Experimental Study of Damage and Defect Detection during Drilling of CFRP Composites

Eshetu Demissie Eneyew

A dissertation

submitted in partial fulfillment of the

requirements for the degree of

Doctor of Philosophy

University of Washington

2014

Reading Committee:

Ramulu Mamidala, Chair

Brian Fabien

Jiangyu Li

Program Authorized to Offer Degree:

Mechanical Engineering

University of Washington

Abstract

Experimental Study of Damage and Defect Detection during Drilling of CFRP Composites

Eshetu Demissie Eneyew

Chair of the Supervisory Committee:

Professor Ramulu Mamidala

Department of Mechanical Engineering

Rejection of parts at the assembly stage due to poor quality hole with drilling induced defect and damages, high rate of drill tool wear, and the formation of gaps when drilling stacks are major problems in the manufacturing of structural components from carbon fiber reinforced plastic (CFRP) composites. Interrupting the drilling process to inspect or monitor these problems during operation increases the cost of production and is a great economic challenge for industries; therefore, there is a great need for on-line monitoring method without interrupting the drilling process. This study will address these problems through various experimental investigations.

Quality of holes and drilling induced damage and defects when drilling CFRP composites laminates were experimentally studied. The influence of drilling parameters, drilling conditions, and the type of surface plies on the resulting quality of the produced hole and on various drilling induced damage and defects were investigated. Drilling induced defects and damages such as drilled hole surface roughness, hole surface morphology, fiber pullout, and delamination were studied through qualitative measurements and SEM examination. In some cases a preliminary investigation on the use of acoustic emission and vibration signal for damage and defect detection was performed.

Analytical models to predict the critical thrust force at the onset of exit ply delamination when drilling unidirectional CFRP composites was developed and proposed using an elliptical delamination zone with clamped boundary condition, and since the load applied by the drill tip is circular, the lateral uniform load is taken over a circular region rather than over an elliptical region. In addition to the analytical model, an experimental investigation was performed through

a punch test on a blind hole to characterize the critical thrust force at the onset of exit ply delamination. The critical thrust force measured from the experimental investigation was compared with the results found by the newly developed analytical model. Comparison of experimentally measured values and predicted values by the new model developed in this study with predicted values of thrust force values at the onset of delamination by other models was presented. Based on this comparison, the predicted values by the new proposed model show better correlation with the experimentally measured values than values predicted by other models.

An experimental investigation on online detection and monitoring of tool wear when drilling CFRP composite laminates was conducted utilizing different signal acquisition systems and signal analysis tools. Two new approaches namely, using the signal amplitude and using output variables from recurrence quantification analysis (RQA) were proposed and studied in this investigation. Thrust force, vibration, acoustic emission, and audio microphone signals were acquired and the variation on the signals signature were studied and correlated to the progression of the drill flank wear. The amplitude of the thrust force and torque increased when flank wear increases, whereas, the amplitudes of acoustic emission and audio microphone signals decreased when flank wear increases. six out of eight of the output variables from the RQA increases with the increase of the drill flank wear, whereas, two of the output variables decrease with the increase of the drill flank wear in both cases of drilling conditions.

In addition, a novel approach to detect the presence of a gap and to estimate the amount of the gap when drilling CFRP composite stacks through various signals was proposed in this investigation. Thrust force, acoustic emission, vibration, and audio microphone signals were acquired when drilling CFRP composite stacks. By introducing preexisting gap between the two plates before drilling, an estimation of the known preexisting gap was performed from the signal profiles. Thrust force signal shows high accuracy of estimating the preexisting gap with a maximum estimation error of 4.17 % in both 0.5 and 1 mm pre-existing gap, whereas, acoustic emission and vibration signal profiles found to be very close in both cases of gaps with an estimation error of 17 % and 5.6 % for 0.5 and 1 mm preexisting gaps respectively. Audio microphone signal delivers comparable estimation accuracy with an average estimation error of 8.63 % and 6.13 % for the preexisting gap of 0.5 mm and 1 mm respectively.

Table of Contents

CHAPTER 5. Damage and Defects when Drilling CFRP Composites …………..……………. 92

List of Figures

List of Tables

Table Page

Acknowledgements

I would like to thank GOD and express my gratitude to the people who help me to get here. First, I would like to give my special thanks to my adviser Professor Mamidala Ramulu for all the help, guidance, and encouragement. For all these years, he was my teacher, mentor, and a father figure. He saw my potential when others do not and took me to his research family. He teach me the value of hard work, dedication, and all the tools I need to have to get here, this was not possible without your encouragement and guidance, thank you again professor.

I also would like to thank Professor Brian Fabien, Professor Jiangyu Li, and Professor Les Atlas for serving in my advisory committee and for their constant support in this process. I also thank all the factuality and stuff of the Mechanical Engineering Department. Wanwisa, Maria, Lucia, and Carey thank you for all the support and encouragement over the years. Thanks to Kevin and Eamon for all the help and training, you gave me in the machine shop. Special thanks to Mr. Bill Kuykendall who helped me in every step of this research whenever I needed help. Thanks to all current and former members of the UW Manufacturing Science and Technology Lab for all the help and encouragement. I extended my acknowledgement to the Boeing Company for generously funding this project.

And last not least I would like to thank to all my families and friends for all the support and love you gave me, without your love, support, and encouragement I would not come this far. Askale, Agegne, Bertukan, Yeshe, Zerihun, Elda, Bety, and Elu, I do not have enough words to thank you all.

CHAPTER 1: INTRODUCTION

Composite materials are materials, which are made of two or more distinct materials, which do not dissolve or merge into each other, but can act together as one structure. Composite materials have been used for thousands of years; adding animal hair to improve strength in pottery works and use of straw reinforced clay in making building bricks [1] are some examples of the early use of composite materials. The need of most modern technologies and industries for materials with a special arrangement of physical and mechanical properties, which cannot be met by conventional metallic alloys and ceramics alone, was answered by the use of advanced (engineered) composite materials. Engineered composite materials are material systems, which contain two or more distinct constituents, which can be synthesized, in order to control the form, amount, and distribution of the constituents in predetermined way, and have unique, useful, and superior properties, that can be determined from the constituent's physical and mechanical properties [2]. These combinations are artificially produced multi-phase materials and would have a better-combined property and structural performance superior than those of the constituent materials acting independently, and a desired distinctive property at the desired level can be achieved by using these artificially engineered composite materials [3].

Structural composite materials have become the choice for structural materials in many applications by providing superior mechanical properties over metallic alloys. These mechanical properties include their light-weight, high strength and stiffness to weight ratio, and ability of maintaining high tensile modulus and strength at elevated temperatures with high corrosion resistance, improved fatigue properties, and high propensity to withstand hostile environmental conditions [4]. Controlling of various parameters of the composite material such as fiber tailoring method, chemical property, proportion of the matrix material, and the interfacial property at the fiber and matrix interface makes it possible to prepare a composite material with a specific mechanical property for a specific structural design. The use of composite materials in modern industries include, but are not limited to, commercial and military aerospace applications, in automotive industries from racing cars to special performance vehicles, in sport and recreational industries from baseball bats to racing bicycles. CFRP composites have been chosen for various main structural component and system manufacturing over other fiber reinforced composite because of their higher specific modulus and specific strength than all other fiber reinforced composite materials [3]. CFRP composites also retain high tensile modulus and high strength at elevated temperatures. These specific properties make CFRP composites a prominent choice for aerospace structural parts and components, where the reduction of structural weight while maintaining the desired mechanical properties is the driving parameter of component design. Fuselage barrel sections, internal web and stringers, as well as control surfaces for aircraft maneuvering are all composed of CFRP composite material.

Even though the manufacturing process technology has advanced to the extent of producing a near-net shape composite laminate, still, it is necessary to perform some machining process in order to facilitate joining and other tasks in the building and assembly of structural components. Joining of these composites to each other or with other material systems is essential in the assembly process of the structural component. Since composites cannot be welded, mechanical joining using fasteners and glue are the only choice to perform this task. For large size holes, the hole can be produced by placing a core in the mold during the lay-up and curing process, but for small size holes, such as for rivets and small fasteners, the holes are produced by drilling. Among composite machining processes, drilling is the most frequently practiced process in the industry [5]. There are various non-traditional drilling technologies such as Water Jet (W.

J.), Abrasive Water Jet (A. W. J.), Electron Discharge Machining (E. D. M.), and Electro Chemical Machining (E. C. M.), which are readily available [107]. However, due to various drawbacks such as matrix melting and moisture absorption up on the application of these operations on fiber-reinforced composites, conventional drilling with twist drill remains the choice for producing small holes in composite materials. Unfortunately, this conventional operation produces various defects, such as, delamination, fiber pull-out, fiber break-out, matrix-crack, shrinkage on the hole diameter, and other damages on the drilled hole because of the anisotropic nature of the fiber-reinforced composite, in which the quality of the hole produced greatly influenced by the condition of the drill tool [107].

High rate of tool wear is one of the challenges in the machining process compared to machining of other material systems. Unlike traditional metallic alloys, the anisotropic property and the abrasive nature of the reinforce fibers expedites the rate of tool wear dramatically. This high rate of tool wear makes producing good quality holes a difficult task when drilling FRP composite materials by demanding frequent inspection of the tool condition and/or changing the drill tool. Inspecting the condition of the drill tool between or during the drilling process manually is not an economical practice and it increases the production cost because of the down time of the machine and the operator time during this task. The presence of a gap between two parts during the joining, assembly, and drilling stack composite materials is another challenge in the assembly stage. Joining of parts after drilling of each part separately is one of the common practices, but this practice is time consuming and labor intensive. Another practice is one – step drilling, where the parts to be joined will be clamped together and drilled together at one-step. In the latter case, poor clamping and chips in the form of dust during the drilling operations create a gap between the two parts and if the operator does not observe this gap, it becomes a big threat for the strength and integrity of the structural component. Drilling is usually the last operation performed on most composite parts, and at this stage, parts are ready for assembly, so any damage introduced at this stage is unaffordable. Nevertheless, this problem persisted, and it is accounted for more than 60% of composite part rejection during quality control in the composite manufacturing industry [6].

The challenges in producing a good quality hole and the need for an automated inspection/detection of quality problems and condition of the drill tool have been acknowledged by researchers in the composites and manufacturing community twenty-five years ago. However, as evidenced by current inspection standards, a reliable solution has yet to emerge. This study targets to address some of the challenges discussed in the production of good quality hole when drilling CFRP composite materials through damage and defect examination, online tool wear monitoring system, online gap detection system, and by developing an analytical exit delamination model. The dissertation has been organized in ten chapters. A brief introduction on CFRP composite materials and challenges in the drilling operation will be presented in Chapter 1, the review on various experimental, analytical, and numerical studies on the drilling of CFRP composite materials will be covered in Chapter 2, and Chapter 3 provides the scope and objectives of this research. Experimental setups, procedures, workpiece material preparation, and measurement techniques will be covered in Chapter 4, damages and defects when drilling CFRP composite laminates will be examined in Chapter 5, and Chapter 6 ply-by-ply cutting action when drilling CFRP composite. Exit delamination model and experimental study on punch test will be presented in Chapter 7, Online tool wear monitoring and online gap detection will be presented in Chapter 8 and 9 respectively. Finally, summary and conclusions of this research followed by recommendation on future work are presented in Chapter 10.

CHAPTER 2: LITERATURE REVIEW

2.1. Introduction

Investigations towards the machining of composite materials have increased considerably over the years in order to understand and enhance the machining process of composite materials. These investigations are mainly based on the existing tools and models from the machining of metallic alloys and some attempt to formulate a new model for machining of composite materials. To understand the cutting mechanisms and the machining process, first some fundamental concepts on conventional metal cutting and the mechanics of drilling will be discussed. Then, the development and the current state of composite machining will be presented. Finally, the experimental, numerical, and analytical investigations on the drilling of fiber-reinforced composites followed by current researches on assessment and monitoring of defects by signal analysis during the drilling of fiber-reinforced composites will be presented.

2.2. Machining of Metals

Material removal process is one of the most machining processes performed in the manufacturing process in order to get the desired shape and size of a component. In general, the material removal process can be classified as cutting, abrasive grinding, and nontraditional material removal process. From these, cutting is the most widely used material removal process, and turning, milling, and drilling are the three main categories of the metal cutting process.

2.2.1. Theory of Metal Cutting

Orthogonal cutting model is an ideal or simplified model used to describe the cutting process, which ignores various complex parts of the cutting geometry, but still useful in describing the mechanics of the cutting process. This ideal model completely suppresses the concept of inhomogeneous strain by assuming the material to behave in a completely homogenous fashion. In orthogonal cutting model, the cutting tool is assumed to have a straight edge, which is perpendicular to the direction of the cut and feed direction. In this model, the tool comprises only two geometric components, the rake angle α and the relief (clearance) angle θ as shown in Figure 2.1.

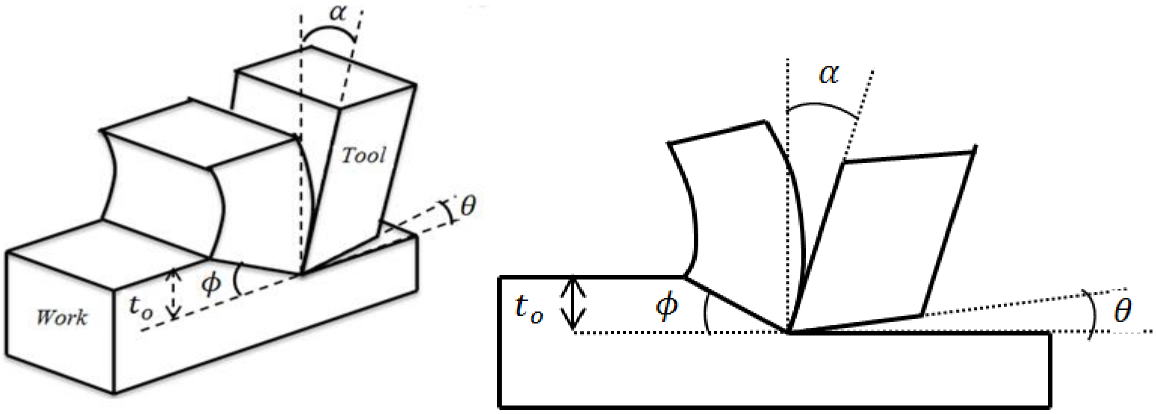

Figure 2.1. Orthogonal cutting model

2.2.2. Mechanism of Chip Formation

At the beginning of the cutting process, the cutting tool is positioned at a certain distance below the top surface of the material being cut; this distance is called the depth of cut t_o, it is also called undeformed chip thickness. As the cutting tool progresses into the material, the material above the shear plane, which is located at an angle of ϕ with respect to the work surface starts to deform by a concentrated shearing action and the chip is produced. The formation and movement of the chip mainly controls the amount of energy consumption during the cutting process. Depending on the type of material being cut and the condition of the cutting process, four basic types of chips: (i) continuous, (ii) discontinuous, (iii) serrated, and (iv) continuous chip with built-up edge (BUE) can be formed. Property of the workpiece, property of the tool material, and the tool geometry are the main variables that affect the chip formation.

The chip formed has always a chip thickness of t_c that is greater than the depth of cut, and this chip thickness can be found by knowing the rake angle α, the shear angle ϕ, and the depth of cut t_o. The ratio of the depth of cut to the chip thickness is called chip thickness ratio (r). Using the geometric relationship as shown in Figure 2.2, this chip thickness ratio can be expressed in terms of the rake angle α, the shear plane angle ϕ, and the length of the shear plane l_s as formulated in Equations (2.1 – 2.3).

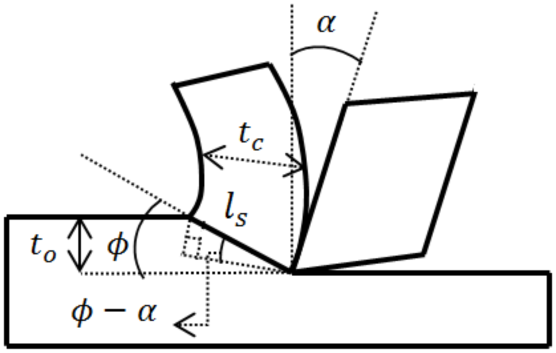

Figure 2.2. Geometric relationship of chip formation

$$r = \frac{t_o}{t_c} \tag{2.1}$$

From the geometric relationship we have

$$t_o = l_s * sin\phi \quad and \quad t_c = l_s * \cos(\phi - \alpha) \tag{2.2}$$

Substituting Equation (2.2) into Equation (2.1) gives

$$r = \frac{sin\phi}{\cos(\phi - \alpha)} \tag{2.3}$$

Solving Equation (2.3) using trigonometric relationship gives the following expression for the shear plane angle ϕ.

$$\phi = \tan^{-1}\frac{r * cos\alpha}{1 - r * sin\alpha} \tag{2.4}$$

The prediction of the shear plane angle ϕ and its relationship with the rake angle α and with other cutting tool geometries plays an important role in the analysis of cutting mechanism and chip formation process. In addition, these angles are the main geometric values in the derivation of cutting force components that cannot be measured directly during the cutting process.

2.2.3. Cutting Forces

In orthogonal cutting model, various force components act on the tool and on the workpiece. The force applied by the cutting tool on the chip can be classified in to two force components which are perpendicular each other as shown in Figure 2.3. These two forces are, the friction force (F), the friction force between the chip and the tool, which resists the flow of chip along the tool face, and the normal force to friction (N), the force normal to the friction force. The vector addition of these two force components gives the resultant force (R), which is oriented at an angle of β relative to the normal force; this angle β is also known as the friction angle. The coefficient of friction μ between the chip and the tool face can be defined using these two force components and the friction angle as shown in Equation (2.5).

$$\mu = \frac{F}{N} = tan\beta \tag{2.5}$$

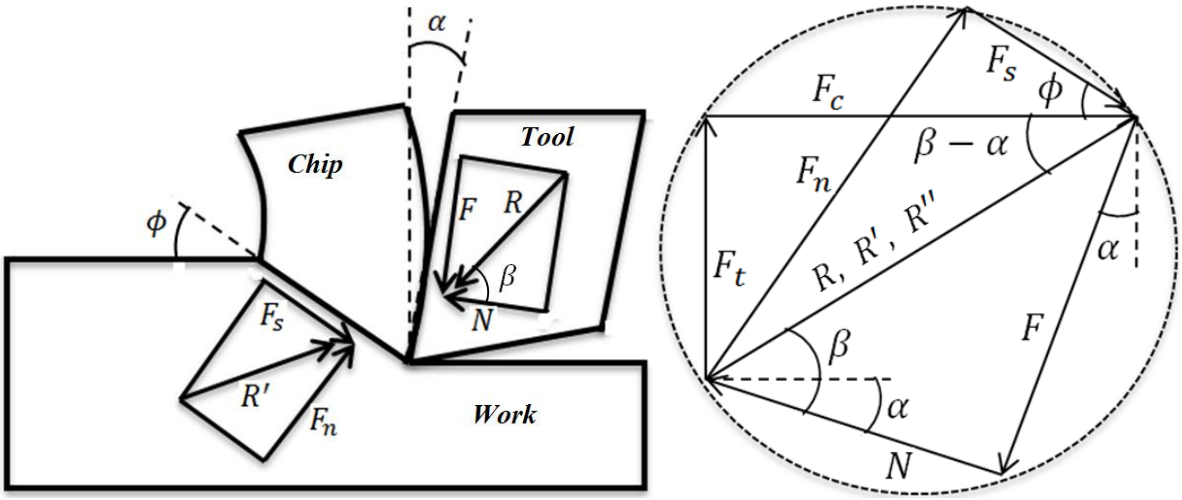

Figure 2.3. Forces acting on the tool and chip (left) and geometric relations of all forces (right)

In addition to the force applied by the tool, the chip is also subjected to two force components exerted by the workpiece, the shear force (F_s), which causes the shear deformation in the shear plane and the normal force to shear (F_n), which is normal to the shear force. Vector addition of these two force components gives the second resultant force R', which must be equal and opposite with the first resultant force R in order to make the forces acting on the chip balanced. All of these force components F, N, F_s, F_n, cannot be measured directly from the cutting process, however, two additional force components, the cutting force F_c, the force in the direction of cutting and the thrust force F_t, the force in the direction of the depth of cut and perpendicular to the cutting force can be directly measured. The third resultant force R'' can be found by vector addition of these two measured force components.

Using the two measured force components and geometric relationships, a series of equation can be derived to express the four force components in terms of the measured force components and geometric quantities as given by Equations (2.6 – 2.9)

$$F = F_c sin\alpha + F_t cos\alpha \tag{2.6}$$

$$N = F_c cos\alpha - F_t sin\alpha \qquad (2.7)$$

$$F_s = F_c cos\phi - F_t sin\phi \qquad (2.8)$$

$$F_n = F_c sin\phi + F_t cos\phi \qquad (2.9)$$

From these force components and the area of the shear plane, it is possible to calculate stress components. Using the geometric relationships shown in Figure 2.4 and the calculated force components, the shear stress τ and the normal stress σ can be derived as expressed by Equations (2.10 – 2.13).

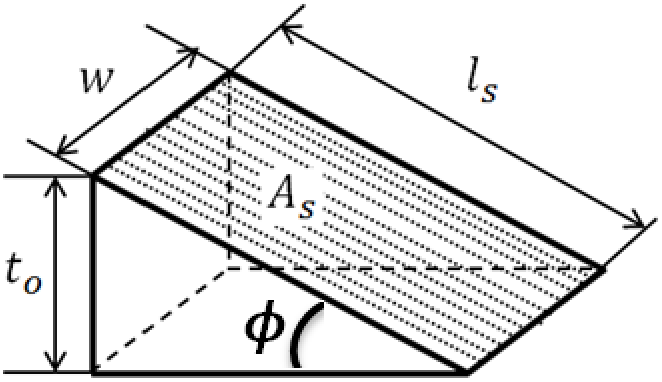

Figure 2.4. Geometric relations of the shear plane

$$\tau = \frac{F_s}{A_s} \qquad (2.10)$$

$$A_s = \frac{t_o w}{sin\phi} \qquad (2.11)$$

By substituting Equation (2.8) and Equation (2.11) into Equation (2.10), the expression for the shear stress can be defined in terms of measured quantities by Equation (2.12).

$$\tau = \frac{(F_c cos\phi - F_t sin\phi\ )Sin\phi}{t_o w} \qquad (2.12)$$

The normal stress in the shear plane can also be found in the same fashion and it is given by Equation (2.13).

$$\sigma = \frac{F_n}{A_s} = \frac{(F_c sin\phi + F_t cos\phi\ )sin\ \phi}{t_o w} \qquad (2.13)$$

2.2.4. Mechanics of the Drilling Process

Drilling is one of the material removal operations used to create a circular hole in the work piece using a multi-point cutting tool. The operation can be performed on a lathe, on a mill, or on a drill press. A quick and precise hole can be produced in this operation, but often reaming and boring may be needed due to rough surface. During the drilling operation, first, the rotating web pierces a small point hole, which is followed by a formation of the chip by the cutting lips (edge), and then the chips are transported out of the hole through the flute of the drill and the drill progress into the workpiece guided by the hole already produced. At the center of the drill, the material is plastically displaced and removed by the chisel edge without a real cutting action. The diameter of the drilled holes usually are larger than the diameter of the drill, but depending on the thermal expansion property of the material being drill, sometimes the drilled hole could have smaller diameter than the diameter of the drill.

2.2.4.1. Drill Geometry

Twist drill is the most commonly used cutting tool in most drilling operations, which has two identical cutting edges designed to produce identical chips. Twist drills have a high length to diameter ratio, and it is composed of three components, shank, body, and drill point. Even though twist drill is composed of many geometric entities, point angle, clearance angle, helix angle, web thickness, and chisel edge angle are mainly considered quantities in the analysis of drilling operation. Figure 2.5 shows the schematic diagrams of a standard twist drill tool with its geometric designations.

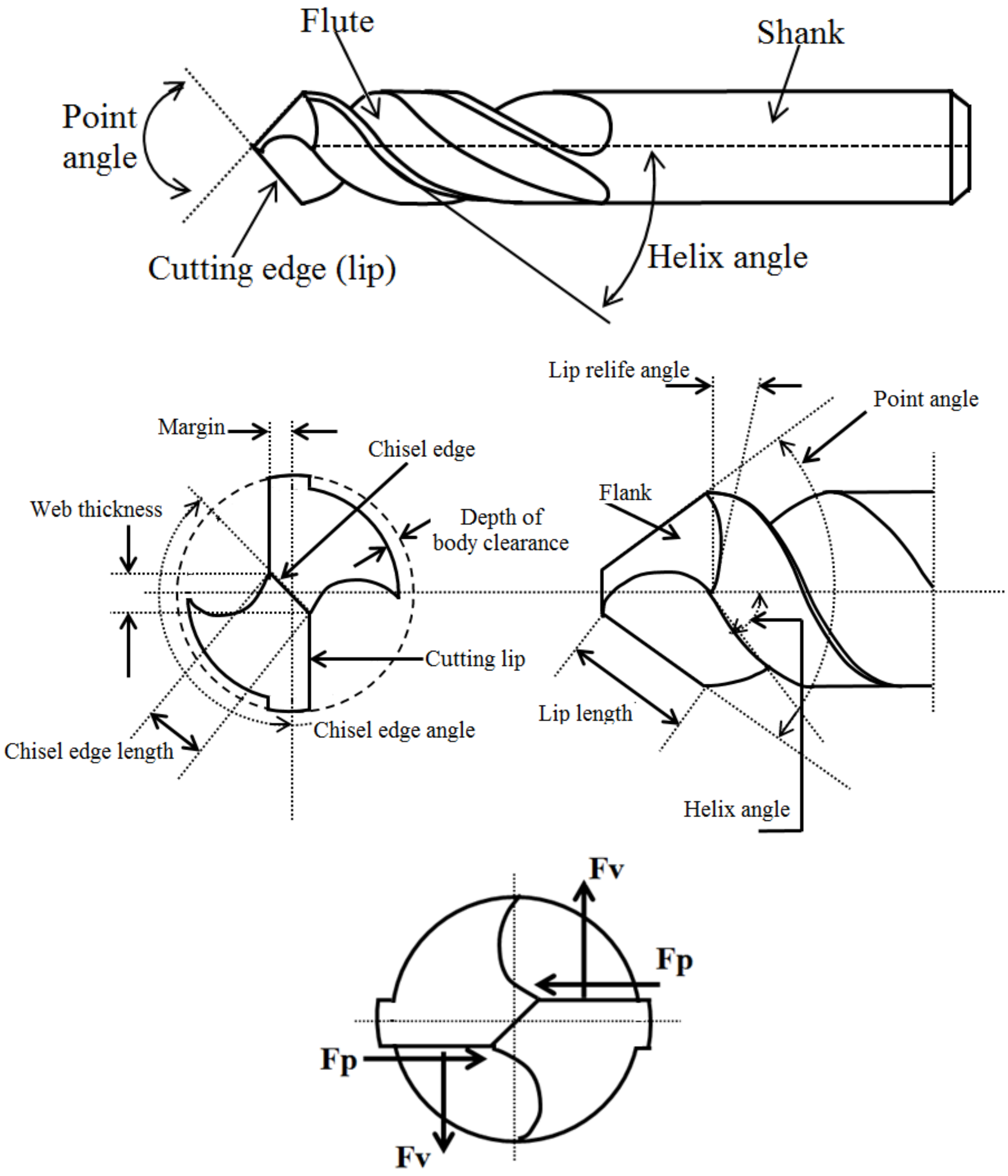

Figure 2.5. Schematic diagrams of the twist drill and resulting forces

The performance and strength of the drill tool can be dictated and affected by these various geometric entities. The web of the drill contributes towards the torsional strength of the drill and strengthens the cutting edge near the drill point. An increase in point angle leads to a freer drilling but it creates less support for the cutting edge since increasing the point angle decreases the web thickness. The helix angle of the drill controls the rake angles and the amount of chip removing capacity, and an increase in helix angle results in freer drilling and fast chip removal capacity at a cost of less support across the cutting edge. This shows that, a special combination of these geometric entities is required in designing a drill tool for various type of drilling operations.

Cutting resistance in drilling consists of:

i) resistance appearing at the lips ,

ii) resistance appearing at the chisel edge, and

iii) resistance appearing at the land.

The first two are due to the undeformed chip plastic strains and due to external friction, whereas, the latter is due to friction against the machined surface. The resultant of cutting resistance forces or thrust force is the sum of the axial components in the direction of the drill axis and the resultant moment or torque is the circumferential force components generated moment.

2.2.4.2. Prediction of Thrust Force and Torque

The mechanics of the drilling process comprises various aspects, which includes but not limited to the work material, cutting tool condition, cutting parameters, and over all cutting process conditions. The quality or performance of the drilling process may be influenced by many variables such as tool condition, type of the drilling machine, position of the work material, cutting environment, power, feed rate, cutting force, and torque. From these, the cutting force and torque are considered the most influential cutting parameters during the analysis of the drilling process.

The two cutting lips and complex point geometries of the twist drill make the prediction and analysis of the thrust force and torque during the drilling operation somewhat difficult. Shaw [7] presented a full analysis on the prediction of thrust force and torque for metal drilling. In this analysis, three basic material removal actions were proposed, (1) cutting by the two cutting lips, (2) cutting action by the web, and (3) extrusion by the web. The torque is influenced only by the first two actions, whereas the trust force is influenced by all the tree actions. Drill diameter (d), feed per revolution (f), length of the chisel edge, (c), and specific cutting energy of the work (u) are taken as primary variables in the analysis of the drilling torque (M). After dimensional analysis is performed on the variable of importance, the relationship between the torque and these variables are given by Equation (2.14).

$$\frac{M}{d^3u} = \psi_1\left(\frac{f}{d}, \frac{c}{d}\right) \tag{2.14}$$

In the absence of a size effect (increase in u with volume deformed at one time), the torque should be expected to vary as the projected area of the drill or as d^2. Thus in the absence of size effect, Equation (2.14) can be expressed as shown in Equation (2.15).

$$\frac{M}{d^3u} = \frac{f}{d}\psi_2\left(\frac{c}{d}\right) \tag{2.15}$$

In drilling, u varies inversely with (fd) $^{0.2}$, therefore, when drilling a given work material having a Brinell hardness of H_B

$$u \sim \frac{H_B}{(fd)^{0.2}} \qquad (2.16)$$

Combining Equation (2.15) and (2.16) gives

$$\frac{M}{d^3 H_B} = \frac{f^{0.8}}{d^{1.2}} \Psi_2 \left(\frac{c}{d}\right) \qquad (2.17)$$

After conducting a number of drilling experiments on heat-treated chrome-nickel steel with sharp drills and dry cutting for a conventional value of $c/d \approx 0.18$, the experimental points are seen to lie on a straight line with an excellent agreement of Equation (2.16). For these tests, Equation (2.16) can be expressed as Equation (2.18).

$$\frac{M}{d^3 H_B} = 0.087 \frac{f^{0.8}}{d^{1.2}} \qquad (2.18)$$

The expression for the thrust force (F_{th}) can be formulated in the same fashion. Based on the geometry of the cutting point of the drill, the thrust force is composed of two components: the thrust force due to the cutting lip (F_{th}, *lip*), and the thrust force due to the chisel edge or web (F_{th}, *web*) as shown in Figure 2.6. The expression for the thrust force after dimensional analysis is given by Equation (2.19), in this expression; the term (Ψ_3) is the contribution to the thrust due to extrusion at the web of the drill.

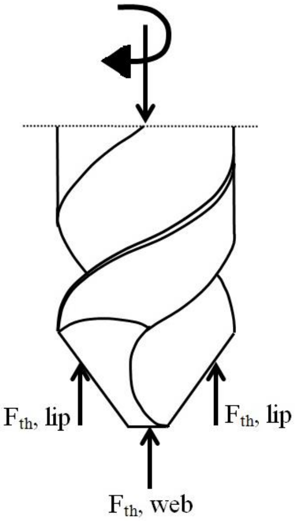

Figure 2.6. Components of the thrust force

$$\frac{F_{th}}{d^2 H_B} = K_1 \frac{f^{0.8}}{d^{1.2}} + \psi_3 \left(\frac{c}{d}\right) \tag{2.19}$$

Where K_1 is a constant for a given work material and drill, and Ψ_3 is some function of *(c/d)*. The component of the thrust force due to the extrusion at the web *(F_{th}, web)* can be written as

$$F_{th,web} = \frac{u\pi c^2}{4} \tag{2.20}$$

Since there should be negligible size effect for the extrusion at the web, $u \sim H_B$ and hence

$$\frac{F_{th,web}}{d^2 H_B} \sim \left(\frac{c}{d}\right)^2 \tag{2.21}$$

From which it follows that

$$\psi_3 \left(\frac{c}{d}\right) = K_2 \left(\frac{c}{d}\right)^2 \tag{2.22}$$

where K_2 is a constant for a given work material and drill.

Since the value of *c/d* for all these drills was approximately 0.18, and from the regression equation, it follows the form given below.

$$\frac{F_{th}}{d^2 H_B} = 0.195\frac{f^{0.8}}{d^{1.2}} + 0.68\left(\frac{c}{d}\right)^2 \qquad (2.23)$$

This equation may be used to estimate the drilling thrust for any material having a Brinell hardness H_B.

2.3 Machining of Fiber Reinforced Plastic (FRP) Composites

Fiber reinforced plastics (FRP) have been used in structural components for many years. Since their first application for an acid resistant tank in 1907 [8], the interest towards fiber reinforced plastic materials have been grown rapidly, and investigations are underway in order to fully characterize and to improve their mechanical property, manufacturing process, and quality control. Since the machining processes and operations on these FRP composites take place before the component is ready for application, optimizing these operations and processes is the driving force of many investigations. Unlike isotropic materials and metallic alloys, where the chip formation mechanism is controlled by shearing, in the machining process of FRP composite materials, local bending at the fiber-matrix interface controls the chip formation, which makes the machining process of FRP composite materials very complicated. In addition, the inhomogeneous and anisotropic nature of FRPs combined with the abrasive nature of the reinforcing material makes the machining process difficult by introducing process-induced damages on the work material and making the cutting tool life short. Depending on the method and technique used, machining process generally categorized as traditional machining and nontraditional machining. Traditional machining includes turning, milling, drilling, and grinding, whereas, laser, water-jet, electro chemical machining, electron discharge, electron deposition, and ultrasonic machining are grouped under nontraditional machining. In this section, some of the investigations done on traditional machining of FRP composite materials will be reviewed under their respective classification as experimental studies, numerical studies, and analytical studies.

2.3.1. Experimental Studies on Machining of FRP Composites

Many experimental investigations have been reported over the years on the machining of FRP composites, and many studies are still underway. Teti et al. [9] have reported an excellent review on the machining of composite materials. On this review, they report that, machining of a composite material depends on the properties and relative content of the reinforcement and the matrix materials as well as on its response to the machining process. The review highlights that the machining of composite materials imposes a special demand on the geometry and wear resistance of the cutting tool. The fiber type, reinforcement architecture, and the matrix content are considered as the most important factors governing tool selection and machining parameter setting. Carbide tools, coated carbide tools, and PCD tools are complimented for yielding good results in terms of tool wear and tool life during the machining of GFRP and CFRP.

The experimental investigation by Koplev et al. [10] is one of the earliest studies on the machining of CFRP composites. In this study, the cutting process, chips, and cutting forces in machining of CFRP are examined by using shaping and quick-stop experiments with a new chip preparation technique. The cutting operation was carried out on a unidirectional composite panel with two cutting directions of parallel and perpendicular to the fiber direction. A reasonably good surface quality was produced when the cutting direction is parallel to the fiber orientation and nearly all the fibers were fractured perpendicular to their longitudinal direction where only a few fibers were smashed, and there were pieces of raked matrix between them. Whereas, when cutting perpendicular to the direction of the fiber, the surface finish was rather poor quality and the whole surface is covered with thin layer of matrix material with a layer of disturbed composite with cracks just below the surface. In addition, two separate effects occurred near the tip of the cutting tool when the cutting direction is perpendicular to the fiber direction. As the tool moves forward, it presses on the material in front of it causing the material to fracture and create a chip and at the same time, it applies a downward pressure on the composite below it, which produces cracks of approximately 0.1 – 0.3 mm in depth in to the specimen. When machining parallel to the fiber direction, the tool also applies pressure, at which chips are produced; but crack is often seen in front of the tool tip indicating that, this crack runs further than the current chip and the cracks on the surface of the specimen only reach a depth of one or two fiber diameters. The chips from the parallel cutting were found to have almost rectangular cross-section, whereas, chips from perpendicular cutting are less regular in shape. Furthermore, upon the examination of the chips produced in both cutting direction, it is found that, the chips have not been subjected to a large plastic deformation as normally seen in metal chips, rather; they consist a series of fractures.

In the study of machining FRP composites, it is necessary to incorporate the quality and integrity of the machined surface of the component in addition to the study of the cutting or machining process and mechanism. Ramulu [11] conducted an in-depth investigation on the machining and surface integrity of FRP composites, which covers the cutting mechanism, cutting forces, surface roughness, and surface integrity. In the study of the cutting mechanism, it was noted that for the 0^0 material, chip formation mechanisms were composed of mode I loading and fracture along the fiber-matrix interface, mode II loading through tool advancement, and fracture perpendicular to the fiber direction under bending loads. In positive fiber orientations between 15^0 and 75^0, the chip formation mechanism includes fracture from compression-induced shear across the fiber axis combined with interfacial shearing along the fiber direction during chip advancement. The material removal mechanism almost in all positive orientations appears to be governed by the in-plane shear properties of the uni-directional material. Chip formation for fiber orientations greater than 75^0 is primarily compression-induced fracture perpendicular to the fibers and inter-laminar shear fracture along the fiber-matrix interface, in which others [10, 12] also observe these mechanisms. In addition, damage to the - 45^0 plies was more extensive through shear failure along the fiber/matrix interface and fracture perpendicular to the fiber direction beneath the trimming plane. Chips produced from trimming - 45^0 plies of the laminate resulted in severe damage below the trimming plane, but the extent of damage was limited due to support provided by adjacent plies. Overall, in the trimming of uni-directional panels, discontinuous chips were observed with primary dependence on fiber orientation. Cutting mechanisms for 0^0 and 45^0 plies were identical to those in the trimming of unidirectional material. However, chip-formation mechanisms in trimming 90^0 and - 45^0 plies of the multi-directional laminate changed due to the support provided by adjacent plies.

The quality of machined surface of FRP is one of the main variable draws a great concern in the machining of FRP composites. Unlike single-phase materials, the surface finish and roughness of FRP machined surface varies depending on the fiber orientation, cutting direction, and the direction of measurement. Ramulu [11] observed that the surface roughness parameters values R_a and R_y in the longitudinal direction were usually higher than those in the positive fiber orientation were and this is attributed to the unique chip formation mechanisms of the 0^0-fiber orientation and bare fibers on the machined surface. The average surface roughness of fiber orientations from 15^0 to 60^0 in both longitudinal and transverse measurement directions exhibited high quality surface finish and the changes on roughness measurements between fiber orientation of 15^0 and 60^0 were very few. Matrix smearing was dominant feature on 45^0 and 90^0 fiber plies, whereas, in the case of - 45^0 plies the dominant feature was the in-depth damage due to fiber pullout and inter-laminar cracking (delamination) which induced deep valleys in profile measurements taken transverse to the trimming direction. Measurements taken parallel to the cutting direction did not indicate the extent of trimming damage, which shows that Ra and Ry alone are not capable of indicating the true surface quality of trimmed FRP.

In an attempt to characterize the effect of tool geometry and operation conditions on the machining of FRP composites, Wang et al. [12, 13] conducted a two- phase experimental study on the orthogonal cutting mechanisms of unidirectional and multi-directional graphite/epoxy composite laminate. In the first phase of this study [12], orthogonal trimming was performed on unidirectional laminate test material with various fiber orientations incorporating both in-situ and post process analysis methods. Since machining of fiber-reinforced materials generally creates numerous tiny chips, which are difficult to handle for examination, during the edge trimming process, “macro chip method” was used in collecting the discontinuous chips with the aid of adhesives. Three different cutting mechanisms were observed during the edge trimming of unidirectional laminate. The chip formation mechanisms in the 0^0 fiber orientation comprised fracture along the fiber/matrix interface attributed to cantilever bending, followed by fracture perpendicular to the fiber direction, whereas, in positive fiber orientations up to 75^0, chip formation was comprised of compression induced shear perpendicular to the fiber axis. Chip release occurred through fracture along the fiber/matrix interface. In the 90^0 and negative fiber orientations, chip formation was composed of both in and out of plane shear fracture along the fiber/matrix interface with severe macro deformation induced by the compressive tool load. The cutting mechanisms observed in this study were presented schematically as shown in Figure 2.7.

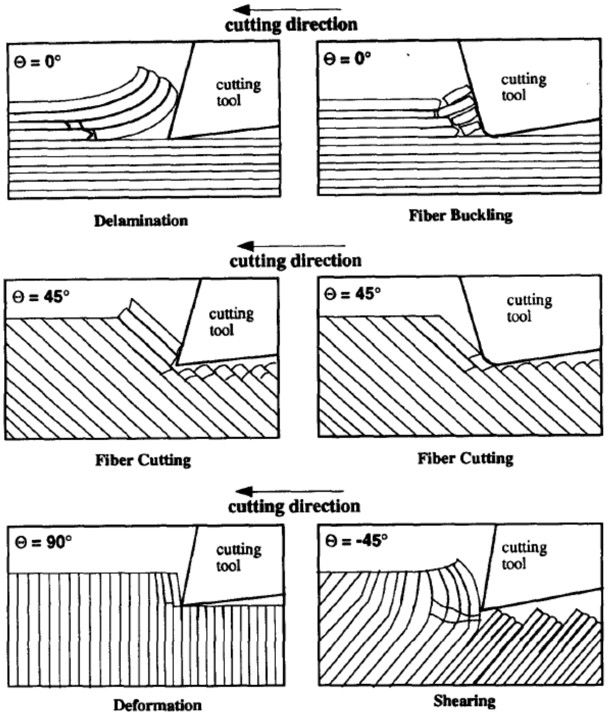

Figure 2.7. Cutting mechanisms in the orthogonal machining of Graphite/Epoxy [12]

This study also shows that chip formation, cutting forces, and surface morphology in edge trimming of unidirectional Gr/Ep were highly dependent on fiber orientation, which also reported by others [11, 19 – 21]. Macro chip studies and high speed photographic observations showed that the chip size decreases with the increase of fiber orientation up to 45^0, whereas, insignificant changes in chip formation were observed for fiber orientations greater than 45^0 where discontinuous powder-like chips were noted. Chip size is also inter-related to the degree of principal cutting force fluctuation. High principal cutting force fluctuations were observed in the 0^0 fiber orientation due to the initiation/propagation mechanisms of chip formation. A decline in principal cutting force fluctuation was observed with increasing positive fiber orientations up to 75^0, and high fluctuations were again noted in trimming when fiber orientations are equal or greater than 90^0. The largest influence of tool geometry on cutting forces was apparent in the magnitude of the resultant normal force on the shear plane when trimming positively oriented material. The lowest resultant cutting force in this study was measured when trimming 0^0 material with a $10^0\alpha/17^0\gamma$ tool. Otherwise, increasing the tool rake angle resulted in an increase in resultant cutting force due to the influence of the thrust force. Specific cutting energy in trimming the unidirectional Gr/Ep was well below than in edge trimming of homogeneous structural materials. The degree of matrix smearing on the machined surface increased with increasing fiber orientation and served to reduce the surface roughness. Average surface roughness (Ra) for positive fiber orientations measured in both longitudinal and transverse directions was almost constant in fiber orientations from 15^0 to 60^0, ranging between 1 and 1.5 µm.

In their second phase of the study [13], orthogonal trimming was performed on multidirectional laminate. The chip formation observed in trimming of the multi-directional Gr/Ep laminate was very similar to that of unidirectional material despite the presence of multiple fiber angles. Support provided by adjacent plies permitted the 90^0 and -45^0 plies to be machined with less significant degrees of damage than in trimming unidirectional material. Post trimming analysis indicated that the range of tool geometry used in this study was insignificant to the chip formation mechanisms. High fluctuations in the principal cutting force were noted which is attributed to the 90^0 plies of the Gr/Ep laminate. Minimum cutting force, in terms of the resultant force was obtained from experiments with a 5^0 rake and 17^0 clearance angle PCD inserts. Empirical modeling suggests that the optimum tool geometry for minimizing the resultant cutting force is constituted by a 6^0 - 7^0 rake with a 17^0 clearance angle. Distinct surface profiles were observed from 0^0, 45^0, 90^0, and -45^0 plies of the edge trimmed laminate due to the differences in chip formation with fiber orientation. Observations of surface profiles from 0^0 and 45^0 unidirectional laminate in Part I [12] were identical to those in trimming of the multi-directional material. Continuous fibers with limited matrix covering were found on the trimmed surface of 0^0 fiber plies, and uniform matrix covered with broken fiber rubble was noted on the 45^0 plies. Fiber/matrix interface shearing was responsible for the interior ply damage of the -45^0 plies and crushed fibers distributed within a matrix covering were noted on the 90^0 fiber plies. Standard surface roughness parameters were not capable of accurately distinguishing the surface quality of the multi-directional laminate due to the inherent damage of -45^0 plies. A more comprehensive description of the machined surface can be obtained from a combination of average surface roughness parameters and statistical parameters from profiles taken transverse to the trimming direction.

Wang and Zhang [14] conducted an experimental investigation on the orthogonal cutting of unidirectional fiber reinforced plastics to understand the machinability of epoxy composites reinforced by unidirectional carbon fibers subjected to orthogonal cutting. This experiment was carried out by modifying a surface grinder where the grinding wheel being replaced by a cutting tool. The study shows that fiber orientation is a key factor, which determines the surface integrity of a machined component and it is reported that a fiber orientation of 90^0 as a critical angle, beyond which a severe subsurface damage will occur. The significant bouncing back of materials after cutting is a characteristic phenomenon associated with the machining of FRPs in which this mechanism is the elastic bending of the high strength fibers. Three distinct deformation zones of chipping, pressing, and bouncing was observed when the fiber orientation is less than or equal to 90^0, however if the fiber orientation is greater than 90^0, fiber bending during cutting will become more significant and the cutting mechanism becomes more complicated. Cutting forces were influenced by fiber orientation, tool rake angle, and depth of cut, where the first was the more influential compared to the latter two. In addition, the curing condition for making the FRPs was attributed for altering the mechanical properties of the material, and for its slight contribution to the change on the cutting forces particularly in the transverse direction, whereas, the cure degree does not influence the surface roughness.

Abrate and Walton [15, 16] investigated traditional and non-traditional machining of composite materials. Drilling, cutting, sawing, routing, and grinding operations were included in their study of traditional machining, whereas, laser, water-jet, electro-discharge, electro-chemical spark, and ultrasonic machining were incorporated in their study of non-traditional machining. In their study of traditional machining [15], they reported, the thrust force and torque applied on the drill bit during drilling operations depend on speed, feed rate, tool geometry, and tool wear, where the type of drill used influences both drill wear and delamination. It is also noted that, positive rake angles are needed to generate the least amount of heat during the cutting process. However, the more positive the rake angle, the more fragile the cutting edge becomes. A small chisel edge angle was recommended as a second element of good tool geometry and to the improvement of the penetration rate. The direction of cut has been accounted for various damages when cutting a unidirectional laminate composite, in which, when the cutting direction is parallel to the fiber orientation (0^o), individual fibers are pulled out, which disagrees from the observation made by others [12]. In addition, when this angle increases, compression and bending occur in the 20^o - 45^o range, the fibers are pulled out of the cut surface and diverted into the cut direction, and the worst surface quality occurs in this range. When the cutting direction is perpendicular to the fiber orientation, fibers are subjected to shear and bending, and surface quality improves. They conclude that, in order to minimize the amount of heat generation and to avoid thermal damage to the part during traditional machining, proper tool geometry and operating conditions must be adopted.

2.3.2. Numerical Studies on Machining of FRP Composites

In addition to experimental investigations, numerical modeling and simulation is one of the valuable tools used to understand and characterize the machining of FRP composites. Since machining of FRP composite involves various numbers of physical phenomenon, numerical modeling and simulation becomes handy in getting a great insight of the machining process ahead of the actual machining takes place. Arola and Ramulu [17] numerically studied the orthogonal cutting of unidirectional fiber reinforced polymer composite using a finite element analysis (FEA) method. They used a dual fracture process to simulate the chip formation incorporating maximum stress and Tsai-Hill failure criteria. This study assumes that the material is locally homogeneous and orthotropic, the incremental plastic, viscoelastic, and thermal strains are negligible with respect to the elastic component, out of plane stresses of the unidirectional laminate is negligible relative to those in the cutting plane, and the cutting tool was defined as a rigid body. The model shows that chip formation and material removal characteristics are particularly fiber orientation dependent, this observation was also made by other experimental studies [11 – 12, 19 – 21]. The extent of the failure envelopes from the FEA simulations corresponds to the magnitude of principal cutting force fluctuation. The simplified two-dimensional model for the orthogonal cutting of unidirectional Gr/Ep predicted the principal cutting forces that agreed very well with experimental values. However, the thrust force predictions were not consistent with dynamometer measurements and failed to comply with experimental trends.

Lasri et al. [18] studied the progressive failure of unidirectional GFRP composites during orthogonal machining using a finite element analyses (FEA). Chip formation process and damage modes such as matrix craking, fiber-matrix debonding, and fiber breaking were modeled by degrading the material properties. Damage analysis was carried out using Hashin, maximum stress, and Hoffman failure criteria. After damage was detected, selective stiffness degradation was applied to the work piece material. In their result, it was demonstrated that, the use of stiffness degradation concept with the appropriate failure criterion responds potentially in a predictable fashion to changes in chip formation process for machining of FRPs. They generalize that, the damage mechanisms in composite laminates include four types of failure modes (i) transverse matrix cracking, (ii) fiber-matrix interface debonding, (iii) fiber rupture, and (iv) inter-ply delamination. In addition, they found that, the composite structure in machining showed a sequence of damage events prior to the complete chip formation.

Rao et al. [19] simulated the orthogonal machining of unidirectional carbon fiber reinforced polymer (UD – CFRP) and glass fiber reinforced polymer (UD – GFRP) composites using finite element method (FEM). Both composite materials were modeled at micro scale as a layered material, considering the fibers and the matrix as separate phases rather than as equally homogenous materials (EHM), whereas, the cutting tool was modeled as a rigid body with a reference point which controls the movement of the cutting tool. Only the region of the work material close to the chip formation zone was modeled in the numerical model in order to keep the problem tractable. They used a two-phase micro-mechanical model with the assumption of elastic fiber and elasto-plastic matrix to estimate the cutting forces during machining. For this simulation of orthogonal machining of UD – CFRP and UD – GFRP, a finite element analysis software tool of ABAQUS v6.5 and a plane strain analysis was used, which is typically used for metal machining. In their result, they found that, the contact pressure varies with the fiber orientation and is less effected by the depth of cut and rake angle for both composites. At the fiber orientation of 90^{o,} both bending at first fiber second matrix interface and crushing at fiber – tool interface causes fiber fracture in CFRP, whereas, bending is the main failure mode in GFRP. Bending increasingly becomes more significant for both material systems as the fiber orientation changes from 90^{o} to 15$^{o.}$ It was also reported that, sub-surface damage depends mainly on fiber orientation, where the maximum value was observed at 90^{o} fiber orientations for both materials and it was more in the GFRP as compared to the CFRP. The chip formation mechanism is dominated by a combination of crushing and tensile failure of the reinforcing fiber. In addition, the matrix, though isotropic, get influenced by these maximum principal stresses at the interface, however, the Von Miss stress are more predominant to deform and subsequently fail the matrix before fiber failure.

Rao et al. [20] investigated the chip formation mechanism in orthogonal machining of unidirectional glass fiber reinforced polymer (UD – GFRP) to develop a finite element model and to simulate the chip formation mechanism of UD – GFRP composite. They used the same material system, process parameter, and tool geometry as used in the above study [19], whereas, a plane stress formulation was used in this study. The portion of the work material adjacent to the cutting tool is modeled using fiber and matrix separately, whereas, portions away from the cutting tool are modeled as EHM. In this model, two fibers, three matrix layers, and two EHM regions are considered as shown in Figure 2.8, and the tool is assumed to be in contact with the first fiber (f_1) after the first matrix (m_1) has been removed prior to the machining simulation. In the simulation, fine mesh is used in the fiber and matrix elements, whereas, a coarse mesh is used in the EHM elements away from the fiber or matrix domain.

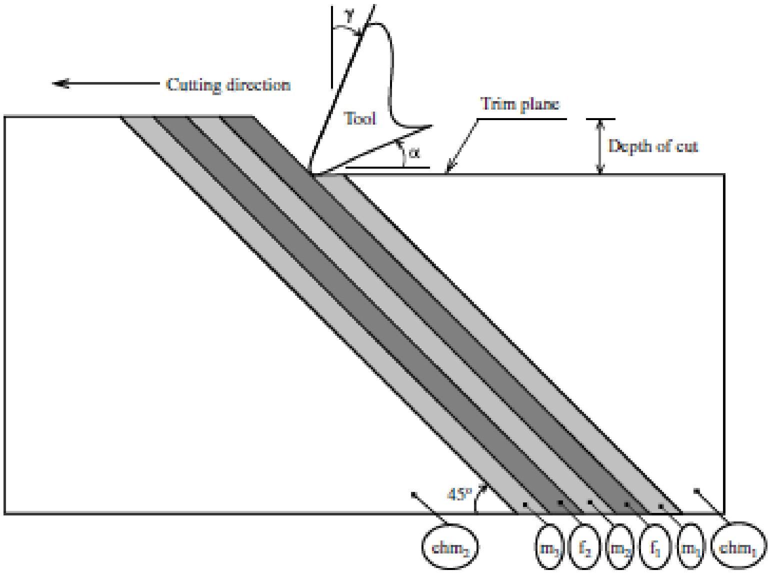

Figure 2.8. The fiber (f_i), matrix (m_i), and EHM (ehm_i) domains for 45^0 fiber orientation [19]

They found that, damage initiates first at the rear face of the matrix (m_2) and spreads towards the rear face of the fiber (f_1). The fiber breakage initiates due to local bending at the fiber (f_1) – matrix (m_2) interface on the rare side of the fiber and propagates towards the front side (tool – fiber contact) of the fiber. In the UD – FRP composites with fiber orientation of $90^{0,}$ for the low depth of cut (0.1 mm), the damage in the matrix reaches the free surface before the fracture of the fiber. Whereas, for the case of higher depth of cut (above 0.15 mm), the damage do not reach the free surface even when complete failure of the fiber occurs, leading to a hanging or loosely attached chip. For other fiber orientations, the damage does not propagate to the free surface for all depth of cut. The maximum damage is observed in the second matrix next to the fiber being cut and the depth of damage in this matrix varied between 60 µm and 115 µm. In the third matrix, the damage reached the maximum value at the fiber orientation of 30^0 and decreases thereafter to zero for 75^0 and 90^0 fiber orientations.

It is been also observed that, discontinuous chips were formed during machining due to the failure of the fiber and the matrix material. The length of the chip depends on the initial contact distance of the tool and the fiber from the trim plane. The chip length at 0.1 mm depth of cut varies between 372 µm and 50 µm as the fiber orientation varies from 15^0 and 90^0. Sub - surface damage occurred due to both matrix cracking and interfacial debonding, this sub-surface damage mainly depends on the fiber orientation, and it is greater when the fiber orientation is 30^0. The numerical simulations show that, for all fiber orientations, irrespective of tool rake angle and depth of cut, matrix damage is the main mode of sub-surface damage rather than the interfacial debonding. Debonding due to opening and shearing modes occurs at the interface. It was noted that, Mode-I fracture is predominant for the higher fiber orientations and Mode-II fracture is predominant for lower fiber orientations.

Carlos et al. [21] studied orthogonal cutting of long fiber composites and developed a model based on finite element method. A macro – mechanical model was developed allowing the simulation of the initiation and completion of the chip during the evolution of the cutting process, where a dynamic approach to chip removal was performed using explicit integration scheme in a FE code. In this study, subsurface damage induced on CFRP was analyzed for different fiber orientations and compared with the results obtained when machining GFRP and numerical model was validated with experimental data obtained from scientific literature for GFRP. In the simulation, a plane stress model was developed using the commercial Finite Element code ABAQUS/Explicit and the model was applied to the cutting simulation of both Glass and Carbon FRP composites. Both materials were modeled with an elastic behavior up to failure, taking into account the anisotropy of the material and the cutting tool was assumed rigid. For the cutting operations, CFRPs are considered as brittle material while GFRPs are cataloged as ductile material. The mesh of the work piece was refined in the zone surrounding the tool tip in order to model the evolution of the damage associated to the chip initiation and evolution accurately. The medium element size at this zone was 5 µm. In this study, a cutting length equal to 2 mm was considered, which is enough to reach steady state conditions during the cutting process and the damage initiation criteria for fiber-reinforced composites was based on Hashin's theory.

In their result, they found that, machining induced sub-surface damage experienced by CFRPs is much reduced than that of GFRPs. GFRPs exhibited large deformation before breakage and extended damage beneath and ahead of the tool tip. However, in the case of CFRPs, the damage was located in the zone of uncut chip in front of the interface, being this zone removed with the chip formation. The chip formation mechanisms and induced damages were strongly dependent on fiber orientation, which is also have been reported by Rao et al. [20]. The effect of bending moment (involving both cracking and crushing damage) was observed for fiber orientations close to the cutting speed direction in CFRPs and the increment in the angle of orientation leads to increased crushing damage beneath the machined surface. It is also reported that, the energy needed to complete the breakage of the elements characterize the composite behavior (brittle/ductile) strongly influencing the chip formation mechanisms and matrix damage, being both phenomena also dependent on the fiber orientation. Machining induced subsurface damage was much reduced for brittle composite (CFRPs) than for ductile composite (GFRPs).

2.3.3. Analytical Studies on Machining of FRP Composites

In addition to the experimental and numerical studies conducted in the machining of fiber reinforced composites, analytical formulation is also attracted many investigators in order to understand the cutting process of FRPs and to offer a simplified analytical solutions for practical applications. Zhang [22] conducted an analytical study to understand some common features in the mechanics modeling of machining composites. Long fiber reinforced composite (LFRC) and ceramic particle reinforced aluminum metal matrix composite (MMC) were considered in this study. In the case of cutting LFRCs, three distinct deformation regions were identified in the cutting zone when the fiber orientation varies between 0^0 and 90^0 as shown in Figure 2.9. The first region, which is in front of the rake face of the cutting tool, resulting in a chip is identified as region 1 or chipping region where fracture occurs at the cross-sections of the fibers and along the fiber-matrix interfaces. Pressure region or region 2 is the deformation region that takes place under the nose of the cutting tool, where the nose pushes down the work piece material. The third deformation zone is region 3 or bouncing region, which involves mainly the bouncing back of the work piece material, which happens under the clearance face of the cutting tool.

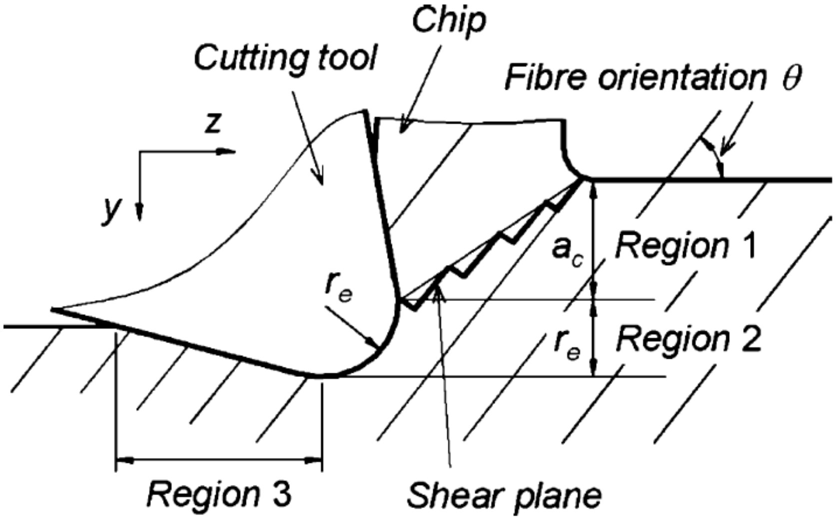

Figure 2.9. Deformation zones when cutting LFRC [22]

The mechanics model of cutting is based on the deformation mechanism discussed above, in such a way, the cutting zone in the model also divided in to three regions and it considers only when the fiber orientation is less than or equal to 90^0. In this model, region 1 has a depth of a_c as shown in Figure 2.14 bounded by the starting point of the tool nose, region 2 have a depth equal to the nose radius, and region 3 starts from the lowest point of the tool. It is assumed that the total force can be calculated by adding up the forces in the entire three regions and the total cutting forces in the vertical and horizontal directions are given by

$$\begin{cases} F_y = F_{y1} + F_{y2} + F_{y3} \\ F_z = F_{z1} + F_{z2} + F_{z3} \end{cases}$$

where F_{yi} and F_{zi} (i = 1, 2, 3) are the corresponding forces in Regions 1–3, defined by

$$\begin{cases} F_{y1} = \tau_1 h a_c \dfrac{cos\phi \tan(\phi + \beta - \gamma_0) - sin\,\phi}{(\tau_1/\tau_2)\cos(\theta - \phi)\, sin\theta - \sin(\theta - \phi)\, cos\theta} \\ F_{z1} = \tau_1 h a_c \dfrac{sin\phi \tan(\phi + \beta - \gamma_0) + cos\phi}{(\tau_1/\tau_2)\cos(\theta - \phi)\, sin\theta - \sin(\theta - \phi)\, cos\theta} \end{cases}$$

$$\begin{cases} F_{y2} = P_{real}(cos\theta - \mu sin\theta) \\ F_{z2} = P_{real}(sin\theta + \mu cos\theta) \end{cases}$$

$$\begin{cases} F_{y3} = \dfrac{1}{2} r_e E_3 h(1 - \mu cos\alpha sin\alpha) \\ F_{z3} = \dfrac{1}{2} r_e E_3 h cos^2\alpha \end{cases}$$

In which $\phi \approx \arctan\left\{\frac{cos\gamma_0}{1 - sin\gamma_0}\right\}$, E_3 is the effective modulus of the workpiece material in region 3, h is the thickness of the workpiece, r_e is the tool nose radius, and v is the minor Poisson's ratio. $P_{\text{real}} = K \cdot P$ is the real resultant force in Region 2 in which the coefficient K is a function of fiber orientation to be determined by experiment, μ is the friction coefficient, τ_1 and τ_2 are the shear strengths of the material, γ_0 is the rake angle of the tool, and β is the friction angle on the rake face. The validity of this model was compared and verified with experimentally measured cutting forces and the model predicts nicely the nature of the cutting force variation when the cutting parameters change. The model has captured the major deformation mechanisms in cutting the LFRCs. The maximum error of the predictions is relatively ~ 30%, and the reason for this error was assumed that experimental measurements were influenced by many factors.

Gururaja and Ramulu [4] studied subsurface stresses generated during orthogonal cutting of unidirectional fiber reinforced plastics using a generalized plane strain anisotropic elasticity formulation. In this study, complete closed form analytical expression for the stress fields for line-load profile acting on continuous homogenous anisotropic half-space have been derived. The orthogonal cutting of FRPs was treated as a half-space problem, where the work piece material during cutting can be approximated as a half-space subjected to a line loading of constant magnitude resultant force R acting at an angle of α with a contact width of 2ε as shown in Figure 2.10. In addition, incremental plastic, viscoelastic, thermal strains, and friction were neglected and furthermore a quasi-static scenario has been considered along with the assumption of generalized plane strain deformation. The UD – FRP composite laminate has been modeled as continuous homogeneous linear elastic half-space.

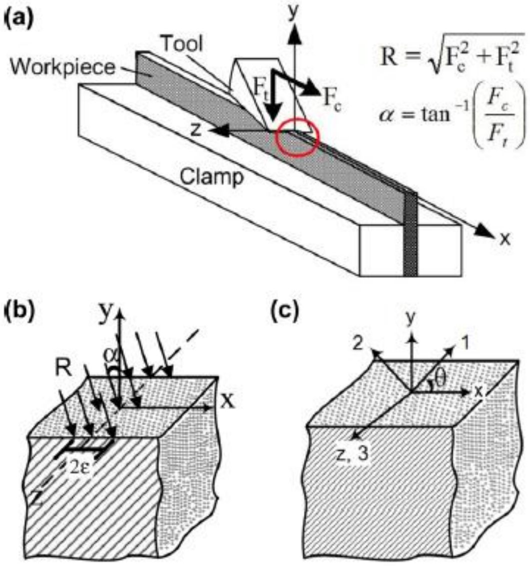

Figure 2.10. Edge trimming process modeling: (a) Cutting process, (b) Line-load with uniform magnitude along z-axis, and (c) Cartesian coordinate definition [4]

In their analysis of subsurface stress, it has been reported that, the stress σ_{yy} decreases more rapidly with increased depth (y/ε) for $\theta = 0^0$ as compared to $\theta = 90^0$ for $\alpha = 0^0$. In addition, for $\theta = 45^0/135^0$, the maximum occurs (approximately) along the direction of θ and the stress-field appear to be mirror image and the same behavior observed for $\alpha = 0^0$. Much of the observations made on σ_{yy} contours also hold for σ_{xx} and τ_{xy} contours. For 0^0 laminate, the stress magnitudes are quite high and decreases significantly with increasing depth while for 90^0 laminate the stress magnitudes are quite low, which is the opposite of the observation from σ_{yy}. For combined load case, $0^0/90^0$ laminates exhibit a symmetric stress field about the $x/\varepsilon = 0$ axis with maximum compressive stress in the leading edge and tensile stress in the receding edge of the load profile. Moreover, the stress profile for $45^0/135^0$ laminates are mirror images and large tensile stress exists in the receding side of the load profile for 135^0 laminate. For applied normal load case, τ_{xy} shows similar behavior as seen in the case of σ_{xx} and $\sigma_{yy.}$ Higher maximum magnitude of τ_{xy} was observed for 0^0 laminate and a lower maximum τ_{xy} magnitude has been seen for the 90^0 laminate. The τ_{xy} distribution for the horizontal load application shows the characteristic stress dispersion. The 90^0 laminate under horizontal load application exhibits a large magnitude of shear stress, whereas, τ_{xy} distribution for the combined load case presents averaged stress fields responses as observed for σ_{yy} and σ_{xx}.

On the continuation of their study [4], Gururaja and Ramulu [23] conducted a study on failure analysis of FRP laminate subsurface to determine and characterize failure envelopes for an assumed loading scenario. In this study, an attempt has been made to understand the failure behavior of a UD–CFRP laminate modeled as a quasi-homogeneous anisotropic half-space subjected to a surface line load acting at an assumed angle using a Tsai–Wu failure criterion. In their failure analysis, they used a parameter of failure index (FI), to facilitate comparison between stress fields of different fiber angles and load angles. For a plane strain condition considering a transversely isotropic laminate, the failure index is expressed by the equation given below. Where the derivation of parameters used in the equation can be found in the referenced material.

$$FI = (F_1\sigma_{11} + F_2(\sigma_{22} + \sigma_{33}) + F_{11}\sigma_{11}^2 + F_{22}(\sigma_{22}^2 + \sigma_{33}^2) + 2F_{12}(\sigma_{11}\sigma_{22} + \sigma_{11}\sigma_{33}) \\ + 2F_{23}\sigma_{22}\sigma_{33} + F_{66}\tau_{12}^2) \geq 1$$

Fiber orientations of 0, 45, 90, and 135 degrees were investigated in the study. The failure behavior of the laminates showed reliance with their respective fiber orientations and the failure contours were indicative of the fiber orientation, with the *FI* = zero contour separating the compressive and tensile zones analogous to stress-analysis plots. When the load was applied along the fiber direction, the contours were not distinct, particularly for α = 45^0 acting on the 135^0 laminate and normal load acting on the 90^0 laminate. Depth of failure was found to be different for tensile/compressive zones. For the hypothetical loading cases, a maximum depth of failure of around 60 µm was found in the tensile zone (behind the line load) for shear loading 135^0 laminate. Maximum failure width occurred for the 90^0 laminate of about 162 µm. Comparison of analytically estimated failure depths with experimental observations reveals that the analytical method is able to replicate the trend observed in experiments.

2.4. Drilling of FRP Composite Materials

Drilling is one of the most important material removal process, which is extensively carried out on fiber-reinforced composite materials. Unlike conventional metallic alloys, the drilling process of FRP composite laminates is difficult in nature with many new damage modes and chip formation mechanisms, which do not occur usually in drilling of metallic alloys. One reason for this is that, the inhomogeneous and anisotropic nature of FRPs make the material removal process different from that of machining of single-phase materials, and unlike metals, in which shearing is the major chip formation mechanism, in composite materials local bending at the fiber-matrix interface seems to be important during chip formation [19]. In addition, the different property of the matrix, fiber, and the interface contribute a great deal for the process-induced damages in the drilling process of FRPs, and this process-induced damage during drilling is accounted for more than 60% of composite part rejection during quality control in the composite manufacturing industry [6].

Drilling is a complex hole forming operation in which the tool penetrates the work material. The material removal process is accomplished through both extrusion and cutting operations. Most studies either address damages incurred to the composite materials during the drilling process or discuss parametric influence of operating conditions on hole quality. On the drilling of composites, their non-homogeneous and anisotropic nature causes many problems. The problems encountered during drilling composites include delamination, fiber pullout, high rate of tool wear, etc. Delamination is one of the severe problems in drilling composites. It is generally regarded as a matrix dominated failure behavior, which usually occurs in the inter-ply region. Delamination can be introduced by three mechanisms; peeling up of the top layer, punching out of the uncut layer nears the exit, and the thermal stress mode. Fiber-pullout is the tearing away of the fiber/matrix from the wall of the machined surface. Shorter tool life is due to abrasion by hard fibers constituents and low thermal conductivity of composite constituents causing local heat accumulation on the cutting tool. Micro-cracks occur in the inter-laminar area or along the fibers. Other problems include hole shrinkage caused by lower flexural strength and presence of powdery chip, which cause health hazard and difficulties on handling of the process.

These problems encountered during drilling of composites need to be confronted. When such defects are present on drilled holes, they are causes of re-work/rejection of parts. These defects initiate crack propagation, and are causes of untimely failure of the composite structure. A number of empirical and analytical studies are performed to understand the drilling characteristics on composites and to reduce the defects on the process. In the following sections, experimental studies, numerical studies, analytical studies, and studies on the use of signal processing as quality control on the drilling of composites will be summarized.

2.4.1. Experimental Studies on the Drilling of FRP Composites

Experimental studies are the leading investigational tools in the understanding and characterization of the drilling process of FRP composite materials and many investigators [5 – 6, 24 – 41, 25 – 26, and 44 – 66] have conducted several experimental studies. Among the experimental investigations conducted related to the drilling process of FRP composite materials, characterizing the influence of various drilling parameters on the quality of drilled holes and relating these drilling parameters with process-induced damage is the focus of many investigators. To minimize damage, therefore, it is important to monitor process variables such as the machining forces and the position of the tool relative to the work piece [24]. Cutting speed, feed rate, and tool materials along with laminate configuration are the most common parameters considered influencing the quality of drilled holes, so characterizing these parameters is essential in order to reduce process-induced damages during drilling of FRP composites. The review of some of these experimental studies is presented in this section.

Abrão et al. [25] conducted a literature survey on the machining of composite materials, more specifically on drilling of glass and carbon fiber reinforced plastic composites. The effect of tool materials and their geometry on the damage of the drilled hole, thrust force, torque, and related parameters (power and specific cutting pressure) together with the quality of the hole, with emphasis on delamination is the leading focus of the survey. They outlined which factors should be considered in order to obtain the best performance from the drilling operation as shown in Figure 2.11. On their review of the machining parameters, they found that in most studies, the drilling investigations were done using a high speed steel (HSS) and tungsten carbide (WC) drills, the cutting speed employed is usually from 20 to 60 m/min, whereas, the feed rate values lower than 0.3 mm/rev are frequently used. Cutting speed is not a limiting factor when drilling polymeric composites, particularly with hard metals, therefore, the use of cutting speeds below 60 m/min is explained by the maximum rotational speed of conventional machining tools. Since drill diameters above 10 mm are rarely reported and the higher cutting speed leads to a higher temperature, which may in turn causes the softening of the matrix material. The use of feed rate below 0.3 mm/rev was associated with the delamination damage caused when this parameter is increased and tungsten carbide tool was reported as a preferred tool when drilling at higher cutting speed.

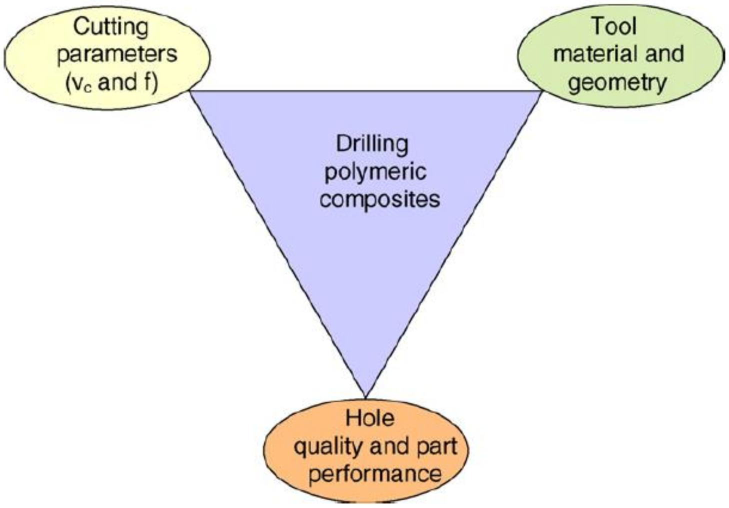

Figure 2.11. Principal aspects to be considered when drilling FRPs [25]

Hocheng and Puw [5] studied drilling of reinforced thermoset and thermoplastics to characterize the material response to the machining process. In their study, they investigated the chip formation and assessed the machinability of two representative materials, thermoset-based or epoxy and thermoplastic-based or acrylonitrile butadiene styrene (ABS) composites to present the different responses to the drilling process using a standard two flute HSS drill of 5 mm. The characteristics of the chip produced during the drilling trial were different for the two materials. In the case of thermoplastics, the chips are produced in continuous and curling form for a wide range of drilling conditions, whereas, in the case of thermosets, the chips were more brittle than thermoplastics, thus the chips tend to fracture earlier, and the chips show exclusive fractures regardless of cutting conditions. In the case of thermosets (carbon/epoxy), higher feed rate produces blockier chips by increasing depth of cut, whereas, higher cutting speed causes early material fracture by elevating the strain rate and reducing chain sliding. The thrust force is found to be proportional to the depth of cut for both materials and the curves for carbon/epoxy show the effect of tool condition in machining. The arithmetic mean (R_a) was used as a surface roughness parameter in dictating the integrity of the machined surface and carbon/epoxy shows a rougher wall than the ABS based material and it was comparable to that of steels for the same operation. A series of mini-fractures in machining of carbon/epoxy, which is a result of the brittle behavior of thermosets and fibers was accounted for roughness of the surface. At lower feed rates and cutting speeds, the fracture is less violent and more controllable (due to lower strain rate) thus produces a smoother surface. More delamination at the entry and exit was reported when drilling thermoset composite than that of the thermoplastic composites.

Sonbaty et al. [26] investigated the influence of some drilling parameters on thrust force, torque, and surface roughness when drilling fiber reinforced composite materials, in which these parameters include the cutting speed, feed rate, dill size, and fiber volume fraction. The drilling operations were conducted on glass fiber reinforced epoxy composite with various values of fiber volume fractions clamped on a back plate using a standard HSS twist drill. The thrust force and torque increased with the increase of feed rate and drill diameter and decreases with the increase of the cutting speed. The increase in fiber volume fraction increases the peak thrust force but does not show significant influence on the torque. This study shows that the cutting speed and feed rate have insignificant effect on surface roughness at speeds ranging from 455 to 1850 rpm, and the highest value of roughness was obtained at higher feed and lowest cutting speed. In general, the surface roughness was improved by increasing the fiber volume fraction and a higher value of surface roughness was observed on holes drilled by a combination of lower fiber volume fraction and low feed. At low feed, the surface roughness increases when the drill diameter increases from 8 to 13 mm, whereas, at high feed, the surface roughness value increases with the increase of the drill diameter up to 10 mm and decreases when the drill diameter increases from 10 to 13 mm. Budan and Vijayarangan [27] also conducted experimental study on GFRP composite laminate to verify the effect of machining parameters and fiber concentration on the surface finish, hole quality, and delamination using an 8 mm diameter HSS drill. They found that, the surface roughness R_a values increases with the increase of drill speed and fiber content, which is not in line with the result reported by [26], where the high fiber content was complemented for better surface roughness. The minimum R_a value was obtained at the lowest values of cutting speed and feed rate. The result also shows that, the influence of the feed rate on the surface roughness value is less than the influence of drill speed and fiber content. The quality of the hole was decreased for the higher fiber content laminates than the lower fiber content laminates, and holes produced at higher feed rates were affected by delamination.

Similarly, Shyha et al. [28] investigated the effect of laminate configuration and feed rate on the cutting performance when drilling holes in CFRP composites. A drilling experiment on a 3 mm thick unidirectional and woven CFRP laminates was performed using uncoated WC twin lipped stepped drills, incorporating a pilot diameter of 1 mm with a 1.5 mm sizing diameter section. The longest tool life was obtained when drilling woven laminates at the higher feed rates and the effect of prepreg form on tool life was only prominent when employing a higher feed rate (up to 44-fold increase in tool life between UD and woven). This study shows that the feed rate was the most influential factor on the thrust force where thrust force increases with the increase of the feed rate and the resulting thrust force at the last hole is approximately 3 times larger than the first hole regardless of the type and form of the prepreg. In most cases, the delamination factor found to be lower at hole exit compared to the corresponding entry position. Feed rate and prepreg form had the most significant effect on first hole entry delamination factor while prepreg type, feed rate, and interaction between prepreg form/feed rate were the main contributing factors for the corresponding exit delamination factor. None of the control variables were found to be statistically significant with regard to last hole entry delamination factor, while only feed rate was shown to influence last hole exit delamination. In addition, for all conditions tested, the drilled hole diameter was found to be undersize by 36 µm (~ 2.5%) to 73 µm (~ 5%) at the end of tool life.

The type and geometry of the drill tool used in the drilling of FRP composites have a great influence in the quality and surface integrity of the hole produced. A number of investigators [29 – 34] conducted experimental study on the effect of tool type and tool geometry on hole quality and drilling forces when drilling FRP composites. Wern et al. [29] investigated the surface texture of holes drilled on composite using two different PCD tipped drill geometries.

The two drills used in this study are drill A that have a diameter of 12.7 mm with an axial rake angle of 27 ^{0} and drill B having a diameter of 13.9 mm with an axial rake angle of 7 ^{0}. Fiber pull out, which caused the pitting phenomenon in the rough surface zone, occurs when the fiber is at negative angle to the cutting direction. The hole surface was partitioned in to four regions of severe surface damage zone and the roughness measurements were taken on these regions as shown in Figure 2.12, and pitting or fiber pullout occurs on plies around regions 1 and 3 while regions 2 and 4 of the ply surface are smooth and covered with matrix. It is also observed that when the cutting edge is at an angle of greater than -5^{0} or less than -80^{0} with the fiber orientation, pitting is not observed on the surface. Drill A produced a surface that had a narrower damage width than that for drill B. While the high rake angle caused the fiber to fracture near the cutting edge producing a surface with less fiber pullout, the low axial rake angle drill generates a surface by pulling out relatively large portions of material. Feed rates have a definite effect on the machined surfaces. Between 0.0254 and 0.1778 mm/rev, the surface roughness decreased with an increase in feed rate. At feed rates above 0.1778 mm/rev, the surface roughness increases with an increased feed. Colligan and Ramulu [30] also conducted experimental study on the formation of macroscopic pitting or fiber pullout caused by the drilling of graphite/epoxy composites using two drill geometries which are identical to drill A and B of [29]. In comparing the performance of the two drill geometries, it was observed that drill point geometry A produced a good hole at or below feed rates of 0.127 mm/rev and pitting was observed at the higher feed rates, whereas, drill B produces a heavily pitted holes at all feed rate levels. The cutting speed and the application of coolant were not significant in determining the formation of pits on the hole surface, rather the feed rate was found to be a significant factor in the formation of pitting. Pitting is strongly related to the orientation of the fibers relative to the cutting edge and has been observed to occur at those points where the fibers are inclined into the advance of the cutting edge at approximately 45^0.

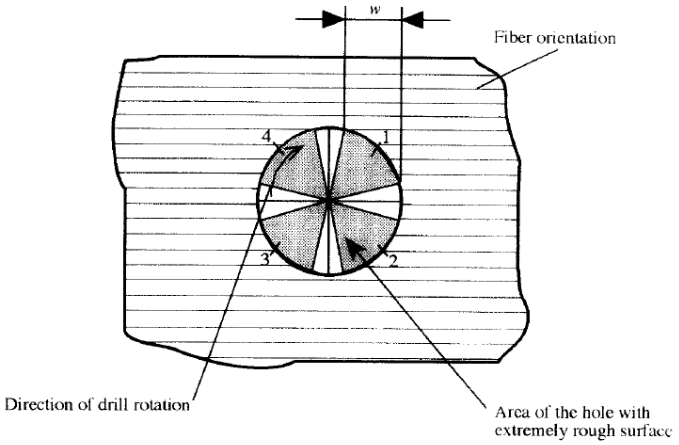

Figure 2.12. Severe surface damage zone in unidirectional ply [29]

Ramulu et al. [31] studied the performance of three drill tools, namely HSS drill, carbide straight flute, and polycrystalline diamond when drilling graphite/bismaleimide (Gr/Bi) composites. The polycrystalline diamond (PCD) four-facet drill produced the highest quality of holes, suffered the least amount of wear, and the thrust force of the PCD drill was one third of that of HSS drill. The carbide drill produced better quality holes, low thrust force, and lower amount of tool wear compared to the HSS drill; however, it produces less quality of holes, higher thrust force, and higher amount of tool wear than the PCD drill. The conventional HSS tooling suffered the most wear and consequently produced a large increase in drilling forces, and these higher forces in turn led to an increase in exit delamination and specimen damage. In addition, tools with helical flutes were found to induce pulling thrust forces and entrance delamination, while those with straight flutes did not. Velayudham and Krishnamurthy [32] studied the effect of point geometry and their influence on thrust force and delamination in drilling of polymeric composites. The performance of normal point geometry tipped carbide drill with point angle of

118^0, web thinned tipped carbide drill with point angle of 85^0, and tripod geometry solid carbide drill were investigated when drilling Glass/Phenolic-woven fabric composite. In general, thrust force increases with the increase of the feed rate for all kind of drill geometry, which is also observed by others [26, 28, and 82]. The thrust force experienced by the tripod geometry drill was found to be almost 60% less than that of the normal point geometry drill, which was attributed to the higher web thickness of the normal point geometry drill. The thrust force of the web thinned tip carbide tool was a little higher than the tripod tool but way less than the normal point geometry drill. From all drill type, tripod point drill results the least damage, whereas, the normal tipped drill produces greater extent of damage. In the case of tripod point drill, peripheral damage was not increased even with the increase of thrust force, whereas, in the case of normal point drill, the delamination factor was increased considerably with the increase of thrust force. Overall, a high quality hole was produced when tripod geometry drill was used.

Lazar and Xirouchakis [33] conducted an experimental analysis of drilling fiber reinforced composite to determine the distribution of the drilling loads and effect of tool geometry on drilling forces using three different drill tools. Tapered drill reamer, 8-facet twist drill, and 2-facet twist drill were used on CFRP and GFRP composite panels utilizing an aluminum backing plate. The 2-facet twist drill generated the maximum amount of axial load per ply, while the maximum tangential load was usually greater for tapered drill reamer. The 8-facet twist drill seems to be the best performer, probably due to the web-thinning feature, which makes the cutting process more efficient in the close vicinity of the chisel edge in comparison with the 2-facet twist drill. Overall, the average maximum thrust over all tested conditions is 3% higher for CFRP than GFRP, while the average maximum torque is 20% higher for GFRP. It was shown that the geometry of the drill (especially the chisel edge area) and the axial feed rate are the most important parameters for lowering the critical loads. In addition, it was suggested that lowering the size of the chisel edge as in the tapered drill reamer or performing an additional web-thinning grinding as in the 8-facet twist drill will make the cutting in close vicinity of the tool axis more efficient and therefore lower the chances of delamination onset. Quan and Zhong [34] experimentally investigated the performance of plated diamond core drill, cemented diamond core drill, HSS twist drill, and HSS twist drill with plated diamond coat when drilling CFRP. The experimental result of this investigation indicates that the HSS twist drill is not competent for making holes on composites and making holes with a solid drill would generate much more chips than that of with a core drill. Under the same test condition, the machining effect of the plated core tool is better than that of the cemented core tool and more satisfying process outcome can be achieved with core tools than with solid drills when making holes in CFRP or GFRP. The result also shows that dry cutting condition (without cooling and flushing air/fluid) is unsuitable for making holes in the composite with the cemented or plated diamond tools.

The effect of coating on the performance of tungsten carbide tool on the resulting drilling forces and hole quality was studied by Murphy et al. [35] using titanium nitride (TiN)-coated drill, diamond-like carbon (DLC)-coated drill, and uncoated drill having four straight flutes. Thrust force and torque were increased as the number of drilled holes increases for all type of drill tools. The result from the go-no-go gauge and diameter measurements 1 mm from the top shows that the uncoated tools perform best with an average of six holes drilled in tolerance; followed by the TiN with just over four holes and by DLC with an average of one. This performance order was reversed when diameter measurements was taken 1 mm from the bottom. The study concludes that overall the use of coatings was found to be of no benefit when machining carbon – epoxy composites. In attempt to study the influence of point angle on the resulting thrust force and torque, Jayabal and Natarajan [36] conducted an experimental study using HSS twist drill with point angles of 90^0, 104^0, and 118^0 when drilling E-glass/polyester composites. This study shows that both the thrust force and torque increased with the increase of the drill point angle. Similarly, Bhatnagar and Jalutharia [37] compared four-facet drill, eight-facet drill, parabolic drill, and Jo-drill when drilling CFRP and GFRP composites and found out the highest thrust force and torque were created by four-facet drill, whereas, the lowest were by eight-facet drill. The thrust and torque by the parabolic drill and Jo-drill were the second and third highest respectively. Mohan [38] also reported the increases of the thrust force and torque with the increase of drill diameter.

From the studies discussed above, we have seen that cutting speed, feed rate, tool materials, and tool geometry along with laminate configuration are the most common parameters considered influencing the quality of drilled holes, so characterizing these parameters is essential in order to reduce process-induced damages during drilling of FRP composites. From all modes of damage, delamination is considered the most threatening damage mode during the drilling process of composite materials. Delamination, in addition of reducing the structural integrity of the laminate, it also causes poor assembly tolerance and has the potential of creating long-term performance deterioration [73]. Delamination has been identified as a resin or matrix failure occurring predominantly in the interplay region of a laminate [75]. Delamination during drilling of composite laminates found to occur at the entrance and exit of the drill bit and the two modes are known as push-out delamination at the exit and peel-up delamination at the entrance respectively, and from these, push-out delamination is the most dangerous damage [24, 73, 75, and 76]. Push-out delamination occurs when the drill progress towards the bottom of the laminate in which the uncut thickness of the laminates decreases. At this stage, the number of plies under the ply which is being cut is also decreases as the drill approaches the bottom the laminate, so less backing support for the ply being cut, at the same time the stress caused by the thrust force gets larger than the inter-laminar strength of the laminates resulting an exit-ply delamination. Peel-up at the entrance occurs when the chisel edge of the drill bit scrape or wear off the first ply or two of the laminate at the entrance. And as the drill progress towards the laminate, the materials which has been scrape is being pulled and tends to move upward along the flute resulting the peeling of the top plies of the laminate. Figure 2.13 shows the schematic representation of the two modes of delamination and some of the Experimental studies on delamination will be presented as follows.

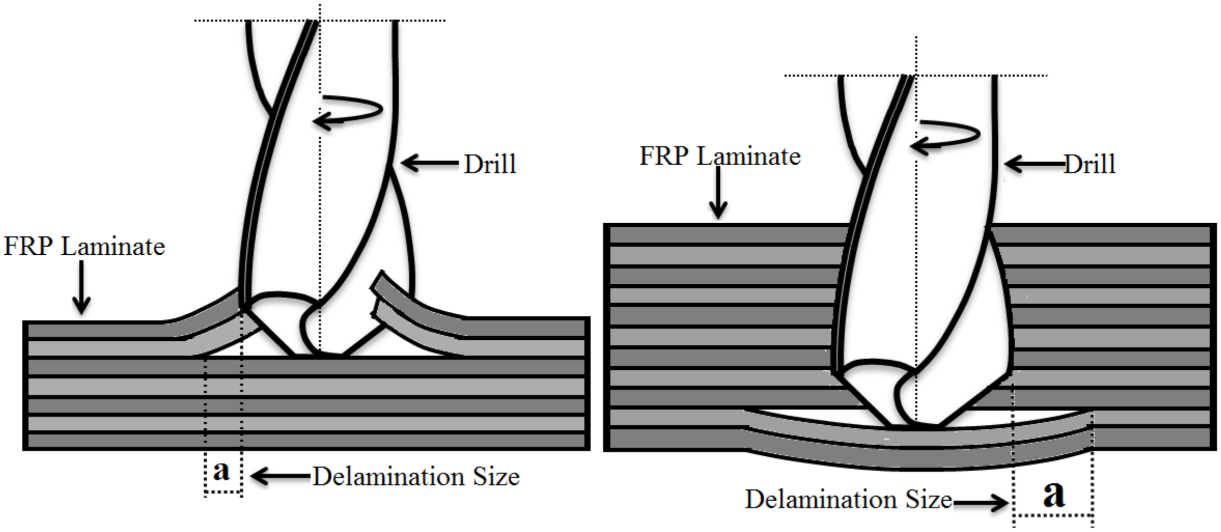

Figure 2.13. Schematic representation of delamination at entrance (left) and at exit (right)

In their experimental study, Dharan and Won [24] investigated the machining parameters and critical characteristics of the tool force response during machining and proposed an intelligent machine tool that can automatically keep the thrust and cutting force below their critical threshold during machining to allow damage-free machining of composite laminate. The experiment was conducted on a woven CFRP composite using a carbide-tipped twist drills of diameter 1/4, 5/16, and 3/8 inch. The study shows that about 50 – 60% of the total thrust force is acting on the chisel edge of the drill, whereas, the portion of the torque acting on the chisel edge is relatively small. The thrust force and torque responses were idealized to represent the different events taking place during machining for the designing of the intelligent control system. The allowable maximum force predicted by the delamination criterion at the tool entry defines the initial feed rate, and once initial contact is made and drilling begins, the control mode will be switched from feed rate/position control to force control. The reference value for the force-position feedback loop will be set to the predicted critical force for the delamination. For a drilling operation completed without delamination, the critical force is increased for the next cycle. If delamination is detected, a signal is sent to the position feedback loop to reduce the feed rate momentarily or to back up the drill by an appropriate amount. It is reported that, this process will allow an immediate and systematic adjustment of the critical force not only at a particular depth where the delamination is taking place but also at other depths and producing damage - free hole will be possible based on the above intelligent control system. Figure 2.14 shows the overall scheme of the proposed intelligent control system.

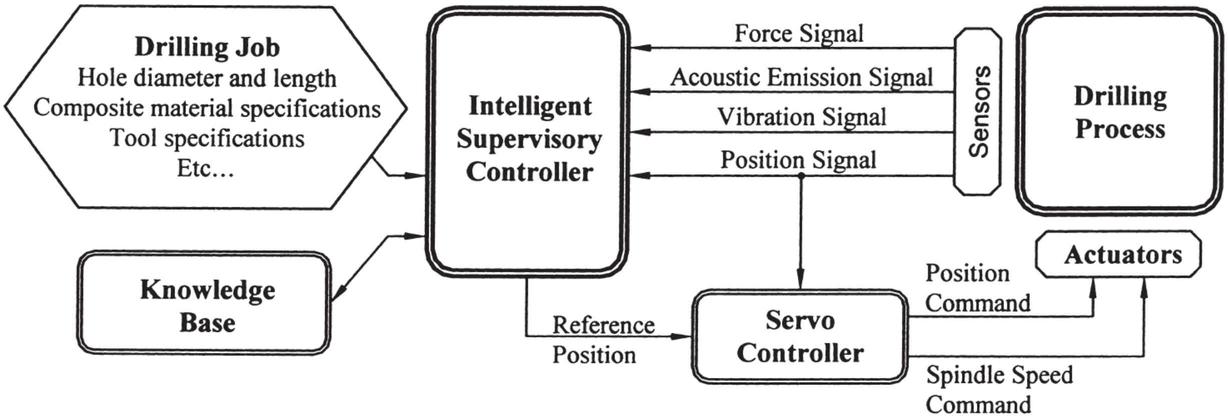

Figure 2.14. Overall scheme of the intelligent control system [24]

The concept of delamination factor (i.e. the ratio of the maximum diameter in the damage zone to the drill diameter$\frac{D_{max}}{D}$) was proposed by Chen [39] in order to analyze and compare the degree of delamination when drilling of CFRP composites. Drilling tests were performed to measure the variation of cutting forces with or without delamination and to measure the flank surface temperature, where an embedded thermocouple inside the drill bit was used for the temperature measurement. The study shows that the effect of cutting speed on the cutting force was insignificant, while both the thrust force and torque increased with the increase of the feed rate, whereas, the flank surface temperature increases with the increase of the cutting speed and decreases with the increase of the feed rate. Regarding the effect of tool geometry on the cutting force, small point angle, small web thickness, large chisel-edge rake angle, and large helix angle was suggested for minimal cutting force. A mathematical correlation between the delamination factor and the average thrust force when drilling unidirectional and multidirectional CFRP composites using a HSS and Carbide drill tool was proposed and given by the following relations.

1. For unidirectional with HSS drill

$$F_d = 0.671 + 0.0487\bar{F_z}$$

2. For unidirectional with Carbide drill

$$F_d = 0.671 + 0.041\bar{F_z} --- for\ \bar{F_z} < 216N$$

$$F_d = 0.671 + 0.011\bar{F_z} --- for\ \bar{F_z} > 216N$$

3. For multidirectional with Carbide drill

$$F_d = 1.285 + 0.011\bar{F_z}$$

Where, $F_d = \frac{D_{max}}{D}$ is the delamination factor and $\bar{F_z}$ is the average thrust force.

Various experimental investigations are underway in an effort to characterize the effect of material type and process parameters on delamination caused by the drilling process, from these experimental studies and analysis of process parameter influence on delamination are the focus by many [40 – 42, 44, and 49]. Even though the practice commonly used in the measurement of delamination size is the direct measurement by digital or optical microscopy, the research community presents various approaches which includes a shadow moiré laser based imaging technique [64], digital image analysis using image digitalization [66], the use of scanner with Corel-Draw software [40], and computerized tomography and C-Scan [43].

Khashaba [40] conducted drilling experiment to study the influence of material variables on the thrust force and delamination. The drilling processes were conducted on five different types of E-glass fiber reinforced thermosetting composites of continuous-winding with filler/polyester, cross-winding/polyester, chopped/polyester, woven/polyester, and woven/epoxy using a new standard HSS drills. The thrust force and torque were increased with increasing feed for continuous-winding and cross-winding composites and the thrust forces of continuous-winding composite are more than three orders of magnitude than those in the cross-winding, woven, and chopped composites. Overall, the constituent materials of the composite specimens, specimen thickness, and machining time show a significant effect on the behavior of thrust force and torque over the machining time and the presence of sand filler in continuous-winding composites not only raised the values of cutting forces and push-out delamination but also increased their values with increasing cutting speed. An inexpensive technique for measuring delamination was introduced by using color flatbed scanner and image software (CorelDraw). The delamination size was increased with increasing feed because of increasing thrust force and push-out delamination is found to be more severe than that of peel-up. For the same fiber shape, both modes of delamination of woven/epoxy composite are lower than woven/polyester composites despite the two composites have a proximately equal thrust forces. Delamination-free hole was achieved when drilling cross-winding composites using variable feed technique. Gaitonde et al. [41] carried out an experimental study on drilling of CFRP composites using cemented carbide drill tool to examine the influence of process parameters, namely, cutting speed, feed rate, and drill point angle on delamination factor. The study reveals that delamination size increase with the increase of feed rate, the increase of point angle, and decreases with the increase of the cutting speed. Overall, a combination of lower values of both feed rate and point angle with higher range of cutting speed gives minimum delamination size. Kilickap [42] also has studied the effect of process parameters on the delamination when drilling GFRP composites using a HSS drill by taking cutting speed, feed rate, and drill point angle as a variable process parameters. It was observed that the delamination factor at exit surface is larger than delamination factor at entrance surface for the same drilling condition. This study shows that delamination factor increased with the increase of feed rate and cutting speed, whereas, others [41] reported delamination factor increases with the increase of feed rate and with the decrease of cutting speed. For the same cutting parameters, delamination factor shows an increase with the increase of point angle, which also reported by [41]. Summary of empirical relationships proposed by various studies to correlate drilling force with feed rate and drill diameter are given in Table 2.1

Table 2.1. Summary of empirical relationships [97]

Work material and Drilling parameters	Thrust force Fz (N), Torque M (N.m)
Unidirectional CFRP T300 /5208, ply thickness = 0.228 mm, laminate thickness = 20 plies, HB = 98 Kg/mm^2. Standard HSS twist drill, diameters = 6.35, 12.7 mm, drill point = 118^o, chisel length = 0.2 d, feed rate up to 0.12 mm/rev .	$F_A = d^2 H_B \left[\frac{1.91 f^{0.4}}{d^{1.2}} + \frac{0.101}{d}\right]$ $F_A = 0.136 H_B d^{0.78} f^{0.4}$
CFRP T300/5208 laminates of different configuration. Cross ply laminate thickness =20 plies, quasi-isotropic laminate thickness = 24 plies, ply thickness = 0.125 mm. Standard HSS twist drill, diameter = 6.35, drill point = 118^o, chisel length = 0.2d, feed rate up to 0.2 mm/rev.	$F_A = 56.3 f^{0.4}$ $F_A = 41.8 f^{0.32}$ $F_A = 43.1 f^{0.22}$
E-glass UD GFRP, ply thickness = 0.228, total laminate thickness = 4mm, Vf = 0.4. Trepanning tool and twist drill diameters = 8, 10, 14 and 16 mm, feed rates = 0.01-0.2 mm/rev, cutting speed = 50 m/min.	$F_A = 48.98 d^{0.242} f^{0.37}$ $F_A = 48.98 d^{0.2783} f^{0.41}$ $M = 0.039 d^{1.571} f^{0.59}$ $M = 0.039 d^{1.529} f^{0.52}$
E-glass chopped fiber mat, laminate thickness = 10 mm, Vf = 0.63, carbide coated drill bit, drill diameters = 6, 10 mm, spindle speed 400 rpm, feed rates = 0.1-0.7 mm/rev.	$F_A = 35.004 (f * d)^{1.3844} - 0.23 d^2$ $M = 0.0064 f^{1.3844} d^{2.9844} + 0.0091 d^2$
Quasi-isotropic layup [0/45]39s of woven CFRP (Toray 300/Fiberite 934), ply thickness = 0.125 mm, laminate thickness = 9.9 mm, Vf = 0.63. Drills: carbide tipped HSS, diameters = 6.35, 7.9 mm, spindle speed = 1000 rpm, feed rates 0.1 – 1.0 mm/rev.	$F_A = 40.77 (f * d)^{0.66} - 0.3 d^2$ $F_A = 3.5 (f * d)^{0.66} - 0.11 d^2$ $F_C = 14.12 (f * d)^{0.66}$ $M = F_C \frac{d}{2}$
Quasi-isotropic layup [0/45]43s of woven AFRP (Kevlar 49/Fiberite 7714) 8.1 mm total thickness. Vf = 0.6. Drills: carbide tipped HSS, diameters = 6.35, 7.9 mm, spindle speed = 300 rpm, feed rates 0.1 – 1.0 mm/rev.	$F_A = 35.84 (f * d)^{0.50} - 0.09 d^2$ $F_A = 30.81 (f * d)^{0.50}$ $M = F_C \frac{d}{2}$

2.4.2. Numerical Studies on the Drilling of FRP Composites

Numerical study and simulation of the drilling process of CFRP composites is one of the many tools used by investigators. Numerical studies often complimented for saving time, money, and for not involving the destroying of a real work material. Even though the number of numerical studies conducted on the drilling of FRP composites is not as much as the experimental studies, several investigators [27, 67 – 71] presented numerical analysis on the drilling process of FRP composites using various methods. Budan and Vijayarangan [27] used a finite element analysis (FEA) model to predict the effect of fiber percentage on the thrust force causing delamination when drilling GFRP laminates. The workpiece is modeled using the apparent properties of cut and uncut laminates and the tool was modeled as an isotropic material. The model assumes that the thrust force causes the delamination, which is perpendicular to the ply surface and since it is required to evaluate the thrust force that causes delamination only around the circumference of the hole, the point angle, which causes delamination at the center portion of the hole was ignored in the construction of the FEA model. The failure criterion assumes that delamination occurs when the critical stress at the interface between the cut and uncut portion of the laminate reaches the inter-laminar tensile strength of the material. Results indicate that there is a decrease in delamination force with the increase of fiber content. From this model, it is reported that the increase in fiber content decreases the thrust force and in turn, this decrease in thrust force causing delamination. The statement in this study that claims the decrease in thrust force causes delamination is in contrary of results reported by others [73, 75 – 76]. In an attempt to study the influence of thrust force and torque on the drilling-induced damage of UD-GFRP composite laminates, a numerical model was developed by Singh and Bhatnagar [67] to model the drilling process using the concept of finite element approach. In this study, the drilling of the composite laminate is modeled as a plate with an inbuilt conical hole as a frustum of a cone at the center of the plate, and this plate is discretized using 3-D solid hexahedron elements that offer versatility in terms of fiber orientation, stacking sequence, and material properties for the laminate. The hole is assumed to be generated because of the transient drilling action and a finite element model for a 4-layer symmetric UD-GFRP composite laminate is developed using a general-purpose software package, NISA, with the appropriate property data. The finite element model of the laminate is shown in Figure 2.15.

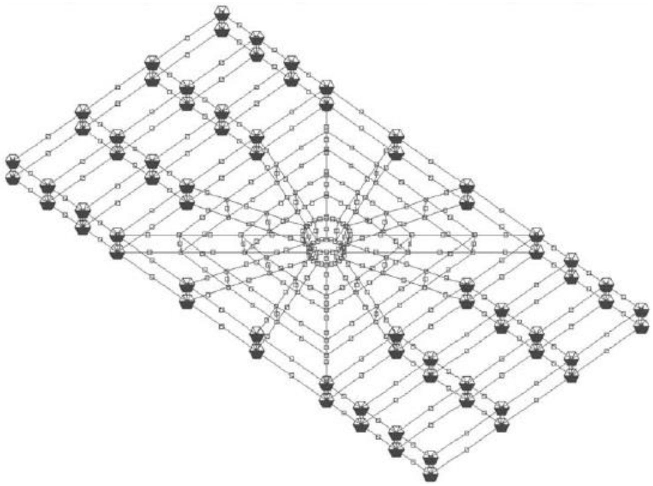

Figure 2.15. Finite element model of transient drilling of UD – GFRP laminate [67]

A static concentrated thrust force acting perpendicular to the plate with torque acting parallel to the surface of the plate is applied and a Tsai-Wu failure criterion is used to predict the failure of the composite laminate. The model shows that, the damage at the drill entry point is less profound than the damage at the end of the hole and the maximum damage for the first layer occurs in the direction of the fibers. The critical thrust force was found to be 42 N when no torque is applied and when torque is applied the critical thrust force dropped to 38 N with a torque of 10 N.cm, which is an indication of that the torque also have an influence on the damage around the drilled hole and should not be ignored completely. In order to validate their analytical model Rahmé et al. [68] developed a numerical model using the “Samcef” software and this model is used to calculate the critical thrust force using failure mechanics approach. In this study, the form of the material located beneath the drill was modeled in terms of a thin circular plate and initial crack was created along the hole circumference. The study shows that the number of elements along the circumference of the hole is the most influential parameter on the results. Figure 2.16 shows the finite element model mesh used in this study.

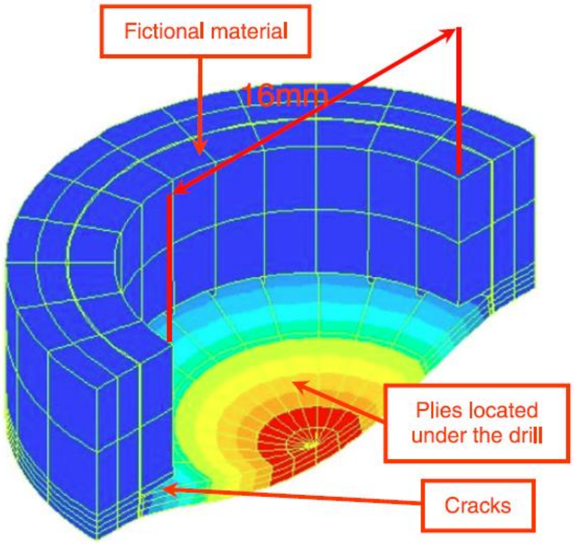

Figure 2.16. Finite element model mesh [68]

The critical thrust force is calculated when the energy release rate in mode I reaches its critical value and the total energy release rate is calculated using a virtual crack extension (VCE). The numerical model shows a good correlation with the analytical model in predicting of the critical thrust force for the uniformly distributed load application case and the maximum error was about 12 %. Rakesh et al. [69] also developed a finite element model to investigate the effect of drill tool geometry on drilling induced damage using a standard finite element package of ABAQUS. This model assumes a discrete rigid drill, downward translational and rotational motion of the drill, plane stress condition, and linear elastic behavior. Three drill point geometries of trepanning drill, twist drill, and jo-drill were considered in the modeling. The Hashin damage initiation criterion is used for more than a single stress component to evaluate different failure modes in different directions, which consider six different damage initiation mechanisms. A further loading after a damage initiation criterion is satisfied causes degradation of the material stiffness coefficient in the modeling of the damage. The prediction of damage area around the drilled hole for the twist drill is found to be larger than the other two drill geometries. The damage area predicted by this simulation process is compared with experimentally found damage area and a close match was reported between the two results. The result given by this study indicates that the numerical simulation predicted the delamination factor approximately 34% higher than the experimentally observed values for all drill geometries under investigation.

Durão et al. [70] used a three-dimensional finite element model including interface finite elements incorporating a cohesive mixed mode damage model to simulate delamination onset and growth induced by drilling for twist drill and C-shape drill tools. The damage model combines aspects of strength-based analysis and fracture mechanics and it is assumed that failure occurs gradually as energy is dissipated in a cohesive zone behind the crack tip. Damage initiation is predicted by using a quadratic stress criterion assuming that normal compressive stresses do not promote damage. This model does not consider the rotational movement of the tool; rather it is more concentrated in the indentation process that occurs by the action of the chisel edge. In this study, they show that the model accurately predicts the maximum thrust force obtained during experimental work and the modeled thrust–displacement curve shape is very similar for both geometries considered. In addition, the orientation of the main delamination area in the model is the same as in experimental result and an orientation angle for the onset of delamination of approximately 22.5^0 from the reference fiber direction of 0^0 has resulted consistently in both experimental and model results. These authors in another study [71] reported same results and Figure 2.17 shows the finite element model for the above two studies.

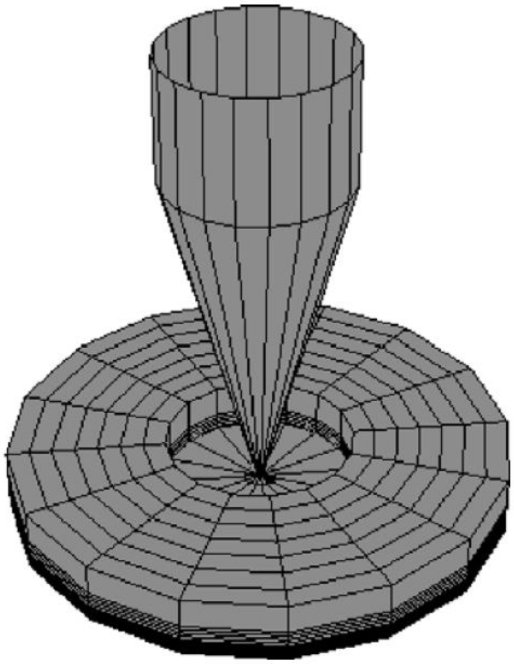

Figure 2.17. Finite element model [71]

2.4.3. Analytical Studies on the Drilling of FRP Composites

Analytical studies are useful tools in modeling and predicting process parameters and resulting outcomes based on the theoretical analysis. When it comes to the analytical studies conducted on the drilling process of FRP composites, most of the studies are dedicated in the prediction of the critical thrust force at which delamination will occur, while some studies focused on predicting the cutting forces throughout the drilling process. A mechanistic model for prediction of torque and thrust force during the drilling of composite materials was developed by Langella et al. [72]. The model is based on an assumption that orthogonal cutting takes place in an infinitesimal instant and acting over an elementary area on the cutting lip and each elementary force is integrated throughout the cutting lip length to calculate thrust and force. A normalized radial coordinate ρ is defined which is equal to the ratio of the radial distance of a cutting point from the axis of the tool measured on a plane perpendicular to the axis (r) to the nominal radius of the drill (*R*). The formulation of this model is mainly focused on the influence of the feed rate (*f*), point angels (*ε*), and the geometric relationship of the drill elements. The main geometric relationships of the drill elements are shown in Figure 2.18.

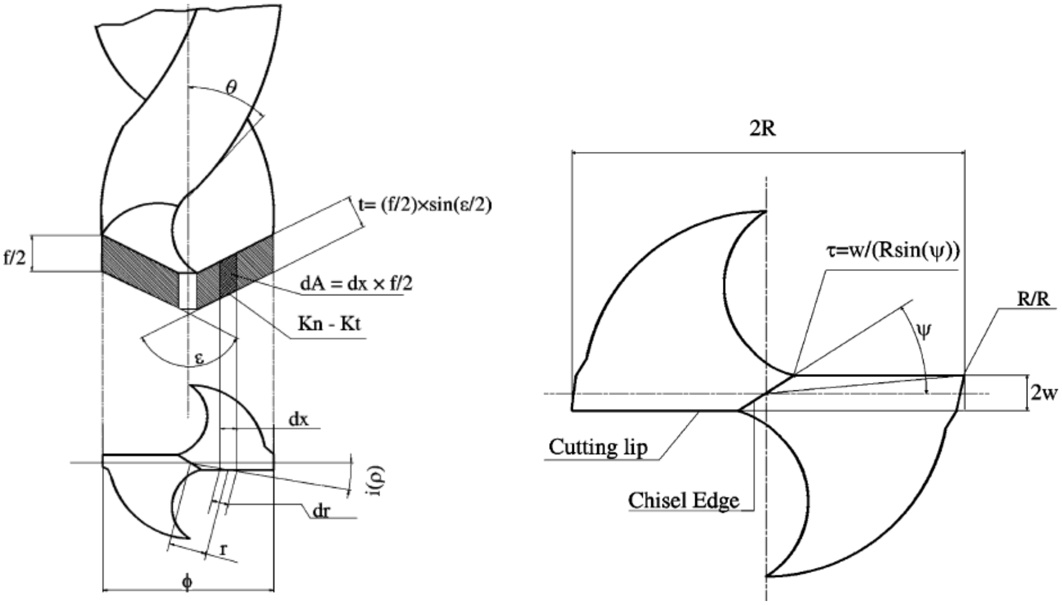

Figure 2.18. Chip load portion and geometric relations [72]

From the definition of normalized radial distance and the geometric relationship, the following equations are formulated knowing that the elementary area dA is a product of dx and *f*/2, where *f* is the feed rate (mm/rev) and *f*/2 is the cutting depth considering that there are two cutting lips.

$$dx = dr\cos\big(i(\rho)\big)\ and\ \rho = {}^{r}/_{R} = \gg dr = Rd\rho \qquad (2.24)$$

And, therefore

$$dx = \cos\big(i(\rho)\big)\, R\, d\rho \qquad (2.25)$$

From Figure 2.18, the following relationship can be deduced.

$$w = \frac{r}{sin(\varepsilon/2)}\sin\big(i(\rho)\big)\; and\; i(\rho) = sin^{-1}\left[\frac{w}{\rho R}\sin(\varepsilon/2)\right] \qquad (2.26)$$

Where ε is the point angle, *w* is half of the thickness of the chisel edge, and *i (ρ)* is the inclination angle of the cutting lip for the tool considered. Here *cos (i (ρ))* can be approximated as follows.

$$\cos\big(i(\rho)\big) = [1 - sin^2 i(\rho)]^{1/2} = \left[1 - \frac{w^2 sin^2(\varepsilon/2)}{\rho^2 R^2}\right]^{1/2}$$

$$= 1 - \frac{w^2 sin^2(\varepsilon/2)}{\rho^2 R^2} \qquad (2.27)$$

To obtain the resultant of all the tangential and vertical forces that are exerted on each cutting lip, an integration is performed in respect of the whole length of the cutting lip as follows.

$$F_v = \int_\tau^1 \left[B \times 10^{-1.089\gamma}\left({}^{f}\!/_{2}\right)^{0.5}\left(1 - \frac{w^2 sin^2(\varepsilon/2)}{2\rho^2 R^2}\right)\right] R\, d\rho \qquad [N]$$

$$F_h = \int_\tau^1 \left[[A + B \times 10^{-1.089\gamma}(f/2)]\left(1 - \frac{w^2 sin^2(\varepsilon/2)}{2\rho^2 R^2}\right)\right] R\, d\rho \qquad [N] \qquad (2.28)$$

The integration limits based on Figure 2.18 are given as:

$$lower = \tau = \frac{w/sin\psi}{{}^{D}\!/_{2}} = \frac{w}{Rsin\psi}$$

$$higher = \frac{R}{R} = 1 \qquad (2.29)$$

Where A and B are coefficients that are to be determined depending on the drill geometry and cutting parameters, γ is the rake angle of the drill, and ψ is the angle of the chisel edge. The thrust force and torque can be calculated from the resolved components of the vertical force (δFr and δFa), which are perpendicular and parallel to the axis respectively as shown in Figure 2.19.

The first component, δFr, is offset by the equivalent and opposite component generated by the other cutting lip, while the second component, δFa, generates a resistant thrust force. To determine the torque value δM, δFh is multiplied by the distance r from the spin axis and to obtain the thrust value δFa it is enough to project δFv in the direction of the axis, i.e. to multiply δFv by sin (ε/2), and these results are given in Equation (2.30). The actual rake angle γ is the sum of two addends of the static and dynamic rake angle, both of which vary in accordance with ρ as shown in Figure 2.19, and it is given in Equation (2.31).

$$T = 2\int_{\tau}^{1} B \times 10^{-1.089\gamma}(f/2)^{0.5}\left(1 - \frac{w^2 sin^2(\varepsilon/2)}{2\rho^2 R^2}\right) \times Rsin(\varepsilon/2)d\rho \quad [\mathrm{N}]$$

$$M = 2\int_{\tau}^{1}\left[[A + B \times 10^{-1.089\gamma}(f/2)]\left(1 - \frac{w^2 sin^2(\varepsilon/2)}{2\rho^2 R^2}\right)\right] \times \rho R^2 d\rho \quad [N\ mm] \qquad (2.30)$$

$$\gamma = \gamma_s + \mu = tan^{-1}\left(\frac{\rho tan\theta}{\sin(\varepsilon/2)}\right) + tan^{-1}\left(\frac{f}{2\pi\rho R}\right) \qquad (2.31)$$

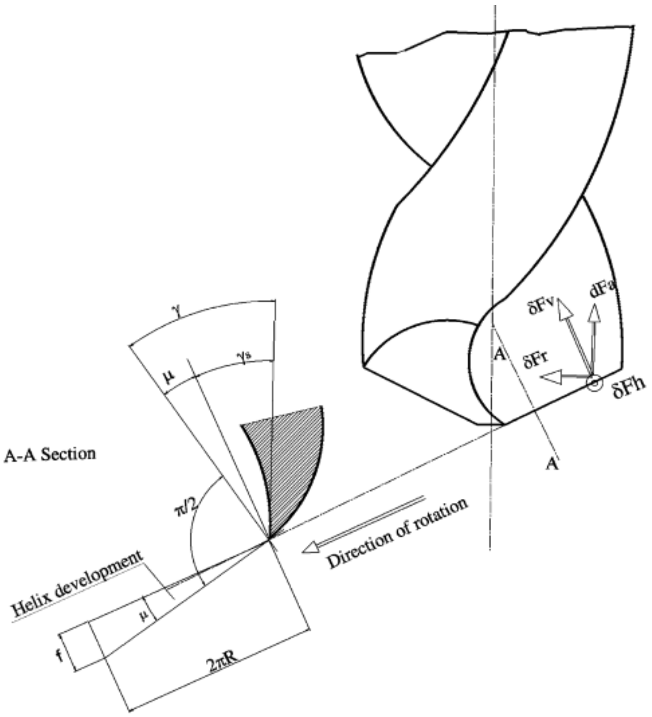

Figure 2.19. The forces exerted on a main cutting lip and the drilling rake angle [72]

The relationships between thrust and torque given above are referred to the whole cutting lip and supply the maximum values measurable during a drilling process performed on composite laminate. To describe the trends of the thrust force and torque values acting on the cutting lip only, the effect of the chisel edge is eliminated by drilling a pilot hole. The variations in thrust and torque, which occur at every instant after the startup of the drilling process, is given by the following relations.

$$T = 2B \times 10^{-1.089\gamma}(f/2)^{0.5} \times \int_{r_p/R}^{r(t)/R} \left(1 - \frac{w^2 sin^2(\varepsilon/2)}{2\rho^2 R^2}\right) \times Rsin\left(\frac{\varepsilon}{2}\right) d\rho \ \ [N]$$

$$M = 2[A + B \times 10^{-1.089\gamma}(f/2)] \times \int_{r_p/R}^{r(t)/R} \left[\left(1 - \frac{w^2 sin^2(\varepsilon/2)}{2\rho^2 R^2}\right)\right] \times \rho R^2 d\rho \quad [N\ mm] \qquad (2.32)$$

Where $r\ (t) = \left(r_p^2 + 2\Delta\left[r_p^2 - (w/2)^2\right]^{0.5} + \Delta^2\right)^{0.5}$ $[mm]$,$\Delta = tfvtan(f/2)$, r_p is the pilot hole radius, *t* is the cutting time, and *v* is the spindle speed. The unknown constants A and B can be calculated based on the following system of equations.

$$B \times 10^{-1.089\gamma} = K_n \ \ [N/mm^2]$$

$$\frac{A}{f/2} + B \times 10^{-1.089\gamma} = K_t \ \ [N/mm^2] \qquad (2.33)$$

Where: *Kn* and *Kt* are specific energies for the vertical and horizontal force respectively.

The value of the trust force due to the chisel edge is given by Equation (2.34) based on the chisel edge rake angle and the specific energy of the chisel edge. Since the contribution of the horizontal component is so small, only the vertical component is considered in the evaluation of the thrust force due to the chisel edge. The values of the specific energies are calculated from the curves of individual experimental tests based on the expressions given by Equation (2.35)

$$T = C \times 10^{-c\gamma_{chisel}} f^{0.5} 2w \;\; [N] \tag{2.34}$$

Where *C* can be calculated $K_{n,chisel} = \; C \times 10^{-c\gamma_{chisel}}$ and

$$\gamma_{chisel} = -(tan^{-1}[tan(\varepsilon/2)\cos(\psi)])$$

$$K_n = \frac{T_{exp}}{2(f/2)^{0.5}\left(\int_{\tau}^{1}\left(1 - \frac{w^2 sin^2(\varepsilon/2)}{2\rho^2 R^2}\right) \times Rsin\left(\frac{\varepsilon}{2}\right) d\rho\right)} \; [N/mm^2]$$

$$K_t = \frac{M_{exp}}{2(f/2)\left(\int_{\tau}^{1}\left(1 - \frac{w^2 sin^2(\varepsilon/2)}{2\rho^2 R^2}\right) \times R^2 d\rho\right)} \; [N/mm^2]$$

$$K_{n,chisel} = \frac{T_{exp}}{f^{0.5} 2w} \; [N/mm^2] \tag{2.35}$$

Ho-Cheng and Dharan [73] studied the phenomenon of delamination damage produced during drilling of composite laminates and proposed a model that relates the delamination of the laminate to drilling parameters and composite material properties. This analysis uses a fracture mechanics approach in which the opening-mode delamination, fracture toughness, and a material parameter were used with a plate model of the laminate. In this model, a center loading of the thrust force on the material through the center of the drill web and a circular crack area under the diameter of the drill was assumed, and an energy balance equation based on linear elastic fracture mechanics (LEFM) was given by Equation (2.36).

$$G\pi(D + 2a)da = F_A\, dx - dU \tag{2.36}$$

Where G is the energy release rate per unit area, D is the diameter of the drill, a is the assumed size of an existing crack length, F_A is the applied thrust force, and U is the stored strain energy. An expression for the critical thrust force at the onset of crack propagation for the case of push-out delamination at the exit was given based on classical plate bending theory as shown in Equation (2.37). Where h in this equation is the uncut depth of the laminate under the tool.

$$U = \frac{8\pi M x^2}{\left(a + \frac{D}{2}\right)^2}$$

Where the displacement x and the moment M are expressed as

$$x = \frac{F_A\left(a + \frac{D}{2}\right)^2}{M} \qquad and \quad M = \frac{Eh^3}{12(1 - v^2)}$$

$$F_A^* = \pi \left[\frac{8G_{IC}Eh^3}{3(1-v^2)}\right]^{1/2} \tag{2.37}$$

Where G_{IC} is the critical strain energy release rate, F_A^* is the critical load at the onset of crack propagation, h is the uncut depth under the tool, E is Young's modulus, and ν is Poisson's ratio. Reasonably good agreement with experimental results for smaller number of plies was reported.

In the case of peel-up model, it was assumed that, the critical peeling force, F_P^*, in the axial direction is related to the horizontal critical cutting force F_C^* by a peeling factor k_p, which is assumed to be a function of tool geometry and friction between the tool and work piece and it is defined by Equation (2.38). Using the same analysis as of push-out model and replacing the uncut depth by the cut thickness, the critical cutting force at the onset of delamination at entrance was derived as shown in Equation (2.39). It has been reported that, the push-out model was verified and showed a good agreement with an existing experimental data, whereas, no experimental data showing entrance damage as a function of the cutting force can be found to compare the peel-up model.

$$k_p = \frac{F_C^*}{F_P^*} \tag{2.38}$$

$$F_C^* = k_p \pi \left[\frac{8G_{IC}E(H-h)^3}{3(1-v^2)}\right]^{1/2} \tag{2.39}$$

Zhang et al. [74] studied the delamination process in drilling of composites and proposed a general closed-form mechanical model for predicting the critical thrust forces at which delamination begins to propagate at different plies. The model is built based on linear fracture mechanics, classical plate bending theory, and mechanics of composites. In this analysis, the energy equation shown in Equation (2.40) was used based on LEFM theory. A clamped delamination zone was assumed, and therefore the boundary conditions for bending were taken as fixed edge.

$$P_C d\omega_o = G_{IC} dA + dU \tag{2.40}$$

Where: P_C is the critical thrust force at which delamination begins to occur, $d\omega_o$ is the displacement of the drill, G_{IC} is the energy release rate per unit area, dA is the area of the crack, and dU is the infinitesimal strain energy.

The constitutive relations between the loading and deformation of a laminate based on the classical laminate theory, equilibrium equation, and boundary condition of the delamination zone along with the ellipticity ratio ($\xi = a/b$) were used to drive the expression for the critical thrust force for multidirectional laminates given by Equation (2.41). Here a and b are half of the delamination size along the fiber direction and normal to the fiber direction respectively. Moreover, it is reported that, this model can be modified and used for different or special laminate lay-up sequences.

$$P_C = \sqrt{\frac{\pi G_{IC}}{\xi(C_3 - K)}} \tag{2.41}$$

In order to check the validity of the model, they conducted experimental drilling with a cutting speed of 12,000 rpm and a feed rate that varies from 0.005 to 0.05 mm/rev using 6 mm tungsten carbide twist drill. They found that, the value of the thrust force increased with the increase of the feed rate and a perfectly good quality hole without delamination was produced at the lower feed rate of 0.005 mm/rev, whereas, a significant amount of delamination was observed at the higher feed rate of 0.05 mm/rev. Overall, it was reported that, the delamination location during the drilling operation is in a good agreement with the experimental results.

Jain and Yang [75] studied the effects of feed rate and chisel edge on delamination in composite drilling, and proposed an analytical model to predict critical thrust force and critical feed rate at which the delamination crack begins to propagate. The analytical model was developed using fracture mechanics, laminate theory, and mechanics of drilling with an assumption of an elliptical delamination shape where the ellipticity ratio (a/b) remains constant and have a clamped boundary condition. Where a and b are half the delamination size along the fiber and transverse directions, respectively. Using the energy balance relation, which is given by Equation (2.42), they drive and proposed the critical thrust force at which the delamination crack begins to propagate, which is given by Equation (2.43).

$$P dw_0 = G dA + dU \tag{2.42}$$

where G is the crack propagation energy, dU is the infinitesimal strain energy, w_0 is the distance moved by the tool, and dA is the increase in the area of the crack.

$$P^* = 3\pi \left(\frac{b}{a}\right) \sqrt{2 G_{IC} D^*} \tag{2.43}$$

Where $D^* = D_{11} + \frac{2(D_{12}+2D_{66})}{3}\left(\frac{a}{b}\right)^2 + D_{22}\left(\frac{a}{b}\right)^4$ and D_{ij} represent the components of the bending stiffness matrix.

The critical thrust force in Equation (2.43) is a function of the ellipticity ratio a/b, and the ellipticity ratio is estimated in terms of the bending stiffness for the possible minimum critical thrust force base on Equation (2.44). From this, the smallest critical thrust force in which there is no delamination below this value is proposed and given in Equation (2.45).

$$\frac{a}{b} = \left(\frac{D_{11}}{D_{22}}\right)^{0.25} \tag{2.44}$$

$$P_C^* = 3\pi^4 \sqrt{\frac{D_{22}}{D_{11}}}\sqrt{2G_{IC}D_C^*} \tag{2.45}$$

Where: $$D_C^* = 2D_{11} + \frac{2(D_{12}+2D_{66})}{3}\sqrt{\frac{D_{11}}{D_{22}}}$$

In addition to the critical thrust force, they also proposed a model for critical feed rate (f^*) for the onset of delamination and this expression is given by Equation (2.46). In this study, a variable feed rate, which starts at high feed rate at the beginning of the drilling process and then decreasing the feed rate progressively, is presented as alternate strategy to avoid delamination. Regarding the effect of the chisel edge, it is reported that, it is possible to reduce the thrust force almost to a third by halving the chisel edge width.

$$f^* = \left\{\frac{d^{1.2}}{1.91}\left[\frac{3\pi}{d^2 H_B}\left(\sqrt[4]{\frac{D_{22}}{D_{11}}}\right)\sqrt{2G_{IC}D_C^*} - \frac{0.101}{d}\right]\right\}^{2.5} \tag{2.46}$$

The model proposed for maximum thrust by Jain and Yang [1994] was

$$P = 0.136H_B d^{0.78} f^{0.4}$$

Further, it was indicated that P varies with $f^{0.317}$ for cross-ply laminates and with $f^{0.224}$ for quasi-isotropic laminates.

Where: d is the drill diameter in mm, H_B is the Brinell hardness number of the material in Kg/mm^2, and f is the feed rate in mm/rev.

Zhang's model [74] presented here is considered as a starting point for the analytical study of predicting the critical thrust force during the drilling process of FRP composites as it succinctly describes the thrust forces in terms of constituent material properties in a closed form for an arbitrary multi-directional laminate. It has been mentioned that a few typographical errors were found in the published work while re-deriving the expressions of strain energy [76], and these errors have been corrected and presented in the final form by Gururaja et al. [76]. The model by Jain et al. required extension to the delamination theory of multi-directional laminates and Zhang et al. [74] carried out this extension. Gururaja and Ramulu [76] studied exit-ply delamination models for drilling of FRPs and proposed a modified exit-ply delamination model. In their modified model, an elliptical delamination zone with clamped boundary condition and a distributed loading has been assumed over the entire delamination zone. The external work done by this distributed load over the elliptical delamination zone has been given by Equation (2.47), where a and b are half the delamination size along the fiber direction and normal to the fiber direction respectively.

$$W = \int_{-a}^{a} \int_{-b\sqrt{1-(x^2/a^2)}}^{b\sqrt{1-(x^2/a^2)}} q.w\, dy\, dx \qquad (2.47)$$

Where: $q = \frac{P_c}{\pi ab}$ $\quad and \quad w = w_o\left(1 - \frac{x^2}{a^2} - \frac{y^2}{b^2}\right)^2 \quad with \quad w_o = C_3 P_c a^2$

Substituting the above expressions back in to Equation (2.47) gives the simplified version of the work done as:

$$W = \frac{P_c^2 C_3}{3} a^2 \tag{2.48}$$

From this and the energy balance equation, they proposed the modified form of critical thrust force expression as:

$$(P_c)_{modified} = \sqrt{\frac{\pi G_{lc}}{\xi\left((C_3/3) - K\right)}} \tag{2.49}$$

Where: ξ= ellipticity ratio (a/b), $K = \frac{\xi}{144\pi D^*}$, and $D^* = D_{11} - \frac{2}{3}(D_{12} - 2D_{66}) - \xi^4 D_{22}$

Figure 2.20 describes Modified Zhang Model yielding the best predictions with experimental observations as compared to other models. A detailed analysis of the Modified Zhang exit-ply delamination model can be found in reference [76]

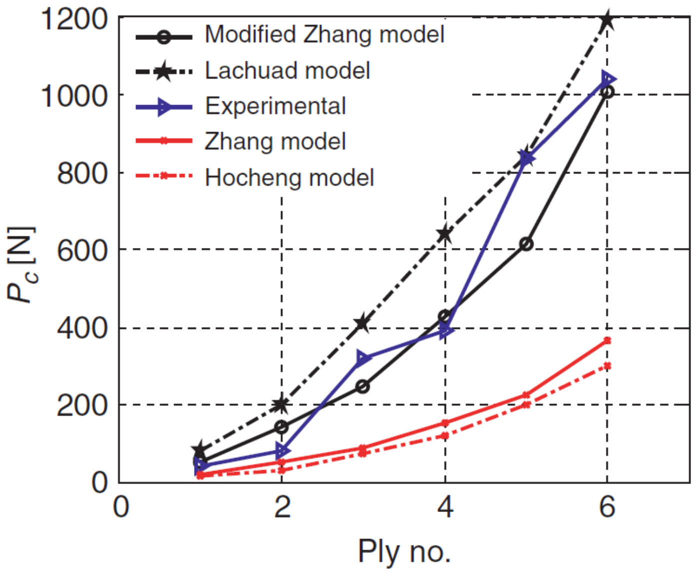

Figure 2.20. Comparison of critical thrust force (Pc) predictions using various models with increasing ply numbers [76]

2.4.4. Hole Quality Assessment by Signal Analysis

As it is has been discussed in the previous sections, many investigations on the drilling of FRP composites are underway including experimental studies, numerical studies, and analytical studies on the area are presented. In recent years, optimizing the quality of drilled holes on FRP composites and developing on process quality monitoring system is a growing interest in the industries. Most studies on the quality of hole during drilling of FRP composites have been relied on the trust force and torque signal analysis to relate damage and defects on drilled holes to process parameters. Several investigation are reported on hole quality assessment using different signal analysis techniques which incorporate acoustic emission (AE) signal, force signal, and vibration signals. Some of the studies conducted on the use different signal analysis on the assessment of hole quality during the drilling of FRP composites will be reviewed in this section.

Drilling and machining experiments were conducted at the University of Washington by material science and technology research group using HSS, PCD, carbide, and cryogenic treated carbide drills on a carbon fiber-reinforced thermoset and thermoplastic composites, namely Graphite/Epoxy, Graphite/PIXA-M (PIXA-M) composites since 1989. Cutting mechanisms were characterized by cutting force signal analysis [77 and 78]. During drilling, force signals were collected from all conditions and analyzed using Fast Fourier Transformations and autoregressive (AR) time series models. Power Spectrums were used to examine the cutting characteristics in the drilling process, whereas, AR coefficients were used to distinguish the cutting signals from autoclaved PIXA-M composites, induction heated PIXA-M composites, conventional carbide drill, and cryogenic treated carbide drills. Their results showed that, composite consolidation process affects the cutting characteristics and surface quality of PIXA-M composites. In drilling of autoclaved PIXA-M composites, deeper fiber pullouts on the machined surface are observed, while matrix smearing is dominant in induction heated PIXA-M composites. High frequency components of the force signal can be found in drilling of autoclaved PIXA-M composites, and it exhibits high sensitivity to burst type cutting force signal and fiber pull-out in the process. A strong correlation between AR coefficients and the cutting characteristics was found. Combinations of model coefficients that maximize the discrimination index seem to depend more strongly on the consolidation processes, rather than on cutting conditions such as drilling speeds and cryogenic treatment of carbide tools.

Mascaro et al. [79] studied the characteristics of acoustic emission from the drilling of CFRP composites and reported the experimental results of AE generated during the drilling of CFRP. They conducted the drilling experiment on a 10 mm thick CFRP plate using standard drill with a constant thrust force and rotational speed of 550 rpm. A standard HSS twist drill of 9 mm diameter, a mill of 9 mm diameter with two cutting blade, and a PCD drill of 7.64 mm diameter were used in this study. V-101 500 KHz wide band transducer and a digital storage oscilloscope at a sampling rate of two mega samples per second were used for the AE signal acquisition. During the drilling process of the full thickness, five AE signals from different depth of drilling were stored and concatenated to make only one representative signal. The study show that, in all drilling configurations, the drilling process produced a characteristic acoustic signature in the frequency range of 150 – 200 kHz, and this frequency band is independent of the tool geometry, rotational speed, and thrust force. The energy of the acoustic signature was sensitive to tool wear and it constitutes a good feature for AE monitoring. In addition, the higher frequencies of the AE were related to the cutting of the carbon fibers.

Rotem [80] studied the characteristics of acoustic emission generated from a hole in a composite laminate. In this study, statistical method of pattern recognition was used to decide the source of detected AE parameters by examining a few parameters from some events. Five parameters: (1) the slope of the amplitude histogram, (2) rise rate of the AE signal, (3) period of the AE signal, (4) the width of the signal, and (5) the frequency spectrum of the signal were chosen in the characterization of the AE signal. Three types of laminates: angle-ply (± 45^0), angle-ply (± 15^0), and unidirectional laminates, which all have a thickness of 1 mm made of 8 plies were used in the experiment. A 5 mm diameter hole was drilled on half of these specimens using a tungsten carbide drill tool and then all the specimens were clamped in a tensile machine with an AE transducer mounted on them, after which they were loaded to 30 % of the failure load. The results from this test were analyzed to give the AE parameters of the signal for use in the pattern recognition method. Fast Fourier Transform (FFT) was carried out on the stored signals, and it did not give a conclusive unique value for the descriptor purpose and therefore a method called Maximum Entropy Spectral analysis were used in the analysis. Where this method filters the coefficients, concentrates the result around one or two values, and is thus more suitable for pattern recognition descriptor. It was reported that, the results from laminates with hole shows less steep slope than the laminates without a hole, whereas, the width of the signal obtained from the laminates with hole become larger than the one without a hole. For the other descriptors, the trend was not uniform. In addition, it was noted that, from the results of the histogram slope, the effect of the hole is to give a unique value for the slope regardless of the laminate construction.

Ravishankar and Murthy [81] studied the application of acoustic emission in drilling of composite laminates. In this study, a 2.5 mm holes were drilled on a 12 ply and 16 ply cross ply glass fiber reinforced plastic (GFRP) using HSS drill tool, and acoustic emission signal was acquired using a 300 kHz broadband piezoelectric-type sensor. The total AE signal obtained during the drilling process was given by the summation of AE signals from different sources as shown in Equation (2.50). In which the sub scripts in the given equation are T is the total, M the matrix, F the fiber, f the friction, and D the delamination.

$$AE_T = AE_M + AE_F + AE_f + AE_D \tag{2.50}$$

Two approaches have been proposed for the signal to source identification in the drilling process. (1) Examine the signal characteristics of each source constituents (macro and/or micro) when drilled separately to quantify the energy levels, and (2) obtain the total signal, which contains energy due to all of the sources, and look for typical parameter/parameters that can characterize the individual sources. Based on the root mean square (rms) value of the AE signal, it was reported that, at a given thrust/feed rate, the complexion of the AE signature changes from the entry to the exit of the drill and an overall change in the signature occurs as the applied thrust increases. The signal levels increase as the drill translates further, where this phenomenon occurs in all of the three mechanisms (contact friction, drilling, and peripheral friction). In addition, the AE signal was dissected in to two parts as static part, which rises up as the drill enters and exits and as dynamic part, containing crests and troughs oscillating about the mean value of the static part. Small spikes were noticed just prior to the highest spike, and the small spike was attributed to the delamination damage at the exit and the highest spike was attributed to the breaking of glass fibers and the local splintering action.

Arul et al. [82] conducted experimental investigation to determine the relationship between AE rms and cutting parameters during drilling of polymeric composites. Drilling trials were performed on 4 mm thick woven GFRP composites using a 6 mm diameter HSS drill with a cutting speed of 9.43 – 30.16 m/min and feed rate of 0.02 – 0.08 mm/rev. AE signal was measured with a Kistler wide band piezoelectric AE sensor, and the thrust force during drilling was also measured using Kistler two-component dynamometer. From the thrust force measurement, it was seen that, the effect of the cutting speed on thrust force was less significant than that of the feed rate, and the thrust force increases with the increase of the feed rate, which is also reported by others [26, 28, and 32]. Two spikes in the AE signal, small and large and were observed and associated with damage modes, where the small spike attributed to delamination, while the large spike for breakage of the glass fibers, which is also reported by others [81]. The power of the AE signal progressively increases with the number of holes drilled, and after 30 holes there is a sudden rise in power of the signal for which, the higher order of stressing of the material resulting in fiber cracking, matrix crazing, and other associated defects was accounted for the rise in power. The AE rms values increased with the increase of cutting speed from 18.85 – 23.56 m/min, and this was taken as indication that, the cutting is good in this region; in the other hand, the decrease of the AE rms value was associated with the deterioration in performance of the drill. Higher order of AE rms also associated with large hole shrinkage, indicating higher order relaxation with hole shrinkage.

Velayudham et al. [83] studied the influence of drilling variables on thrust, torque, and vibration signals when drilling glass fiber reinforced laminated composites with higher order of fiber volume fraction. They used Wavelet Packet Transform (WPT) to characterize the vibration signal acquired through an accelerometer, which was mounted on the specimen, and thereby to evaluate the status of the tool and to study the cutting mechanism. From the observation made on thrust force and torque, the best possible machining condition was reported at drilling speed of 80.4 m/min and feed rate of 315 mm/min. A good correlation between vibration power spectrum and wavelet packet transform was also reported. A predominant peak appeared in the power spectrum at a frequency of approximately 1500 Hz was attributed as an indicator of tool performance induced defects such as delamination, whereas, debonding was associated with relatively low frequency components. In the other hand, lower order level of wavelet coefficients were attributed to the uniform and clean cutting of fibers. A rapid increase in vibration power and corresponding wavelet coefficient was related to a critical tool wear.

Hossein et al. [84] employed acoustic emission sensing for online detection of process-induced damage during drilling of composites and wavelet based signal processing was used in the study. The drilling experiment is carried out on a unidirectional and cross ply E-glass fiber reinforced polyester resin composite using a standard HSS twist drill of diameter 10 mm. Acoustic emission signal was collected using PCI-2 system with broad band piezoelectric transducer sensor. The study shows that, the AE rms values increased with the increase of cutting speed from 9.42 to 15.7 m/min, which was cited as an indication of a good cutting condition for this region. When the cutting speed increases above 15.7 m/min, the AE rms value start decreasing, which is also related to deterioration in the performance of the drill and associated rubbing as indicated by high amplitude, low frequency peak as well as low rms value (low energy release). An optimal drilling condition during drilling was chosen based on the lowest thrust force measured and at this optimum drilling condition, relatively higher amplitude of AE rms values associated with dominant higher frequency peaks was observed. A dominant frequency range of delamination was established from the wavelet analysis. When drilling the unidirectional laminate, this dominant frequency range is found to be from 62.5 – 125 KHz, whereas, when drilling the cross ply laminate is from 125 – 250 KHz.

2.5. Summary

In composite manufacturing and assembly, 60% of part rejection is accounted due to defective or poor quality hole. In recent years, investigating the response of CFRP composites towards various machining process have become the foremost interest of many researchers. In attempt to avoid or reduce process induced damages during the machining and drilling of FRP composite materials numerous studies have been conducted and are underway. From these studies, selected materials on experimental studies, numerical studies, analytical studies, and the use of signal analysis on the machining mainly on drilling of FRP composites are reviewed in this chapter. The main outcomes of this review can be summarized as follows.

1. Most of the investigations were focused on characterizing the drilling process of FRP composites in terms of cutting forces, surface roughness, and delamination. Results of these investigations were used to correlate the quality the drilled hole to various drilling parameters such as cutting speed, feed rate, laminate configuration, and drill geometry.
2. The dominant process induced damage during the drilling process was found to be delamination. According to most of the studies, exit-ply or push-out delamination is the most dangerous of all damage type and a substantial amount of experimental studies were concentrated on empirically relating delamination to thrust force.
3. Most of the analytical studies on the drilling of FRP composites are focused on the prediction of the critical thrust force at which delamination will occur.
4. Studies focused on the investigation of fiber pullout during drilling are very limited compared to the coverage given to the study of delamination.

5. The numerical studies and simulation of the drilling process of FRP composites are very fewer than the work done on other machining processes of FRP composites.

6. Limited investigations are reported on on-line defect monitoring during drilling of composites materials using acoustic emission and vibration signal analysis. However, there is no study available either on the quantification of damage or on-line monitoring of drilling defects of composite materials.

CHAPTER 3: RESEARCH OBJECTIVES

In aerospace industry, part rejection at the assembly stage due to drilling induced defect and a high rate of tool wear are major economic problems. It is neither practical nor economical to inspect for drilling induced defects and to measure the condition of the drill tool for each hole drilled during or between each operation, so developing on-line monitoring method is a vital concern for industries. In this study, a new approach has been proposed utilizing, force analysis, acoustic emission analysis, and vibration signal analysis to examine the relationship between signal response and drilling induced damage and defects. In addition, a novel approach of using an audio microphone signal analysis was employed to develop an on-line tool wear monitoring system and on-line detection of gaps when drilling CFRP stacks is proposed.

This research investigated drilling induced damages and defects experimentally when drilling different types of CFRP composites through surface roughness, drilling forces, fiber pullout measurement, delamination measurement, and study of drilled hole surface morphology. The relationship between drilling induced damages and drilling conditions and parameters will be investigated experimentally. On-line detection and monitoring of tool wear will be developed using an audio microphone as an acoustic sensor in addition to using drilling forces and acoustic emission signals. Developing of an on-line detection and estimation of gaps when drilling CFRP composite stacks using an audio microphone as an acoustic sensor along with thrust force, acoustic emission, and vibration signals will be carried out in this research. In addition, critical thrust force at the onset of delamination will be experimentally investigated through a punch test and an analytical model to predict critical thrust force at the onset of delamination using linear elastic fracture mechanics (LEFM) and plate bending theory will be developed.

The main objectives of this research are experimental investigation of process-induced damage and defects when drilling CFRP composites materials, developing an on-line monitoring system for monitoring of the condition of the drill tool and for detection of gaps when drilling CFRP composite stacks, and develop an analytical model of critical thrust force at the onset of delamination. These objectives are summarized as follows.

1. Damage and defects when drilling CFRP composite materials
    - Experimental study of drilling induced damage and defects such as surface roughness and morphology, fiber pullout, and delamination. Characterize the type and severity of these damage and defects through SEM examination and study the influence of drilling conditions and process parameters on the resulting damages and defects. Derive equations for thrust force prediction based on Shaw's thrust force equation.
2. Ply-by-Ply cutting action when drilling CFRP composites
    - Perform a systematic study with a series of experimental blind hole drilling on a unidirectional CFRP composites at various depths with various depths ranging from two plies up to fourteen plies with increments of two ply thickness and study the cutting mechanism and peel-up delamination through optical and SEM microscopy.
3. Exit delamination model and experimental verification
    - Conduct experimental investigation of critical thrust force at the onset of delamination through a punch test and develop an analytical model for the critical thrust force at the onset of delamination using linear elastic fracture mechanics (LEFM)

4. On-line detection and monitoring of tool wear
    - Investigate drill wear when drilling multi-directional and uni-directional CFRP laminates using HSS and carbide drill tools and acquire force, acoustic emission, and audio microphone signals. Process the acquired signals and develop an on-line detection and monitoring of drill wear using the amplitude of the acquired signals and recurrence quantification analysis (RQA) method.
5. On-line detection and estimation of gaps when drilling CFRP composite stacks
    - Conduct experimental drilling on CFRP stacks and collect force, acoustic emission, vibration, and audio microphone signals. Perform signal processing on acquired signals and develop a method for on- line detection and estimation of gaps when drilling CFRP composite stacks.

CHAPTER 4: EXPERIMENTAL SETUP AND PROCEDURES

4.1. Introduction

To achieve the objectives of this research, different types of experimental investigations on the drilling process of FRP composites and drilling induced damages and defects were conducted. Four types of signals were acquired during the drilling operation followed by inspection and measurement of drilling induced damage and defects. In this chapter, drill tool materials used, experimental setup, workpiece materials, experimental procedures, measurement methods of various signals, damage inspection, and detailed information on hardware and software used in this research will be presented.

4.2. Workpiece Materials and Specimen Preparation

The Boeing Company kindly donated all work piece materials used in this experimental investigation. Two types of multidirectional laminates, quasi-isotropic laminate, and unidirectional laminates are the four types of CFRP laminates used in this study. The two multi-directional CFRP materials have similar stacking sequence having a thickness of 7.62 mm and 39 plies with an average ply thickness of 195 µm but have different surface ply. Where the former have a surface ply made of fiberglass dry scrim on both tool and bag side, whereas, the latter is with a plain weave fabric as the exterior surface plies on both sides. These panels were made with a symmetrically repeated ply layup of [0/45/-45/90] to obtain the desired thickness with a fiberglass dry scrim and a plain weave fabric as a surface plies, where details of the layup will be discussed in chapter 5. The third material is a quasi-isotropic CFRP laminate composed of 10 plies having a thickness of 2 mm with an average ply thickness of 200 µm and it is made up of symmetrical stacking sequence of $[0,45,90,-45,0]_s$. The fourth material is a unidirectional

CFRP laminated with an average ply thickness of 192 µm and three different thicknesses of 6.35, 12.7, and 19.05 mm were used in this investigation.

All materials were prepared to the desired size for various experimental studies. An abrasive water jet was used for cutting work pieces from the large panel to various sizes required. Most of the specimens were cut to the size of 76 by 101 mm, 76 by 152 mm, 101 by 152 mm, and 127 by 178 mm based on the requirements of different experiments conducted in this study. Each specimen was inspected for surface and edge flaws or defects, which might be caused during the cutting, and preparation process before the experiment is conducted on it.

4.3. Drill Tool Materials

In this investigation, high-speed steel twist drill (HSS), carbide twist drill, and polycrystalline diamond (PCD) eight-facet drill were used to conduct the drilling experiments. The HSS drill tools were purchased from a distributer, whereas, the carbide drill tools, which are a product of ultra-tool, were purchased directly from the manufacturer. The eight-facet PCD drill is a product of STF precision and was acquired from the manufacturer. Basic geometric values of these drill tools are given in Table 4.1, whereas, and their optical images are shown in Figure 4.1.

Table 4.1. Basic geometric values of the drill tools

Drill Tool	Point Angle (Degrees)	Helix Angel (degrees)	Lip Length (mm)	Flute Length (mm)	Overall Length (mm)
HSS	118	25	4	72	108
Carbide	118	25	3.8	50.8	82.6
PCD	--	25	---	26	75

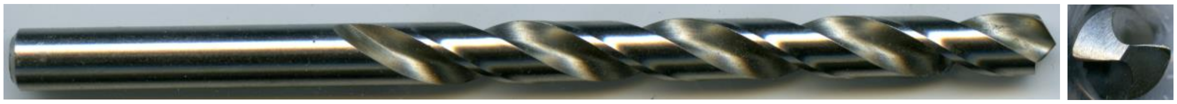

(a) HSS Drill

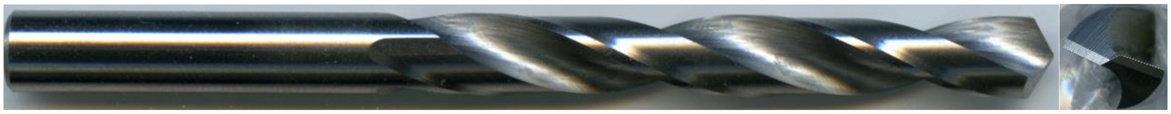

(b) Carbide Drill

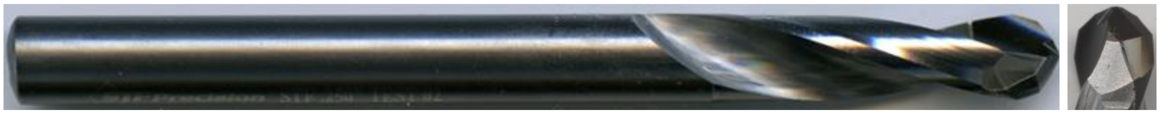

(c) Eight-facet PCD Drill

Figure 4.1. Optical images of drill tools used

4.4. Experimental Work

The experimental part of this investigation is mainly consist of conducting experimental drilling operation and measuring drilling forces, acoustic emission signals, vibration signals, and recording audio microphone signals during the drilling process followed by inspection and measurement of drilling induced damage and defects. The experimental setup, hardware, and software used for various measurements, damage inspection, damage measurement, and other experimental works will be presented in the following sections.

4.4.1. Machining System

All drilling operation in this investigation was carried out using a Haas TM1P three – axis milling machine, which is equipped with Kistler Type 9123C rotating dynamometer except one set of punch test experiment presented in chapter 7, where Kistler Type 9257BA plate dynamometer was used instead of rotating dynamometer. The machining center is shown in Figure 4.2. The spindle of this mill is a direct speed belt drive with a maximum rated power of 5.6 kW, a maximum rotational speed of 6000 rpm, and a maximum feed rate of 10.2 m/min. The allowable travels in the X, Y, and Z-axis are 762, 305, and 406 mm respectively. The machine is equipped with a tool changer, which have capacity of holding 10 tools and maximum tool diameter of 89 mm. Detailed technical specification data for the machining system is given in Appendix A. 1.

Figure 4.2. Haas TM1P three – axis milling machine

4.4.2. Work Holding Fixture

A custom modular adjustable fixture was fabricated from steel to hold and consistently locate the work piece. The fixture is adjustable so that a work piece of various sizes from 25.4 to 127 mm in width can be accommodated with an increment of 25.4 mm. The fixture has a capability of accommodating a work piece with a maximum length of 203 mm and the thickness of the work piece can vary as needed. Figure 4.3 shows the schematic diagram of the modular fixture.

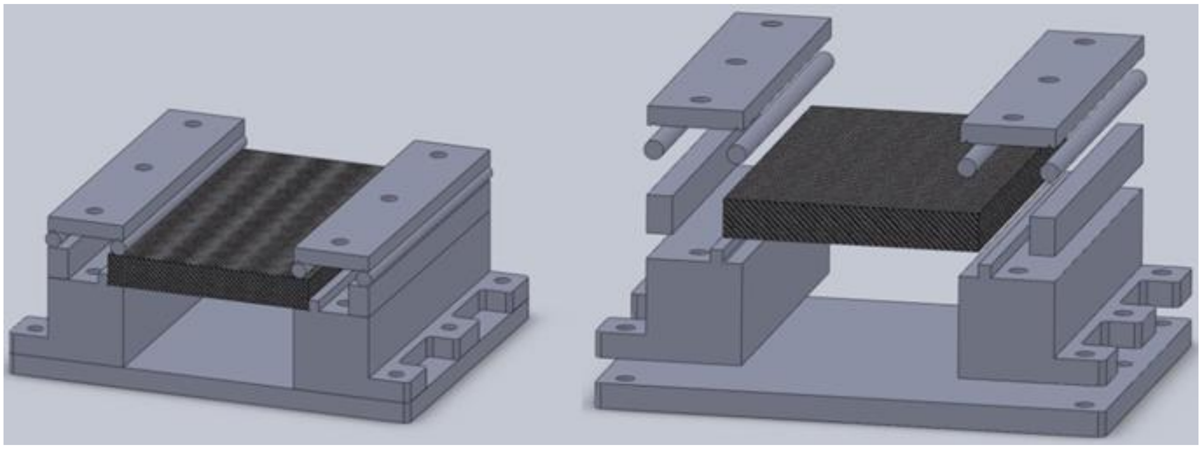

Figure 4.3. Schematic diagram of the custom made modular fixture

The drilling operation was carried out using a high speed steel (HSS), carbide, and polycrystalline diamond (PCD) twist and eight facet drills, with different drilling parameters of cutting speed varying from 1500 – 6000 RPM, and feed rate from 50 – 320 μm/rev. In the drilling operation, four different signals namely, drilling force signals, acoustic emission, accelerometer, and microphone signals were acquired with the appropriate data acquisition systems based on the target of the experiment. Description and methodology of acquiring these signals are given in the following sections.

4.4.3. Drilling Forces Measurement

Measurement of drilling forces were accomplished by using Kistler Type 9123C rotating dynamometer and Kistler Type 5223 signal conditioning box along with Kistler DynoWare DAQ pc software – input via pci DAQ card. The output format of the system for the measured quantities was ASCII. The sampling rate of 7.8 kHz was used in the force signal measurements. Detailed technical specification data for the drilling forces measurement system is given Appendix A. 2. For each drilled hole, different force components such as force in the x-direction (F_x), force in the y-direction (F_y), force in the z-direction (F_z), and the torque (M_z) were measured and from these measured force components, the tangential force (F_t) and the radial force (F_r) were calculated. From all these measured drilling forces, the thrust force and torque were the two primary force quantities used in the analysis of this investigation. The schematic representation of drilling forces measurement system is shown in Figure 4.4. Kistler Type 9257BA plate dynamometer was used for the punch test experiment discussed in chapter 7.

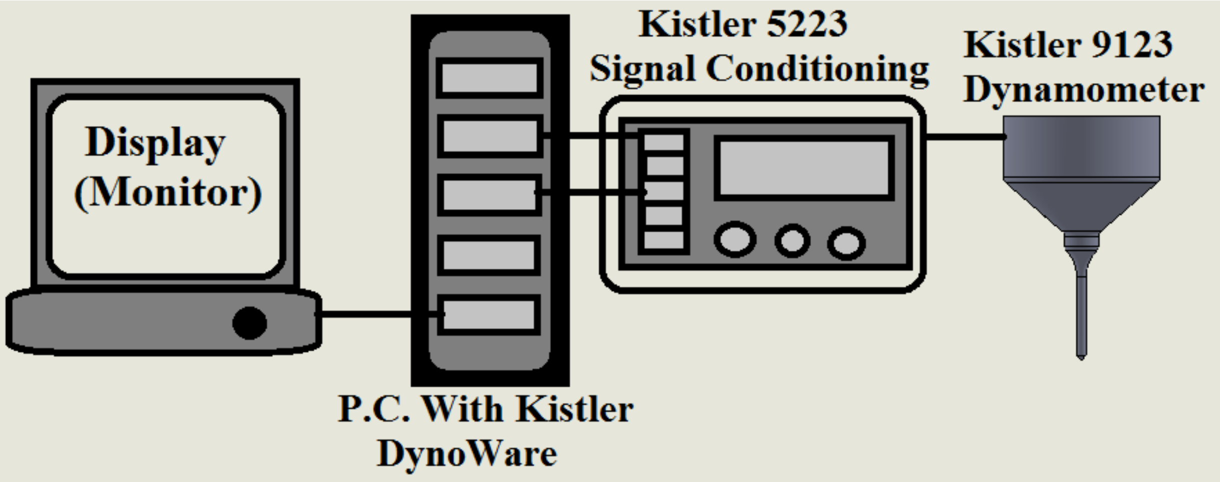

Figure 4.4. Schematic diagram of drilling forces measurement system

4.4.4. Vibration signal Measurement

Two Wilcoxon 732A single-axis high frequency accelerometers were used to acquire and measure the vibrational signal during the drilling experiment. The accelerometers have a sensitivity of 10 mV/g and a maximum acceleration range of 4900 m/s^2. Model P704B general – purpose power unit powered by 9 V. alkaline battery with BNC signal input – output connectors were used for power supply. National Instruments NI 9234 signal acquisition module and Lab View data acquisition software with a sampling rate of 50 thousand samples per second were used to capture the vibration signal. Technical specification data for the high frequency accelerometer is tabulated in Appendix A. 3. The two accelerometers were attached to the work piece and positioned 90^0 each other using a screw on a pre-drilled hole to the work piece. An optical image of the location of the two accelerometers and detailed view of the accelerometer sensor are shown in Figure 4.5.

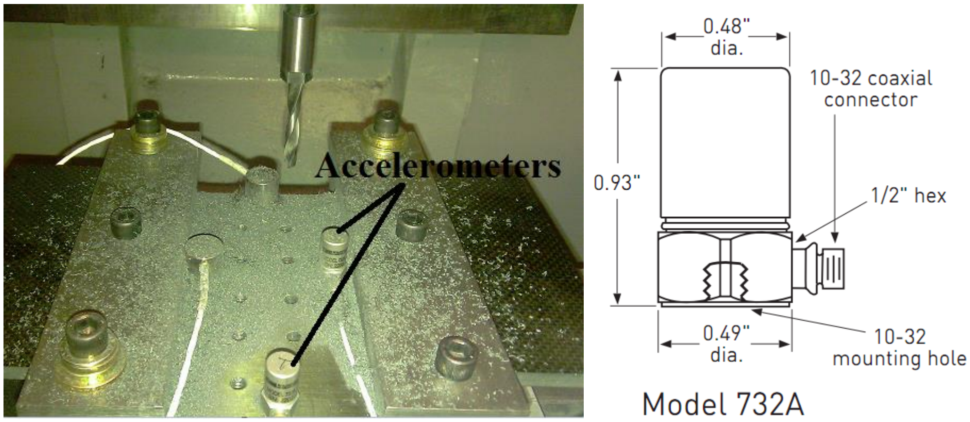

Figure 4.5. Location of accelerometers (left) and detailed view of accelerometer (right)

4.4.5. Acoustic Emission Measurement

Acoustic emission (AE) signal was acquired using a Physical Acoustic PCI-2 AE system with AEwin PCI-2 software and WIN-POST post processing software along with two WD wideband acoustic sensors and 2/4/6 pre-amplifier. The PCI-2 system is equipped with 2 channels, AE data acquisition and digital signal processing system on a full-size PCI card and it uses 18 bit A/D conversion, 40 mega samples/second acquisition with sample averaging, and automatic offset control. The systems used in the acoustic emission data acquisition are listed in Table 4.2.

Table 4.2. List of systems used in AE measurement

Name	Type	Make
AE system	PCI-2 AE system 2-channel card	Physical Acoustic
Software	AEwinPCI-2 and WIN-POST	Physical Acoustic
Amplifier	1220-5054,2/4/6 Preamplifier	Physical Acoustic
Sensor	WD wideband differential sensor	Physical Acoustic

The two-wideband AE sensors were positioned 90^0 each other in most cases and attached to the work piece using Sonotech Ultragell II coupling gel. Figure 4.6 shows an optical image of the placements of acoustic emission sensors. During the drilling operation, main AE signal characteristics such as energy, count, rms, power, rise time, average frequency, and peak frequency were measured. The main AE signal processing features and specifications are tabulated in Appendix A. 4. Schematic representation of acoustic emission measurement system is shown in Figure 4.7.

Figure 4.6. Optical image of AE sensor placement

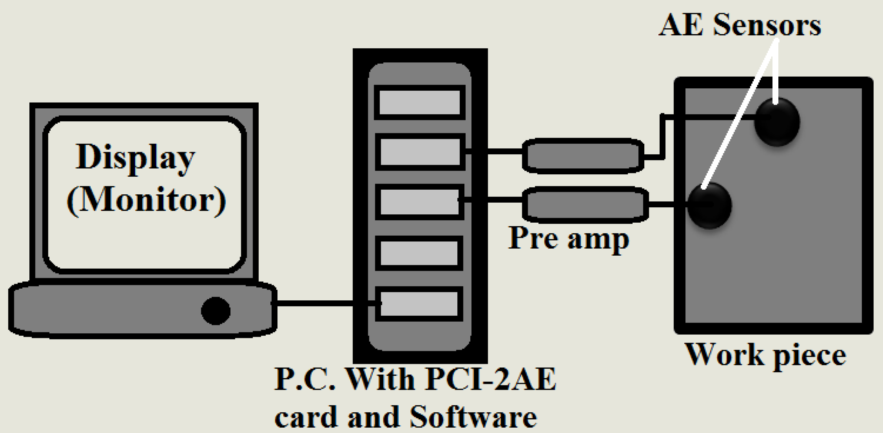

Figure 4.7. Schematic diagram of acoustic emission measurement system

4.4.6. Air-coupled Audio Signal Recording

In addition to Physical Acoustic PCI-2 AE system, an air-coupled audio signal recording system was used by utilizing a Sony ECM-719 audio microphone recorder. This microphone has a frequency response of 100 Hz – 15 kHz. National Instruments NI 9234 signal acquisition module and Lab View data acquisition software were used to capture and record the acoustic signal from the audio microphone. The microphone was mounted on the modular fixture through a bracket made of steel sheet. Figure 4.8 shows an optical image of the mounting and placement of the stereo microphone and schematic diagram of the audio signal recording system. The schematic diagram of all measuring systems as an integrated system is shown in Figure 4.11.

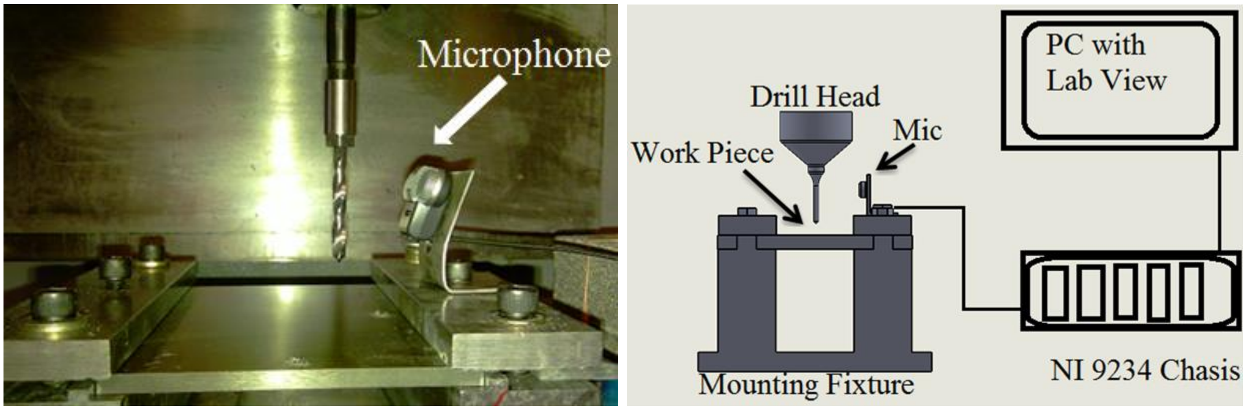

Figure 4.8. Optical image of microphone placement (left) and audio signal recording system (right)

4.5. Inspection and Measurements of Damage

After the drilling operation, drilled holes were inspected and examined for possible drilling induced damages and defects. Micro-Vu Toolmakers microscope, which has a magnification range from 35 to 205 X and Nikon digital microscope were used to inspect and measure all possible drilling induced micro and macro damages on the top and bottom surface of the hole to evaluate circularity. Once the necessary measurements and images of the full hole has been taken, the work pieces with a drilled holes were sectioned in to two halves using a diamond circular saw and/or band saw in order to utilize access for inspection of the drilled hole surface. Figure 4.9 shows a schematic representation of how sectioning was made after the drilling was done.

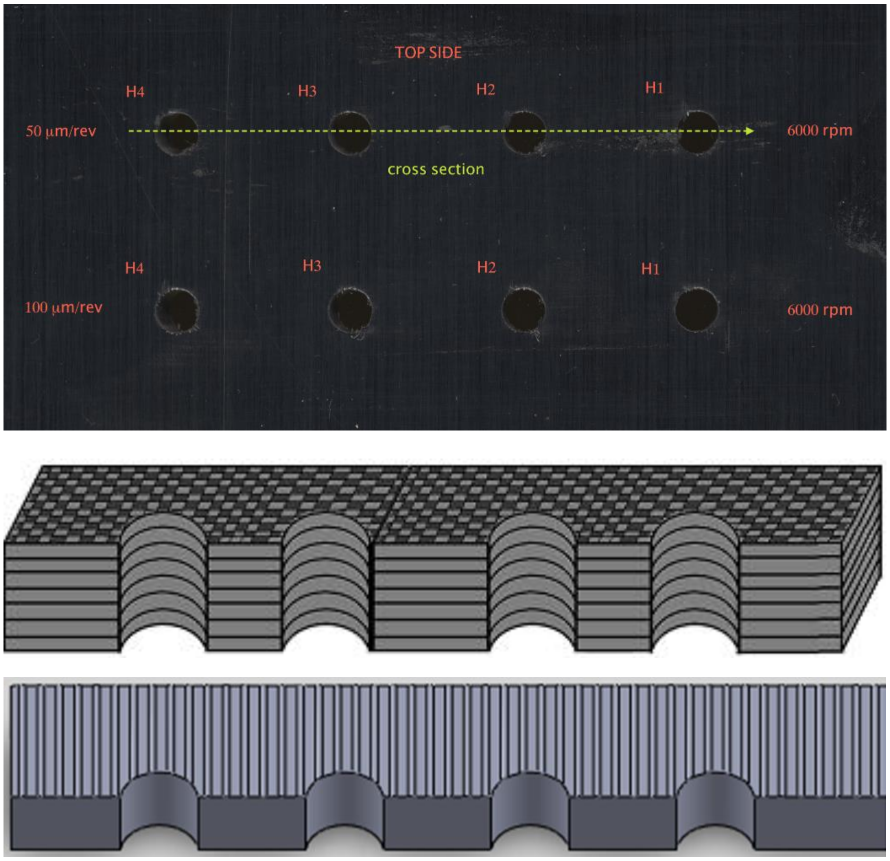

Figure 4.9. Schematic diagram of sectioned work piece

After the sectioning of the holes, various damage and defect inspections and measurements were performed. MahrSurf XR20 surface profilometer with a probe stylus radius of 2 µm and a cut-off length of 0.8 mm was used to measure the surface roughness of the sectioned surface of drilled holes. Once surface roughness measurement and inspection of damage and defects using the above two microscopes is completed, the sectioned holes were cut out individually in order to prepare samples for electron scanning microscopy (SEM) for further inspection. FEI Sirion scanning electron microscopy was used for detailed damage analysis and inspection. An optical image and a schematic representation of a sample prepared by sectioning holes individually for SEM inspection is shown in Figure 4.10.

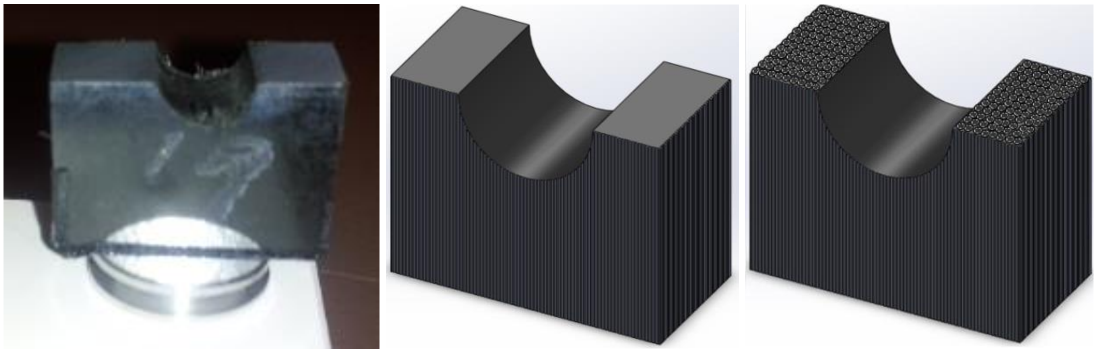

Figure 4.10. An optical image (left) and schematic representation of sectioned SEM sample (right)

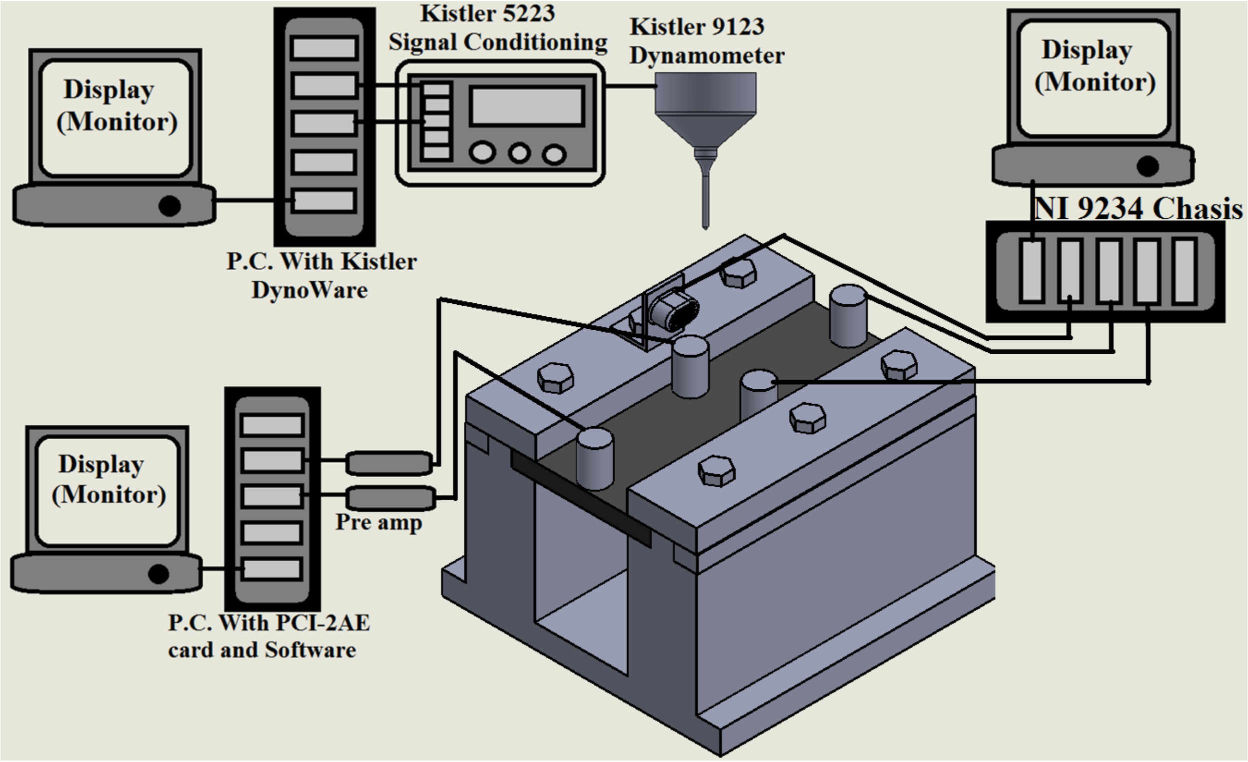

Figure 4.11. Schematic diagram of the complete experimental setup

CHAPTER 5: DAMAGE AND DEFECTS WHEN DRILLING CFRP COMPOSITES

5.1. Introduction

The drilling process of CFRP composite materials is more complex than the drilling of metallic alloys, as the drilling of CFRP composites introduces process induced damage and defects, which do not occur in the drilling of metallic alloys. The inhomogeneous and anisotropic property of FRP composites and the abrasive nature of the reinforcing fibers along with the complexity of the cutting tool geometry make the production of a good quality hole a difficult task by creating process-induced damages and defects during the drilling process. FRP drilling induced damage, which may compromise structural integrity, includes spalling, delamination, fiber pullout, matrix crack, matrix smearing, and fiber breakout. More than 60% of composite part rejections at the assembly stage are due to poor quality of drilled holes [6]. While suppressing some drilling induced damage could be achieved by optimizing drilling parameters such as cutting speed, feed rate, and tool geometry, eliminating all rejectable defects remain a big challenge. Figure 5.1 shows a schematic representation of common drilling induced damage and defects when drilling CFRP composites.

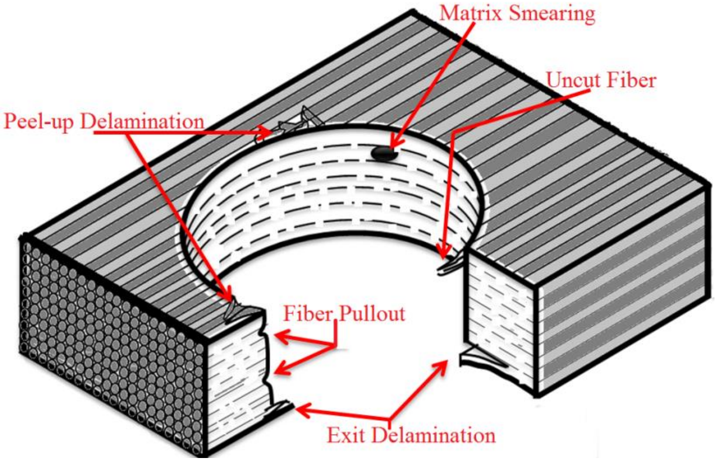

Figure 5.1. Schematic representation of common drilling induced damage and defects

The chip formation mechanism is a controlling factor that makes drilling of FRP composites complex and different from drilling of traditional metallic alloys. In metallic machining, shearing is the major chip formation mechanism, whereas, in the case of FRPs local bending at the fiber-matrix interface controls the chip formation. During the drilling of FRP composite materials, the cutting edge encounters the reinforcing fibers at different angle at every instant of the cutting action (drilling process). The interaction angle between the cutting direction and the orientation of the reinforcing fiber varies based on the location of the cutting edge throughout the circumference and the stacking orientation of each individual plies. Based on the angle of interaction, the main cutting mechanisms are take place by delamination, by fiber buckling, by fiber cutting, by deformation, and by shearing (by plow up). Most of the damage and defects occurred during the drilling process are dependent (related) to this interaction angle between the cutting direction and fiber orientation. The major areas (sectors) of the interaction angles and four major cutting mechanisms as stated in the review are adopted and shown in Figure 5.2, related with drilling process cutting mechanisms. The process repeats itself during circumferential and axial travel of the drill.

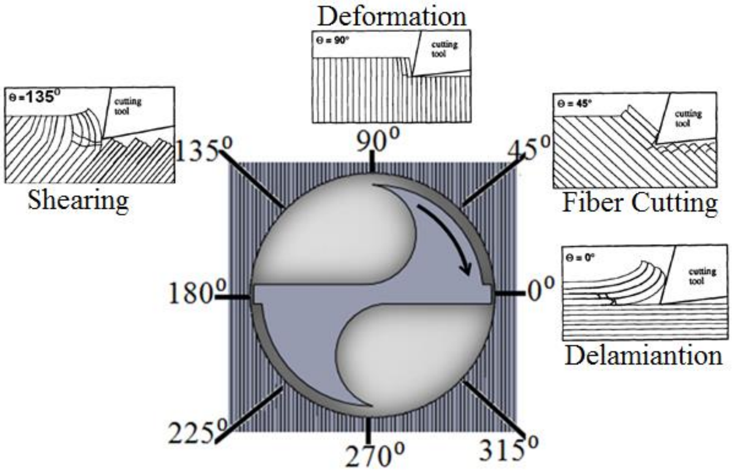

Figure 5.2. Schematic of major sectors of fiber-cutting edge interaction angles and cutting mechanisms (adapted from [12])

Figure 5.3 shows an SEM images of most common drilling induced damages and defects. Exit delamination and fiber pullout are the most severe process induced defects. The amount, location, and severity of these drilling induced damage and defects vary depending on the type and geometry of drill tool used, drilling conditions, and the stacking sequence of the CFRP composite. An experimental investigation of drilling induced damage and defects when drilling CFRP composites composed of different types of stacking sequence using a 6.35 mm carbide twist drill and an eight-facet PCD drill will be presented in this chapter. The experimental conditions and material used are given in Table 5.1.

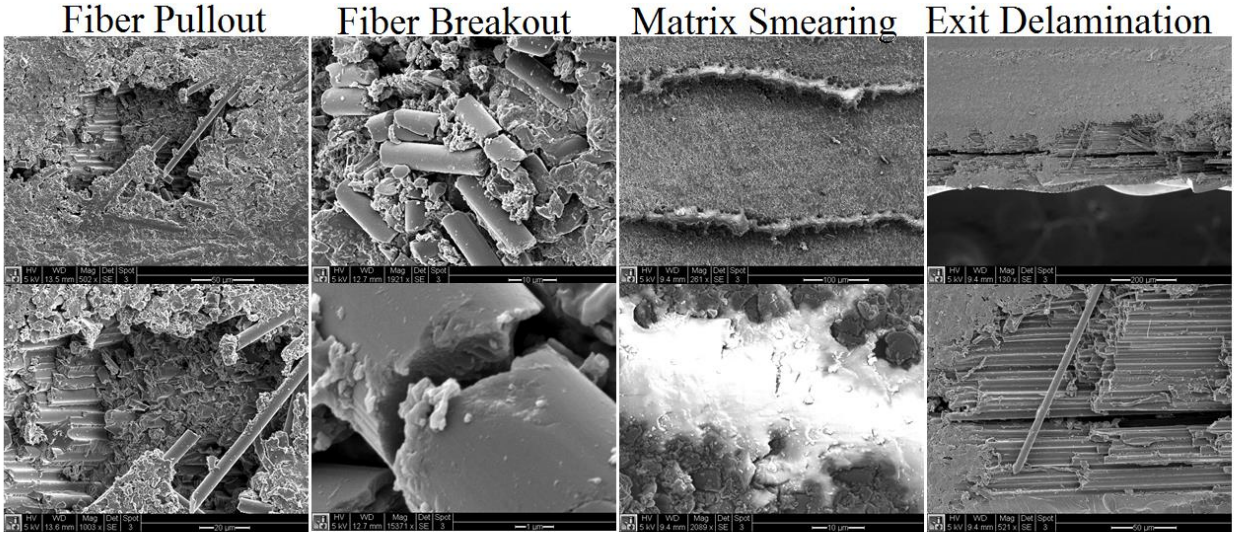

Figure 5.3. An SEM image of common drilling induced damage and defects

Table 5.1. Experimental conditions and material used

Work Piece Material	Signal Acquired	Drill Tool	Cutting Speed (rpm)	Feed Rate (µm/rev)
7.62 mm multi-directional CFRP with fiberglass scrim surface ply	Cutting Forces and Vibration	Carbide	3000 and 6000	50, 100, 150, and 200
7.62 mm multi-directional CFRP with woven fabric surface ply	Cutting Forces			
2 mm quasi-isotropic CFRP	Cutting Forces and AE			
6.35 mm uni-directional CFRP	Cutting Forces	PCD	1500, 3000, 4500, and 6000	64, 128, 192, 256, and 320

5.2. Drilling of Multi-Directional CFRP Composites

Experimental investigation on damage and defects when drilling multi-directional CFRP composites was conducted. Two sets of experimental studies were carried out on two multi-directional CFRP laminates, which have similar stacking sequence except the surface plies using a carbide twist drill. The experimental setup, material preparation, inspection techniques, and other experimental related information are given in detail in chapter four. In this part of the investigation, drilling induced damage and defects including, surface roughness and morphology, fiber pullout, and delamination were evaluated. The relationship between drilling parameters and drilling forces will be presented along with a model for thrust force prediction through Shaw's equation.

5.2.1. Multi-Directional CFRP with Fiberglass Dry Scrim Surface Ply

A series of experimental drilling was conducted on a 7.62 mm thick multi-directional CFRP composite laminate consists of 39 plies with an average ply thickness of 195 μm, which have a stacking sequence of $\left[(90,-45,0,45)_{4s},0,90,0,\overline{90}\right]_{s}$. Drilling forces were acquired during the drilling process. The influence of drilling parameters such as feed rate and cutting speed on the resulting thrust force and torque was studied and based on Shaw's equation a thrust force prediction was made. The quality of the drilled hole was examined and drilling induced damages and defects including surface roughness measurement, fiber pullout, and delamination were studied and will be presented in the following sections.

5.2.1.1. Drilling Forces

From the measured drilling forces, thrust force and torque are the two forces considered in this study. Figure 5.4 shows typical profiles for the thrust force and torque at 6000 rpm cutting speed and feed rate of 100 µm/rev. The trend in the profiles of thrust force and torque is similar for all cutting speed and feed rates. The behavior or the trend of the thrust force can be classified in to four main regions based on the position of the drill tool as it progress through the work material and these regions are illustrated in Figure 5.5.

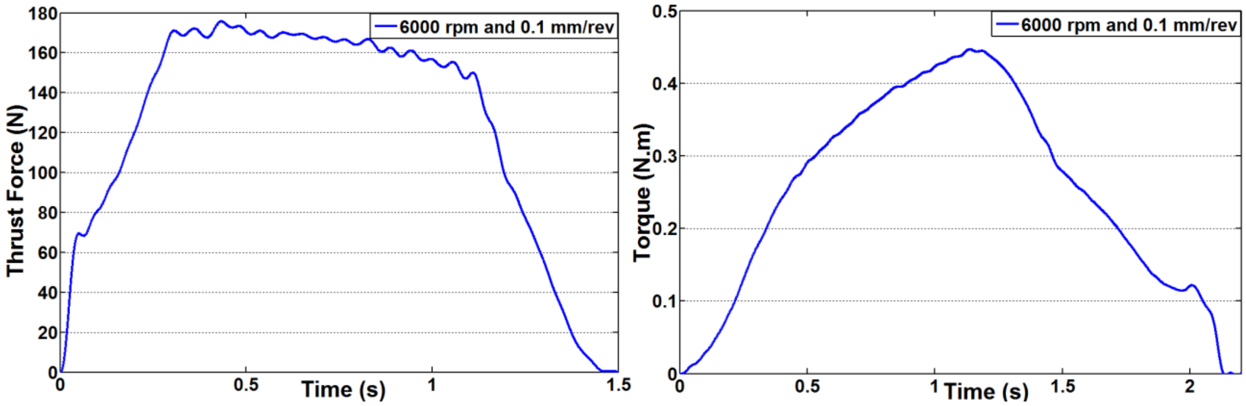

Figure 5.4. Typical thrust force (left) and torque (right) profiles

In the first region, the thrust force increases from zero with a steep slope when the drill tip contact and penetrate trough the work material with scraping the top most ply by the chisel edge until the cutting edge starts the cutting action. Then in the second region, the thrust force keep increasing with a less steep slope compared to the first region up to the point where the cutting edge is fully engaged in the cutting action. Once the full cutting edge is engaged in the cutting process and the drill body is inside the work material, the thrust force profile stays relatively at the same level compared to the increase seen in the first two regions until the drill tip approaches the last few plies as shown in region three. The number of uncut plies is getting less so do the resistance to the cutting process, so in turn, the thrust force starts decreasing slowly until the drill tip penetrates the last ply. In the last phase of the cutting process as the cutting edge exits the work piece fully, the thrust force shows a rapid decrease and goes to zero as shown in region four. Whereas, the torque profile did not show the same behavior as of the thrust force in all four regions, instead, it increases as the drill progress towards the work piece and it keep increasing with a less slope after region two until the end of the cutting process and the rotation of the drill stops completely.

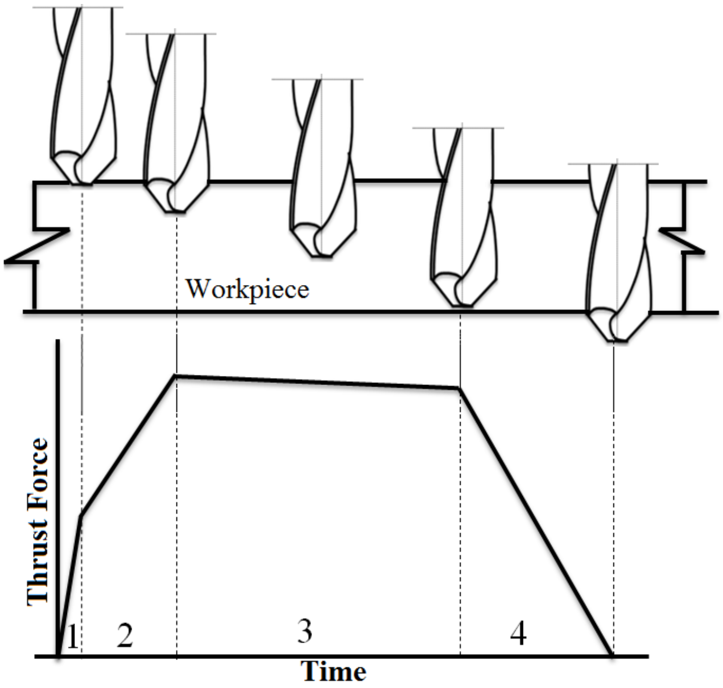

Figure 5.5. Schematic representation of thrust force as a function of drill position

The influence of drilling parameters on the resulting thrust force and torque is shown in Figure 5.6. Both the torque and thrust force increased with the increase of the feed rate and decreased when the cutting speed increased. The influence of the cutting speed on thrust force and torque is less than the influence of the feed rate. The change seen on the magnitude of the torque due to the change in drilling parameters was higher than the change seen on the magnitude of the thrust force. When the feed rate doubles from 100 to 200 µm/rev, the torque increased by 30 %, whereas, the thrust force increased by 25 %, and when the cutting speed doubles from 3000 to 6000 rpm, the torque decreased by 15.5 %, whereas, the thrust force decreased by 7.2 %. In general, a combination of higher cutting speed and lower feed rate found to minimize the resulting drilling forces when drilling CFRP composite materials.

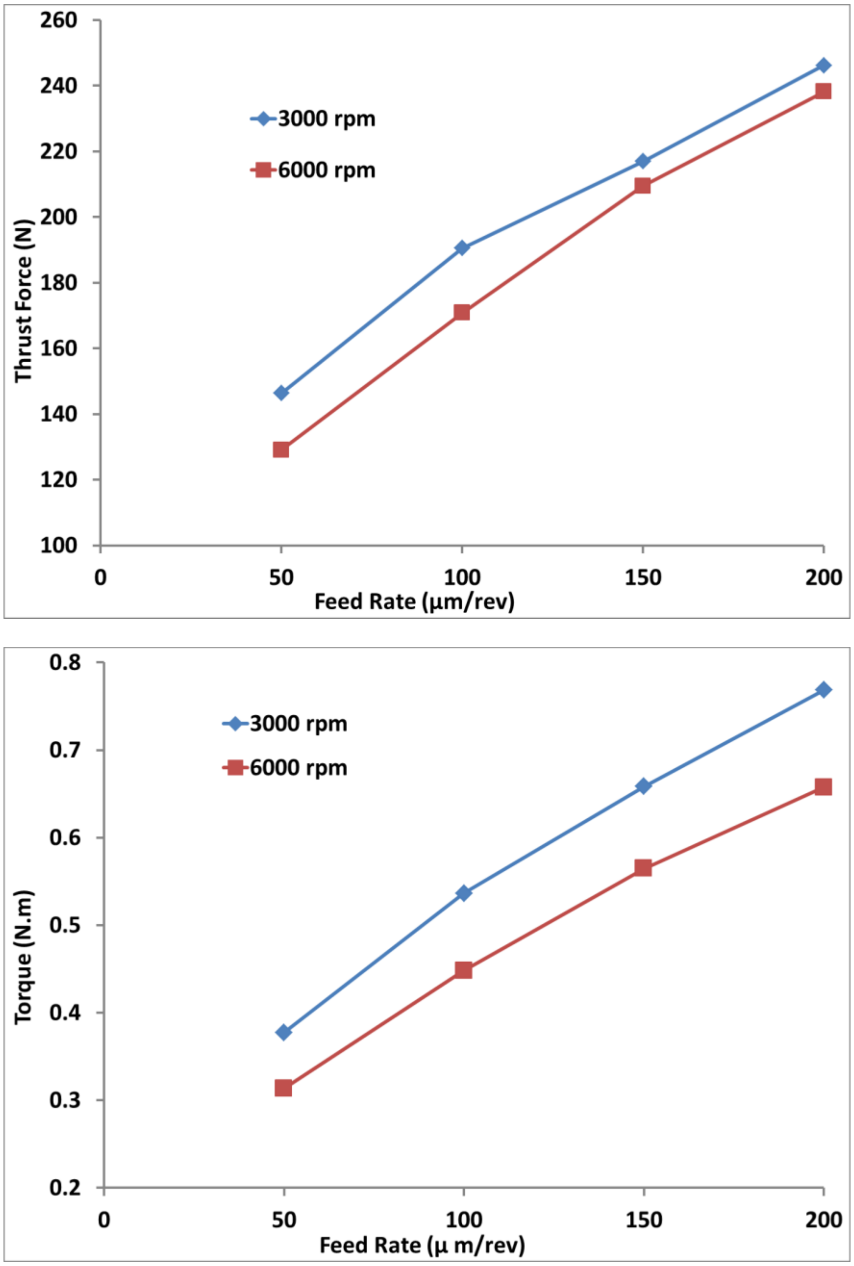

Figure 5.6. Influence of drilling parameters on thrust force (top) and torque (bottom) magnitudes

5.2.1.2. Analytical Model for Thrust Force Based on Shaw's Equation

Even though performance of the drilling operation and the qualities of the produced hole are influenced by many variables, cutting force and torque are considered the most influential cutting variables when drilling CFRP composite materials. Milton C. Shaw presented a full analysis on the prediction of thrust force when drilling metallic alloys in his book "metal cutting principle" and this analysis is discussed in chapter two. Adopting Shaw's equation [7], an attempt was made for prediction of the thrust force and the approaches used for this prediction are given as follows.

From Shaw's equation, we have

$$\frac{T}{d^2 H_B} = K_{13} s^{2a} \, \frac{f^{1-a}}{d^{1+a}} \left[\frac{1-\frac{c}{d}}{\left(1+\frac{c}{d}\right)^{a}} + K_{14} \left(\frac{c}{d}\right)^{1-a} \right] + K_{12} \left(\frac{c}{d}\right)^{2} \tag{5.1}$$

Here the value given by $\frac{c}{d}$ is constant for a given drill geometry, so we can combine these values to the corresponding constants and get the following constants:

$$K_{13} s^{2a} \left[\frac{1-\frac{c}{d}}{\left(1+\frac{c}{d}\right)^{a}} + K_{14} \left(\frac{c}{d}\right)^{1-a} \right] = K_{15} \tag{5.2}$$

And $$K_{12} \left(\frac{c}{d}\right)^{2} = K_{16} \tag{5.3}$$

Therefore, by plugging Equation (5.2) and (5.3) in to Equation (5.1) we will have:

$$\frac{T}{d^2 H_B} = K_{15} \, \frac{f^{1-a}}{d^{1+a}} + K_{16} \tag{5.4}$$

Multiplying both sides by $d^2 H_B$ yields:

$$T = H_B K_{15}\,\frac{f^{1-a}}{d^{1+a}}d^2 + H_B K_{16} d^2 \tag{5.5}$$

Since the hardness value is also a material constant, it can be combined with the corresponding constants to get just only two constants as given below:

$$H_B K_{15} = K_1 \quad \textit{and} \quad H_B K_{16} = K_2 \tag{5.6}$$

Finally, we have

$$T = K_1 (f * d)^{1-a} + K_2 d^2 \tag{5.7}$$

The value of the constant ***a*** in Equation (5.7) is the slope of the graph log (***u***) versus log (***fd***) in which the value of the specific energy ***u*** can be calculated from experimentally measured values of the torque (*M*) as shown in Equation (5.8) below.

$$u = \frac{8M}{fd^2} \tag{5.8}$$

Here, ***f*** is the feed rate in mm/rev and ***d*** is the drill diameter in mm.

The values of the required constants were calculated based on the above equations. Once the value of the specific energy is calculated using Equation (5.8) and experimentally measured values of the torque at 3000 rpm, the value of ***a*** was computed from the slope of the graph log (*u*) versus log (*f* * *d*) as shown in Figure 5.7. Using this value, the values of the two remaining constants were calculated for both cutting speeds used in this part of the experiment and these values are given in Table 5.2. The final equations used in the prediction of the thrust force are given in Equation (5.9), whereas, the measured values of the thrust force versus the predicted values are shown in Figure 5.8.

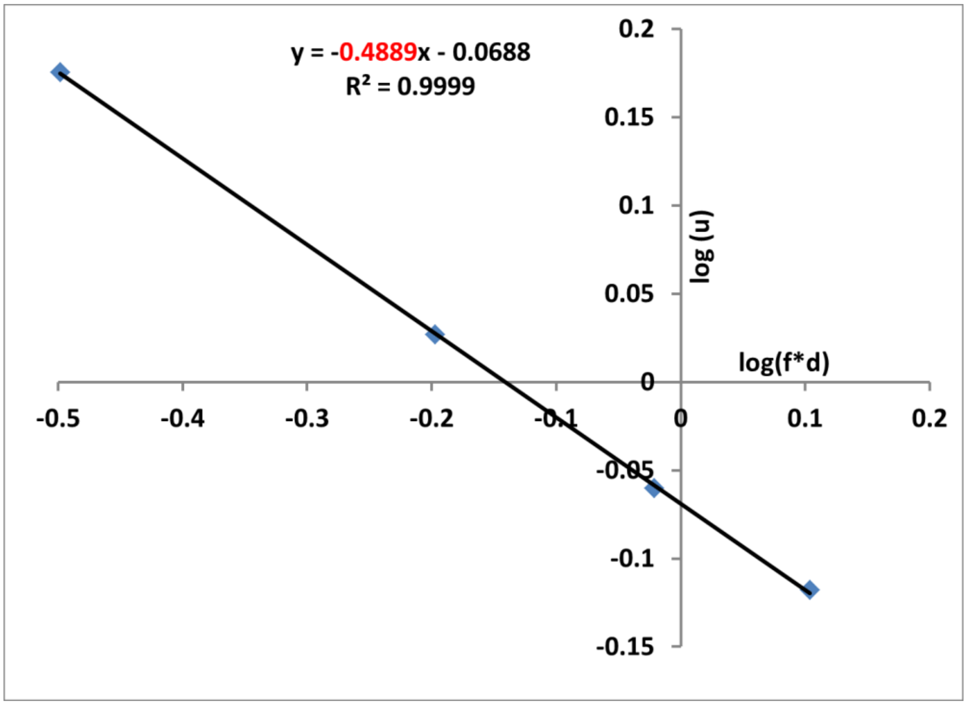

Figure 5.7. Log (u) versus log (f*d) plot for fiberglass scrim surface ply

Table 5.2. Values of calculated constants for each cutting speed

Cutting Speed	Drill Diameter	K_1	K_2	a
3000 rpm	6.35 mm	174.22	1.225	0.489
6000 rpm	6.35 mm	190.33	0.573	0.489

$$T = 174.22(f \times d)^{0.511} + 1.225d^2, for\ 3000\ rpm$$

$$T = 190.33(f \times d)^{0.511} + 0.573d^2, for\ 6000\ rpm \tag{5.9}$$

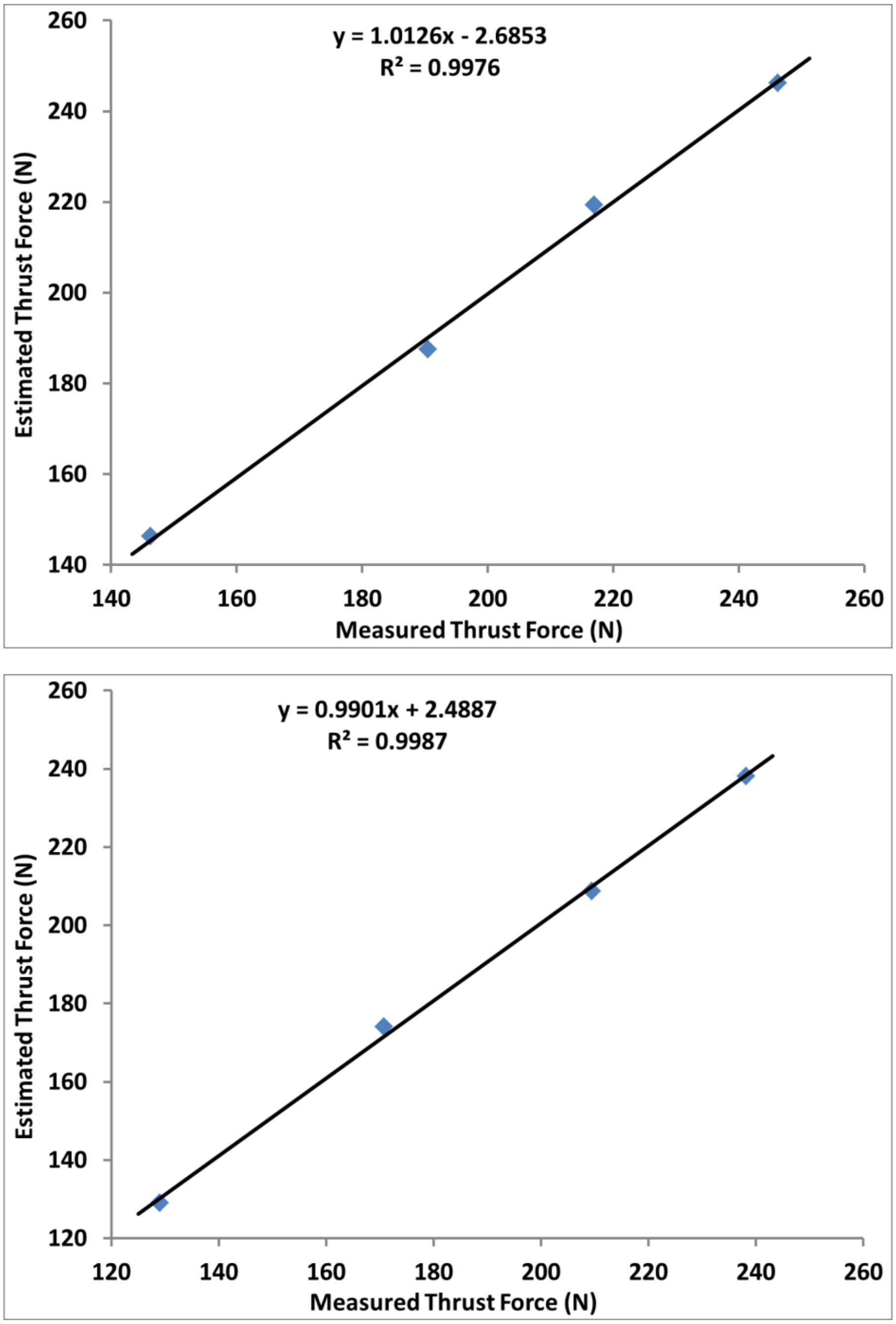

Figure 5.8. Measured and predicted thrust force values at 3000 rpm (top) and 6000 rpm (bottom)

5.2.1.3. Surface Roughness

After the drilling process, each hole was sectioned for surface roughness measurements and optical inspection of the drilled hole surface following the procedure discussed in chapter four. Figure 5.9 shows a typical optical image of a hole surface. As it can be seen from this figure, the defects on the surface of the hole are periodic in nature, which repeats itself based on the ply orientation. In addition to the periodic appearance, the defects are not uniform or similar around the circumference of the hole, and for this reason, it is necessary to take surface roughness at various sectors around the circumference of the hole in order to get a full measure of the hole surface roughness.

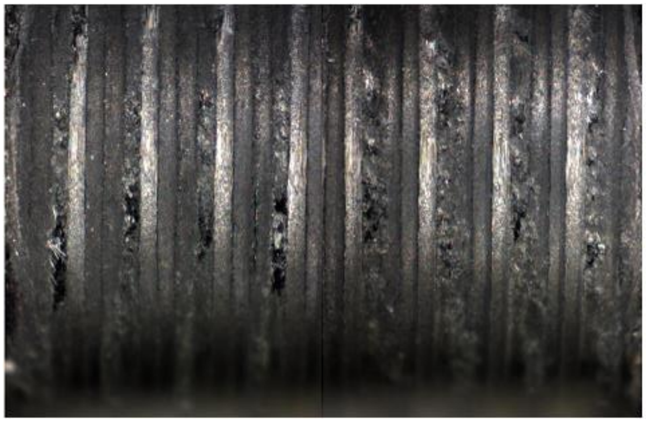

Figure 5.9. Optical image of sectioned hole surface

During the drilling of FRP composite materials, the cutting edge encounters the reinforcing fibers at different angles at every instant of the cutting action (drilling process). The interaction angle between the cutting direction and fiber orientation varies based on the position of the cutting edge along the circumference and stacking orientation of each individual plies. Based on the angle of interaction, the primary cutting mechanisms are accomplished by delamination, fiber buckling, fiber cutting, deformation, and shearing. These four major cutting mechanisms take place during the axial and circumferential travel of the drill and based on these cutting mechanisms, eight sectors or regions were selected for surface roughness measurement. Figure 5.10 shows schematic diagram of the eight locations (sectors) selected for surface roughness measurement and since the holes were sectioned across the line connecting 0^0 and 180^0, surface roughness measurements were not taken at these two locations.

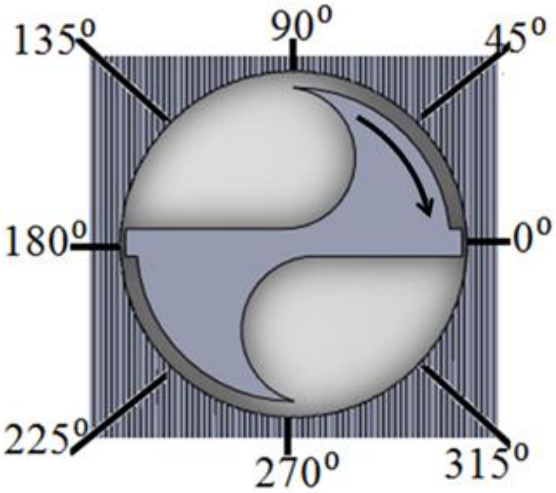

Figure 5.10. Schematic diagram of the eight regions selected for roughness measurements

Roughness measurements were taken across the drilling direction at six different locations around the circumference of the hole using Mahr Surface Profilometer with a probe (stylus) radius of 2.5 µm. Parametric quantities, such as: arithmetic mean roughness (R_a), maximum peak-to-valley (R_t), root mean square roughness (R_q), and ten point average surface roughness (R_z), which describe the surface of the hole were evaluated from the surface roughness profiles. These parametric quantities varied relative to the location of the measurement and drilling conditions. Figure 5.11 shows the surface profiles of a hole drilled at 6000 rpm and 200 µm/rev at six different locations and the values of the surface roughness parameters corresponding to these surface profiles are given in Table 5.3.

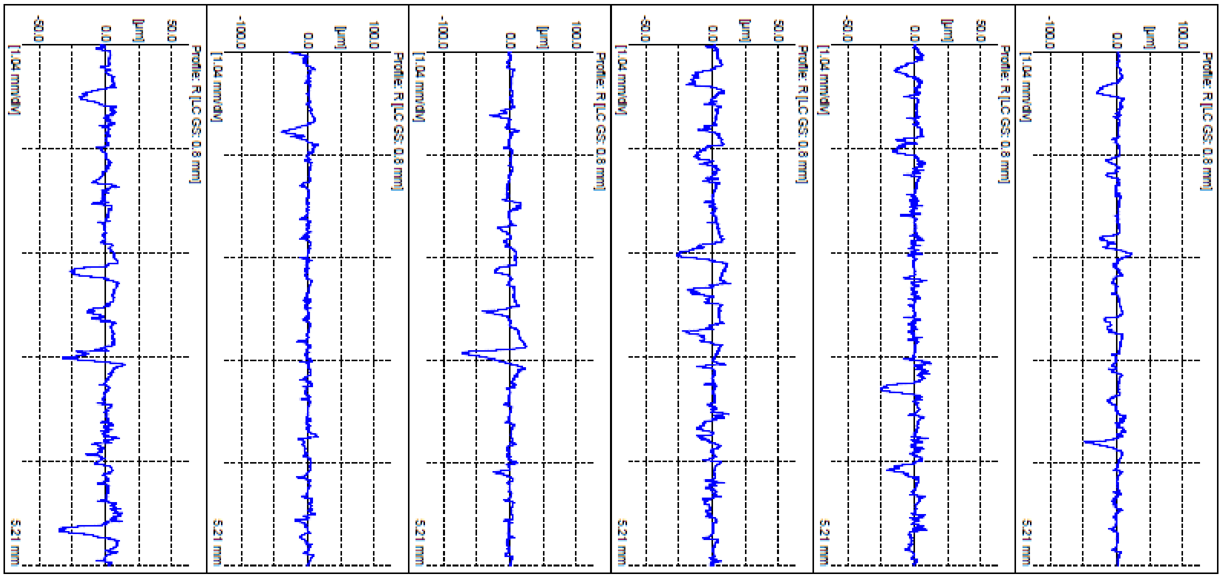

Figure 5.11. Surface profiles at different location of a hole drilled at 6000 rpm and 200 µm/rev

Table 5.3. Variation of roughness parameters around a hole at 6000 rpm and 200 µm/rev

Parameter	45^0	90^0	135^0	225^0	270^0	315^0
R_a (µm)	4.96	3.88	5.91	4.51	3.39	5.29
R_q (µm)	7.44	5.85	10.27	6.22	5.15	7.77
R_z (µm)	36.37	31.33	50.69	28.65	26.21	40.18
R_t (µm)	49.31	55.99	95.27	39.83	38.08	70.79

As it can be inferred from Figure 5.11 and Table 5.3, the values of surface roughness parameters are dependent on where the measurements were taken for a single hole. The values of surface roughness parameters were found to be higher at locations where the interaction angle between the cutting direction and fiber orientation is 135^0 and 315^0 for all surface measurements taken and for all drilling conditions. In order to present the variation of roughness parameters around the circumference of the hole visually, a radar plot was plotted and shown in Figure 5.12 for the maximum peak-to-valley (R_t) values from a hole drilled at 6000 rpm and 200 µm/rev. The surface profiles for all drilled holes are shown in Appendix B. 1, whereas, the roughness parameter values are given in Appendix B. 2.

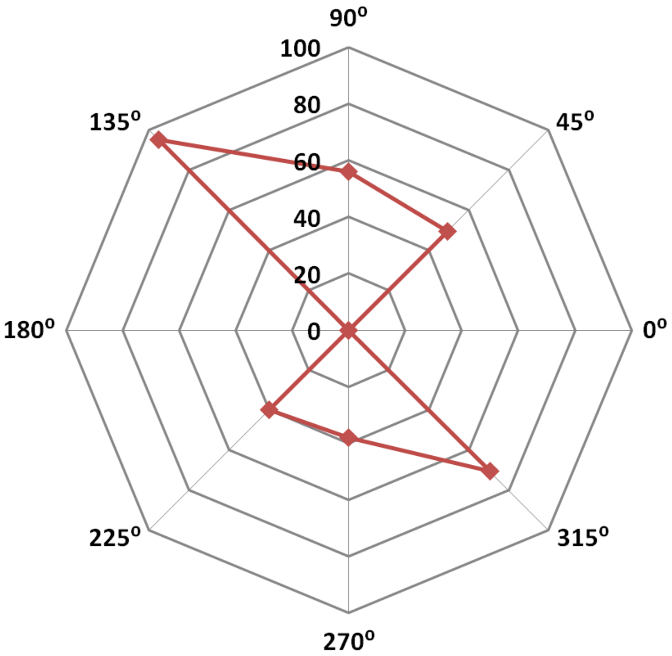

Figure 5.12. Circumferential variation of maximum peak-to-valley (R_t) values

5.2.1.4. Fiber Pullout and Surface Morphology

The surface topography and texture of each drilled holes were extensively studied using optical imaging in order to characterize and evaluate the damage and defect regions. After an optical imaging of the sectioned halve of the hole surface was taken, a close-up image was captured at eight locations from each sectioned halves of the hole surface given sixteen images for each single hole as shown in Figure 5.13 (a). From the close-up look of imaging section two and six shown in Figure 5.13 (b), one can see that the occurrence of drilling induced damage/defects are periodic in nature appearing in every other three plies and there is no significantly observed defect or fiber pullout at the middle plies. The occurrences of these periodic fiber pullout defects are associated with the orientation of individual plies in the stacking sequence, which is mainly composed of $\pm 45^0$ ply orientation except some occurrence at other plies. There is no significant fiber pullout was observed at the middle of the hole where the plies at the middle are composed of plies with 0^0 and 9^0 orientation. All optical images showing the topography and morphology of the sectioned hole surface for all drilling conditions are shown in Appendix C.

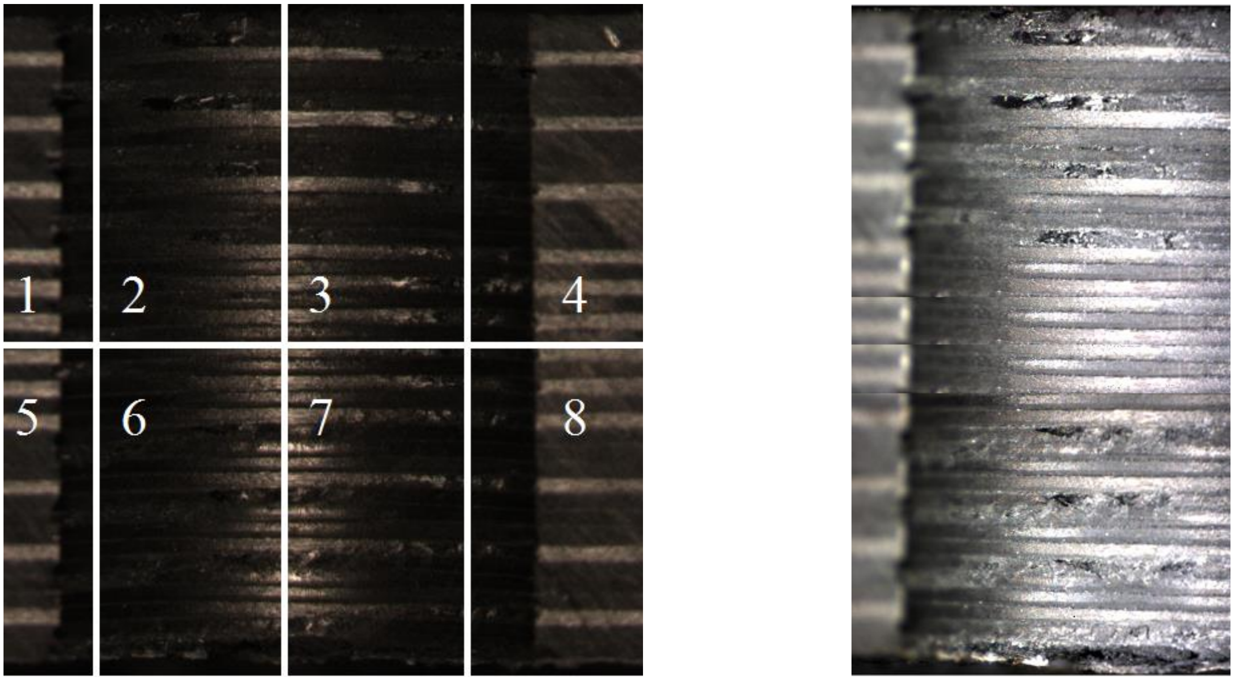

(a) Location of imaging (b) Close-up look of section 2 and 6

Figure 5.13. Optical image of sectioned hole surface

From the study on the optical images of the hole surface, fiber pullout is the major defect observed drilling induced damage. An optical image of a typical edge of sectioned hole with fiber pullout is shown in Figure 5.14. As it can be seen from the optical image, the fiber pullout appears in a periodic fashion and it is hard to take a measure of the depth and width of the fiber pullout because of the poor surface quality of the edges. To make the measurement of the fiber pullout as accurate as possible, after the optical image was taken each sectioned edge was polished using a rotating table polisher before performing fiber pullout measurement.

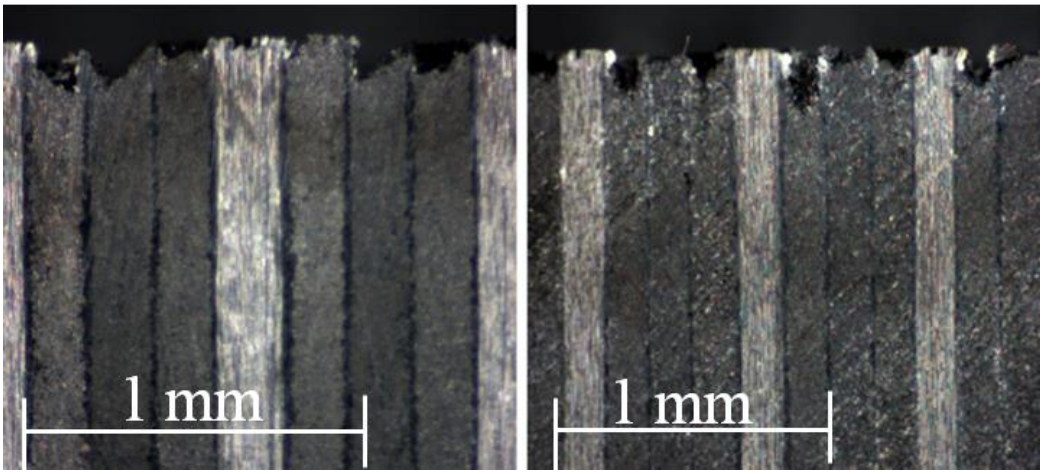

Figure 5.14. Optical images of sectioned edges with fiber pullout at 6000 rpm and 50 μm/rev

The amount of fiber pullout was measured using a Toolmakers microscope and it was quantified by its width and height. Figure 5.15 shows an optical image of a polished edge of a sectioned hole with fiber pullout and a schematic representation of the method used for fiber pullout measurement. The measured values of width and depth of the fiber pullout for two cutting speed and two feed rates are given in Table 5.4. The occurrence and location of fiber pullout mainly depends on the interaction angle between cutting direction and orientation of the fibers and/or stacking sequence of the individual plies. The location and the magnitude of fiber pullout observed in this study are mainly influenced by the orientation of each individual ply in the stacking sequence rather than the drilling condition. Almost all fiber pullout observed in this study were occurred on plies that have an orientation of $\pm 45^0$ in the stacking sequence except some rare occurrence on plies with 0^0 and 90^0 orientation in the stacking sequence. The width of the fiber pullout measured varies from half ply thickness up to one ply thickness, whereas, the depth of fiber pullout varies from 43 μm up to 328 μm. The full values of measured fiber pullout width and depth for all drilling conditions along with the stacking orientation of each individual ply is given in Appendix D.

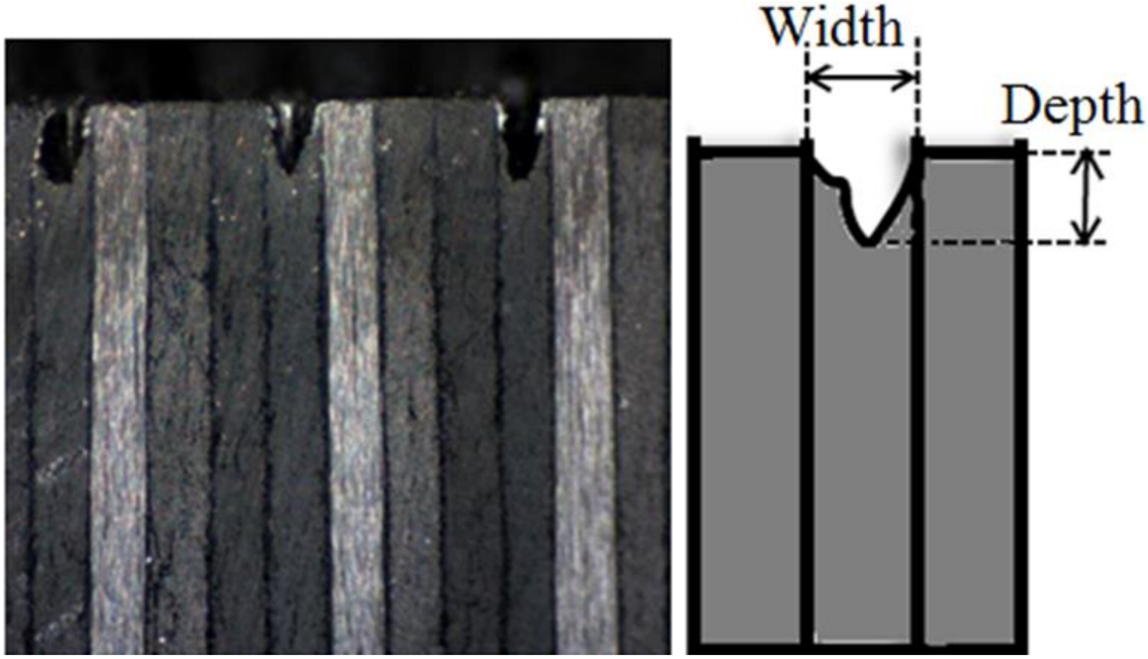

Figure 5.15. Optical image of polished edge with fiber pull out (left) and schematic representation of fiber pullout measurement

Table 5.4. Measured values of fiber pullout width and depth at different drilling conditions

Cutting Speed (rpm)	Ply Orientation (degrees)	Ply Number	Width (µm)		Depth (µm)	
			At 50 µm/rev	At 200 µm/rev	At 50 µm/rev	At 200 µm/rev
3000	-45	2nd	158.5	137.8	71.2	57.3
	-45	6th	172.9	158.5	243.2	229.4
	-45	10th	151.6	-	234	-
	-45	14th	149.3	144.7	183.5	119.3
	-45	26th	121.7	167.7	103.2	162.9
	-45	30th	135.5	188.4	123.9	169.8
	-45	34th	158.5	137.8	100.9	80.3
	-45	38th	156.2	163.1	126.2	176.7
6000	45	4th	135.6	163.1	165.2	91.7
	90	5th	186.1	172.3	94.2	89.7
	45	8th	142.4	174.6	179	114.7
	45	12th	209.1	156.2	160.8	121.6
	45	16th	158.5	172.3	213.5	126.2
	45	24th	140.1	176.9	119.3	174.3
	45	28th	144.7	165.4	247.8	121.6
	45	32nd	140.2	144.7	144.6	169.8
	45	36th	135.6	112.6	328.1	158.3

In most cases, the measured values of fiber pullout depth found to be higher at the lower level of feed rates and the higher level of cutting speed over the length of the hole drilled. For the case presented in Table 5.4, fiber pullout depth measured at the feed rate of 50 μm/rev was higher 70 % of the time than the measured value of fiber pullout depth for both levels of cutting speeds. This may be explained by the mechanism of fiber pullout, which is the tearing away of the fibers/matrix from the wall of the drilled surface, the slower the feed rate the longer the cutting edge stays in contact with individual plies so the tearing action before the cutting edge engaged with another tearing action on another ply. So the longer the tearing time and the contact of the cutting edge with a single ply, the deeper the tearing action and results deeper fiber pullout than the fiber pullout depth caused by a higher feed rate. Figure 5.16 shows a comparison of fiber pullout depth between the feed rates of 50 μm/rev and 200 μm/rev at the cutting speed of 6000 rpm.

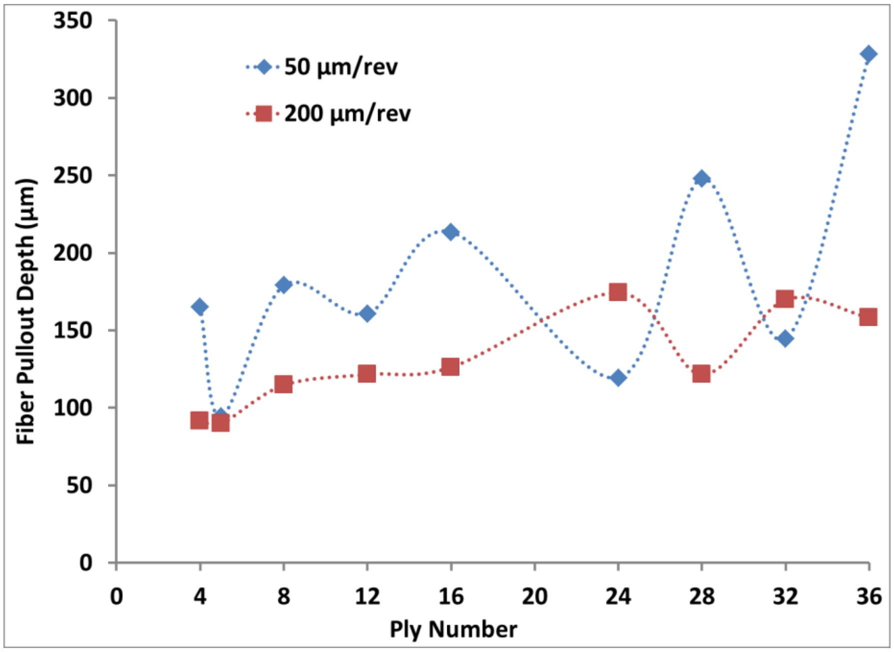

Figure 5.16. Comparison of fiber pullout depth at cutting speed of 6000 rpm

5.2.1.5. Delamination

Delamination is one of the most severe process induced damage/defect when drilling CFRP composite materials and generally it is regarded as matrix dominated failure behavior, and usually occurs in the inter-ply region. Delamination can be introduced by three mechanisms; peeling up of the top layer, punching out of the uncut layer near the drill exit, and through thermal stress. From these, exit ply delamination is the most common mode of delamination when drilling CFRP composite materials. Exit delamination occurs when the drill progresses towards the bottom of the material being drilled where the uncut thickness of the laminates decreases. At this stage, the number of plies under the ply being cut also decreases as the drill approaches the bottom of the laminate, so there is less backing support for the plies being cut. At the same time, the stress caused by the drilling thrust force becomes larger than the inter-laminar shear strength of the laminate and this leads to an exit-ply delamination. The resulting thrust force as the drill progresses towards the bottom of the laminate mainly controls exit ply delamination. Figure 5.17 shows a schematic representation of exit ply delamination along with an optical image of exit delamination.

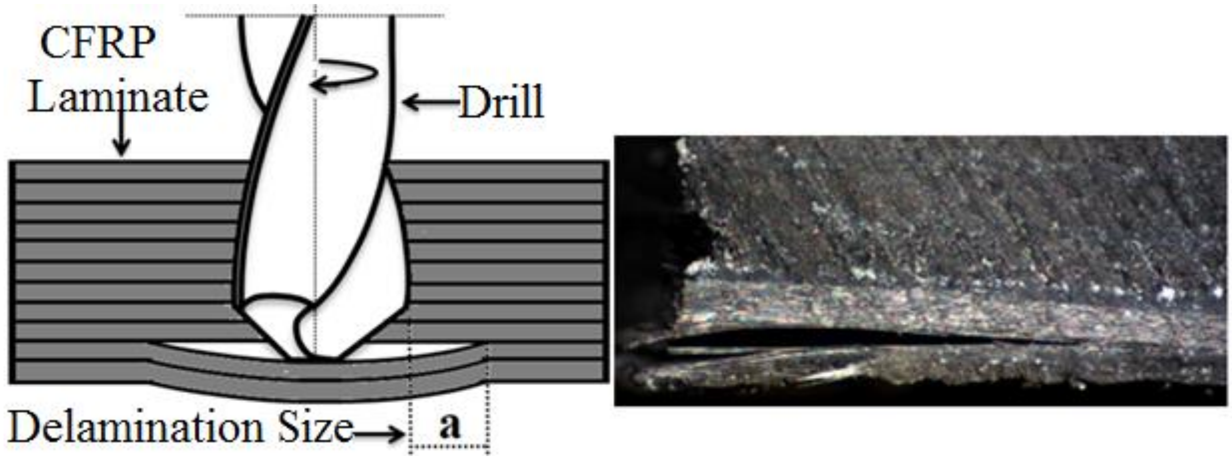

Figure 5.17. Schematic representation (left) and optical image of exit ply delamination (right)

Cutting Speed (rpm)	Feed Rate (µm/rev)	Entrance	Exit
3000	50	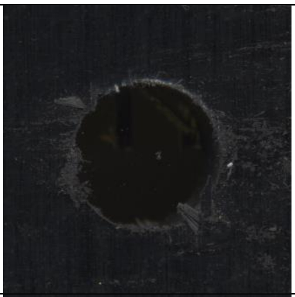	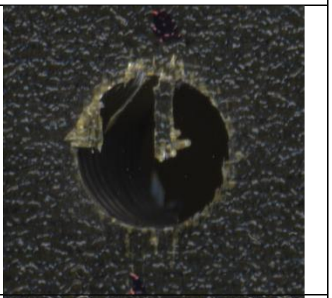
	200	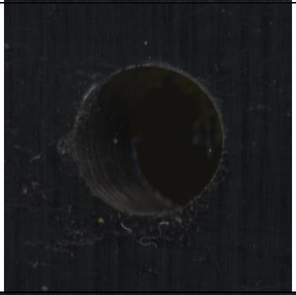	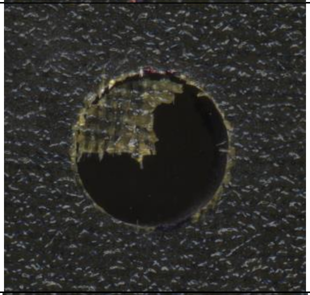
6000	50	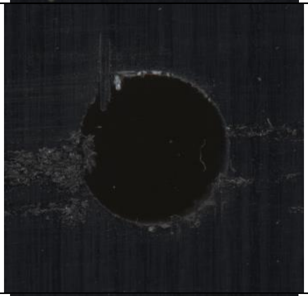	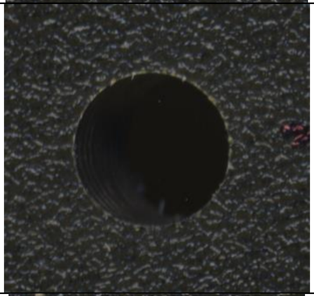
	200	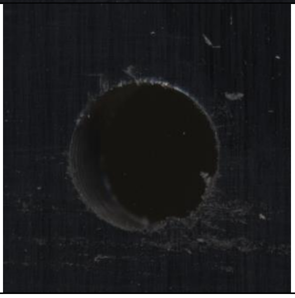	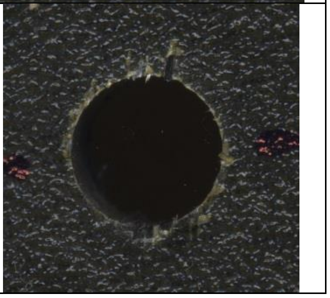

Figure 5.18. Optical macrograph of holes at the entrance and exit of the drill

Figure 5.18 shows an optical macrograph of hole at the entrance and exit of the drill produced at two different cutting speeds, using minimum and maximum feed rate. Note that the amount of delamination at drill exit is much larger than the delamination observed at the entrance of the drill. The fiber breakout due to peel-up delamination at the drill entry is much smaller in comparison to the damage induced by delamination at the drill exit. More uncut fibers were observed at the drill exit at the lower level of cutting speed than the higher level of cutting speed. At cutting speed of 6000 rpm, there is no uncut fibers at the drill exit in both cases of feed rates but the amount of delamination seen at higher feed rate at the drill exit was much larger than the amount of delamination seen at lower feed rate. The amount of delamination at the drill exit was measured using a Toolmakers microscope and expressed in terms of delamination factor, which is a normalized quantity that is determined by dividing the diameter of the circle that circumscribed the maximum delamination by the nominal diameter of the drill used to produce the hole. Figure 5.19 shows a schematic representation of the delamination factor determination.

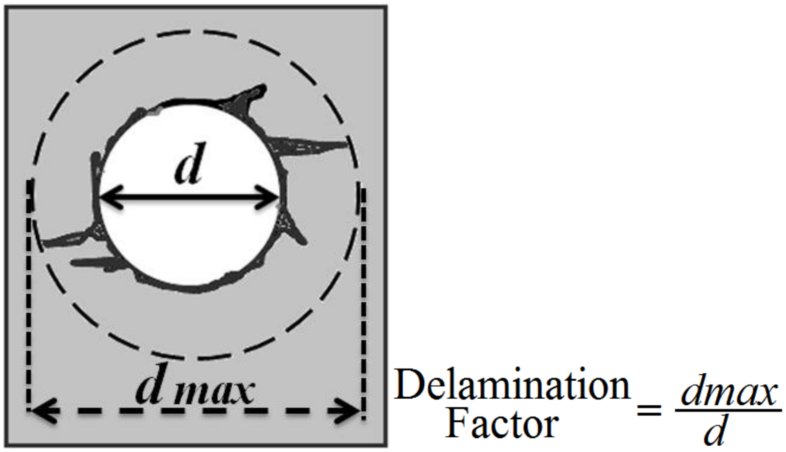

Figure 5.19. Schematic representation of delamination factor determination

Delamination at the drill exit increased when the feed rate increases and decreased when the cutting speed increases resulting minimal exit delamination when drilling with a combination of higher cutting speed and lower feed rate. The maximum delamination factor measured was 1.68 when drilling at 3000 rpm and 50 µm/rev and the minimum delamination factor was 1.11 when drilling at 6000 rpm and 50 µm/rev. The values of delamination factor at the drill exit at lower and higher level of feed rates for cutting speed of 6000 rpm are given in Table 5.5, whereas, the complete calculated values of delamination factor are given in Appendix E. At the cutting speed of 6000 rpm, delamination factor shows an average increase of 18 % when the feed rate increased from 50 to 200 µm/rev. Figure 5.20 shows a surface plot of delamination factor at lower and higher combination of cutting conditions.

Table 5.5. Delamination factor values for two feed rate levels at 6000 rpm

Hole Number	Feed Rate (µm/rev)	
	50	200
1	1.158	1.563
2	1.117	1.216
3	1.116	1.526
4	1.173	1.283
Average	1.141	1.397
STDEV	0.029	0.173

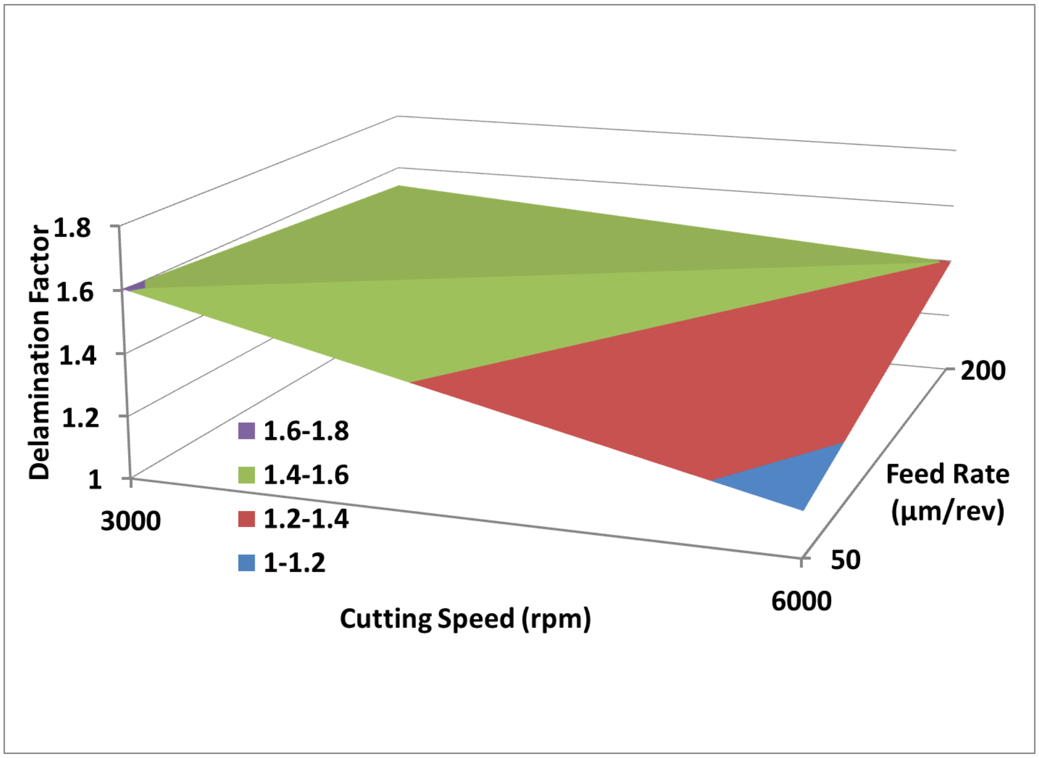

Figure 5.20. Surface plot of delamination factor at different combination of cutting conditions

5.2.1.6. Correlation of Damage Size with Vibration Signal Amplitude

During the drilling process of this part of experimental investigation, vibration signals were acquired using two high frequency accelerometers, where details of vibration signal acquisition and setup is discussed in chapter four. The acquired vibration signal then processed using a demodulation signal processing technique with three steps, where these processing steps are shown in Figure 5.21. The signal processing for the vibration signal analysis was carried out at the University of Washington Department of Electrical Engineering Interactive Systems Design Laboratory. Graduate student Daniel Tidwell and Professor Les atlas performed the vibration signal processing.

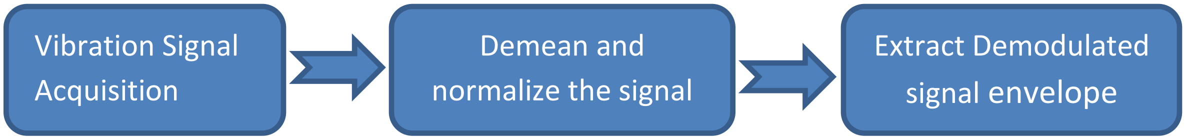

Figure 5.21. Block diagram of signal processing procedure

The raw vibration signal acquired from the accelerometer before processing is shown in Figure 5.22 (a), and this raw signal is processed by demodulation signal processing technique, which uses DEMON (Demodulated Noise) spectrum given by Equation (5.10), which is different from other standard conventional signal processing techniques. Figure 5.22 (b) shows raw vibration signal profile after Demeaned and normalized. After the process of Demean and normalization of the raw vibration signal, the demodulated signal envelope was extracted and is shown in Figure 5.22 (c). At this stage, the vibration signal from the accelerometer is ready for correlation between damage size and amplitude of demodulated signal envelopes.

$$S_{D,dB}(\omega) = 10log_{10}\left\{\left|\sum_{n} x^2(n)e^{-j\omega n}\right|\right\} \qquad (5.10)$$

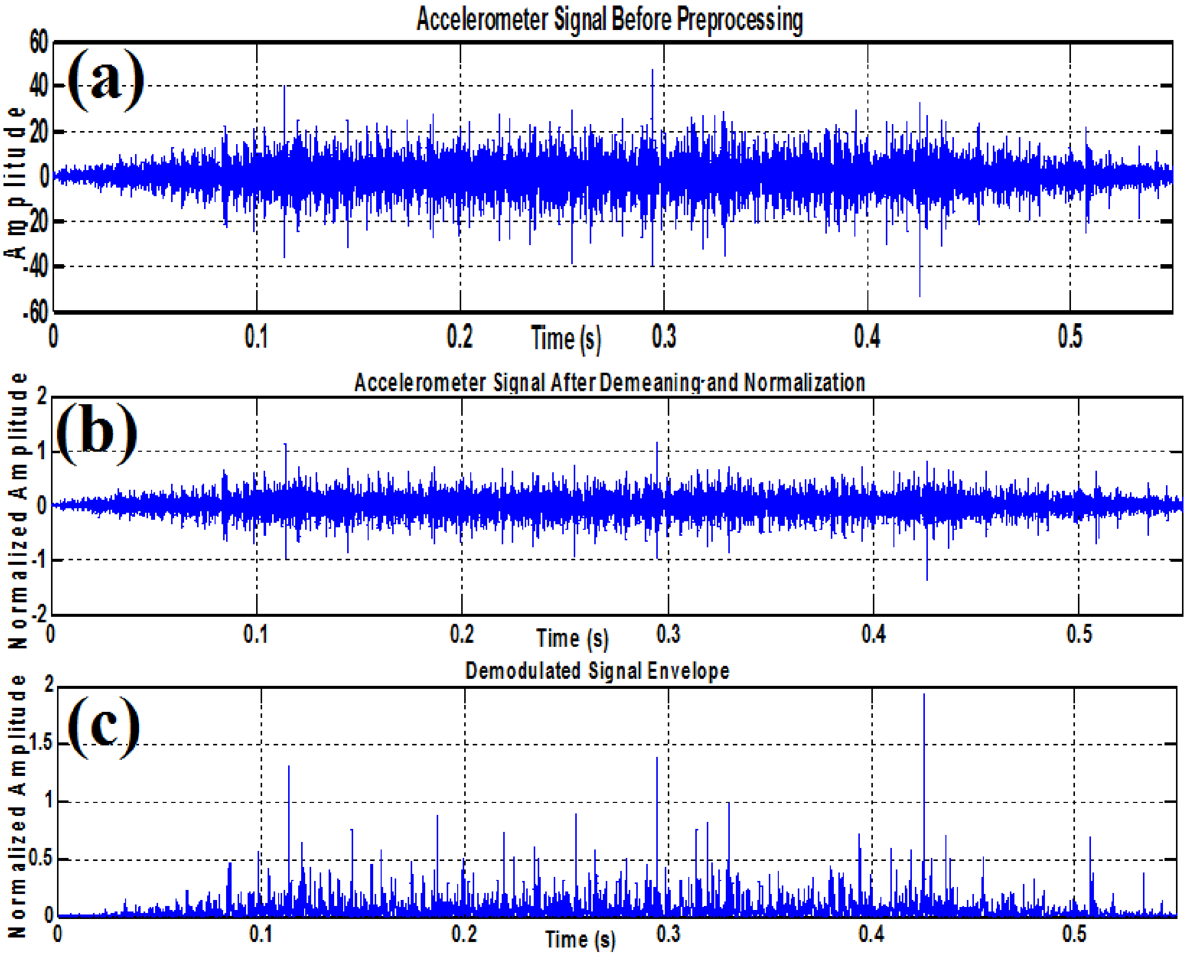

Figure 5.22. Profiles of raw (a), demeaned and normalized (b), and demodulated envelope (c) of vibration signals

From the location of drilling induced damage, the time, when the damage occurred was calculated and correlated with the spike points in the amplitude of the demodulated signal envelope. In this correlation, the time for any point on the drill to pass one ply is calculated from the cutting speed, feed rate, and ply thickness using the relationship given by Equation (5.11).

$$Time\ to\ pass\ one\ ply\ (s) = \frac{Ply\ thickness\ (mm) \times 60}{Cutting\ Speed\ (rev/min) \times Feed\ rate\ \left({}^{mm}/_{rev}\right)} \qquad (5.11)$$

The time at the demodulated signal starts at zero is where the drill (chisel edge) makes the first contact with the work piece and since, the chisel edge leads the center of the cutting edge, which is taken as a reference point for the location of the damage, and directly matching the time from zero is not realistic. The time correlation between the spikes of the demodulated amplitude and the location of the damage is made by adding the time required for the center of the cutting edge to reach a point after the chisel edge passes the same point. Using this approach, first the location of drilling induced damages were identified as shown in Figure 5.23, and then the relative time when the center of the cutting edge passes through these damage locations is correlated with the amplitude of the spike on the demodulated signal envelope. Figure 5.24 shows the correlation of spikes on demodulated signal amplitude spikes with the location of damages.

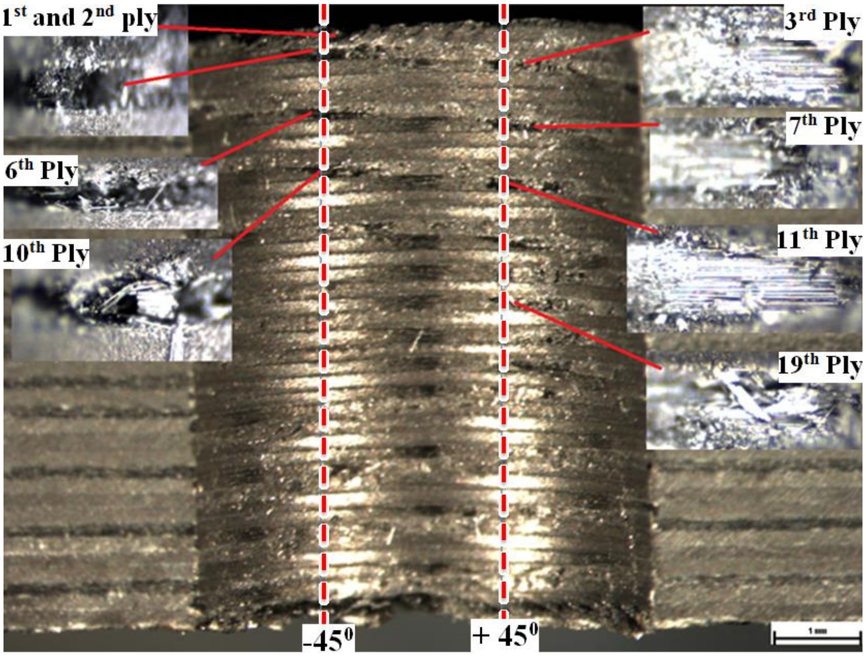

Figure 5.23. Identification of damage location for the hole drilled at 6000 rpm and 200 µm/rev

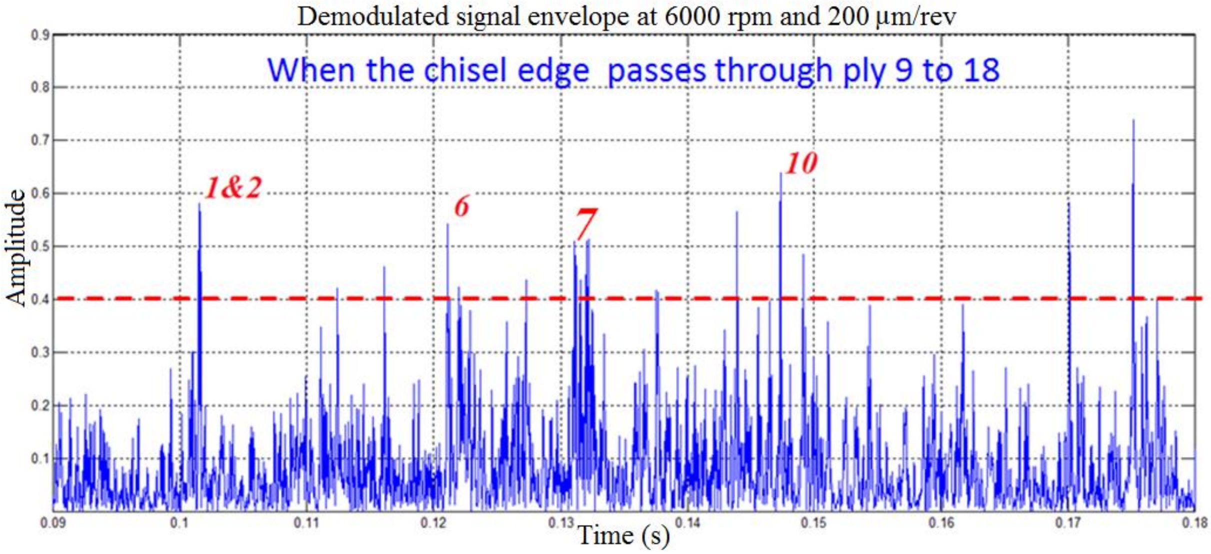

Figure 5.24. Correlation of damage location with demodulated envelope amplitude spikes

Five damages at various ply locations has been identified from three holes drilled with a cutting speed of 6000 rpm and feed rate of 200 µm/ rev and correlated with the spikes of the modulated signal amplitude where the location of the damages were the same for all holes. The length of these damages was measured using a Toolmakers microscope and the length is then correlated with the corresponding amplitudes of the demodulated signal envelope. Figure 5.25 shows the correlation plot for damage length and amplitude of demodulated signal envelope. The damage length measured shows a good correlation with the corresponding amplitude of the demodulated signal envelope with an average coefficient of determination value of 0.83. For the best and reliable damage detection, considering the damage area is suggested instead of just the damage length in the future.

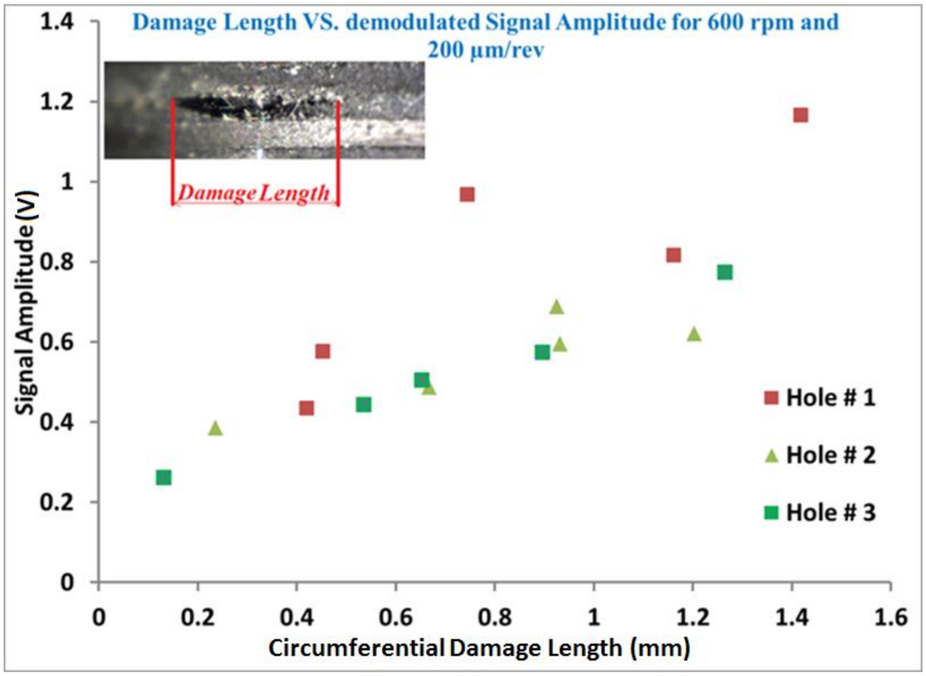

Figure 5.25. Damage width versus vibration signal amplitude

5.2.2. Multi-Directional CFRP with Woven Fabric Surface Ply

A series of experimental drilling was conducted on a 7.62 mm thick multi-directional CFRP composite laminate consists of 39 plies with an average ply thickness of 195 µm. The top and bottom plies of the laminate are made of woven fabric and the rest 37 plies are arranged with a stacking sequence of $\left[(90,45,0,-45)_{4s},0,90,\overline{0}\right]_s$. This part of the investigation is almost identical to the experimental investigation presented in the previous section except that the surface plies used in this case are woven fabric plies rather than fiberglass scrim.

5.2.2.1. Drilling Forces

Thrust force and torque are the two drilling forces deliberated in this part of the investigation. The trend reflected on the profiles of the thrust force and torque is similar for all combinations of cutting conditions except the changes in the magnitude at different levels of cutting speeds and feed rates. The trend observed in the profiles of the thrust force can be categorized in to four main regions based on the position of the drill tip through the thickness of the material being drilled, which is the same as the trend discussed in section 5.2.2.1 with the schematically represented shown in Figure 5.5. The magnitude of the thrust force and torque increased when the feed rate increased and decreased with the increase of the cutting speed. The change in magnitude of the torque due to cutting parameters was higher than the change in thrust force magnitude. When the feed rate doubles from 100 to 200 µm/rev, the torque increased by 31 %, whereas, the thrust force increased by 27 %, and when the cutting speed doubles from 3000 to 6000 rpm, the torque decreased by 18.5 %, whereas, the thrust force decreased by 11 %. Typical thrust force and torque profiles when drilling at 6000 rpm cutting speed and feed rate of 100 µm/rev are shown in Figure 5.26.

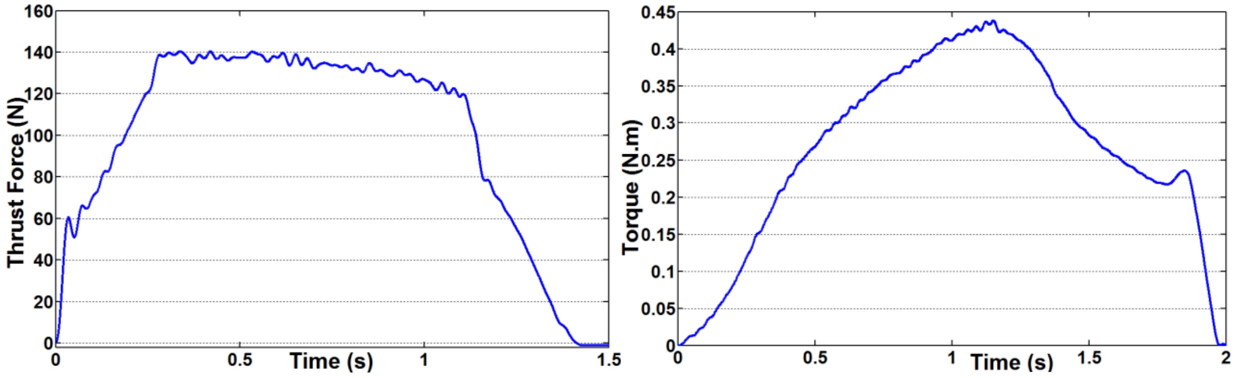

Figure 5.26. Typical thrust force (left) and torque (right) profiles

Even though the two multi-directional CFRP laminates used in the investigation of this section and the previous section are similar except the type of their surface ply, the resulting drilling forces were found to be different. The influence of the surface ply on the magnitude of the thrust force was higher than the influence on magnitude of the torque. The thrust force measured when drilling CFRP laminate with surface ply of fiberglass scrim was higher than the woven fabric surface ply by 14.6 % at 3000 rpm and by 18 % at 6000 rpm, whereas, the torque was 1.7 % higher at 3000 rpm and 5 % higher at 6000 rpm. Figure 5.27 shows the comparison of thrust force and torque at lower and higher cutting speed for the two types of surface plies.

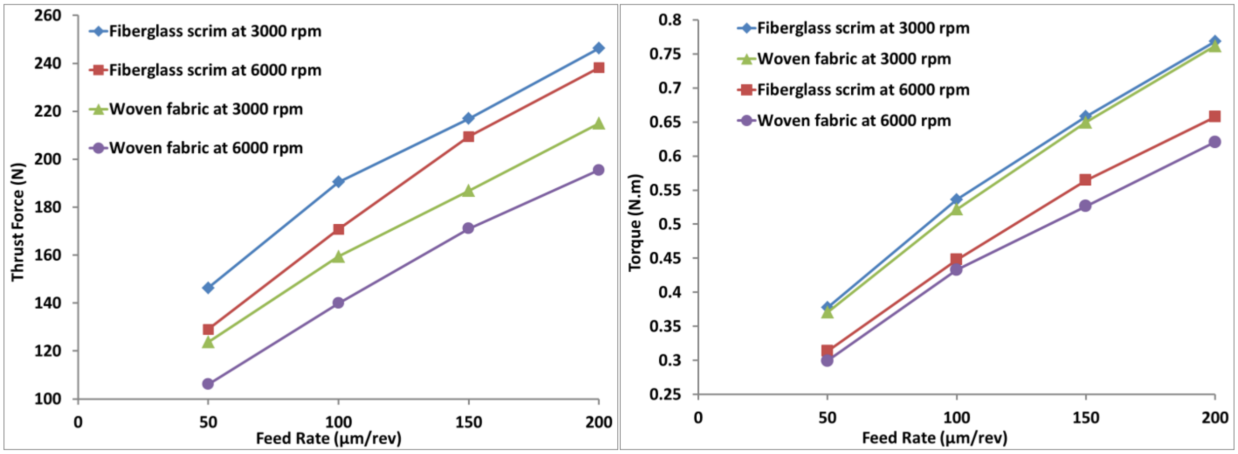

Figure 5.27. Comparison of thrust force and torque for two types of surface plies at different cutting speeds

5.2.2.2. Thrust Force Prediction through Shaw's Equation

As it was discussed in section 5.2.12, drilling forces are influential variables for the quality of the hole produced when drilling CFRP composite laminates. A prediction of the thrust force was performed based on the Shaw's equation, which discussed in detail in chapter two. Using Equations (5.1) to (5.8) and the slope of the graph log (u) versus log $(f * d)$ shown in Figure 5.28, the three constants required for thrust force prediction was computed and given in Table 5.6 and the final equation used to the prediction of thrust force is given in Equation (5.12). Prediction of the thrust force was performed through these equations and the measured values of thrust force versus the predicted values are shown in Figure 5.29.

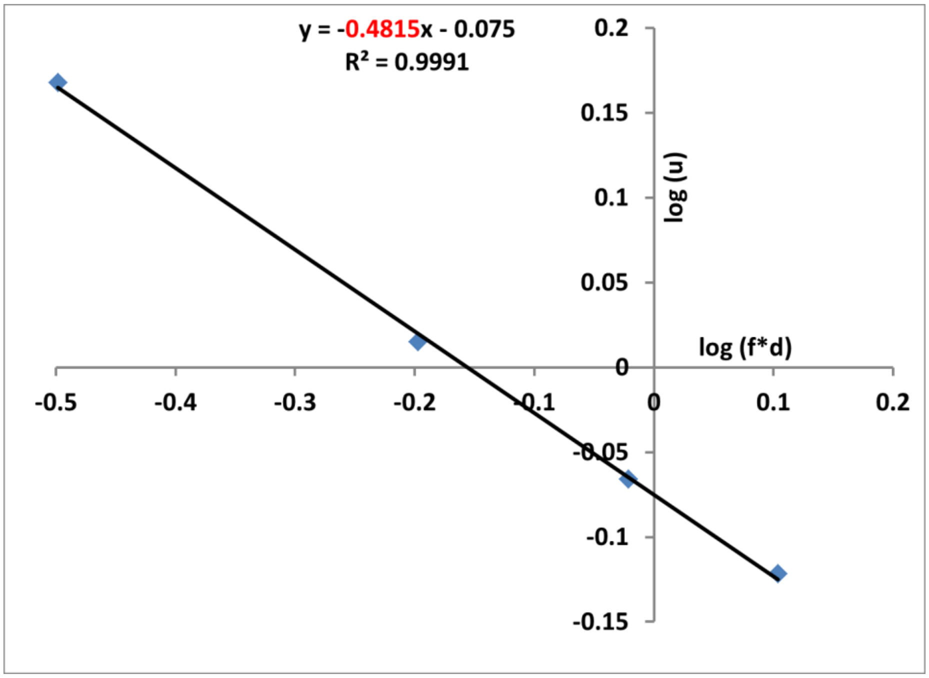

Figure 5.28. Log (u) versus log (f*d) plot for woven fabric surface ply

Table 5.6. Values of calculated constants for each cutting speed

Cutting Speed	Drill Diameter	K_1	K_2	a
3000 rpm	6.35 mm	157.18	0.917	0.482
6000 rpm	6.35 mm	154.04	0.523	0.482

$$T = 157.18(f \times d)^{0.518} + 0.917d^2, for\ 3000\ rpm$$

$$T = 154.04(f \times d)^{0.518} + 0.523d^2, for\ 6000\ rpm \qquad (5.12)$$

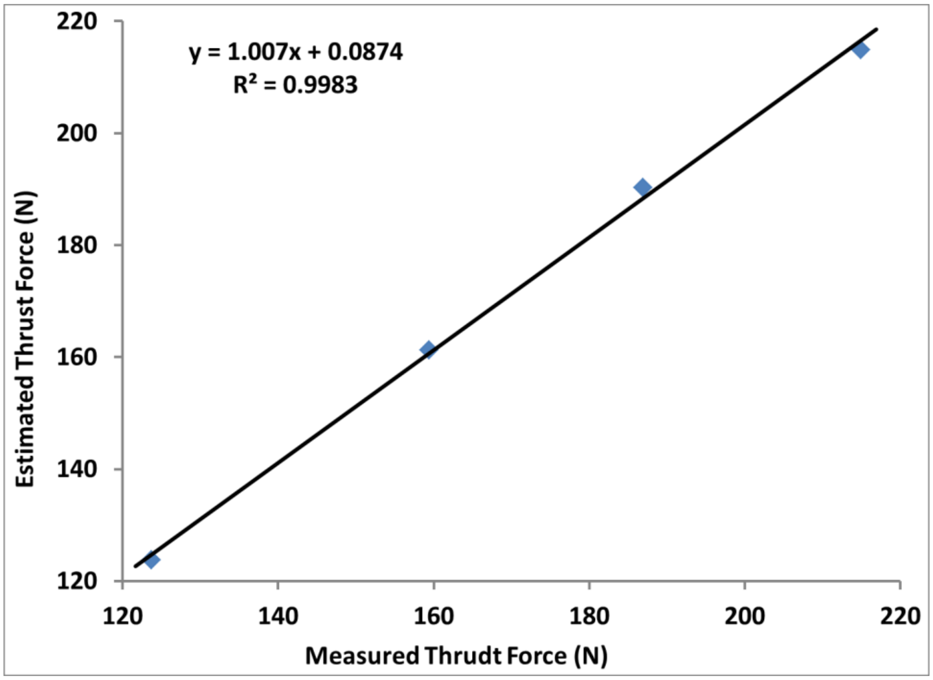

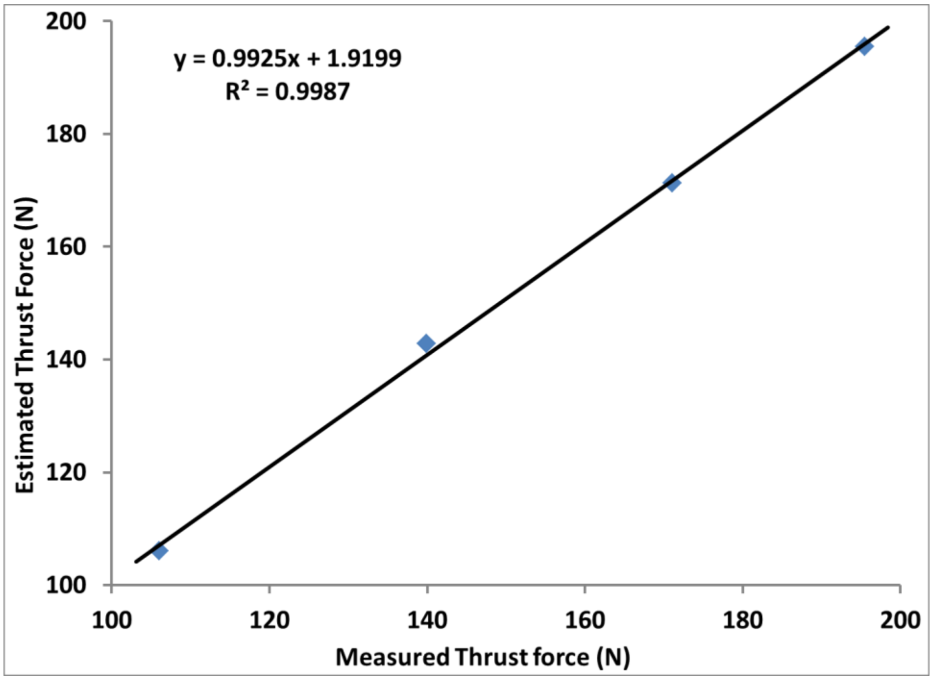

Figure 5.29. Measured and predicted values of thrust force at 3000 rpm (top) and 6000 rpm (bottom)

5.2.2.3. Surface Roughness

Surface roughness of the sectioned holes surface was measured at six locations through similar procedure used in section 5.1.2.3. Parametric quantities, such as: arithmetic mean roughness (R_a), maximum peak-to-valley (R_t), root mean square roughness (R_q), and ten point average surface roughness (R_z), which describe the surface of the hole were evaluated from the surface roughness profiles. These parametric quantities varied relative to the location where the measurement was taken. Figure 5.30 shows the variation of the maximum peak-to-valley (R_t) values for different measurement location around the hole for drilling condition of 6000 rpm and 200 µm/rev.

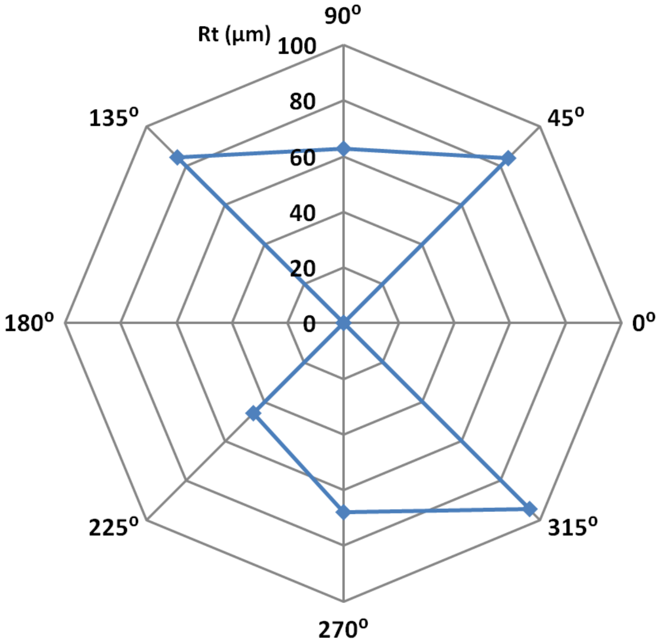

Figure 5.30. Variation of the maximum peak-to-valley (R_t) value around the hole

The values of surface roughness parameters were mainly influenced by the location of measurement, which is related to the interaction angle between the cutting direction and the fiber and/or individual ply orientation as shown in Figure 5.10. Higher values of surface roughness parameters were measured on locations where the interaction angle is 135^0 and 315^0 for all surface roughness measurements taken and for all drilling conditions. Surface roughness profiles of a hole drilled at cutting speed of 6000 rpm and at 200 µm/rev feed rate at six locations is shown in Figure 5.31, whereas, the values of surface roughness parameters for the corresponding profiles is given in table 5.7. The surface profiles for all drilled holes are shown in Appendix F. 1, whereas, the roughness parameter values are given in Appendix F. 2.

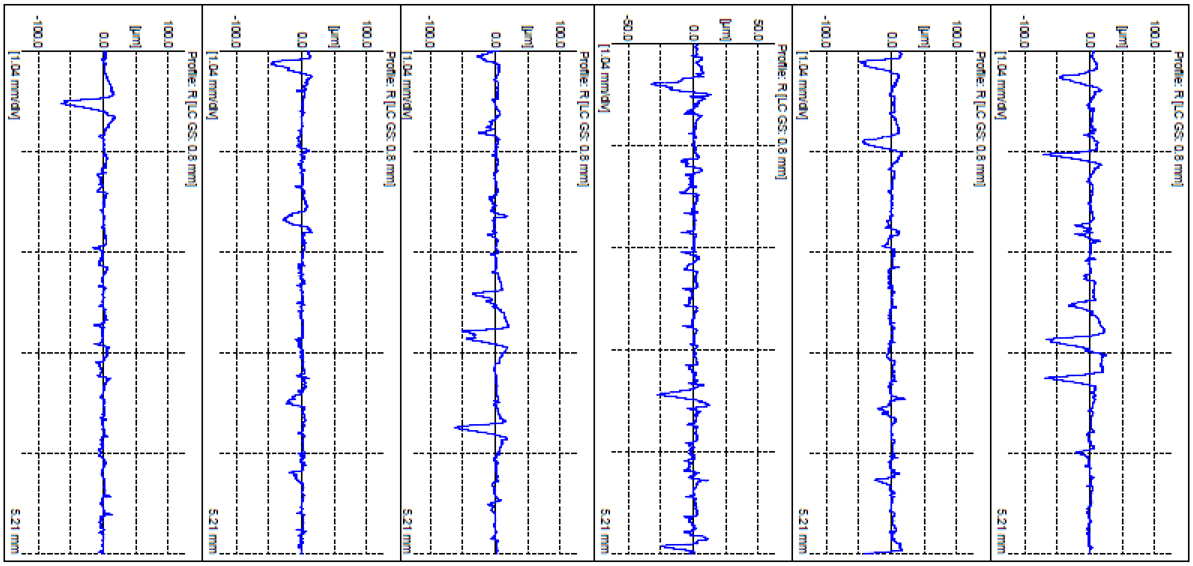

Figure 5.31. Surface profiles at different location of a hole drilled at 6000 rpm and 200 µm/rev

Table 5.7. Variation of roughness parameter around the a hole at 6000 rpm and 200 µm/rev

Parameter	45^0	90^0	135^0	225^0	270^0	315^0
R_a (µm)	4.16	4.31	6.35	3.34	5.32	8.08
R_q (µm)	8.06	7.32	10.72	5.29	9.03	13.65
R_z (µm)	34.20	35.79	48.44	30.21	41.90	70.89
R_t (µm)	83.98	62.63	84.20	45.69	68.07	94.64

5.2.2.4. Fiber Pullout and Surface Morphology

The morphology of the drilled hole surface was similar to the surface morphology of the multi-directional CFRP laminate with fiberglass scrim surface ply. The observed fiber pullout appears in a periodic fashion as discussed in section 5.2.1.4 and shown in Figure 5.13 in the same section. The depth and width of fiber pullout was measured using a Toolmakers microscope through the same procedure used in the case of CFRP laminate with fiberglass scrim surface ply and the measurement method shown in Figure 5.15. The occurrence of the fiber pullout was greatly associated with the orientation of individual plies in the stacking sequence in which more than 90 % of the measured fiber pullout occurs whenever the orientation of individual plies in the stacking sequence is ±45^0. The depth of fiber pullout varies from 50 to 258 µm, whereas, the width of fiber pullout measured varies from half to one ply thickness. Depth of fiber pullout measured at the lower feed rate was higher than fiber pullout depths at the higher level of feed rate 60 % of the time. Figure 5.32 shows the variation of fiber pullout depth with feed rate at cutting speed of 6000 rpm. The width and depth of fiber pullout for two feed rates and two cutting speeds is given in Table 5.8, whereas, the complete list of measured fiber pullout depth and width is given in Appendix G.

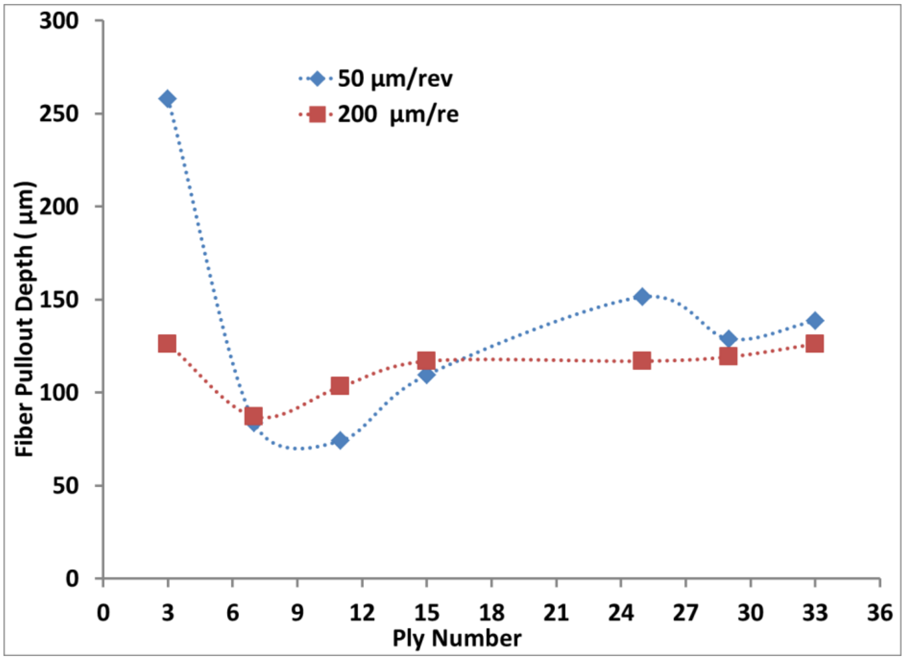

Figure 5.32. Variation of fiber pullout depth with feed rate at 6000 rpm

Table 5.8. Width and depth of fiber pullout for two feed rates and two cutting speeds

Cutting Speed (rpm)	Ply Orientation (degrees)	Ply Number	Width (µm)		Depth (µm)	
			At 50 µm/rev	At 200 µm/rev	At 50 µm/rev	At 200 µm/rev
3000	45	3rd	197.6	142.4	73.4	146.8
	45	7th	156.2	166.7	94.1	130.8
	45	11th	174.6	167.7	73.4	123.9
	45	15th	199.9	151.6	110.1	105.5
	-45	23rd	142.4	119.4	119.3	91.8
	45	25th	149.3	179.2	126.2	96.4
	45	29th	176.9	174.6	119.3	55.1
	-45	31st	---	144.7	---	149.1
	45	33rd	159.3	151.6	112.3	50.5
	45	37th	165.4	---	121.6	---
6000	45	3rd	148.5	160.8	257.9	126.2
	45	7th	154.9	147	83.8	87.2
	45	11th	148.5	140.1	74.2	103.2
	45	15th	177.6	148	109.6	117
	45	25th	167.9	153.9	151.5	117
	45	29th	133.5	159	128.9	119.3
	45	33rd	158.1	165.4	138.7	126.2
	45	37th	145.2	---	183.8	---

5.2.2.5. Delamination

Delamination at the exit of the drill was measured employing similar procedures used when measuring exit delamination of holes drilled on CFRP laminates with fiberglass scrim surface plies in section 5.2.1.5. Figure 5.33 shows an optical macrograph of holes at the entrance and exit of the drill tool at different combinations of drilling conditions. The amount of delamination observed at the exit was higher than that of the entrance for all cutting speed and feed rate levels. More uncut fibers were seen at drill exit at the low level of the cutting speed than the higher level of cutting speed, which is also observed in the case of CFRP laminate with fiberglass scrim surface ply. The amount of delamination at the entrance and exit of the drill observed in the case of woven fabric surface plies was smaller compared to the delamination occurred on fiberglass scrim surface ply. An optical macrograph of the drill entrance and exit for lower and higher levels of feed rates at the cutting speed of 6000 rpm for both surface plies is shown in Figure 5.34.

Cutting Speed (rpm)	Feed Rate (µm/rev)	Entrance	Exit
3000	50	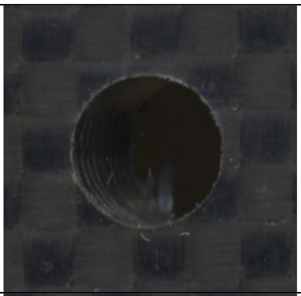	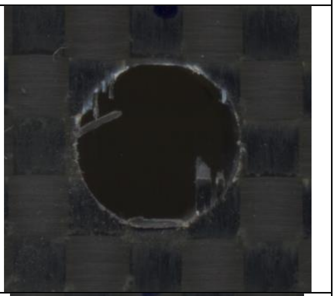
	200	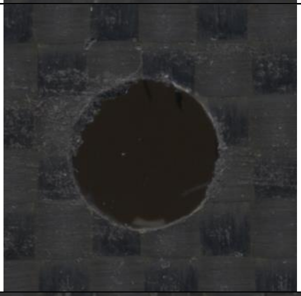	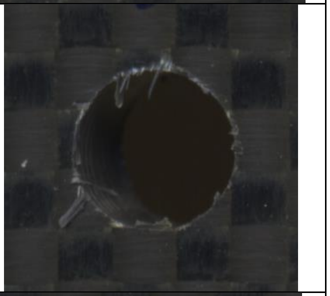
6000	50	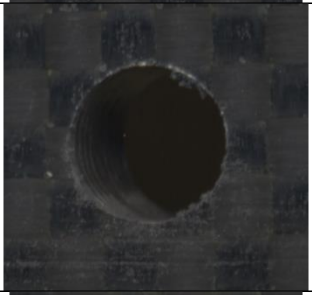	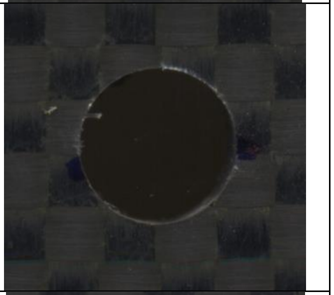
	200	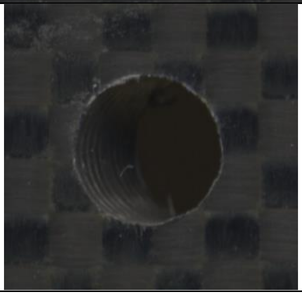	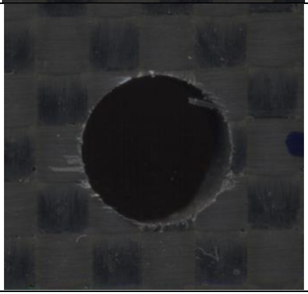

Figure 5.33. Optical macrograph of holes at drill entrance and exit at different drilling conditions

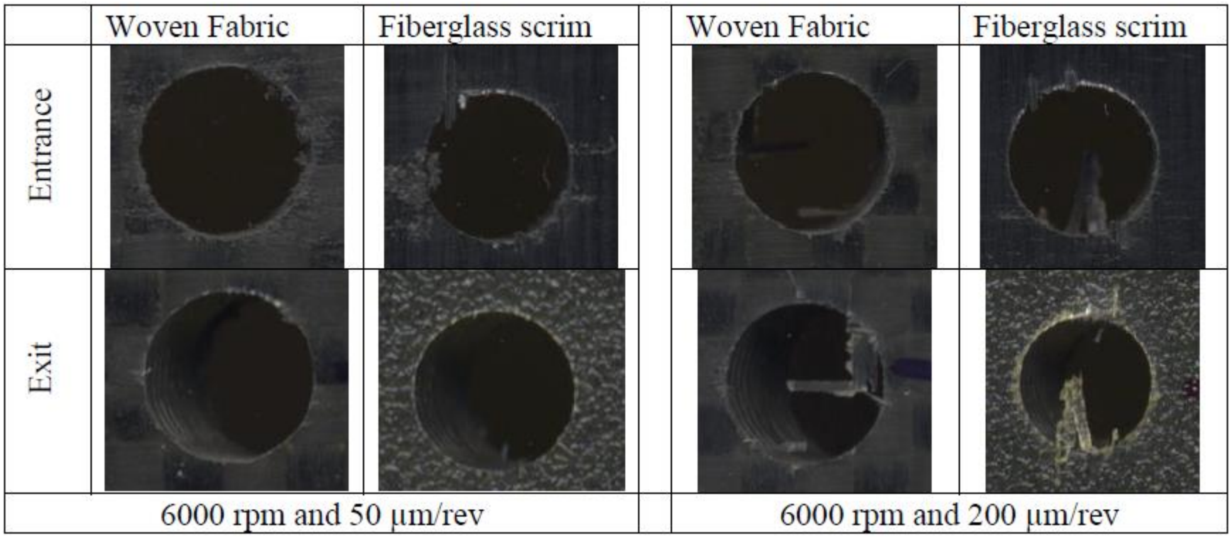

Figure 5.34. Optical macrograph of the drill entrance and exit for both surface plies

The measured size of exit delamination is expressed in terms of delamination factor, which is a normalized quantity that is determined by dividing the diameter of the circle that circumscribed the maximum delamination by the nominal diameter of the drill used to produce the hole as shown in Figure 5.19. Delamination factor increased with the increase of feed rate while the change in delamination factor was not that significant when the cutting speed increased or decreased. When the feed rate increased from 50 to 200 µm/rev, delamination factor increased by 12.4 % and by 8.8 % at cutting speeds of 3000 rpm and 6000 rpm respectively. Figure 5.35 shows the surface plot of delamination factor for different combinations of drilling conditions. Delamination factor at the exit for woven fabric surface ply was lower than that of the fiberglass scrim surface ply by 20.7 % at cutting speed of 3000 rpm and by 11.2 % at cutting speed of 6000 rpm. Delamination factor values at the lower and higher levels of feed rates for cutting speed of 6000 rpm is given in Table 5.9, whereas, delamination factor values for all combinations of drilling conditions is given in Appendix H.

Table 5.9. Delamination factor values for low and high levels of feed rate at 6000 rpm

Hole Number	Feed Rate (μm/rev)	
	50	200
1	1.18	1.23
2	1.18	1.36
3	1.12	1.16
4	1.11	1.27
Average	1.15	1.26
STDEV	0.04	0.08

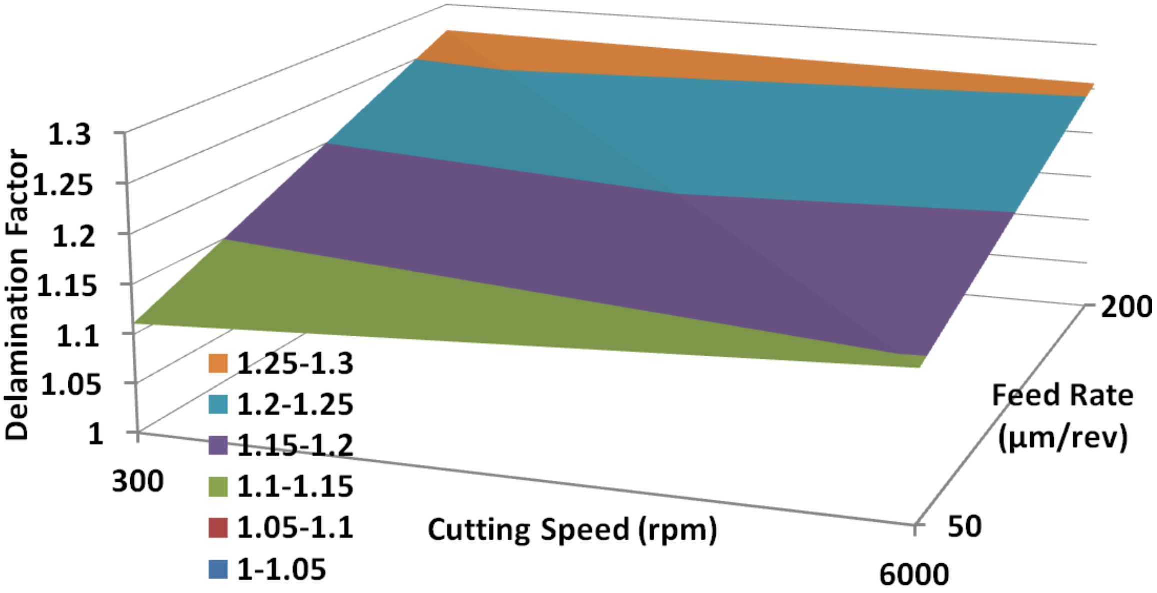

Figure 5.35. Surface plot of delamination factor at different combination of drilling condition

5.2.3. Summary on Drilling of Multi-Directional CFRP Composites

Experimental investigation on process induced damage and defects when drilling multi-directional CFRP composite laminates was conducted in this part of the study. Two multi-directional CFRP composite laminates having similar stacking sequence but different surface plies namely fiberglass scrim and woven fabric surface plies were used in this investigation. Process induced damages and hole quality were investigated through surface roughness measurement, fiber pullout and surface morphology, and exit delamination. The influence of drilling parameters such as cutting speed and feed rate on drilling forces was studied and a thrust force prediction was made through the modification of Shaw’s equation. Vibration signal was acquired and an attempt to correlate damage size with vibration signal amplitude was made.

Thrust force and torque increased with the increase of feed rate and decreased when the cutting speed increases in both case of multi-directional CFRP laminates. The influence of feed rate on the drilling forces was more pronounced than the influence of the cutting speed. The magnitude of drilling forces for the woven fabric surface ply was lower than the drilling forces of fiberglass scrim surface ply. The values of surface roughness parameters and fiber pullout depth varied based on the location of measurement and orientation of individual plies in the stacking sequence. Fiber pullout depth was higher where the ply orientation is $\pm 45^0$. Delamination factor at the exit of the drill increased when the feed rate increases for both surface plies and decreased when the cutting speed increases for fiberglass scrim surface ply case, however cutting speed influence on delamination factor was not significant in the case of woven fabric surface ply. Lower delamination factor was resulted when drilling woven fabric surface ply compared to fiberglass scrim surface ply.

5.3 Drilling of Quasi-Isotropic CFRP Composites

For this part of the investigation, a series of experimental drilling was carried out on a 2 mm thick quasi-isotropic CFRP laminate made up of 10 plies each having a ply thickness of 200 μm in a symmetrical stacking sequence of $[0,45,90,-45,0]_s$ using a 6.35 mm carbide twist drill tool. Detailed information on experimental setup, procedure, and material preparation can be found in chapter four. Two levels of cutting speed and four levels of feed rates were used in this experiment and the drilling was repeated four times for each combination of feed rate and cutting speed giving a total of 32 holes. Cutting force and acoustic emission signals were acquired during the drilling operation, whereas, the texture and surface morphology of the drilled hole surface was intensively studied through scanning electron microscopy (SEM).

5.3.1. Thrust Force

Figure 5.36 shows a typical thrust force and torque profiles acquired when drilling at cutting speed of 6000 rpm and feed rate of 100 µm/rev. The magnitude of thrust force was greatly influenced by the feed rate, whereas, the influence of cutting speed on thrust force is less significant as seen in the previous sections. When the feed rate increased from 50 to 200 µm/rev, the magnitude of the thrust force increased by 38 % when drilling at 3000 rpm and by 35 % when drilling at 6000 rpm, however when the cutting speed increased from 3000 to 6000 rpm, the thrust force increased only by 3 %. One thing to note here is, in other investigations discussed in previous sections thrust force decreases when cutting speed increase, which is not the case in this part of the study. The change in thrust force magnitude due to change in drilling conditions is shown in Figure 5.37.

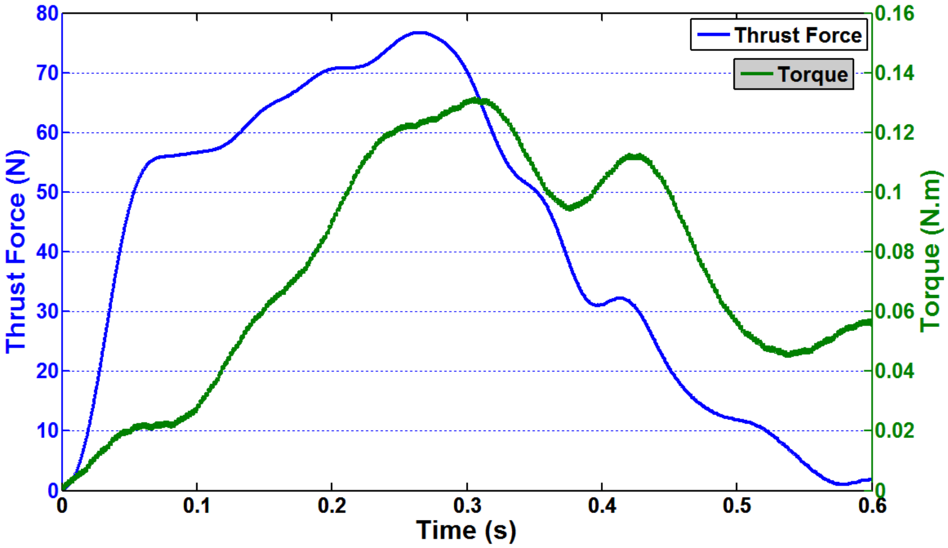

Figure 5.36. Typical thrust force and torque profile at 6000 rpm and 100 µm/rev

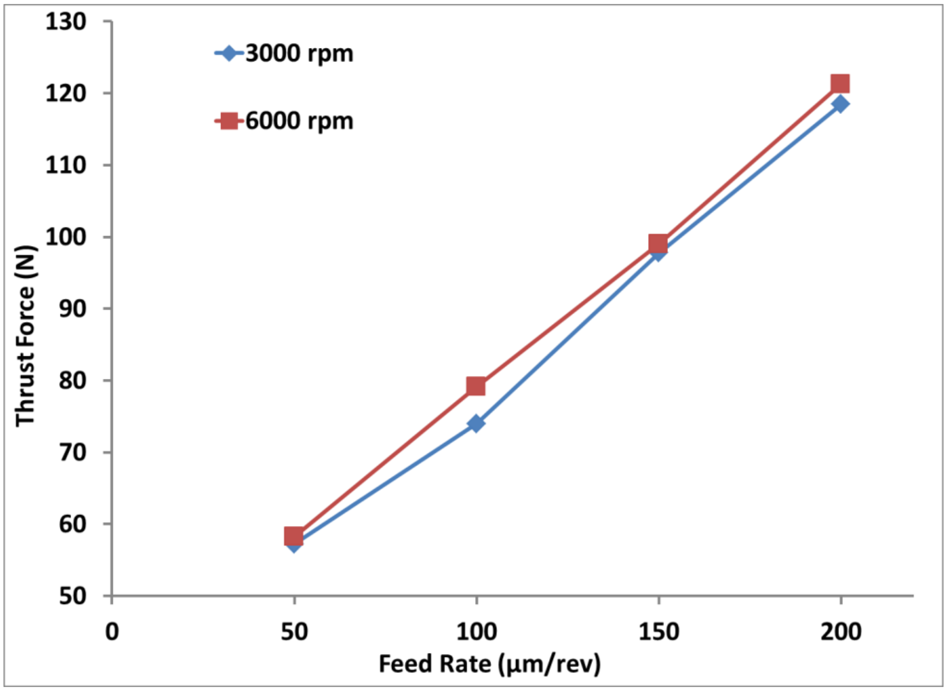

Figure 5.37. Thrust force variation with drilling conditions

Figure 5.38 shows the magnitude of thrust force versus feed rate for holes drilled at 6000 rpm, and as it can be seen in the plot, thrust force magnitude did not show that much variation from one hole to the next for the same combination of drilling condition, which shows the repeatability of the experiment. Using the analysis of variance, the significant factors and their interaction effects were identified in terms of cutting speed and feed rate. Based on the measured thrust force and the ANOVA, a linear regression model for the hole production process was developed using Design Expert software. The effect of drilling condition on the thrust force is modeled by using ANOVA analysis and the surface response model result is given in Table 5.10. The effect of drilling conditions on the resulting thrust force from the model is shown in Figure 5.39.

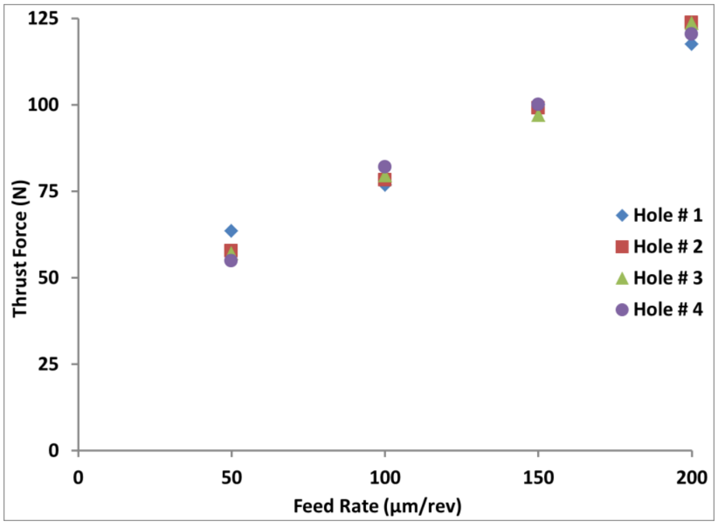

Figure 5.38. Thrust force versus feed rate for each drilled hole at 6000 rpm

Table 5.10. ANOVA Table

Source	Sum of Squares	DF	Mean Square	F Value	p-value prob>F
Model	17069.07	3	5689.69	662.32	< 0.0001
A-Speed	39.65	1	39.65	4.62	0.0405
B-Feed	17026.62	1	17026.62	1982.01	< 0.0001
AB	2.79	1	2.79	0.33	0.5732
Residual	240.54	28	8.59		
Cor Total	17309.6	31		**$R^{\wedge 2}$= 0.9861**	
Thrust = 35.36824+3.01804E-4*Speed+396.78155*Feed+3.5226E*Speed*Feed					

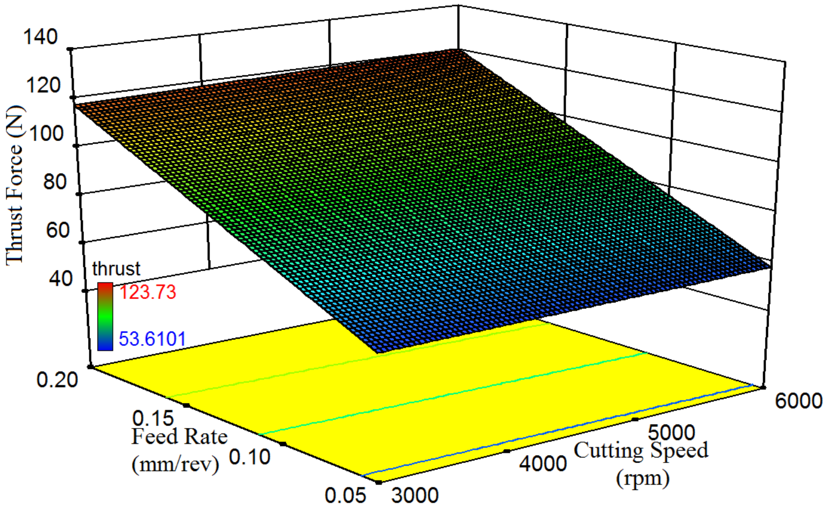

Figure 5.39. Thrust force model graph

5.3.2. Surface Morphology

The surface morphology of the drilled hole surface was studied using SEM imaging to identify type of drilling induced damage and defects. Figure 5.40 shows an optical macrograph of the CFRP laminate after an edge trimming. Note that the occurrence of fiber pullout in the fourth and seventh plies, which both have a ply orientation of -45 degree in the stacking sequence showing the influence of individual ply orientation in the stacking sequence on the resulting surface morphology. As expected, drilling induced damages are observed on the surface of the produced hole as shown in the case of edge trimming cutting mechanism and as discussed in section 5.2, where fiber pullout is observed mainly when ply orientation is -45 degree.

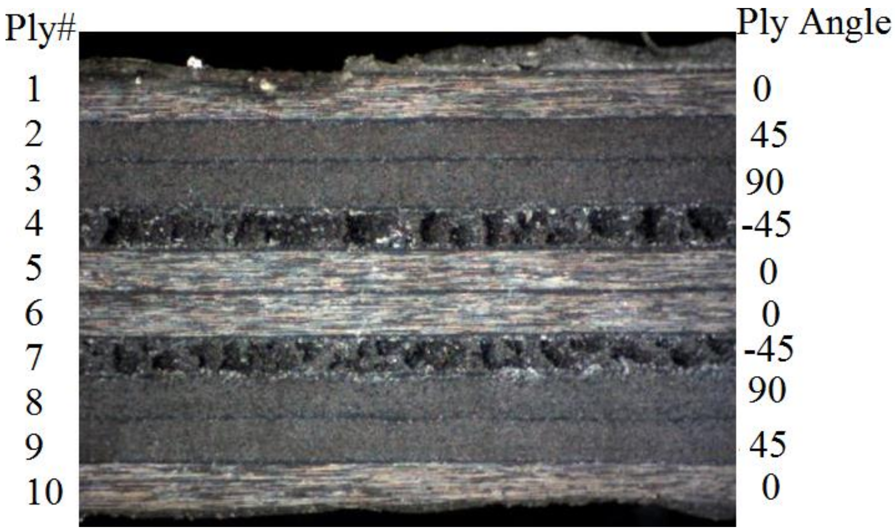

Figure 5.40. Optical macrographs of CFRP laminate after edge trimming

Unlike the edge trimming process, where the cutting tool travels in a linear path and the interaction angle between the cutting direction and ply orientation is the same through the trimming process, the drilling process is different in this aspect. In drilling, the drill tool encounters each plies at different angle as the tool travels circumferentially and the relative cutting angle between the cutting direction and fiber orientation changes continually. The interaction or relative cutting angle between the cutting direction and fiber orientation changes every quarter rotation, where + 45 degree becomes – 45 degree resulting fiber pullout mainly on second, fourth, seventh, and ninth ply. Figure 5.41 shows an SEM image of halve surface of drilled hole at 3000 rpm and 50 µm/rev.

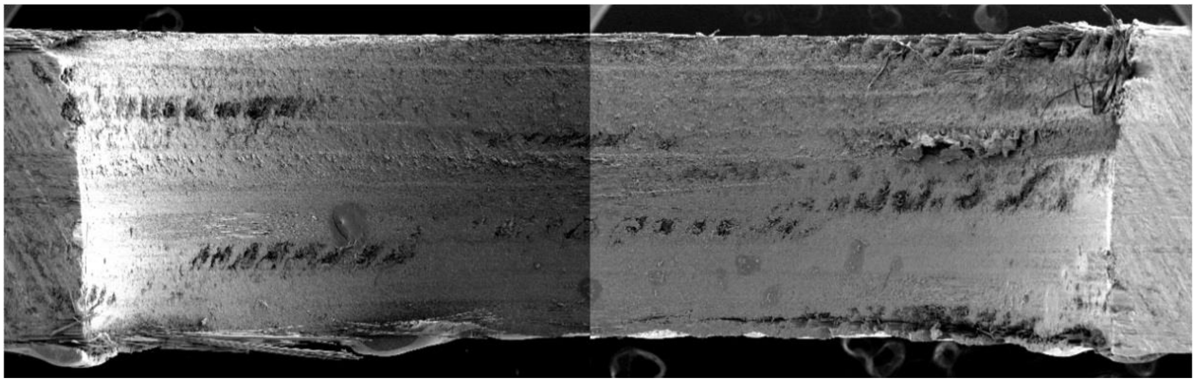

Figure 5.41. SEM image of halve surface of drilled hole at 3000 rpm and 50 µm/rev

In this SEM study, fiber pullout, fiber breakout, exit delamination, and matrix crack were mainly observed surface defects or damages. Most of the fiber pullout and fiber breakout damages were occurred on the second, fourth, seventh, and ninth plies when the ply orientation is ± 45 degree. Whereas, the occurrence of exit delamination and matrix crack were not influenced by ply orientation. The existence of bare fibers completely separated from the matrix due to matrix (resin) poor area at the entrance of the drill was another damage/defect observed in addition to fiber pullout, fiber breakout, delamination, and matrix crack. Figure 5.42 shows SEM images of bare fibers at the drill entrance when drilling with 50 µm/rev at 3000 rpm and 6000 rpm. SEM images of major drilling induced damages/defects observed in this part of the investigation are given in Figure 5.43, whereas, additional SEM micrographs for hole drilled at a combinations on lower and higher levels of feed rate and cutting speed are given in Appendix I.

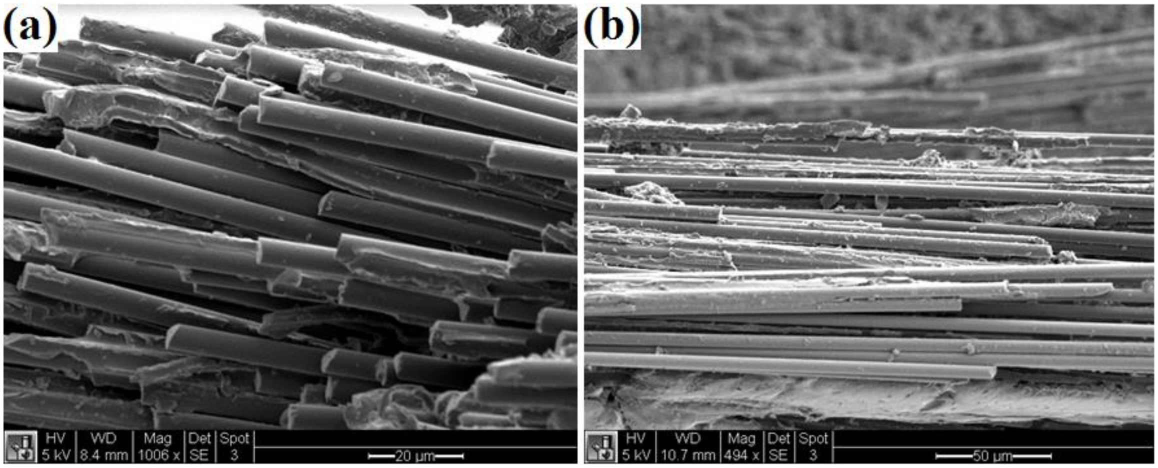

Figure 5.42. Bare fibers at the drill entrance (a) at 3000 rpm and (b) at 6000 rpm

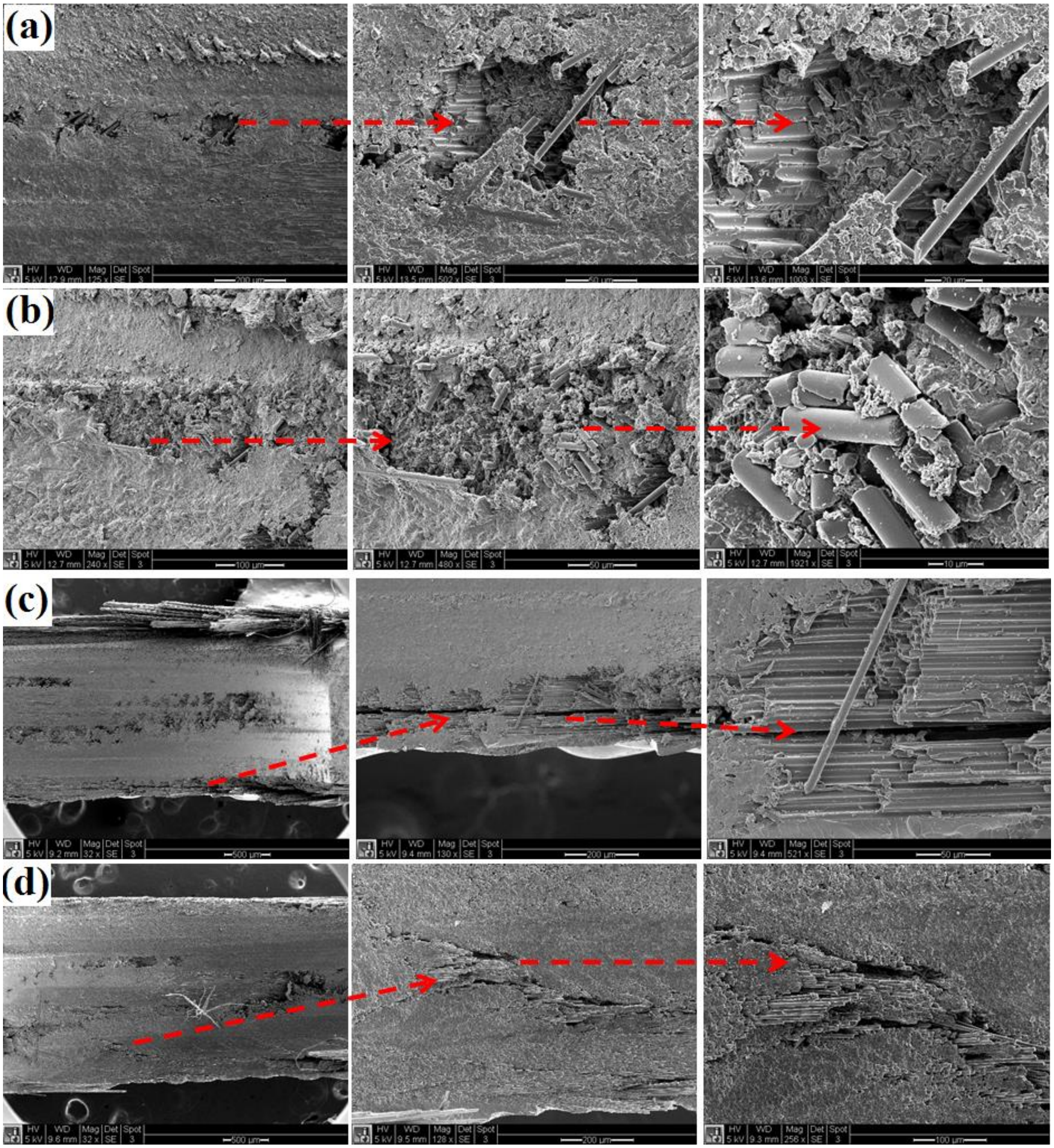

Figure 5.43. SEM images of drilling induced damage and defects when drilling quasi-isotropic CFRP laminate (a) fiber pullout, (b) fiber breakout, (c) exit delamination, and (d) matrix crack

5.3.3. Acoustic Emission Signal

Acoustic emission (AE) signal was acquired during the drilling process using a Physical Acoustic PCI-2 AE system and WD wideband acoustic sensor, where detailed information on the measurement system and procedures can be found in chapter four. Figure 5.44 shows a typical acoustic emission raw signal profile acquired when drilling at a feed rate of 100 µm/rev and 3000 rpm cutting speed. All acquired acoustic emission raw signal shows more or less similar profile trend except some variation on the occurrence, location, and amplitude of signal spikes. The complete array of raw acoustic emission signals profiles for all drilled holes are given in Appendix J.

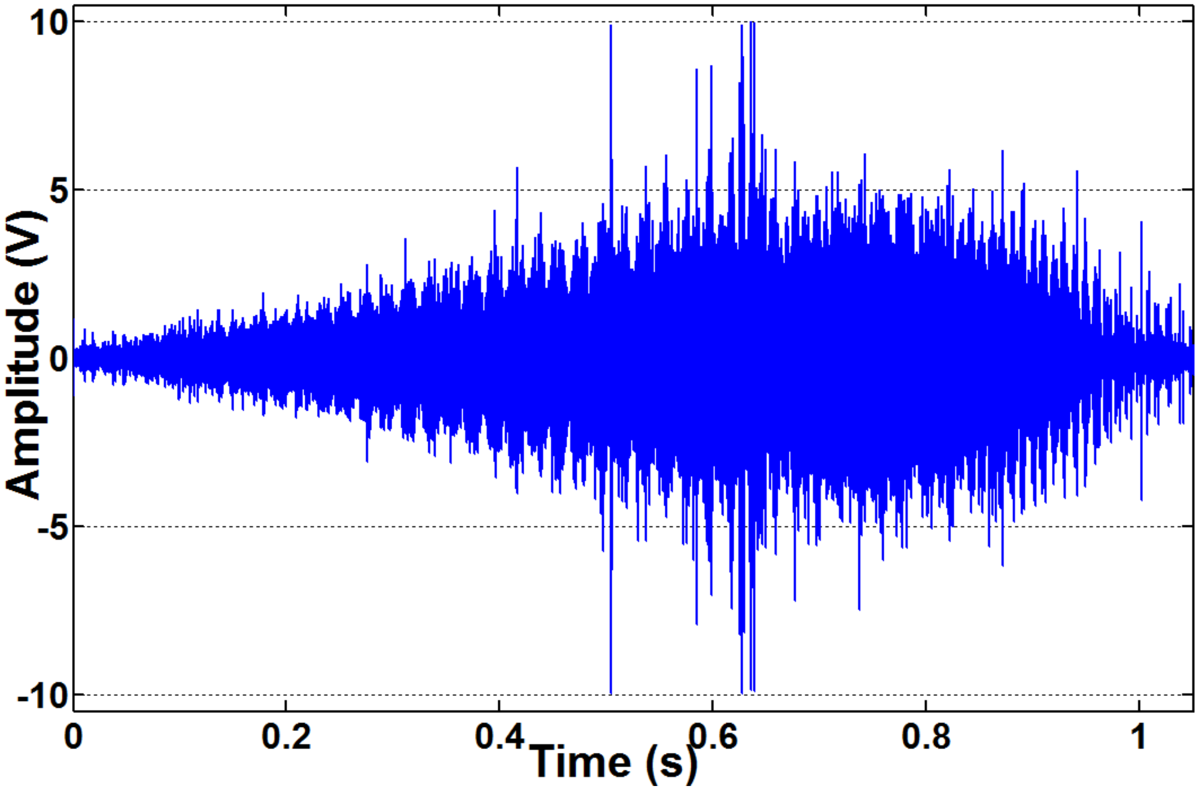

Figure 5.44. Typical profile of acoustic emission raw signal

From the profile of the raw acoustic signal shown in Figure 5.44, there are two large spikes in the amplitude of the acoustic emission signal, which is also observed in most of the acquired signals. Since the location of the center of the cutting edge as it progress through the material being drilled can be calculated using Equation (5.11), it is possible to correlate these amplitude spikes with the location of the cutting edge using the time mark of these spikes. For this, the raw acoustic emission signal was first processed using a Hilbert transform. Figure 5.45 shows a plot for the upper (positive) part of squared Hilbert envelope with the time stamp for the two spikes when drilling at a feed rate of 100 μm/rev and cutting speed of 3000 rpm.

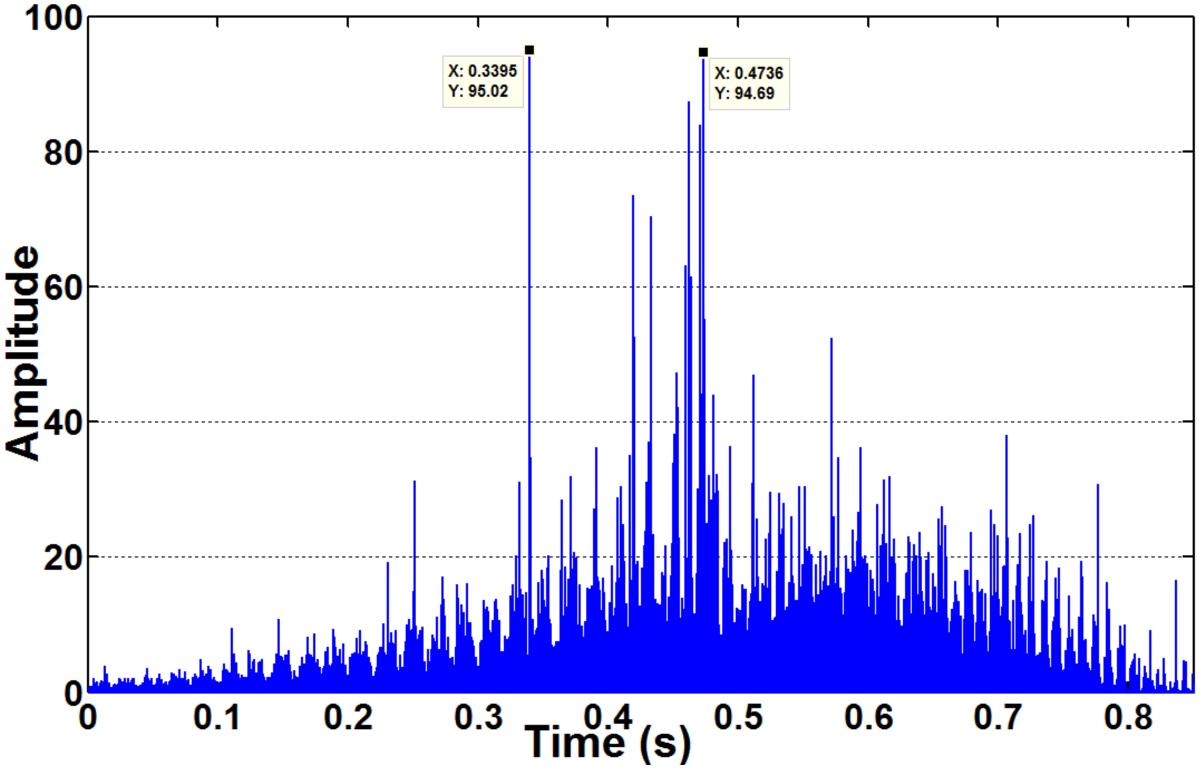

Figure 5.45. Squared Hilbert envelope when drilling at a 100 μm/rev and 3000 rpm

The time difference between the two spikes is can be found by subtracting the time stamp, which is 0.134 second. For this particular case of 100 µm/rev feed rate and cutting speed of 3000 rpm, the cutting edge travels at 5 mm/s giving a distance of 0.671 mm between the two spikes and since the thickness of each ply is 0.2 mm, the number of plies between the spikes is 3.3 plies. The first spike occurs at 0.3395 second, which means for the cutting edge traveling at 5 mm/s, it occurred after the center of the cutting edge travels 1.7 mm. Knowing that the center of the cutting edge is 1 mm far from the tip of the drill, gives the distance traveled by the center of the cutting edge from the first ply to the first spike, which is 0.7 mm or 3.5 ply thickness. From this, it is possible to determine that the two spikes occurred when the center of the cutting edge passes through the fourth and seventh ply, which both plies have a stacking orientation of -45 degree.

As it is discussed and shown in Figure 5.40, sever fiber pullout is expected on the fourth and seventh plies because of their ply orientation. Examination of the SEM image also confirm that these spikes are really caused by the high level of acoustic signal due to the tearing away of fibers from the surface of the hole in the formation of the fiber pullout. In addition to these two large spikes, another spike at 0.572 second was observed in the same signal profile where the center of the cutting edge passes the ninth ply and matrix crack was occurred at this location. Form the study of the above acoustic emission profile and similar events observed in other holes, spikes in squared Hilbert envelope with amplitude greater than 80 are associated with the occurrence of fiber pullout and amplitude greater than 50 are associated with matrix crack. Figure 5.46 shows SEM image of fiber pullouts on fourth and seventh ply and matrix crack on the ninth ply, whereas, Figure 5.47 shows these damages on the squared Hilbert envelope.

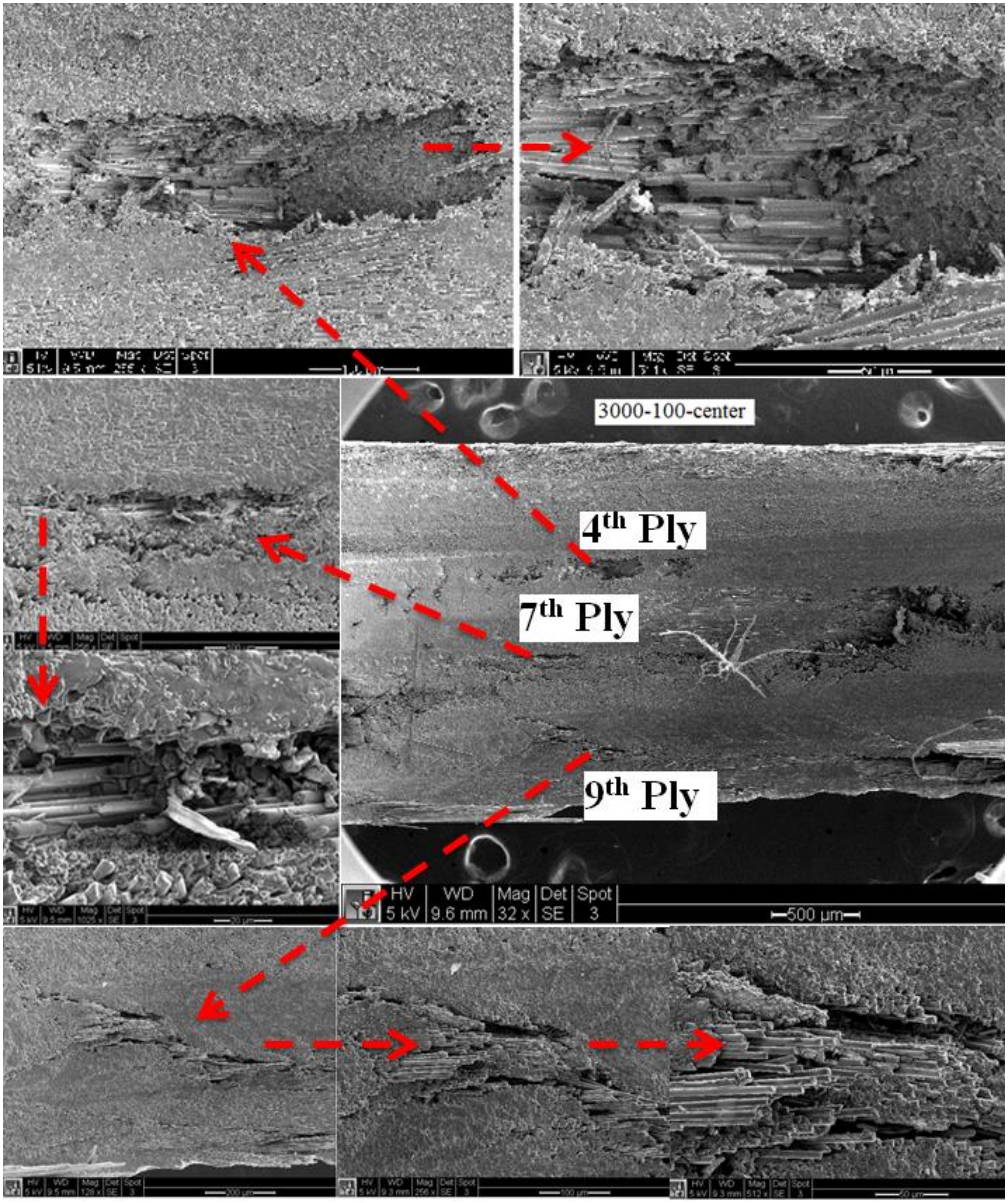

Figure 5.46. SEM images of fiber pullout and matrix crack related to signal spikes

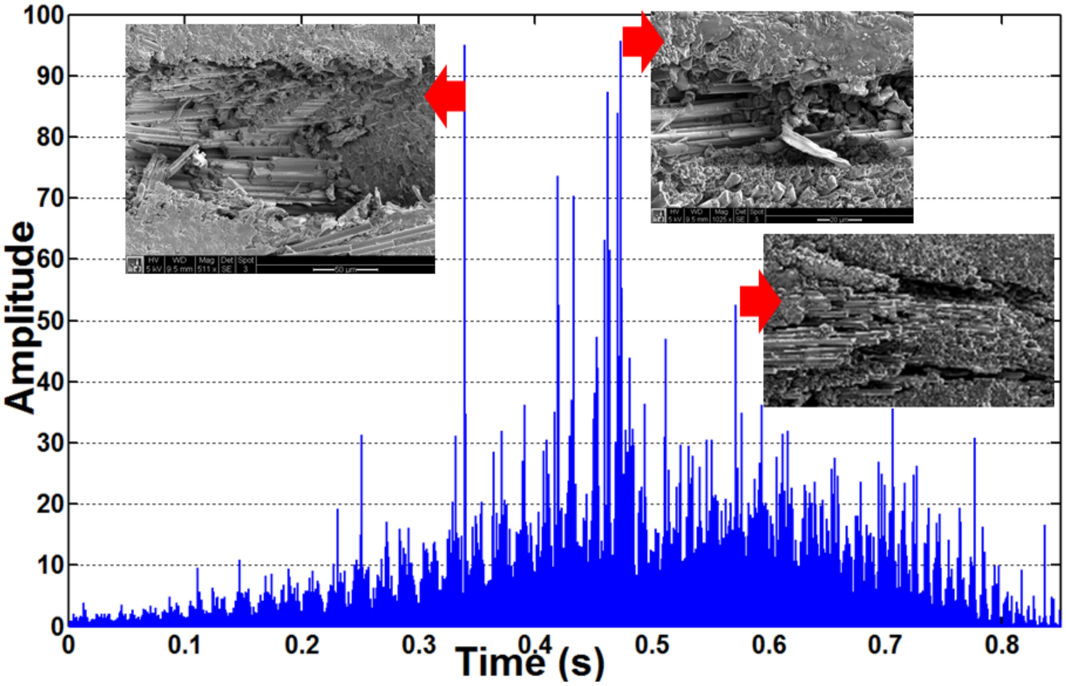

Figure 5.47. Damage and AE amplitude correlation

5.4. Drilling of Uni-Directional CFRP Composites

An experimental investigation on the drilling of unidirectional carbon fiber reinforced plastic (UD-CFRP) composite was conducted using polycrystalline diamond (PCD) tipped eight facet drill. The experimental setup, procedure, and material preparation can be found in chapter four. The quality of the drilled hole surface was examined through surface roughness measurements and by scanning electron microscopy (SEM). All drilling was conducted in dry condition without the use of coolant. The experimental plan was designed using Design Expert by taking cutting speed and feed rate as experimental factors at different level. Using the analysis of variance, the significant factors and their interactions effect were identified in terms of cutting speed and feed rate. Based on the measured data (drill forces, surface roughness and delamination) and the ANOVA, a multiple linear regression model for the hole production process was developed using of the form as shown in Equation (5.13).

$$y(x) = C_0 + \sum_i C_i x_i + \sum_i C_{ii} x_i^2 + \sum_{j>i} \sum C_{ij} x_i x_j \qquad (5.13)$$

In which the following are the coefficients:

C_0 = Constant
C_i = First order or linear effect
C_{ii} = Second order or quadratic effect
C_{ij} = Interaction effects

The variables are the parameters and denoted as follows:

x_1 = speed (RPM)
x_2 = feed rate (µm/rev)

Based on a design of experiments approach, the software then performs an Analysis of Variance (ANOVA) in order to determine the effects of each variables on each of the responses analyzed. The equations for thrust force, torque, surface roughness, and delamination factor follow in the next section. Depending on the model used to fit the data, individual effects and interaction effects can be determined as significant with respect to each response. Once these effects are determined, an equation is generated using the various effects to fit the specified model.

5.4.1. Drilling Forces

Typical representations of the thrust force and torque profiles are shown in Figure 5.48 for two different cutting speeds with varying feed rate. The trend of thrust force and torque profiles displayed similar behavior for all combinations of drilling conditions as the drill progresses through the work material. Thrust force and the torque both show an increasing trend with the increase of the feed rate for all cutting speeds, whereas, both thrust force and torque amplitudes decreased with the increase of the cutting speed. The resulting drilling forces were more influenced by the feed rate compared to the influence by the cutting speed.

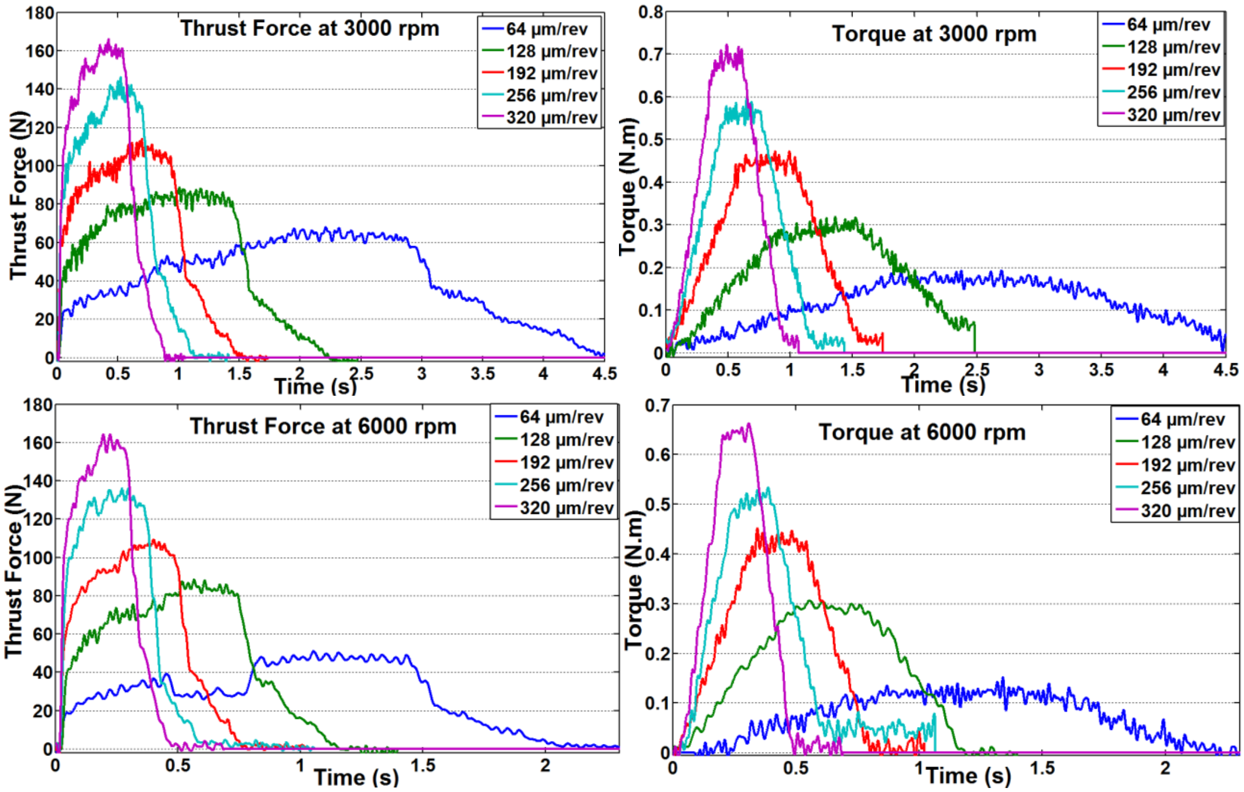

Figure 5.48. Thrust force and torque profiles at 3000 and 6000 rpm for various feed rates

The effect of drilling conditions on the thrust force and torque is modeled by using ANOVA analysis and the surface response models, where detail information of the ANOVA model is given in Appendix K. Figure 5.49 shows the influence of drilling parameters such as cutting speed and feed rate on resulting drilling forces. When the cutting speed increases from 1500 to 6000 rpm, both thrust force and torque decreased by an average of 9.4% and 15.6% respectively over all feed rates, whereas, when the feed rate increases from 64 to 320 µm/rev, thrust force and torque both showed an average increase by 63.9 % and 75.9 % respectively over all cutting speeds. The influence of drilling parameters was more profound on torque compared to their influence on the thrust force.

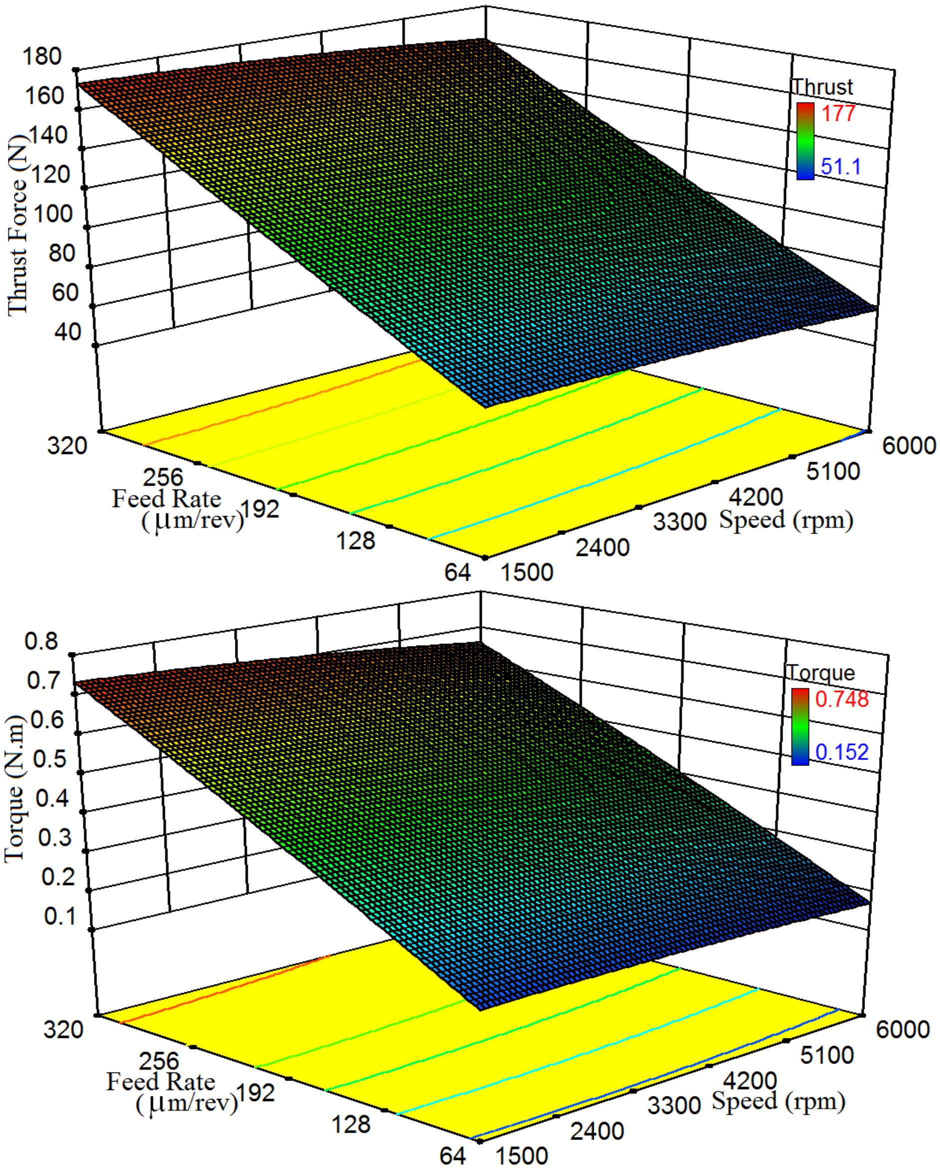

Figure 5.49. Influence of drilling condition on thrust force and torque

A prediction of the thrust force was performed based on the Shaw's equation, which is discussed in detail in chapter two and derived in section 5.2 through Equations (5.1) to (5.8). The three constants required for thrust force prediction was computed for each cutting speed and given in Table 5.11. By substituting these constants in to Equation (5.7) the resulting thrust forces for each cutting speed were computed and the values of measured and predicted thrust forces is shown in Figure 5.50.

Table 5.11. Values of constants for thrust force prediction

Cutting Speed	Drill Diameter	K_1	K_2	a
1500 rpm	6.35 mm	79.42	0.572	0.131
3000 rpm	6.35 mm	69.26	0.789	0.131
4500 rpm	6.35 mm	69.88	0.821	0.131
6000 rpm	6.35 mm	80.86	0.252	0.131

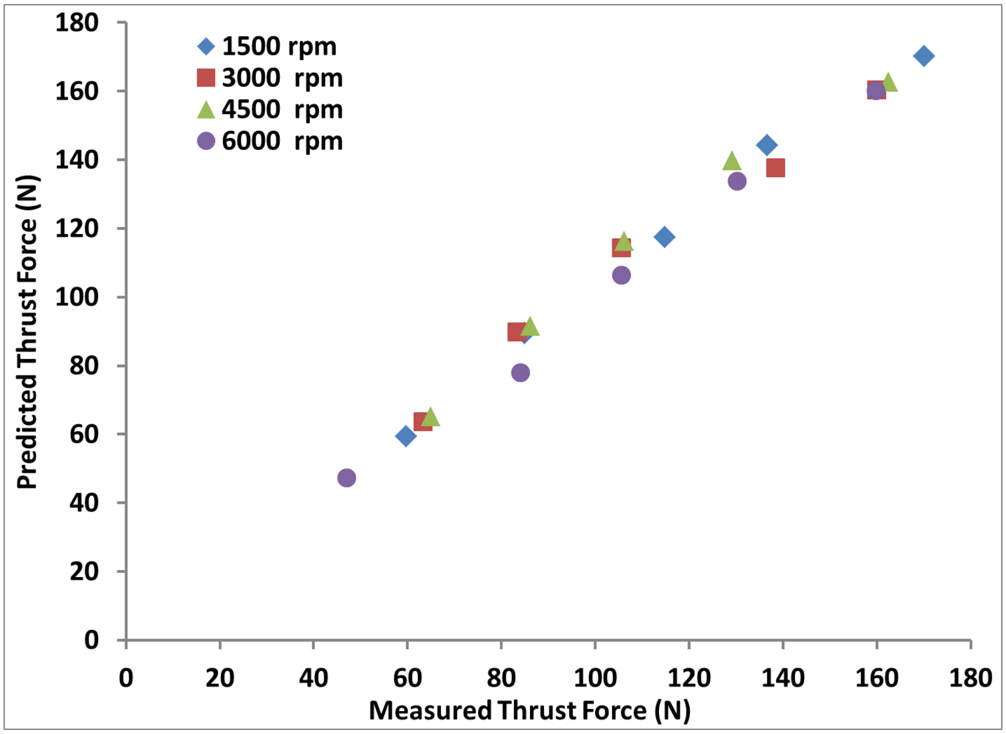

Figure 5.50. Measured and predicted values of thrust forces

5.4.2. Surface Roughness

Surface roughness measurements of the sectioned hole were taken at six different locations/regions as discussed in section 5.2 and shown in Figure 5.10. Typical surface profiles recorded from holes drilled with a combination of higher level of cutting speed with lower level of feed rate and lower level of cutting speed with higher level of feed rate are shown in Figure 5.51. The surface describing parameters namely, the average surface roughness, R_a; maximum peak-to-valley height, R_t; root mean square roughness, R_q; and ten point average surface roughness, R_z; were evaluated from the surface roughness profiles. Surface profiles and roughness parameter values for all combinations of cutting speeds and feed rates are given in Appendix L. 1 and L. 2 respectively.

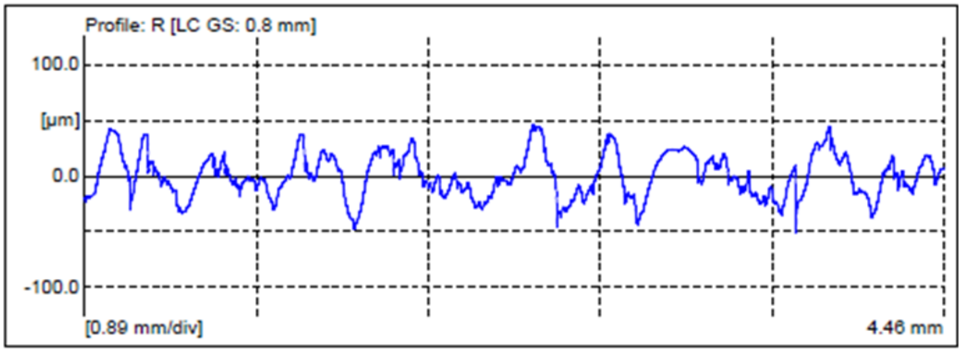

(a) 1500 rpm and 320 µm/rev

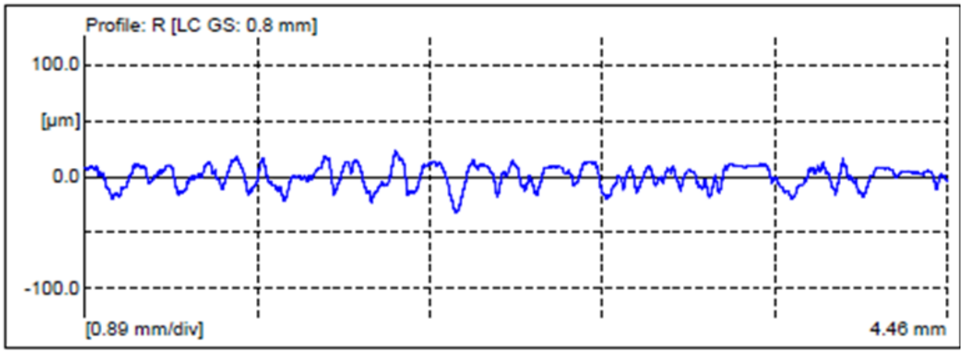

(b) 6000 rpm and 64 µm/rev

Figure 5.51. Typical surface profiles

Figure 5.52 shows a radar plot of the values of surface describing parameters R_a, R_t, R_q, and R_z at lower-level and higher-level combinations of cutting speed and feed rate. Note that the values of the average surface roughness, R_a and R_q shown in Figure 5.52 (a) and Figure 5.52 (c) respectively are smaller than other surface roughness parameters R_z and R_t shown in Figure 5.52 (d) and Figure 5.52 (b) respectively as expected and reported by other studies [1, 5, and 82]. The measured values of both surface roughness parameters (R_t and R_z) found to be higher in two regions where the angle of interaction (relative cutting angle) between the cutting direction and the fiber orientation is 135^0 and 315^0. In addition, as it can be seen from the Figure 5.52, both R_t and R_z displayed the same trend regardless of the cutting speed or feed rate. Based on these observations, it is clear that R_t is best describing parameter to describe not only the average surface roughness but also the fiber pull out as well. Surface roughness height variation is dominated by the feed rate regardless of the speed used.

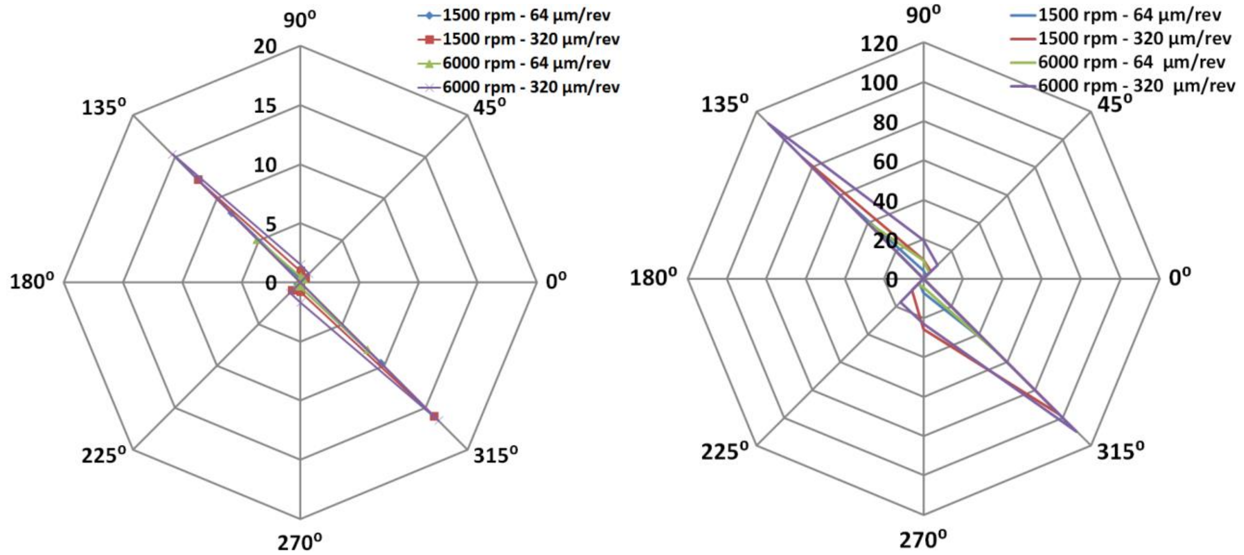

(a) Average surface roughness (Ra)

(b) Average maximum peak to valley roughness (R_t)

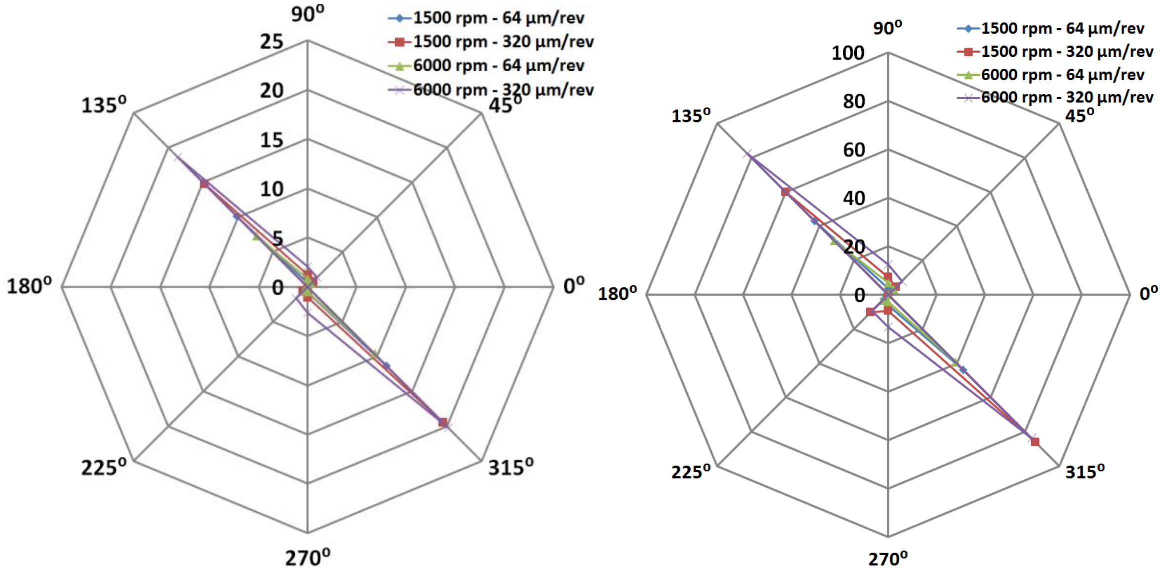

(c) Average root mean square roughness (R_q)

(d) 10 point average surface roughness (R_z)

Figure 5.52. Surface roughness values at different combinations of drilling conditions

From the ANOVA analysis given in Appendix L. 3, a model for surface roughness parameters of R_a and R_t were developed to study the influence of cutting parameters on surface roughness and presented in Figure 5.53. A lower value of both parameters has been measured at 6000 rpm than the 1500 rpm for the same feed rate of 64 µm/rev, whereas, for the feed rate of 320 µm/rev, lower value has been measured at the cutting speed of 1500 rpm than that of 6000 rpm. From this, it is clear that, it is possible to produce a better surface with a combination of high cutting speed and low feed rate. At the higher cutting speed, a better surface is produced at a feed rate of 64 µm/rev, which is one third of the ply thickness.

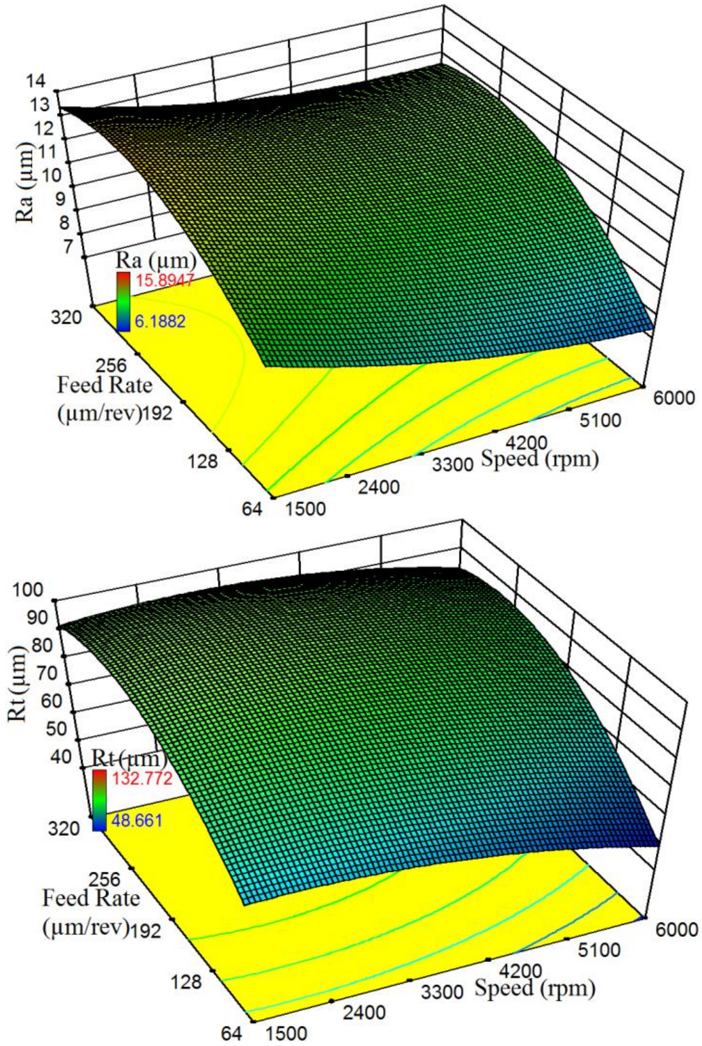

Figure 5.53. Influence of drilling conditions on R_a (top) and R_t (bottom)

5.4.3. Drilled Surface Morphology

An extensive SEM analysis was done to evaluate the surface morphology of the drilled hole surfaces and to document drilling induced defects and damages. Figure 5.54 shows typical drilling induced defects and damages observed in the SEM analysis of this investigation, whereas, more SEM micrographs of the hole surface and drilling induced damage and defects are given in Appendix M. Measurements of damage showed that the fiber breakout at entry shown in Figure 5.54 (a) is no more than one ply deep, the fiber pull out shown in Figure 5.54 (b and c) was slightly over half the ply thickness, and the delamination shown in Figure 5.54 (d) was two ply thicknesses deep. Since the maximum surface roughness was measured on two points (135^0 and 315^0), it is necessary to verify the region of the damage sector.

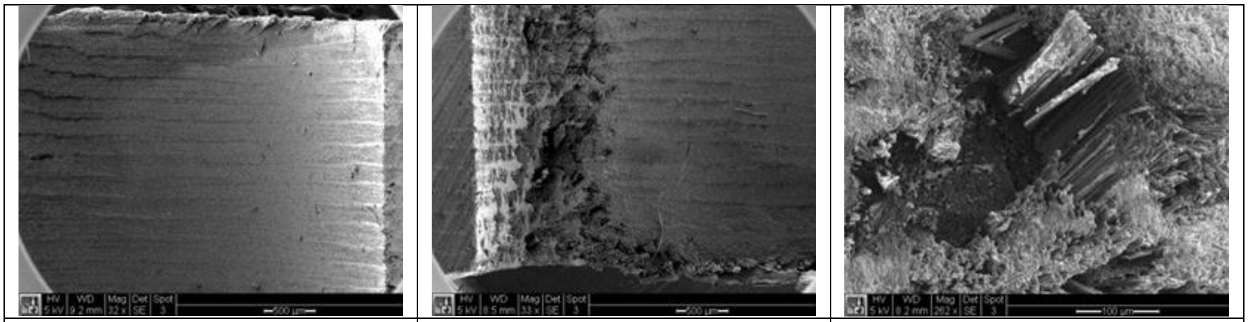

(a) Hole cross-section and minor damage at the drill entry.(1500 rpm, 320 µm/rev)

(b) Damage region and fiber pullout (1500 rpm, 320 µm/rev)

(c) Magnified image of fiber pull out region (1500 rpm, 320 µm/rev)

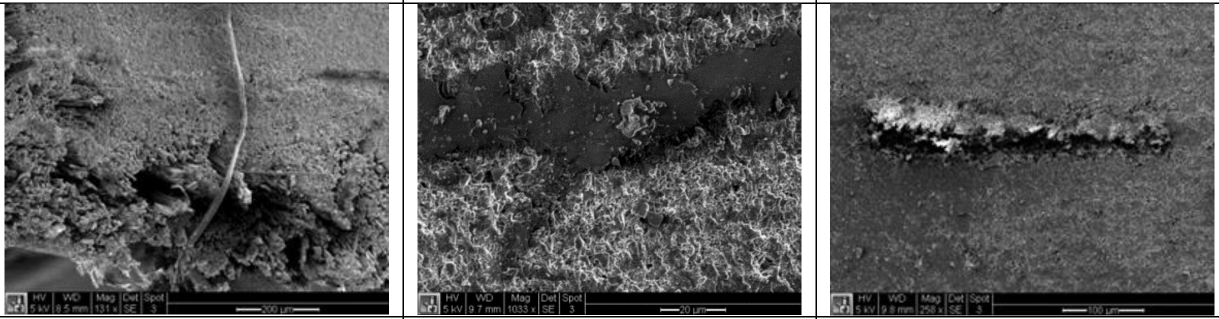

(d) Delamination at the drill exit (1500 rpm, 320 µm/rev)

(e) Charcoal mark of matrix (3000 rpm and 192 µm/rev)

(f) Internal delamination (4500 rpm and 320 µm/rev)

Figure 5.54. SEM micro graphs of typical drilling induced damages on the hole surface

Figure 5.55 shows an SEM micrograph of the two halves of the hole surface with damage sectors or regions. From the SEM image, it was observed that fiber pullout has occurred continuously in a sector rather than just at a point, and this sector approximately covers an average angle of 30 – 35^0. As it can be seen in the SEM micrographs, the surface roughness/fiber pullout in these two regions/sectors was uniform from the top to the bottom of the hole. Within these experimental conditions, the two sectors are found from 135^0 – 175^0 and 315^0 – 355^0 as shown in Figure 5.55. The SEM image indeed shows the two sectors where the surface roughness/fiber pullout is higher confirming the result shown in Figure 5.52 that the highest value of surface roughness parameters were measured in these two sectors namely at 135^0 and 315^0.

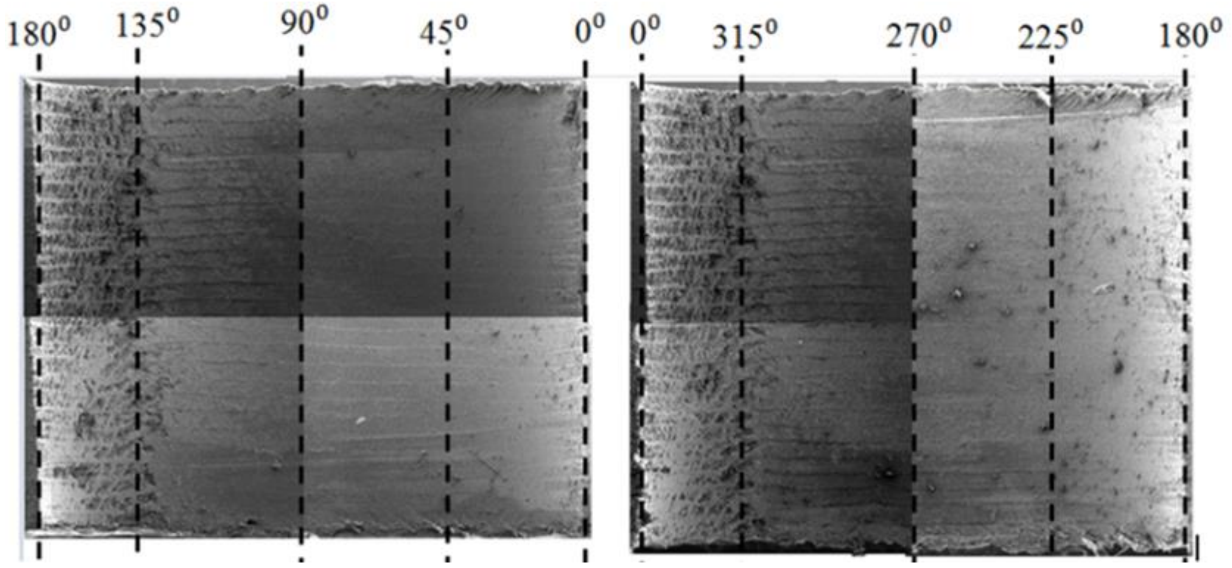

Figure 5.55. SEM micrograph of the two halves of the hole surface and damage sectors

For further investigation of the relationship between thrust force and these damage sectors, thrust force profile for one complete revolution of the drill for a hole drilled at 4500 rpm was plotted and shown in Figure 5.56. As it can be inferred from the plot, the trust force varies significantly throughout the rotation of the drill which is an indication of the resistance of the material to the cutting action varies with the relative cutting angle between the cutting direction and the fiber orientation. This variation of the thrust force can also represent the cutting action that takes place around the circumference of the hole. The magnitude of the thrust forces noticeably varies from position to position or sector to sector. The rotational profile of the thrust force reveals that there are two unloading sectors in each rotation approximately around at 135^0 and 315^0, where fiber pullout was dominant in these sectors. The circumferential variation of thrust force along with the results of fiber pullout and surface roughness confirms that the resulting hole surface quality is clearly influenced by the cutting mechanism and interaction angle between the cutting direction and fiber/ply orientation as discussed in section 5.1.

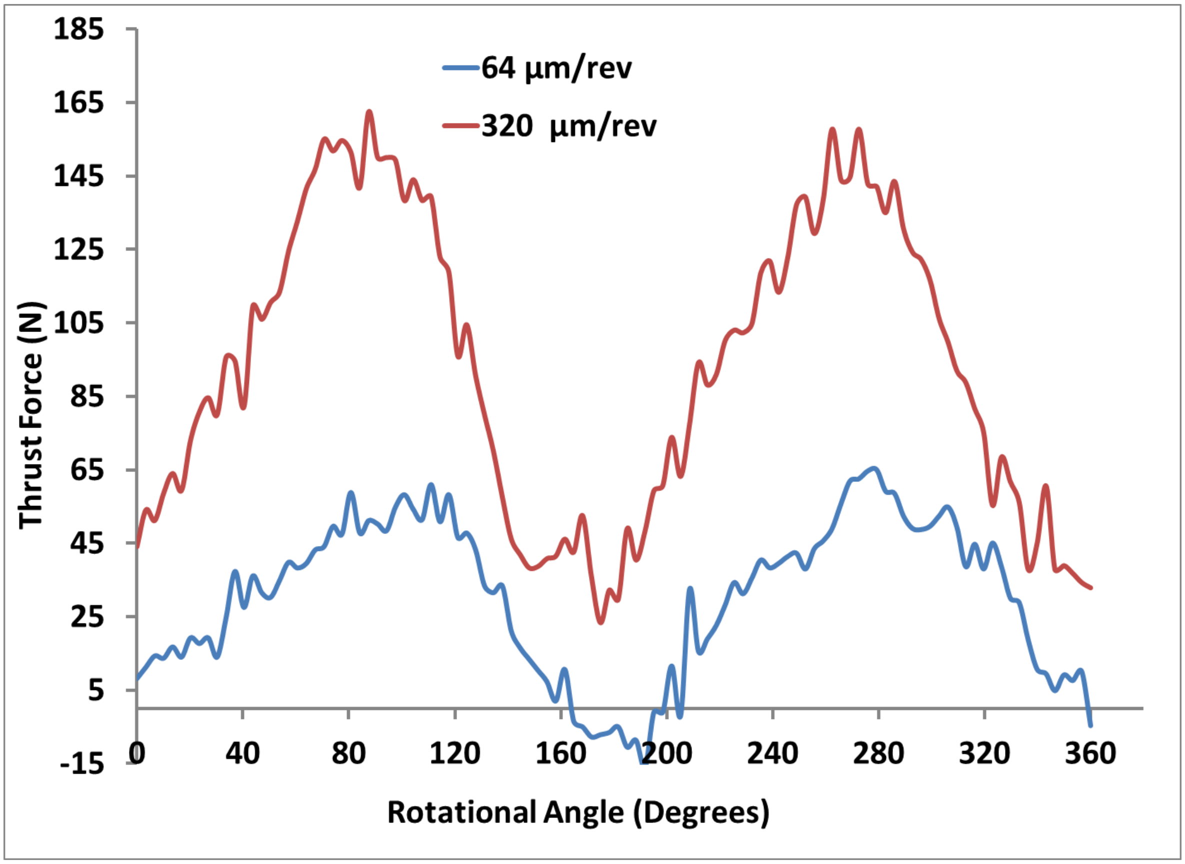

Figure 5.56. Rotational variation of thrust force at full engagement of the cutting edge

5.4.4. Delamination

Delamination at the entrance and exit side of the drill was measured using Toolmakers microscope through the same methodology discussed in section 5.2 and the amount of delamination is expressed in terms of delamination factor as shown in Figure 5.19. An optical macrograph of delamination at the drill entrance and exit for combinations of lower and higher levels of cutting speed and feed rate is shown in Figure 5.57, whereas, optical macrographs of delamination for all drilled holes are given in Appendix N. Delamination at the exit side of the drill is much severe compared to delamination at the entrance for all combinations of cutting speeds and feed rates. As it can be seen from the figure, better hole was produced at a combination of higher speed and lower feed rate. Delamination at the entrance and exit was reduced by 15 % when the cutting speed increased from 1500 to 6000 rpm at the lower feed rate level. Note that even though the sizes of the holes are equal for all holes, it looks different in the figure because holes with large delamination were zoomed out to include the delamination area.

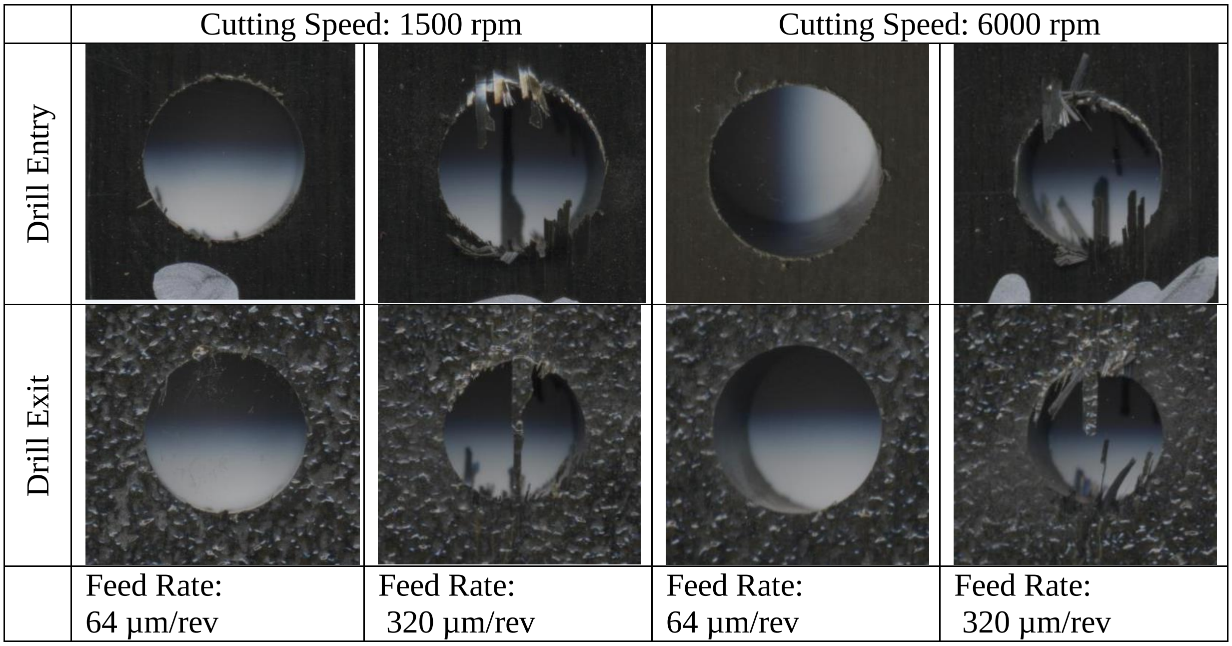

Figure 5.57. Optical macrograph of delamination at the drill entrance and exit

Delamination factor was calculated from the measured delamination and based on delamination factor and ANOVA a multiple linear regression model was developed. Figure 5.58 shows the influence of drilling conditions on delamination factor for peel-up (drill entry) and push down (drill exit) delamination. Delamination factor at the exit was always higher than the drill entry regardless of the cutting speed and feed rate. Delamination factor was found to be linearly related to cutting speed and feed rate at the drill entry or for peel-up delamination, whereas, it is non-linearly related to cutting speed and feed rate at the drill exit or for exit delamination. Aerospace application acceptable delamination factor of less than 1.4 for a 6.35 mm diameter drill was achieved when the feed rate is less than or equal to one-third of the ply thickness. In this investigation, optimal drilling condition to keep delamination factor less than 1.4 was found to be 64 µm/rev of feed rate with the cutting speeds of 4500 to 6000 rpm.

The influence of feed rate on delamination factor at the entry and exit was higher than the influence of cutting speed, which is also seen in drilling forces and surface roughness parameters. Delamination factor for entry and exit delamination increased when the feed rate increases and decreased when the cutting speed increases. When the feed rate increases from 64 to 320 µm/rev, delamination factor increased by an average of 42.5 % and 40.4 % at the drill entry and exit respectively, whereas, when the cutting speed increases from 1500 to 6000 rpm, delamination factor decreased by an average of 20.5 % and 13.9 % at the drill entry and exit respectively. The lowest delamination factor at the drill entry was measured when drilling with a cutting speed of 6000 rpm and 64 µm/rev, whereas, the lowest delamination factor at the drill exit was measured when drilling with a cutting speed of 4500 rpm and 64 µm/rev. Over all, delamination at drill entry and exit can be significantly minimized by a combination of higher cutting speed and lower feed rate, and from this investigation, a feed rate of one-third of the ply thickness was found to be an optimal feed rate to minimize delamination at drill entry and exit.

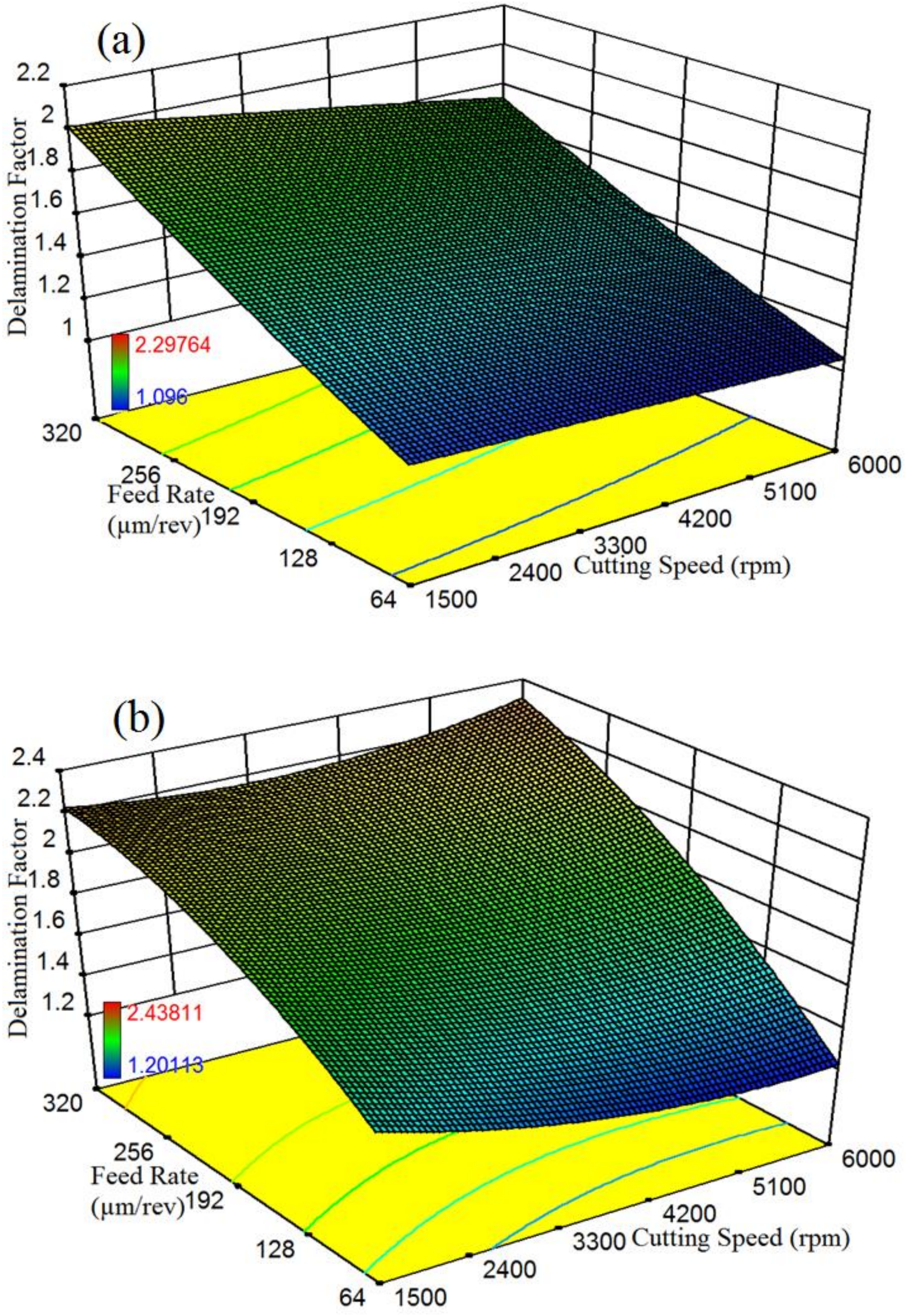

Figure 5.58. Influence of drilling conditions on delamination factor (a) at entry and (b) at exit

5.5. Conclusion

Quality of holes and drilling induced damages and defects when drilling uni-directional and multi-directional CFRP composite laminates were experimentally investigated. The influence of drilling parameters and conditions on the resulting quality of produced holes and other drilling induced damages and defects was investigated. The quality of drilled holes was characterized in terms of surface roughness measurement and drilling induced damages and defects. Drilling induced defects and damages such as drilled hole surface roughness, hole surface morphology, fiber pullout, and delamination were studied through qualitative measurements and SEM examination. Drilling force such as thrust force and torque were evaluated and related to various process induced damages and defects. In some cases a preliminary investigation on the use of acoustic emission signal and vibration signal for damage and defect detection was performed. From the results and observations made in this investigation, the following concluding remarks are drawn.

1. Thrust force and torque increased with the increase of feed rate and decreased with the increase of cutting speed and the influence of the feed rate on cutting forces was more pronounced than the influence caused by the cutting speed for all types of CFRP laminates studied. Thrust force prediction equation was derived based on Shaw’s prediction equations and a prediction of thrust force was performed with an average determination coefficient of 0.98 for all CFRP laminates.
2. Thrust force amplitudes varies significantly over the rotational position of the drill when drilling uni-directional CFRP laminate and a lower value of the thrust force was observed around the rotational angles of 135^0 and 315^0.

3. In all types of CFRP laminates, rougher surface regions/sectors were observed along the circumference of the hole, which runs throughout the hole depth. Maximum values of average surface roughness parameters (R_a, R_q, $R_{z,}$ and R_t) were occurred (measured) when the angle of interaction between the cutting direction and the ply orientation is 135^0 and 315^0 along the circumference of the hole. Better hole surface quality with minimum surface roughness was obtained with a combination of higher cutting speed and lower feed rate in all cases of CFRP laminates.
4. In the case of multi-directional CFRP laminate, fiber pullout occurred in a periodic fashion based on the orientation of individual plies in the stacking sequence, whereas, in the case of uni-directional CFRP laminate, fiber pullout was observed in two regions where the angle of interaction between the cutting direction and the fiber orientation is from 135^0 - 175^0 and 315^0 - 355^0.
5. When drilling multi-directional CFRP laminate, fiber pullout depth varied from 43 µm to 328 µm based on the orientation of individual plies in the stacking sequence, whereas, width of fiber pullout was found to be varied from one half to one ply thickness. Fiber pullout depth was higher where the orientation of individual plies in the stacking sequence is $\pm 45^0$. Surface roughness parameter maximum peak-to-valley height R_t was found to be sensitive parameter to characterize fiber pullout depth.
6. Delamination factor increased when the feed rate increases and decreased with the increase of the cutting speed for all CFRP laminates. The amount of delamination factor resulted when drilling multi-directional CFRP laminates was lower than the delamination factor when drilling uni-directional CFRP laminate. Between the multi-directional laminates, delamination factor when drilling multi-directional CFRP laminate with

woven fabric surface ply was lower than the delamination factor measured when drilling multi-directional CFRP laminate with fiberglass scrim surface ply. Over all, delamination factor was minimized when drilling with a combination of higher cutting speed and lower feed rate.

7. Correlation between the amplitude of demodulated vibration signal and damage (fiber pullout) length was performed when drilling multi-directional CFRP laminate with fiberglass scrim surface ply. The damage length measured shows a good correlation with the corresponding amplitude of the demodulated signal envelope with an average coefficient of determination value of 0.83. For the best and reliable damage detection, considering the damage area is suggested instead of just the damage length in the future.
8. The relationship between drilling induced damages and acoustic emission signal amplitude was studied. From this study, spikes in squared Hilbert envelope with amplitude greater than 80 are associated with the occurrence of fiber pullout and those with amplitude greater than 50 are associated with matrix crack.

CHAPTER 6: PTY-BY-PLY CUTTING ACTION WHEN DRILLING CFRP COMPOSITES

6.1. Introduction

The complexity of the cutting action and mechanism when drilling CFRP composite was discussed in chapter five and the cutting mechanism was examined for fully drilled holes. During the drilling of FRP composite materials, the cutting edge encounters the reinforcing fibers at different angle at every instant of the cutting action (drilling process). The interaction angle between the cutting direction and the orientation of the reinforcing fiber varies based on the location of the cutting edge throughout the circumference and the stacking orientation of each individual plies. For this, an experimental investigation of ply-by-ply cutting action was conducted on a unidirectional CFRP laminate through blind holes and results of this investigation will be presented in this chapter.

6.2. Experimental Setup and Procedure

A 6.35 mm thick unidirectional CFRP laminate composed of 33 plies with a ply thickness of 192 μm was prepared from a large panel by cutting to a size of 127 by 178 mm using a circular diamond saw. A blind hole was drilled with various depths ranging from two plies up to fourteen plies with increments of two ply thickness using a 6.35 mm carbide twist drill with cutting speed of 3000 rpm and feed rate of 100 μm/rev. Drilling force was acquired during the drilling process. The drilled blind holes were inspected for possible damages through optical microscope and scanning electron microscopy. An optical images of blind holes drilled at various depth is shown in Figure 6.1.

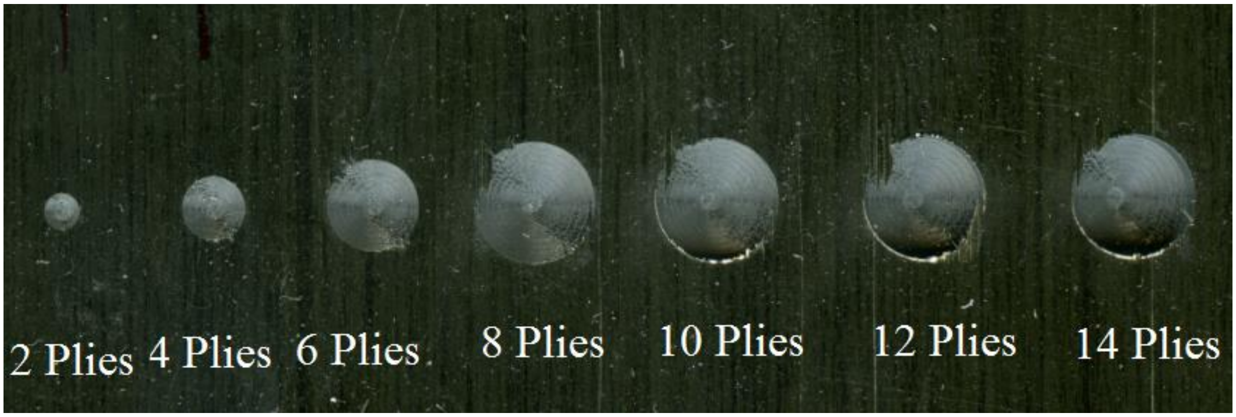

Figure 6.1. Optical images of blind holes at various depth

6.3. Thrust Force

Figure 6.2 shows thrust force and torque profiles for the blind holes drilled with various depths ranging from two plies up to fourteen plies with increments of two ply thickness. The thrust force profile shows same trend for all numbers of plies drilled and the change in magnitude of thrust force when the numbers plies drill increased was relatively constant (similar). The magnitudes of the thrust force for the numbers of plies drilled are shown in Figure 6.3, whereas, the numeric values of the thrust force and the percent increase in thrust force magnitudes with the increase of numbers of plies drilled is given in Table 6.1.

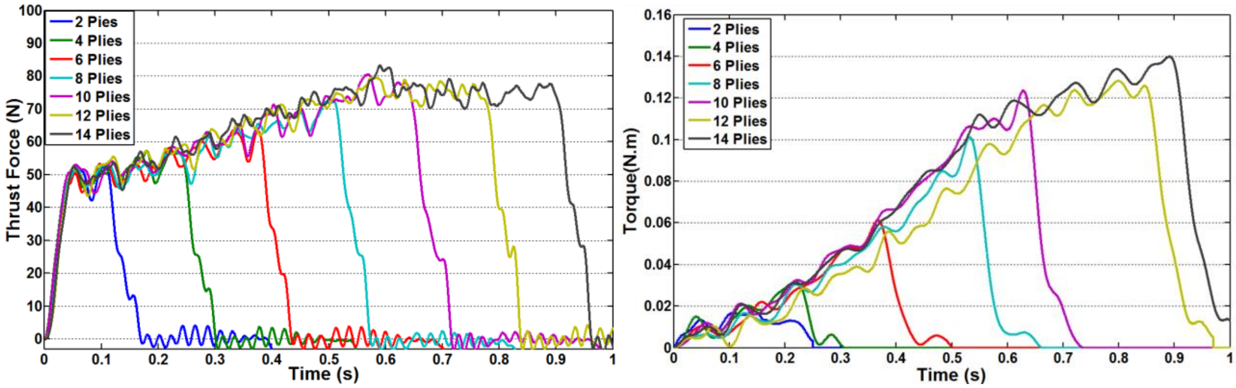

Figure 6.2. Thrust force profiles (left) and torque profiles (right) for numbers of plies drilled

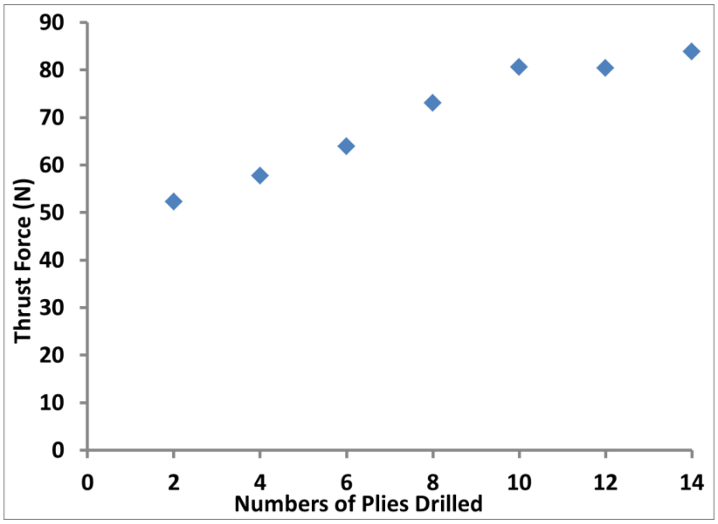

Figure 6.3. Thrust force magnitudes for numbers of plies drilled

Table 6.1. Increment of thrust force magnitudes for numbers of plies drilled

Numbers of plies drilled	Thrust Force (N)	Increment (N)	% increase
2	52.254		
4	57.694	5.44	9.43
6	63.934	6.24	9.76
8	72.999	9.06	12.42
10	80.612	7.61	9.44
12	80.390	-0.22	-0.28
14	83.875	3.49	4.16

As it can be seen from Figure 6.3 and Table 6.1, thrust force magnitude show a relatively constant increment when the number of plies drilled increases. When the numbers of drilled plies increases from two to ten, the thrust force magnitude increased by an average of 10% for every increase of two plies and the change in thrust force magnitude was negligible when the numbers of plies drilled increased from ten to twelve. The change in thrust force magnitude for numbers of plies drilled greater than ten where the cutting edge and body of the drill fully engaged inside the material was smaller compared to the changes seen for numbers of plies drilled less than ten. Large portion of the thrust force is due to the penetration of the first one or two plies and once the drill penetrates the top ply, the magnitude of the thrust force due to the cutting of each individual plies is much less than the thrust force caused by the penetration action.

6.4. Inspection of Drilled Surface

The drilled surface was examined through optical imaging to investigate possible damage and defects induced by the cutting action. Optical images of the drilled surface for each numbers of plies drilled are shown in Figure 6.4. As it was discussed in chapter five, drilling induced damages were observed in specific sectors or regions on all cases of numbers of plies drilled. Looking at the center of the blind holes one can see the fibers are smashed and crashed together by the chisel edge with a rotational pattern in the direction of the drill rotation. In addition to the crashing of fibers at the contact of the chisel edge, a rougher and rugged surface is seen at two sectors when the interaction angle between the fiber orientation and cutting direction is -45 degrees. The same damage sector or region was also seen in all investigations studied and discussed in chapter five due to the cutting mechanism of drilling FRP composites as shown in Figure 5.2.

A new phenomenon about the occurrence of peel-up delamination was observed in this investigation. Peel-up delamination or delamination at the drill entrance was considered to occur by the cutting action of the chisel edge and all earlier studies reported that it occurs when the chisel edge scratches and peeled off the top plies. As it can be seen from the optical images in Figure 6.4, no peel-up delamination is occurred when the numbers of plies drilled are below six and it starts occurring when the numbers of plies drilled are six and above. The vertical length of the cutting edge (lip) measured parallel to the drill axis used in this investigation is 1.17 mm and if we divide this length by the ply thickness we found that the drill must cut six plies to drill a depth of 1.17 mm. After the depth of 1.17 mm or after cutting six plies, the cutting edge is fully inside the material and the body of the drill starts entering the work piece at which the occurrence of peel-up delamination starts.

Numbers of plies drilled	Full Image	Magnified Image
2		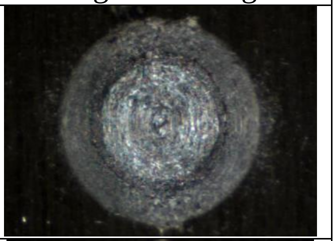
4	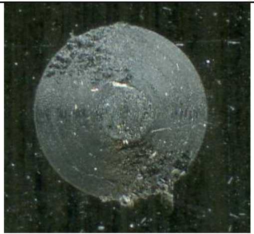	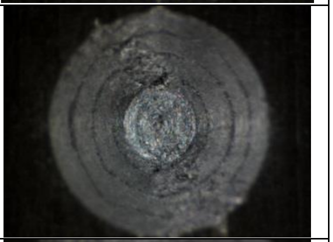
6		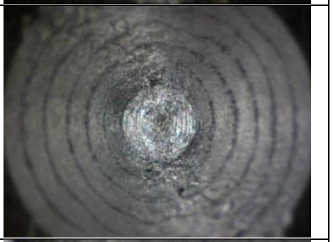
8		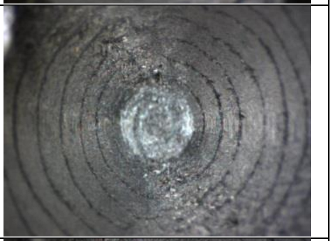
10	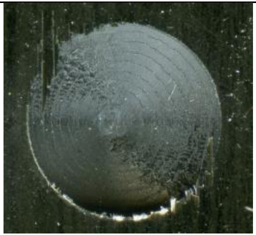	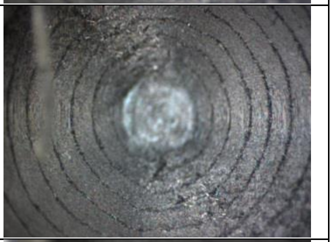
12	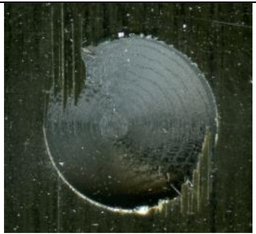	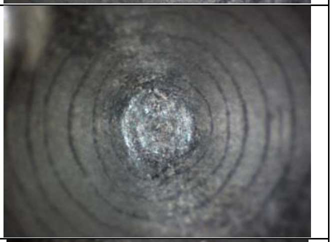
14		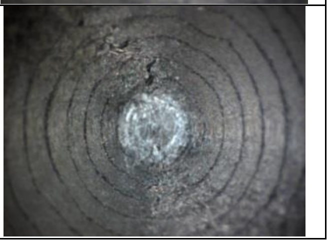

Figure 6.4. Optical images of the drilled surface for each numbers of plies drilled

From this, it is clear that the chisel edge did not create (cause) peel-up delamination rather peel-up delamination is caused when the drill flute starts engaging or entering the work piece. Delamination at the drill entrance occurred after the cutting edge is completely inside the work material and as soon as the flute of the drill made contact the work piece material. In addition to this, all peel-up delamination were occurred on the same location when the interaction angle between the fiber orientation and cutting direction is -45 degree. An SEM image of peel-up delamination for the numbers plies drilled from eight to twelve is shown in Figure 6.5. As it can be seen in the SEM micrographs, peel-up delamination occurred at the same orientation on all cases of numbers of plies drilled.

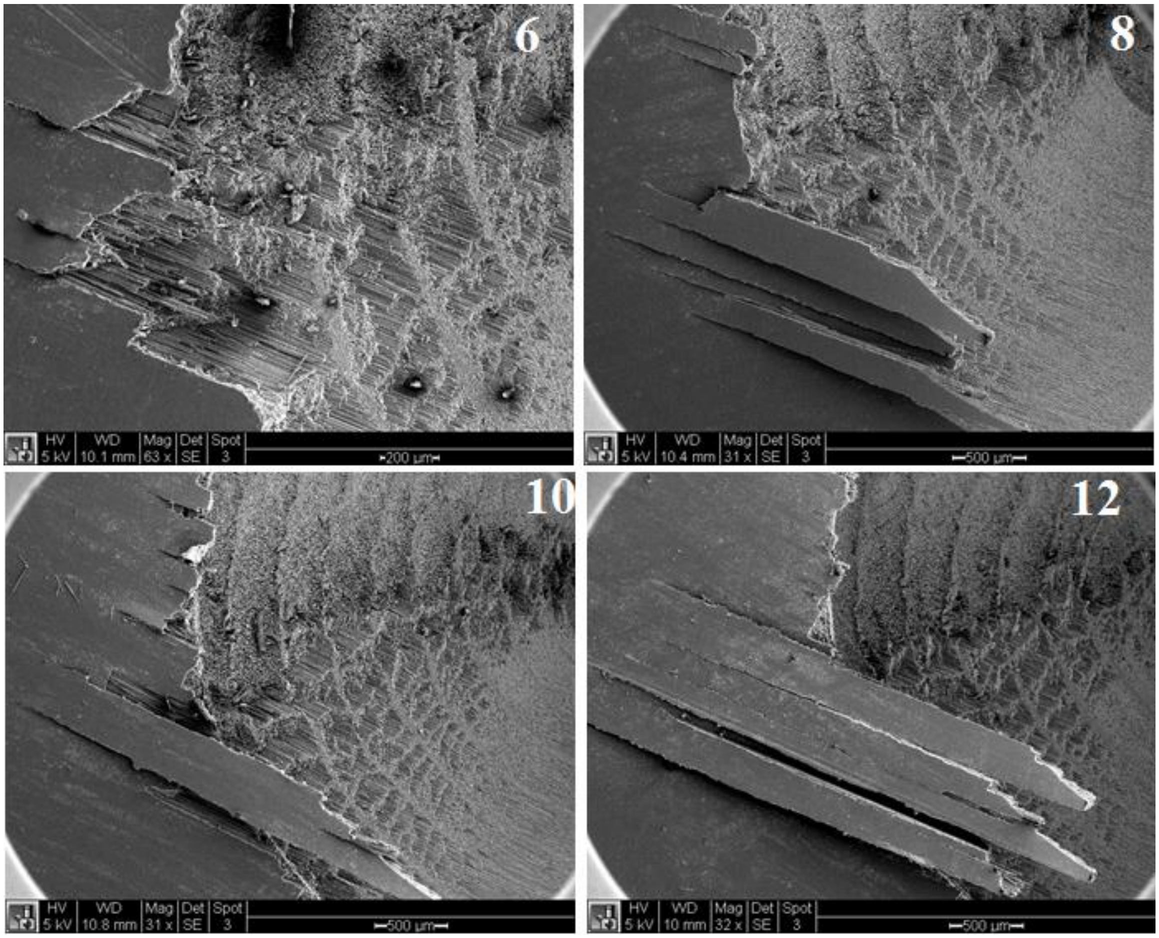

Figure 6.5. SEM micrograph of peel-up delamination

CHAPTER 7: ANALYTICAL MODEL OF EXIT DELAMINATION AND EXPERIMENTAL VERIFICATION

7.1. Introduction

Exit delamination is regarded as the most dangerous mode of delamination of all when drilling FRP composites because of its contribution to the reduction of structural strength and stiffness over the life of the structural component. Over the years, many experimental, analytical, and numerical investigations have been conducted to address this problem. A comprehensive review of these various studies conducted in order to address the problems and challenges caused by exit ply delamination when drilling FRP composite laminates is given in chapter two. In this chapter, an analytical model for predicting critical thrust force at the onset of exit ply delamination will be presented and compared with the existing models. In addition, experimental investigation conducted through a punch test on a blind hole to characterize the critical thrust force at the onset of exit ply delamination will be discussed. Finally, the critical thrust force measured from the experimental investigation will be compared with the developed analytical model.

7.2. Model Derivation

Developing analytical model for prediction of critical thrust force at the onset of exit ply delamination is not a new topic and many studies [73 – 76] reported analytical models for exit ply delamination using Griffith’s failure/fracture theory. From these, Hocheng model [73] was the earlier model and it assumes a circular crack or fracture surface below the cutting tool. Later a new model proposed by Jain [75] considered an elliptical delamination zone under the drill tool, which is more appropriate for FRP materials since the propagation of crack in not uniform in the longitudinal and transverse direction of FRP laminates. Zhang [74] also considered an elliptical delamination zone and his model was modified by Gururaja [76] by considering distributed load acting on the entire elliptical zone, which was considered as a point load in the case of Zhang model [74].

This study presents analytical exit delamination model for prediction of critical thrust force at the onset of exit ply delamination when drilling uni-directional CFRP composites based on linear elastic fracture mechanics (LEFM) and plate bending theory. In the derivation of the model, an elliptical delamination zone was considered. Since the load applied by the drill tip is circular, the lateral uniform load was taken over a circular region rather than over elliptical region. Figure 7.1 shows the elliptical delamination zone and the circular lateral uniform loading region where a and b are the major and minor axis of the elliptical delamination zone respectively. The radius of the circular lateral uniform loading region is also the minor radius of elliptical delamination zone represented by letter b.

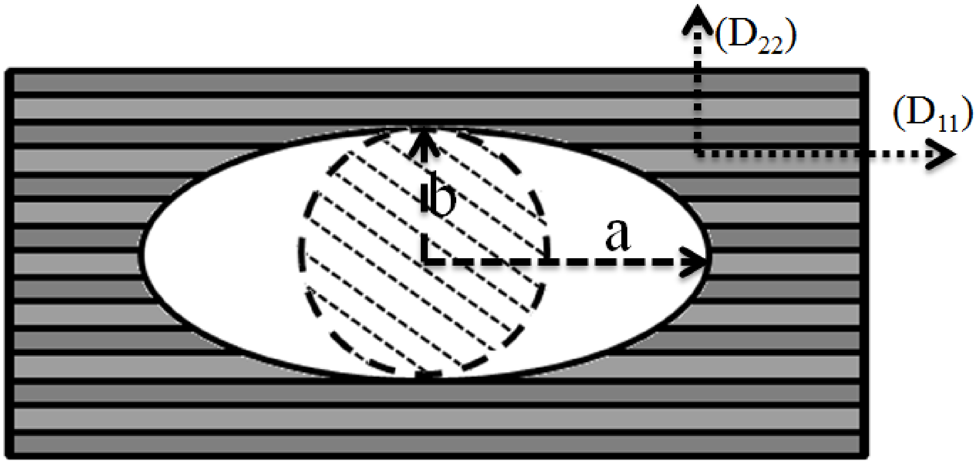

Figure 7.1. Schematic representation of delamination zone and lateral loading region

The energy balance equation can be written as shown in Equation (7.1) based on LEFM

$$P_c dw_o = G_{IC} dA + dU \tag{7.1}$$

Where P_c is the critical thrust force at the onset of exit ply delamination, dw_o is the displacement of the drill tip, G_{IC} is the energy release rate per unit area, dA is the increment of the crack area, and dU is the infinitesimal strain energy.

For uni-directional FRP laminate, the twisting-bending components D_{16} and D_{26} equals to zero and the extension-bending coupling the [B] matrix also equals to zero. Based on these, the constitutive relationship between moment and curvature can be expressed in the form as shown in Equation (7.2). Where [M] is the moment, [D] is bending stiffness, and [k] is curvature.

$$\begin{bmatrix} M_x \\ M_y \\ M_{xy} \end{bmatrix} = \begin{bmatrix} D_{11} & D_{12} & 0 \\ D_{12} & D_{22} & 0 \\ 0 & 0 & D_{66} \end{bmatrix} \begin{bmatrix} k_x \\ k_y \\ k_{xy} \end{bmatrix} \tag{7.2}$$

The displacement (W) of an elliptical plate and the displacement field (w_o) in closed form were derived by Bert [98] and are given here in Equation (7.3) and (7.4) respectively.

$$W = w_o \left(1 - \frac{x^2}{a^2} - \frac{y^2}{b^2}\right)^2 \tag{7.3}$$

Where a and b are major and minor axis of the elliptical region.

$$w_o = \frac{q}{C_{33}} \tag{7.4}$$

$$wher, \qquad C_{33} = \frac{24D_{11}}{a^4} + \frac{24D_{22}}{b^4} + \frac{16(D_{12} + D_{66})}{a^2 b^2}$$

Where q is the lateral uniform load over the circular region of radius b shown in Figure 7.1 and the relationship between q and Pc can be expressed according to Equation (7.5).

$$q = \frac{P_c}{\pi b^2} \tag{7.5}$$

By defining an ellipticity ratio $= \frac{a}{b}$, and substitute it in to Equation (7.5) we get

$$q = \frac{P_c \xi^2}{a^2} \tag{7.6}$$

Substituting the value of q in Equation (7.6) in to Equation (7.4) and simplifying it we have the following:

$$w_o = \frac{P_C \xi^2 / a^2}{C_{33}}$$

$$w_o = \frac{P_c \xi^2 a^2}{24\pi\left[D_{11} + \frac{2}{3}\xi^2(D_{12} + D_{66}) + \xi^4 D_{22}\right]} \tag{7.7}$$

$$letting\ \ D^* = \left[D_{11} + \frac{2}{3}\xi^2(D_{12} + D_{66}) + \xi^4 D_{22}\right] \tag{7.8}$$

By plugging the value in Equation (7.8) back to Equation (7.7) yields Equation (7.9)

$$w_o = \frac{P_c \xi^2 a^2}{24\pi D^*} \tag{7.9}$$

Upon differentiating Equation (7.9) with respect to a, we get dw_o as expressed in Equation (7.10)

$$dw_o = \frac{P_c \xi^2 a da}{12\pi D^*} \tag{7.10}$$

The strain energy for uni-directional FRP laminate can be written as:

$$U = \frac{1}{2} \iint_s [k]^T [D][k] dy dx \tag{7.11}$$

Where s is the limit of integration over the elliptical region given by $\frac{x^2}{a^2}+\frac{y^2}{b^2}-1 \leq 0$, [D] is the bending stiffness matrix, and the components of the curvature matrix [k] are given by Equation (7.12).

$$k_x = -\frac{\partial^2 W}{\partial x^2},\ k_y = -\frac{\partial^2 W}{\partial y^2},\ and\ k_{xy} = -2\frac{\partial^2 W}{\partial x \partial y} \qquad (7.12)$$

Applying the limits of integration, the strain energy can be written as follows:

$$U = \frac{1}{2}\int_{-a}^{a}\int_{-\frac{b}{a}\sqrt{a^2-x^2}}^{\frac{b}{a}\sqrt{a^2-x^2}}[k]^T\,[D][k]dydx \qquad (7.13)$$

Plugging the values of Equation (7.3) and Equation (7.12) in to Equation (7.13) and solving the integration yields the following:

$$U = 4\pi w_o^2\left[\frac{D_{11}b}{a^3}+\frac{2D_{12}}{3ab}+\frac{D_{22}a}{b^3}+\frac{4D_{66}}{3ab}\right] \qquad (7.14)$$

Substituting the values of w_o and the ratio a/b in the above equation by Equation (7.9) and by the ellipticity ratio ξ respectively and after performing simplification and rearranging we will have the following expression for the strain energy.

$$U = \frac{P_c^2\xi^3a^2}{144\pi(D^*)^2}\left[D_{11}+\frac{2}{3}\xi^2(D_{12}+D_{66})+\xi^4D_{22}\right] \qquad (7.15)$$

Substituting the right hand part of Equation (7.15) with Equation (7.8) gives the final expression for the strain energy as follows:

$$U = \frac{P_c^2\xi^3a^2}{144\pi D^*} \qquad (7.16)$$

By differentiating Equation (7.16) with respect to a, we can find the expression for dU as given below

$$dU = \frac{P_c^2 \xi^3 ada}{72\pi D^*} \qquad (7.17)$$

The increment in the crack area dA can be expresses in the following relation

$$dA = \pi(a + da)(b + db) - \pi ab$$

$$dA = 2\pi bda = \frac{2\pi ada}{\xi} \qquad (7.18)$$

Now plugging the values of Equations (7.10), (7.17), and (7.18) into Equation (7.1), we get:

$$\frac{P_c^2 \xi^2 ada}{12\pi D^*} = \frac{G_{IC} 2\pi ada}{\xi} + \frac{P_c^2 \xi^3 ada}{72\pi D^*} \qquad (7.19)$$

Solving Equation (7.19) for the critical thrust force $P_{c,}$ we get the final equation for the critical thrust force at the onset of exit ply delamination as given in Equation (7.20) below.

$$P_c = \frac{12\pi}{\xi^{3/2}} \sqrt{\frac{G_{IC} D^*}{6-\xi}} \qquad (7.20)$$

The components of the bending stiffness matrix were computed using the following equation:

$$D_{11} = \frac{E_{11} h^3}{12(1-v^2)}, D_{22} = \frac{E_{22} h^3}{12(1-v^2)}, D_{12} = \frac{v E_{22} h^3}{12(1-v^2)}, and\ D_{66} = \frac{G_s h^3}{12} \qquad (7.21)$$

Where h is the thickness of uncut ply

The ellipticity ratio was related to the bending stiffness in the following equation

$$\xi = \left(\frac{D_{11}}{D_{22}}\right)^{1/3} \qquad (7.22)$$

The material properties used in the model are taken from [76] and are given in Table 7.1.

Table 7.1. Material properties used in the model

E_{11} (GPa)	E_{22} (GPa)	G_s (GPa)	v	G_{IC} (N/mm)	Ply Thickness (μm)
144	8.7	4.14	0.3	150	195

Using material properties given in Table 7.1 with Equations (7.20) to (7.22), a prediction of critical thrust force at the onset of exit ply delamination was made using the analytical model developed up to six plies and the results are given in Table 7.2, and plotted in Figure 7.2.

Table 7.2 Predicted values of thrust force values for various uncut plies

Number of Plies left	1	2	3	4	5	6
Thrust Force (N)	37.50	106.06	194.84	299.98	419.23	551.10

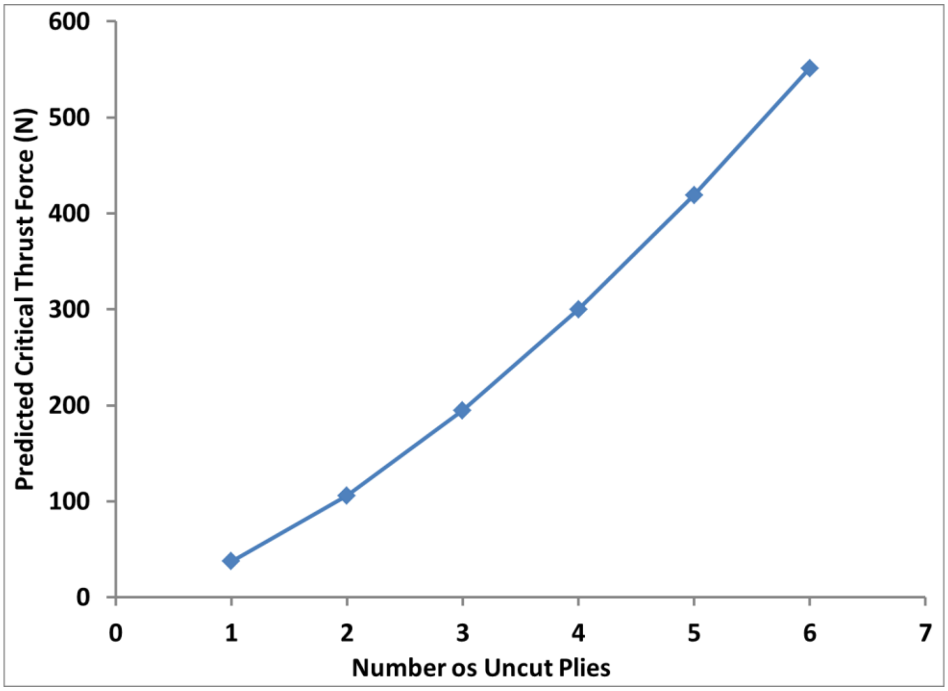

Figure 7.2. Prediction of critical thrust force at the onset of exit ply delamination

7.3. Experimental Study on Critical Thrust Force

In order to investigate the amount of critical thrust force at the onset of delamination at various plies under the drill tip, an experimental study was conducted through a punch test. The experiment was conducted for a numbers of uncut plies left below the drill tip. The experimental setup, procedures, and results are presented in the next sections.

7.3.1. Experimental Setup and Procedures

In this investigation, a unidirectional CFRP composite panel having a thickness of 19.406 mm and an average ply thickness of 195 μm were used. The work pieces were prepared by cutting to a size of 102 by 76 mm from a large panel using an abrasive water jet. Two holes with a diameter of 10 mm were drilled in each test piece in order to facilitate clamping them with the plate dynamometer. After preparing the test coupons, a blind hole was drilled at the center of each coupon at various depths using a 6.35 mm carbide twist drill. The depth of the blind hole at each coupon was varied according to the desired number of plies (thickness) leftover at the bottom of each coupon. The depth of blind holes for each coupon along with the thickness of the uncut ply under (below) the blind hole is tabulated in Table 7.3. A rectangular support was prepared from steel tube to utilize a free space between the test coupon and the plate dynamometer and in order to allow free delamination without back support around the hole. A punch was machined from hardened steel with a tip diameter equal to the chisel edge length of the drill used for drilling the blind hole. Figure 7.3 shows the rectangular steel tube support and the hardened steel punch.

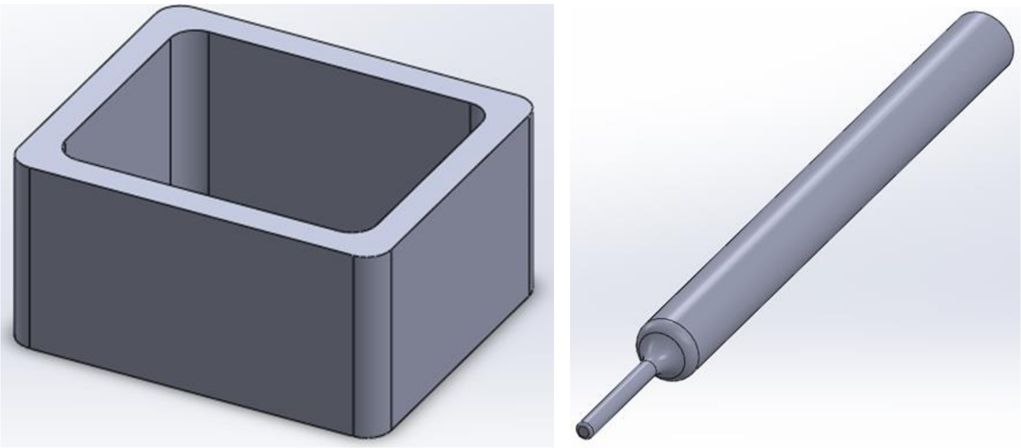

Figure 7.3. Rectangular steel tube support (left) and hard steel punch (right)

Table 7.3 Depth of blind holes and number of uncut plies

Coupon Number	Depth of Blind Hole (mm)	Thickness of Uncut plies (mm)	Number of Uncut Plies
1	19.016	0.390	2
2	18.626	0.780	4
3	18.236	1.170	6
4	19.211	0.195	1
5	18.821	0.585	3
6	18.431	0.975	5

The experiment was carried out on a Haas TM1P milling machine equipped with Kistles Type 9257BA plate dynamometer and Kistler signal conditioning box along with Kistler DynoWare DAQ pc software – input via pci DAQ card and the output format of the system was ASCII. A Physical Acoustic PCI-2 AE system with AEwin PCI-2 software and WIN-POST post – processing software along with WD wideband acoustic sensor was used to acquire acoustic emission (AE) signals during the punch test. The AE sensor was attached to the work piece using Sonotech Ultragell II coupling gel. The work piece was clamped on the plate dynamometer with two 10 mm hexagonal bolts with the support of a rectangular steel tube. The schematic representation of the experimental setup along with detailed section view is shown in Figure 7.4. Blind holes were drilled on each coupon with a 6.35 mm carbide twist drill leaving the desired thickness (number of plies) at the bottom (end) of the plate. After the blind hole was made, the remaining part of the blind hole, which is the uncut portion, was punched using the hardened steel punch at vertical feed rate of 1 mm/min. The thrust force and AE signals were recorded for the punching portion of this experiment.

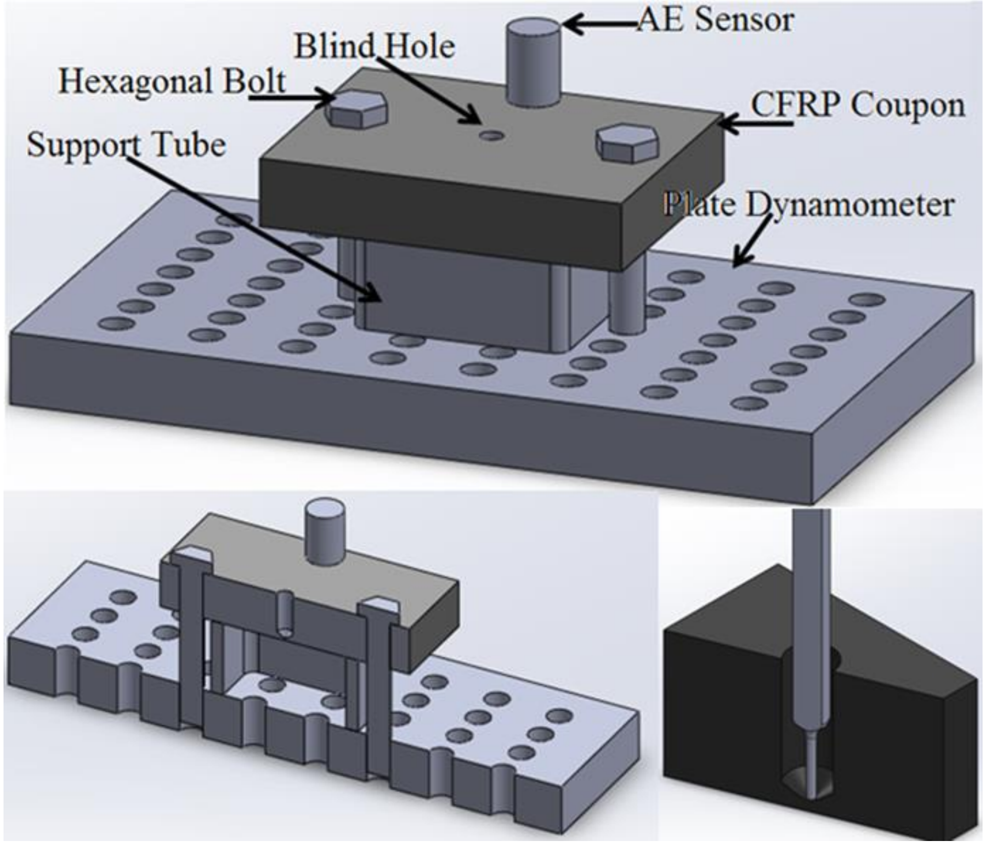

Figure 7.4. Schematic diagram of the experimental setup

7.3.2. Results and Discussions

Figure 7.5 shows the thrust force profiles at the onset of delamination for the six punch tests. The thrust force increased with the increase of the uncut plies left over. The thrust force increased gradually upon the increment of the numbers of the uncut plies almost for all increments of uncut plies except the big jump observed when the number of uncut plies (leftover plies) increased from four to five plies where the trust force was increased by 52%. The maximum value of the thrust force before it starts decreasing was considered the thrust force at the onset of delamination. The value of the thrust force at the onset of delamination is given in Table 7.4. The values of critical thrust force at the onset of delamination for the corresponding number of plies are shown in Figure 7.6.

Table 7.4 Thrust force values for various uncut plies

Number of Plies left	1	2	3	4	5	6
Thrust Force (N)	101	160	170	211	439	567

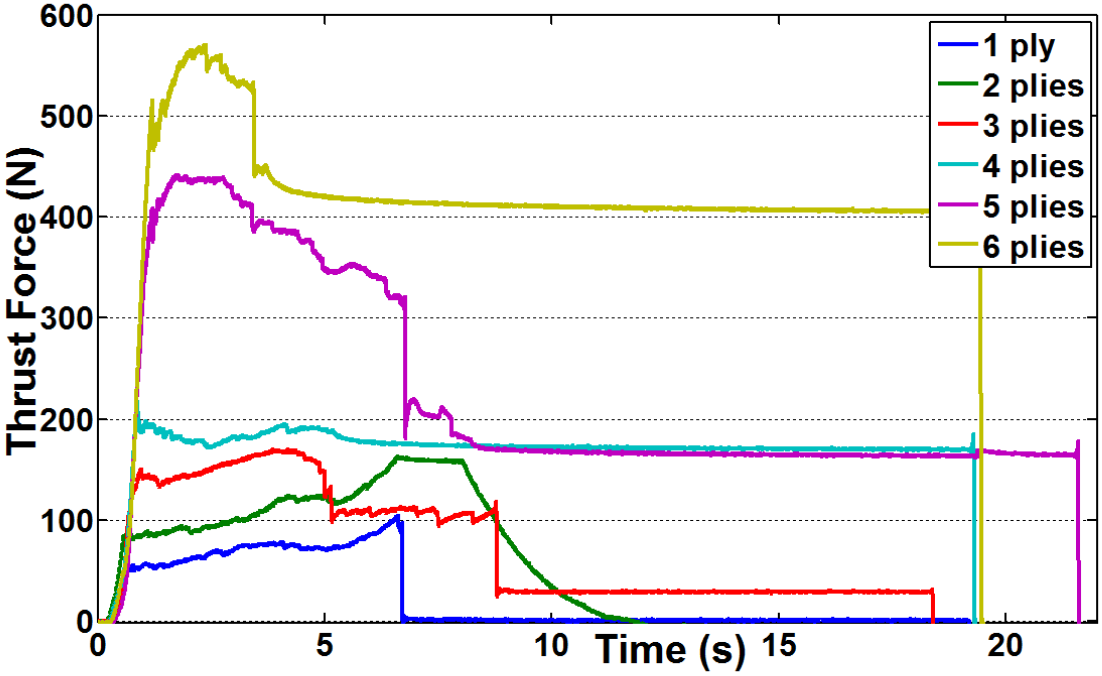

Figure 7.5. Thrust force profiles for the punch test

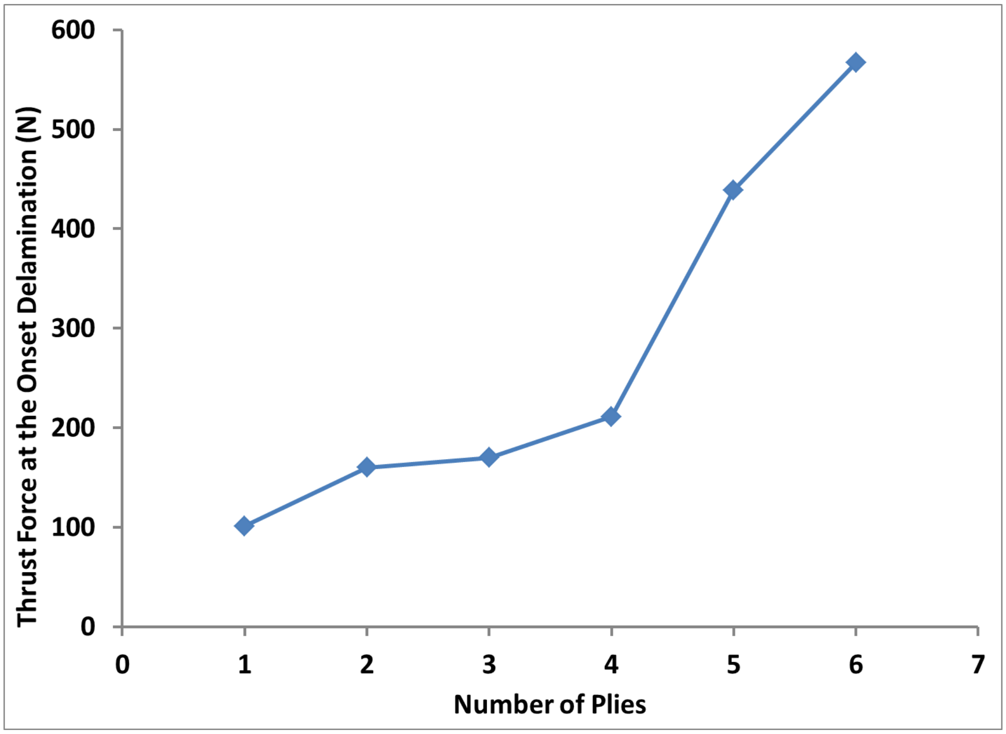

Figure 7.6. Experimental values of critical thrust force at the onset of exit ply delamination

Acoustic emission (AE) signal was collected during the punch test and a representative plot for the AE signal profile is given in Figure 7.7. As it can be seen from the plot, a large spike in the amplitude of the AE signal is recorded followed by smaller spikes. The first and large spike is an indication of the occurrence of the main delamination and the smaller spikes following the large spike are from the smaller delamination and consecutive smashing or breaking action of the fibers occurred after the first one. The average value of the amplitude of the first (highest) spike for all punch tests is found to be 80 dB, which can be used as a reference value for the detection of delamination.

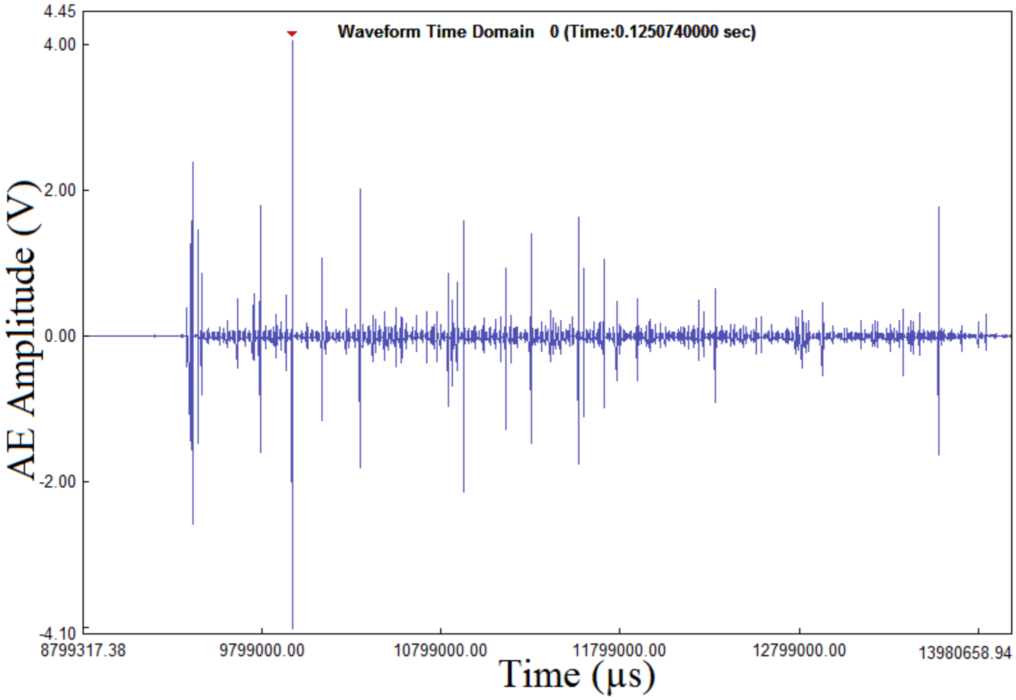

Figure 7.7. Representative plot for the AE signal profile

The drilled holes were sectioned after the punch test was conducted using a circular diamond saw. The optical image of the sectioned hole was taken using a Toolmakers microscope and these optical images are given in Table 7.5. The optical image of the sectioned holes reveals that delamination does not occur exactly at the interface of two consecutive plies rather it is found to occur in a single ply. The location of delamination seen in these optical images of sectioned holes is not in the line of ply interface as it is assumed and reported in many studies; rather it appears inside in a single ply (lamina). In addition, for most cases, a recurring incident of delamination accompanied by smashing and crashing of fibers was observed following the occurrence of the first delamination.

Table 7.5. Optical image of sectioned holes

Number of Ply left	Full	Right side close up
1	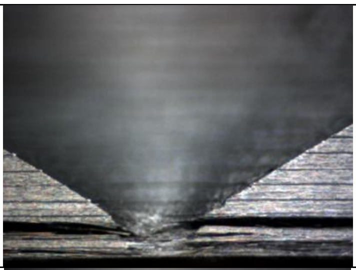	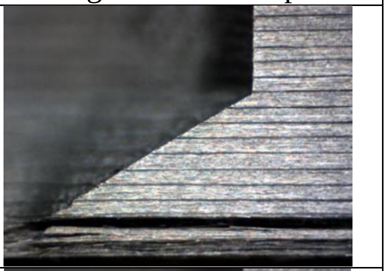
2	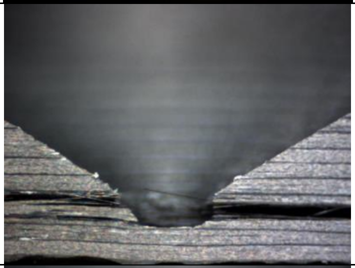	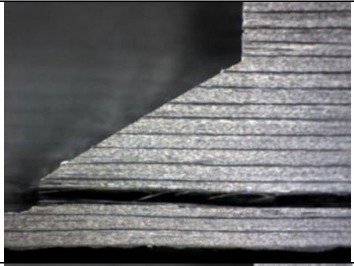
3		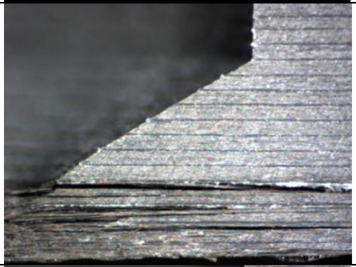
4	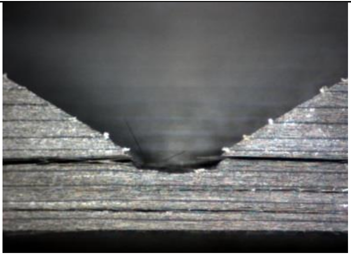	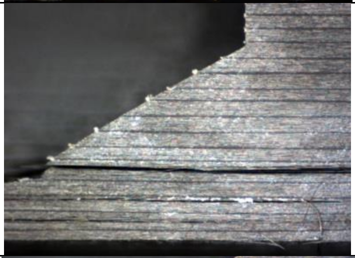
5	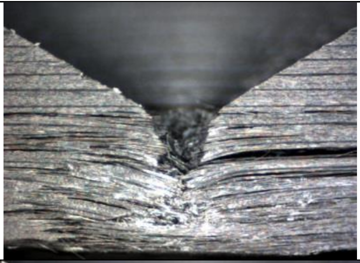	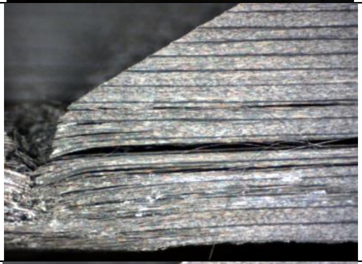
6	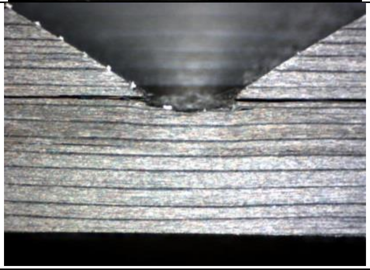	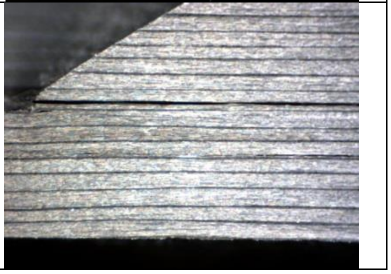

The values of the critical thrust force at the onset of delamination measured experimentally and predicted by using the new analytical model are given in Table 7.6 and the comparison plot for the two results is shown in Figure 7.8. The prediction made by the used of the analytical model was lower than the experimentally measured values when the numbers of uncut plies is less than or equal to two. For the numbers of uncut plies greater than two, the analytical model prediction was close to the experimentally measured values especially when the numbers of uncut plies are three, five, and six. The predicted values by the model when the number uncut plies are three and four were higher than the experimental values by 12.7 % and 29.7 % respectively, whereas, the predicted values were lower than the experimental values for the number of uncut plies five and six by 4.7 % and 2.9 % respectively.

Table 7.6. Measured and predicted critical thrust force at the onset of delamination

Number of Uncut Plies	Thrust Force at the Onset of Delamination (N)	
	Experimental measurement	Analytical Model Prediction
1	101	37.50
2	160	106.06
3	170	194.84
4	211	299.98
5	439	419.23
6	567	551.10

Experimentally measured values of the thrust force at the onset of delamination and predicted values using the new analytical model were compared with other values reported by other numerical models. Predicted thrust force values from Hocheng’s delamination model [73], Gururaja’s modified exit delamination model [76], and Zhang’s delamination model [74] are the studies considered for the comparison. The values of thrust force at the onset of delamination predicted by the new analytical model and by the three models mentioned above along with the experimentally measured values in this study are given in Table 7.7.

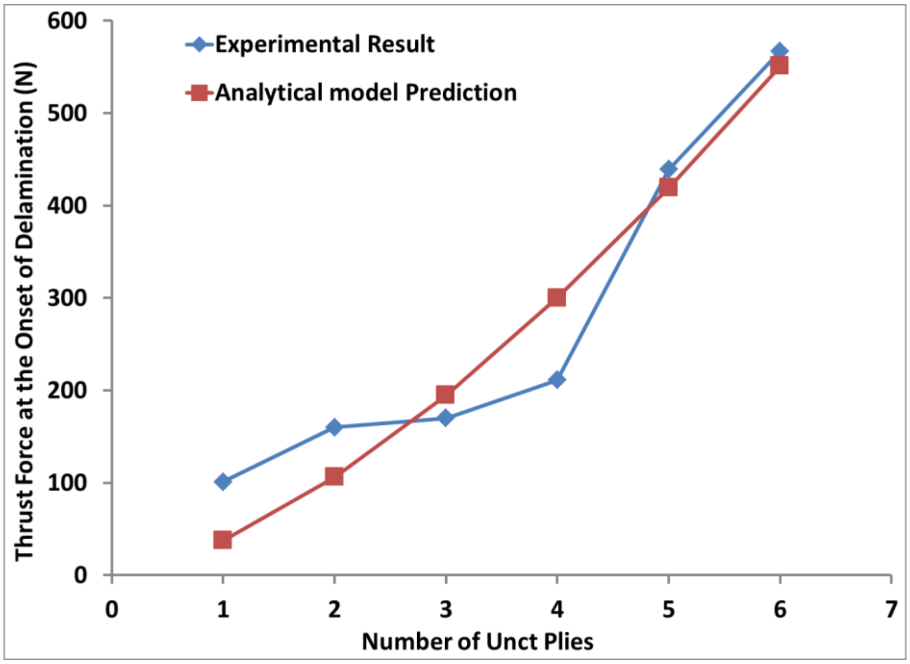

Figure 7.8. Comparison of experimentally measured and model prediction values of thrust force

Table 7.7. Comparison of experimental, new model prediction, and other model predictions

Number Of Uncut plies	Critical Thrust Force at the Onset of Delamination (N)				
	Experimentally Measured	Predicted by New Model	Predicted by Hocheng Model	Predicted by Gururaja Model	Predicted by Zhang Model
1	101	37.50	15	52.18	18.45
2	160	106.06	32	145.3	51.38
3	170	194.84	74	252.66	89.33
4	211	299.98	120	437.74	154.86
5	439	419.23	200	633.19	223.86
6	567	551.10	300	1033.87	365.5

The thrust force values at the onset of delamination measured experimentally in this study are higher than the values predicted by all models considered when the numbers of leftover or uncut plies are one and two. Both the experimentally measured values and predicted values by the new model are higher than the prediction made by Hocheng’s model and Zhang’s model for all six plies. The thrust force values predicted by Gururaja’s model were higher than the thrust force values predicted by the new model for all uncut plies and higher than the experimentally measured values for the numbers of uncut plies from three – six. From all three models chosen for this comparison, Gururaja’s model was the closest to the experimentally measured values when the numbers of uncut plies are one and two, however when the numbers of uncut plies are greater than two, the model prediction higher than the experimentally measured values in this study. Over all, based on the comparison and the results presented, the new model developed in this study is more close to the experimentally measured values. Figure 7.9 shows a comparison of experimentally measured values and predicted values by the new model developed in this study with predicted values by other models mentioned above of thrust force values at the onset of delamination.

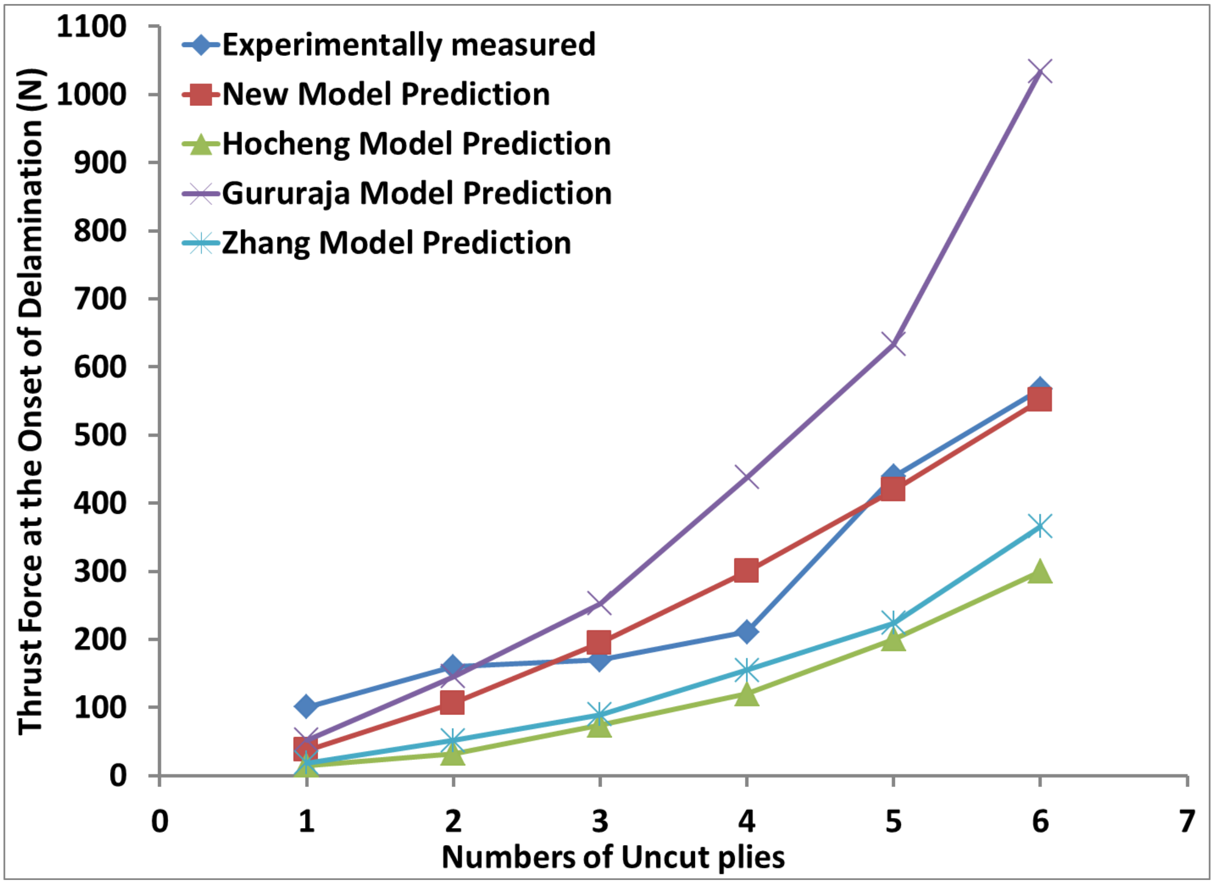

Figure 7.9. Critical thrust force values for numbers of uncut plies from all models

7.4. Conclusion

An analytical model to predict the critical thrust force at the onset of exit ply delamination when drilling uni-directional CFRP composites was proposed and an experimental investigation was performed through a punch test to determine the thrust force at the onset of delamination. The results and observations made in this investigation are summarized by the following concluding remarks.

1. An analytical model to predict the critical thrust force at the onset of exit ply delamination when drilling uni-directional CFRP composites was proposed based on LEFM and plate bending theory.
2. An elliptical delamination zone with clamped boundary condition was considered in the formulation of the model. In addition, since the load applied by the drill tip is circular, the lateral uniform load is taken over a circular region rather than over an elliptical region.
3. A punch test was carried out in order to measure the critical thrust force experimentally at the onset of exit ply delamination when drilling uni-directional CFRP composites and an acoustic emission signal was also acquired to investigate the amplitude of the acoustic signal at the onset of exit ply delamination.
4. Large spike in the amplitude of the acoustic emission signal was observed at the onset of main delamination followed by smaller spikes from the smaller delamination and consecutive smashing or breaking action of the fibers. The average value of the amplitude of the first (highest) spike for all punch tests is found to be 80 dB, which can be used as a reference value for the detection of delamination.
5. The optical image of the sectioned holes reveals that delamination does not occur exactly at the interface of two consecutive plies, rather it is found to occur in a single ply. The

location of delamination seen in these optical images of sectioned holes is not in the line of ply interface as it is assumed and reported in many studies; rather it appears inside in a single ply (lamina).

6. Comparison of experimentally measured values and predicted values by the new model developed in this study with predicted values by other models of thrust force values at the onset of delamination was presented. Based on this comparison, the predicted values by the new proposed model show better correlation with the experimentally measured values than values predicted by other models.
7. Since the influence of shear stress from the torsional component of the drilling force not included in any of the existing models, it is necessary to incorporate this component of the drilling force in the future modification of existing models. Yet, the new proposed model yields better prediction of the critical thrust force at the onset of exit ply delamination when drilling uni-directional CFRP composites.

CHAPTER 8: ONLINE DETECTION AND MONITORING OF TOOL WEAR

8.1. Introduction

Even though FRP composite materials provide many advantages over traditional metallic alloys and other material systems, there are many challenges in the manufacturing and machining of FRP composites. The quality of holes produced during the drilling of fiber reinforced composite materials is one of the controlling factors for the resulting structural strength and surface integrity. However, quality of holes produced greatly influenced by the condition of the drill tool. High rate of tool wear is one of the challenges in the machining process compared to machining of other material systems. Unlike traditional metallic alloys, the anisotropic property of composite materials and the abrasive nature of the reinforce fibers expedites the rate of tool wear dramatically. This high rate of tool wear makes producing of good quality holes a difficult task when drilling FRP composite materials by demanding frequent inspection of the tool condition and/or changing the drill tool. Inspecting the condition of the drill tool between or during the drilling process manually is not an economical practice and it increases the production cost because of the down time of the machine and the operator during this task. A new approach of an online monitoring of drill tool wear will be presented in this chapter. This new approach utilizes two different methods namely, the signal amplitude and recurrence quantification analysis (R. Q. A.).

8.2. Monitoring using Signal Amplitude

In this part of the investigation, various signals were acquired and processed to correlate the change in the signal amplitude with the amount of flank wear measured in the drilling process. Experimental drilling was conducted using high speed steel (HSS) and carbide twist drills on a multi-directional $\left([(90,-45,0,45)_{4s},0,90,0,\overline{90}]_s\right)$ and a uni-directional CFRP composite laminates. Both the HSS and carbide drill tools are standard length twist drills with a point angle of 118^0 and a helix angle of 25^0. The experimental conditions are given in Table 8.1. The experimental setup along with the signal acquisition and measurement system is discussed in detail in chapter four. Flank wear of the drill tool was measured at different stage of the drilling process using toolmaker's microscope. Figure 8.1 shows the schematic representation of the cutting edge of the drill and flank wear measurement method.

Table 8.1. Experimental conditions of monitoring using signal amplitude

Material	Drill Tool	Cutting Speed (rpm)	Feed Rate (µm /rev)	Signal Acquired
7.62 mm Multi-Directional CFRP	6.35 mm diameter HSS	6000	200	AE, Mic, Force, and Accelerometer
19.05 mm Uni-Directional CFRP	12.7 mm diameter HSS	6000	100	Mic
	6.35 mm diameter Carbide	3000	100	Mic, AE, and Force
			200	
		6000	100	
			200	

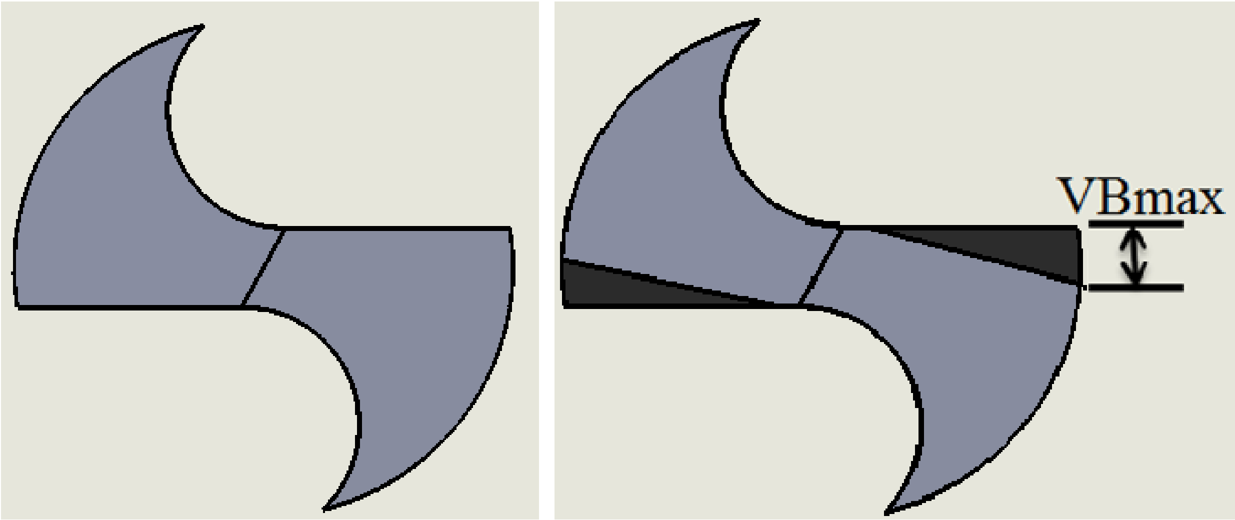

Figure 8.1. Schematic representation of cutting edge of the drill and flank wear measurement

8.2.1. Monitoring when Drilling Multi-Directional CFRP using HSS Drill

A 7.62 mm multi-directional CFRP composite laminate with a stacking sequence of $\left(\left[(90,-45,0,45)_{4s},0,90,0,\overline{90}\right]_s\right)$ composed of 39 plies with an average ply thickness of 195 µm was used for this part of the investigation. Twenty five holes were drilled on the test coupon using a 6.35 mm HSS twist drill. Thrust force, torque, acoustic emission, accelerometer, and audio microphone signals were acquired during the drilling process. Flank wear measurements of the cutting edge were taken at 3.1 mm from the center (axis) of the drill for every five holes drilled. The results from recorded signals will be presented in the following sections. Figure 8.2 (a) shows an optical image of the drill cutting edge for new (sharp) drill and the progression of the flank wear for every five holes drilled and Figure 8.2 (b) shows an optical image of the edge rounding of the cutting edge after drilling twenty-five holes.

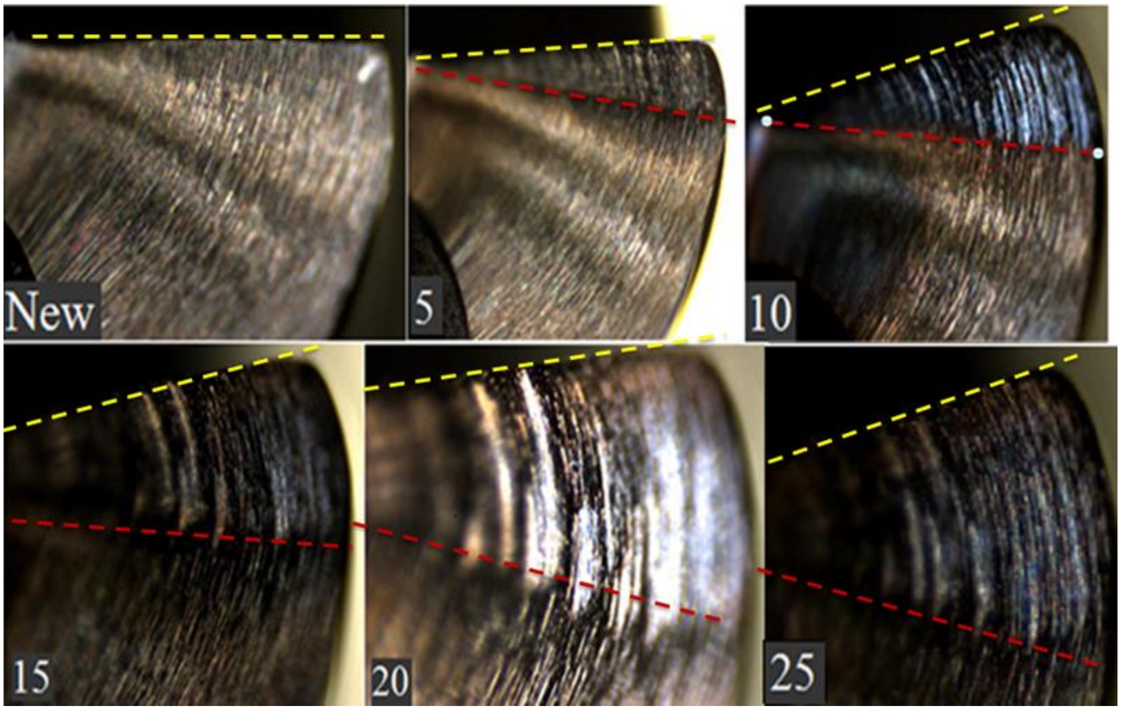

Figure 8.2. (a) Optical images of drill cutting edge as received and for every five holes drilled

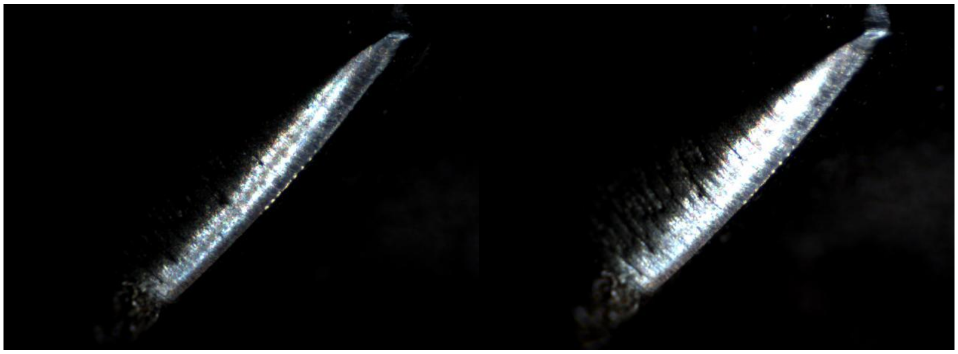

Figure 8.2. (b) Optical images of cutting edge rounding after drilling twenty-five holes

Table 8.2 shows the amount of flank wear measured for every five holes and Figure 8.3 shows the amount of flank wear measured versus the number of holes drilled. The amount of flank wear sustained by the cutting lip found to be higher in the first five holes compared to the tool wear progression seen after the first five holes. During the drilling of the first five holes, the cutting edge went from sharp (new) to a flank wear of 583 µm, then the progression of the flank wear become less once the cutting edge suffers this much of flank wear. The rate of flank wear progression over the amount of drilled material is shown in Figure 8.3. As it can be seen from this plot, the rates of flank wear decreases when the amount of material drilled increases. The highest flank wear progression is recorded in the beginning of the drilling process when the cutting tool goes from being sharp to sustain some amount of flank wear. Once the cutting edge suffered a considerable amount of flank wear and lost its sharpness leading to edge rounding, the drill cutting edge endures the wear and the rate of wear progression decreases compared to the rate of progression observed on the first 10 holes in the beginning of the drilling process.

Table 8.2. Flank wear measurements

Number of Drilled Holes	5	10	15	20	25
Drilling distance (mm)	38.1	76.2	114.3	152.4	190.5
Flank wear (mm)	0.583	0.804	0.940	1.094	1.400
Wear area on one edge (mm^2)	0.886	1.221	1.428	1.662	2.123

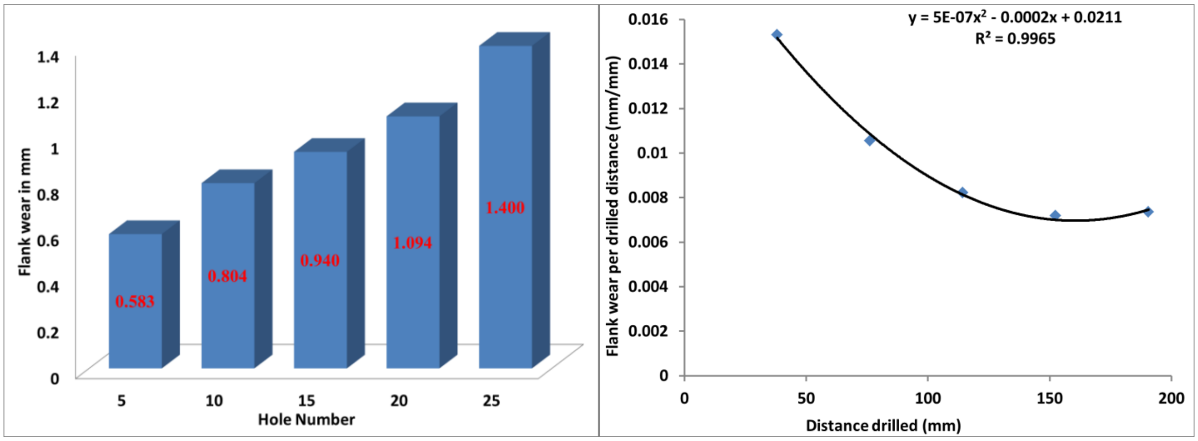

Figure 8.3. Flank wear for number of holes (left) and flank wear rate for material drilled (right)

8.2.1.1. Thrust Force

Thrust force is one of the four signals acquired in order to correlate the signals amplitude to the amount of tool wear measured. The thrust force profile for the first hole and for every five holes is shown in Figure 8.4. The thrust force profile shows a large increase when the number of drilled holes increases from one to five holes, however, the rate of increase observed between every fifth holes after the fifth hole was relatively similar. A 60% increase of thrust force was seen between the first and the fifth hole, after the fifth hole, the rate of increase in thrust force become smaller and smaller for each increase of five holes. The lowest increase in thrust force was an 8.7 % increase when the number of hole drilled increases from twenty to twenty-five.

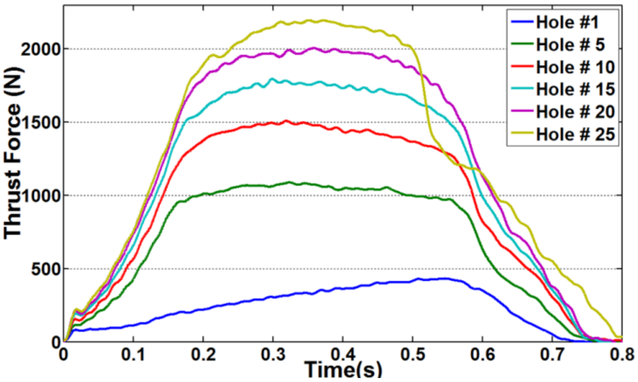

Figure 8.4. Thrust force profiles for every five hole

Figure 8.5 shows the relationship of thrust force amplitude with the number of drilled holes and the amount of flank wear. Thrust force increased with the increase of flank wear and the relationship between thrust force and flank wear can be approximated to a second order polynomial with the coefficient of determination of 0.9965. By establishing a threshold amount of flank wear where drill tool should be changed, the corresponding thrust force amplitude for the threshold flank wear can be calculated and used to monitor the condition of the drill tool online without interrupting the drilling process. From this, we can see that thrust force can be used as tool wear estimation tool except that the investment required for thrust force acquisition system could be expensive. Other than the economical concern, the use thrust force amplitudes for online monitoring of tool wear when drilling CFRP composites demonstrates its capability in this study.

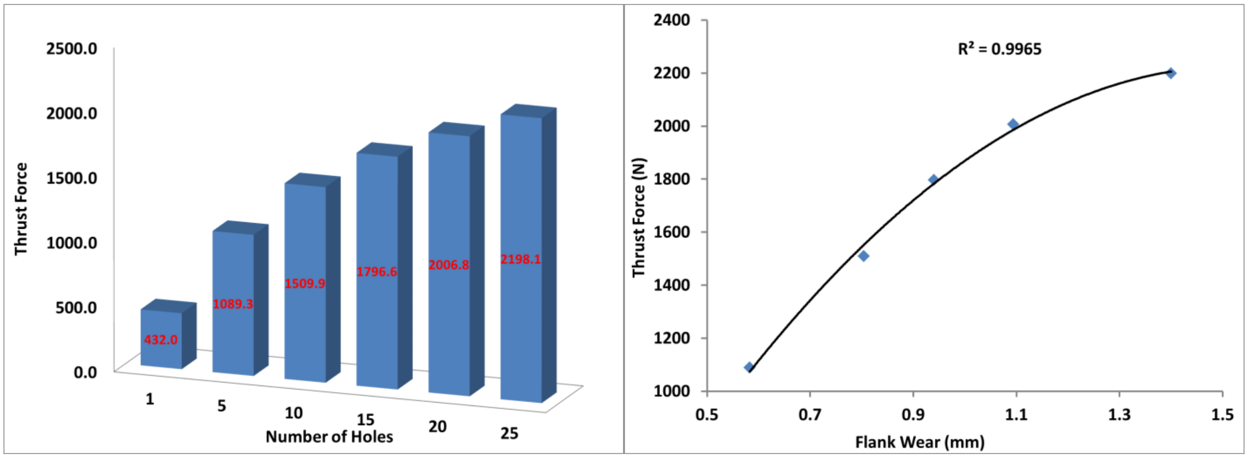

Figure 8.5. Relationships of trust force with number of holes (left) and with flank wear (right)

Flank wear estimation was performed through the polynomial fit equation found from flank wear versus thrust force graph and using the thrust force amplitude as an input parameter. All estimations of the flank wear done through the thrust force amplitude was found to be an overestimate of the measured flank wear. The average estimation error achieved by using thrust force amplitude as an input parameter was 14 % of over estimation and the maximum error was 19.3 % of over estimation. Measured and estimated flank wear values are given in Table 8.3 and the estimated values versus measured values of flank wear are plotted and shown in Figure 8.6.

Table 8.3. Measured and estimated flank wear using thrust force amplitude

Hole Number	Measured Flank Wear (mm)	Estimated Flank Wear (mm)	Estimation Error (%)
5	0.583	0.669	12.9
10	0.804	0.879	8.6
15	0.940	1.124	16.4
20	1.094	1.356	19.3
25	1.400	1.605	12.8

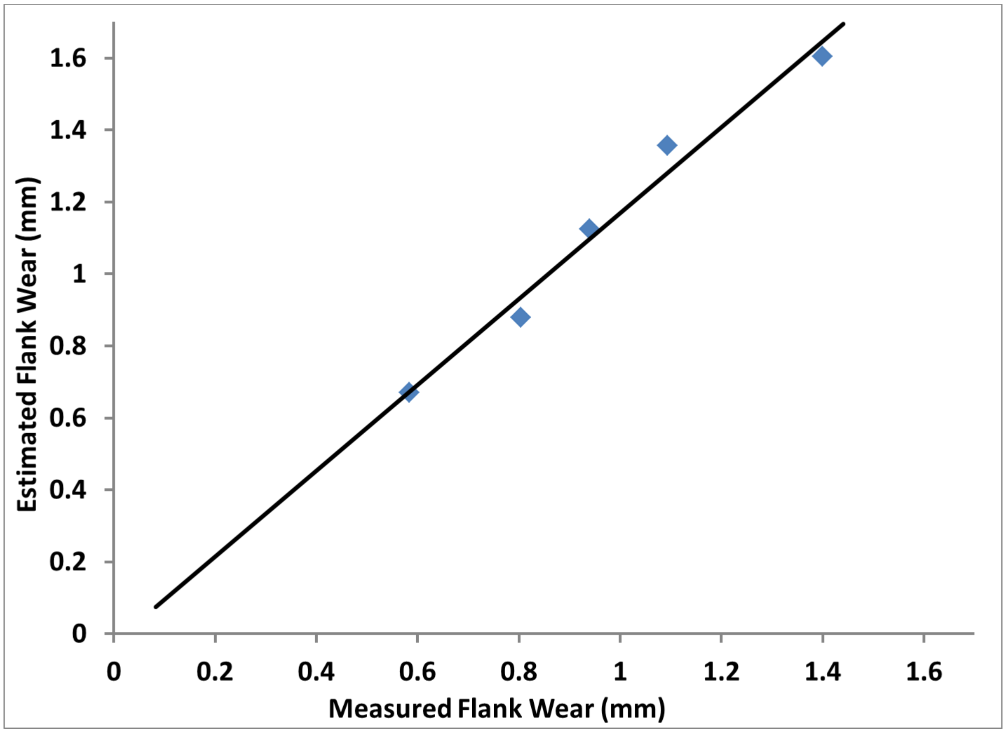

Figure 8.6. Measured and estimated flank wear by using thrust force amplitude

8.2.1.2. Torque

Figure 8.7 shows the variation in torque profiles when the number of drilled hole increased. The observed variation on the torque amplitude is not as large as the variation observed on thrust force amplitude. The amplitude of torque increased by 21.4 % when the number of drilled hole increased from one to five, however, for holes five to twenty, the increase in torque amplitude was relatively similar for each five holes drilled which was around 6 %. No significant increase on torque amplitude was observed after the twentieth hole.

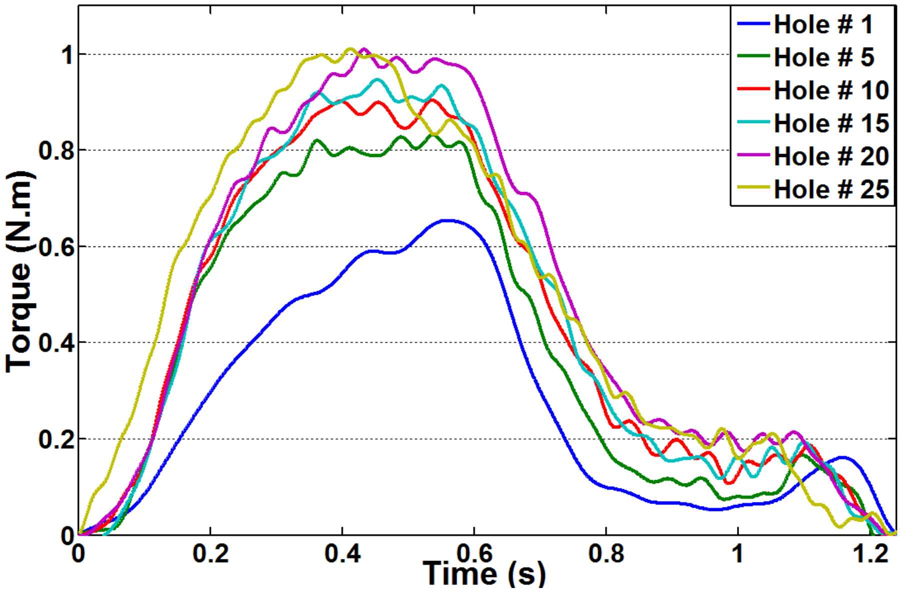

Figure 8.7. Torque profiles for every five holes drilled

The relationship between the torque amplitude and measured flank wear is shown in Figure 8.8 where an increasing trend in the amplitude of the toque is observed with the increase of the flank wear. The amplitude of the torque increased by 17.5 % when the flank wear progressed from 0.583 to 1.094 mm, however when the flank wear increased from 1.094 to 1.4 mm, the increase in the amplitude of torque was negligible with a value of 0.12%. This shows that torque is less sensitive to the progression of flank wear compared to thrust force.

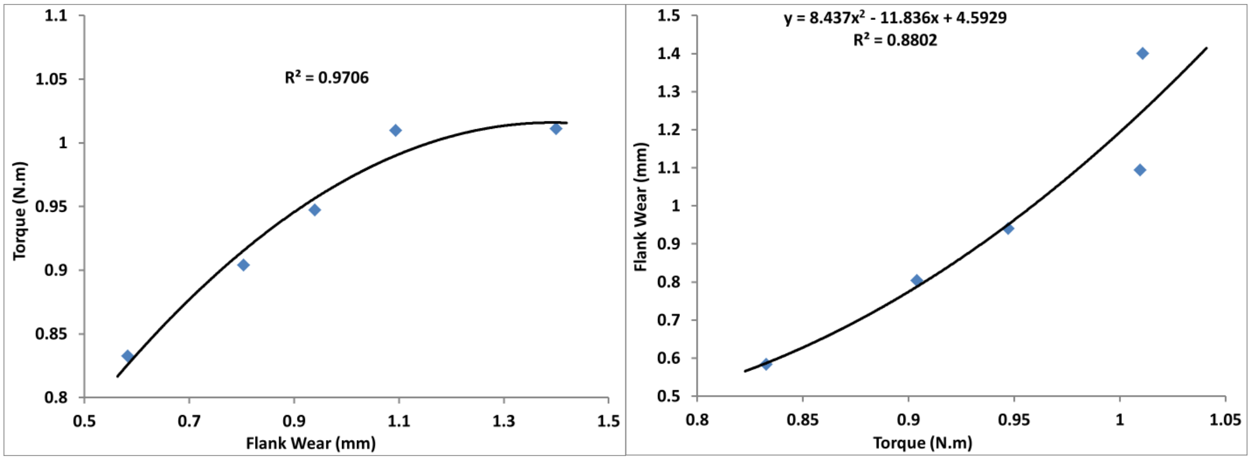

Figure 8.8. Relationship between torque and flank wear

Using the polynomial fit equation, which correlates the torque amplitude with the measured values of flank wear as shown in Figure 8.8, an estimation of the flank wear was performed and the values of flank wear estimation are given in Table 8.4. The accuracy of estimation achieved by the use of torque was higher than the estimation accuracy achieved by using thrust force amplitude. The average estimation error found in estimating flank wear through the amplitude of torque profile was 5.6 % with a maximum estimation error of ± 12 %. Figure 8.9 shows estimated flank wear versus measured flank wear, which gives a coefficient of determination of 0.88.

Table 8.4. Measured and estimated flank wear using torque amplitude

Hole Number	Measured Flank Wear (mm)	Estimated Flank Wear (mm)	Estimation Error (%)
5	0.583	0.587	0.68
10	0.804	0.788	-1.99
15	0.940	0.952	1.24
20	1.094	1.244	12.03
25	1.400	1.250	-12.02

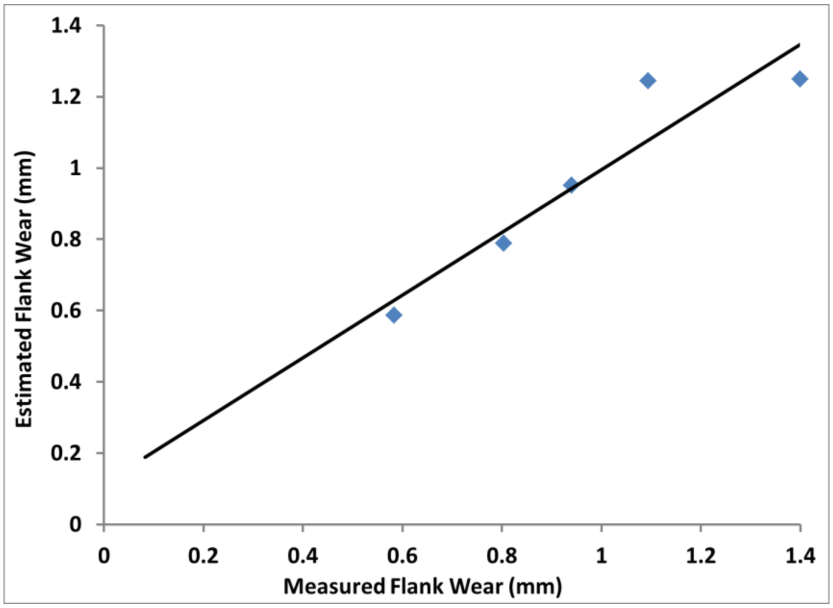

Figure 8.9. Estimated and measured values of flank wear using amplitude of torque

8.2.1.3. Acoustic Emission and Vibration Signals

Acoustic emission and accelerometer signals were also acquired and studied in order to correlate the change in signal amplitude with the amount measured of tool wear. The amplitude from these signal acquisition systems found to be depend on the distance (location) of the sensors and since the acoustic emission sensors and the accelerometers were placed at fixed location, the distance between drilled holes and the sensors vary for each hole. Figure 8.10 show the locations of sensors and drilled holes, where AE represent the acoustic emission sensor, AC represent the location of the accelerometers, and AM represents the location of the audio microphone which will be discussed in the next section. The variation on the amplitudes of AE and AC signals for all drilled holes is shown in Figure 8.11. Typical accelerometer and acoustic emission raw signal profiles acquired when drilling the first hole is given in Figure 8.12 and the variation on the signal amplitude due to sensor location is seen clearly despite the fact the signal was acquired while drilling one hole. Because of the anisotropic nature of CFRP composites, the wave propagation medium varies based on the relative distance between the sensor location and the hole being drilled and based on the relative orientation of the fibers. Due to the dependency of the amplitudes on the location of the drilled holes, the amplitudes from these sensors were not convenient to correlate the amount of measured tool wear. The distance between the sensors and the hole as well as orientation of sensors should kept constant (similar) for each drilled hole in order to use the signals from these sensors for tool wear monitoring purpose.

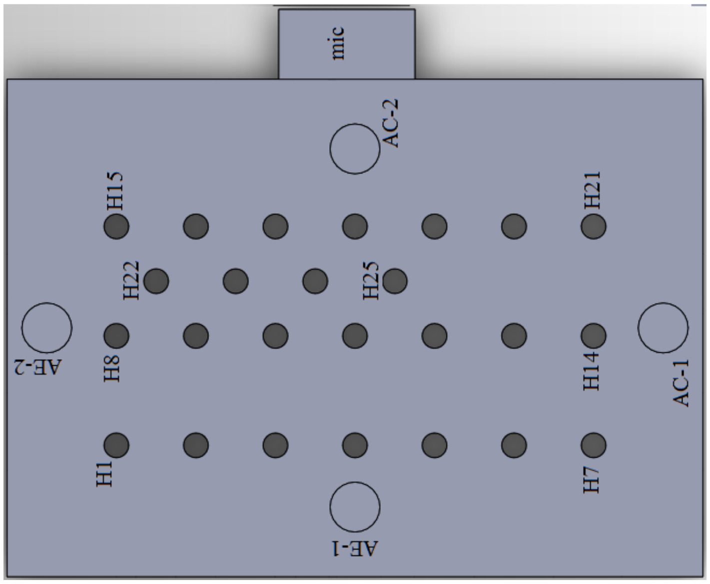

Figure 8.10. Schematic representation of sensor location and hole position

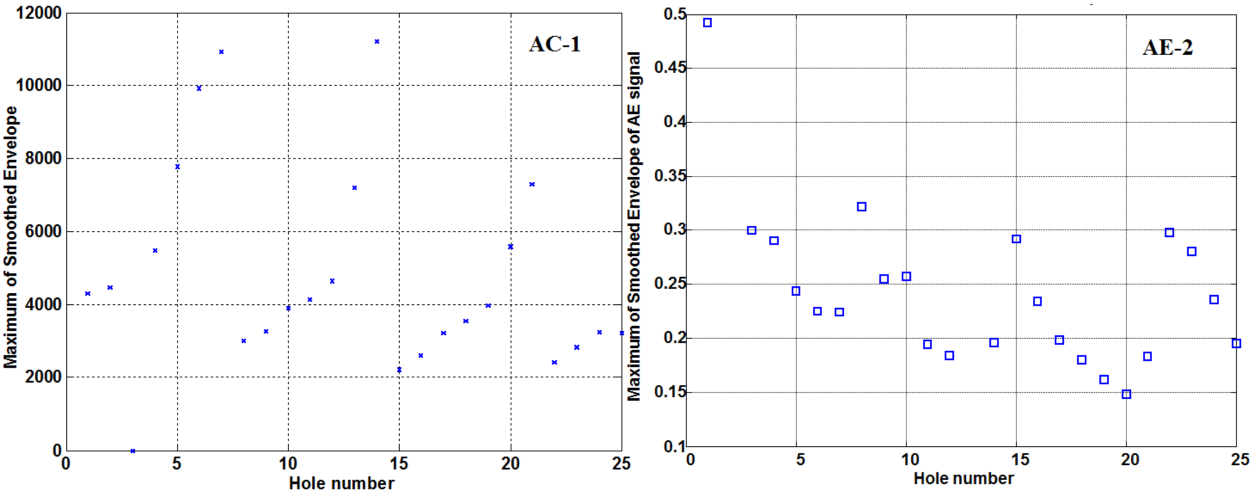

Figure 8.11. Amplitude of accelerometer signal (left) and acoustic emission signal (right)

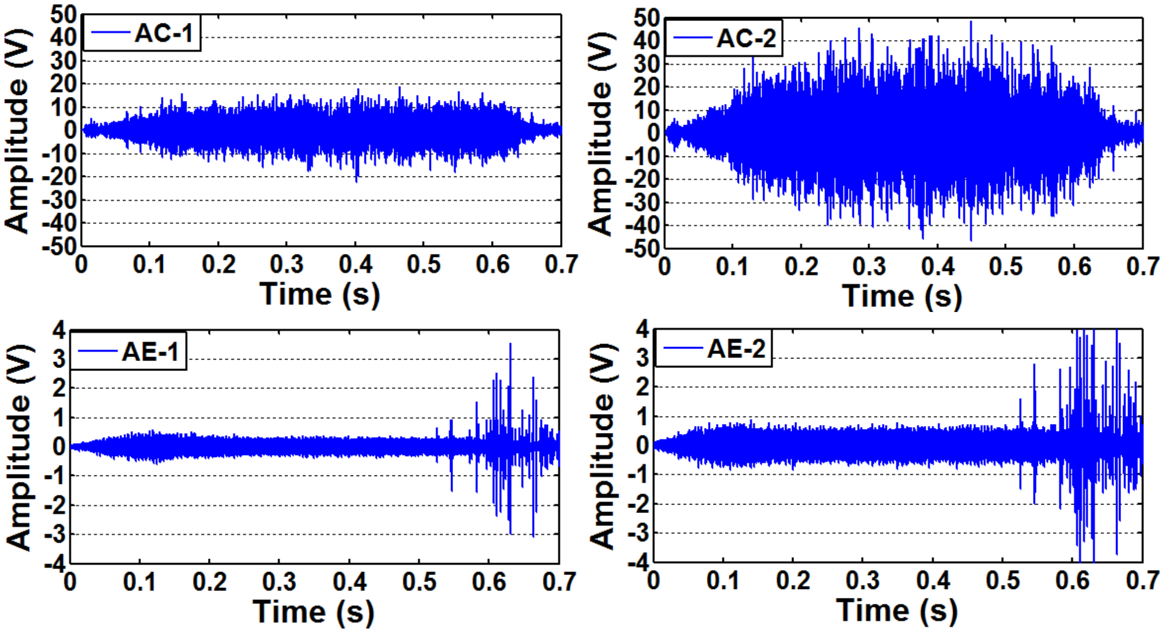

Figure 8.12. Typical raw signal profiles of accelerometer (top) and acoustic emission (bottom) from hole number one

8.2.1.4. Audio Microphone Signals

An air coupled audio microphone (AM) was used to record the acoustics generated by the cutting action during the drilling operation. The change in amplitude relative to the progression of the tool flank wear was studied. Figure 8.13 shows raw signal profiles of the audio microphone for the first and twenty-fifth hole for comparison. The amplitude of the raw signal from the audio microphone decreases as the number of drilled holes increases, which can be seen in Figure 8.13. The raw signal profiles for all twenty-five holes are given in Appendix O.

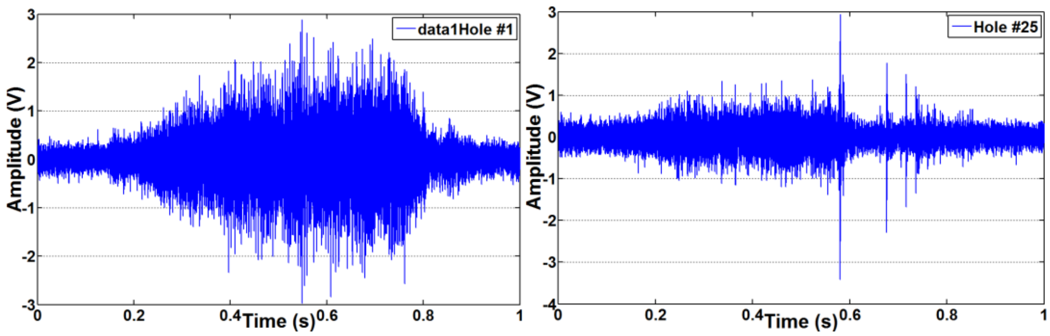

Figure 8.13. Audio microphone raw signal profiles of the first and twenty-fifth hole

The raw audio microphone acoustic signal is then filtered and smoothed through a low-pass filter in order to eliminate the noise and to correlate the amplitude with the amount of measured flank wear. The magnitude of the maximum amplitude of the filtered signal decreases when the number of hole drilled increased. The maximum amplitude of the smoothed signal and the amount of flank wear for every five holes is given in Table 8.5. To get a normalized quantity, the number of drilled holes was multiplied by the thickness of the CFRP plate used in this study and listed in the table as the distance traveled by the drill. Flank wear was measured starting at the fifth hole and onwards for every five holes drilled or every 38.1 mm of material drilled.

Table 8.5. Maximum amplitude of smoothed signal and flank wear

Number of Holes Drilled	Distance traveled by the drill (mm)	Maximum amplitude of smoothed signal (V)	Flank wear (mm)
1	7.62	4.88	----
5	38.1	3.99	0.58
10	76.2	3.12	0.80
15	114.3	1.90	0.94
20	152.4	1.79	1.09
25	190.5	1.49	1.40

Figure 8.14 shows the maximum amplitudes of the acoustic signal from the audio microphone. The amplitude of the AM signal decreased with a steep slope when the number of drilled hole increase from one to fifteen, and when the number of drilled holes increased from fifteen to twenty five, the rate of decreasing of the amplitude gets smaller compared to the rate when the number of holes increased from one to fifteen. The correlation of maximum amplitude of the smoothed signal with the number of holes drilled gives a coefficient of determination of 0.986, but from the trend of the data points in Figure 8.14, one can see that the rate of change in the amplitude of the AM signal become smaller after the fifteenth hole. If we break down the regression line in to two parts at the fifteenth hole, a better coefficient of determination value of

0.996 will be for hole numbers 1 – 15, whereas, for the hole numbers from fifteen to twenty five, the coefficient of determination becomes 0.93 which is lower than the value found with one regression line. Figure 8.15 shows the maximum amplitude of the signal for the number of holes drilled with two regression lines.

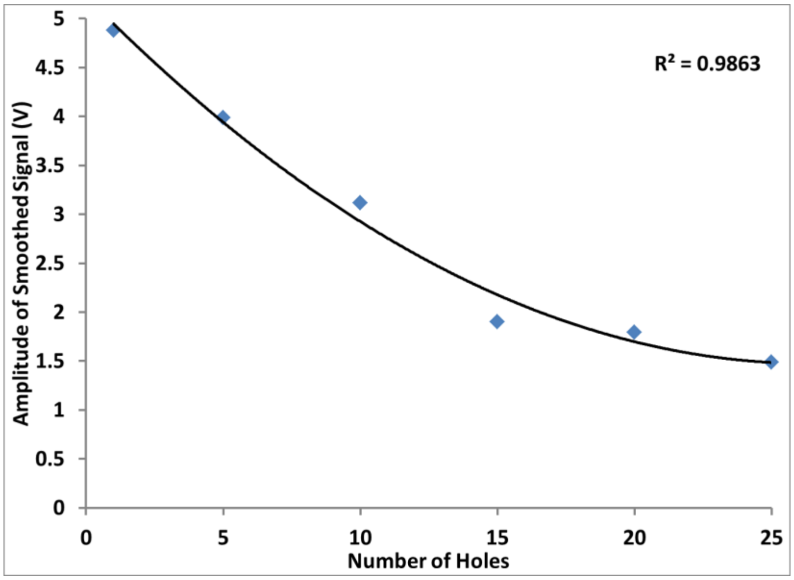

Figure 8.14. Maximum amplitude of smoothed signals for number of holes drilled

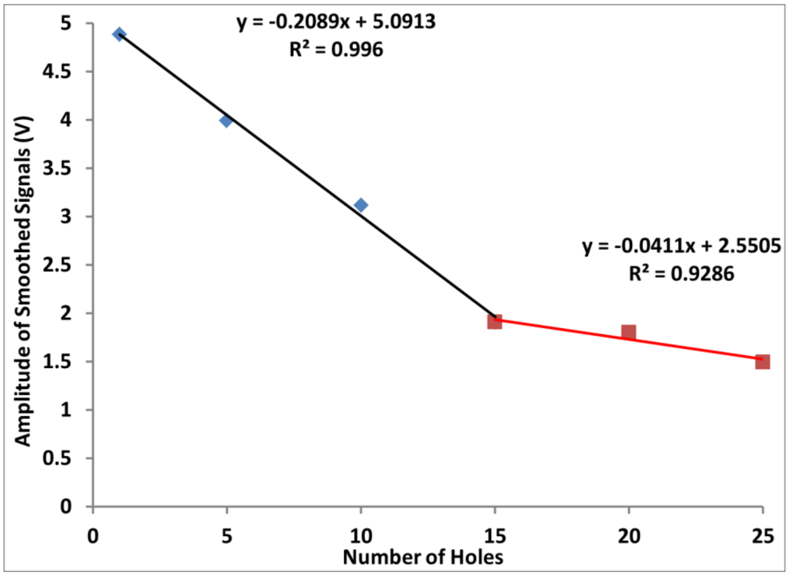

Figure 8.15. Maximum amplitude of smoothed signals for number of drilled holes with two regression lines

In addition to the correlation of the maximum amplitude of the smoothed microphone signal to the number of drilled holes, correlation with the amount of flank wear also studied. Figure 8.16 shows the relationship between the maximum amplitude of the microphone signal and the amount of measured flank wear in this study. The correlation between the amplitude and amount of flank wear can be approximated with a second-degree polynomial, which gives a coefficient of determination of 0.952. From this, it is possible to estimate the amplitude of the AM signal for a specific or predetermined amount of wear to monitor the condition of the tool without interrupting the drilling process. For known (pre-determined) wear limit where the drill tool should be changed, the corresponding value of the signal amplitude for that amount of flank wear limit can be determined (calculated) using this relationship and can be used to warn the operator to change the drill tool.

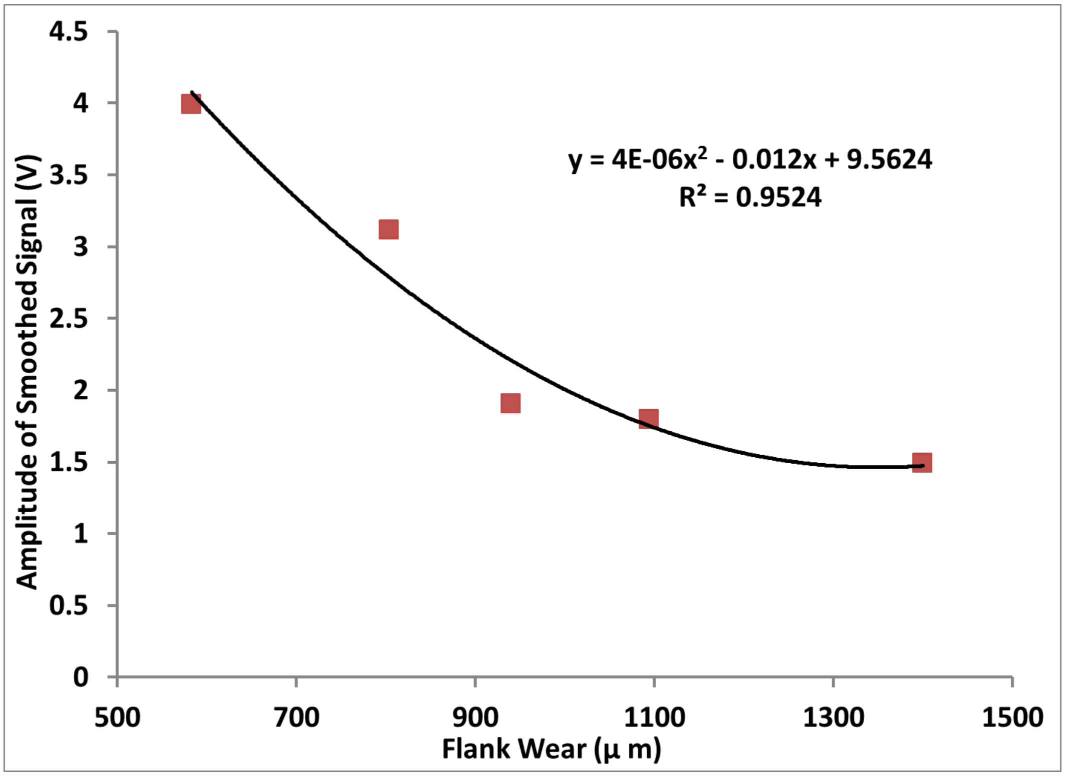

Figure 8.16. Amplitude of smoothed microphone signal for flank wear

The amplitude of the smoothed signal also can be used as an input parameter to determine (estimate) the amount of flank wear sustained by the drill tool and for online monitoring of the condition of the drill during the drilling operation. Figure 8.17 shows the plot for flank wear versus the maximum amplitude of the filtered microphone signal in which the two values are related by a power regression line with a coefficient of determination of 0.92. Using the power equation of the regression from this plot and using the amplitude of the smoothed signal as an input, the amount of flank wear expected was estimated (predicted) and the measured and estimated values of the flank wear are plotted in Figure 9.18. The average error in estimating the amount of flank wear by the amplitude of the AM signal was 7.24 % with a maximum over estimation error of 11.8 % and a maximum under estimation error of 10 %.

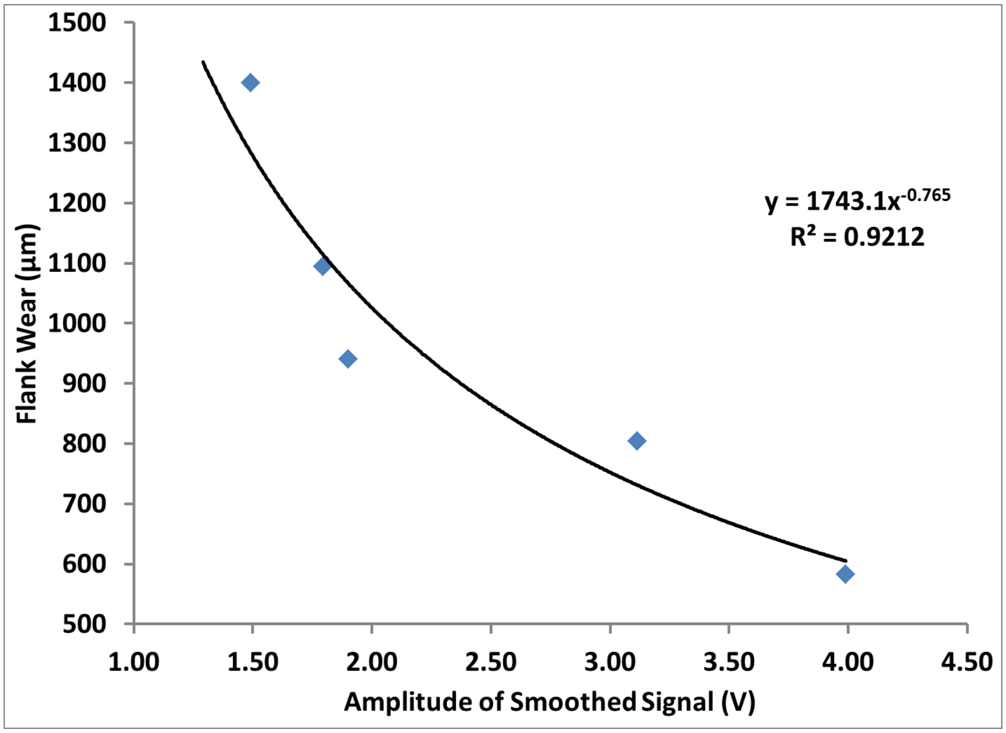

Figure 8.17. Flank wear versus amplitude of smoothed microphone signal

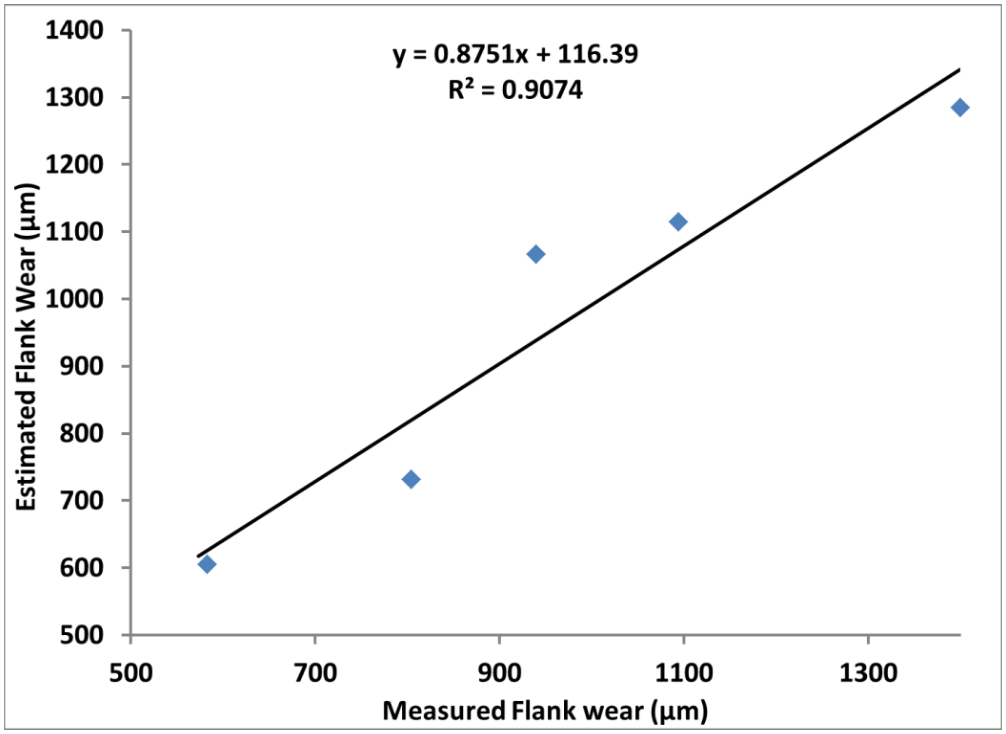

Figure 8.18. Measured and estimated flank wear using microphone signal amplitude

8.2.2. Monitoring when Drilling Uni-Directional CFRP using HSS Drill

A 19.05 mm thick uni-directional CFRP composite laminate composed of 99 plies with an average ply thickness of 192 µm was used for this part of the study. Six holes were drilled on the test coupon using a 12.7 mm HSS twist drill at a cutting speed of 6000 rpm and 100 µm/rev feed rate. Tool wear measurements were taken for every two drilled holes after drilling of the 2nd, 4th, and 6th hole. Audio microphone signal was acquired during the drilling process. The results from the microphone signal will be presented in the following section. Figure 8.19 shows optical images of new (as received) sharp cutting edge and the progression of the flank wear for every two holes drilled. The amount of measured flank wear for every two holes along with the amount of material drilled is given in Table 8.6.

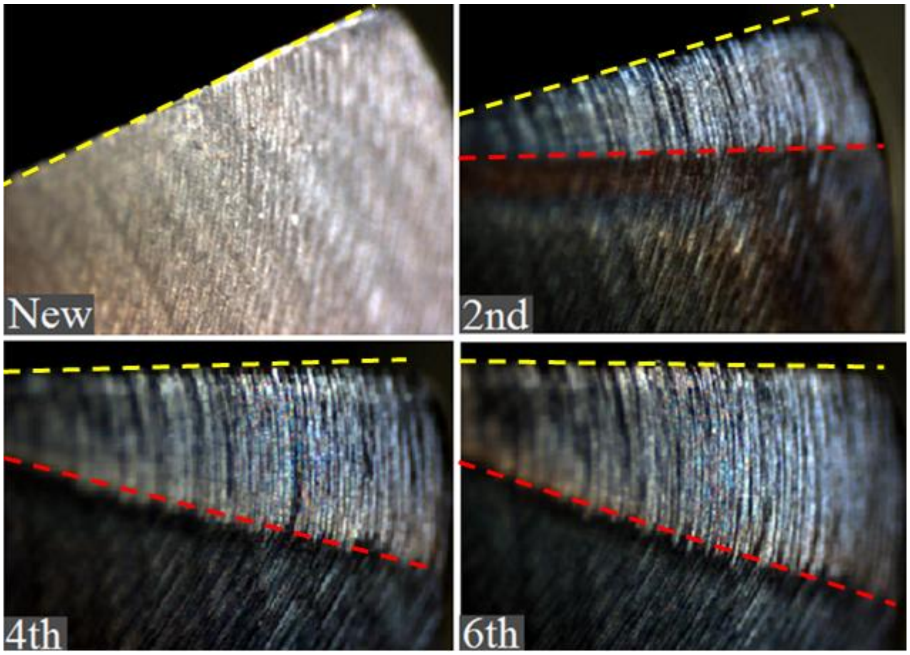

Figure 8.19. Optical images of new and worn cutting edge for every two holes

Table 8.6. Flank wear measurements for drilled holes

Number of Holes	Amount of material drilled (mm)	Flank Wear (mm)
2	38.1	0.997
4	76.2	1.337
6	114.3	1.607

Flank wear measurement shows that the cutting edge suffered a large amount of wear during the first two holes compared to the progression of the wear after the second hole, where the cutting edge worn largely from being sharp to a flank wear of 0.997 mm after drilling just two holes or 38.1 mm of material. The progression of the flank wear was less compared to the progression seen from new tool to drilling of two holes, with 25 % increase when the number of drilled holes increased from two to four and 17 %, and a 25 % increase when the number of drilled holes increased from four to six. Figure 8.20 shows the relationship between flank wear and the number of drilled holes, and the relationship between the flank wear and number of holes drilled can be approximated with a regression line with a determination coefficient of 0.9956.

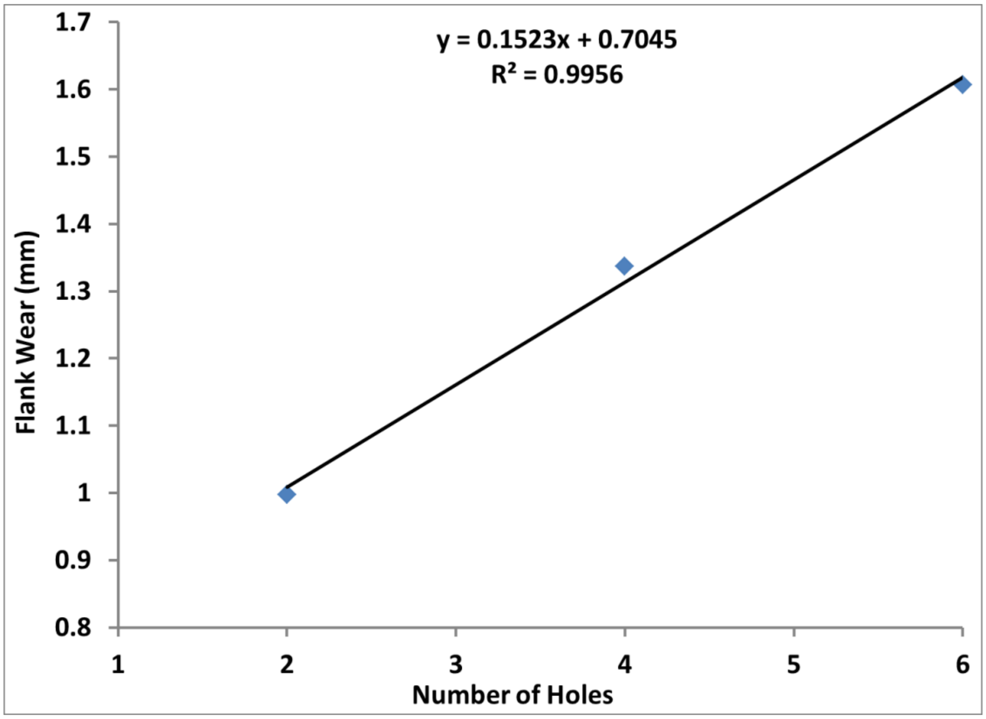

Figure 8.20. Relationship between flank wear and the number of drilled holes

8.2.2.1. Audio Microphone Signal (AMS)

The acoustics of the cutting action was recorded using an air-coupled audio microphone (AM) during the drilling operation and the variation in the amplitude of the acoustic signal was studied. Figure 8.21 shows the raw acoustic signal profiles of the second hole and the sixth hole and the plot of the raw signal profiles collected for the rest of drilled holes are given in Appendix P. The amplitude of the raw signal of the sixth hole is lower than that of the second hole, which also been seen in the previous sections (studies) where the amplitude of the acoustic signal decreases when the number of drilled holes increased.

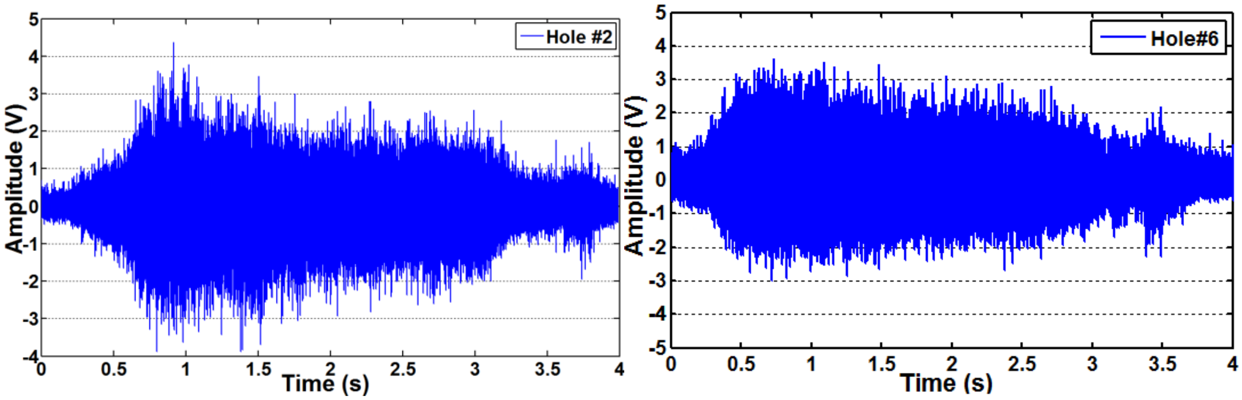

Figure 8.21. Raw signal profiles of AM for the second and sixth hole

The raw acoustic signals from the audio microphone was filtered and smoothed through a low-pass filter in order to eliminate the noise and to correlate the amplitude of the AM signal with the flank wear measurement. As it was seen in previous sections, the maximum amplitude of the smoothed signal also decreased when the number of drilled holes increased. The maximum amplitude of the filtered signal for each hole along with the normalized quantity of amount of material drilled which the number of holes drilled multiplied by the thickness of the CFRP plate used in this part of the study is given in Table 8.7.

Table 8.7. Maximum amplitude of smoothed signal and number of holes

Number of Holes Drilled	Amount of Material Drilled (mm)	Maximum Amplitude of Smoothed Signal (V)	Flank Wear (mm)
1	19.05	0.831	--------
2	38.1	0.779	0.997
3	57.15	0.689	--------
4	76.2	0.676	1.337
5	95.25	0.620	--------
6	114.3	0.615	1.607

Figure 8.22 shows the maximum amplitude of the audio microphone signal for the number of drilled holes. The decreasing trend of the signal amplitude when the numbers of drilled holes increased from one to six can be approximated with an average linear slope of

4.5 %, whereas, the change (slope) between the fifth and the sixth hole is only 0.5%. The decreasing trend of the maximum amplitude of the signal follows a second-degree polynomial with a determination coefficient of 0.977. The decreasing trend of the maximum amplitude of the AM signal when the number of drilled holes increased was also seen in the previous sections.

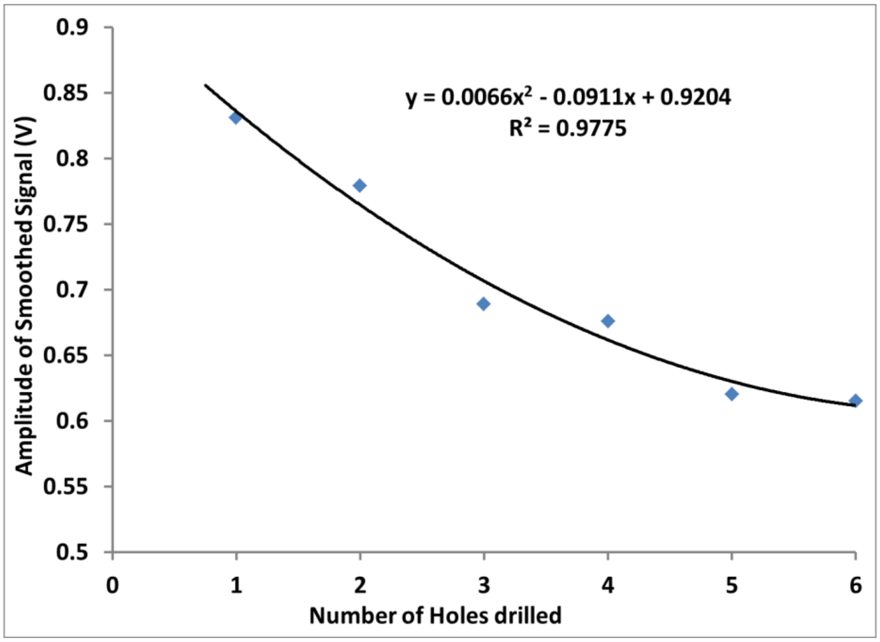

Figure 8.22. Maximum amplitude of smoothed signal for the number of drilled holes

Correlation of the maximum amplitude of the audio microphone signal with the flank wear also considered in addition to the correlation made with the number of drilled holes. Figure 8.23 shows the relationship between the maximum amplitude of the microphone signal and the flank wear sustained by the cutting edge. As the case discussed in the previous sections (studies), the amplitude of the audio microphone signal decreased when the flank wear increases. The correlation between the measured flank wear and the smoothed amplitude shows a linear relationship with a coefficient of determination of 0.99. From this relationship, it is possible to estimate (predicted) the amount of flank wear sustained by the cutting tool using the value of maximum amplitude as an input parameter. The maximum error in estimating the flank wear by using the AM amplitude value as an input parameter for this part of the study was only 2 %, which shows the proficiency of the proposed method to monitor the condition of the drill (cutting) tool online without interrupting the drilling process.

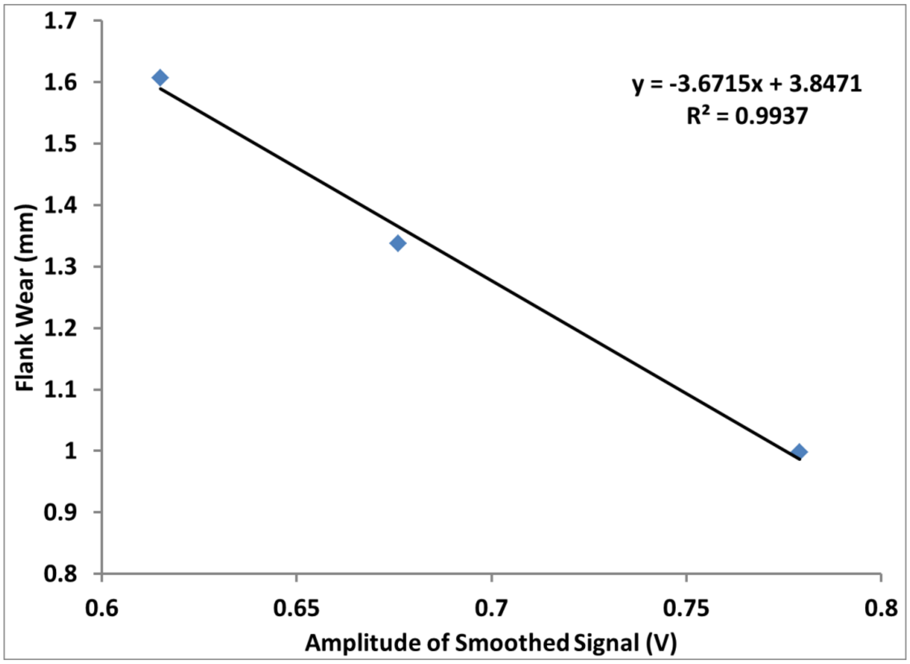

Figure 8.23. Flank wear and smoothed signal amplitude

8.2.3. Monitoring when Drilling Uni-Directional CFRP using Carbide Drill

A 19.05 mm thick uni-directional CFRP laminate composed of 99 plies that have an average ply thickness of 192 µm was used for this part of the investigation. Four set of drilling experiments with various combination of drilling conditions were conducted using a 6.35 mm carbide twist drill, where the drilling conditions are given in Table 8.8. 320 holes were drilled on the test coupons, 80 holes for each drilling conditions and flank wear measurements were taken for every ten drilled holes. Thrust force signal, audio microphone signal, and acoustic emission signals were acquired during the drilling operations and the correlation of flank wear with the amplitude of these acquired signals will be discussed in the next sections. Figure 8.24 shows representative optical images of the cutting edge and flank wear progression for each tenth hole drilled taken from drilling condition I and optical images of the cutting edge and flank wear progression for the remaining drilling conditions are given in Appendix Q. The amount of flank wear measured for every tenth hole for all four drilling conditions is tabulated in Table 8.9.

Table 8.8. Drilling condition combinations

Drilling Condition	Cutting Speed (rpm)	Feed Rate (μm/rev)	Number of Hole Drilled
I	3000	200	80
II	3000	100	80
III	6000	100	80
IV	6000	200	80

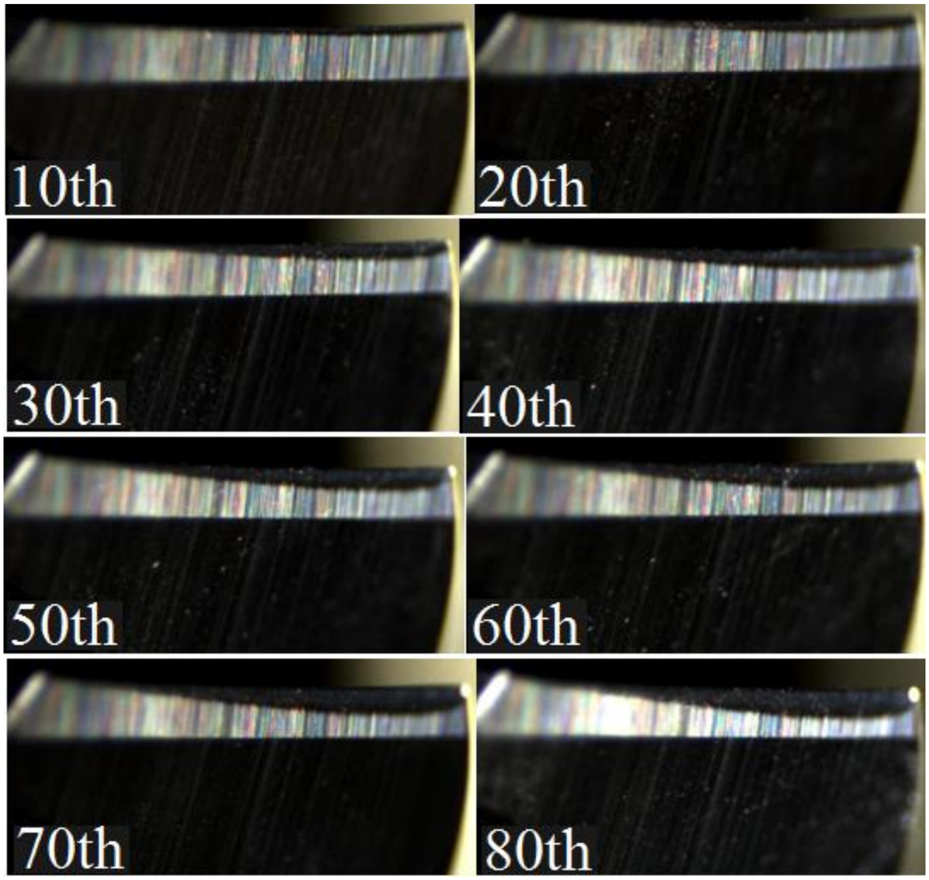

Figure 8.24. Representative optical image of the cutting edge from drilling Condition I

Table 8.9. Flank wear measurements for every tenth hole

Number of Holes Drilled	Material Drilled (mm)	Flank Wear (µm)			
		Condition I	Condition II	Condition III	Condition IV
10	190.5	61.3	68.1	64.5	53.7
20	381.0	84.0	96.8	83.5	86.2
30	571.5	117.0	123.7	119.4	103.3
40	762.0	136.0	148.4	128.6	116
50	952.5	147.0	173.4	155	134.9
60	1143.0	183.1	189.7	180.8	148.4
70	1333.5	194.0	232.8	203.4	167.8
80	1524.0	209.0	254.9	216.2	184

As it can be inferred from Table 8.9, the measured flank wear increased relatively in a constant rate when the number of drilled hole increased from ten to eighty for all cases of drilling conditions. Figure 8.25 shows the amount of measured flank wear for every tenth hole of all the four drilling conditions where the flank wear displays a linear increase with the increase of the number of drilled holes, where the change in flank wear did not show a large variation between the consecutive measurements (holes). The values of flank wear measured at each holes appears to be relatively close to each other for all drilling conditions until the number of drilled hole is forty, and a variation on flank wear between each drilling conditions were observed when the numbers of drilled hole is more than forty. The maximum flank wear sustained by the cutting edge is 254.9 µm after drilling of 80 holes or after drilling of 1524 mm of material with drilling condition II. Whereas, in the case of the previous studies using HSS drill, the cutting edge suffers a flank wear of 580 µm and 997 µm just after drilling 38.1 mm of material for 6.35 mm and 12.7 mm HSS drills respectively. This shows that carbide drill didn’t suffer half of the flank wear that the HSS drill suffered even the carbide tool drills 40 times more material than that the HSS tool.

To better understand the progression of the flank wear, the normalized value of the flank wear progression, which is measured flank wear divided by the amount of material drilled was calculated. Figure 8.26 shows flank wear per drilled distance for the total amount of material drilled in all drilling conditions. The largest observed variation on the value of the flank wear per drilled distance was an average of 42 % decrease for all drilling conditions when the amount of material drilled increased from 190.5 mm to 381 mm, after that all the variation were less than 15 % for amount of material drilled from 381 to 1524 mm. The relationship between flank wear per the amount of material drilled and distance of material drilled can be approximated by a power curve.

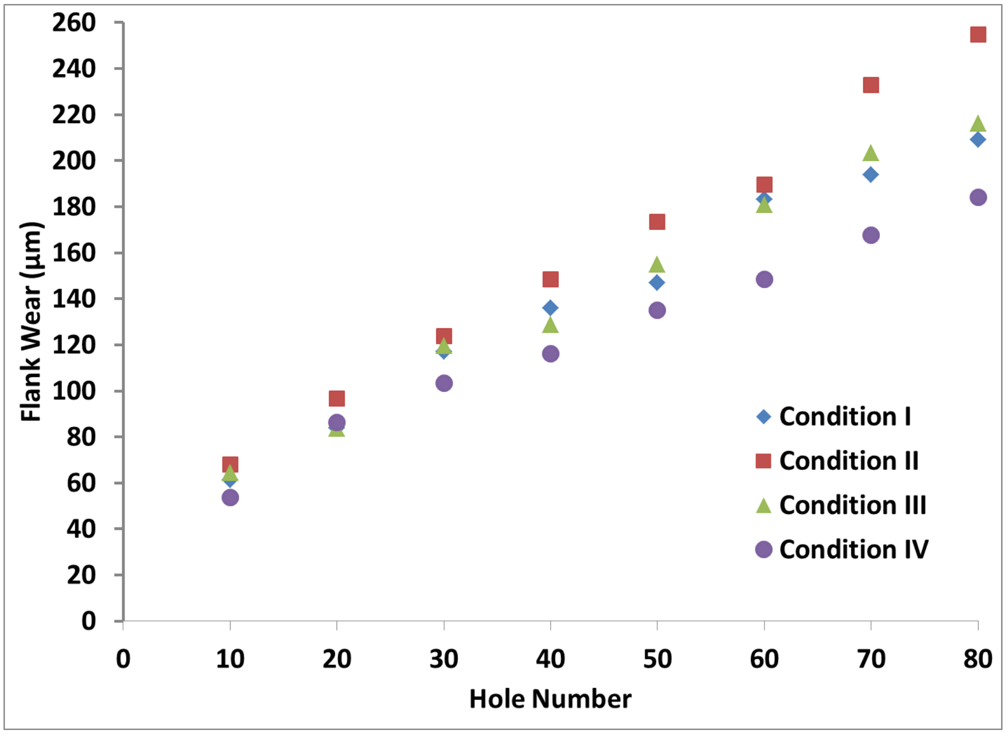

Figure 8.25. Amount of flank wear for number of holes drilled

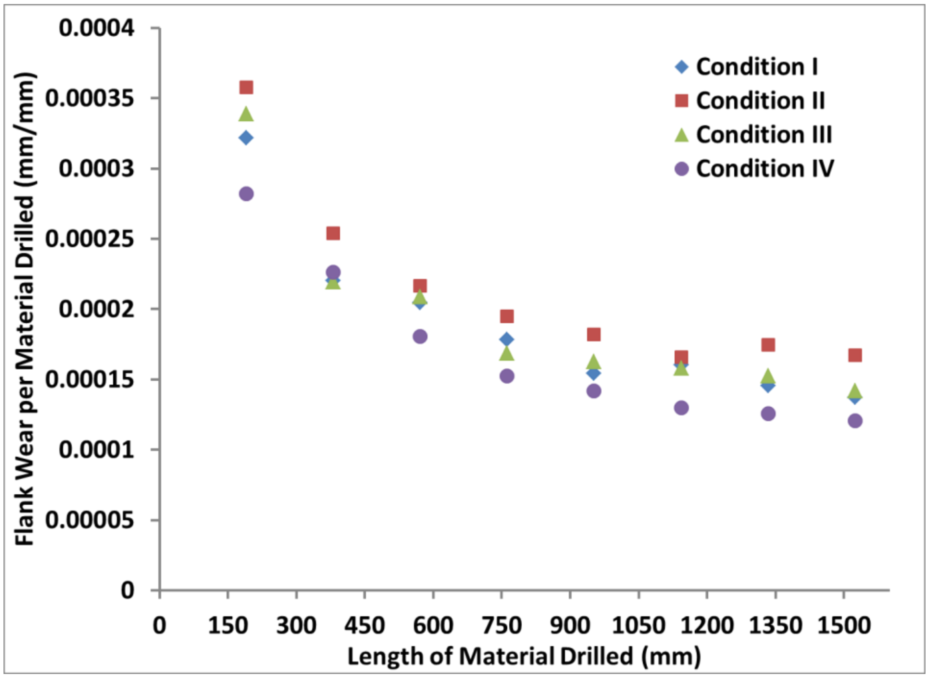

Figure 8.26. Flank wear rate for the amount of material drilled

8.2.3.1. Thrust Force

Thrust force was measured for the first hole and then for every tenth drilled hole and a representative thrust force profile from drilling condition I and IV is shown in Figure 8.27, whereas, thrust force profiles for drilling conditions II and III are given in Appendix R. The amplitude of the thrust force shows a gradual increasing trend as the number of drilled holes increased with an average increasing rate of 8 % for each consecutive measurement over all drilling conditions except for the first and tenth holes. The thrust force amplitude increased by 33 % when the number of holes drilled increases from one to ten and increased by 16 % when the number of holes drilled increases from ten to twenty.

The thrust force increased only by 33 % when the amount of material drilled increases from 19.05 mm to 190.5 mm when a carbide tool is used, whereas, when using a HSS drill tool the thrust force increased by 60 % when the amount of material increases from 7.62 mm to 38.1

mm. Moreover, when using HSS tool, the trust force was 432 N just for drilling 7.62 mm of material, whereas, for the carbide tool even after drilling 1524 mm of material the thrust force is only 306 N. Figure 8.28 shows the relationship between the value of the thrust force amplitude and the number of drilled holes for the first and every tenth holes drilled for all drilling conditions.

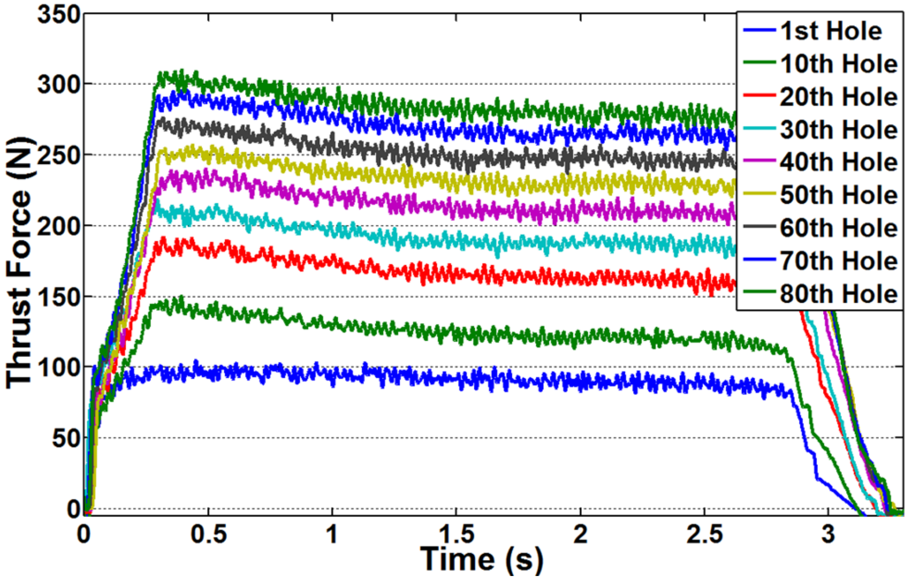

(a) Drilling Condition I

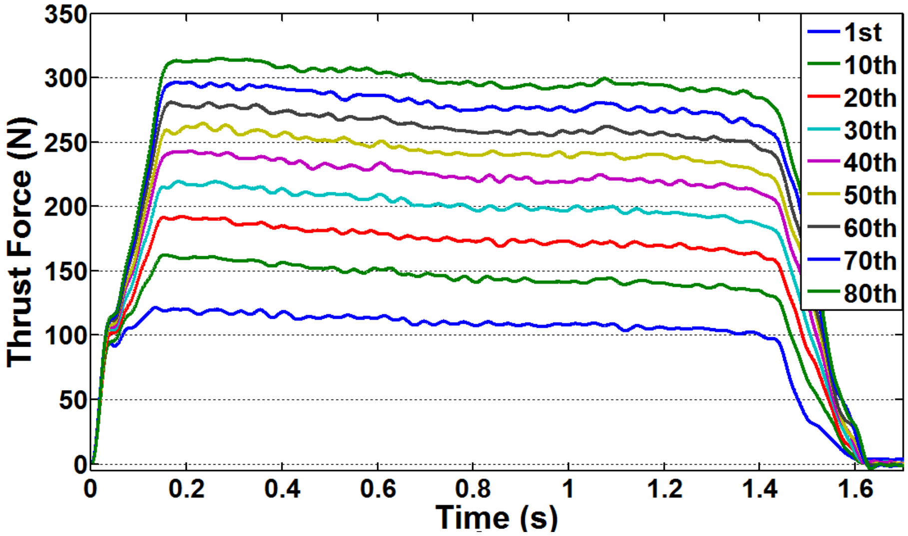

(b) Drilling Condition IV

Figure 8.27. Representative thrust force profiles from drilling condition I and IV

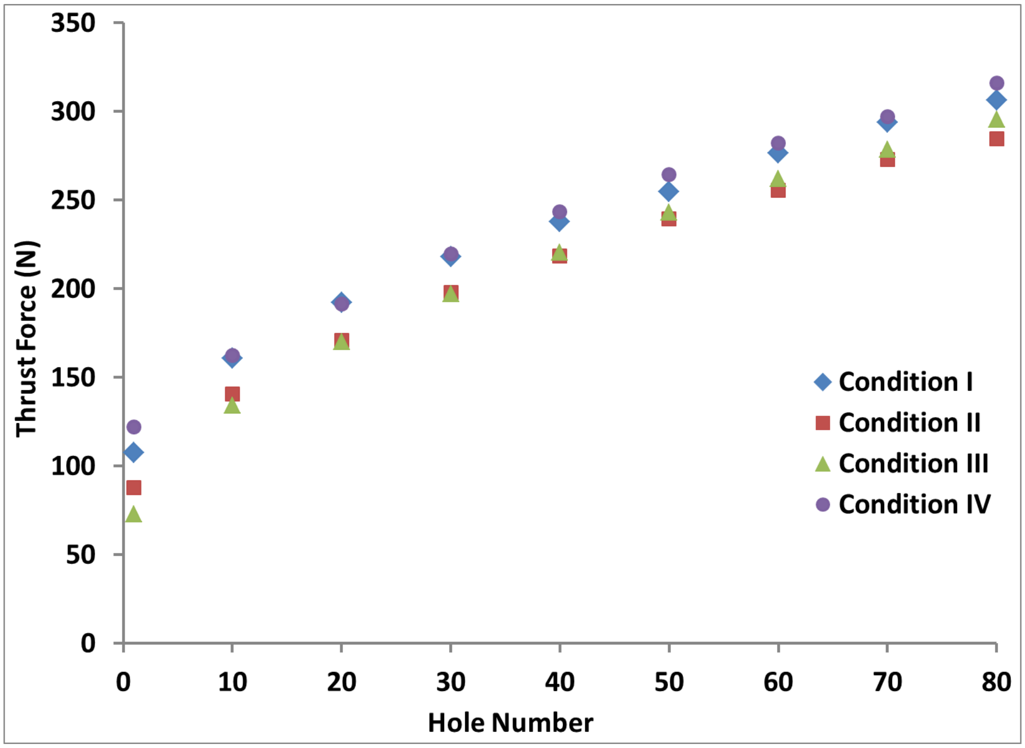

Figure 8.28. Thrust force values for the first and every tenth hole over all drilling conditions

The values of measured flank wear and amplitude of thrust force exhibits relatively a linear correlation over all combinations of drilling conditions. Figure 8.29 shows the relationship between the amount of flank wear and the amplitude of thrust force from the four drilling conditions used. The magnitude of thrust force amplitude increased from 134.4 to 316 N when the amount flank wear increased from 54 to 255 µm over all combinations of drilling conditions used in this investigation. As it can be seen from figure 8.29, the coefficient of determination value for flank wear versus thrust force plot is above 0.97 for all combinations of drilling conditions so it is possible to use this relationship to estimate flank wear using thrust force amplitude as an input parameter. As it was shown in the previous sections using HSS drill tool, thrust force amplitude is a great tool for estimating flank wear and monitoring the condition of the cutting tool better than any of the signals considered in this study.

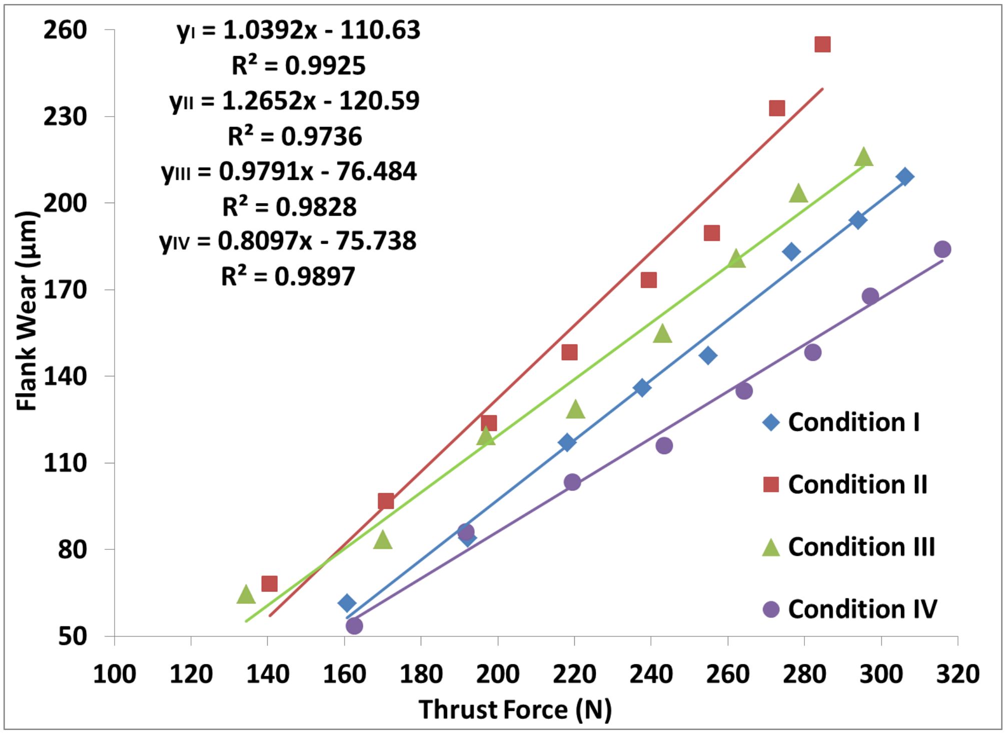

Figure 8.29. Relationship between flank wear and thrust force over four drilling conditions used

From the four regression line equations shown in Figure 8.29, an expression was deduced to express flank wear in terms of thrust force amplitude by taking an average of the four regression line equations. Using this expression and thrust force amplitude as an input parameter, an estimation of flank wear from measured thrust force amplitude was performed and the measured and estimated values of the flank wear for all drilling conditions are given in Figure 8.30. This shows that thrust force amplitude can be used as an input parameter for estimation of flank wear and serves as a significant tool in online monitoring of the condition of drill tool without interrupting the drilling operation.

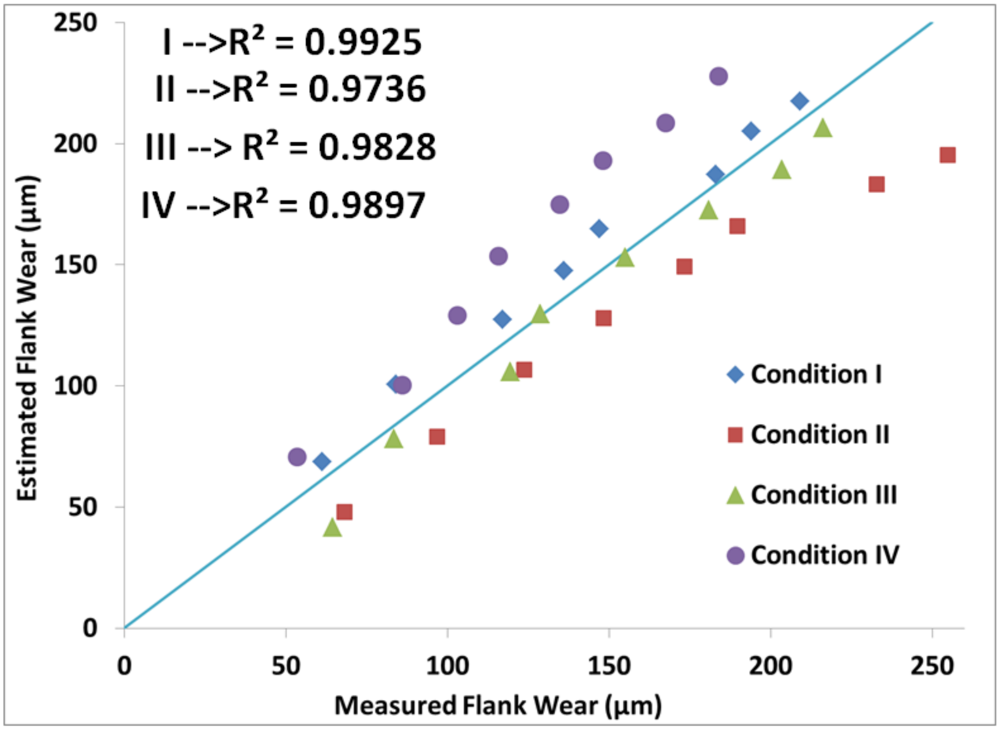

Figure 8.30. Measured and estimated values of flank wear over the four drilling conditions

8.2.3.2. Torque

The observed variation on the torque profile when the number of drilled holes increased for drilling conditions I and IV are given by Figure 8.31 and torque profiles for drilling conditions II and III are given in Appendix S. The observed variation on the torque amplitude is not as large as the variation observed on thrust force profiles. The amplitude of torque increased by an average of 25 % over all drilling conditions when the number of drilled hole increased from one to 10, however, for holes ten to eighty, the increase in torque amplitude was relatively small with an average increase of 8 % over all drilling conditions. This shows that torque amplitude is less sensitive to the progression of tool wear compared to that of thrust force amplitude.

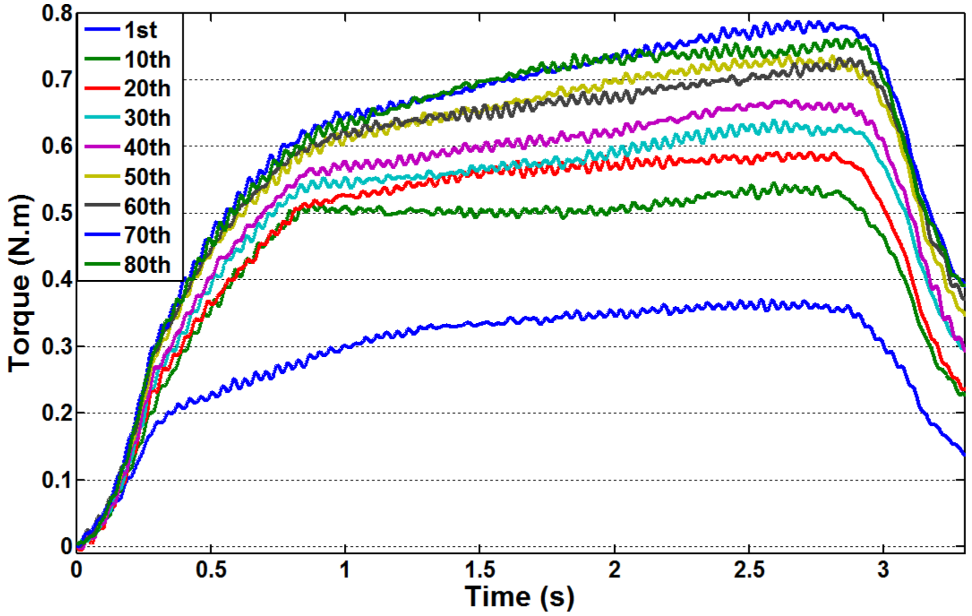

(a) Drilling Condition I

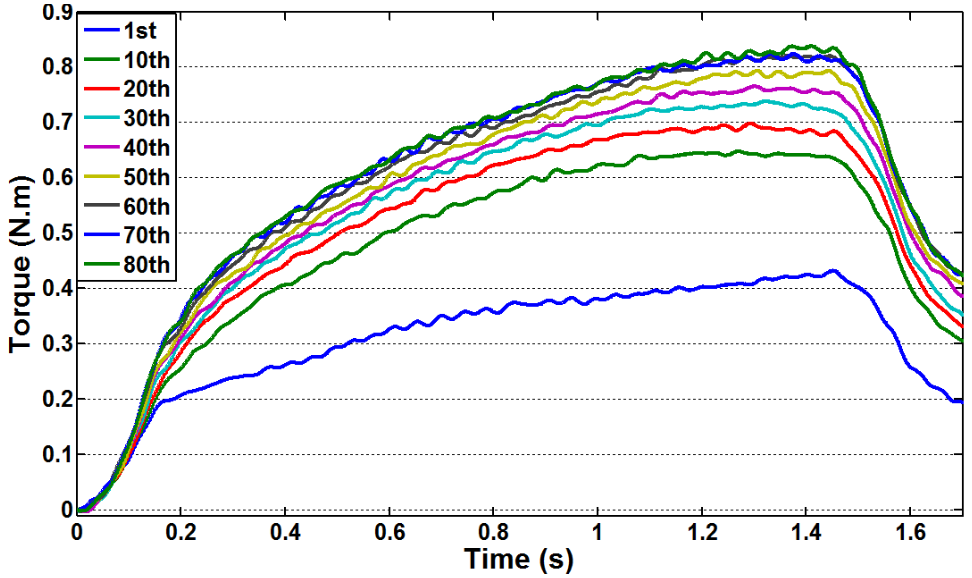

(b) Drilling Condition IV

Figure 8.31. Profiles of the torque measurement from drilling conditions I and IV

Figure 8.32 shows the relationship between the value of torque measurement and the number of drilled holes for the first and every tenth holes drilled for all drilling conditions. The value of the torque amplitude varies with the drilling condition used, whereas, variation of this magnitude was not observed in the case of thrust force magnitude. The lowest value of the torque magnitude was measured when the drilling condition is a combination of higher cutting speed and lower feed rate, in this case drilling condition III, which is also true for the case of thrust force magnitude.

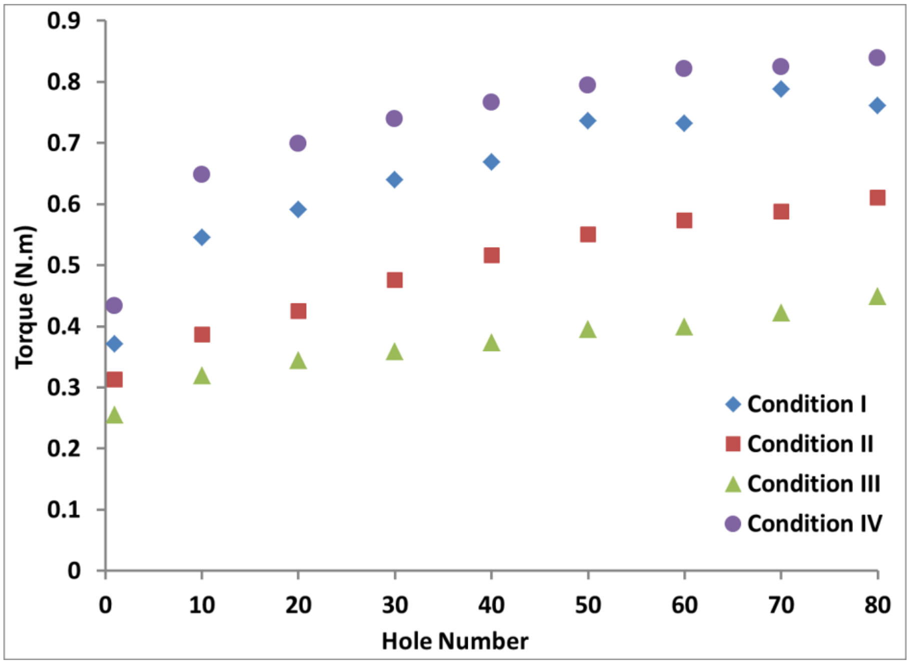

Figure 8.32. Torque values for first and for every tenth hole drilled over all drilling conditions

8.2.3.3. Audio Microphone (AM) Signal

The acoustic signals were recorded using an audio microphone (AM) during the drilling operation starting from the twentieth hole to the eightieth hole for every tenth drilled hole of the drilling condition I, II, and IV. Figure 8.33 shows a representative profile of the raw audio microphone signal for the twentieth and eightieth hole from condition I. The plots of the raw signal profile for the rest of drilled holes and drilling conditions are given in Appendix T. The raw signal profile becomes noisier when the number of drilled holes increased and the amplitude of the raw signal decreased with the increase of the number of holes drilled as it was observed in the other audio microphone signals discussed in the previous sections.

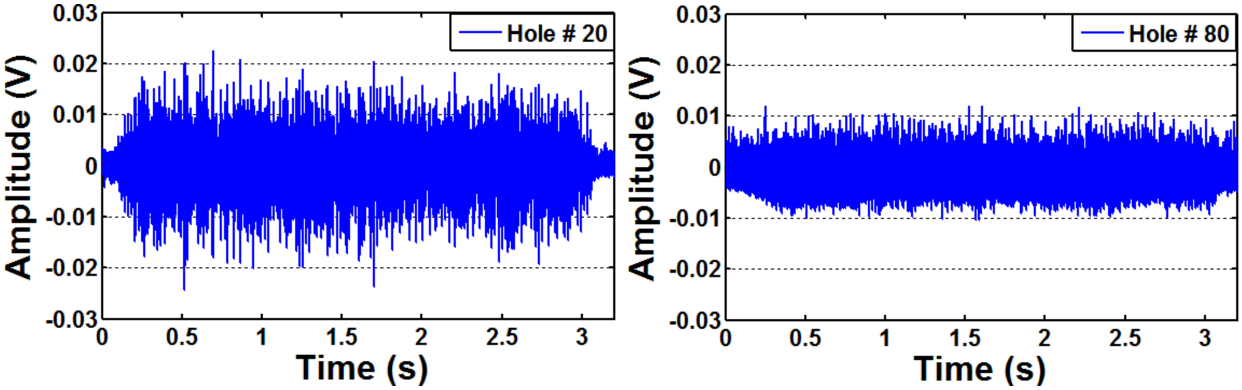

Figure 8.33. Raw microphone signal profiles for the twentieth and eightieth hole for condition I

In order to make a correlation between the amplitude of the audio microphone signal and the flank wear measurement the noise of the raw signal should be eliminated, for this, the raw signal was filtered through a low-pass filter. The amplitude of the raw signal profile was amplified by a factor of a thousand before filtering. The amplitude of the smoothed (filtered) signal decreased when the number of holes increases, which also the case for all experimental investigations covered in the previous sections. The amplitude of the 20th hole was lower than the 30th hole in the case of drilling condition II and IV and in the fourth drilling condition, the amplitude of the 80th hole was found to be lower than the 70th hole where these events were not observed in other part of this study. The amplitudes of the filtered audio microphone signals with the number of holes drilled and the amount of materials drilled for the three drilling conditions are given in Table 8.10. The amount of material drilled is a product of the material thickness and the number of drilled holes.

The values of the maximum amplitude of the smoothed (filtered) audio microphone signal for every tenth drilled hole starting from the twentieth to the eightieth hole for the three drilling conditions are given in Figure 8.34. The amplitude of the AM signal was decreased by an average of 27 % when the number of drilled hole increased up to 60 and after the 60th hole, the

AM amplitude shows only an average of 11 % decrease over the three drilling condition. The decreasing trend of the microphone signal was also observed in studies discussed in previous sections and can be correlate with flank wear to monitor the condition of the cutting tool.

Table 8.10. Amplitude of filtered audio microphone signal

Hole Number	Material Drilled (mm)	Amplitude of Smoothed Signal (V)		
		Condition I	Condition II	Condition IV
20	381.0	1.947	1.0834	0.556
30	571.5	1.833	1.2662	0.588
40	762.0	1.776	1.2149	0.4845
50	952.5	1.277	1.0645	0.398
60	1143.0	1.091	0.9518	0.365
70	1333.5	0.962	0.9436	0.303
80	1524.0	0.935	0.901	0.4665

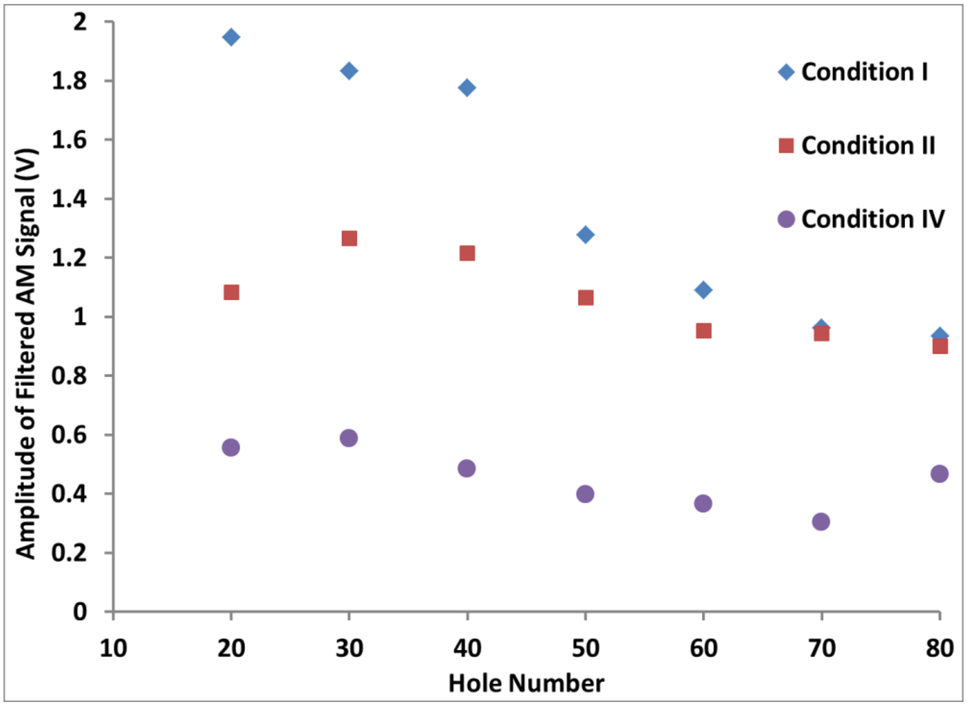

Figure 8.34. Amplitude of audio microphone signal for number of drilled holes

Figure 8.35 shows the relationship between the amounts of measured flank wear and the maximum amplitude of the audio microphone signal for drilling condition I. The relationship between the two values can be approximated through a linear regression line with a coefficient of determination value of 0.9083. The amplitude of the AM signal can be correlated with the value of the flank wear based on this relationship of linear regression equation and can be used to estimate flank wear values from AM amplitude for online monitoring of the cutting tool condition. The amount of flank wear values were estimated through the linear regression equation from Figure 8.35 using the amplitude of filtered AM signal as an input parameter. The maximum errors in estimating the flank wear was an over estimate of 15.67 % for the twentieth hole and an under estimate of 16.89 % for the fortieth hole, whereas, the minimum error was an over estimate of 0.18 % for the sixtieth hole. The values of measured and estimated flank wear using AM amplitude as an input parameter for drilling condition is given in Table 8.11.

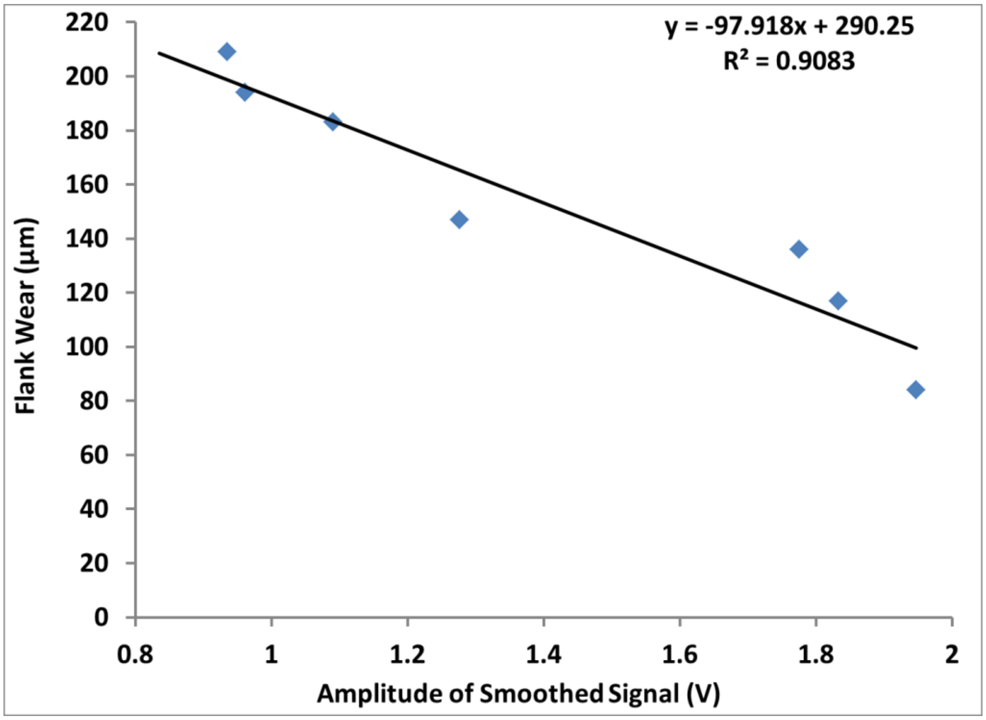

Figure 8.35. Flank wear as a function of audio microphone amplitude for condition I

Table 8.11. Measured and estimated flank wear

Hole Number	Measured Flank Wear (μm)	Estimated Flank Wear (μm)	Error (%)
20	84.0	99.6	15.67
30	117.0	110.8	-5.63
40	136.0	116.3	-16.89
50	147.0	165.2	11.02
60	183.1	183.4	0.18
70	194.0	196.1	1.05
80	209.0	198.7	-5.19

8.2.3.4. Acoustic Emission (AE) Signal

In addition to the thrust force, torque, and audio microphone signals, acoustic emission signal was also acquired for this part of the study. From the results of section 8.2.1.3, it was found that acoustic emission signal is highly path dependent due to the anisotropic nature of CFRP composites, which makes the acoustic wave propagation medium varies based on the relative distance between the sensor location and the hole being drilled and based on the relative orientation of the fibers. To avoid this path dependency, the location of the acoustic emission sensor relative to the hole being drilled was kept constant by moving the acoustic emission sensor and positioning it at same distance near the hole being drilled. Representative profiles of the raw AE signal from drilling condition III are given in Figure 8.36 for the tenth and eightieth hole, whereas, the plots of raw signal profiles for the rest of drilled holes and drilling conditions are given in Appendix U. The amplitude of the raw signal decreased slowly when the number of drilled holes increased but the variation of the raw signal amplitude between consecutive measurements are not as high (large) as the amplitude variation seen in other signals considered in this study.

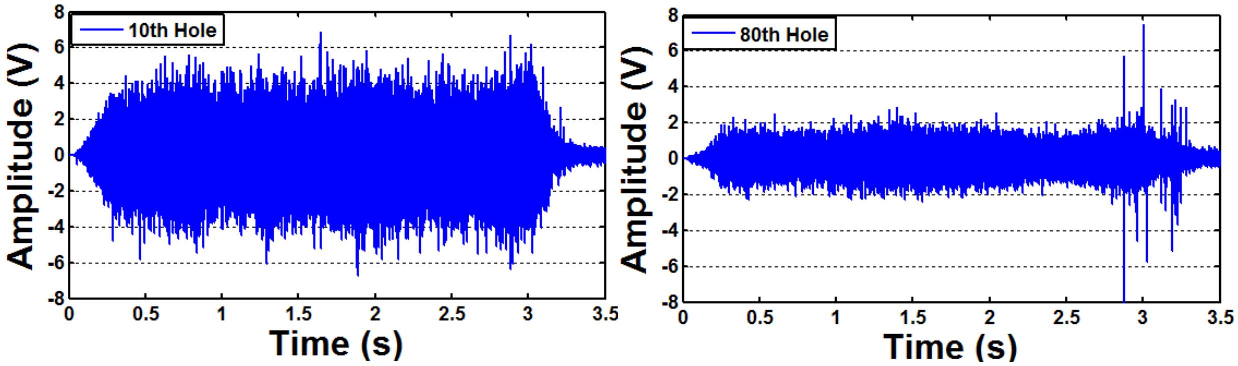

Figure 8.36. Representative profiles of raw AE signal for 10th and 80th hole from condition III

To quantify the variation of the acoustic emission signal amplitude and to make a correlation between the amplitude of the acoustic emission signal and the measured flank wear, the raw signal was filtered and smoothed trough a low-pass filter. The amplitudes of filtered acoustic emission signal for the number of drilled holes along with the amount of material drilled for all drilling conditions are given in Table 8.12. The amplitude of the AE signal decreased when the number of drilled holes increases except some observed outliers in one or two cases shown in Table 8.12. Other than these outliers, the decreasing trend of acoustic emission signal amplitude was observed for all drilling conditions as it was observed on other signals discussed in earlier sections.

Table 8.12. Amplitude of filtered acoustic emission signal

Hole Number	Material Drilled (mm)	Smoothed AE amplitude (V)			
		Condition I	Condition II	Condition III	Condition IV
10	190.5	0.748	0.389	0.733	0.965
20	381.0	0.772	0.280	0.541	0.737
30	571.5	0.711	0.255	0.361	0.710
40	762.0	0.702	0.268	0.411	0.703
50	952.5	0.663	0.227	0.392	0.525
60	1143.0	0.682	0.186	0.392	0.520
70	1333.5	0.664	0.213	0.352	0.523
80	1524.0	0.630	0.189	0.322	0.549

Figure 8.37 shows the amplitude of filtered acoustic emission signals for the number of holes drilled over all drilling conditions. The amplitude of the AE signal decreased over all drilling conditions by various amount from 4.89 to 50.7 % when the number of drilled holes increased from 10 to 30, whereas, when the numbers of drilled hole increased beyond forty, the `amplitude decreases slowly by an average of 5 % over all drilling conditions. When the number of drilled holes increased from ten to eighty, the amplitude of the AE signal decreased by an average of 42 % over all drilling conditions. As it can be seen from Figure 8.37, the amplitude of AE signal shows a good sensitivity to the change of the condition of the cutting tool up to the 50th hole, which is equivalent to an average flank wear of 152 µm over all drilling conditions. After the cutting edge of the drill sustains 152 µm of flank wear, or drilled 50 holes, the sensitivity of acoustic emission signal amplitude towards the progression of flank wear decreases compared to the sensitivity observed for holes less than fifty.

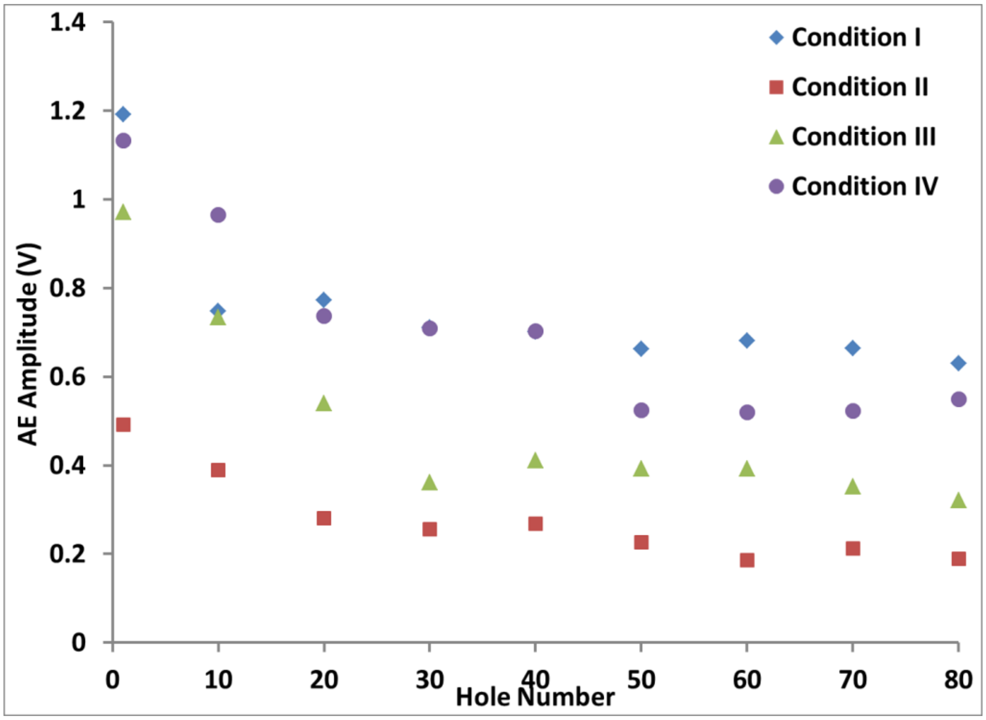

Figure 8.37. Amplitude of acoustic emission signal for the number of drilled holes

Figure 8.38 shows the values of flank wear as a function of the filtered acoustic emission signal amplitudes for drilling condition I. The relationship between the two values is approximated by a linear regression line with coefficient of determination value of 0.837. The amplitude of the AE signal can be correlated with the value of the flank wear based on this relationship of linear regression equation and can be used to estimate flank wear values from AE amplitude for online monitoring of the cutting tool condition. Expected values of flank wear were estimated through the linear regression equation from Figure 8.38 using the amplitude of filtered acoustic emission signal as an input parameter. Measured and estimated flank wear values are plotted in Figure 8.39. The estimation of flank wear values using the amplitude of acoustic emission signals as an input parameter was calculated and the maximum estimation error found was + 31 % and – 32 % for hole numbers ten and twenty respectively. Other than these two holes, the maximum estimation error found for the number of drilled holes from thirty to eighty was ± 16 %. Even though the estimation error is found to be higher than the estimation errors found by using audio microphone and thrust force, acoustic emission signal can be utilized for tool condition monitoring with appropriate adjustments.

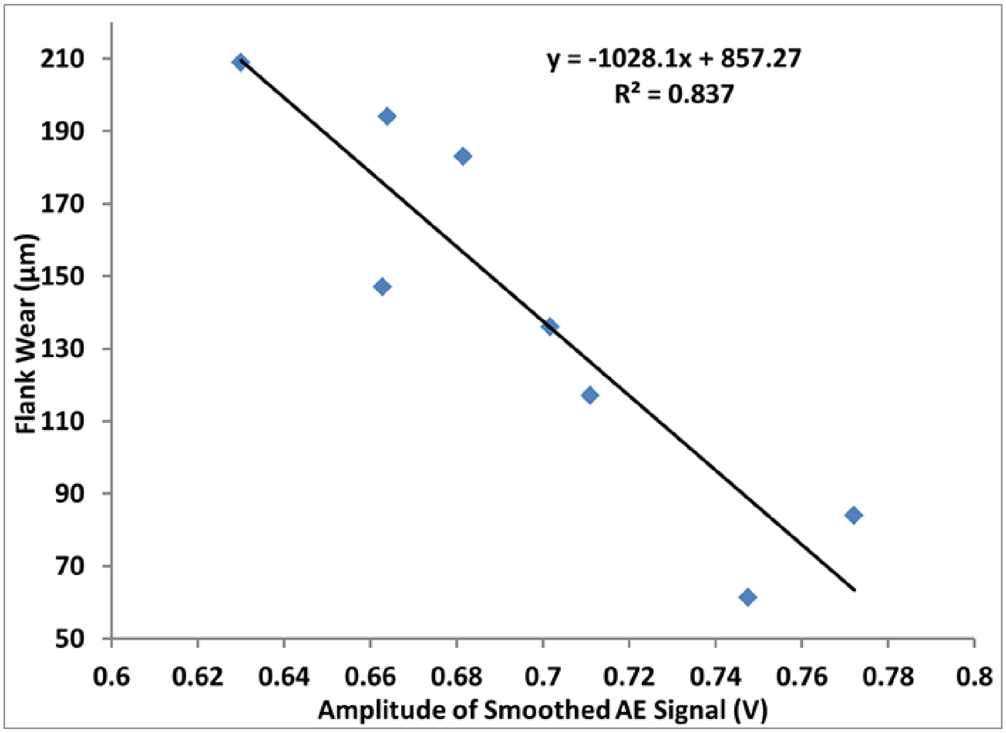

Figure 8.38. Flank wear as a function of filtered AE signal amplitude for condition I

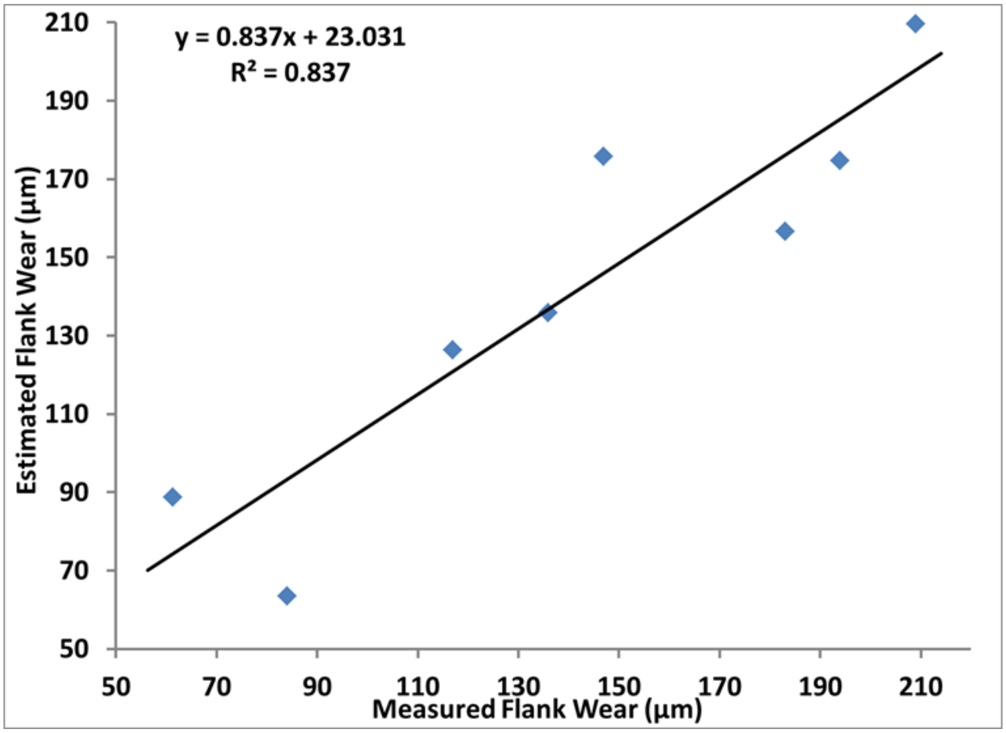

Figure 8.39. Measured and estimated values of flank wear using AE signal amplitude

8.3. Monitoring through Recurrence Quantification Analysis (R. Q. A)

This section presents the application of recurrence quantification analysis (RQA) as an analysis tool for the acoustic signal recorded through an audio microphone for on – line detection and monitoring of tool wear when drilling CFRP composite materials. The notion of a recurrence is for any ordered series (time or spatial); a recurrence is simply a point that repeats itself. Recurrence quantification analysis is an analysis tool, which quantifies the number and duration of recurrences of a dynamic system presented by its phase space trajectory, and it is known to provide useful information even for short, non-stationary, and noisy system. This quantification is based on the recurrence plot and recurrence analysis. Recurrence analysis is also a graphical method, which was introduced by Eckmann et al. [100 and 101], which is designed to locate hidden recurring patterns, non-stationary, and structural changes. Recurrence plot (RP), visual recurrence analysis (VRA), and recurrence quantification analysis (RQA) will be discussed in the following sections.

8.3.1. Recurrence Plot (RP)

Recurrence plots are graphical tools (devices) especially suited to detect hidden dynamic patterns and nonlinearities in a given data based on Takens's theorem [102]. The theorem states that it is possible to recreate a topologically equivalent picture of the original multidimensional system behavior by using the time series of a single observable variable using the method of time delay. The reconstructing of these equivalent vectors from a given scalar series is shown below. Figure 8.40 shows examples of a representative recurrence plot along with the corresponding time series plot for an audio microphone signal acquired when drilling CFRP composite. Main features of the recurrence plot and their interpretation is given in Table 8.13.

Let a be a given one-dimensional scalar time series as shown below;

$$a = (a_1, a_2, a_3, \ldots.., a_T) \tag{8.1}$$

From this one-dimensional scalar time series of length T a family of new vectors called embedded vectors will be constructed as shown in the equation bellow.

$$A_i = \left(a_i, a_{(i+\tau)}, a_{(i+2\tau)}, \ldots.., a_{(i+(m-1)\tau)}\right) \tag{8.2}$$

Where: $i = 1$ to T, τ is the time delay (lag), and m is the embedding dimension.

The new family of vector A_i then represents the multidimensional process of the time series as a trajectory in m-dimensional space. Recurrence plots are symmetrical $N \times N$ arrays in which a point is placed at (i, j) whenever a point A_i on the trajectory is close to another point A_j. How close the two points A_i and A_j each other is expressed by calculating the Euclidian distance between the two normed vectors as $\|A_i - A_j\| \leq r$, where r is a fixed radius. Other norms such as minimum or maximum can also be used in this calculation. The two vectors considered recurrent if the distance lays between the radiuses and can be graphically indicated by a dot.

The number of newly constructed vectors (N) is given by equation (8.3)

$$N = T - (m - 1)\tau \tag{8.3}$$

The sequence of embedded vectors recreates the original dynamics only if the values of m and τ are chosen properly, in particular, for Takens's theorem to hold m must be

$$m \geq 2d + 1 \tag{8.4}$$

Where: d is the original (unknown) systems dimension.

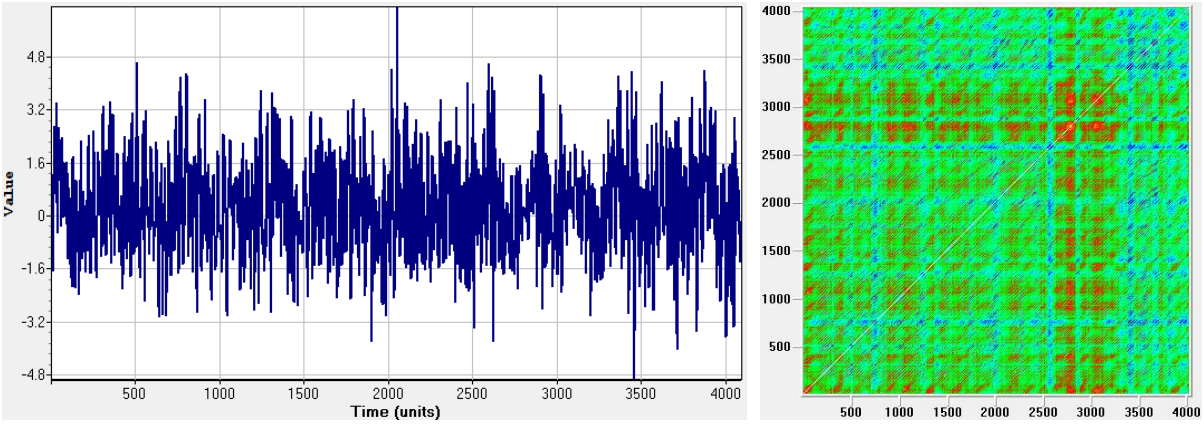

Figure 8.40. Time series plot (left) and its corresponding recurrence plot (right)

Table 8.13. Main features of recurrence plot and their interpretation

Recurrence Plot Feature	Interpretation
Homoginity	Stationary process
Fading to the upper left and lower right corners	Nonstationarity: the process contains a trend or drift
Disruptions	Nonstationarity: some states are rare or far from the normal; transitions may have occurred
Digonal lines parallel to the main diagonal	The states evolution is simmilar at different times and suggests a deterministic process
Digonal lines orthogonal to the main diagonal	The states evolution is simmilar at different times but with inverse time
Vertical and horizontal lines	Some states do not change or chenge slowly for some time
Isolated single points	Heavy flactuation in the process
Periodic patterns	Cycles, the time distance between periodic patterns corspond to period

8.3.2. Visual Recurrence Analysis (VRA)

Visual recurrence analysis (VRA) is a software package for topological analysis, qualitative and quantitative assessment, and nonparametric prediction of nonlinear and chaotic time series. Some VRA software packages are available freely in the public domain. This software packages calculates the time delay and the embedded dimension values, which are the main input parameters for the recurrence quantification analysis. The average mutual information function introduced by Fraser and Swinney [103] serves as a good estimate for the time delay τ. This function yields the first local minimum of the auto correlation and this first local minimum is the optimal time delay value for the embedded vectors. For selecting the embedding dimension, false nearest neighbor method was introduced by Kennel et al. [104] as an efficient tool to find the minimum required embedding dimension m. The VRA computes the time delay (lag) and embedding dimension using average mutual information and false nearest neighbor method respectively. In addition to calculating the input parameters, it gives the recurrence plot and computes various recurrence quantification analysis variables.

8.3.3. Recurrence Quantification Analysis (RQA)

Even though recurrence plots provide graphical representation of hidden dynamic patterns and nonlinearities in a given data, they do not deliver any quantification. Zbilut and Webber [105] introduced the concept of RQA and developed several strategies to quantify features of such plots originally pointed out by Eckmann et al [100 and 101] to provide objective quantification of important aspects shown by recurrence plot. The development of the recurrence quantification leads to the computation of several descriptive statistical variables. Percent recurrence, percent determinism, laminarity, trapping time, Ratio, entropy, maxline, and trend are the main descriptive variables in the recurrence quantification. Detailed explanation of each variable is given below.

- Percent recurrence (REC) is the measure of the percentage of recurrence points in the recurrence plot excluding the main diagonal. High value of percent recurrence indicates the periodic nature of the process. REC is defined as:

$$REC = \frac{1}{N^2}\sum_{i,j=1}^{N} r_{ij} \qquad (8.5)$$

where: r_{ij} is an element of the recurrence matrix.

- Percent determinism (DET) is the measure of the percentage of recurrence points that form diagonal lines. High value of percent determinism indicates that the given signal exhibit a deterministic structure. DET is defined as:

$$DET = \frac{\sum_{l=l_{min}}^{N} l.P(l)}{\sum_{i,j=1}^{N} r_{ij}} \tag{8.6}$$

  where *l* is the length of the diagonal lines on the recurrence plot and *P (l)* is the histogram of the lengths l of the diagonal lines.

- Laminarity (LAM) is a measure of the percentage of recurrence points that form vertical lines and it is defined as:

$$LAM = \frac{\sum_{v=v_{min}}^{N} v.P(v)}{\sum_{v=1}^{N} v.P(v)} \tag{8.7}$$

  where *P (v)* is the frequency distribution (histogram) of the lengths *v* of the vertical lines, which have a length of at least v_{min}.

- Trapping time (TT) is the average length of vertical lines or structures, which is an estimate of the mean time that the system will stay at a specific state or how long the state will be trapped.

$$TT = \frac{\sum_{l=l_{min}}^{N} lP_v(l)}{\sum_{l=l_{min}}^{N} P_v(l)} \tag{8.8}$$

- Ratio (RATIO) is the ratio of percent determinism over percent recurrence and can be used to detect transition between states.

$$RATIO = N^2 \frac{\left(\sum_{l=l_{min}}^{N} lP(l)\right)}{\left(\sum_{l=1}^{N} lP(l)\right)^2} \tag{8.9}$$

- Entropy (ENT) is the Shannon entropy of the distribution of the diagonal line lengths *p (l)*, which is also a measure of how much information is needed to recover a system.

$$ENT = -\sum_{l=l_{min}}^{N} p_{(l)} ln p(l) \qquad (8.10)$$

- Max-Line (L max) is the longest diagonal line segment measured parallel to the main diagonal, which has been shown to be inversely proportional to the largest Lyapunov exponent.
- Trend (TREND) is the slope of the least square regression of local recurrence as a function of displacement from the main diagonal, which is expressed in unites of percent local recurrence per thousand points. Trend is a measure of how stationary a given system is and indicates the paling of recurrence plot towards its edge.

8.3.4. Experiments

For this part of the investigation, two sets of drilling experiments were conducted on two unidirectional CFRP composites one having a thickness of 6.35 mm and the other having a thickness of 19.05 mm using a 12.7 mm HSS twist drill. Acoustic signal was acquired through an audio microphone during the drilling process. The experimental conditions for the two sets of experiments are given in Table 8.14. Flank wear measurements were taken for every fifth hole drilled in the case of condition-I and for every other hole drilled in the case of condition-II. Figure 8.41 shows an optical image of the cutting edge of a new (sharp) drill and the progression of the flank wear for condition-II.

Table 8.14. Summary of experimental conditions

Condition	Condition-I	Condition-II
Material thickness (mm)	6.35	19.05
Number of holes drilled	15	6
Cutting speed (rpm)	600	600
Feed rate (μm/rev)	200	100

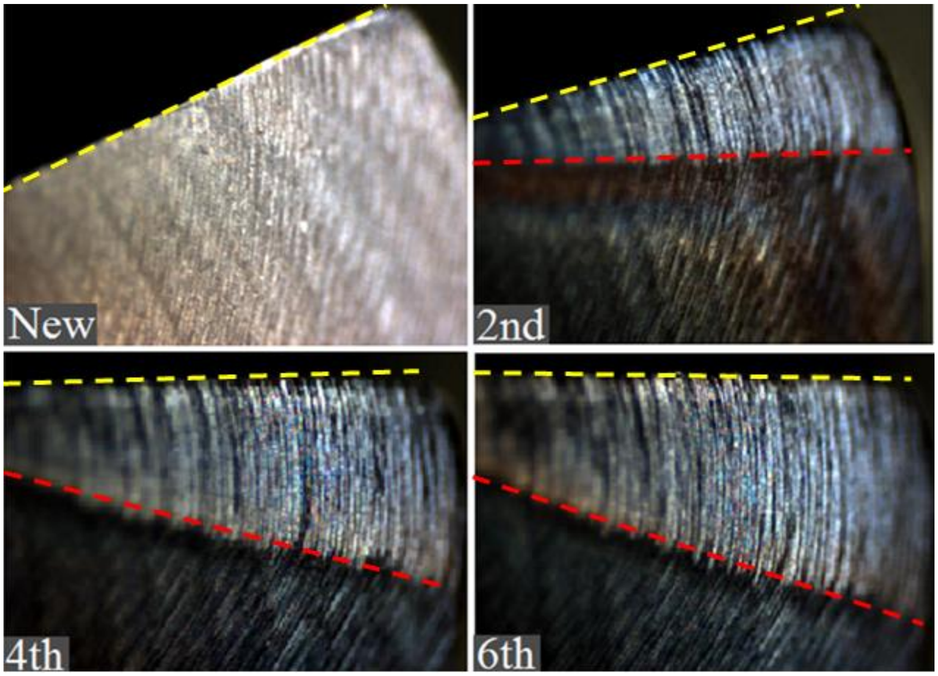

Figure 8.41. Optical image of sharp and worn cutting edge

The amplitude of the raw microphone signal was multiplied by a hundred and 4000 data points were selected after half of the cutting edge is engaged into the work piece, then these data points were converted in to formatted text format in order to use the visual recurrence analysis tool. For the RQA analysis, the microphone signals corresponding to the flank wear measurements were used. Table 8.15 gives the amount of flank wear measured with the corresponding distance of material drilled for both drilling condition. Then the microphone raw signals were loaded to the VRA software for RQA analysis in order to correlate the output variables of the RQA to the measured flank wear.

Table 8.15. Flank wear measurements and drilling distance

Number of drilled hole		Distance drilled (mm)		Flank wear (mm)	
Condition-I	Condition-II	Condition-I	Condition-II	Condition-I	Condition-II
5	2	31.75	38.1	0.943	0.997
10	4	63.5	76.2	1.212	1.337
15	6	95.25	114.3	1.435	1.607

8.3.5. Analysis Procedure and Results

The analysis and computation of RQA output variables was done using VRA software. The procedures followed to generate the recurrence plot and RQA output variables are as follows:

- The formatted text file loaded to VRA
- Time delay (lag) was computed through average mutual information analysis
- Embedded dimension was computed through false nearest neighbor analysis using the computed time delay as an input parameter. The maximum dimension was set to 30.
- Using the time delay and embedded dimension, RQA analysis was performed and RQA output variables were computed.

During the RQA analysis, An Euclidean method for to calculate the distances between vectors in the reconstructed state space, absolute method for rescaling the recurrence matrix, and Lowest number of upward diagonal recurrent points required to define a deterministic line were used in the analysis. In addition, the threshold radius was set to 1.5 in all RQA analysis for both conditions. Figure 8.42 shows the average mutual information plot for computing the time delay.

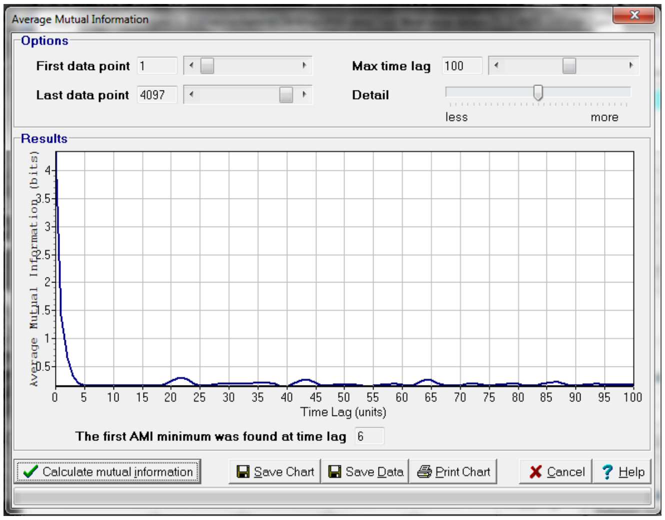
Average Mutual Information

First data point 1
Last data point 4097
Max time lag 100

The first AMI minimum was found at time lag 6

Figure 8.42. Average mutual information plot for condition-II with 0.977 mm flank wear

After computing the time delay through average mutual information analysis, false nearest neighbor analysis was performed using the time delay as an input parameter for calculating the embedded dimension. Figure 8.43 shows a plot of nearest neighbor analysis and as it is given in the bottom of the plot the optimal global embedded dimension for this plot is found to be 28. Using the same procedure, average mutual information and nearest neighbor analysis were performed for both drilling conditions and the time delay and optimal embedded dimension values were calculated. The values of time delay and embedded dimensions for both drilling conditions along with the flank wear measurement are given in Table 8.16.

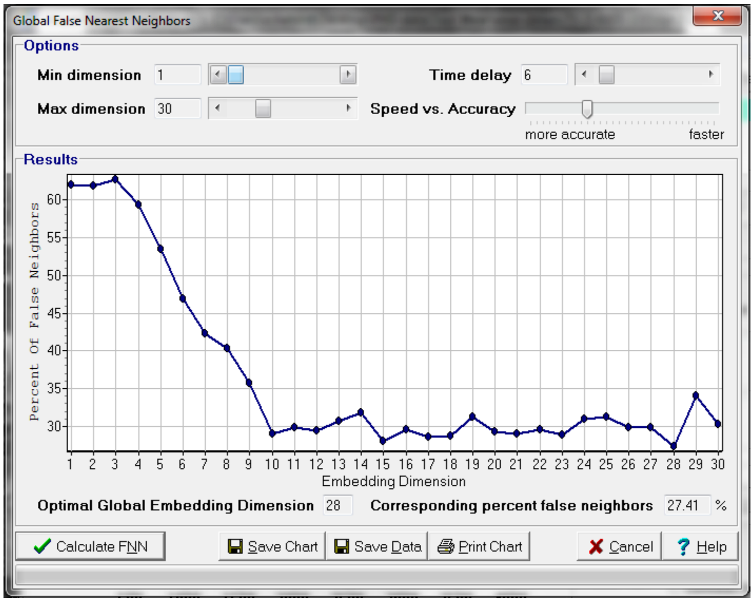
Global False Nearest Neighbors

Options

Min dimension 1

Max dimension 30

Time delay 6

Speed vs. Accuracy

Results

Optimal Global Embedding Dimension 28

Corresponding percent false neighbors 27.41 %

Figure 8.43. Nearest neighbor plot for condition-II with 0.977 mm flank wear

Table 8.16. Time delay and embedded dimension values

Drilling Condition	Distance drilled (mm)	Flank wear (mm)	Time delay τ	Embedded dimension *m*
I	31.75	0.943	5	18
	63.5	1.212	5	15
	95.25	1.435	5	16
II	38.1	0.997	6	28
	76.2	1.337	7	21
	114.3	1.607	10	14

Using the values of time delay and embedded dimension, the recurrence plots were generated for all drilling and flank wear conditions. Figure 8.45 shows the recurrence plots for the two drilling conditions with the corresponding flank wear measurement. As it can be seen from these recurrence plots, there is a change in the pattern, distribution of color, the length of the diagonal lines, and the density of vertical and horizontal lines when the level of wear increases in both drilling conditions. However, recurrence plot does not give any quantification about the source signal and the precise meanings of these patterns are unknown rather than serving as a general qualitative tool. In order to get a quantitative measure, performing recurrence quantification analysis (RQA) is required.

For these recurrence plots to be quantified RQA analysis is performed for both drilling conditions at all wear levels. In addition to the values of time delay and embedded dimension, other input parameters should be specified for the RQA analysis. These input parameters are grouped in three categories as evolution, distance, and phase space. The distance category consists the start of the first epoch, the end of the first epoch, data shift, and number of epochs, whereas, the distance category consists the method, rescaling, line, and radius. The phase space category is the category for time delay and embedded dimension. The input parameters required for the RQA analysis are listed below.

- First epoch start determines the position in the data file where the first epoch starts.
- First epoch end determines the position in the data file where the first epoch ends.
- Data shift determines the number of points to be shifted between epochs
- Epochs determines the number of times to repeat the recurrence plot analysis within the epoch window sliding down the input data set.

- Method determines the method used to calculate the distance between vectors in the reconstructed state space (Euclidean, Min norm, or max norm).
- Rescaling determines the method of rescaling the recurrence matrix (absolute, mean, or max).
- Line determines the lowest number of upward diagonal recurrence points required to define a deterministic line.
- Radius determines the maximum Euclidean distance at and below which recurrence points are defined and displayed.

In the RQA analysis, the first epoch was started at the first data file and ends at the end of the data file, whereas, the data shift has been set to zero since no data shift is necessary and all data files were analyzed as one epoch. To calculate the distances between vectors in the reconstructed state space Euclidean method, absolute method for rescaling the recurrence matrix, line was set to be two, and the threshold radius was set to 1.5 in all analysis. Figure 8.44 shows the RQA window.

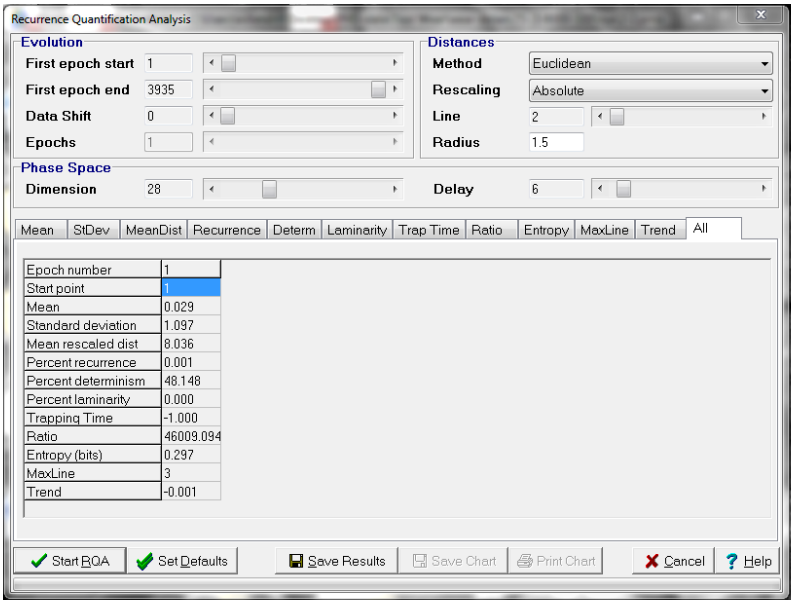

First epoch start: 1
First epoch end: 3935
Data Shift: 0
Epochs: 1
Method: Euclidean
Rescaling: Absolute
Line: 2
Radius: 1.5
Dimension: 28
Delay: 6

Epoch number	1
Start point	1
Mean	0.029
Standard deviation	1.097
Mean rescaled dist	8.036
Percent recurrence	0.001
Percent determinism	48.148
Percent laminarity	0.000
Trapping Time	-1.000
Ratio	46009.094
Entropy (bits)	0.297
MaxLine	3
Trend	-0.001

Figure 8.44. The recurrence quantification analysis window

Condition-I		Condition-II	
Wear	Recurrence Plot	Wear	Recurrence Plot
0.943	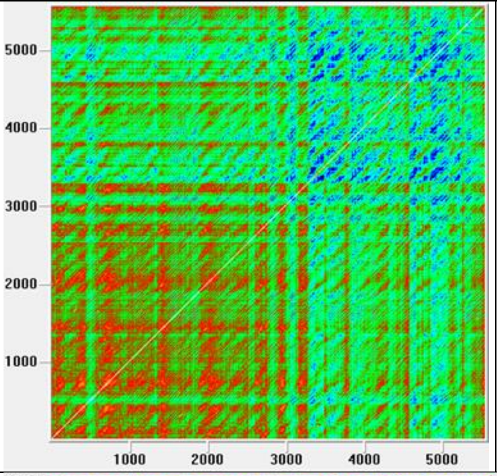	0.997	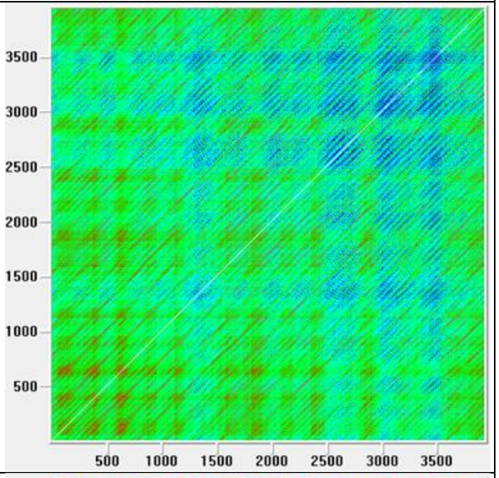
1.212	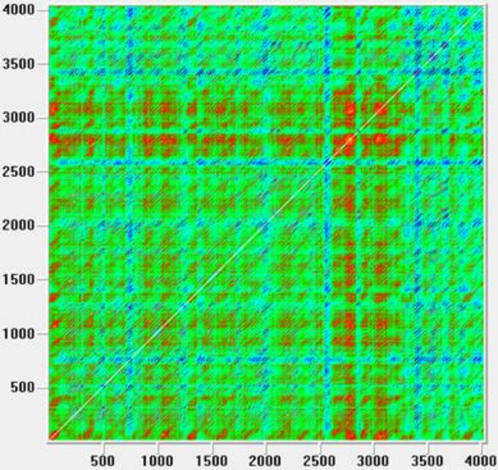	1.337	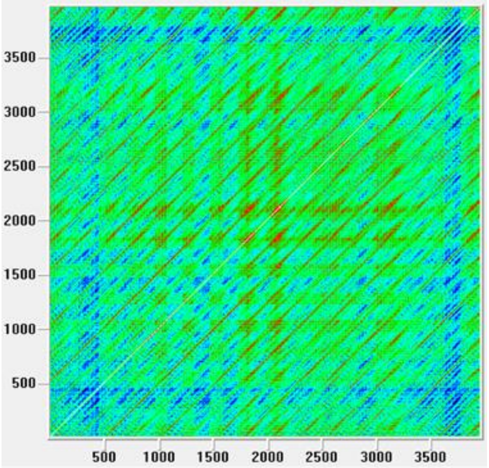
1.435	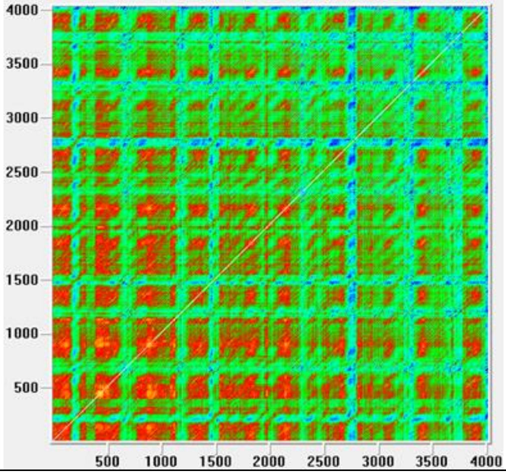	1.607	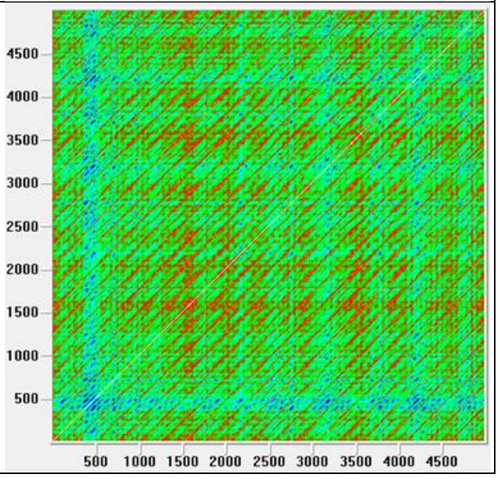

Figure 8.45. Recurrence plots for different wear level

8.3.5.1. RQA Output Variables and Wear for Drilling Condition-I

Following the procedure discussed in the previous section, RQA analysis is performed for all drilling conditions, and the results for drilling condition one will be discussed here and for case of drilling condition-II will follow in the next section. The summary of the RQA output variables along with the corresponding wear for drilling condition-I is given in Table 8.17. All of the RQA output variables except for the trend and ratio increased when the amount of flank wear increases. The influence of flank wear on the output variables of the RQA analysis is plotted and given in Figure 8.46. Looking at these plots, six of the output variables, which increased with the increase of the flank wear, can be grouped in to two categories based on their rate of increase between the two transition points on the value of flank wear, which are from a flank wear of 0.943 to 1.212 mm and from 1.212 to 1.435 mm. Percent recurrence, percent laminarity, and maxline show similar rate of increase between the transition flank wear ranges, whereas, the percent determinism, trapping time, and entropy show the same rate of increases between these transition ranges. The ratio and the trend values decreased when the flank wear increased in different rate.

Table 8.17. Summary of RQA output variables for drilling condition-I

Drilling distance (mm)	31.75	63.5	95.25
Flank wear (mm)	0.943	1.212	1.435
Percent recurrence	0.001	0.006	0.038
Percent determinism	35.659	71.652	77.291
Percent laminarity	0.000	5.804	43.902
Trapping time	-1.000	2.000	2.155
Ratio	42534.7	12965.1	2060.0
Entropy (bits)	1.221	1.957	2.005
Maxline	4.000	45.000	186.000
Trend	-0.001	-0.005	-0.032

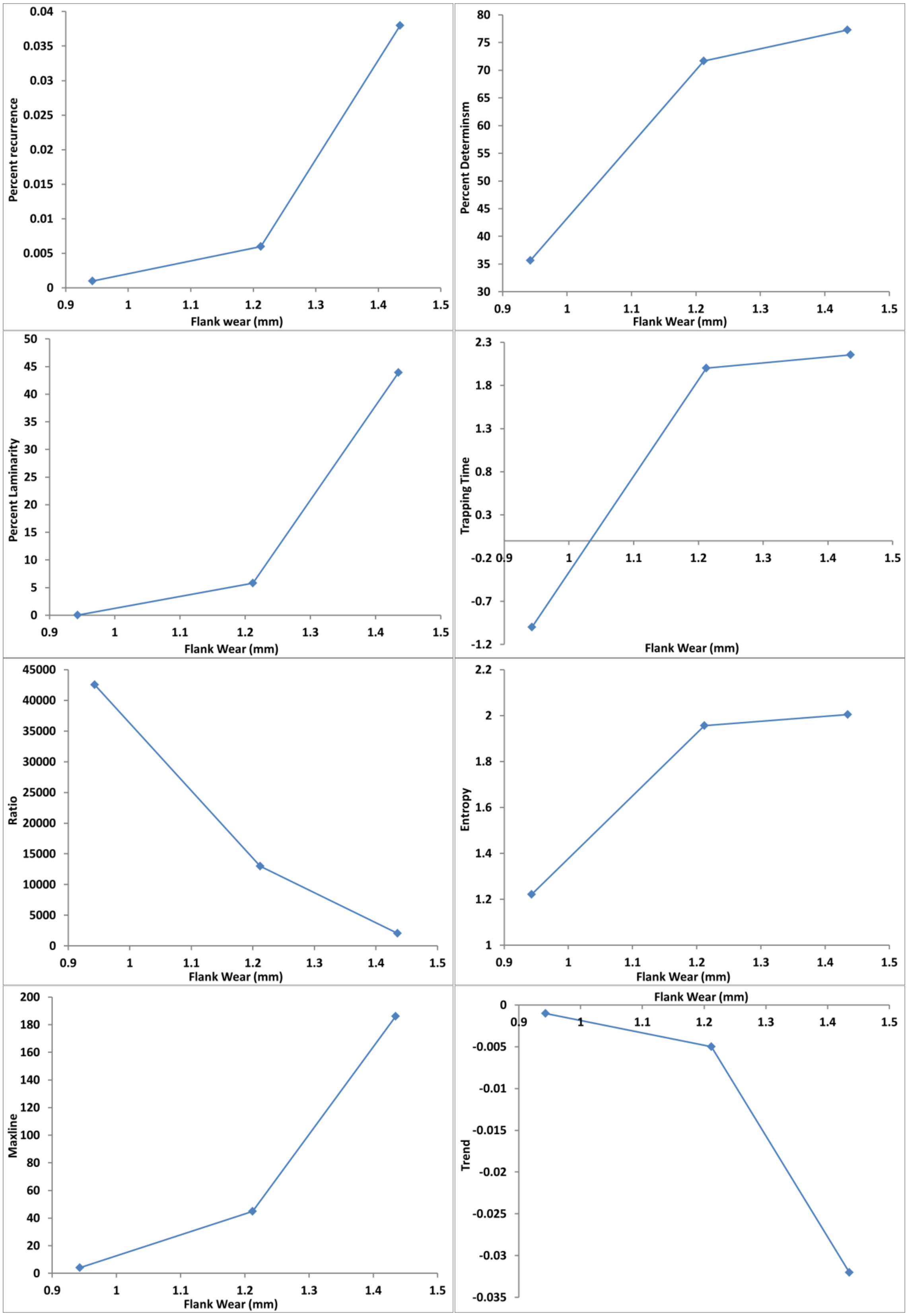

Figure 8.46. RQA output variables and flank wear for drilling condition-I

From the eight RQA output variables computed in the analysis, six of the variables increased with the increase of the flank wear, whereas, two of the output variables decreased when the flank wear increased. The rate of change (slope of output variables versus flank wear line) in the values of these RQA output variables is found to be different for the two regions of flank wear progression. Where the first region represents the progression of the flank wear from 0.943 to 1.212 mm with 22.2 % increase and the second region represents the progression of the flank wear from 1.212 to 1.435 mm with 15.5 % increase. The rate of increase or the slope for percent recurrence, percent laminarity, and maxline in the second region of flank wear progression was 7.7, 7.9, and 4.2 times higher than the first region of flank wear progression respectively. In the case of percent determinism, trapping time, and entropy, the rate of increase in their value during the second region of flank wear progression was 5.3, 16, and 12 times lower than the rate of increase observed in the first region of flank wear progression respectively. The ratio and trend values decreased when the flank wear increased in a variable rate.

8.3.5.2. RQA Output Variables and Wear for Drilling Condition-II

Analysis of RQA was performed for drilling condition-II following the same procedure and input parameters used in the case of drilling condition-I and the RQA output variables computed in the same fashion as drilling condition-I. The summary of values for RQA output variables along with the drilling distance and flank wear is given in Table 8.18. From eight output variables considered, the value of six output variables increased with the increase of flank wear, whereas, the values for two variables decreased when the flank wear increased. The output variables which showed an increase in their value when flank wear increased are the same as those variables in drilling condition-I. Figure 8.47 shows the plots of RQA output variables versus the amount of flank wear measured for drilling condition-II.

Table 8.18. Summary of RQA output variables for drilling condition-II

Drilling distance (mm)	38.1	76.2	114.3
Flank wear (mm)	0.997	1.337	1.607
Percent recurrence	0.001	0.014	0.056
Percent determinism	48.148	56.530	86.944
Percent laminarity	0.000	3.105	48.350
Trapping time	-1.000	2.000	2.071
Ratio	46009.1	4040.7	1553.3
Entropy (bits)	0.297	1.726	2.378
Maxline	3.000	104.000	1004.000
Trend	-0.001	-0.013	-0.037

As it is been observed in the case of drilling condition-I, the RQA output variables percent recurrence, percent determinism, percent laminarity, trapping time, entropy, and maxline increased when flank wear increase, whereas, ratio and trend decreased with the increase of the flank wear. The rate of increase or the slope of these variables found to be varying for the two regions of flank wear progression. The first region is when the flank wear increased from 0.997 to 1.337 mm and the second is when the flank wear increased from 1.337 to 1.607 mm. The rate of increase of present recurrence, percent determinism, percent laminarity, and maxline in the second region when the flank wear increases by 16.8 % was 4.1, 4.6, 18.3, and 11.2 times higher than the rate observed in the first region when the flank wear shows a 25.4 % increase. In the case of trapping time, the rate of increase in the first region was 33.6 times higher than the rate of increase seen in the second region while the entropy shows somewhat similar rate of increase in both regions. The values of the trend and the ration decreased with the increase of the flank wear at different rate. For comparison reason, the RQA output variables versus the amount of measured flank wear for drilling condition I and II are plotted together and shown in Figure 8.48.

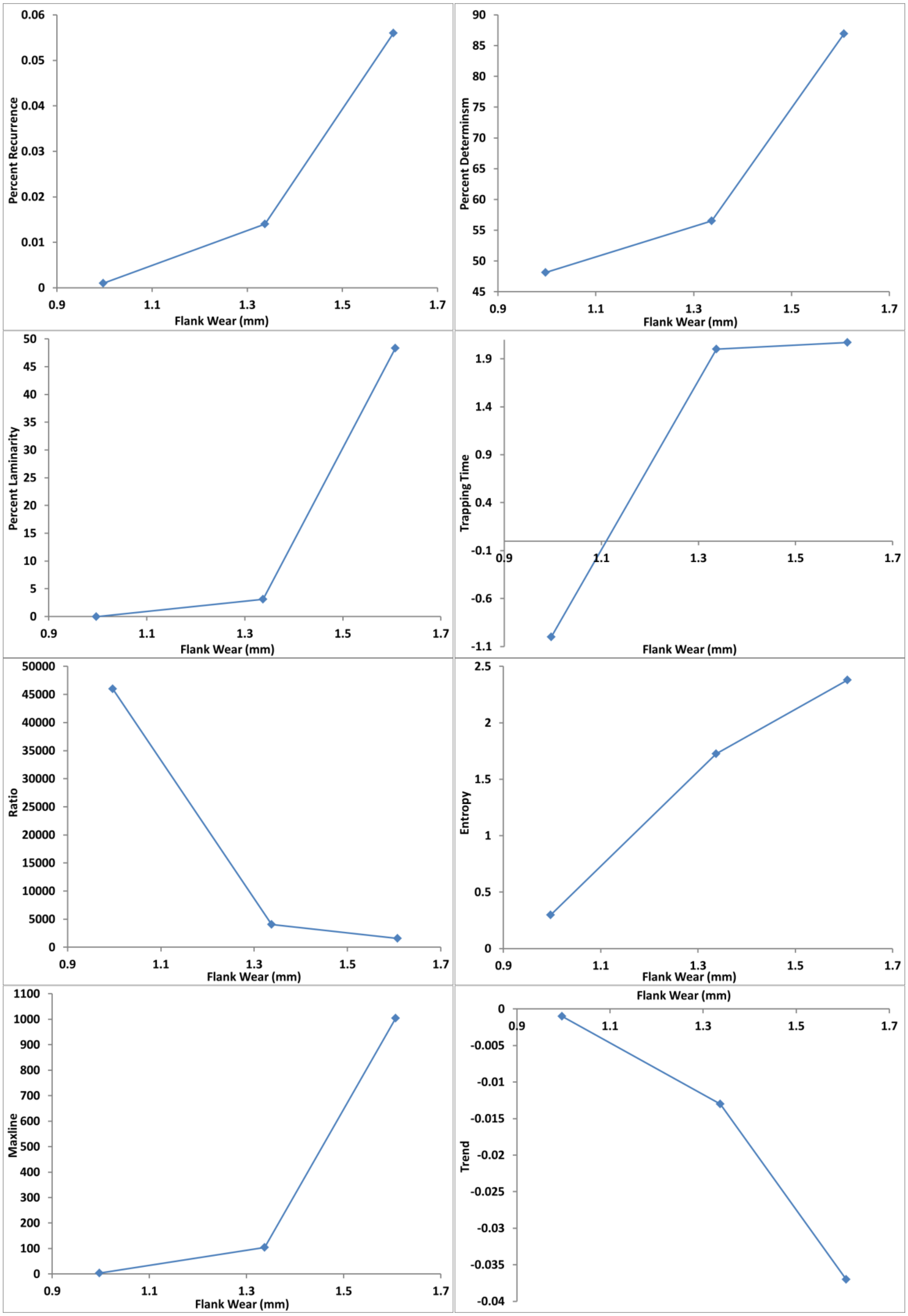

Figure 8.47. RQA output variables and flank wear for drilling condition-II

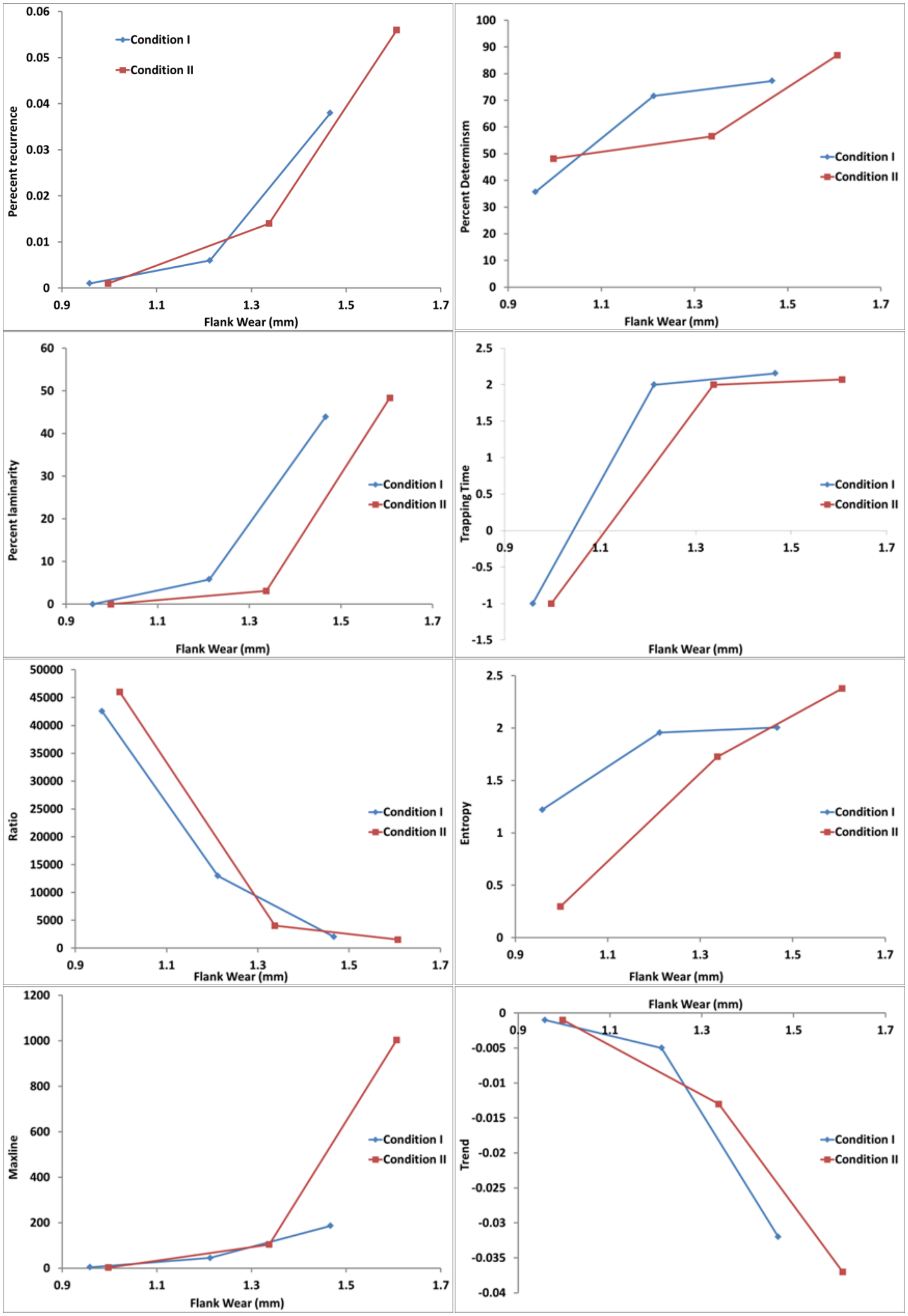

Figure 8.48. RQA output variables and flank wear for drilling condition I and II

8.3.6. Summary

Recurrence plot generation and recurrence quantification analysis was performed on audio microphone signal acquired during the drilling of unidirectional CFRP composites in order to see the correlation between RQA output variables and drill flank wear. Two drilling conditions were used in this investigation and the results from the RQA analysis and flank wear measurements were discussed in the previous sections. The output variables from the RQA analysis show similar behavior in both drilling conditions with different level of flank wear progression and the influence of flank wear progression on the output variables of the RQA analysis was clearly observed. In general, this investigation shows that recurrence quantification analysis can be used as analysis tool for audio microphone raw signal to detect and monitor flank wear progression when drilling CFRP composite laminates.

8.4. Tool Wear and Hole Quality

The quality of the hole produced when drilling CFRP composite materials is significantly influenced by the condition of the drill tool. As it is been discussed in the previous sections, the condition of the drill tool is one of the controlling factor in the resulting drilling forces and in turn, the magnitude of drilling forces has great impact on the quality of the hole produced. Increasing of thrust force magnitude and excessive heat generation are mainly resulted when the drill tool gets worn and dull. When the cutting edge of the drill tool gets worn out and dull, various defects such as matrix smearing, delamination, and geometrical variation of the hole will occur during the drilling process of CFRP composite material. In this section some of hole quality issues created because of tool wear will be presented.

8.4.1. Tool Wear and Surface Roughness

In order to investigate the effects of tool wear on the resulting surface quality of the hole, roughness measurements were taken at six different locations around the circumference of the holes drilled for tool wear experiment discussed in section 8.2.4. The combinations of drilling conditions used for this part of the investigation are given in Table 8.8. Parametric quantities, such as: arithmetic mean roughness (R_a), maximum peak-to-valley (R_t), root mean square roughness (R_q), and ten point average surface roughness (R_z), which describe the surface of the hole were evaluated from the surface roughness profiles. The values of surface roughness describing parameters measured at the location where the interaction angle between the cutting direction and fiber orientation is 0^0 increased when the number of drilled holes increases. At this orientation, the cutting mechanism is more of slicing or splitting of the fibers longitudinally and as the cutting edge of the drill is worn, the cutting action is more of chopping with a dull cutting edge resulting an increase in the surface irregularity. Figure 8.49 shows surface roughness values measured at a location where the interaction angle between the cutting direction and fiber orientation is 0^0 for drilling Condition I, whereas, surface roughness values for all drilling conditions measured at this location are plotted and given in Appendix V.

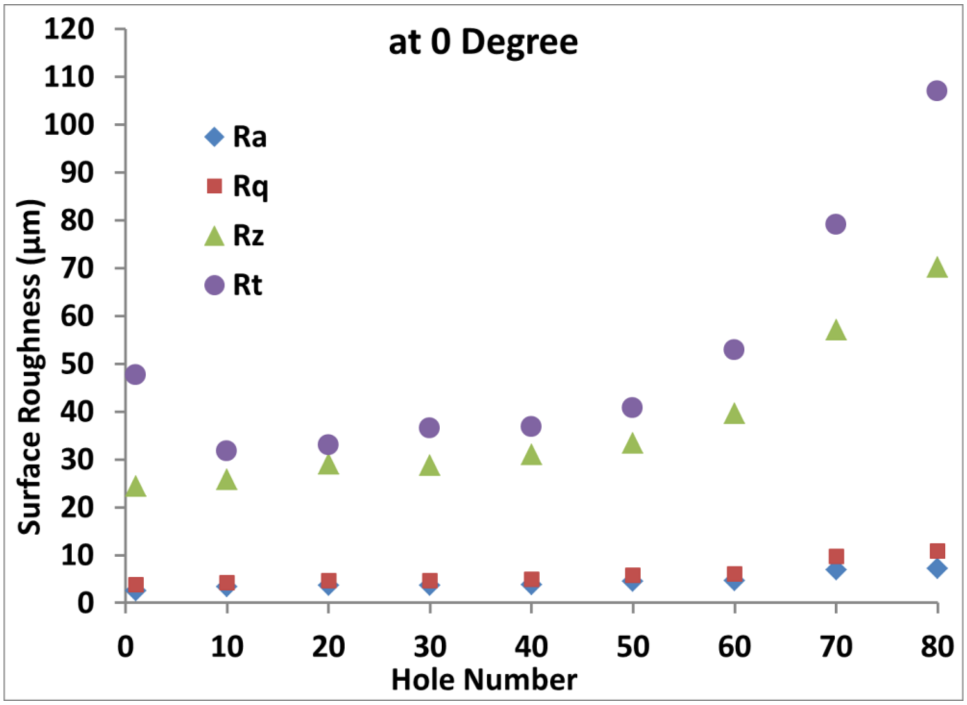

Figure 8.49. Surface roughness values at interaction angle of 0^0 for drilling condition I

Unlike the values of surface roughness describing parameters measured at the location where the interaction angle between the cutting direction and fiber orientation is 0^0, the values measured at locations where the interaction angle is -45^0 decreased when the number of drilled holes increases. Figure 8.50 shows surface roughness values measured at a location where the interaction angle between the cutting direction and fiber orientation is -45^0 for drilling condition I, whereas, surface roughness values for all drilling conditions measured at this location are plotted and given in Appendix W. The cutting mechanism at this interaction angle takes place by shearing of the fibers and as the cutting edge of the drill tool worn out the cutting action is more of crashing of the fibers and a rougher surface is expected as the tool wear increases. Even though, the values of the surface roughness parameters decreased as the amount of drill wear increases it not an indication of a good surface quality of the hole, rather the roughness of the surface and fiber pullouts are covered by melted matrix smeared over the surface of the hole. As the cutting edge of the drill tool worn out, the cutting action is more of extrusion and rubbing than cutting, which leads to excessive heat generation due to high friction and brute force applied by the worn drill tool causing melting of the matrix material, which smeared and filled the rougher surfaces of the hole. From this, it is clear that surface roughness alone cannot be used as a tool to characterize hole quality when drilling CFRP composite materials.

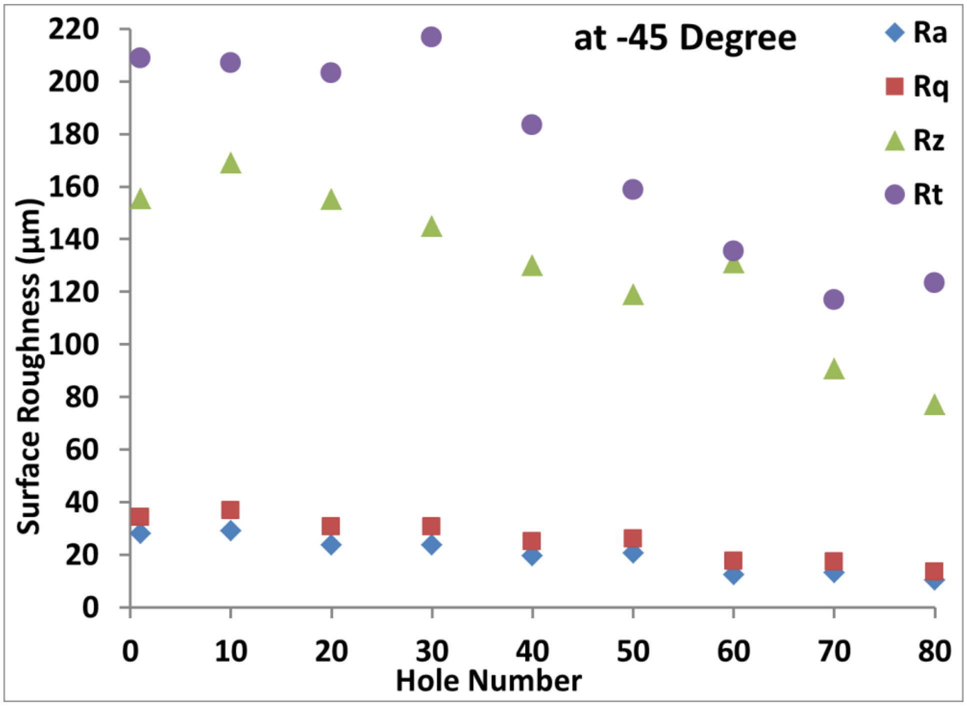

Figure 8.50. Surface roughness values at interaction angle of -45^0 for drilling condition I

8.4.2. Tool Wear and Hole Circularity

To characterize the influence of drill tool wear on the resulting circularity of the drilled hole, circularity measurements at the drill entrance was conducted for the holes drilled for tool wear experiment discussed in section 8.2.4. The combinations of drilling conditions used for this part of the investigation are given in Table 8.8. The circularity of the holes at the drill entrance was measured using Toolmakers microscope for drilling conditions II, III, and IV. Figure 8.51 shows an optical representation of runoff points of circularity error for hole number one and eighty from drilling condition II, whereas, these optical representation for all holes and drilling conditions are given in Appendix X.

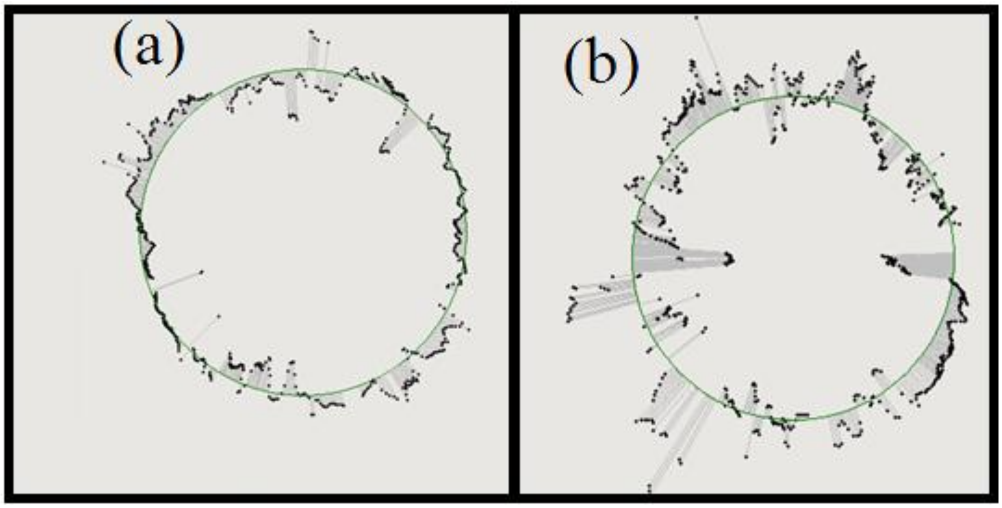

Figure 8.51. Optical representation of runoff points of circularity error for 1st hole (a) and 80th hole (b) from drilling condition II

Figure 8.52 shows the relationship between circularity error and number of drilled holes for the three drilling conditions considered here. As it can be seen from the figure, the errors on the circularity of the hole at drill entrance increased when the number of drilled holes and tool wear increases. The minimum circularity error of 0.0991 mm was measured from the 1st hole drilled at drilling condition II, whereas, the maximum circularity error of 0.3281 mm was measured from the 1st hole drilled at drilling condition II. The minimum circularity error was measured from the first hole for all drilling conditions and the maximum circularity error was measured from the 70th hole for drilling conditions II and IV and from 80th hole for drilling condition III.

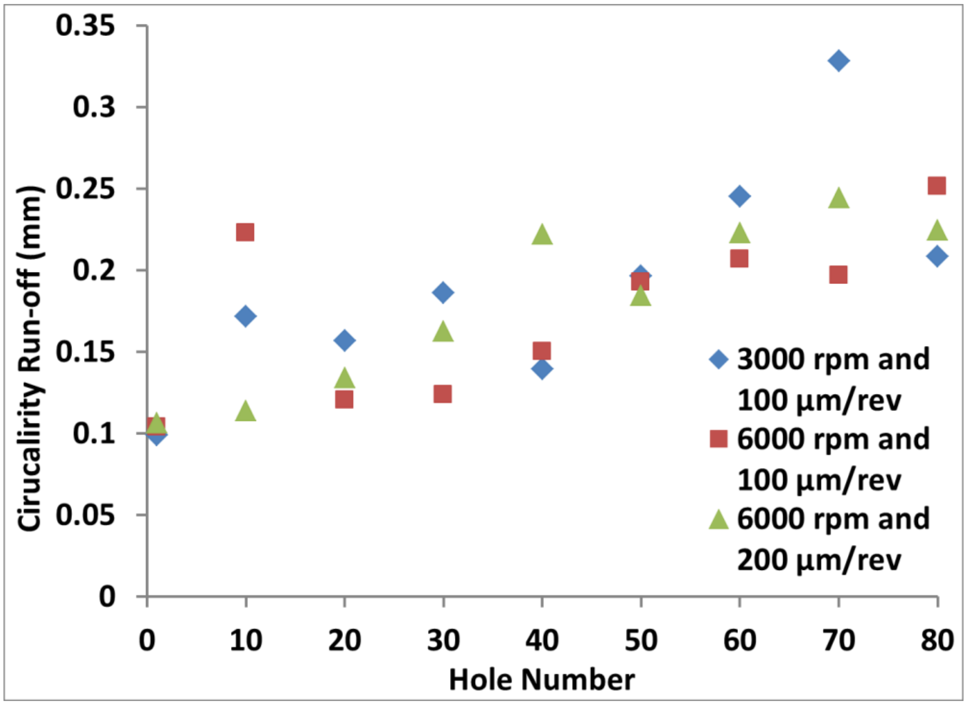

Figure 8.52. Relationship between circularity error and number of drilled holes

8.4.3. Tool Wear and Diameter Variation

Variation in the diameter of drilled holes is one of the geometrical errors caused by the condition of the drill when drilling CFRP composite materials. Diameter measurement at the entrance of the drill tool was taken using Toolmakers microscope from the holes drilled for the tool wear experiment discussed in section 8.2.4 where the combinations of drilling conditions used for this part of the investigation are given in Table 8.8. The variation on the diameter of the hole at the drill entrance for the number of drilled hole is shown in Figure 8.53. As it can be seen in the figure, after the first hole the diameter of the hole at the drill entrance decreases as the numbers of drilled holes increased for all conditions except the 50th and 60th hole drilled at 3000 rpm and 100 µm/rev. The largest variation in diameter was measured at the 80th hole drilled at 6000 rpm and 200 µm/rev, where the diameter decreased from its nominal diameter of 6.35 mm to 6.2059 mm. When the cutting edge of the drill loses its sharpness and worn out, it extrude and pressed away some fibers instead of cutting and as the drill tool extracted the pressed down fibers spring back causing hole shrinkage.

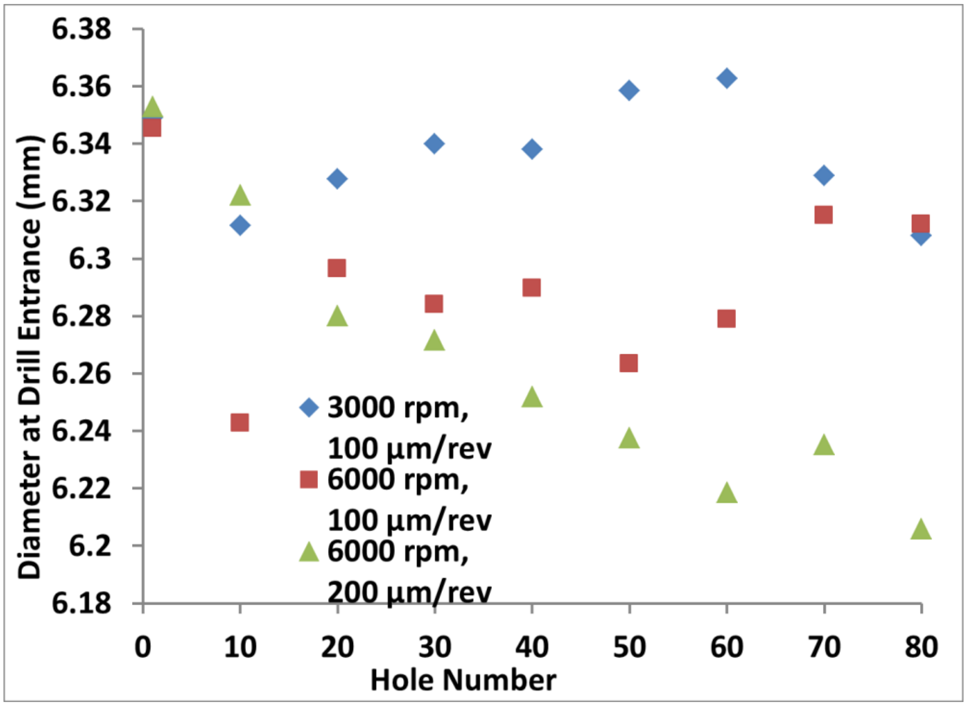

Figure 8.53. Variation on diameter of the hole at the drill entrance for the number of drilled hole

8.4.4. Tool Wear and Delamination

As it have been discussed in the previous chapters, delamination is the most severe process induced damage/defect and exit ply delamination is the most common mode of delamination when drilling CFRP composite materials. The condition of the drill tool is one of the controlling factors that causes exit ply delamination by contributing to the increase of drilling forces as the cutting edge of the drill tool worn out. Two sets of experiments conducted on a 19.05 mm thick uni-directional CFRP composite laminate composed of 99 plies with an average ply thickness of 192 µm using a HSS drill tool were considered to investigate the effect of tool wear on the location of exit ply delamination. The locations of exit ply delamination were measured using KrautKramer USN60 ultrasonic flow detector.

In the first set of the experiment, six holes were drilled on the CFRP laminate at cutting speed of 6000 rpm and feed rate of 100 µm/rev using a 12.7 mm HSS drill tool. Flank wear measurements were taken for every two holes drilled, whereas, location of exit ply delamination from the drill exit side was measured for all six holes and measured values of flank wear, delamination location from the exit side, and the numbers of delaminated are given in Table 8.19. The relationship between delamination distance from the bottom the plate and measured flank wear is shown in Figure 8.54. The location where delamination occurred measured from the bottom of the plate and the numbers of plies delaminated increased when the flank wear increases as expected, since the higher the tool wear the higher the thrust force resulting more plies to delaminated. As it is discussed in chapter 7, the numbers of plies delaminated at the exit is mainly influenced by the magnitude of thrust force and it is seen in chapter 8 that the magnitude of the thrust force increases when the amount of tool wear increased.

Table 8.19. Values of flank wear, delamination location, and the numbers of delaminated

Hole Number	Flank Wear (mm)	Delamination Location from Exit Side (mm)	Numbers of Plies Delaminated
1	----	3.25	17
2	0.997	4.00	21
3	----	3.50	18
4	1.337	5.00	26
5	----	5.50	29
6	1.607	6.50	34

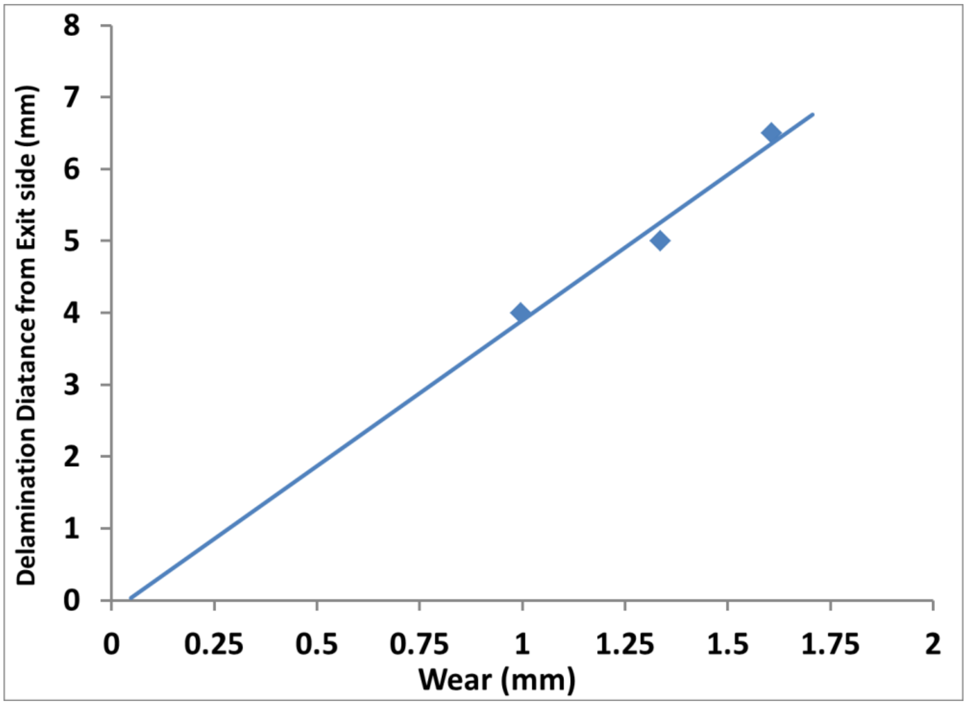

Figure 8.54. Effects of tool wear on delamination location (distance)

The second set of the experiment conducted on the CFRP laminate at cutting speed of 6000 rpm and feed rate of 200 μm/rev using a 6.35 mm HSS drill tool and eight holes were drilled on the work piece. Flank wear measurements were taken for every two holes drilled, whereas, location of exit ply delamination from the drill exit side was measured for each holes except for the 3rd hole and measured values of flank wear, delamination location from the exit side, and the numbers of delaminated are given in Table 8.20.

Table 8.20. Values of flank wear, delamination location, and the numbers of delaminated

Hole Number	Flank Wear (mm)	Delamination Location from Exit Side (mm)	Numbers of Plies Delaminated
1	----	1.38	7.15
2	0.617	2.50	12.99
3	----	----	----
4	0.713	3.25	16.89
5	----	3.50	18.19
6	0.861	3.75	19.49
7	----	4.00	20.79
8	1.048	4.00	20.79

Figure 8.55 shows the relationship between delamination distance from the bottom the plate and measured flank wear. As it seen in first set of experiment above, the location where delamination occurred measured from the bottom of the plate and the numbers of plies delaminated increased when the flank wear increases. These observations display how tool wear highly affects the quality of hole produced in many aspects when drilling CFRP composite laminates. The quality of the hole produced when drilling CFRP composites can be influenced in many factors such as speed, feed rate, and tool geometry in which all influences the hole quality by controlling the resulting drilling forces and heat generation during the drilling process. Even though optimization of these factors is possible to minimize the resulting drilling forces and heat generation, without appropriate tool wear monitoring method, controlling the quality of drilled hole is not possible.

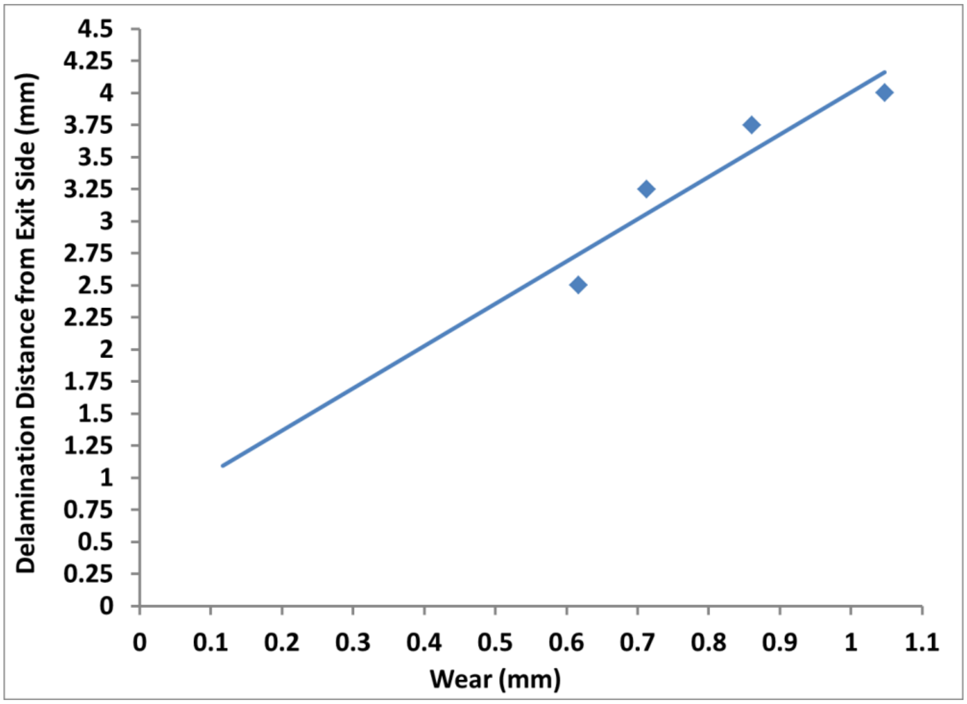

Figure 8.55. Effects of tool wear on delamination location (distance)

8.5. Conclusion

An experimental investigation on online detection and monitoring of tool wear when drilling CFRP composite laminates was conducted utilizing different signal acquisition systems and signal analysis tools. Two new (novel) approaches namely, using the signal amplitude and using output variables from recurrence quantification analysis (RQA) were proposed and studied in this investigation. Thrust force, vibration, acoustic emission, and audio microphone signals were acquired and the variation on the signals signature were studied and correlated to the progression of the drill flank wear. Drill tool flank wear measurements were taken when drilling uni-directional and multi-directional CFRP composite laminates having various thicknesses using HSS and carbide drill tool. Based on the observation made from the results of this investigation the following concluding remarks have been made.

1. The amplitude of thrust force increased when the amount of flank wear increased, and using the thrust force amplitude as an input parameter flank wear was estimated with an average error of 5.7 % and 0.5 % when drilling multi-directional CFRP using HSS drill and uni-directional CFRP using carbide drill respectively.
2. The amplitude of the audio microphone signal decreased when the amount of flank wear increases. Using the amplitude of the audio microphone amplitude as input parameter flank wear was estimated with an average error of 7.8 %, 2 %, and 16 % when drilling multi-directional CFRP using HSS drill, uni-directional CFRP using HSS drill, and uni-directional CFRP using carbide drill respectively.
3. The amplitudes of vibration and acoustic emission signals found to be path dependent and were not used in estimating flank wear except in one case where the location of the acoustic emission sensor was changed for each hole in order to keep a constant path when

drilling uni-directional CFRP using carbide drill. In this particular case, the amount of flank wear was estimated using the acoustic emission signal amplitude with a maximum error of 32 % for the tenth and twentieth hole and 16 % for holes from thirty to eighty.

4. An air-coupled audio microphone was proven to detect the variations in acoustic signature when the condition of the cutting edge of the drill too changes during drilling CFRP composite laminates.
5. Six out of eight of the output variables from the RQA increases with the increase of the drill flank wear, whereas, two of the output variables decrease with the increase of the drill flank wear in both cases of drilling conditions.
6. The output variables from the RQA analysis show similar behavior in both drilling conditions with different level of flank wear progression and the influence of flank wear progression on the output variables of the RQA analysis clearly observed.
7. Over all, the capability of the two proposed approaches in this investigations for online detection and monitoring of the condition of the drill tool when drilling CFRP composite laminate have been demonstrated.
8. An air-coupled audio microphone signal was competent in drill wear monitoring in both proposed approaches.
9. Effect of tool wear on the quality of holes produced was investigated and hole circularity error at the drill entrance and the numbers of plies delaminated at the drill exit increased when tool wear increases, whereas, diameter of the hole at the drill entrance decreased when tool wear increases.
10. It was found that surface roughness value could not be used to characterize the quality of holes when drilling CFRP composite laminates.

CHAPTER 9: ONLINE DETECTION AND ESTIMATION OF GAPS WHEN DRILLING CFRP COMPOSITE STACKS

9.1. Introduction

Drilling is the most frequently executed operation in order to utilize holes for joining composite parts each other or with other material systems in the assembling process. Joining of parts after drilling of each part separately is one of the common practices, but this practice is time consuming and labor intensive. Another practice is one – step drilling, where the parts to be joined will be clamped together and drilled together at one-step. In the latter case, poor clamping and chips in the form of dust during the drilling operations create a gap between the two parts and if the operator does not observe this gap, it becomes a big threat for the strength and integrity of the structural component. In this chapter, experimental investigation conducted to develop on-line gap detection and estimation method when drilling composites stacks using multiple sensors will be presented.

In attempt to avoid the uncertainty of the presence of gaps between stacks and to eliminate the inspection for gaps after every drilled hole, a novel approach for on-line gap detection and estimation when drilling CFRP composite stacks through various signal profiles was proposed. Experimental investigation of the proposed method was carried out on quasi-isotropic- quasi CFRP composite stacks. Thrust force, vibration, acoustic emission, and audio microphone signals, were acquired during the experiment. A pre-determined gap was introduced between the stacks of CFRP plates in the investigation. The results from this experimental study reveal the potentials of the proposed approach for on-line gap detection and estimation when drilling CFRP composite stacks.

9.2. Experimental Setup and Procedures

For this part of the investigation, drilling experiments were conducted on two quasi-isotropic CFRP stacks with pre-determined gaps. Two quasi-isotropic CFRP laminates each composed of 10 plies having a thickness of 2 mm with an average ply thickness of 200 µm and is made up of symmetrical stacking sequence of $[0,45,90,-45,0]_s$ clamped each other as a tack were used for this part of the investigation. Test coupons were cut to a size of 77 by 102 mm using an abrasive water jet. A two – side adhesive tape having a thickness of 0.5 mm and a width of 20 mm is used to create a predetermined gap between the two CFRP plates. Three different conditions; only air (without adhesive tape) between the two plates, 0.5 mm tape between the two plates, and 1 mm tape between the two plates were used in this investigation. In addition to the drilling force measurements, vibration signal, an audio microphone signal, and acoustic emission signals were acquired during the drilling operation and details of these signal acquisition systems are given in chapter four. 6.35 mm diameter standard carbide twist drill and four combinations of cutting conditions were used for the drilling of these CFRP stacks. The combinations of cutting conditions are listed in Table 9.1. A schematic representation of the experimental setup and sensor placement is shown in Figure 9.1, whereas; Figure 9.2 shows the sectional view and detailed view of the setup assembly.

Table 9.1. Combinations of cutting parameters

Drilling condition	1	2	3	4
Cutting Speed (rpm)	3000	3000	6000	6000
Feed Rate (µm/rev)	200	100	100	200

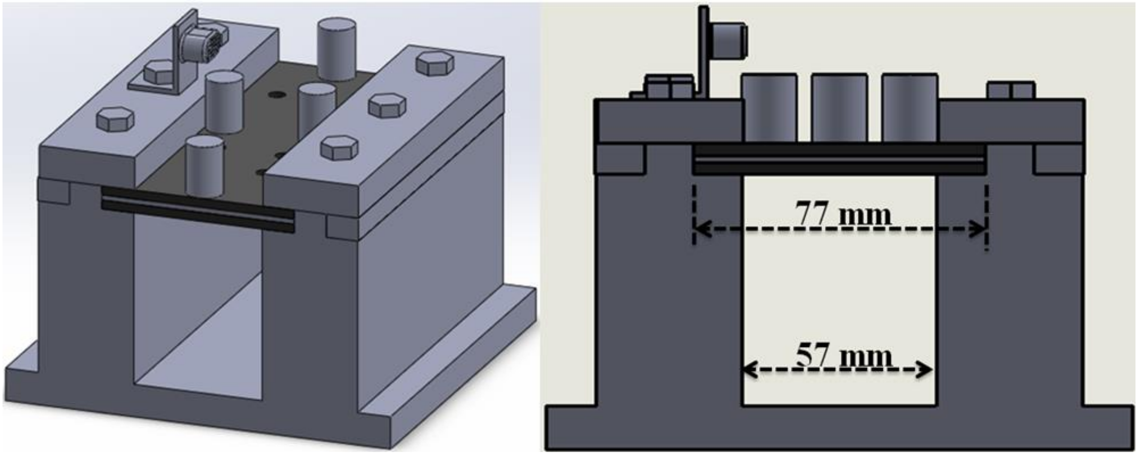

Figure 9.1. Schematic representation of experimental setup and sensor placement

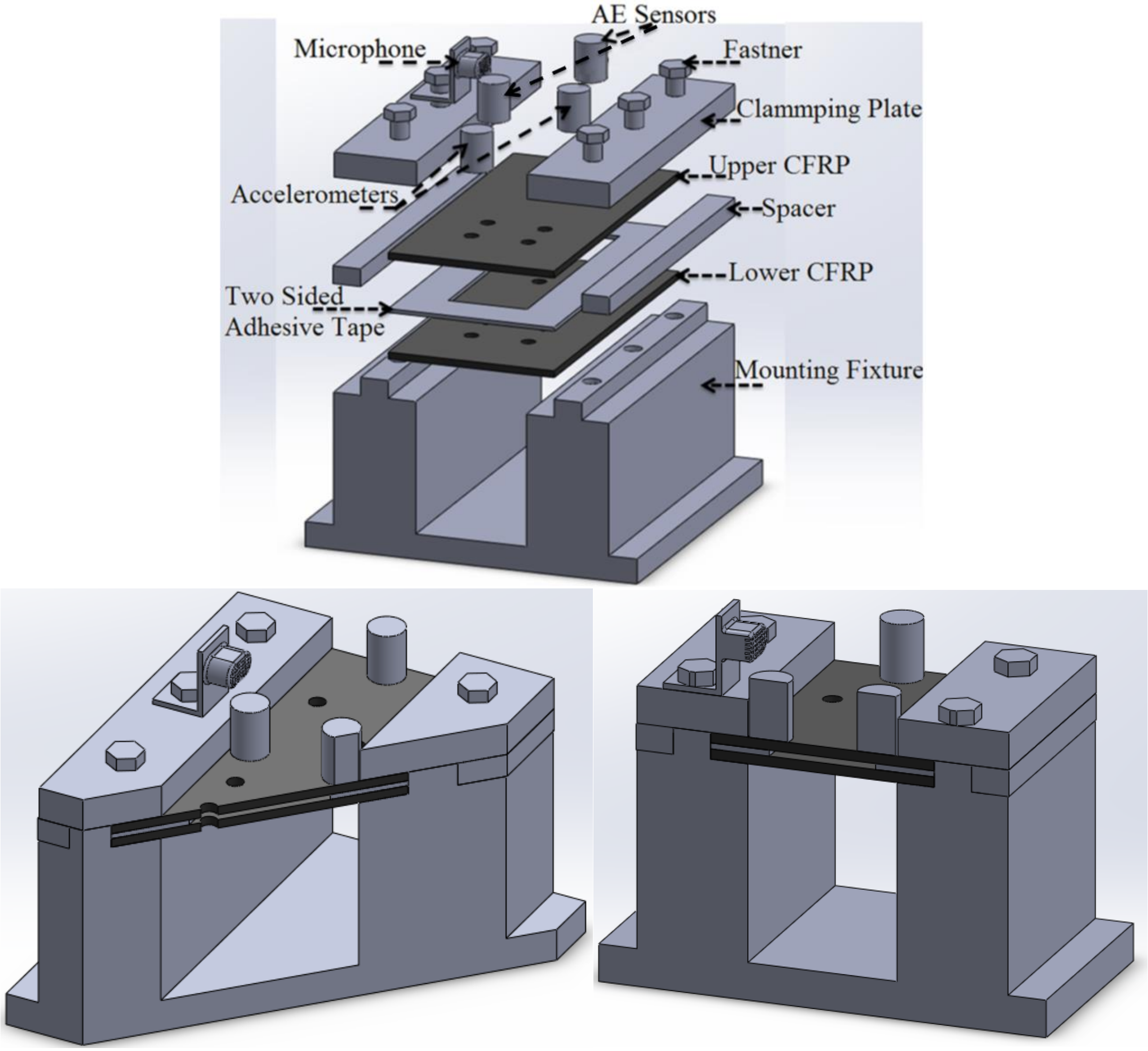

Figure 9.2. Sectional and detailed view of experimental setup assembly

9.3. Result and Discussion

After the experimental drilling operations have been carried out, each acquired signals were converted into the appropriate format for plotting and further processing. The raw signal profiles from the four signal acquisition systems were plotted to make a visual observation of the signals and to plan the next step of signal processing. Figure 9.3 shows representative plots of the raw signal profiles of the four different signals acquired in this investigation. A decrease in the value of amplitude is seen in all raw signal profiles approximately at the middle of the drilling process. In which this deceasing trend (behavior) of the amplitude could be ascribed by the transition point of the drill tip from the top CFRP plate to the lower CFRP plate through the existing gap created by the introduction of the adhesive tape around the edge between the two CFRP plates.

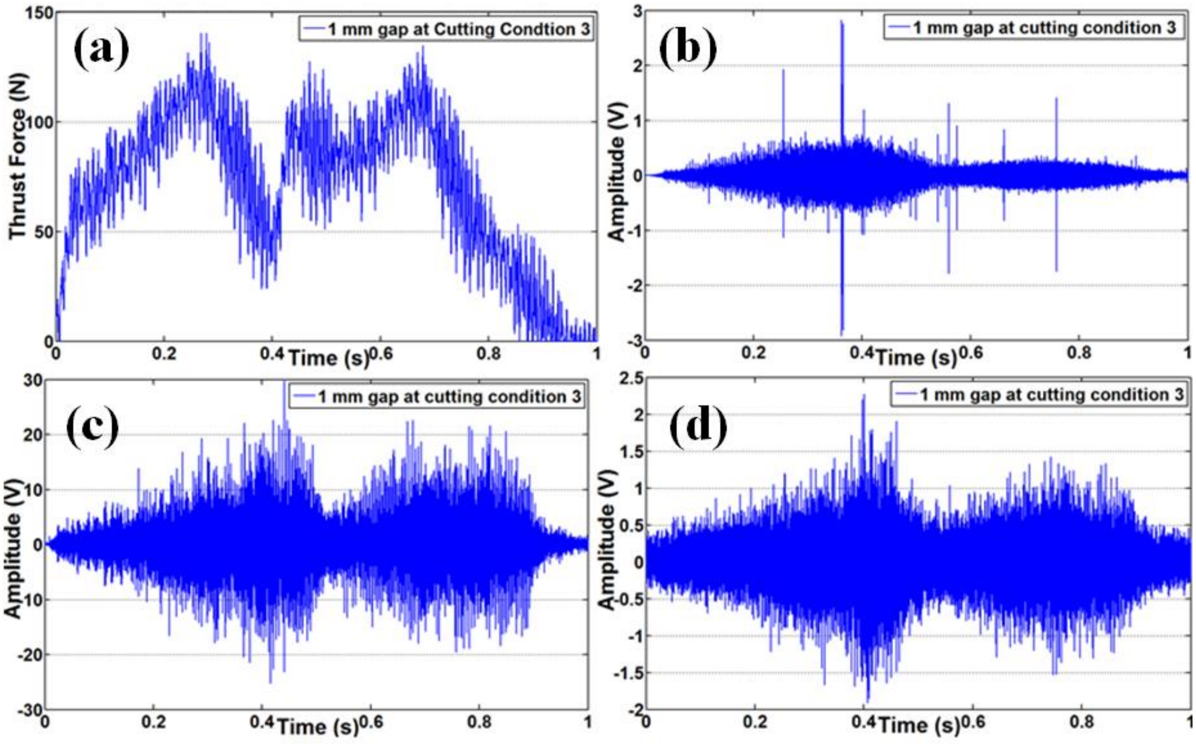

Figure 9.3. Raw signal profiles for (a) Thrust force, (b) Acoustic emission, (c) Accelerometer, and (d) Microphone signals

9.3.1. Detection using Thrust Force Signals

Raw signal profiles of the thrust force in Figure 9.3 (a) reveals that there is a valley in the amplitude profile when the drill tip passes from the upper plate to lower plate. In order to relate this to the amount of the existing gap, the raw signal was filtered through a low-pass filter. Figure 9.4 shows a filtered profile of the thrust force for the cutting condition three where 1 mm gap is introduced between the two CFRP plates. From this plot, two points Xa and Xb were selected which indicate two major locations of the drill tip during the drilling action. The first point Xa is the point where the drill tip exits the last ply on the upper plate and the second point Xb is the point where the drill tip makes contact with the first or the top ply of the lower plate. The reasoning behind the selection of point Xa is that, after attaining the maximum value, the thrust force start decreasing when the drill tip approaches to the last ply, and upon penetrating of the last ply, there is a bump on the thrust force profile. The thrust force keep decreasing during the exit of the drill and goes to zero unless the drill encounters a resistance from a new surface, in this case, the thrust force start increasing again at point Xb, which is the indication of that the drill tip reaches the top ply of the second plate and start drilling the lower plate.

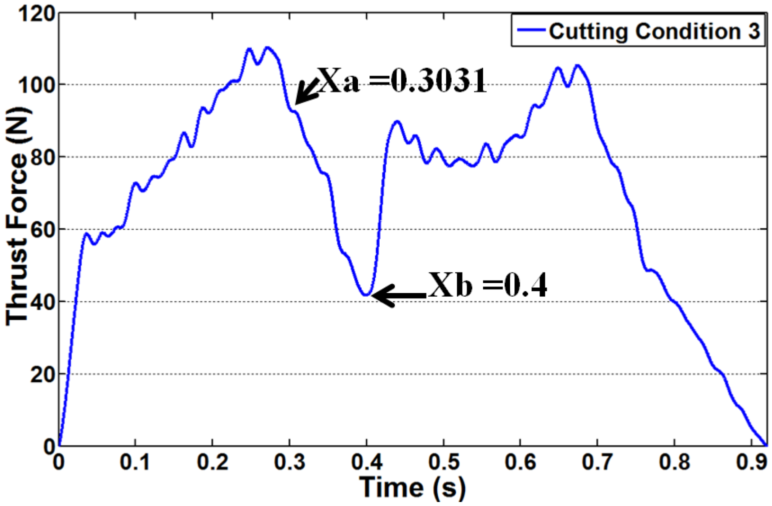

Figure 9.4. Smoothened thrust force profile and selection of points

Once these two points, which identify the position of the drill tip have been identified, it is possible to calculate the distance between these two point which is also the distance between the last (bottom) ply of the top plate and the first (top) ply of the lower plate by getting their time mark. How fast the drill tip travels downward can be calculated from the cutting speed and feed rate, then by multiplying the down ward vertical speed of the drill tip with the time difference between the two points Xa and Xb, it is possible to get the distance between the two points, which is also the gap between the two plates. For the case shown in Figure 9.4, the drilling conditions used are 6000 rpm and 100 µm/rev with a pre-existing gap of 1 mm, and the prediction of the gap between the two plates is given below as an example.

Down ward travel speed of drill tip = feed rate * cutting speed

= 6000 rev/min*100 µm/rev =100 rev/s *0.1 mm/rev

=10 mm/s

Time difference between the two points = T (Xb) – T (Xa) = 0.4 s – 0.3031 s

= 0.0969 s

Gap between the two plates = travel speed * time difference

= 10 mm/s * 0.969 s

= **<u>0.97 mm</u>**

This gives a prediction of 97 % with 0.03 mm error.

9.3.1.1. When 1 mm Gap between the Stacks

Using the procedure discussed above, the trust force signals for the case when there is 1 mm preexisting gap were filtered and the two points of drill tip locations were identified. Figure 9.5 shows the filtered thrust force signals with the locations of the two points for the 1 mm pre-existing gap. The method of detection of gaps when drilling quasi-isotropic CFRP stacks using thrust force profile shows a promising result by predicting the preexisting gap with an average error of 3%. In order to see whether this new method of gap detection using thrust force profile works with different combinations of drilling conditions or not, the prediction of the preexisting 1 mm gap was calculated for four different combinations of drilling conditions and the maximum error of estimating the preexisting gap between the stacks using this method was 4%. The estimated values for the preexisting 1 mm gap for different combination of drilling conditions are given in Table 9.2.

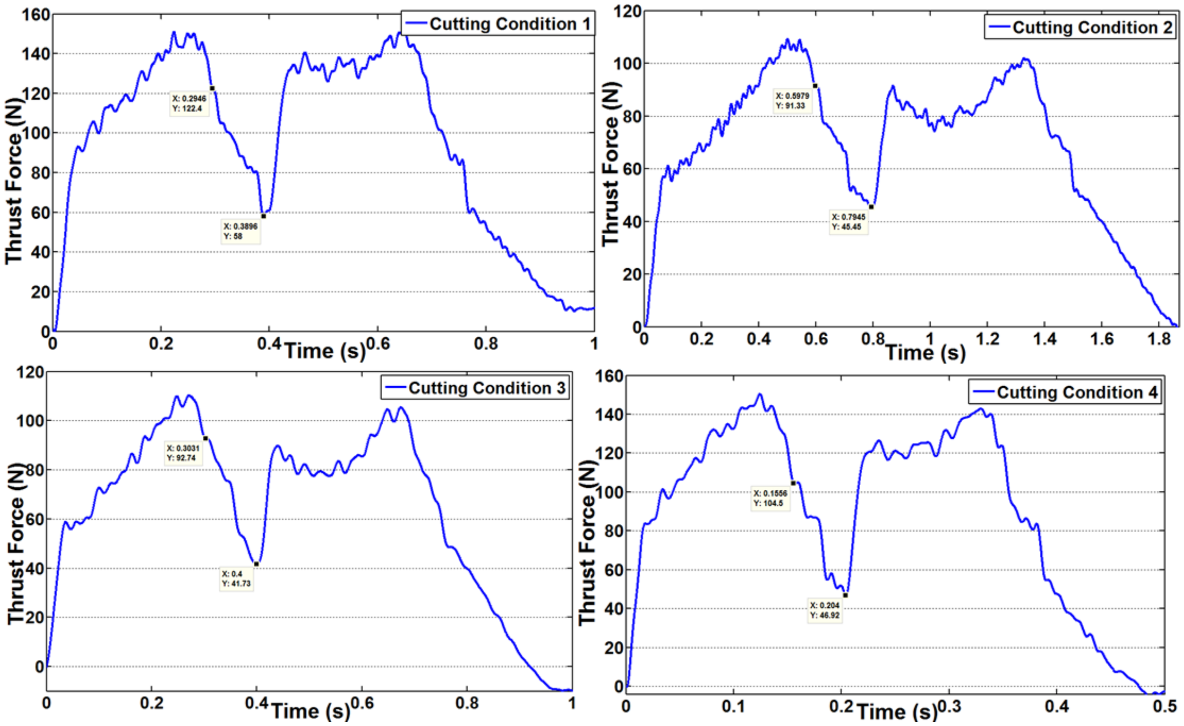

Figure 9.5. Thrust force profiles for 1 mm preexisting gap for different cutting conditions

Table 9.2. Predicted values for the preexisting 1 mm gap for different drilling conditions

Run Order	Cutting Speed (rpm)	Feed Rate (μm/rev)	Preexisting Gap (mm)	Predicted Gap (mm)	Error (%)
1	3000	200	1	0.95	-3
2	3000	100	1	0.98	-2
3	6000	100	1	0.97	-3
4	6000	200	1	0.96	-4

9.3.1.2. When 0.5 mm Gap between the Stacks

For the case of 0.5 mm gap, a single layer of the adhesive tape was used around the edge between the two CFRP plates to introduce the preexisting gap. The procedure used in locating the position of the drill tip and method of estimating the amount of gap between the stacks are the same as of the 1 mm preexisting gap. In this part of the investigation, the thrust force signal for the fourth cutting condition was not acquired properly due to the late starting of the acquisition system. Figure 9.6 shows filtered thrust force signal profiles with the location of the two points for the 0.5 mm preexisting gap. From the filtered signals and the locations of the drill tip, the gap between the two CFRP plates was estimated and the estimation results are given in Table 9.3. The maximum error in estimating the gap was found to be 4.17 % lower than the known preexisting gap during cutting condition two, whereas, in the case of cutting condition three, 100 % estimation was achieved. Over the three drilling conditions, the average estimating error found in estimating the preexisting gap was 2.07 %.

Table 9.3. Predicted values for the preexisting 0.5 mm gap for different drilling conditions

Run Order	Cutting Speed (rpm)	Feed Rate (μm/rev)	Preexisting Gap (mm)	Predicted Gap (mm)	Error (%)
1	3000	200	0.5	0.49	-2.04
2	3000	100	0.5	0.48	-4.17
3	6000	100	0.5	0.5	0.00

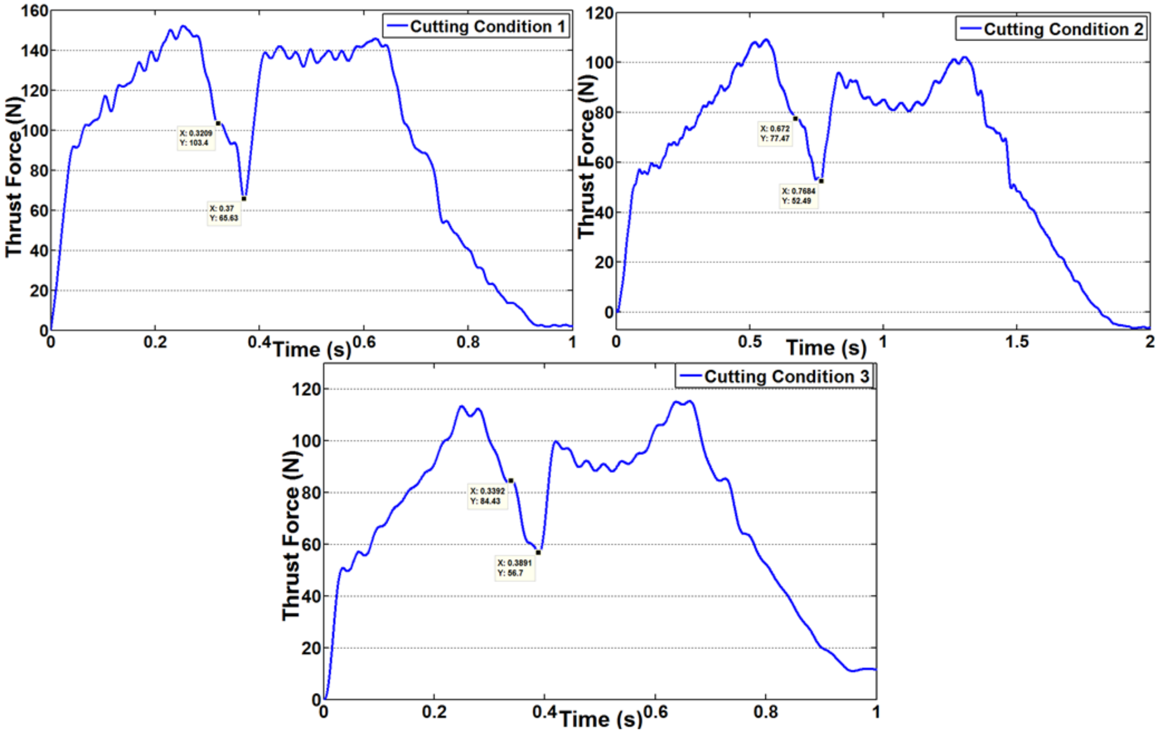

Figure 9.6. Thrust force profiles for 0.5 mm preexisting gap for different cutting conditions

9.3.1.3. Only Air Gap between the Stacks

The third experimental investigation was conducted without introducing any preexisting gap. The two CFRP plates were stacked (placed) one over the other; where the contact surface is consists of one tooling side and one bagging side. Figure 9.7 shows thrust force profiles of the four cutting conditions when drilling the two stacks without introducing a preexisting gap. The thrust force profile shows a sharp valley around the middle instead of a continuous trend, which indicates the drill tip is passing the interaction of the two plates. Even though there is no preexisting gap, since the bag side of the CFRP plate is a rougher surface, there exists an air gap when the bag side of the top plate rests on the tool side of the bottom plate. The presence of this air gap between the two surfaces causes the sharp valley on the thrust force profile, which is also observed on the profiles of the other signals considered in this investigation. In order to determine the amount of this air gap created by the interaction of the bag side of the top plate and the tool side of the bottom plate, surface roughness measurement was done on both surfaces. Surface roughness describing parameter R_t, which is a measure of maximum peak to valley height of a profile was considered to estimate the air gap between the two surfaces and the values of roughness describing parameter R_t measured in longitudinal and transverse direction are given in Table 9.4. From the surface roughness measurement, the maximum possible air gap between the two surfaces can be approximated in the range of 103 – 133 µm.

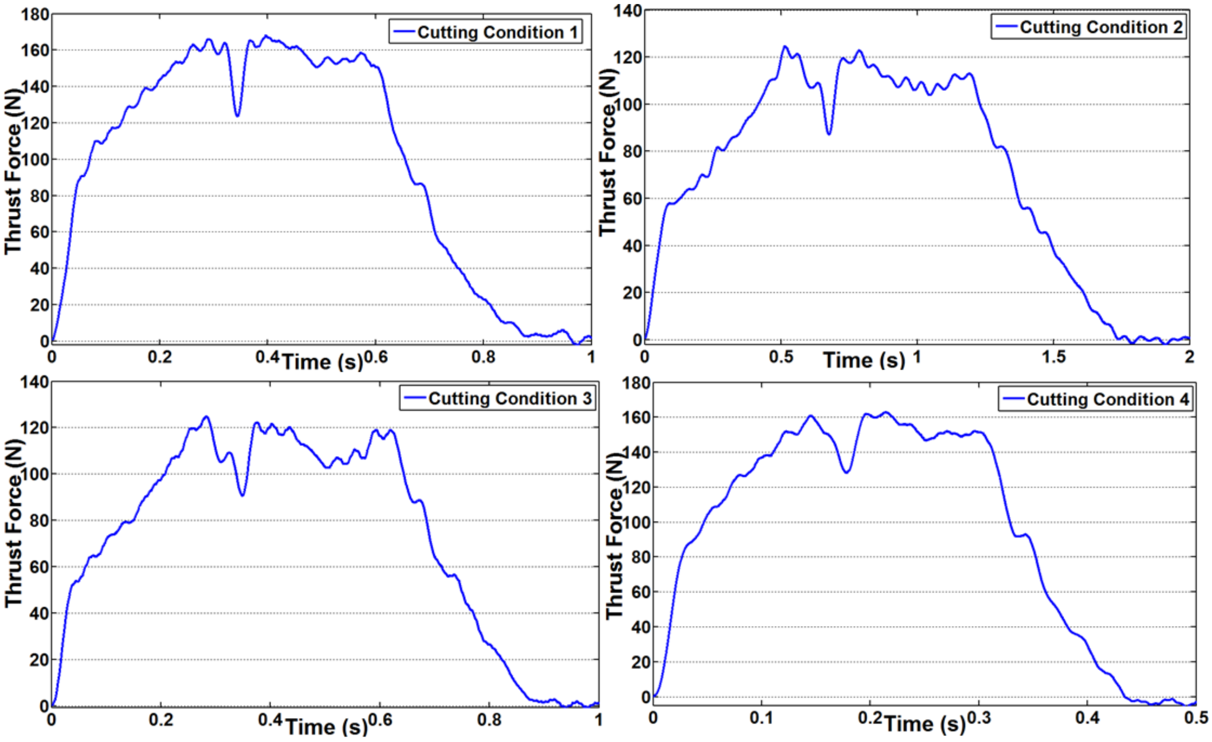

Figure 9.7. Thrust force profiles for no preexisting gap for different cutting conditions

Table 9.4. R_t Values of tool side and bag side surfaces

Measurement Direction	R_t Values (µm)	
	Tool Side	Bag Side
Longitudinal	7.2	95.9
transversal	6.6	126.7

Over all, the proposed method for online detection of gaps using the thrust force profile demonstrates its competence in detecting of gaps when drilling CFRP – CFRP stacks. The method shows its potential for predicting (estimating) the presence of a gap when drilling CFRP stacks by predicting the preexisting gap introduced between the stacks in this experimental investigation and the maximum error found in estimating the preexisting gaps was less than 5%.

9.3.2. Detection using Acoustic Emission Signals

The change in the amplitude trend seen on thrust force profile also has been observed on the raw acoustic emission signals when the drill progresses from the top plate to the bottom plate. As it is shown in Figure 9.3 (b), the amplitude of the AE signal decreases when the drilling is on the bottom plate than it was on the top plate. This is because the AE sensor is attached to the top plate, the propagation of the acoustic wave from the bottom plate travels through three mediums; bottom plate, air, and the top plate before it reaches the AE sensor, so the amplitude of the acoustic wave from the bottom plate it is expected to be smaller than the top plate. Even though this change of acoustic amplitude can be used as an indication for the existence of an air medium or a gap between the stacks being drilled, more analysis is needed in order to predict (estimate) the amount of gap exists between the two plates.

In order to identify the changes in acoustic signature, the raw signal was analyzed in two-step procedure. First, the absolute value of the raw AE signal was computed, then to eliminate the noise and to see the changes in the signal trend, the computed absolute value of the raw signal was filtered through a low-pass filter. Figure 9.8 shows t a representative plots for the absolute value of the raw signal and the corresponding filtered signal. The filtered signal profile in Figure 9.8 (b) shows similar profile signature as seen in the thrust force profile upon the drill exits the top plate and enters the bottom plate. The same hypothesis used to identify the location of the drill tip at the exit of the top plate and at the entrance of the bottom plate in the analysis of the thrust force profile was also used in the analysis of the acoustic emission profile. Applying the same method used in the previous section to the filtered AE signal, the two location of the drill tip are identified as shown in Figure 9.8 (b).

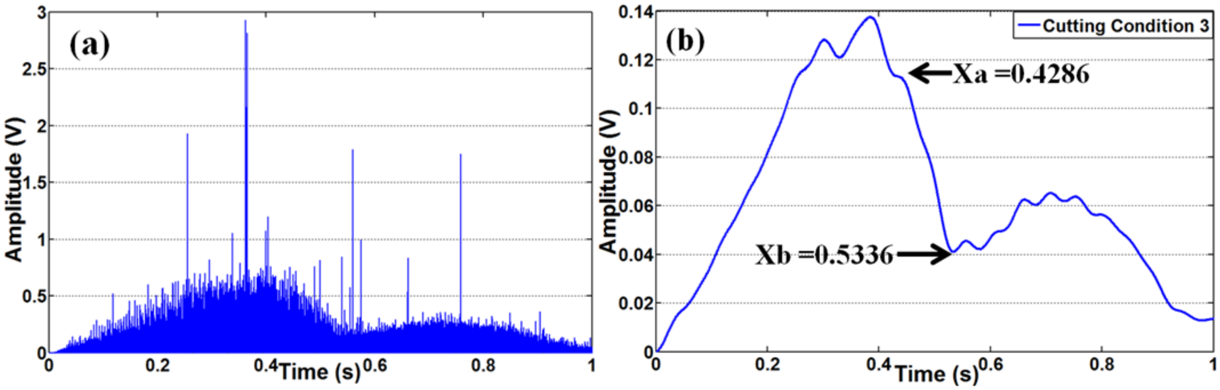

Figure 9.8. Typical acoustic emissions profiles of (a) absolute values and (b) filtered signal

9.3.2.1. When 1 mm Gap between the Stacks

The acoustic emission signals acquired when drilling CFRP stacks with a 1 mm preexisting gap were analyzed using the procedure discussed in previous section. The profiles of filtered acoustic emission signals for a preexisting gap of 1 mm for all drilling conditions are given in Figure 9.9. Based on the location of the drill tip when it exits the top plate and enters the bottom plate, the amount of gap between the stacks was estimated for all drilling conditions and the estimated values of the gap is given in Table 9.5. The maximum error found in estimating the preexisting gap using the acoustic emission signal was a 9.1 % over prediction at drilling condition four, whereas, the minimum error was a 4.2 % under prediction at cutting conditions one and two. For a preexisting gap of 1 mm, the average error in estimating the gap between the CFRP stacks using acoustic emission signal was 5.58 %.

Table 9.5. Predicted values for 1 mm preexisting gap for different drilling conditions

Run Order	Cutting Speed (rpm)	Feed Rate (μm/rev)	Preexisting Gap (mm)	Predicted Gap (mm)	Error (%)
1	3000	200	1	0.96	-4.2
2	3000	100	1	0.96	-4.2
3	6000	100	1	1.05	4.8
4	6000	200	1	1.10	9.1

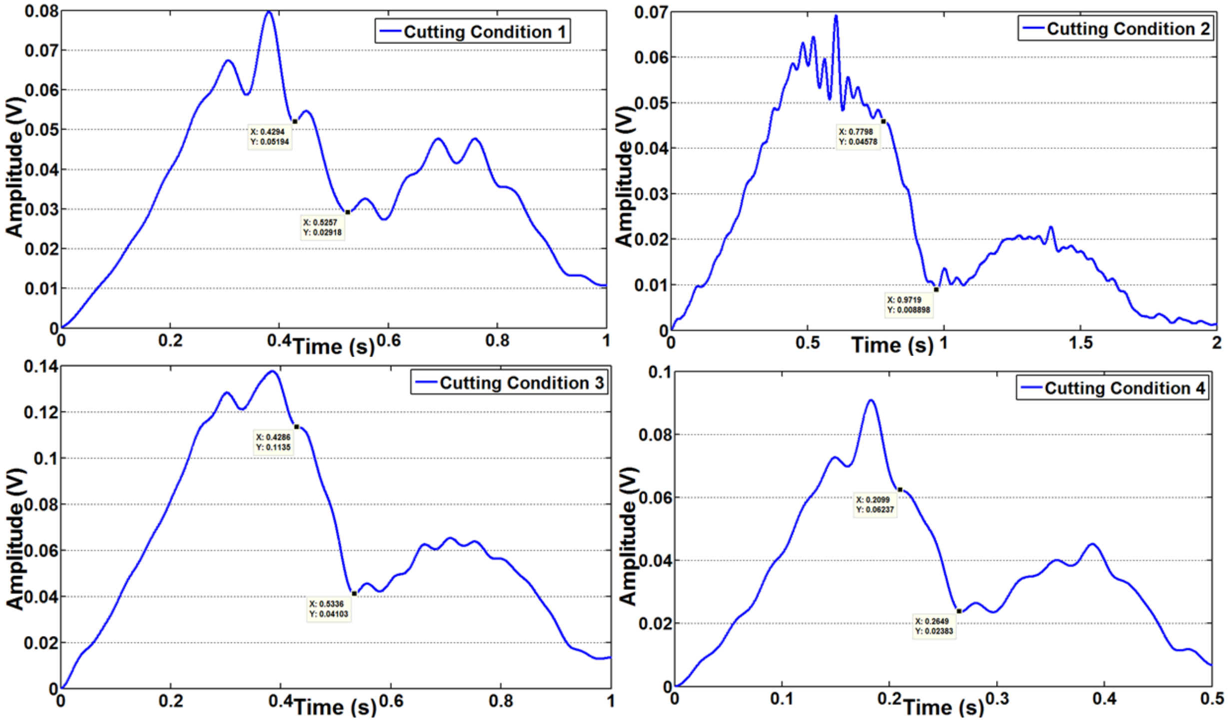

Figure 9.9. Acoustic emission profiles for 1 mm preexisting gap at various drilling conditions

9.3.2.2. When 0.5 mm Gap between the Stacks

An estimation of the gap for a preexisting gap of 0.5 mm was investigated through the same technique used in the case of 1 mm preexisting gap. The profiles for the acoustic emission signals for 0.5 mm preexisting gap at different drilling conditions are shown in Figure 9.10. From the filtered acoustic emission signal, an estimation of the amount of gap present between the two plates was performed and the values of the estimation are given in Table 9.6. The accuracy of estimating the gap between the two plates with a preexisting gap of 0.5 mm was found to be lower than the estimation accuracy found in the case of 1 mm preexisting gap. The maximum error in estimating the gap between the two plates was found to be 24.24 % during drilling condition two, whereas, the lower error of estimation was 9.09 % during drilling condition of one. For preexisting gap of 0.5 mm, the estimation of gap using acoustic emission signal showed an average over estimation error of 16.62 %.

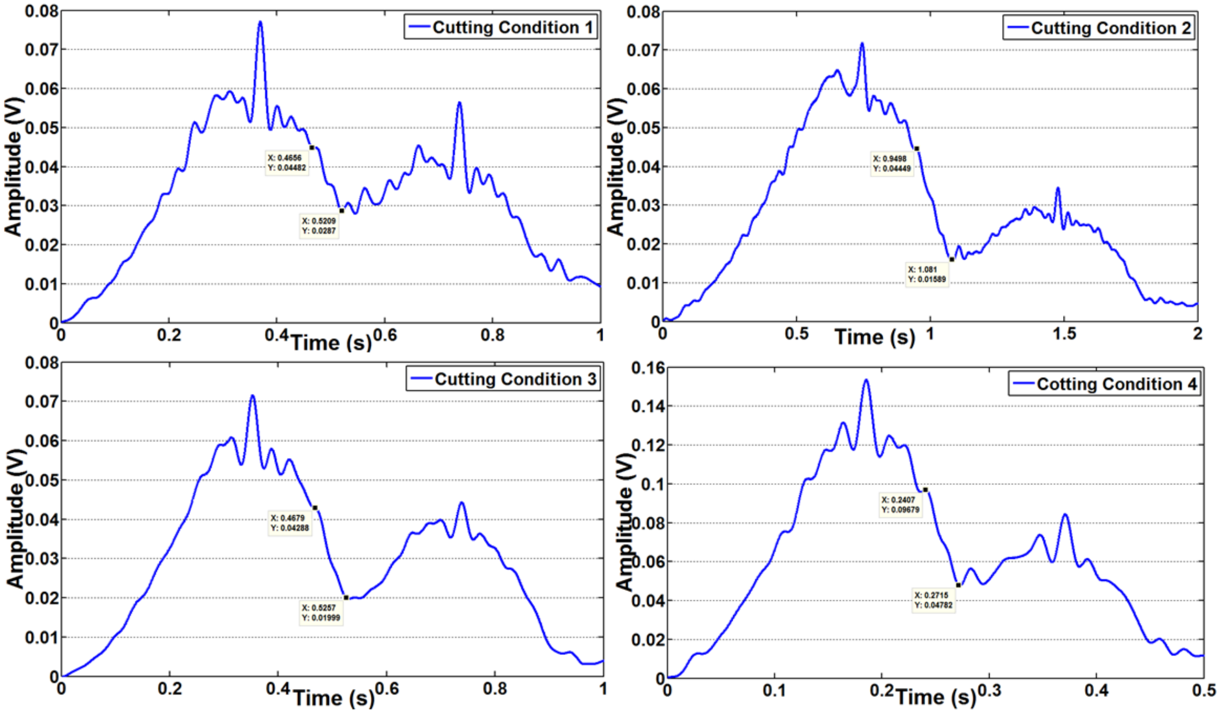

Figure 9.10. Acoustic emission profiles for 0.5 mm preexisting gap at various drilling conditions

Table 9.6. Predicted values for the preexisting 0.5 mm gap for different drilling conditions

Run Order	Cutting Speed (rpm)	Feed Rate (µm/rev)	Preexisting Gap (mm)	Predicted Gap (mm)	Error (%)
1	3000	200	0.5	0.55	9.09
2	3000	100	0.5	0.66	24.24
3	6000	100	0.5	0.58	13.79
4	6000	200	0.5	0.62	19.35

9.3.2.3. Only Air Gap between the Stacks

Figure 9.11 shows the profiles of acoustic emission signal at different drilling conditions when there is no preexisting gap introduced except the air gap created by the interaction of the bagging side and tooling side surfaces of the two plate. Even though there is a small valley in the profiles of the acoustic emission signals, the depth of the valley is very small compared to the depth of the valley observed in thrust force signals. There is no profoundly distinct point observed in order to identify the location of the drill tip at the exit of the top plate and the entrance of the bottom plate to make an estimation of the air gap exist between the two plates.

The proposed approach of online detection of gap using an acoustic emission signal when drilling CFRP composite stacks demonstrates promising results especially when the gap between the two composite stacks is greater than 0.5 mm. Even though the 16.62 % average estimation error found for estimating of the 0.5 mm preexisting gap looks large compared to the 5.8 % average estimation error found in estimating the 1 mm preexisting gap, it is an encouraging result which can be improved by modifying some of the signal analysis parameters and setup conditions.

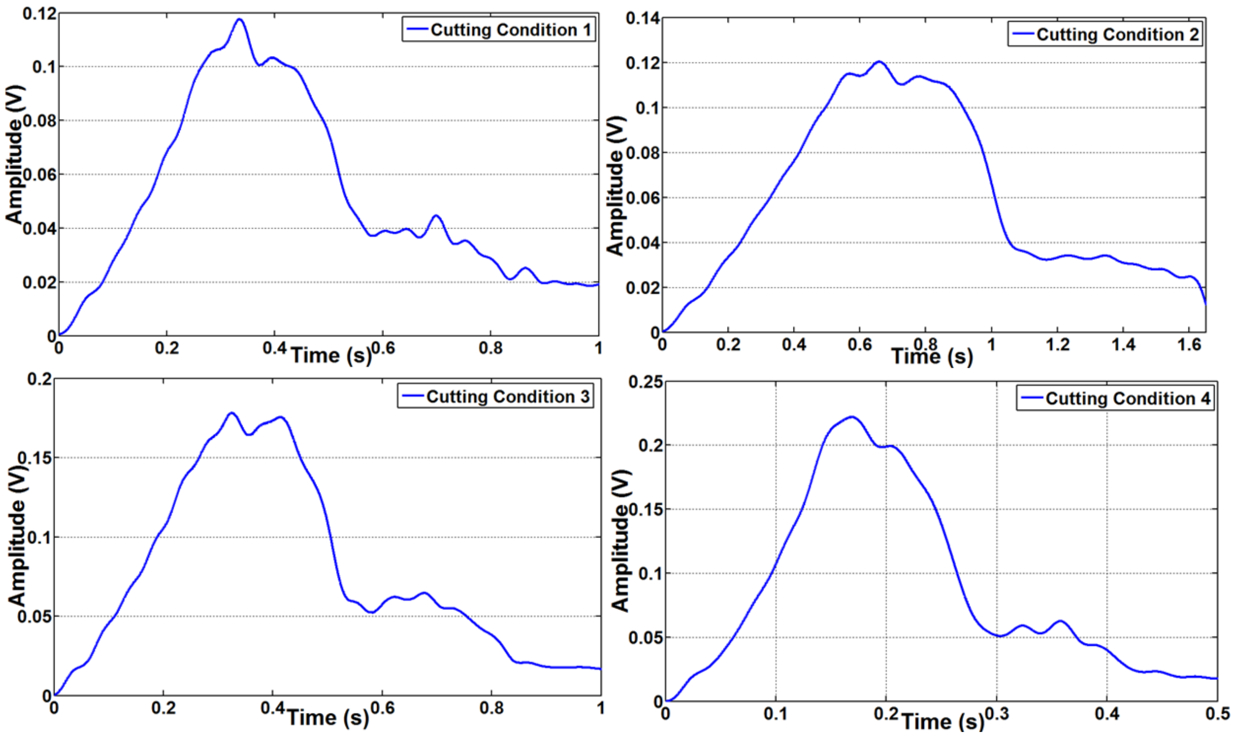

Figure 9.11. Acoustic emission profiles for no preexisting gap at various drilling conditions

9.3.3. Detection using Accelerometer (Vibration) Signals

The vibration signal acquired from the accelerometers displays a variation in amplitude where the drill point exits the top plate and enters the bottom plate like the thrust force and acoustic emission signal profiles, and this variation in amplitude can be seen in Figure 9.3 (c). The raw signal was processed by the same fashion used in the analyzing of the acoustic emission signal, first by computing the absolute value of the raw signal and then filtering through a low-pass filter to quantify the distance between the variations of the amplitude. Figure 9.12 shows repetitive plots for the absolute value of the raw signal and the corresponding filtered signal. The profile of the filtered vibration signal shows similar signatures seen in the acoustic emission signal when the drill exits the top plate and enters the bottom plate. The two points labeled as Xa and Xb on Figure 9.12 (b) are the point where the drill tip exits the top plate and enters the bottom plate respectively as used in the above two section of thrust force and acoustic emission signal analysis. Using these two locations of the drill tip, an estimation of the gap between the two plates for three different preexisting gaps of 1 mm, 0.5 mm, and only air gap between the two plates were made.

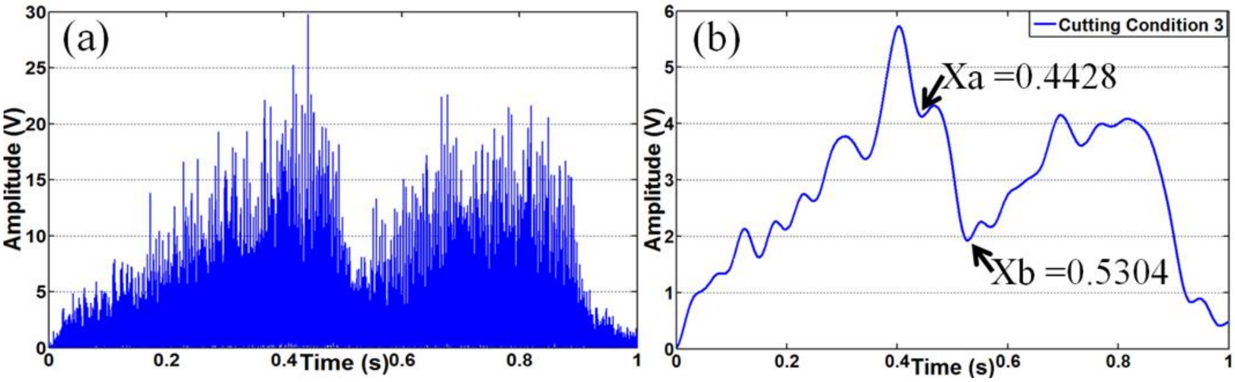

Figure 9.12. Typical vibration signal profiles of (a) absolute values and (b) filtered signal

9.3.3.1. When 1 mm Gap between the Stacks

The vibration signals acquired from the accelerometer when drilling the CFRP stacks with a 1 mm preexisting gap were processed in the same as of the acoustic emission signals and the profiles of the filtered vibration signal at different drilling conditions are shown in Figure 9.13. From the identified locations of the drill tip, an estimation of the gap between the two CFRP composite plates was made for all four drilling conditions. The most accurate estimation was found during drilling condition one with a 1.01 % under estimation, whereas, the largest error in estimating the gap between the stacks was found in drilling condition three with an under estimation of 13.6 %.

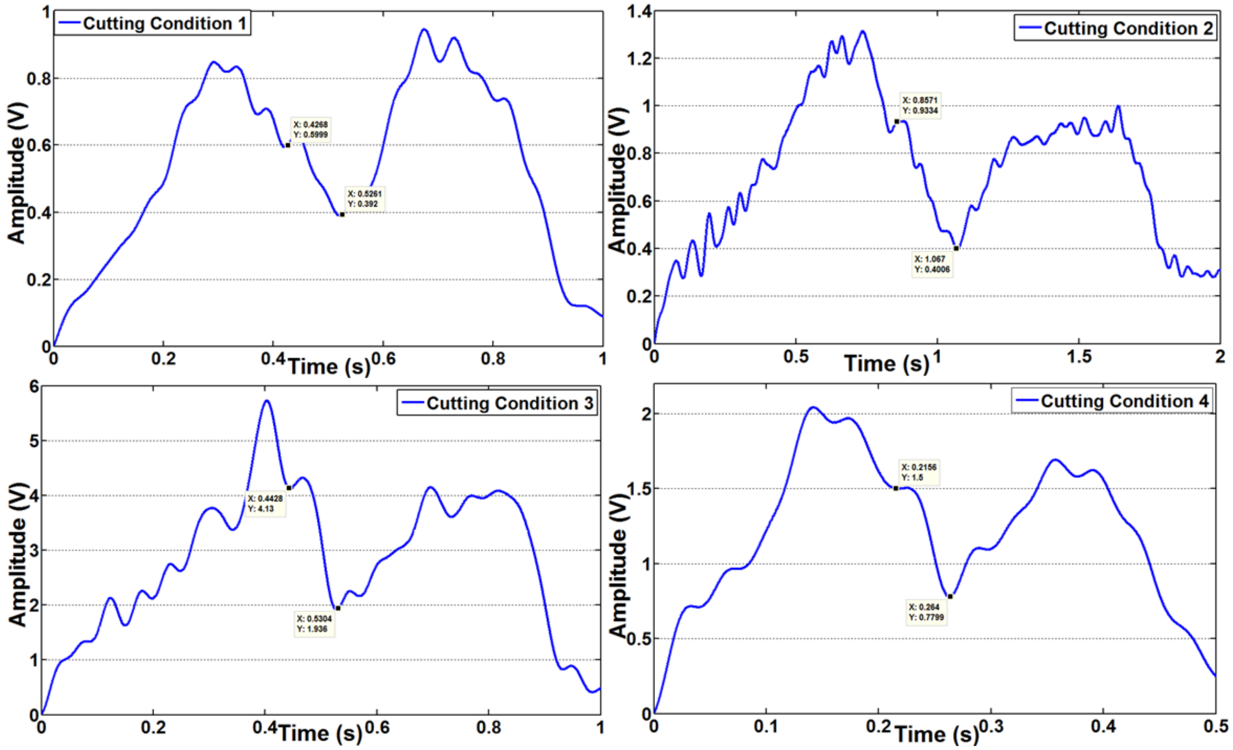

Figure 9.13. Vibration signal profiles for 1 mm preexisting gap at various drilling conditions

The average estimation error found in estimating a 1 mm preexisting gap over all four drilling conditions was 5.62 %, which is relatively close to the average estimation error of 5.58 % found in the use of acoustic emission signal for the same preexisting gap. The predicted (estimated) values for the 1 mm preexisting gap at various combinations of cutting conditions are given in Table 9.7. All the estimations made for the pre-existing gap of 1 mm using the accelerometer signal were overestimate except that of drilling condition three.

Table 9.7. Predicted values for 1 mm preexisting gap for different drilling conditions

Run Order	Cutting Speed (rpm)	Feed Rate (μm/rev)	Preexisting Gap (mm)	Predicted Gap (mm)	Error (%)
1	3000	200	1	0.99	-1.01
2	3000	100	1	1.05	4.76
3	6000	100	1	0.88	-13.6
4	6000	200	1	0.97	-3.1

9.3.3.2. When 0.5 mm Gap between the Stacks

For the drilling of CFRP composite stacks with a preexisting gap of 0.5 mm, the vibration signals from the accelerometer was processed in the same way discussed in the case of 1 mm pre-existing gap. Figure 9.14 shows the vibration signal profiles for a preexisting gap of 0.5 mm at different drilling conditions. The identification of the drill tip location was found to be a bit trickier because there are many variations on the signal profiles compared to the profiles of a 1 mm preexisting gap. The estimation error found in the estimation of the preexisting gap of 0.5 mm was higher than the error found in estimation of the 1 mm preexisting gap. The minimum error of over estimating by 1.96 % was found in drilling condition three, whereas, the maximum error of over estimating the pre-existing gap by 30.6 % was found in drilling condition two. All of estimation errors in the case of 0.5 mm preexisting gap was found to be over estimation of the pre-existing gap, which is different than the case of 1 mm preexisting gap where under estimation was observed in three of the four drilling conditions. The estimation technique using the vibration signal for 0.5 mm preexisting gap case was not as accurate as of 1 mm preexisting gap. Over the four drilling condition, the average error in estimating the 0.5 mm preexisting gap was found to be an over estimation by 17.8 %. Estimated values for the pre-existing 0.5 mm gap are given in Table 9.8.

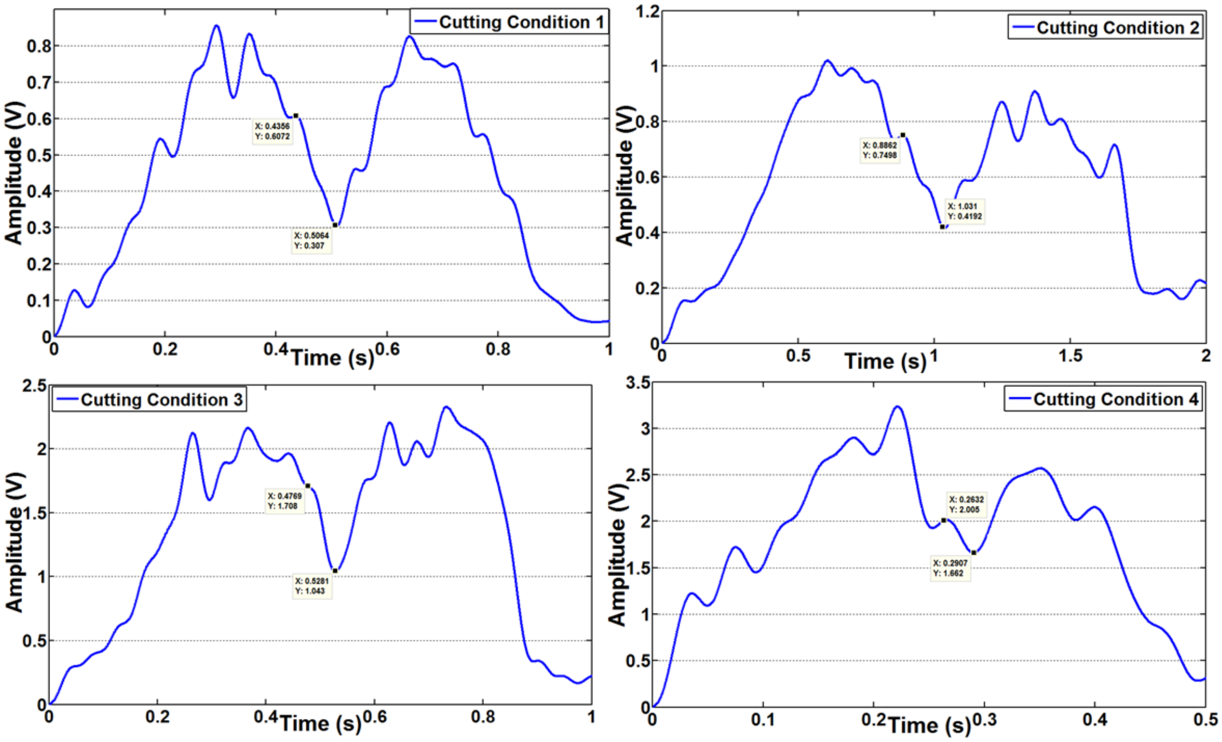

Figure 9.14. Vibration signal profiles for 0.5 mm preexisting gap at different drilling conditions

Table 9.8. Predicted values for the preexisting 0.5 mm gap for different drilling conditions

Run Order	Cutting Speed (rpm)	Feed Rate (μm/rev)	Preexisting Gap (mm)	Predicted Gap (mm)	Error (%)
1	3000	200	0.5	0.71	29.6
2	3000	100	0.5	0.72	30.6
3	6000	100	0.5	0.51	1.96
4	6000	200	0.5	0.55	9.09

9.3.3.3. Only Air Gap between the Stacks

The profiles of vibration signals from the accelerometer when drilling CFRP composite stacks without introducing any preexisting gap is shown in Figure 9.15 for all drilling conditions considered in this investigations. Even though there is an air gap between the two CFRP plates ranging from 103 to 133 μm, which is created by the surface roughness of the bagging side of the top plate as discussed in the previous sections, there is no clear indication of this air gap displayed in the vibration signal profiles. While there are small valleys on the profiles of the signal around the middle of the drilling process, it was impossible to identify the location of the drill tip at the exit of the top plate and entrance of the bottom plate.

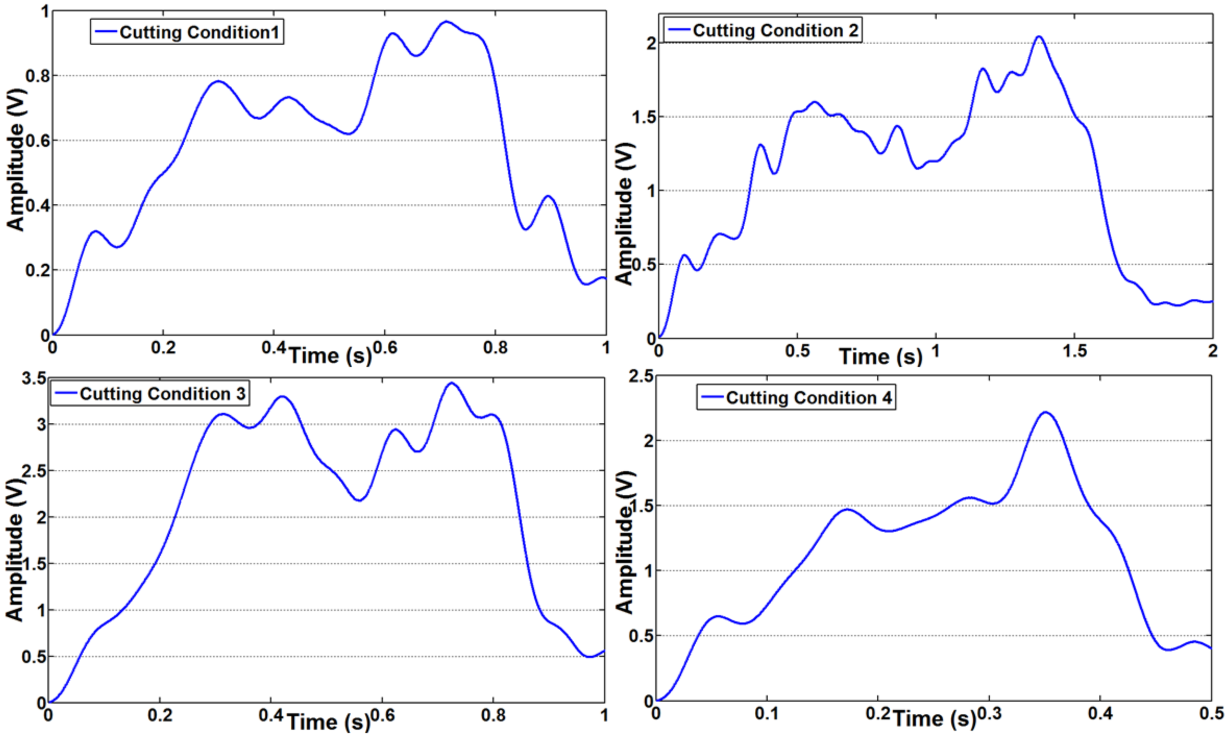

Figure 9.15. Vibration signal profiles without a preexisting gap at different drilling conditions

The results from the vibration signal acquired through the accelerometer for detection and prediction of gap when drilling CFRP composite stacks showed the viability of the proposed and method in this investigation of gap detection. The use of vibration signal for estimating gaps between CFRP plates when drilling CFRP composite stacks conveyed the same level of accuracy found in the use of acoustic emission signal in estimating a preexisting gap in both cases of 0.5 and 1 mm. The estimation accuracy attained using vibration signal was less than the estimation accuracy achieved by thrust force signals, but the use of vibration signal through accelerometer comes with the advantage of minimal coast of hardware and software compared to the investment required for thrust force measurement.

9.3.4. Detection using Audio Microphone Signals

Using an audio microphone as acoustic signal acquisition tool for detecting and predicting gaps when drilling CFRP composite stacks is the fourth proposed method in this investigation. Audio microphones can be a prominent choice from the economic standpoint compared to the other three signal acquisition systems considered in this investigation. As it can be inferred from Figure 9.3 (d), the raw acoustic signal acquired using an audio microphone has relatively similar profile to that of the vibration and acoustic emission signals. The signal processing techniques and the identification of drill tip locations discussed in the vibration signal and acoustic emission signal analysis have been used in the analysis of the acoustic signal from the audio microphone. Typical absolute value and filtered acoustic signal profiles from the audio microphone are shown in Figure 9.16.

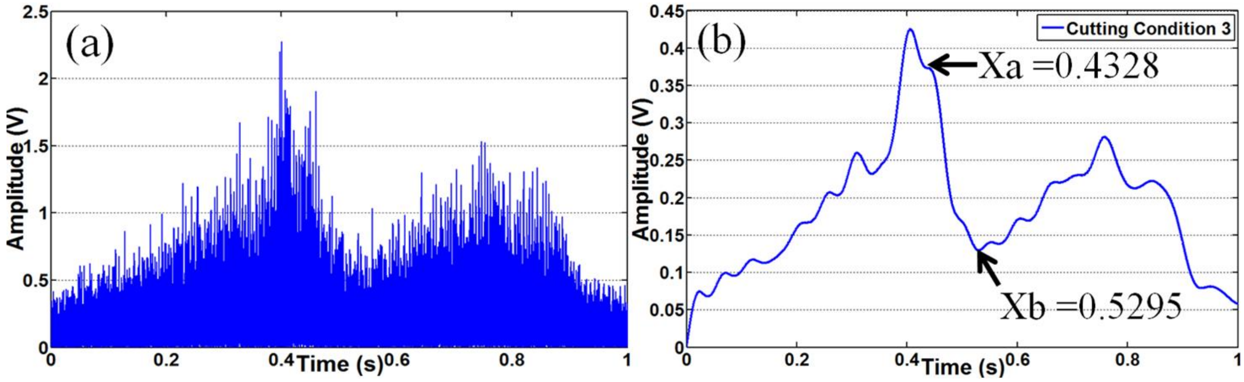

Figure 9.16. Typical audio microphone profiles of (a) absolute values and (b) filtered signal

9.3.4.1. When 1 mm Gap between the Stacks

Figure 9.17 shows the profiles of the audio microphone signal when drilling CFRP composites stacks with a 1 mm preexisting gap at different drilling conditions. From the time stamp identified as the location of the drill tip at the exit of the top plate and entrance of the bottom plate, an estimation of the preexisting gap was made. The lowest estimation error was found at the drilling condition three by underestimating the existing gap by 3.1 %, whereas, the largest estimating error was underestimation by 12.36 % at drilling condition four. The error associated with the estimation of existing gap when drilling CFRP stacks utilizing an audio microphone as a sensor was found to be relatively the same with errors found in the use of acoustic emission and accelerometer signals. The overall error in estimating a 1 mm preexisting gap using audio microphone was 6.13 %. Estimation values for 1 mm preexisting gap at different drilling conditions are given in Table 9.9.

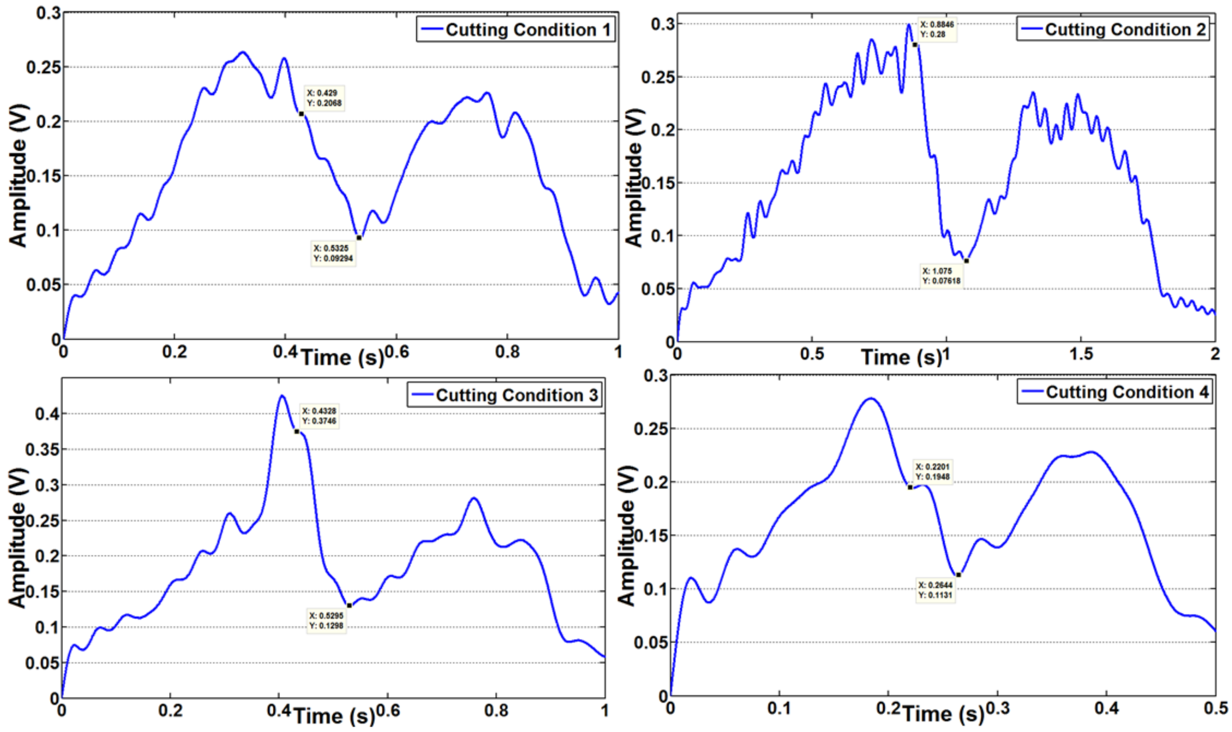

Figure 9.17. Audio microphone profiles for 1 mm preexisting gap at various drilling conditions

Table 9.9. Predicted values for the preexisting 1 mm gap for different drilling conditions

Run Order	Cutting Speed (rpm)	Feed Rate (μm/rev)	Preexisting Gap (mm)	Predicted Gap (mm)	Error (%)
1	3000	200	1	1.04	3.8
2	3000	100	1	0.95	-5.26
3	6000	100	1	0.97	-3.1
4	6000	200	1	0.89	-12.36

9.3.4.2. When 0.5 mm Gap between the Stacks

Audio microphone signal profiles when drilling CFRP composite stacks with a 0.5 mm preexisting gap are given in Figure 9.18. There is a lot of fluctuation in the signal profiles for 0.5 mm preexisting gap case compared the profiles of 1 mm preexisting gaps. Following the same procedure as the other cases discussed in the previous sections, estimation of the gap between the two CFRP plates was made. The lowest estimation error was found at drilling condition four by overestimating the preexisting gap by 1.96 % and the largest estimation error was at drilling conditions one and two by overestimating the gap by 15.25 %. For the case of preexisting 0.5 mm gap over all drilling conditions, the average estimation error found in estimating the gap between the two CFRP plates using an audio microphone signals was 8.63 %. The errors were overestimating the gap in all drilling conditions except condition three. Estimation values for 0.5 mm preexisting gap at different drilling conditions are given in Table 9.10.

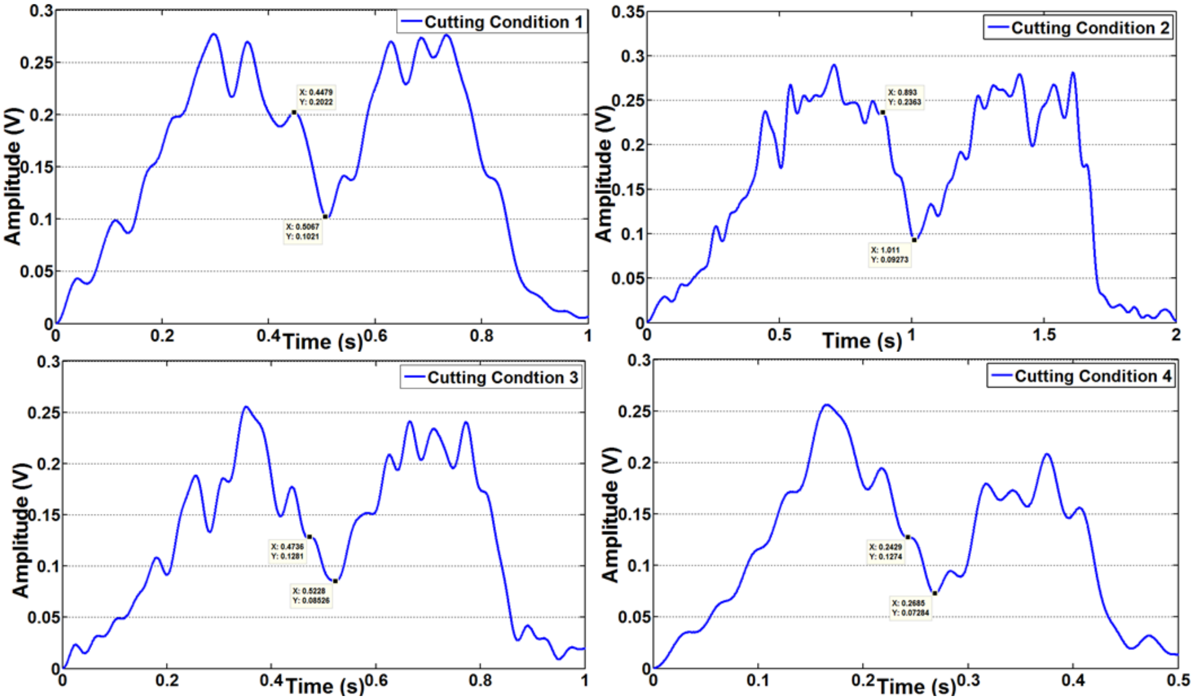

Figure 9.18. Audio microphone profiles for 0.5 mm preexisting gap at various drilling conditions

Table 9.10. Predicted values for the preexisting 0.5 mm gap for different drilling conditions

Run Order	Cutting Speed (rpm)	Feed Rate (µm/rev)	Preexisting Gap (mm)	Predicted Gap (mm)	Error (%)
1	3000	200	0.5	0.59	15.25
2	3000	100	0.5	0.59	15.25
3	6000	100	0.5	0.49	-2.04
4	6000	200	0.5	0.51	1.96

9.3.4.3. Only Air Gap between the Stacks

The audio microphone signal profiles for the drilling of CFRP composite stacks without an introduction of a preexisting gap where only air between the two plates are shown in Figure 9.19. As it can be seen from these profiles, there is no a distinct trend which can be used to identify the location of the drill tip at the exit of the top plate and the entrance of the bottom plate. As it have been discussed in the previous sections, the air gap created by the interface of the two CFRP plate is too small to be identified and make an estimation from the audio microphone signal profiles.

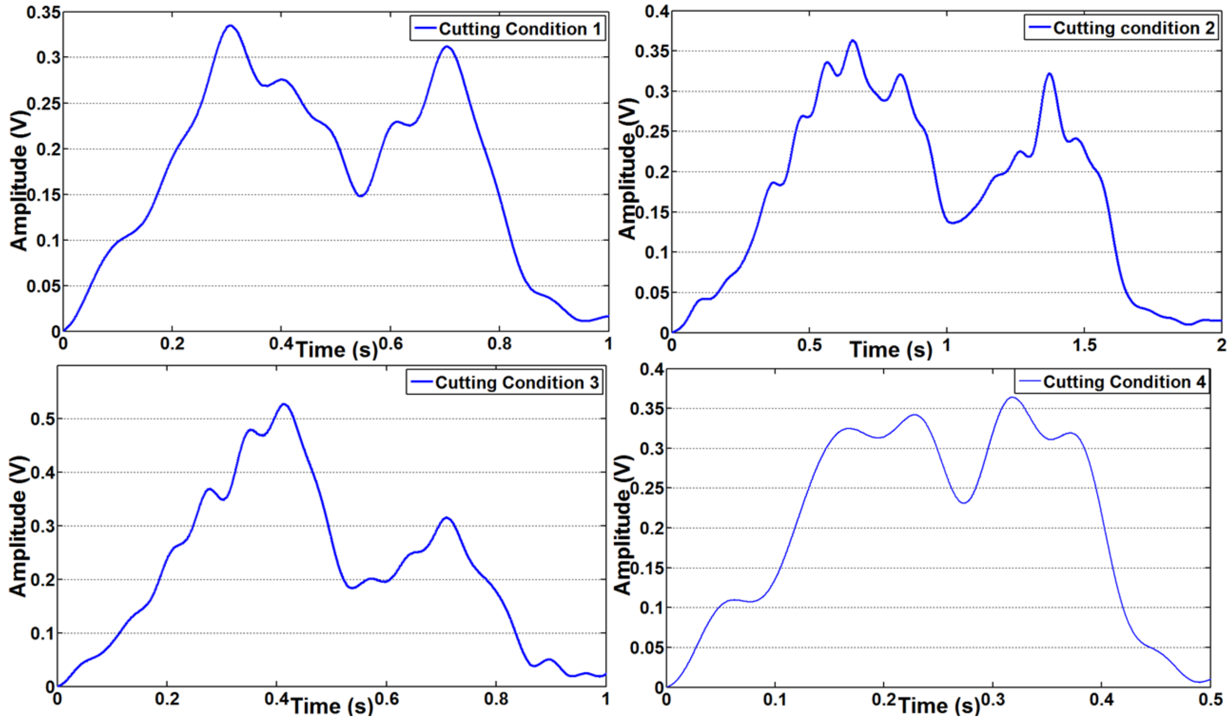

Figure 9.19. Audio microphone profiles without a pre-existing gap at different drilling conditions

Utilizing an audio microphone as acoustic signal acquisition sensor for detection and estimation of gaps when drilling CFRP composite stacks was found to be a better alternative than other expensive sensors and acquisition systems. The level of accuracy attained by using an audio microphone in the estimation of a 1 mm preexisting gap is relatively close to the estimation accuracies achieved by using acoustic emission and vibration signals. However, for the case of 0.5 mm preexisting gap, the estimation accuracy achieved by using an audio microphone was much better than the estimation accuracies found by the use of accelerometer and acoustic emission signal profiles. Moreover, when it comes to cost effectiveness, the investment required for the audio microphone is 100 times less than that of acoustic emission and even more cheaper than the investment required to acquire the force signals. Over all, the proposed method for detecting and estimating gaps through audio microphone signal profiles has demonstrate its proficiency in detecting and estimating gaps between CFRP composite stacks while drilling with in an average estimation error of 6.13 % and 8.6 % for 1 mm and 0.5 mm preexisting gaps respectively. The minimum, maximum, and average estimation errors found in the estimation of pre-existing gap of 1 mm and 0.5 mm for all signal acquisition systems considered in this investigation are given in Table 9.11.

Table 9.11. Comparison of estimation error for all type signal used

Pre-existing Gap (mm)	Type of Signal Used	Estimation Error (%)		
		Minimum	Maximum	Average
1	Thrust Force	2	4	3
	Acoustic Emission	4.2	9.1	5.58
	Vibration	1.01	13.6	5.62
	Audio Microphone	3.1	12.36	6.13
0.5	Thrust Force	0	4.17	2.07
	Acoustic Emission	9.09	24.24	16.62
	Vibration	1.96	30.6	17.8
	Audio Microphone	1.96	15.25	8.63

9.4. Conclusion

A novel approach to detect the presence of a gap and to estimate the amount of the gap when drilling CFRP composite stacks through various signals was proposed in this investigation. Four signal acquisition systems namely thrust force, acoustic emission, accelerometer (vibration), and audio microphone were used to acquire signals when drilling CFRP composite stacks. By introducing pre-existing gap between the two plates before drilling, an estimation of the known pre-existing gap was performed from the signal profiles. From the results and observations made in this investigation, the following concluding remarks have been made.

1. The competency of proposed method was demonstrated in detecting and estimating existing gaps when drilling CFRP composite stacks.
2. Thrust force signal shows high accuracy of estimating the pre-existing gap with a maximum estimation error of 4.17 % in both 0.5 and 1 mm pre-existing gap.

3. Estimations of preexisting gaps made though acoustic emission and vibration signal profiles found to be very close in both cases of gaps with an estimation error of 17 % and 5.6 % for 0.5 and 1 mm preexisting gaps respectively.
4. The level of accuracy achieved in estimating pre-existing gap by using audio microphone signal was comparable with the level of accuracy achieved by acoustic emission and vibration signal for the case of 1 mm gap with an average estimation error of 6.13 %.
5. The estimation made by using audio microphone signal for the case of 0.5 mm preexisting gap delivers much higher accuracy than the accuracy found by the acoustic emission and vibration signals with an average estimation error of 8.63 %.

Overall, the results of this investigation revealed the competency of the proposed method for detecting and estimating gap when drilling CFRP composite stacks. The level of accuracy attained in estimating gap between CFRP stacks using thrust force signal profiles found to be much higher than the level of accuracy attained by using all other signal profiles considered in this investigation, however the investment required to for thrust force signal acquisition system is higher than the investment required for other three acquisition systems combined. On the other hand, the level of accuracy achieved in estimating the gap by using an audio microphone signal is much higher than the accuracy achieved by using vibration and acoustic emission signal and the audio microphone provides additional advantage over the two signal acquisition systems when it comes to the amount of investment required. For these reasons, the audio microphone signal is the favorable choice of signal acquisition system for the proposed approach of online detection and estimation of gap when drilling CFRP composite stacks.

CHAPTER 10: CONCLUSIONS AND RECOMMENDATIONS FOR FUTURE STUDY

Experimental study of damage and defect detection during drilling of carbon fiber reinforced plastic (CFRP) composite materials conducted in this investigation was presented. Concluding remarks based on key findings and results of this investigation followed by recommendations for future study will be presented in this chapter.

10.1. Process Induced Damage and Defects during Drilling of CFRP Composites

Quality of holes and drilling induced damages and defects when drilling uni-directional and multi-directional CFRP composite laminates were experimentally investigated. The influence of drilling parameters and conditions on the resulting quality of the hole produced and other drilling induced damages and defects was investigated. Drilling induced defects and damages such as drilled hole surface roughness, hole surface morphology, fiber pullout, and delamination were studied through qualitative measurements and SEM examination. Drilling force such as thrust force and torque were evaluated and related to the various process induced damages and defects. In some cases a preliminary investigation on the use of acoustic emission signal and vibration signal for damage and defect detection was performed.

Trust force and torque increases with the increase of feed rate and decreases with the increase of cutting speed and the influence of the feed rate on cutting forces was more pronounced than the influence caused by the cutting speed for all types of CFRP laminates studied. Thrust force prediction equation was derived based on Shaw’s prediction equations and a prediction of thrust force was performed with an average determination constant of 0.98 for all CFRP laminates. The magnitude of thrust force varies significantly over the revolution of the drill when drilling uni-directional CFRP laminate and lower value of the thrust force was observed around the rotational angles of 135^0 and 315^0. Maximum values of average surface roughness parameters (R_a, R_q, $R_{z,}$ and R_t) were occurred (measured) when the angle of interaction between the cutting direction and the ply orientation is 135^0 and 315^0 along the circumference of the hole.

The occurrence of fiber pullout when drilling multi-directional CFRP laminate was in a periodic fashion based on the orientation of individual plies in the stacking sequence, whereas, in the case of uni-directional CFRP laminate, it was occured in two regions where the angle of interaction between the cutting direction and the fiber orientation is from 135^0 - 175^0 and 315^0 - 355^0. The depth of fiber pullout varied 43 µm to 328 µm when drilling multi-directional CFRP laminate based on the orientation of individual plies in the stacking sequence, whereas, width of fiber pullout was found to be varied from one half to one ply thickness. Fiber pullout depth was higher where the orientation of individual plies in the stacking sequence is $\pm 45^0$ and surface roughness parameter maximum peak-to-valley height Rt was found to be sensitive parameter to characterize fiber pullout depth.

Delamination factor increased when the feed rate increases and decreased with the increase of the cutting speed for all CFRP laminates. The amount of delamination factor resulted when drilling multi-directional CFRP laminates was lower than the delamination factor when drilling uni-directional CFRP laminate. Between the multi-directional laminates, delamination factor when drilling multi-directional CFRP laminate with woven fabric surface ply was lower than the delamination factor measured when drilling multi-directional CFRP laminate with fiberglass scrim surface ply. Over all, delamination factor was minimized when drilling with a combination of higher cutting speed and lower feed rate.

Correlation between the amplitude of demodulated vibration signal and damage (fiber pullout) length was performed when drilling multi-directional CFRP laminate with fiberglass scrim surface ply. The damage length measured shows a good correlation with the corresponding amplitude of the demodulated signal envelope with an average coefficient of determination value of 0.83. For the best and reliable damage detection, considering the damage area is suggested instead of just the damage length in the future. In addition, the relationship between drilling induced damages and acoustic emission signal amplitude was studied. From this study, spikes in squared Hilbert envelope with amplitude greater than 80 are associated with the occurrence of fiber pullout and those with amplitude greater than 50 are associated with matrix crack.

10.2. Ply-by-Ply Cutting Action and Peel-up Delamination

Experimental investigation of ply-by-ply cutting action was conducted on a unidirectional CFRP laminate through a blind hole was drilled with various depths ranging from two plies up to fourteen plies with increments of two ply thickness. The drilled blind holes were inspected for possible damages through optical microscope and scanning electron microscopy. Thrust force magnitude show a relatively constant increment when the number of plies drilled increases. When the numbers of drilled plies increases from two to ten, the thrust force magnitude increased by an average of 10% for every increase of two plies and the change in thrust force magnitude was negligible when the numbers of plies drilled increased from ten to twelve. The change in thrust force magnitude for numbers of plies drilled greater than ten where the cutting edge and body of the drill fully engaged inside the material was smaller compared to the changes seen for numbers of plies drilled less than ten. Large portion of the thrust force is due to the penetration of the first one or two plies and once the drill penetrates the top ply, the magnitude of the thrust force due to the cutting of each individual plies is much less than the thrust force caused by the penetration action.

A new phenomenon about the occurrence of peel-up delamination was observed in this investigation. Peel-up delamination or delamination at the drill entrance was considered to occur by the cutting action of the chisel edge and all earlier studies reported that it occurs when the chisel edge scratches and peeled off the top plies. From this, it is clear that the chisel edge did not create (cause) peel-up delamination rather peel-up delamination is caused when the drill flute starts engaging or entering the work piece. Delamination at the drill entrance occurred after the cutting edge is completely inside the work material and as soon as the flute of the drill made contact the work piece material.

10.3. Exit Ply Delamination when Drilling Uni-Directional CFRP Composites

An analytical model to predict the critical thrust force at the onset of exit ply delamination when drilling uni-directional CFRP composites based on LEFM and plate bending theory was proposed and an experimental investigation was performed through a punch test to determine the thrust force at the onset of delamination. An elliptical delamination zone with clamped boundary condition was considered in the formulation of the model. In addition, since the load applied by the drill tip is circular, the lateral uniform load is taken over a circular region rather than elliptical region. A punch test was carried out in order to measure the critical thrust force experimentally at the onset of exit ply delamination when drilling uni-directional CFRP composites and an Acoustic emission signal was also acquired to investigate the amplitude of the acoustic signal at the onset of exit ply delamination. Large spike in the amplitude of the acoustic emission signal was observed at the onset of main delamination followed by smaller spikes from the smaller delamination and consecutive smashing or breaking action of the fibers. The average value of the amplitude of the first (highest) spike for all punch tests is found to be 80 dB, which can be used as a reference value for the detection of delamination. Optical image of the sectioned holes reveals that delamination does not occur exactly at the interface of two consecutive plies rather it is found to occur in a single ply. The location of delamination seen in these optical images of sectioned holes is not in the line of ply interface as it is assumed and reported in many studies; rather it appears inside in a single ply (lamina).

Comparison of experimentally measured values and predicted values by the new model developed in this study with predicted values by other models of thrust force values at the onset of delamination was presented. Based on this comparison, the predicted values by the new proposed model show better correlation with the experimentally measured values than values predicted by other models.

10.4. On-line Detection and Monitoring of Tool Wear

Two new (novel) approaches namely, using the signal amplitude and using output variables from recurrence quantification analysis (RQA) of audio microphone signal were proposed for on-line detection and monitoring of tool wear when drilling CFRP composites. Thrust force, vibration, acoustic emission, and audio microphone signals were acquired and the variation on the signals signature were studied and correlated to the progression of the drill flank wear.

The amplitude of thrust force increased when the amount of flank wear increased, and using the thrust force amplitude as an input parameter flank wear was estimated with an average error of 5.7 % and 0.5 % when drilling multi-directional CFRP using HSS drill and uni-directional CFRP using carbide drill respectively. The amplitude of the audio microphone signal decreased when the amount of flank wear increases. Using the amplitude of the audio microphone amplitude as input parameter flank wear was estimated with an average error of 7.8 %, 2 %, and 16 % when drilling multi-directional CFRP using HSS drill, uni-directional CFRP using HSS drill, and uni-directional CFRP using carbide drill respectively. However, amplitudes of vibration and acoustic emission signals found to be path dependent and were not used in estimating flank wear except in one case where the location of the acoustic emission sensor was changed for each hole in order to keep a constant path when drilling uni-directional CFRP using carbide drill. In this particular case, the amount of flank wear was estimated using the acoustic emission signal amplitude with a maximum error of 32 % for the tenth and twentieth hole and 16 % for holes from thirty to eighty.

Six out of eight of the output variables from the RQA increases with the increase of the drill flank wear, whereas, two of the output variables decrease with the increase of the drill flank wear in both cases of drilling conditions investigated in this study. Output variables from the RQA analysis show similar behavior in both drilling conditions with different level of flank wear progression and the influence of flank wear progression on the output variables of the RQA analysis was observed clearly. Air-coupled audio microphone was proven to detect the variations in acoustic signature when the condition of the cutting edge of the drill too changes during drilling CFRP composite laminates. The capability of the two proposed approaches in this investigations for online detection and monitoring of the condition of the drill tool when drilling CFRP composite laminate have been demonstrated. Air-coupled audio microphone signal was competent in drill wear monitoring in both proposed approaches.

10.5. On-line Detection and Estimation of Gaps when Drilling CFRP Stacks

A novel approach to detect the presence of a gap and to estimate the amount of the gap when drilling CFRP composite stacks through various signals was proposed. By introducing pre-existing gap between the two plates before drilling, an estimation of the known pre-existing gap was performed from the signal profiles. The competency proposed method was demonstrated in detecting and estimating existing gaps when drilling CFRP composite stacks. Thrust force signal shows high accuracy of estimating the pre-existing gap with a maximum estimation error of 4.17 % in both 0.5 and 1 mm pre-existing gap. Estimation of preexisting gaps made though acoustic emission and vibration signal profiles found to be very close in both cases of gaps with an estimation error of 17 % and 5.6 % for 0.5 and 1 mm preexisting gaps respectively. The level of accuracy achieved in estimating preexisting gap by using audio microphone signal was comparable with the level of accuracy achieved by acoustic emission and vibration signal for the case of 1 mm gap with an average estimation error of 6.13 %. Whereas, the estimation made by using audio microphone signal for the case of 0.5 mm preexisting gap delivers much higher accuracy than the accuracy found by the acoustic emission and vibration signals with an average estimation error of 8.63 %.

The level of accuracy attained in estimating gap between CFRP stacks using thrust force signal profiles found to be much higher than the level of accuracy attained by using all other signal profiles considered in this investigation, however the investment required to for thrust force signal acquisition system is higher than the investment required for other three acquisition systems combined. On the other hand, the level of accuracy achieved in estimating the gap by using an audio microphone signal is much higher than the accuracy achieved by using vibration and acoustic emission signal and the audio microphone provides additional advantage over the two signal acquisition systems when it comes to the amount of investment required. For these reasons, the audio microphone signal is the favorable choice of signal acquisition system for the proposed approach of online detection and estimation of gap when drilling CFRP composite stacks.

10.6. Recommendations for Future Study

Based on the observations and outcomes of this investigation, the following recommendations for future study are made as an extension of this study.

1. More work should be done in the analysis and processing of acoustic emission and vibration signal to correlate signal signatures to drilling induced damage and defects and towards developing in process detecting method of damages and defects when drilling CFRP composite laminates.
2. The influence of shear stress from the torsional component of the drilling force should be incorporated in the future modification of exit ply delamination model.
3. Continuous work is recommended on tool wear monitoring system in order to develop a data bank and set threshold values of signal amplitude for different drilling conditions. In addition, more experimental study is recommended using a hand held drill and attaching the audio microphone on the drill.
4. The study on detection of gaps should continue in a factory setting in addition to the present study conducted in a laboratory setting.

REFERENCES

[1]. King Jams Bible, Exodus 5:7.

[2]. M. Ramulu, ME450, Composite materials & Design, Lecture Notes, University of Washington, 2010.

[3]. William D. Callister, Jr., Material Science and Engineering, John Wiley & Sons, Inc. 7th edition, 2007.

[4]. S. Gururaja and M. Ramulu, “Analytical Formulation of Subsurface Stresses During Orthogonal Cutting of FRPs”, Composites: Part A, Vol. 41, 2010, pp. 1164-1173.

[5]. H. Hocheng and H. Y. Puw, “On Drilling Characteristics of Fiber-Reinforced Thermoset and Thermoplastics”, Int. J. Mach. Tools Manufact. Vol. 32, No. 4, 1992, pp. 583-592.

[6]. Edoardo Capello, Antonio Langlela, Luigi Nele, Alfonso Paoletto, Loredana Santo, and Vincenzo Tagliaferri, Drilling polymeric Matrix Composite, Chapter 6.

[7]. Milton C. Shaw, Metal Cutting Principles, Oxford University Press, 1984.

[8]. Serope Kalpakjian, “Manufacturing Processes for Engineering Materials”, Addison-Wesley, 3rd edition, 1997.

[9]. R. Teti, “Machining of Composite Materials”, University of Naples Federico II, Italy.

[10]. A. Koplev, Aa. Lystrup, and T. Vorm, “The Cutting Process, Chips, and Cutting Forces in Machining CFRP”, Composites, Vol. 14, No. 4, 1983, pp. 371-376.

[11]. M. Ramulu, “Machining and surface Integrity of Fiber-Reinforced Plastic Composites”, Sãdhanã, Vol. 22, Part 3, 1997, pp. 449-472.

[12]. D. H. Wang, M. Ramulu, and D. Arola, “Orthogonal Cutting Mechanisms of Graphite/Epoxy Composite. Part I: Unidirectional Laminate”, Int. J. Mach. Tools Manufact. Vol. 35, No. 12, 1995, pp. 1623-1638.

[13]. D. H. Wang, M. Ramulu, and D. Arola, “Orthogonal Cutting Mechanisms of Graphite/Epoxy Composite. Part II: Muti-Directional Laminate”, Int. J. Mach. Tools Manufact. Vol. 35, No. 12, 1995, pp. 1639-1648.

[14]. X. M. Wang and L. C. Zhang, “An Experimental Investigation into Orthogonal Cutting of Unidirectional Fibre Reinforced plastics”, International Journal of Machine Tools and Manufacture, Vol. 43, 2003, pp. 1015-1022.

[15]. S. Abrate and D. A. Walton, “Machining of Composite Materials, Part I: Traditional Methods”, Composite Manufacturing, Vol. 3, No. 2, 1992, pp. 75-83.

[16]. S. Abrate and D. A. Walton, “Machining of Composite Materials, Part II: Non-Traditional Methods”, Composite Manufacturing, Vol. 3, No. 2, 1992, pp. 85-94.

[17]. D. Arola and M. Ramulu, “Orthogonal Cutting of Fiber-Reinforced Composites: a Finite Element Analysis” Int. J. Mech. Sci. Vol. 39, No. 5, 1997, pp. 597-613.

[18]. L. Lasri, M. Nouari, and M. El. Mansori, “Modeling of Chip Separation in Machining Unidirectional FRP Composites by Stiffness Degradation Concept” Composite Science and Technology, Vol. 69, 2009, pp. 684-692.

[19]. G. Venu Gopala Rao, P. Mahajan, and N. Bhatnagar, “Micro-Mechanical Modeling of Machining of FRP Composite – Cutting Force Analysis” Composite Science and Technology, Vol. 67, 2007, pp. 579-593.

[20]. G. Venu Gopala Rao, Puneet Mahajan, and Naresh Bhatnagar, “Machining of UD-GFRP Composites Chip Formation Mechanism”, Composite Science and Technology, Vol. 67, 2007, pp. 2271-2281.

[21]. Carlos Santiuste, Xavier soldani, and Maria Henar Miguélez, "Machining FEM Model for Long Fiber Composites for Aeronautical Components" Composite Structures, Vol. 92, 2010, pp. 691-698.

[22]. L. C. Zhang, "A Discussion on Mechanics Modeling", Journal of Material Processing Technology, Vol. 209, 2009, pp. 4548-4552.

[23]. Suhasini Gururaja and Mamidala Ramulu, "Failure Analysis of a Fibrous Composite Half-Space Subjected to Uniform Surface load", Journal of Engineering Materials and technology, Vol. 131, 2009, pp. 1-8.

[24]. C. K. H. Dharan and M. S. Won, "Machining Parameters for An Intelligent Machining System for Composite laminate", International Journal of machine Tools & Manufacture, Vol. 40, 2000, pp. 415-426.

[25]. A. M. Abrão, P. E. Faria, J. C. Camos Rubio, P. Reis, and J. Paulo Davim, "Drilling of Fiber Reinforced Plastics: A Review", Journal of Materials Processing Technology, Vol. 186, 2007, pp. 1-7.

[26]. I. El-Sonbaty, U. A. Khashaba, and T. Machaly, "Factors Affecting the Machinability of GFRP/Epoxy Composites" Composite Structures, Vol. 63, 2004, pp. 329-338.

[27]. D. Abdul Budan and S. Vijayarangan, "Quality Assessment and Delamination Force Evaluation in Drilling Glass Fiber- Reinforced Plastic Laminates – a Finite element Analysis and Linear Elastic Fracture Mechanics Approach", Proc. Instn. Mech Engrs, Vol. 216, Part B: J engineering manufacture, 2010, pp. 173-182.

[28]. Shyha, Soo, Aspinwall, and Bradley, "Effect of Laminate Configuration and Feed Rate on Cutting Performance When Drilling Holes in Carbon Fiber Reinforced Composites" Journal of Materials Processing Technology, Vol. 210, 2010, pp. 1023-1034.

[29]. C.W. Wern, M. Ramulu, and K. Colligan, "A Study of the Surface Texture of Composite Drilled Holes" J. of Materials Processing Technology, Vol. 37, No.1-4, February 1993, pp. 373-389.

[30]. K. Colligan and M. Ramulu, "An Experimental Investigation into Pitting of Hole Surfaces When Drilling Graphite/Epoxy," Processing Fabrication and Manufacturing of Composite Materials, ASME Bound Volume, MD-Vol. 35,1992, pp. 11-25.

[31]. M. Ramulu, P. Young, and H. Kao, “Drilling of Graphite/Bismaleimide Composite Material” Journal of Materials engineering and performance, Vol. 8(3), 1999, pp. 330-338.

[32]. A. Velayudham and R. Krishnamurthy, “Effect of Point Geometry and Their Influence on Thrust and Delamination in Drilling of polymeric Composites” Journal of Materials Processing Technology, Vol. 185, 2007, pp. 204-209.

[33]. Mihai-Bogdan Lazar and Paul Xirouchakis, “Experimental Analysis of Drilling Fiber Reinforced Composites” International Journal of machine Tools and Manufacture, Vol. 51, 2011, pp. 937-946.

[34]. Yanming QUAN and Wenwang ZHONG, “Investigation on Drilling-Grinding of CFRP” Front. Mech. Eng. China, Vol. 4. No. 1, 2009, pp. 60-63.

[35]. C. Murphy, G. Byrne, and M. D. Gilchrist, “The Performance of coated Tungsten Carbide drills when Machining Carbon Fiber-Reinforced Epoxy Composite materials” Proc. Instn. Mech. Engrs, Vol. 216, Part B, 2002, pp. 143-152.

[36]. S. Jayabal and U. Natarajan, “Influence of Cutting Parameters on Thrust Force and Torque in drilling of E-Glass/Polyester Composites” Indian Journal of Engineering & Materials Sciences, Vol. 17, 2010, pp. 463-470.

[37]. Naresh Bhatnagar and Mukesh Kumar Jalutharia, " Prediction of thrust Force and Torque when drilling Composite Materials" Int. J. Materials and Product Technology, Vol. 32, Nos. 2/3, 2008, 213-225.

[38]. N. S. Mohan, A. Ramachandra, and S. M. Kulkarni, "Machining of Fiber-Reinforced Thermoplastics: Influence of Feed and Drill Size on Thrust Force and Torque during Drilling" Journal of Reinforced Plastics and Composites, Vol. 24, No. 12, 2005, pp. 1247-1257.

[39]. Wen-Chou Chen, "Some Experimental Investigations in The Drilling of Carbon Fiber-Reinforced Plastics (CFRP) Composite Laminates", Int. J. Tools Manufacture, Vol. 37, No. 8, 1997, pp. 1097-1108.

[40]. U. A. Khashaba, "Delamination in Drilling GFR-Thermoset Composites" Composite Structures, Vol. 63, 2004, pp. 313-327.

[41]. V. N. Gaitonde, S. R. Karnik, J. Campos Rubio, A. Esteves Correia, A. M. Abrão, and J. Paulo Davim, "Analysis of Parametric Influence on Delamination in High-Speed Drilling of Carbon Fiber Reinforced Plastic Composites" Journal of Materials Processing Technology, Vol. 203, 2008, pp. 431-438.

[42]. Erol Kilickap, "Investigation into the Effect of drilling Parameters on Delamination in Drilling GFRP" Journal of Reinforced Plastics & Composites, Vol. 29 (23), 2010, pp. 3498-3503.

[43]. C. C. Tsao and H. Hocheng, " Computerized Tomography and C-Scan for Measuring Delamination in the Drilling of Composite Materials using Various Drills" International Journal of machine Tools and Manufacture, Vol. 45, 2005, pp. 1282-1287.

[44]. V. Schulze, C. Becke, K. Weidenmann, and S. Dietrich, “Machining Strategies for Hole Making in Composites With Minimal Workpiece Damage by Directing the Process Force Inwards”, Journal of Materials Processing, Vol. 211, 2011, pp. 329-338.

[45]. S. Arul, L. Vijayaraghavan, S. K. Malhotra, and R. Krishnamurthy, “The Effect of Vibratory Drilling on Hole Quality in Polymeric Composites”, International Journal of Machine Tools & Manufacture, Vol. 46, 2006, pp. 252-259.

[46]. M. Ramulu, T. Branson, and D. Kim, “A study on the Drilling of Composite and Titanium Stacks” Composite Structures, Vol. 54, 2001, pp. 67-77.

[47]. D. Kim and M. Ramulu, “Drilling Process Optimization for Graphite/Bismaleimide – Titanium Alloy Stacks” Composite Structures, Vol. 63, 2004, pp. 101-114.

[48]. D. Kim and M. Ramulu, “Study on the Drilling of Titanium/Graphite Hybrid Composites” Journal of Engineering Materials and Technology, Vol. 129, 2007, pp. 390-396.

[49]. R. Piquet, B. Ferret, F. Lachaud, and P. Swider, “ Experimental Analysis of Drilling Damage in Thin Carbon/Epoxy Plate using Special drills” Composites: Part A 31, 2000, pp. 1107-1115.

[50]. E. Brinksmeier, S. Fangmann, and R. Rentsch, “Drilling of Composites and Resulting Surface Integrity” CIRP Annals-Manufacturing Technology, Vol. 60, 2011, pp. 57-60.

[51]. Sanjay Rawat and Helmi Attia, “Characterization of the Dry High Speed Drilling Process of Woven Composites using Machinability Maps Approach” CIRP Annals-Manufacturing Technology, Vol. 58, 2009, pp. 105-108.

[52]. D. Arola and M. L. McCain, “Surface Texture and the Stress Concentration Factor for FRP Components with Holes” Journal of Composite Materials, Vol. 37, No. 16, 2003, pp. 1439-1460.

[53]. R. Kažys, Mažeika, and E. Žukauskas, “Investigation of Accurate Imaging of the Defects in Composite Materials using Ultrasonic Air-Coupled Technique” 4th International Conference on NDT, 2007, pp. 1-7.

[54]. Shigehiko Sakamoto, Yusuke Kajiwara, and Heiji Yasui, “ Precision drilling of CFRP (Carbon Fiber Reinforced Plastics) with Coated Tools, Department of Advanced Mechanical Systems, Kumamoto University, 2-39-1, Kurokami, Kumamoto, JAPAN.

[55]. V. Krishnaraj, S. Vijayarangan, and G. Suresh, “An Investigation on High Speed Drilling of Glass Fiber Reinforced Plastic (GFRP)” Indian journal of Engineering and Material Sciences, Vol. 12, 2005, pp. 189-195.

[56]. Erween Abd. Rahim, Kamaruddin Kamdani and Safian Sharif, “ Performance Evaluation of Uncoated Carbide Tool in High Speed drilling of Ti64Al4V” Journal of Advanced Mechanical Design, Systems, and Manufacturing, Vol. 2, No. 4, 2008, pp. 522-531.

[57]. E. Brinksmeier and R. Janssen, “Drilling of Multi-Layer Composite materials Consisting of Carbon Fiber Reinforced Plastics (CFRP), Titanium, and Aluminum” Annals of the CIRP, Vol. 51/1, 2002, pp. 87-90.

[58]. D. Kim, M. Ramulu, and X. Doan, “Influence of Consolidation process on the Drilling Performance and Machinability of PIXA-M and PEEK Thermoplastic Composites” Journal of Thermoplastic and Composite Materials, Vol. 18, 2005, 195-217.

[59]. Sanjay Rawat and Helmi Attia, “Wear Mechanisms and Tool Life Management of WC-CO Drills during Dry High Speed drilling of Woven carbon Fibre Composites” Wear, Vol. 267, 2009, pp. 1022-1030.

[60]. G. Dipaolo, S. G. Kapoor, and R. E. Devor, “An Experimental Investigation of the Crack Growth Phenomenon for Drilling of Fiber-Reinforced Composite Materials” Journal of Engineering for Industry, Vol. 118, 1996, pp. 104-110.

[61]. B. K. Hinds and M. Treanor, “Drilling of Printed Circuit Boards: Factors Limiting the Use of Smaller Drill Sizes” Proc. Instn. Mech. Engrs., Vol. 214, Part B, 2000, pp. 35-45.

[62]. Eiichi Aoyama, Hiromich Nobe, and Toshiki Hirogaki, “Drilled Hole Damage of Small Diameter Drilling in Printed Wiring Board” Journal of Materials Processing Technology, Vol. 118, 2001, 436-441.

[63]. Dae-Wook Kim and M. Ramulu, “Process Optimization on the Drilling of Composite-Titanium Stacks” Proceedings of ESDA, MAN044, 2002, pp. 1-14.

[64]. M. A. Seif, U. A. Khashaba, and R. Rojas-Oviedo, “Measuring Delamination in Carbon/Epoxy Composites Using a Shadow Moiré Laser Based Imaging Technique” Composite Structures, Vol. 79, Issue 1, 2007, pp. 113-118.

[65]. Redouane Zitoune, Vijayan Krishnaraja, and Francis Collombet, “Study of Drilling of Composite Materials and Aluminum Stack” Composite Structures, Vol. 92, Issue 5, 2009, pp. 1246-1255.

[66]. J. Paulo Davim, J. Campos Rubio, and A. M. Abrao, “A Novel Approach Based on Digital Image Analysis to Evaluate the Delamination Factor after Drilling Composite Laminates” Composites Science and Technology, Vol. 67, 2007, pp. 1939-1945.

[67]. I. Singh and N. Bhatnagar, “Drilling-Induced Damage in Uni-Directional Glass Fiber Reinforced Plastic (UD-GFRP) Composite Laminates” Int. J. Adv. Manuf. Technology, Vol. 27, 2006, pp. 877-882.

[68]. Pierre Rahmé, Yann London, and Frédéric Lachaud, “Analytical Models of composite Material Drilling” Int. J. Adv. Manuf. Technology, Vol. 52, 2011, pp. 690-617.

[69]. P. K. Rakesh, V. Sharma, I. singh, and D. Kumar, “Delamination in Fiber Reinforced Plastics: A Finite Element Approach” Engineering, Vol. 3, 2011, pp. 549-554.

[70]. L. M. P. Durão, M. F. S. F. de Moura, and A. T. Marques, “Numerical Simulation of the Drilling Process on Carbon/Epoxy Composite laminates” Composites, Vol. 37, Part A, 2006, pp. 1325-1333.

[71]. L. M. P. Durão, M. F. S. F. de Moura, and A. T. Marques, “Numerical Prediction of Delamination Onset in Carbon/Epoxy Composites Drilling” Engineering Fracture Mechanics, Vol. 75, 2008, pp. 2767-2778.

[72]. A. Langella, L. Nele, and A. Maio, “A Torque and Thrust Prediction Model for Drilling of Composite Materials” Composites Vol. 36, Part A, 2005, pp. 83-93.

[73]. H. Ho-Cheng and C. K. H. Dharan, “Delamination During Drilling in Composite Laminates”, Journal of engineering for Industry, Vol. 112, 1990, pp. 236-239.

[74]. L-B Zhang, L-J Wang, and X-Y Liu, “A Mechanical Model for Predicting Critical Thrust Force in Drilling Composite Laminates, Proc. Instn. Mech Engrs, Vol. 215, Part B, 2001, pp. 135-146.

[75]. S. Jain and D. C. H. Yang, “Effect of Feed rate and Chisel Edge on Delamination in Composite Drilling”, Journal of Engineering for Industry, Vol. 115, 1993, pp. 398-405.

[76]. S. Gururaja and M. Ramulu, “Modified Exit-ply Delamination Model for Drilling FRPs”, Journal of Composite Materials, Vol. 43, No. 05, 2009, pp. 483-500.

[77]. D. Kim, and M. Ramulu, "Frequency Analysis and Process Monitoring in Drilling of Composite Materials", Advanced Composites Letters, Vol. 13, No. 4, 2004, pp. 185-192.

[78]. M. Ramulu, D. Kim and G. Choi, “Frequency Analysis and Characterization in Orthogonal Cutting of Glass Fiber Reinforced Composites" Composites, Vol. 34, Part A, 2003, pp. 949-962.

[79]. Benoit Mascaro, Vincent Gibiat, Marie Bernadou, and Yves Esquerre, “Acoustic Emission of the Drilling of Carbon/Epoxy Composites” Forum Acusticum, Budapest, 2005, pp. 2823-2827.

[80]. A. Rotem, “The Characteristics of Acoustic Emission from a Hole in a Composite Laminate”, Composite Science and Technology, Vol. 25, 1986, pp. 271-282.

[81]. S. R. Ravishankar and C. R. L. Murthy, “Application of Acoustic Emission in Drilling of Composite Laminates” NDT & E International, Vol. 33, 2000, pp. 429-435.

[82]. S. Arul, L. Vijayaraghavan, and S. K. Malhotra, “Online Monitoring of Acoustic Emission for Quality Control in Drilling of Polymeric Composites” Journal of Materials Processing Technology, Vol. 185, 2007, pp. 184-190.

[83]. A. Velayudham, R. Krishnamurthy, T. Soundarapandian, “Evaluation of Drilling Characteristics of High Volume Fraction Fibre Glass Reinforced Polymeric Composite” International Journal of Machine Tools and Manufacture, Vol. 45, 2005, pp. 399-406.

[84]. Hossein Heidary, Amir Refahi Oskouei, Milad Hajikhani, Behrooz Moosaloo, and Mehdi Ahmadi Najafabadi, “Acoustic Emission Signal Analysis by Wavelet Method to Investigate Damage Mechanisms during Drilling of Composite Materials” Proceedings of The ASME ESDA 2010, pp. 409-416.

[85]. V. Chandrasekharan, S. G. Kapoor, and R. E. Devor, “A Mechanistic Approach to Predicting the Cutting Forces in Drilling: with Application to Fiber-Reinforced Composite Materials” Journal of Engineering for Industry, Vol. 117, 1995, pp. 559-570.

[86]. Mustapha Elhachimi, Serge Torbaty, and Pierre Joyot, “Mechanical Modeling of High Speed Drilling 1: Predicting Torque and Thrust” International Journal of Machine Tools and Manufacture, Vol. 39, 1999, pp. 553-568.

[87]. Anish Paul, S. G. Kapoor, and R. E. Devor, “A chisel Edge Model for arbitrary Drill Point Geometry” Journal of manufacturing Science and engineering, Vol. 127, 2005, pp. 23-32.

[88]. V. Chandrasekharan, S. G. Kapoor, and R. E. Devor, “A Mechanistic Approach to Predicting the Cutting Forces in Drilling: with Application to Fiber-Reinforced Composite Materials” Machining of Advanced Composites, Vol. 45, 1993, pp. 33-51.

[89]. Juhchin A. Yang, Venkatraman Jaganathan, and Ruxu Du, “A New Dynamic Model for Drilling and Reaming Process” International Journal of Machine Tools and Manufacture, Vol. 42, 2002, pp. 299-311.

[90]. Frédéric Lachaud, Robert Piquet, Francis Collombet, and Laurent Surcin, “Drilling of Composite Structures” Composite Structures, Vol. 52, 2001, pp. 511-516.

[91]. M. S. Won and C. K. H. Dharan, “Chisel Edge and Pilot Hole Effects in Drilling Composite laminates” Journal of Manufacturing Science and Engineering, Vol. 124, 2002, pp. 242-247.

[92]. Chung-Chen Tsao and Wen-Chou Chen, “Prediction of the Location of Delamination in the Drilling of Composite Laminates” Journal of Materials Processing Technology, Vol. 70, 1997, pp. 185-189.

[93]. H. Hocheng and C. C. Tsao, “Comprehensive Analysis of Delamination in Drilling of Composite Materials with Various Drill Bits” Journal of Materials Processing Technology, Vol. 140, 2003, pp. 335-339.

[94]. H. Hocheng and C. C. Tsao, “The Path towards Delamination-Free drilling of Composite Materials” Journal of Materials Processing Technology, Vol. 167, 2005, pp. 251-264.

[95]. Jin Pyo Jung, Geun Woo Kim, and Kang Yong Lee, “Critical Thrust Force at delamination Propagation during Drilling of Angle-Ply Laminates” Composite Structures, Vol. 68, 2005, pp. 391-397.

[96]. S. Arul, D. Samuel Raj, L. Vijayaraghavan, S. K. Malhotra, and R. Krishnamurthy, “Modeling and Optimization of Process Parameters for Defect Toleranced Drilling of GFRP Composites” Materials and Manufacturing Processes, Vol. 21, 2006, pp. 357-365.

[97]. M. Ramulu, ME599, Machining & Surface Integrity of Advanced Composites, Lecture Notes, University of Washington, 2011.

[98]. Charles W. Bert, “Closed-Form Solution of an Arbitrary Laminated, Anisotropic, Elliptic Plate Under Uniform Pressure” Journal of Elasticity, Vol. 11, No. 3, 1981, pp. 337-340.

[99]. Mark E. Tuttle, “Structural Analysis of Polymeric Composite Materials” Marcel Dekker, INC. New York, 2004.

[100]. P. Collet and J. P. Eckmann, “On the Abundance of Chaotic Behavior in One Dimension” Annals of the New York Academy of Sciences, 1980.

[101]. J. P. Eckmann, S. Oliffson Kamphorst, and D. Ruelle, “Recurrence Plots of Dynamic System “Europhysics Letters, Vol. 4 (9), 1987, pp. 973-977.

[102]. Floris Takens, “Detecting Strange Attractors in Turbulence” Mathematisch Instituut, Groningen, Holland.

[103]. Andrew M. Fraser and Harry L. Swinney, “Independent Coordinates for Strange Attractions from Mutual Information” Physical Review A, Vol. 33, No. 2, 1986, pp. 1134-1140.

[104]. Matthew B. Kennel, Reggie Brown, and Henry D. I. Abarbanel, “Detecting Embedding Dimension for Phase-Space reconstruction using a Geometrical Construction” Physical Review A, Vol. 45, No. 6, 1992, pp. 3403-3411.

[105]. Joseph P. Zbilut and Charles L. Webber Jr., “Recurrence Quantification Analysis” Wiley Encyclopedia of Biomedical Engineering, Copyright © 2006 John Wiley & Sons, Inc.

[106]. M. Ramulu, ME559, “Introduction to Fracture Mechanics”, Lecture Notes, University of Washington, Seattle, 2010.

[107]. M. Ramulu, ME599, “Machining & Surface Integrity of Advanced Composites”, Lecture Notes, University of Washington, Seattle, 2011.

[108]. Eshetu D. Eneyew, “Effect of Loading Rate on Carbon Fiber Reinforced Plastic (CFRP) Properties” Master of Science Thesis, University of Washington, Seattle, 2010.

[109]. Peter Scott Young, “Drilling Forces in Graphite Reinforced Composites”, Master of Science Thesis, University of Washington, Seattle, 1995.

[110]. Suhasini Gururaja, “Stress Analysis of Machining Damage in Laminated Polymeric Composites” PhD Dissertation, University of Washington, Seattle, 2008.

[111]. Dea-Wook Kim, “Machining and Drilling of Hybrid Composite Materials” PhD Dissertation, University of Washington, Seattle, 2002.

[112]. Chien Wei Wernm “Fiber and Fiber-Matrix Interface Effects on the Orthogonal Cutting of Fiber Reinforced Plastics” PhD Dissertation, University of Washington, Seattle, 1995.

Curriculum Vitae

Eshetu Demissie Eneyew

Education

PhD. March 2014
Mechanical Engineering, University of Washington, Seattle, WA
Dissertation: *Experimental Study of Damage and Defect Detection during Drilling of CFRP Composites*

MSME – 2010
Mechanical Engineering, University of Washington, Seattle, WA
Thesis: *Effect of Loading Rate on Carbon Fiber Reinforced Plastic (CFRP) Properties*

BSME – 2009
Mechanical Engineering, University of Washington, Seattle, WA

AS – 2007
Applied Science, North Seattle Community College, Seattle, WA

AS – 1999
Industrial Education Technology, Adama University, Nazareth, Ethiopia

Diploma – 1996
Auto Mechanics, Bure Agro Technical School, Bure, Etiopia

Research Areas

- Drilling of composite materials
- Process development of advanced materials
- Mechanical properties of composite materials
- Machining induced damage and defects on composite materials
- Drill tool technologies for composite materials

Professional Experience

Teaching Assistant, 2014
Department of Mechanical Engineering, University of Washington, Seattle, WA
- ME 559 – Introduction to fracture mechanics

Pre-Doctoral Research Associate II, 2011-2014
Department of Mechanical Engineering, University of Washington, Seattle, WA

Developed technology for damage and defect detection during drilling of CFRP composite materials. Lead and assist a team of research associates and scientists in their research.

Pre-Doctoral Research Associate I, 2010-2011

Department of Mechanical Engineering, University of Washington, Seattle, WA

Planned and conducted various tests and experiments for damage and defect detection during drilling of CFRP composite materials. Collected analyzed experimental data, wrote and submitted reports, and gave presentations on submitted reports

Graduate Research Assistant, 2009-2010

Department of Mechanical Engineering, University of Washington, Seattle, WA

Conducted experimental investigation on the influence of loading on rate the mechanical properties of CFRP composite laminate structures. Collected analyzed experimental data, wrote and submitted reports, and gave presentations on submitted reports

Undergraduate Research Assistant, 2008-209

Department of Mechanical Engineering, University of Washington, Seattle, WA

Analyzed an electric harvesting mechanism when mechanical stress applied to a piezo-electric material and quantified the amount of electric charge that could be generated for a given amount of mechanical stress. Assisted on research projects, performed experiments, analyzed results, and prepared laboratory reports

Math and Science tutor, 2006

North Seattle Community College, Seattle, WA

Helped college students on their mathematics, physics, and engineering studies

Machinist, Summers of 2006/7/8

Creative Wood Working Corporation, Woodinville, WA

Operate and run various wood working machines on the production floor

Teacher, 2002-2004

Damot High School, Finote Selam, Ethiopia

- Technical and Engineering Drawing

Mechanic, 2001-2002

Water Works Construction Enterprise, Bahir Dar, Ethiopia

Perform regular maintenance and repair on water well drilling rigs, pumps, trucks, and various hydraulic and pneumatic systems

Manager and Lead Technician, 1999-2001

Eshet General Metal works and Pump Maintenance, Bahir Dar, Ethiopia

Manage the production of office and home furniture, manufacture machine parts, repair and install water pumps, and perform various welding and sheet metal works

Journal Publications

- E. D. Eneyew and M. Ramulu, “Multi-Sensor Detection and Estimation of Gaps when Drilling CFRP Composite Stacks”, *ASME International Mechanical Engineering Congress and Exposition*, Montreal, Canada. Nov 2014, Paper No. IMECE2014-38732

- J. Miller, E. D. Eneyew and M. Ramulu, “Machining and Drilling of CFRP Composites”, *SAMPE Journal*, Vol. 49, No. 2, March-April, 2013 , pp. 36-46
- E. D. Eneyew and M. Ramulu, “Tool Wear Monitoring Using Microphone Signals and Recurrence Quantification Analysis when Drilling Composites” *Advanced Materials Research*, Vol. 7, 2013, pp. 239-244
- E. D. Eneyew and M. Ramulu, “Effect of Surface Ply on the Quality of the Hole when Drilling Multi-Directional CFRP Composites”, *Advanced Materials Research,* Vol. 330, 2013, pp. 117-122
- E. D. Eneyew and M. Ramulu , “Hole Surface Quality and Damage when Drilling Unidirectional CFRP”, *Proceedings of the ASME 2012 International Mechanical Engineering Congress and Exposition*, Houston, TX, Nov 2012, Paper No. IMECE2012-88426

Submitted For Publication

- E. D. Eneyew and M. Ramulu, “Multi-Sensor Monitoring of Tool Wear when Drilling CFRP Composite using Carbide Drill”, *International Journal of Machine Tool design and Manufacturing*
- E. D. Eneyew and M. Ramulu, “On-line Detection and Estimation of Existing Gap when Drilling CFRP Composite Stacks”, *ASM E Journal of Manufacturing Science and Engineering*
- E. D. Eneyew and M. Ramulu, “Study of Cutting Mechanism through Ply-by-Ply Cutting Action of Drilling CFRP Composites”, *Composite Science and Technology*
- E. D. Eneyew and M. Ramulu, “ Analytical Mode of Critical Thrust Force at the Onset of Exit-Ply Delamination”, *Composite Structures*

Conference Presentations

- “On-line Detection of Delamination when Drilling Composite Materials using Stereo Microphone Signal”, *International Conference on Computational and Experimental Engineering and Sciences,* April 2013, Bellevue, WA
- “On-line Monitoring of Drill Wear using Stereo Microphone when Drilling CFRP Composite Materials”, *ASM International, AeroMat Conference and Exposition*, April 2013, Bellevue, WA
- “Effect of Surface Ply on the Quality of the Hole when Drilling Multi-Directional CFRP Composites”, *SME, Composite Manufacturing,* 2013, Long Beach, CA
- “Hole Surface Quality and Damage when Drilling Unidirectional CFRP”, *ASME International Mechanical Engineering Congress and Exposition,* Nov 2012, Houston, TX
- “Piezo-Electric energy Harvesting”, *University of Washington 12th Annual Undergraduate Research Symposium*, 2009, Seattle, WA

APPENDIX A – TECHNICAL SPECIFICATION OF MACHINING AND DATA ACQUISITION SYSTEMS

A. 1 MACHINING CENTER TECHNICAL DATA

Table A. 1. Hass TM-1P milling machine specification

		S. A. E. Unit	Metric Unit
Travels	X Axis	30 "	762 mm
	Y Axis	12 "	305 mm
	Z Axis	16 "	406 mm
	Spindle Nose to Table (~ min)	4 "	102 mm
	Spindle Nose to Table (~ max)	20 "	508 mm
Work Table	Length	47.75 "	1213 mm
	Width	10.5 "	267 mm
	T-Slot Width	5/8 "	16 mm
	T-Slot Center Distance	4.00 "	101.6 mm
	Number of Std T-Slots	3	3
	Max Weight on Table (evenly distributed)	1000 lb.	454 kg evenly distributed
Spindle	Max Rating	7.5 hp.	5.6 kW
	Max Speed	6000 rpm	6000 rpm
	Max Torque	33 ft-lb @ 1200 rpm	45 Nm @1200 rpm
	Drive System	Direct Speed Belt Drive	Direct Speed Belt Drive
	Taper	CT or BT 40	CT or BT 40
	Bearing Lubrication	Grease packed	Grease packed
	Cooling	Air Cooled	Air Cooled
Feed Rates	Rapids on X	400 in/min	10.2 m/min
	Rapids on Y	400 in/min	10.2 m/min
	Rapids on Z	400 in/min	10.2 m/min
	Max Cutting	400 in/min	10.2 m/min
Axis Motors	Max Thrust X	2000 lb.	8896 N
	Max Thrust Y	2000 lb.	8896 N
	Max Thrust Z	2000 lb.	8896 N
Tool Changer	Type	Carousel	Carousel
	Capacity	10	10
	Max Tool Diameter (full)	3.5 "	89 mm
	Max Tool Weight	12 lb.	5.4 kg
	Tool-to-Tool (average)	5.7 sec	5.7 sec
	Chip-to-Chip (average)	6.5 sec	6.5 sec
General	Air Required	4 scfm, 100 psi	113 L/min, 6.9 bar
	Machine Weight	3240 lb.	1470 kg

A. 2 TECHNICAL SPECIFICATIONS OF FORCE MEASUREMENT SYSTEMS

Table A. 2. Technical specifications of Kistler Type 9123C rotating dynamometer

Speed	Maximum (rpm)	10 000
Range 1 FSO	F_x, F_y (kN)	- 5 ……5*, -3…..3**
	F_z (kN)	- 20……..20
	M_z (Nm)	- 200…...200
Range 2 FSO (switch table)	F_x, F_y (N)	- 500……500
	F_z (kN)	- 2……..2
	M_z (Nm)	- 20……20
Overload range 1	%	20
Threshold	F_x, F_y (N)	< 1
	F_z (N)	< 4
	M_z (Nm)	< 0.04
Sensibility (Range 1)	F_x, F_y (mV/N)	≈ 2
	F_z (mV/N)	≈ 0.5
	M_z (mV/N)	≈ 50
Linearity	% FSO	≤ ± 1
Hysteresis	% FSO	≤ 1
Crosstalk	$F_x \leftrightarrow F_y$ (%)	≤ ± 2
	$F_z \rightarrow F_{x,\,y}$ (%)	≤ ± 3
	$F_{x,\,y} \rightarrow F_z$ (%)	≤ ± 3
	$M_z \rightarrow F_z$ 1 N/Ncm	≤ ± 0.01
Natural frequency measured without telemetry	fn (kHz)	≈ 2
Operating temperature range	^{0}C	0…..60
Coolant pressure	bar	≤ 70
Degree of protection		IP67
weight	kg	≈ 3

* Force application point on the top plate area

** Force application point 100 mm above top plate area

Table A. 3. Technical specifications for Kistler Type 5223 signal conditioner

Ratio range 1 / range		2 10
Number of channels		5
Number of ranges per channel		2
Cut-off frequency per channel	f-cutoff (kHz)	1
Sampling rate per channel	(kHz)	7.8
Resolution/tolerance	bit/%	12/±0,025
Signal output (FSO)	(V)	±10
Output connector (analog signal)		5 x BNC neg. 15 pin D-Sub
Operating temperature range	^{0}C	0………60
Power supply (switchable)	V/AC	230/115
	%	+15/-22
	Hz	48….62
Power consumption	VA	≈ 30
Weight	kg	8
Interface for remote control		RS-232C

A. 3 TECHNICAL SPECIFICATIONS OF VIBRATION MEASUREMENT SYSTEMS

Table A. 4. Technical specifications of high frequency accelerometers

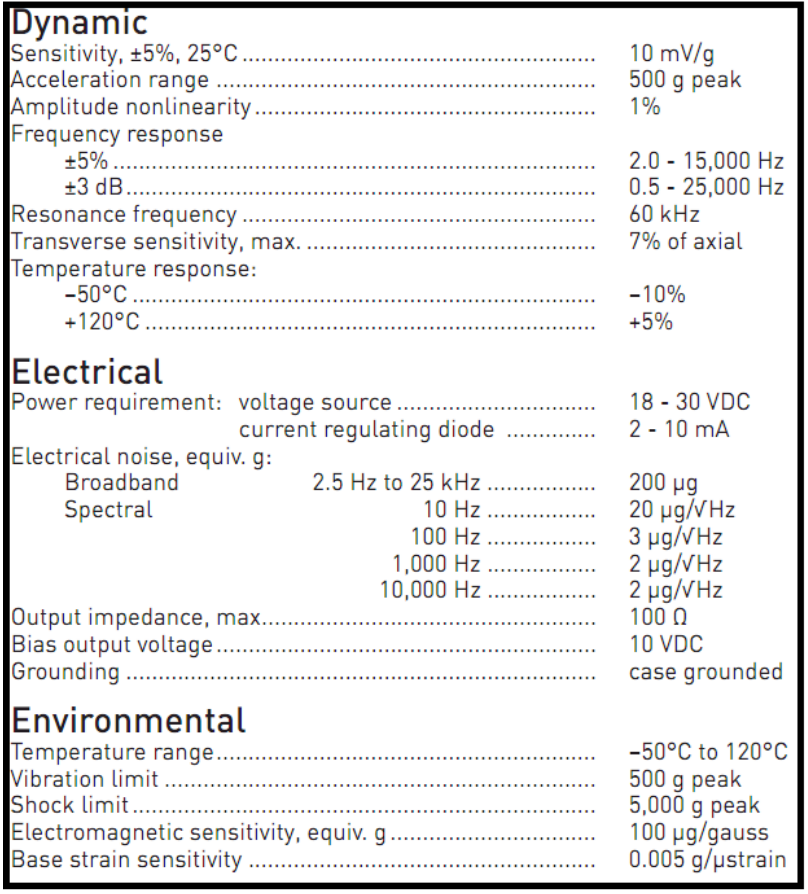

Dynamic	
Sensitivity, ±5%, 25°C	10 mV/g
Acceleration range	500 g peak
Amplitude nonlinearity	1%
Frequency response	
±5%	2.0 - 15,000 Hz
±3 dB	0.5 - 25,000 Hz
Resonance frequency	60 kHz
Transverse sensitivity, max.	7% of axial
Temperature response:	
−50°C	−10%
+120°C	+5%
Electrical	
Power requirement: voltage source	18 - 30 VDC
current regulating diode	2 - 10 mA
Electrical noise, equiv. g:	
Broadband 2.5 Hz to 25 kHz	200 µg
Spectral 10 Hz	20 µg/√Hz
100 Hz	3 µg/√Hz
1,000 Hz	2 µg/√Hz
10,000 Hz	2 µg/√Hz
Output impedance, max.	100 Ω
Bias output voltage	10 VDC
Grounding	case grounded
Environmental	
Temperature range	−50°C to 120°C
Vibration limit	500 g peak
Shock limit	5,000 g peak
Electromagnetic sensitivity, equiv. g	100 µg/gauss
Base strain sensitivity	0.005 g/µstrain

A. 4. AE ACQUISITION PROCESSING FEATURES AND SPECIFICATIONS

Table A. 5. AE signal processing features and specifications

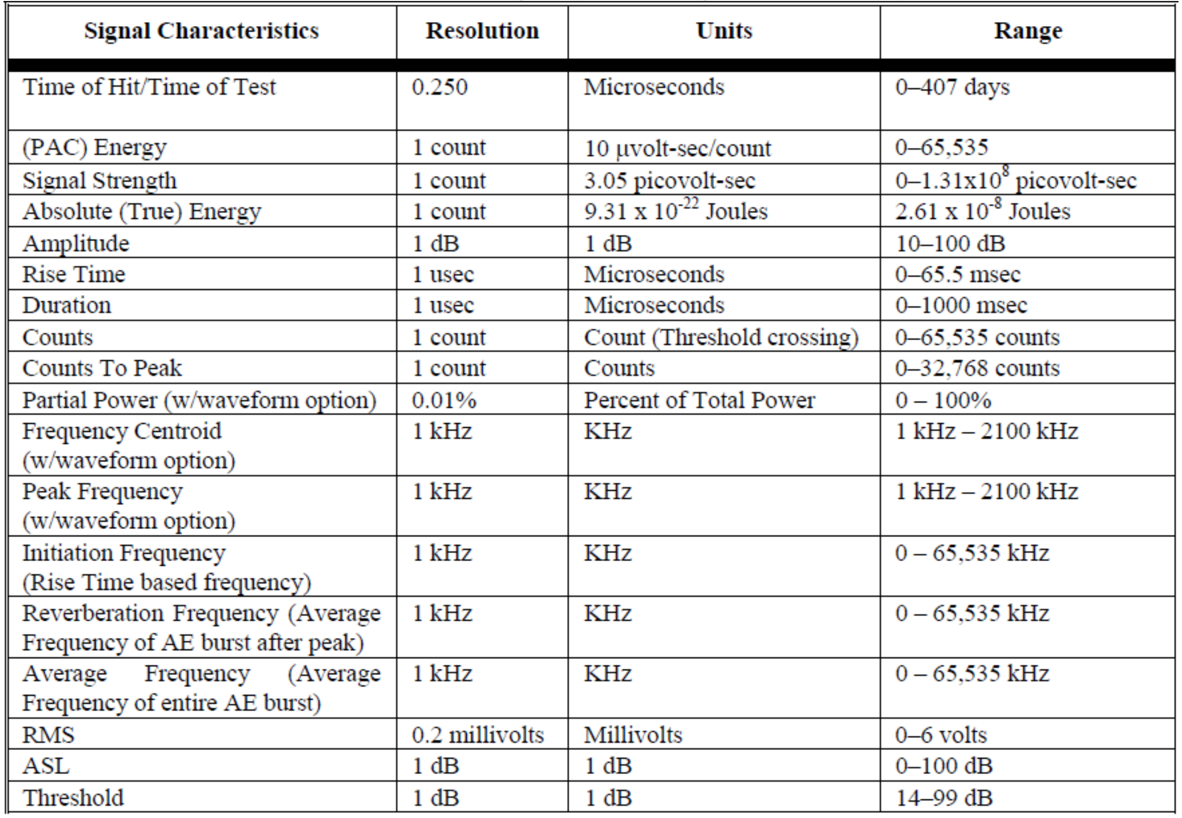

Signal Characteristics	**Resolution**	**Units**	**Range**
Time of Hit/Time of Test	0.250	Microseconds	0–407 days
(PAC) Energy	1 count	10 µvolt-sec/count	0–65,535
Signal Strength	1 count	3.05 picovolt-sec	0–1.31x10^{8} picovolt-sec
Absolute (True) Energy	1 count	9.31 x 10^{-22} Joules	2.61 x 10^{-8} Joules
Amplitude	1 dB	1 dB	10–100 dB
Rise Time	1 usec	Microseconds	0–65.5 msec
Duration	1 usec	Microseconds	0–1000 msec
Counts	1 count	Count (Threshold crossing)	0–65,535 counts
Counts To Peak	1 count	Counts	0–32,768 counts
Partial Power (w/waveform option)	0.01%	Percent of Total Power	0 – 100%
Frequency Centroid (w/waveform option)	1 kHz	KHz	1 kHz – 2100 kHz
Peak Frequency (w/waveform option)	1 kHz	KHz	1 kHz – 2100 kHz
Initiation Frequency (Rise Time based frequency)	1 kHz	KHz	0 – 65,535 kHz
Reverberation Frequency (Average Frequency of AE burst after peak)	1 kHz	KHz	0 – 65,535 kHz
Average Frequency (Average Frequency of entire AE burst)	1 kHz	KHz	0 – 65,535 kHz
RMS	0.2 millivolts	Millivolts	0–6 volts
ASL	1 dB	1 dB	0–100 dB
Threshold	1 dB	1 dB	14–99 dB

APPENDIX B – SURFACE ROUGHNESS RESULTS FOR MULTI-DIRECTIONAL CFRP WITH FIBERGLASS SCRIM SURFACE PLIES

An abbreviation symbols were used in the measurement and presentation of surface roughness parameters as well as in surface profile plots. The designation of these abbreviations is shown in Figure B. 1.

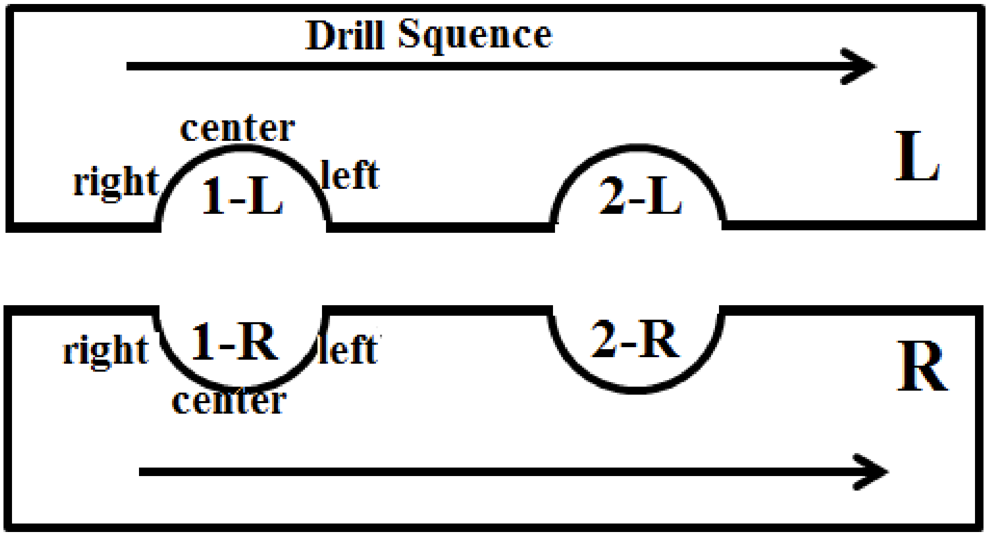

Figure B. 1. Designation of abbreviations used in surface roughness results and profiles

B. 1 SURFACE ROUGHNESS PROFILES FOR MULTI-DIRECTIONAL CFRP WITH FIBERGLASS SCRIM SURFACE PLIES

Surface roughness profiles for holes drilled on multi-directional CFRP composite with fiberglass scrim surface plies are given in Table B. 1. The given profiles are taken at six different locations for each hole as shown in Figure B. 1 for lower and higher level combinations of feed rate and cutting speed.

Table B. 1. Surface profiles for multi-directional CFRP with fiberglass scrim surface plies

Speed	Feed	Section	Location	Profiles
3000 rpm	50 µm/rev	1-L	Center	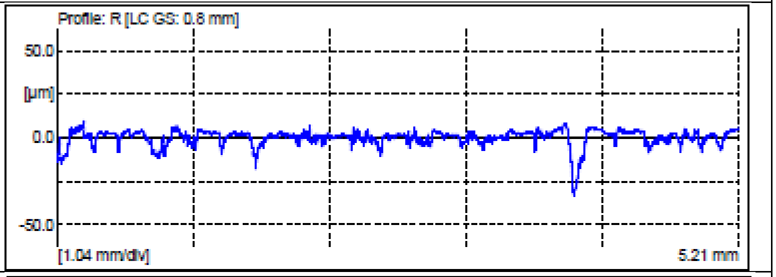
		1-L	Left	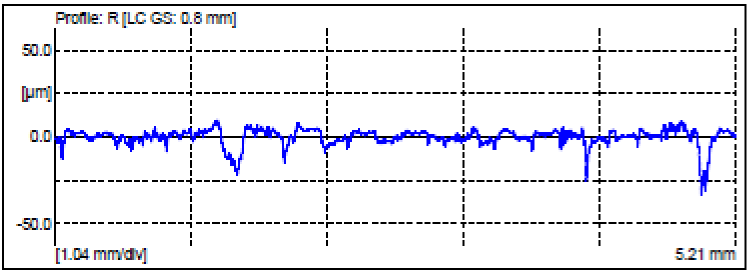
		1-L	Right	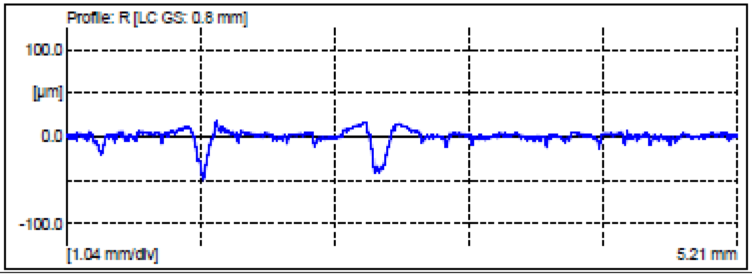
		1-R	Center	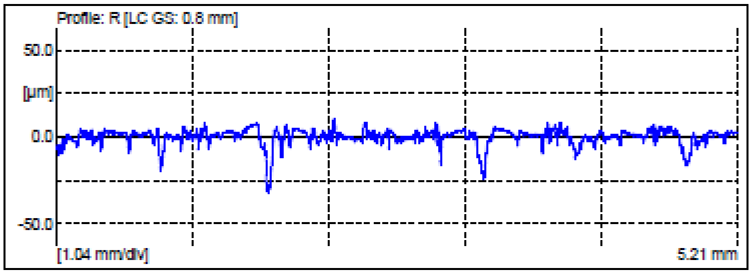
		1-R	Left	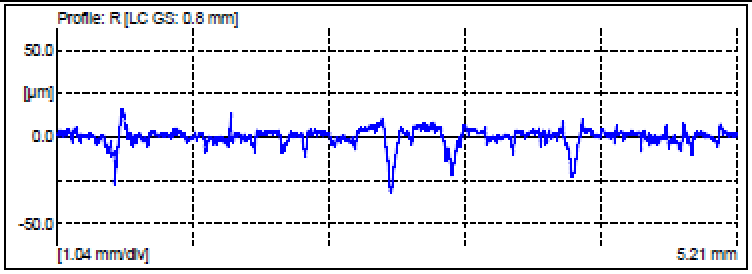
		1-R	Right	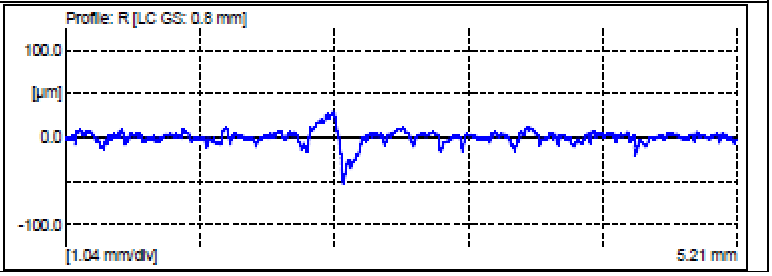

Table B. 1. Continued

Speed	Feed	Section	Location	Profiles
3000 rpm	50 µm/rev	2-L	Center	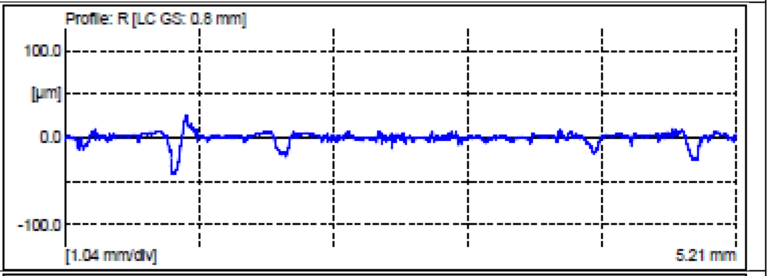
		2-L	Left	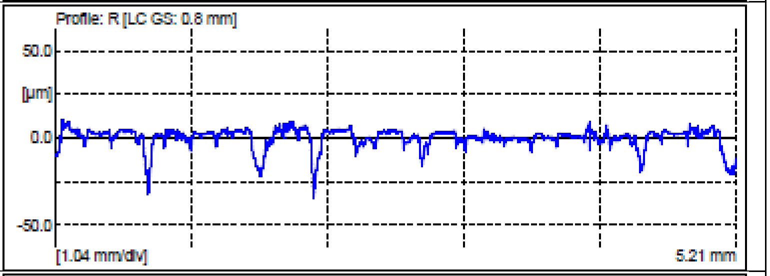
		2-L	Right	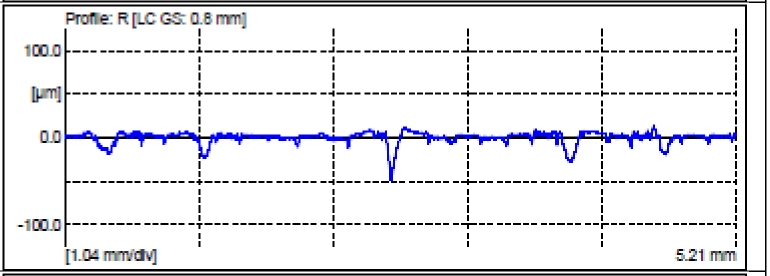
		2-R	Center	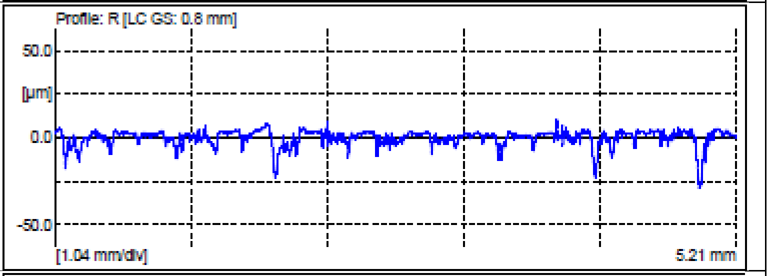
		2-R	Left	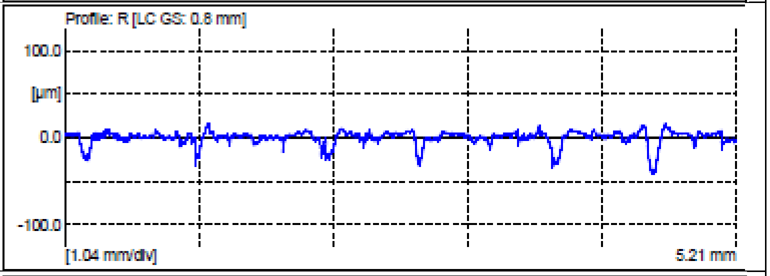
		2-R	Right	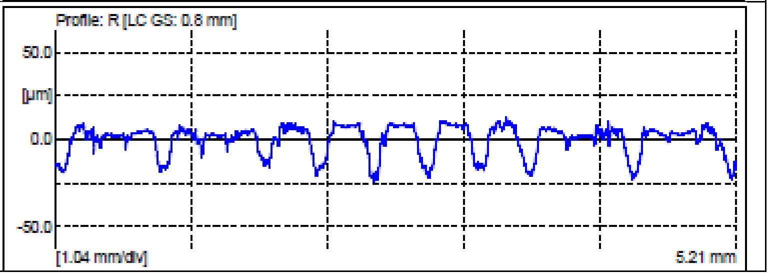

Table B. 1. Continued

Speed	Feed	Section	Location	Profiles
3000 rpm	200 µm/rev	1-L	Center	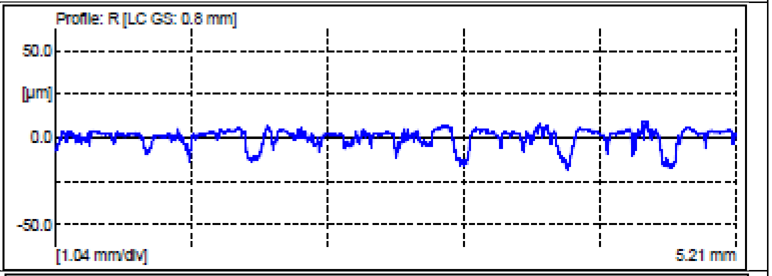
		1-L	Left	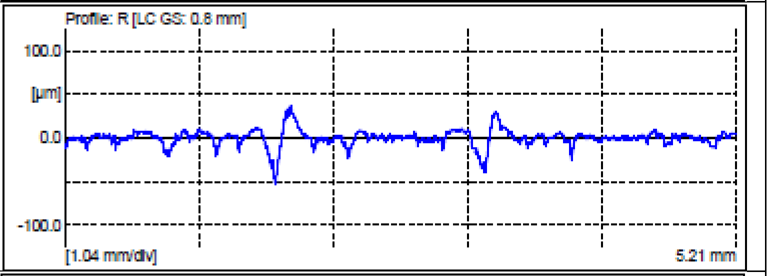
		1-L	Right	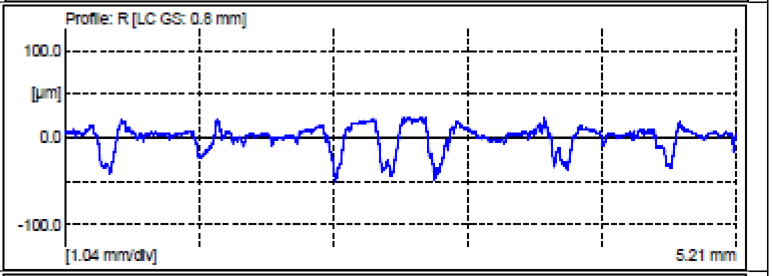
		1-R	Center	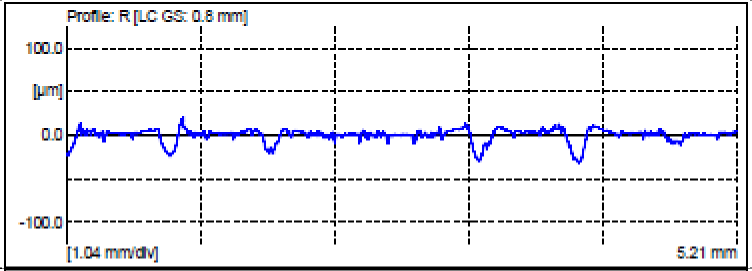
		1-R	Left	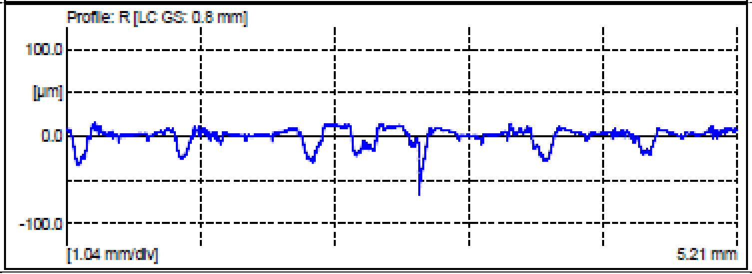
		1-R	Right	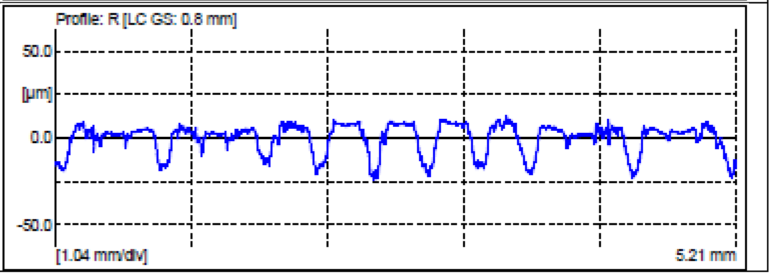

Table B. 1. Continued

Speed	Feed	Section	Location	Profiles
3000 rpm	200 µm/rev	2-L	Center	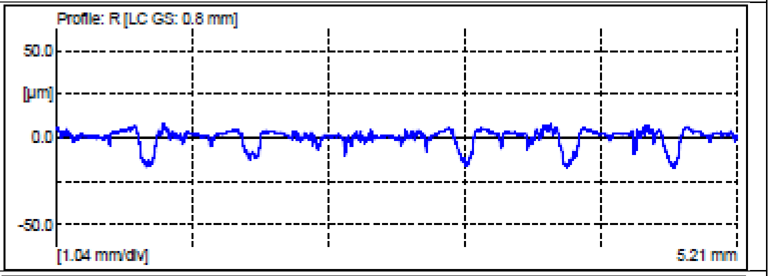
		2-L	Left	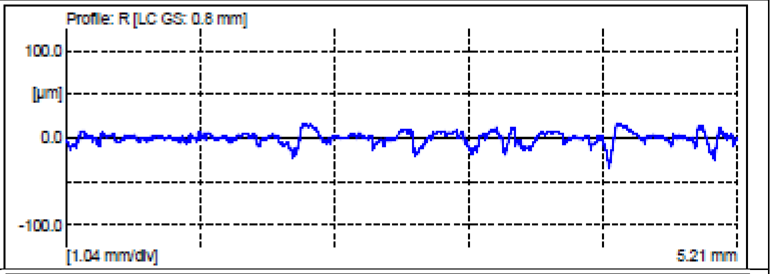
		2-L	Right	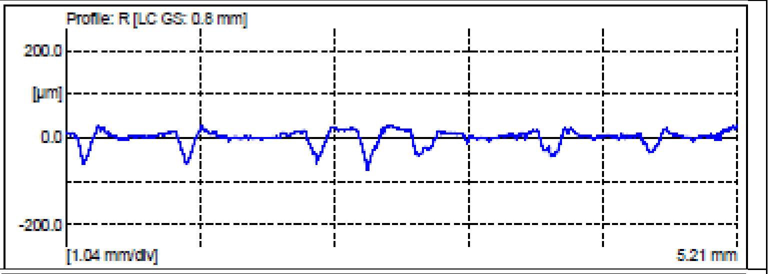
		2-R	Center	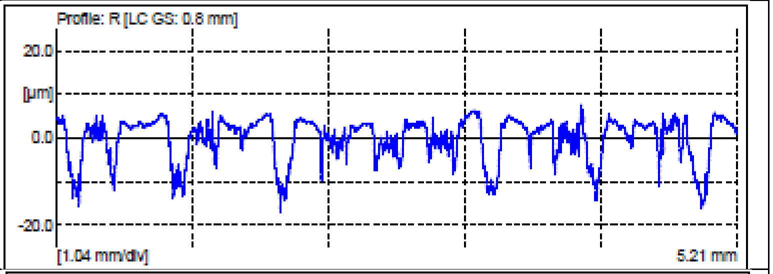
		2-R	Left	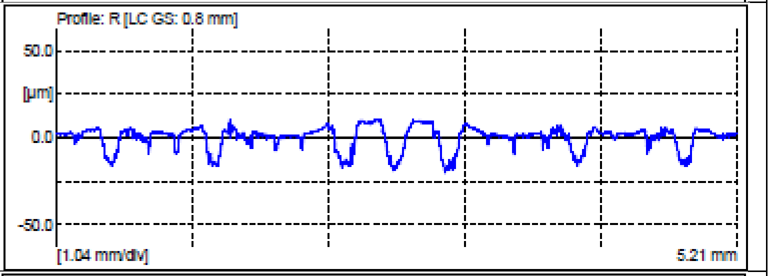
		2-R	Right	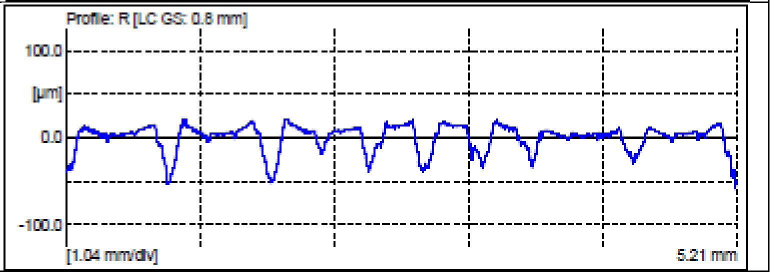

Table B. 1. Continued

Speed	Feed	Section	Location	Profiles
6000 rpm	50 µm/rev	1-L	Center	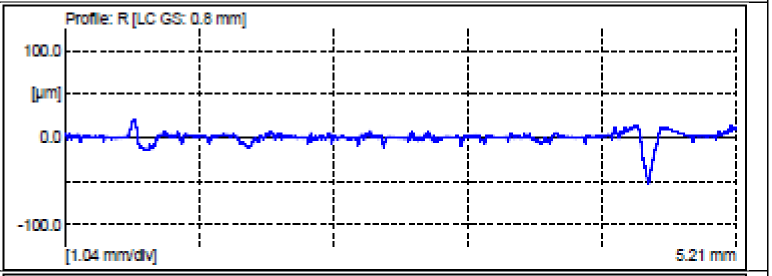
		1-L	Left	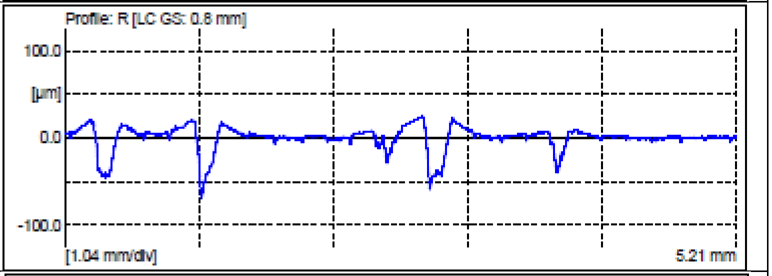
		1-L	Right	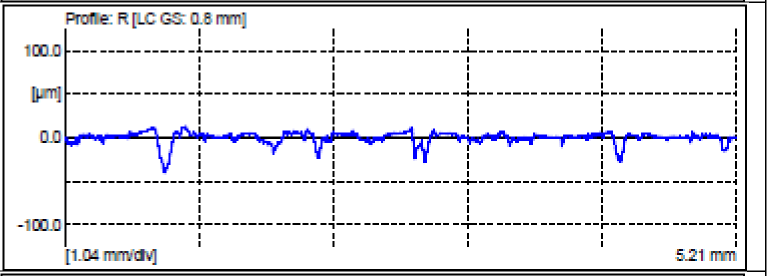
		1-R	Center	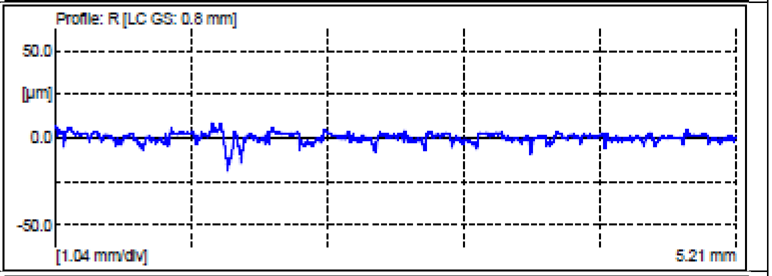
		1-R	Left	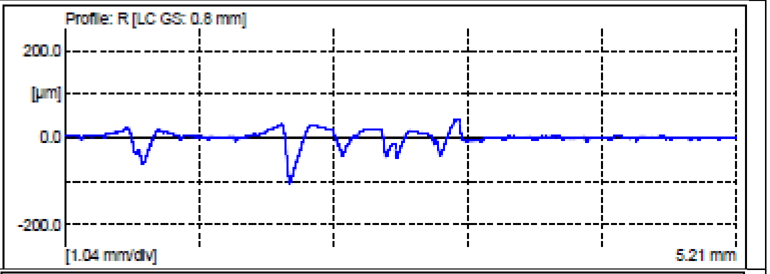
		1-R	Right	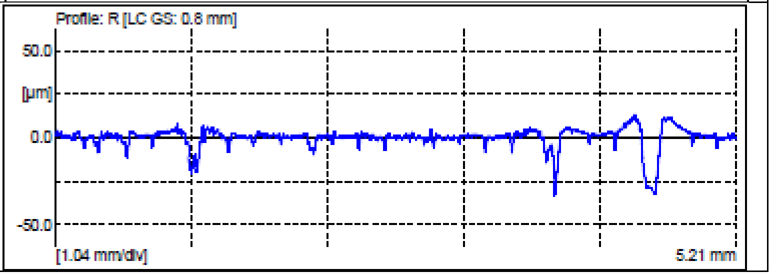

Table B. 1. Continued

Speed	Feed	Section	Location	Profiles
6000 rpm	50 µm/rev	2-L	Center	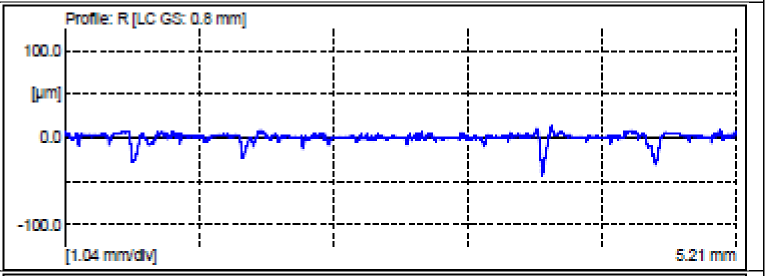
		2-L	Left	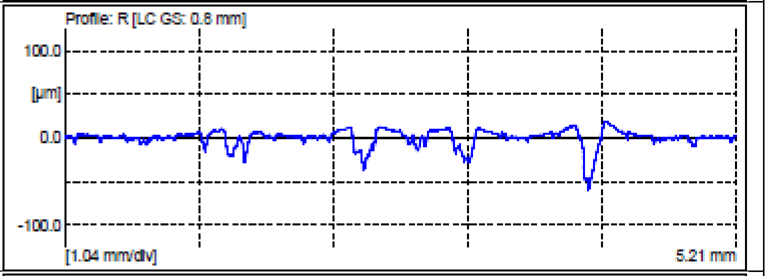
		2-L	Right	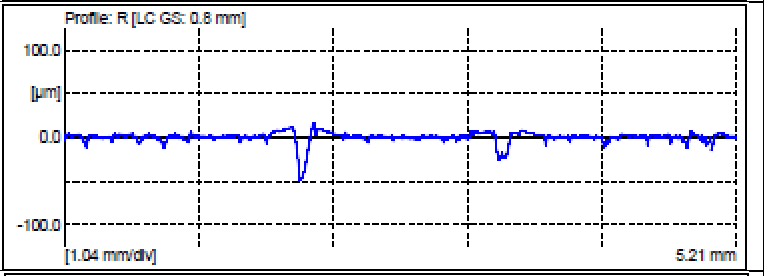
		2-R	Center	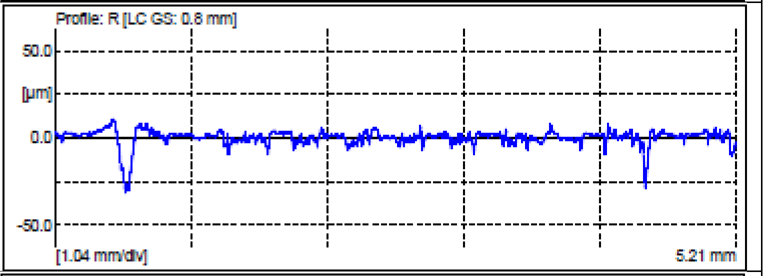
		2-R	Left	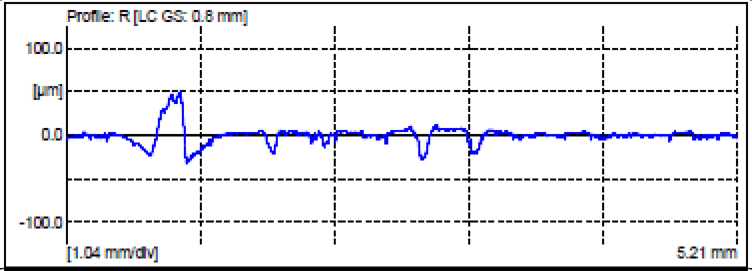
		2-R	Right	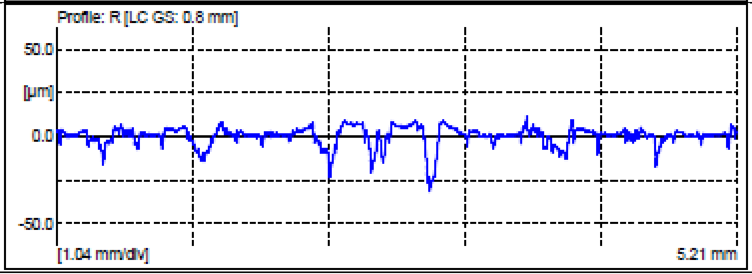

Table B. 1. Continued

Speed	Feed	Section	Location	Profiles
6000 rpm	50 µm/rev	3-L	Center	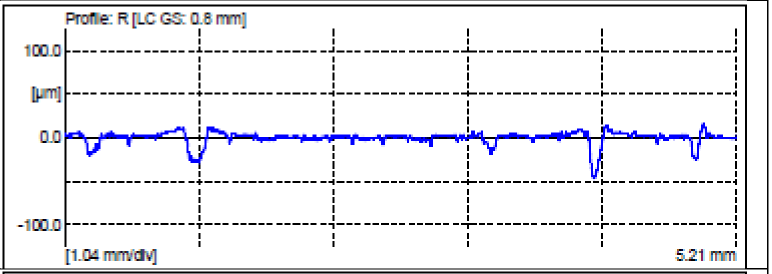
		3-L	Left	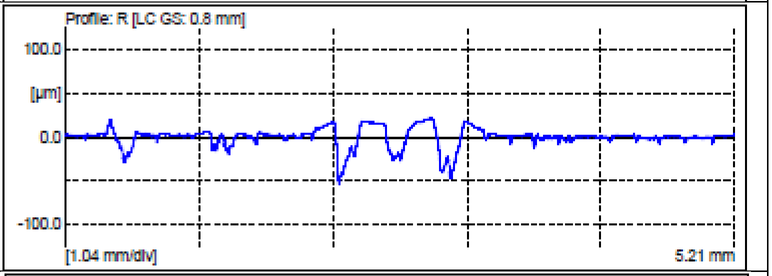
		3-L	Right	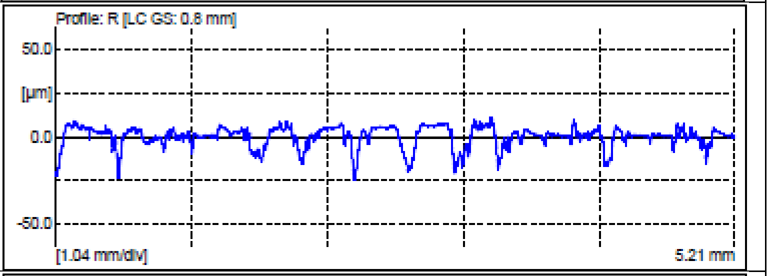
		3-R	Center	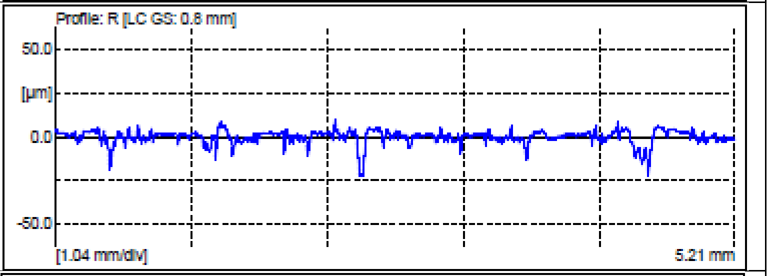
		3-R	Left	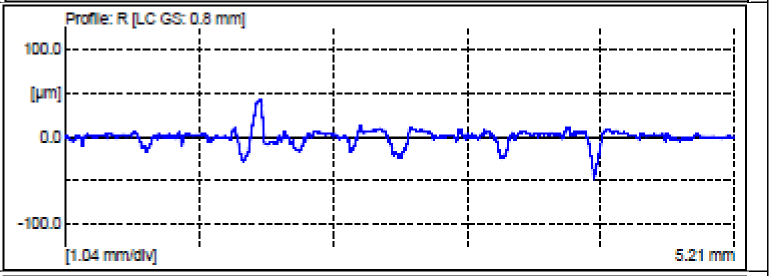
		3-R	Right	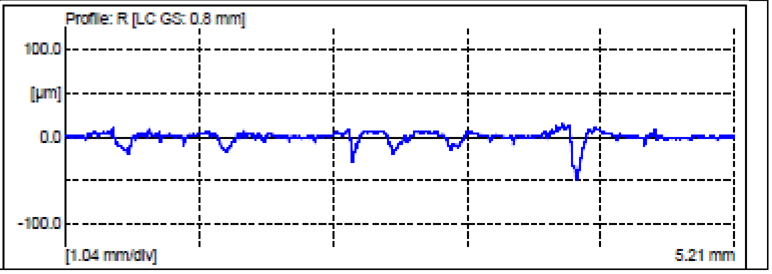

Table B. 1. Continued

Speed	Feed	Section	Location	Profiles
6000 rpm	50 µm/rev	4-L	Center	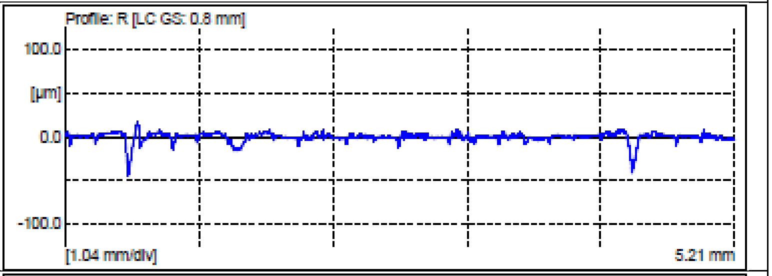
		4-L	Left	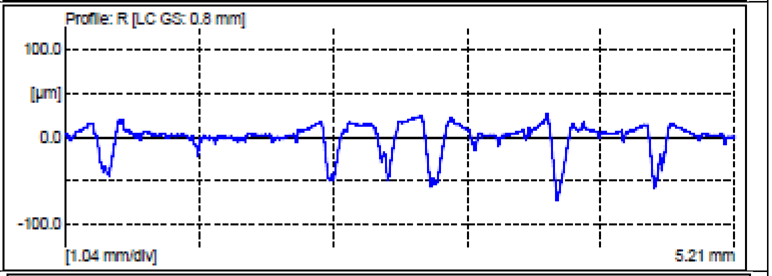
		4-L	Right	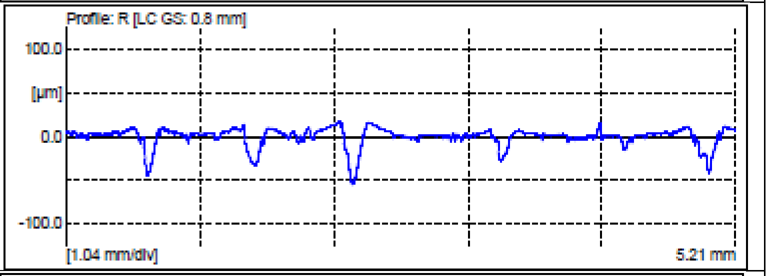
		4-R	Center	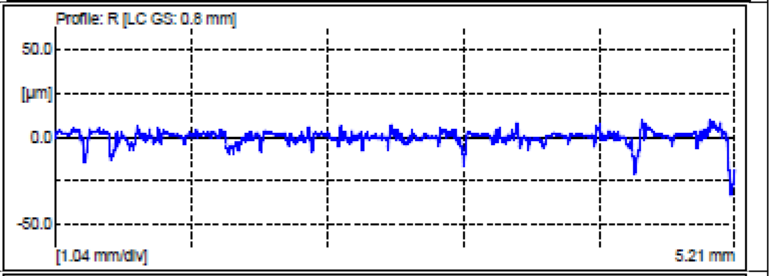
		4-R	Left	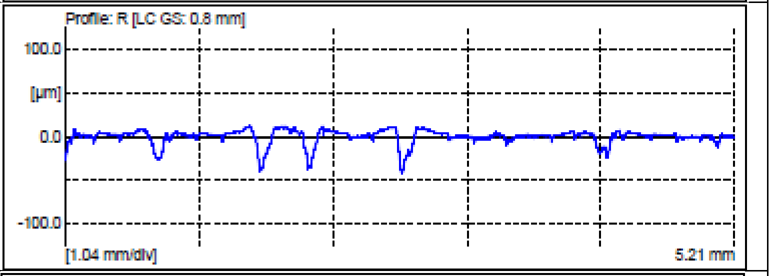
		4-R	Right	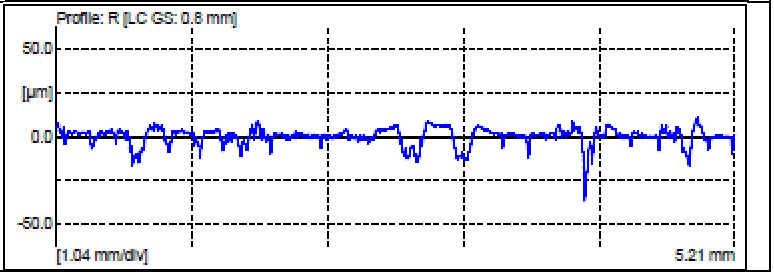

Table B. 1. Continued

Speed	Feed	Section	Location	Profiles
6000 rpm	200 µm/rev	1-L	Center	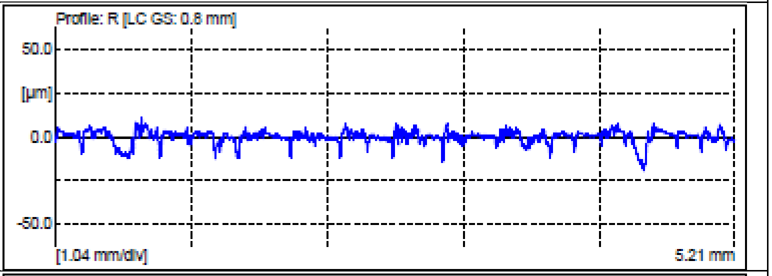
		1-L	Left	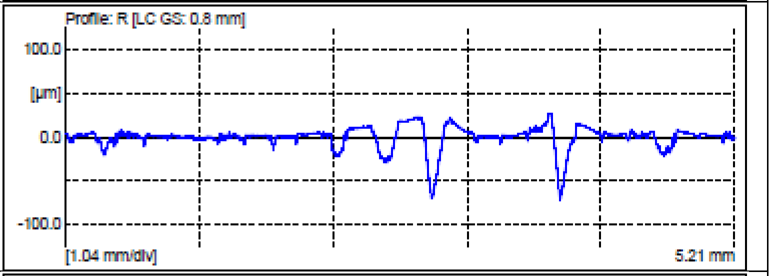
		1-L	Right	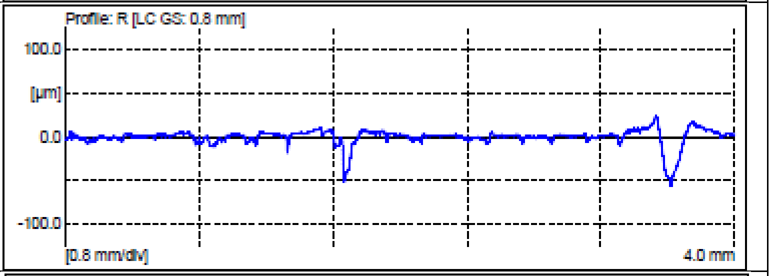
		1-R	Center	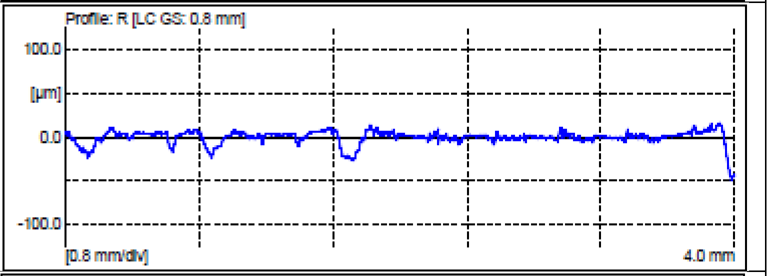
		1-R	Left	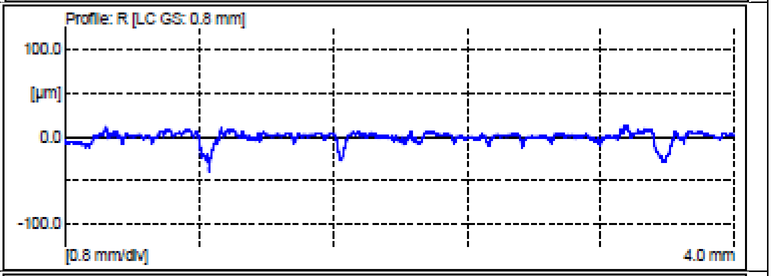
		1-R	Right	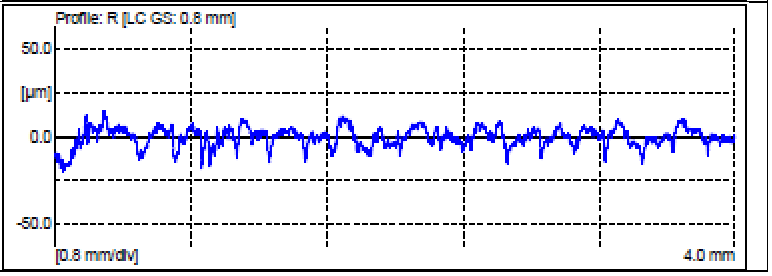

Table B. 1. Continued

Speed	Feed	Section	Location	Profiles
6000 rpm	200 µm/rev	2-L	Center	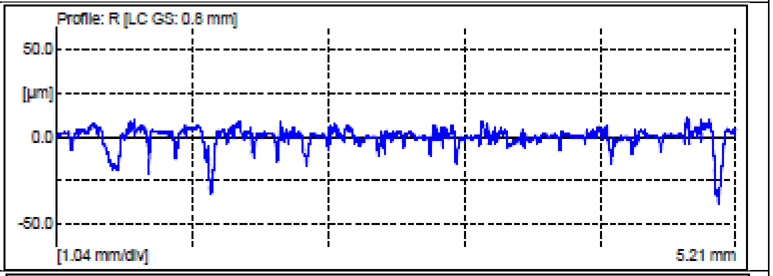
		2-L	Left	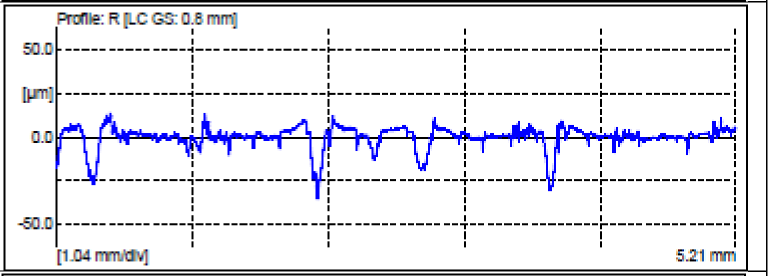
		2-L	Right	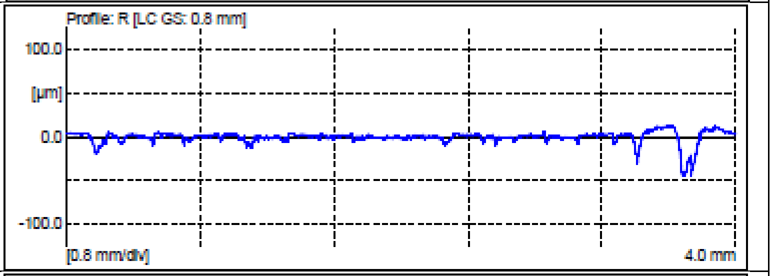
		2-R	Center	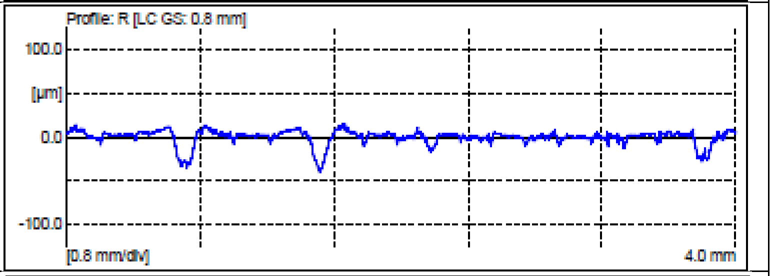
		2-R	Left	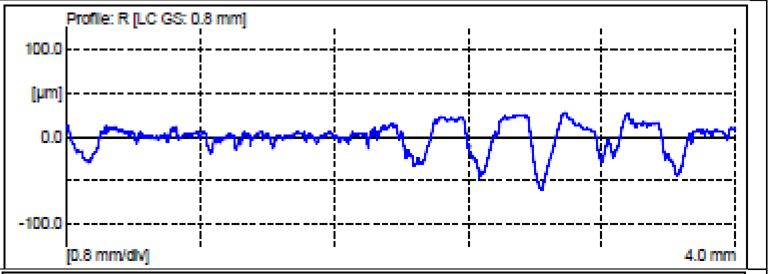
		2-R	Right	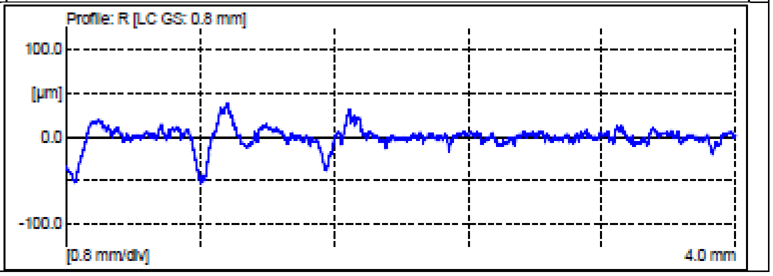

Table B. 1. Continued

Speed	Feed	Section	Location	Profiles
6000 rpm	200 µm/rev	3-L	Center	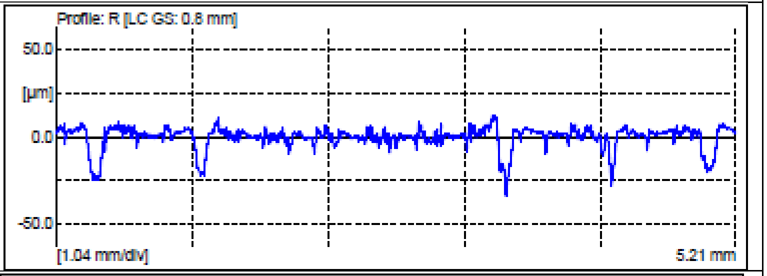
		3-L	Left	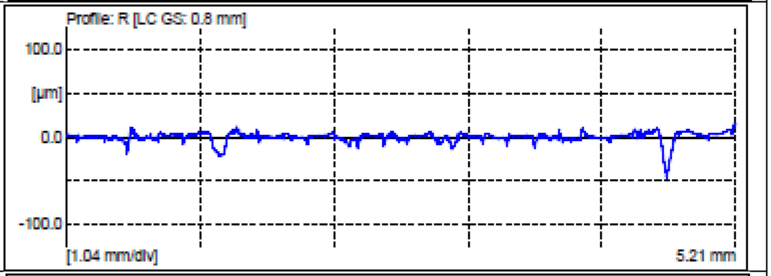
		3-L	Right	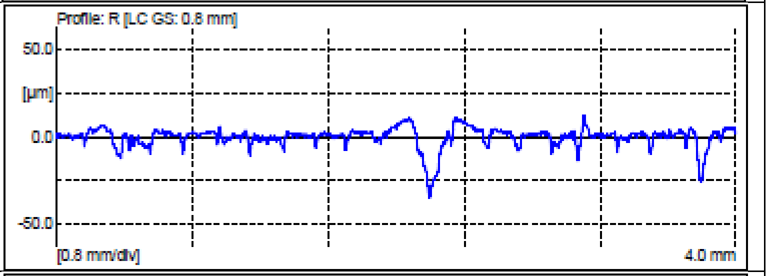
		3-R	Center	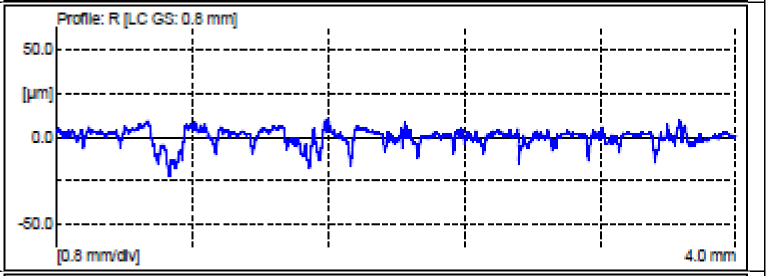
		3-R	Left	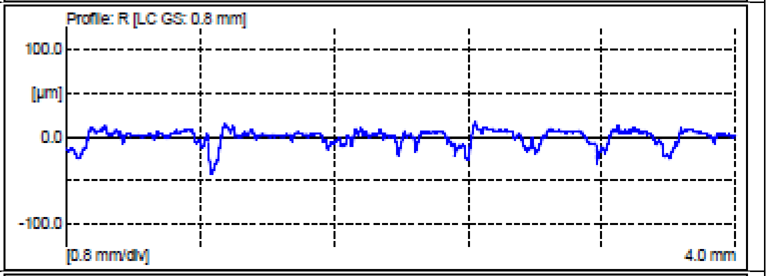
		3-R	Right	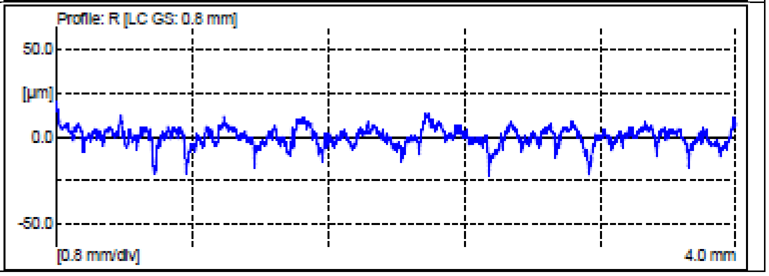

Table B. 1. Continued

Speed	Feed	Section	Location	Profiles
6000 rpm	200 µm/rev	4-L	Center	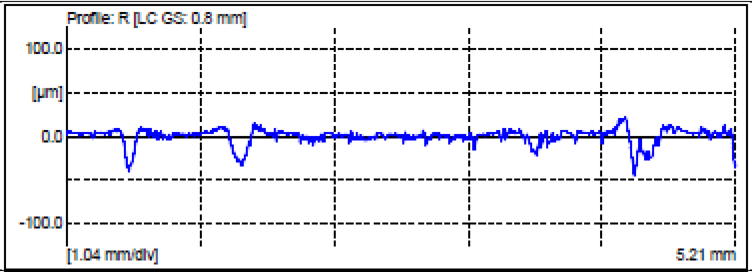
		4-L	Left	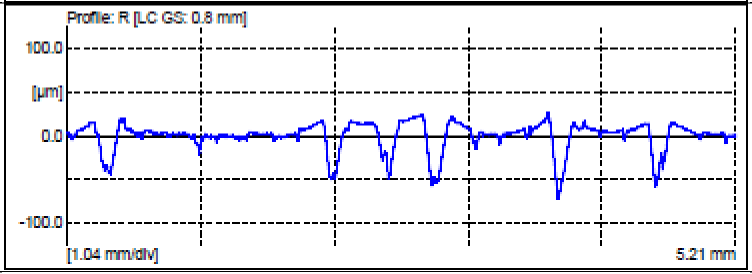
		4-L	Right	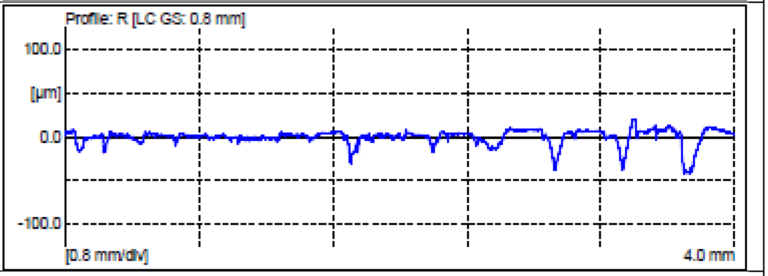
		4-R	Center	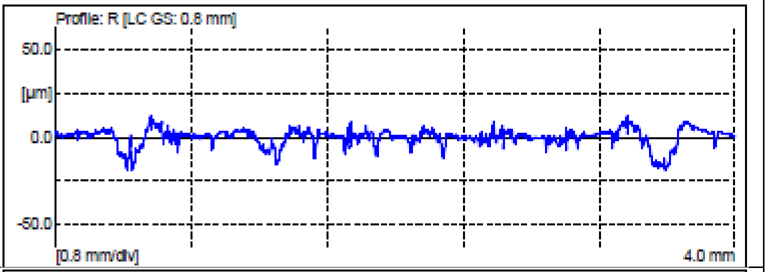
		4-R	Left	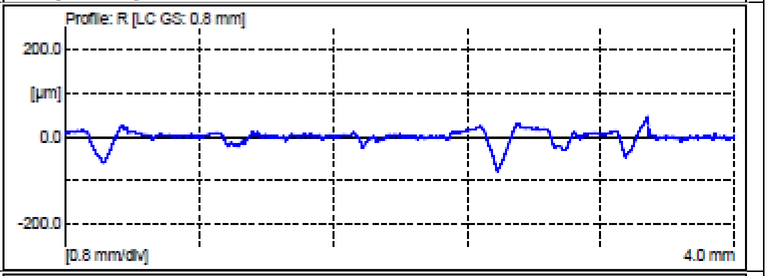
		4-R	Right	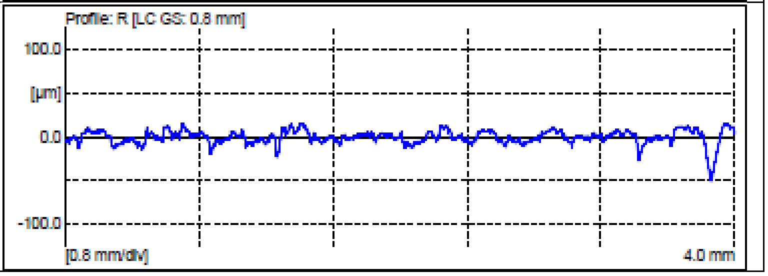

B. 2 ROUGHNESS PARAMETER VALUES FOR MULTI-DIRECTIONAL CFRP WITH FIBERGLASS SCRIM SURFACE PLIES

Table B. 2. Roughness parameter values for fiberglass scrim surface ply multi-directional CFRP

Speed	Feed	Section	Location	Ra (µm)	Rq (µm)	Rz (µm)	Rt (µm)
3000 rpm	50 µm/rev	1-L	Left	3.263	4.987	25.824	43.162
			Center	3.081	4.647	24.105	42.660
			Right	4.715	8.288	40.736	66.384
		1-R	Left	3.408	5.195	32.554	48.154
			Center	3.027	4.748	29.173	42.090
			Right	4.784	7.919	40.377	81.932
		2-L	Left	3.784	5.752	30.834	45.193
			Center	3.913	6.838	35.612	67.397
			Right	4.309	6.855	36.569	61.617
		2-R	Left	5.236	8.081	45.837	57.825
			Center	3.135	4.621	28.265	39.890
			Right	3.041	4.144	24.574	30.692
	200 µm/rev	1-L	Left	5.675	9.168	48.207	89.011
			Center	3.690	4.959	23.094	28.157
			Right	10.003	13.964	59.471	74.076
		1-R	Left	7.022	9.936	50.017	82.163
			Center	4.982	7.559	31.386	52.710
			Right	6.596	8.393	31.794	35.954
		2-L	Left	4.834	6.757	34.399	50.925
			Center	3.467	4.921	22.295	25.149
			Right	12.057	17.177	80.488	103.554
		2-R	Left	4.788	6.414	24.981	30.541
			Center	3.841	4.881	20.110	24.110
			Right	11.471	15.234	67.174	79.869
6000 rpm	50 µm/rev	1-L	Left	8.259	13.907	58.735	93.705
			Center	3.550	6.638	30.275	74.234
			Right	4.323	6.844	35.470	52.881
		1-R	Left	9.752	17.033	66.641	147.524
			Center	1.922	2.680	15.154	27.308
			Right	3.260	5.950	29.860	45.808
		2-L	Left	6.158	9.815	40.616	77.507
			Center	3.206	5.715	35.012	55.660
			Right	3.236	6.432	29.423	63.887
		2-R	Left	5.524	9.878	36.727	80.675
			Center	2.768	4.612	24.786	42.192
			Right	3.790	5.641	28.014	42.849

Table B. 2. Continued

Speed	Feed	Section	Location	Ra (µm)	Rq (µm)	Rz (µm)	Rt (µm)
6000 rpm	50 µm/rev	3-L	Left	6.683	10.941	39.992	74.580
			Center	4.366	7.583	37.717	63.157
			Right	4.360	6.035	28.841	36.041
		3-R	Left	6.478	8.751	43.295	59.160
			Center	3.480	4.727	25.908	35.880
			Right	4.085	6.835	33.851	63.465
		4-L	Left	6.486	11.217	48.985	107.301
			Center	3.114	5.533	33.796	61.141
			Right	6.682	10.746	54.302	71.711
		4-R	Left	5.219	8.447	38.833	53.902
			Center	2.547	4.165	25.067	43.314
			Right	3.354	4.957	28.075	47.782
	200 µm/rev	1-L	Left	7.505	12.871	54.442	98.399
			Center	2.596	3.734	21.704	30.383
			Right	5.061	9.257	39.229	79.968
		1-R	Left	4.146	6.407	32.817	53.455
			Center	4.982	7.559	31.386	52.710
			Right	4.152	5.379	26.833	34.392
		2-L	Left	4.126	6.601	36.276	49.444
			Center	3.513	5.786	31.947	48.784
			Right	3.841	6.861	25.269	57.877
		2-R	Left	11.695	16.077	56.703	87.864
			Center	5.286	8.331	37.256	57.701
			Right	7.388	12.208	52.516	91.784
		3-L	Left	3.455	5.758	32.865	61.714
			Center	4.064	6.395	32.924	46.258
			Right	6.765	11.270	52.246	87.546
		3-R	Left	6.478	8.751	43.295	59.160
			Center	3.480	4.727	25.908	32.880
			Right	3.968	5.203	31.660	41.665
		4-L	Left	10.747	16.449	76.780	98.914
			Center	5.811	8.872	42.018	65.814
			Right	5.577	8.765	37.156	62.660
		4-R	Left	10.076	15.890	71.665	126.214
			Center	3.390	4.901	34.228	31.299
			Right	5.586	7.845	36.520	65.967

APPENDIX C – OPTICAL MACROGRAPHS OF SECTIONED HOLES FOR MULTI-DIRECTIONAL CFRP WITH FIBERGLASS SCRIM SURFACE PLIES

Drilled holes were sectioned in to two halves for investigation of the surface of the drilled hole and optical macrographs of these sectioned holes for higher level and lower level combinations of the feed rate and cutting speed are given in Table C. 1.

Table C. 1. Optical macrographs of sectioned holes for multi-directional CFRP with fiberglass scrim surface ply.

Speed	Feed	Hole	Left halve	Right halve
3000 rpm	50 μm/rev	1	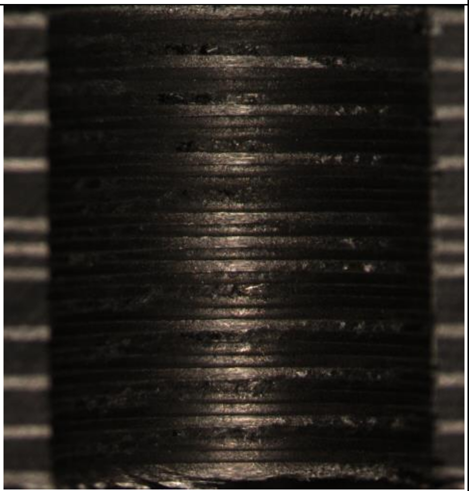	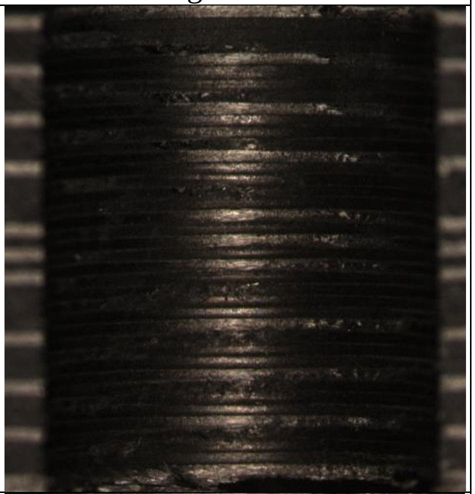
		2	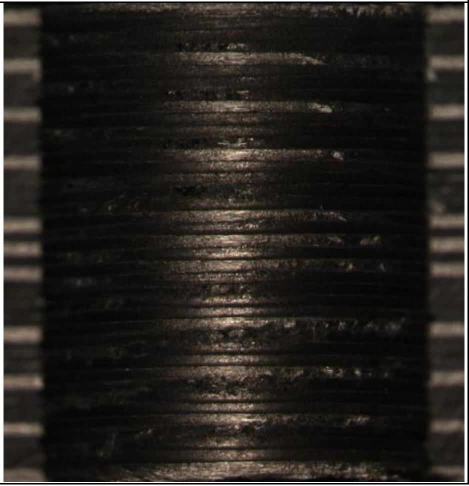	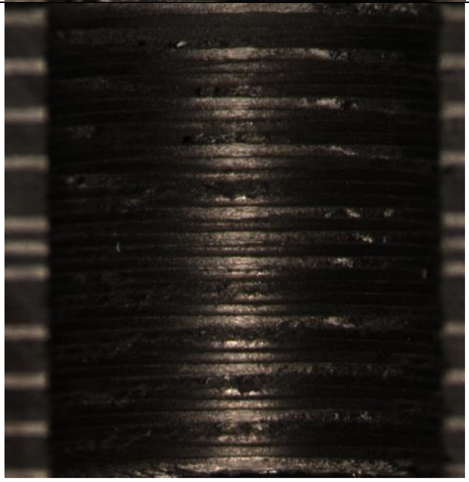

Table C. 1 Continued

Speed	Feed	Hole	Left halve	Right halve
3000 rpm	200 µm/rev	1	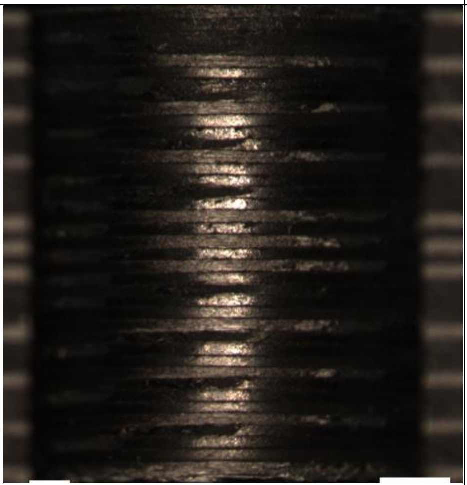	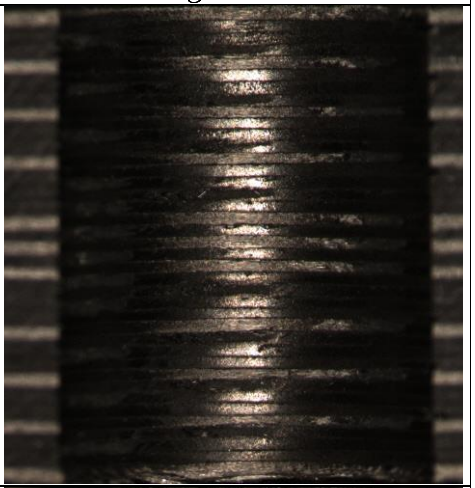
		2	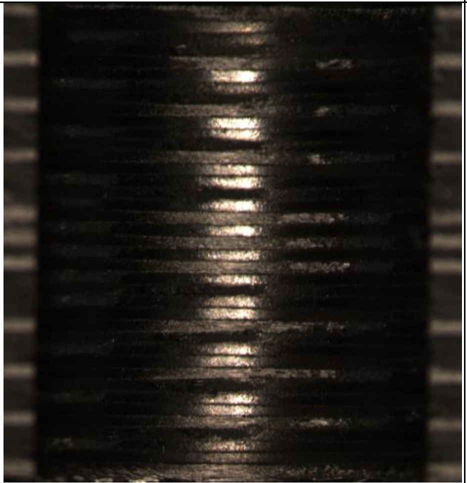	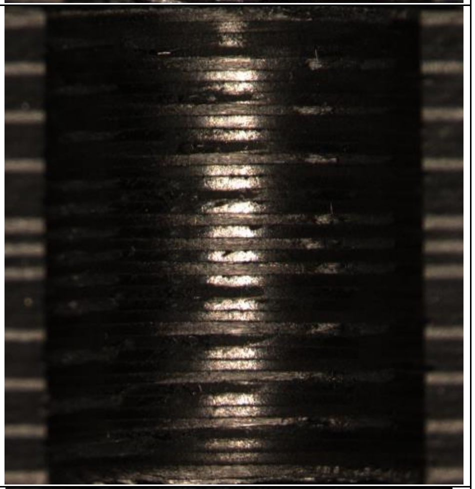
6000 rpm	50 µm/rev	1		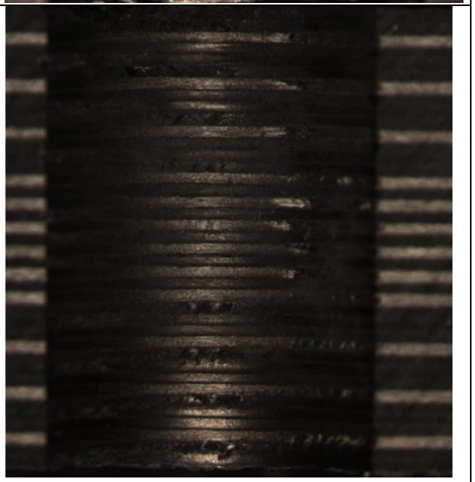

Table C. 1 Continued

Speed	Feed	Hole	Left halve	Right halve
6000 rpm	50 µm/rev	2	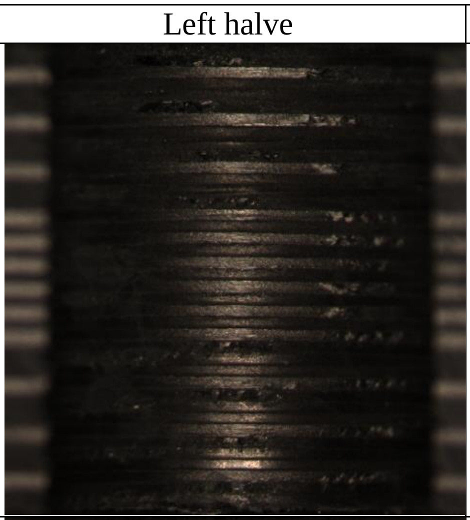	
		3		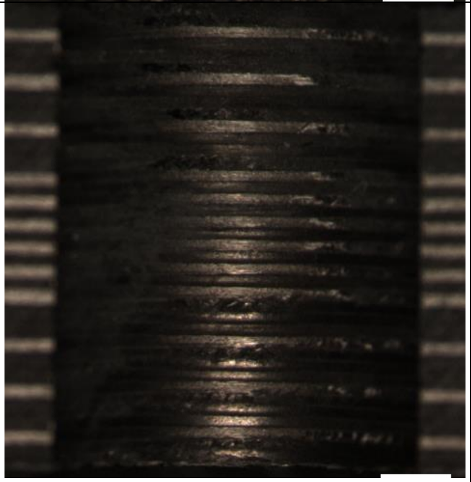
		4	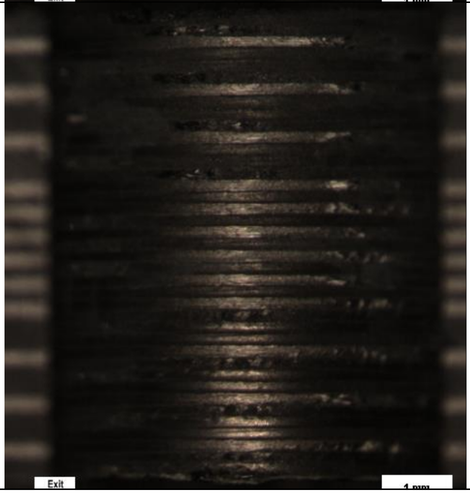	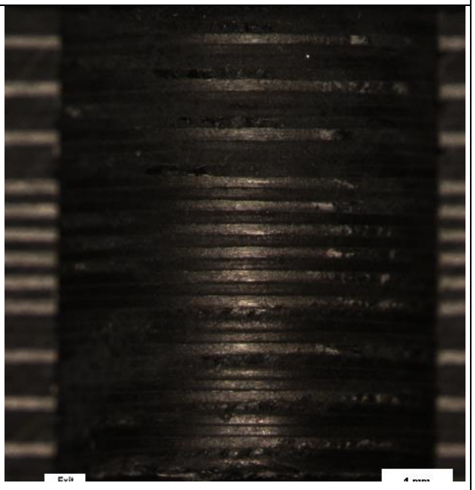

Table C. 1 Continued

Speed	Feed	Hole	Left halve	Right halve
6000 rpm	200 µm/rev	1	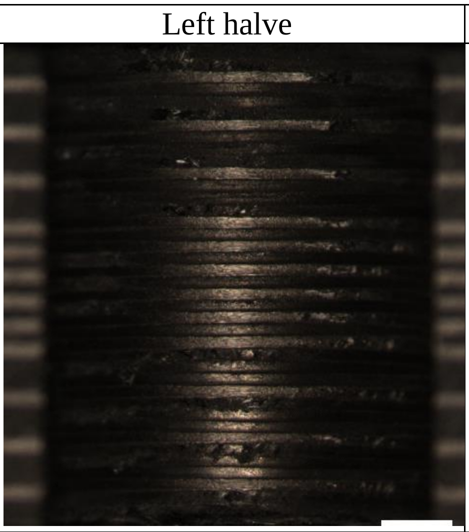	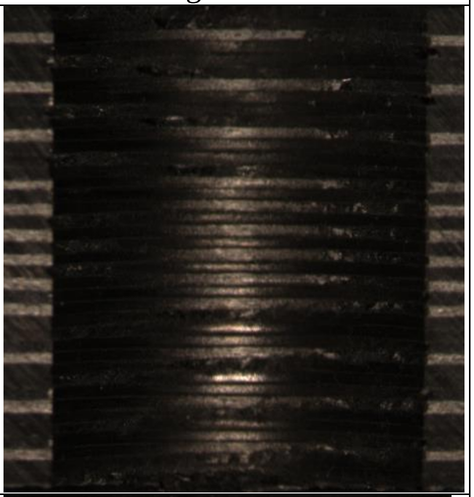
		2	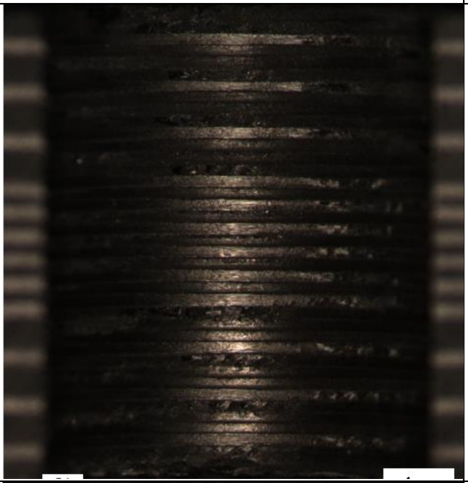	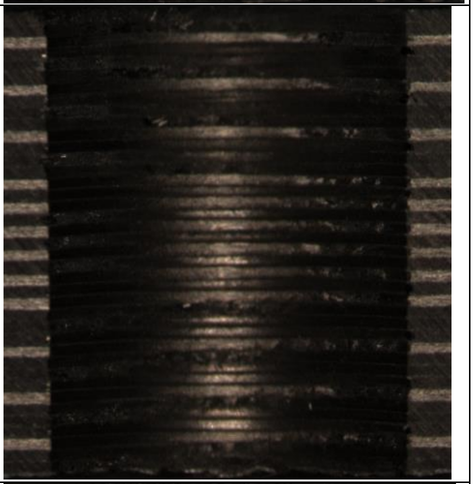
		3	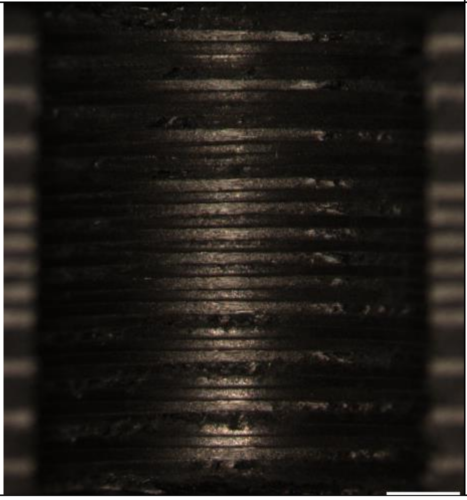	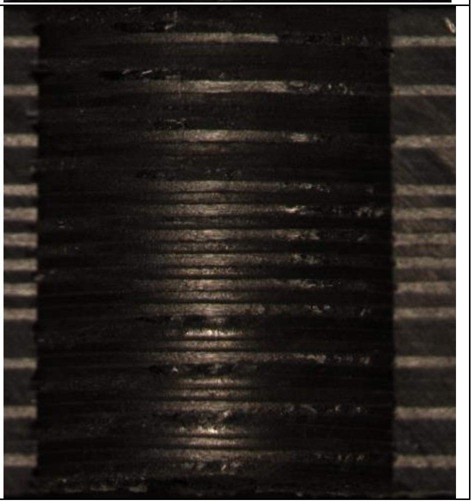

Table C. 1 Continued

Speed	Feed	Hole	Left halve	Right halve
6000 rpm	200 μm/rev	4	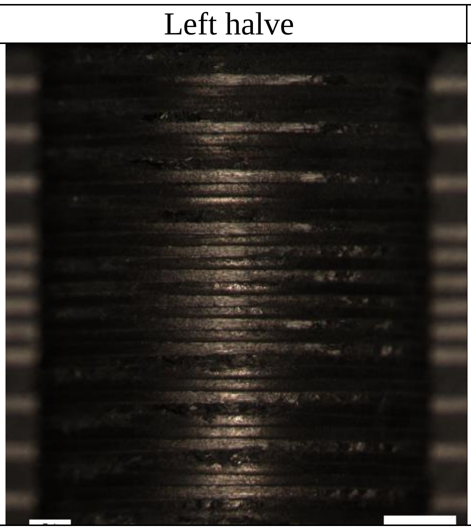	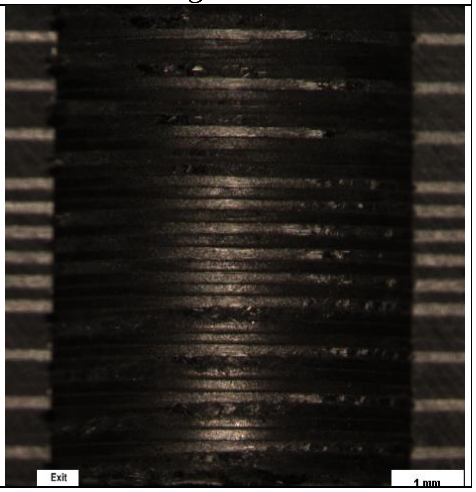

After the optical image of the sectioned halves of the hole was taken, more magnified images were taken at eight locations for each sectioned halve and the images are given in Table C. 2. The locations of imaging area are shown in Figure C. 1.

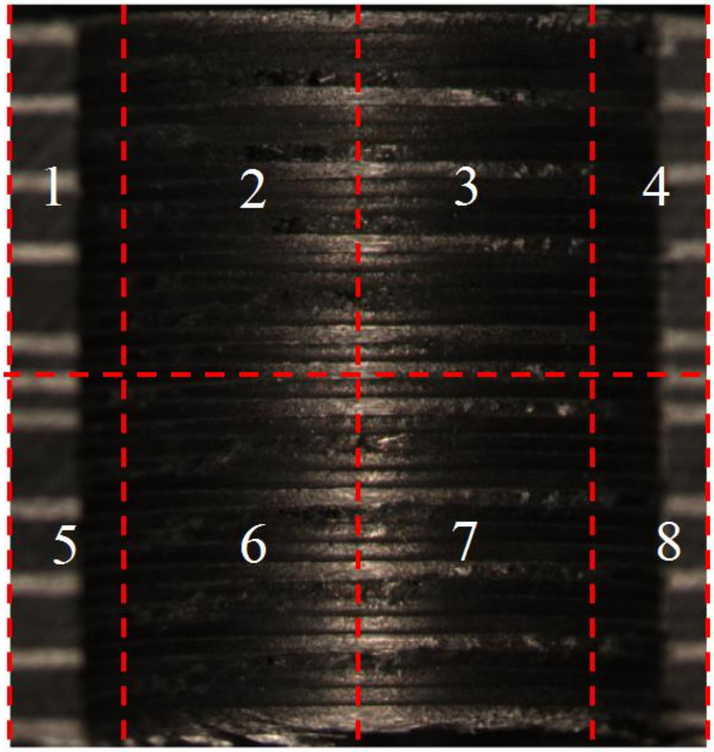

Figure C. 1. Designation of imaging area

Table C. 2. Optical macrographs of hole surface at different locations for multi-directional CFRP with fiberglass scrim surface ply.

Speed	Feed	Hole	Imaging Area – 1	Imaging Area – 4
3000 rpm	50 µm/rev	1-L	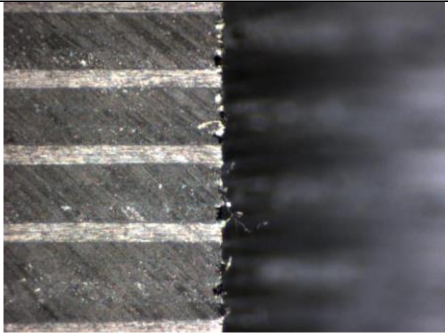	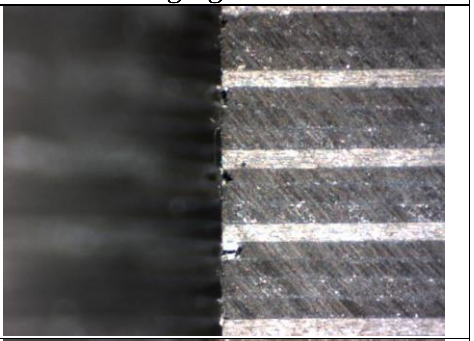
		1-R	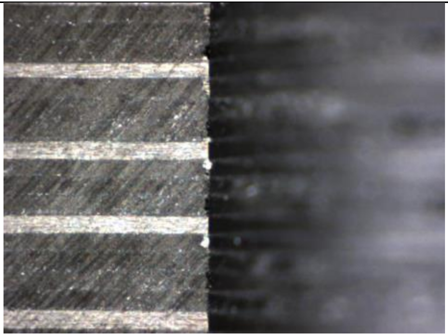	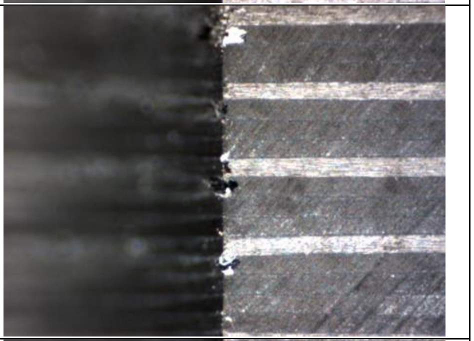
		2-L	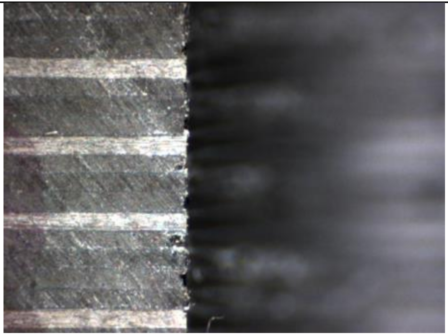	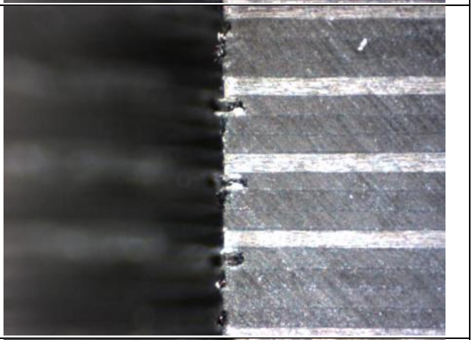
		2-R	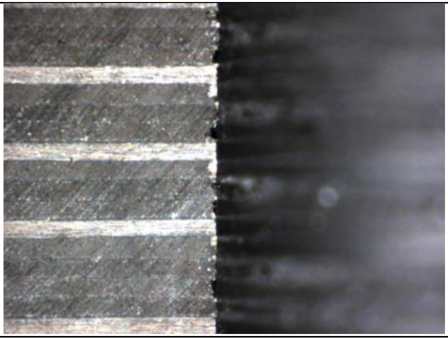	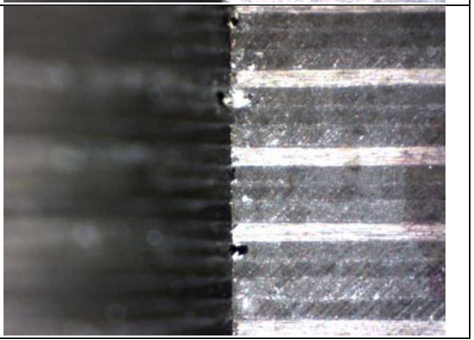

Table C. 2. Continued

Speed	Feed	Hole	Imaging Area – 2	Imaging Area – 3
3000 rpm	50 µm/rev	1-L	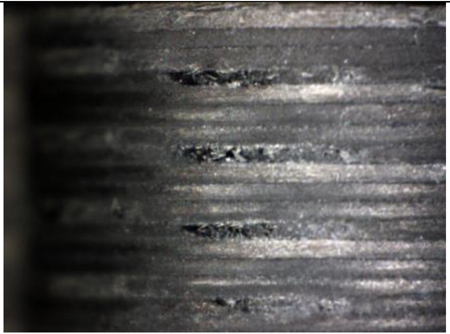	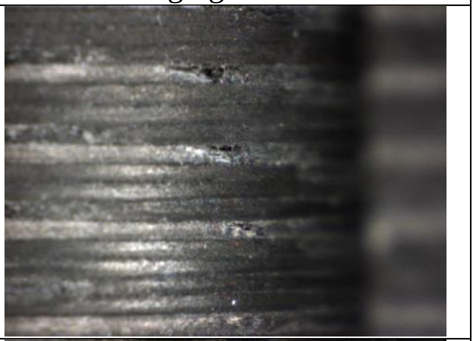
		1-R	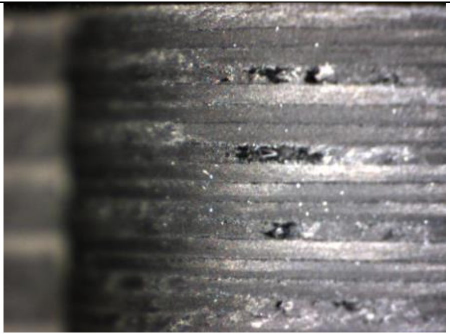	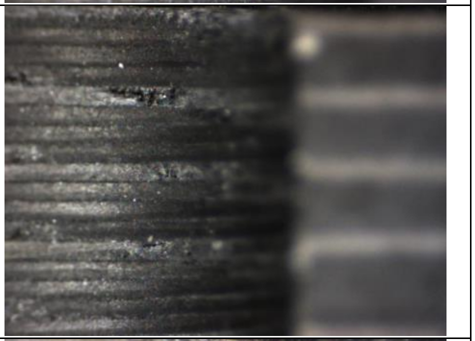
		2-L	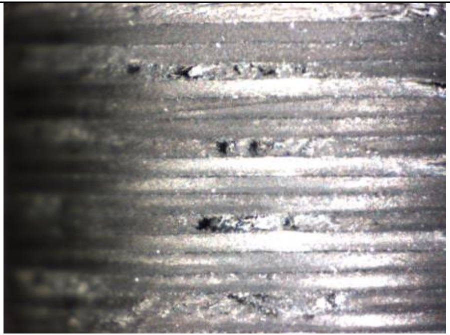	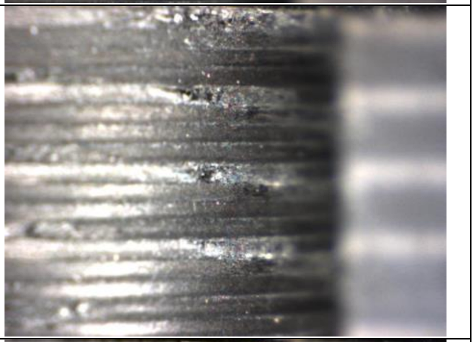
		2-R	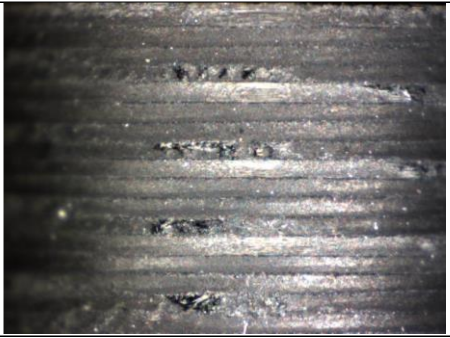	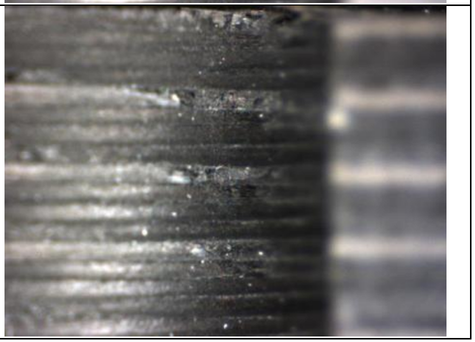

Table C. 2. Continued

Speed	Feed	Hole	Imaging Area – 5	Imaging Area – 8
3000 rpm	50 µm/rev	1-L	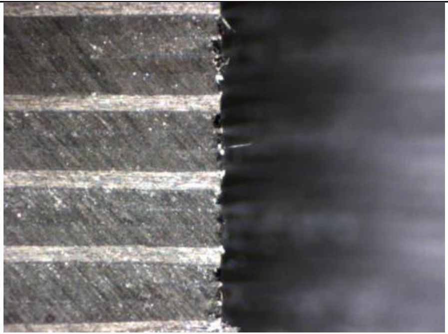	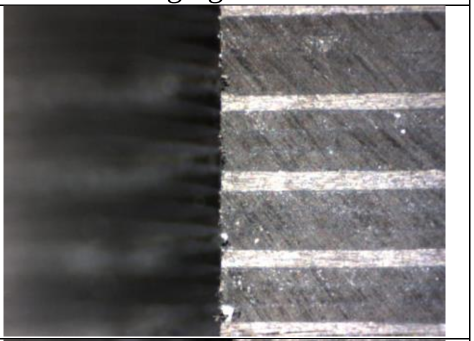
		1-R	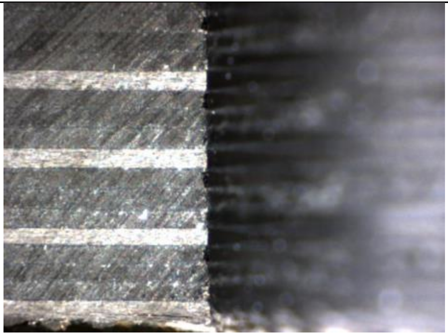	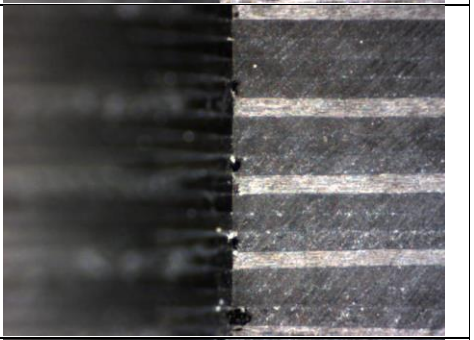
		2-L	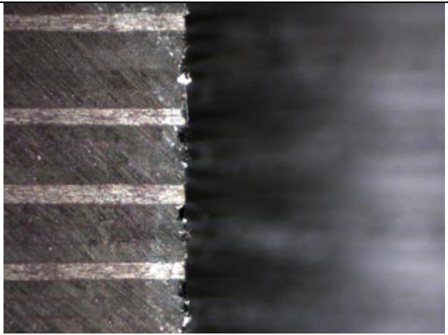	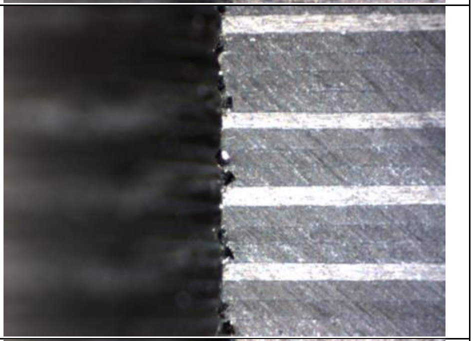
		2-R	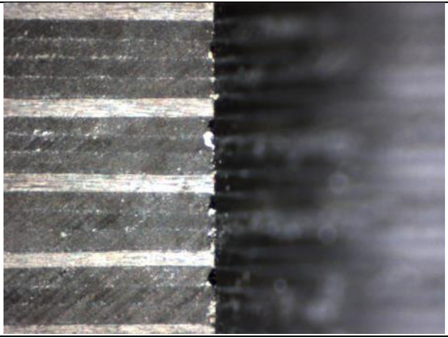	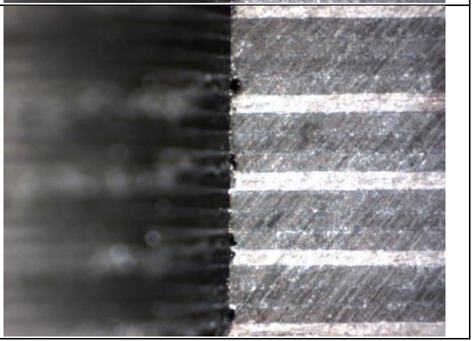

Table C. 2. Continued

Speed	Feed	Hole	Imaging Area – 6	Imaging Area – 7
3000 rpm	50 µm/rev	1-L	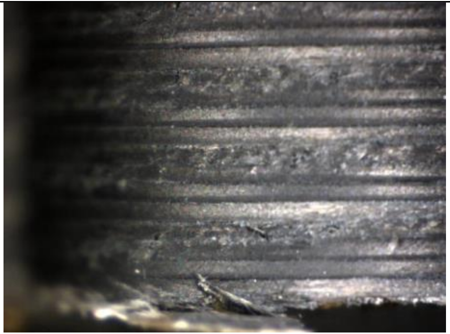	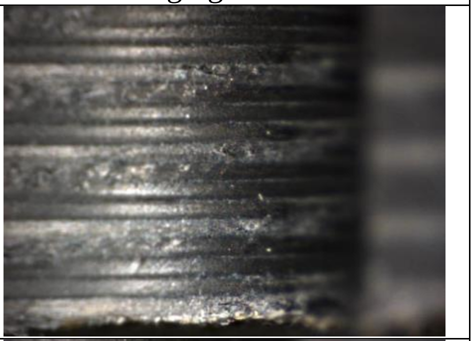
		1-R	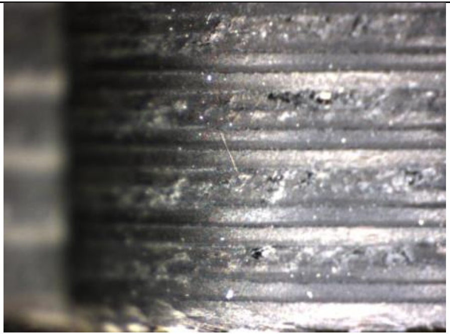	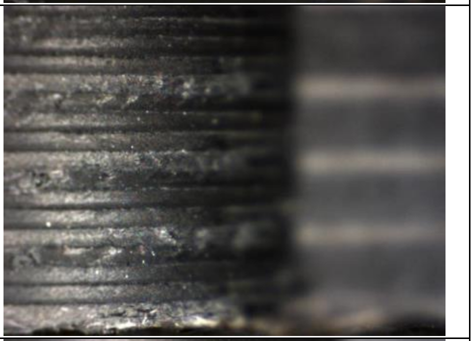
		2-L	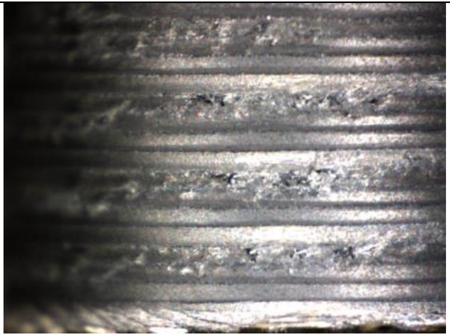	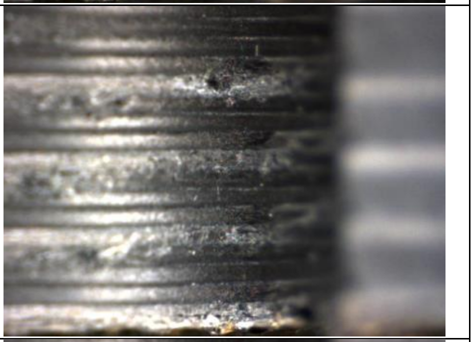
		2-R	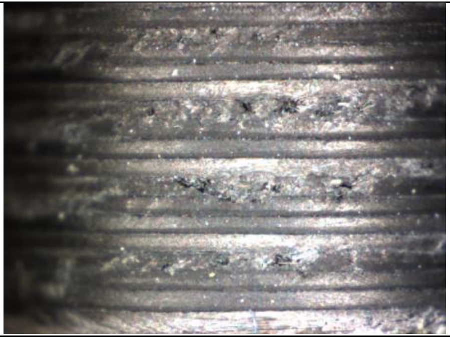	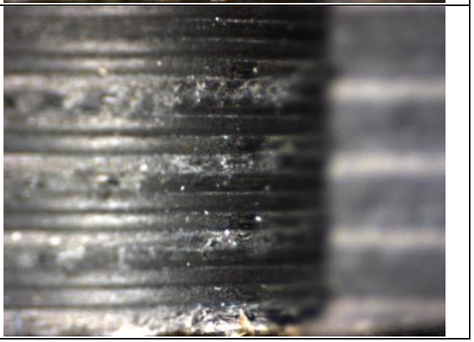

Table C. 2. Continued

Speed	Feed	Hole	Imaging Area – 1	Imaging Area – 4
3000 rpm	200 μm/rev	1-L	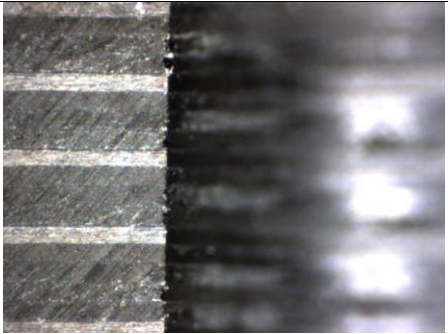	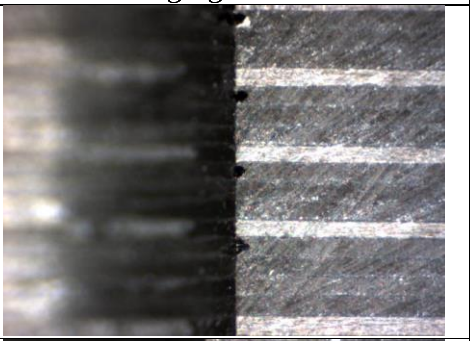
		1-R	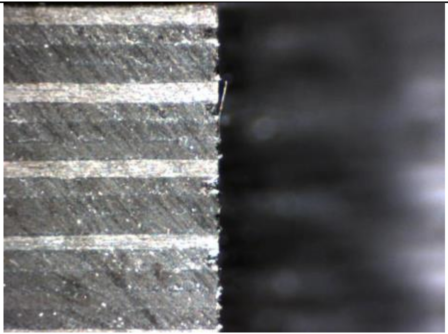	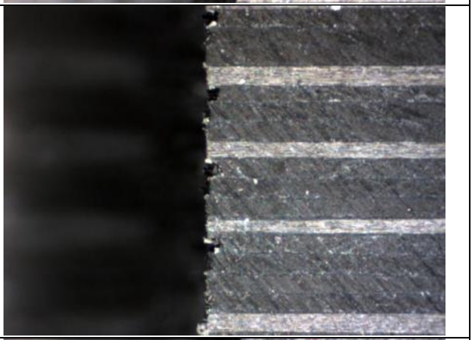
		2-L	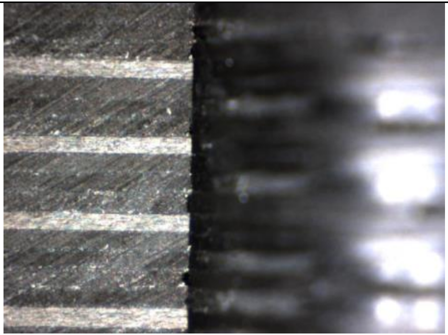	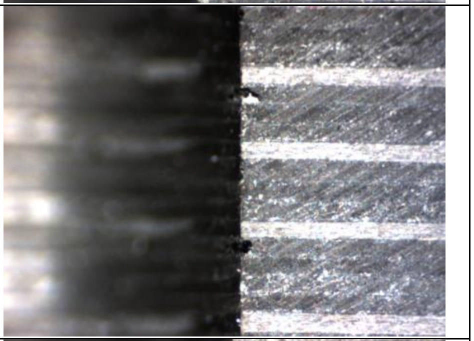
		2-R	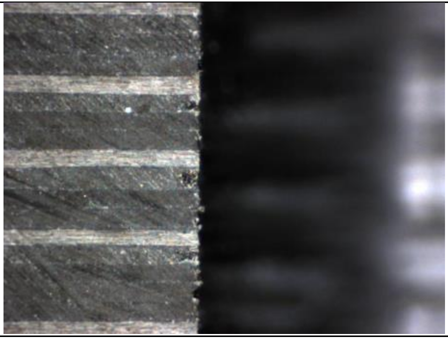	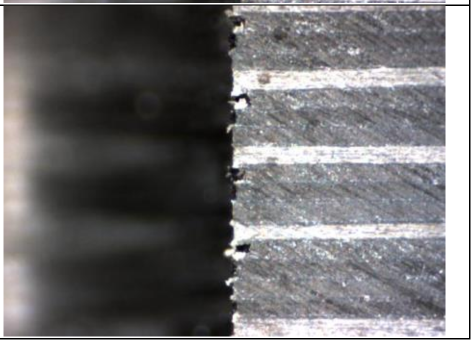

Table C. 2. Continued

Speed	Feed	Hole	Imaging Area – 2	Imaging Area – 3
3000 rpm	200 µm/rev	1-L	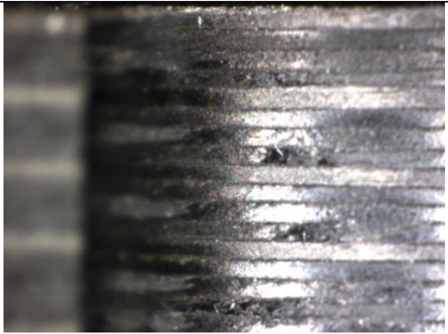	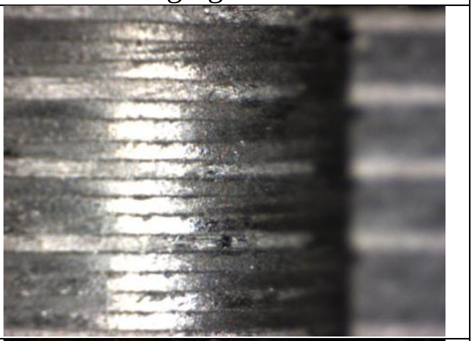
		1-R	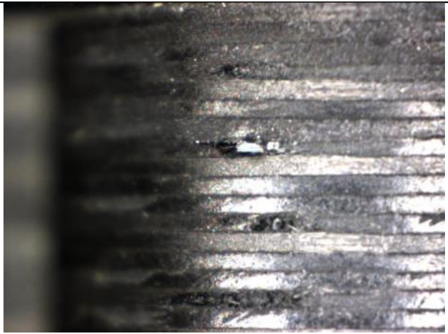	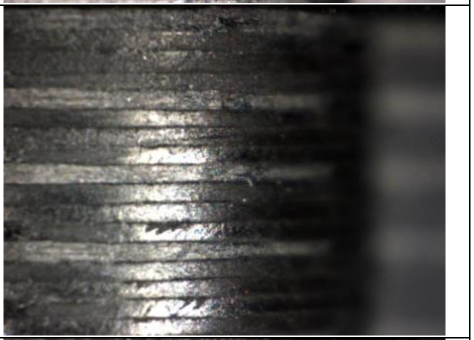
		2-L	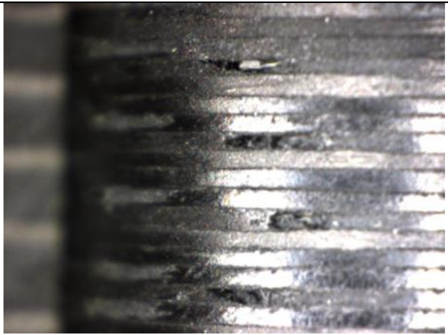	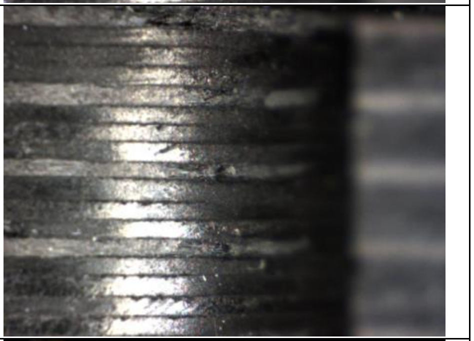
		2-R	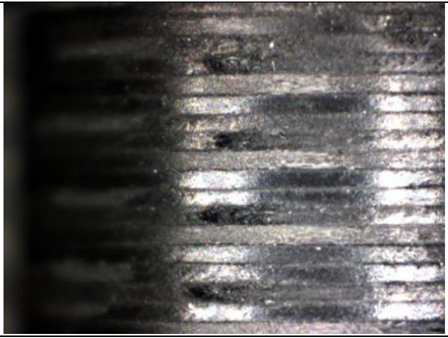	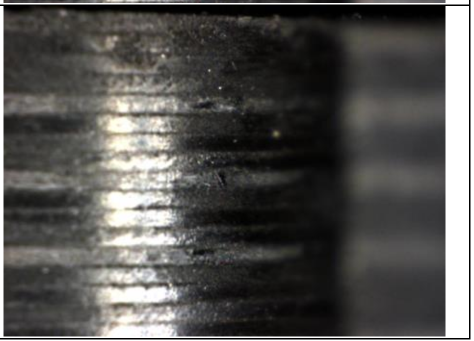

Table C. 2. Continued

Speed	Feed	Hole	Imaging Area – 5	Imaging Area – 8
3000 rpm	200 µm/rev	1-L	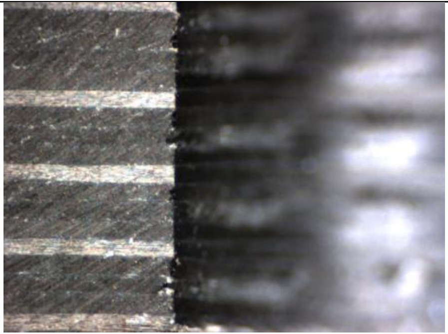	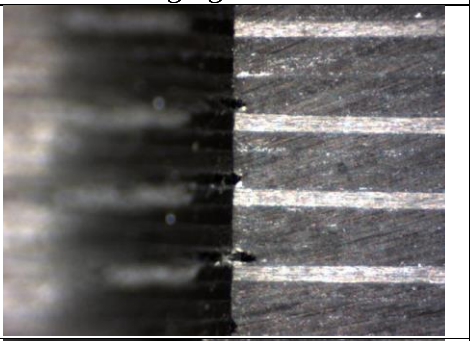
		1-R	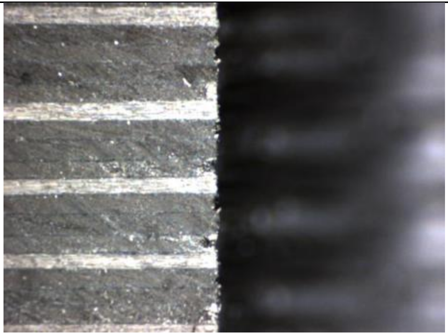	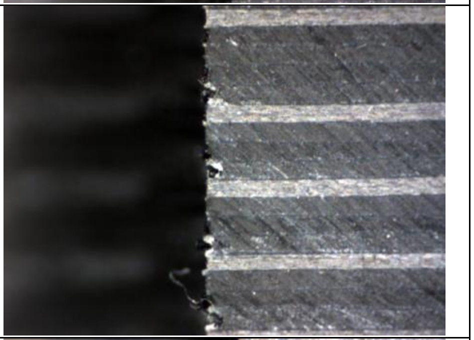
		2-L	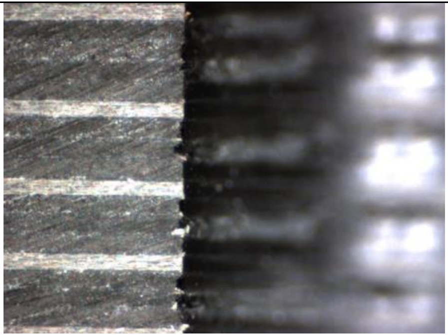	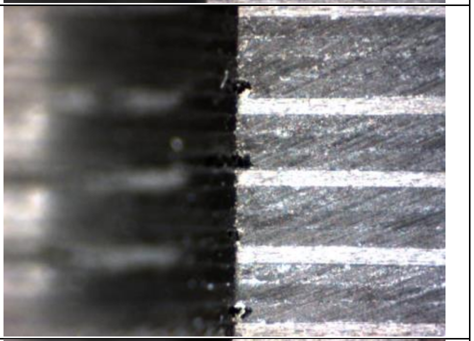
		2-R	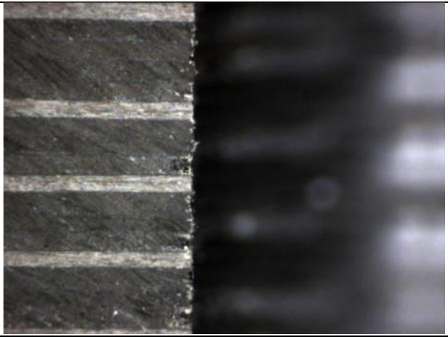	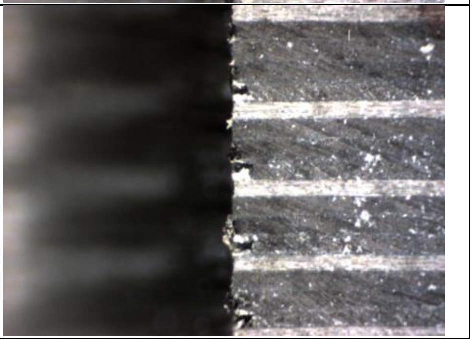

Table C. 2. Continued

Speed	Feed	Hole	Imaging Area –6	Imaging Area – 7
3000 rpm	200 µm/rev	1-L	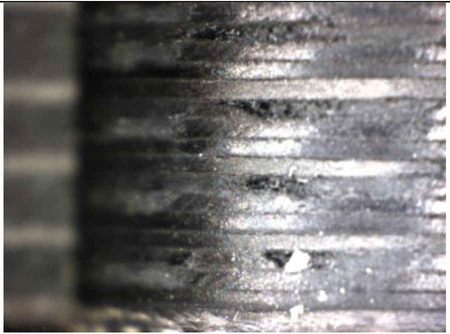	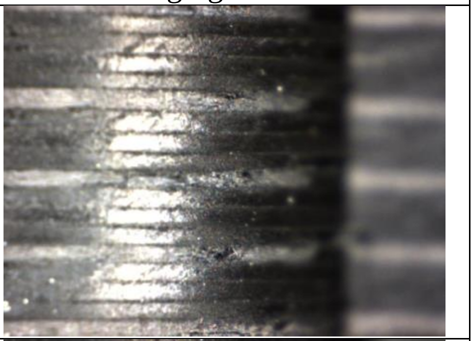
		1-R	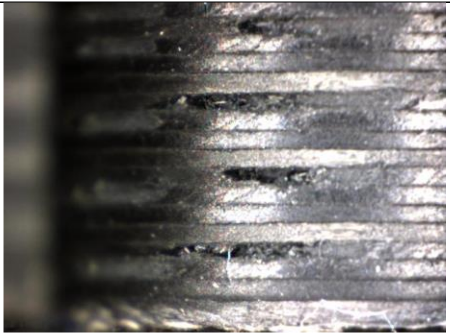	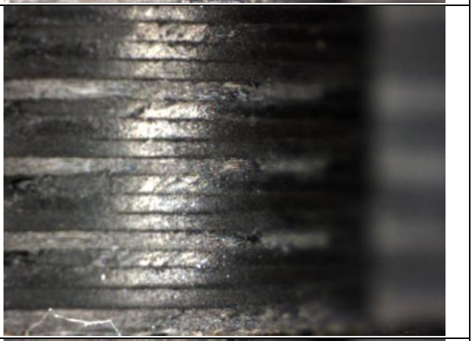
		2-L	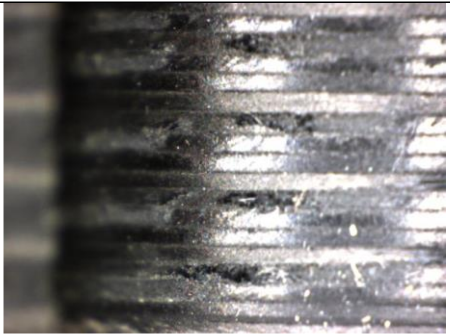	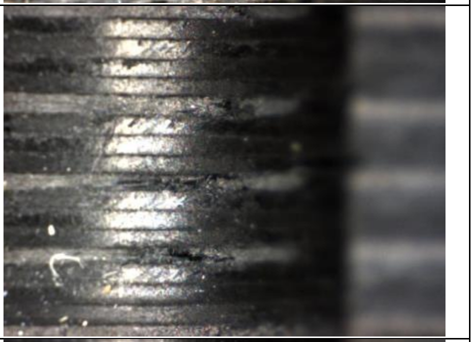
		2-R	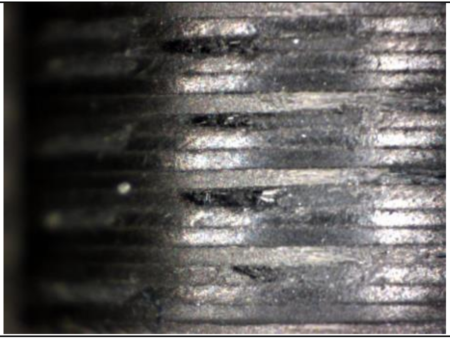	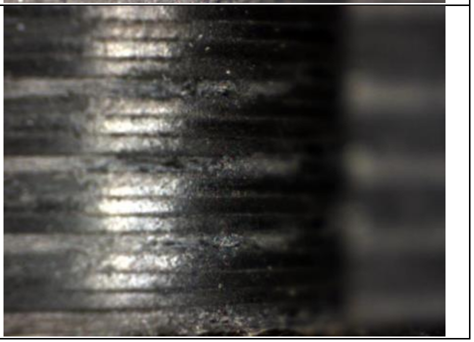

Table C. 2. Continued

Speed	Feed	Hole	Imaging Area – 1	Imaging Area – 4
6000 rpm	50 μm/rev	1-L	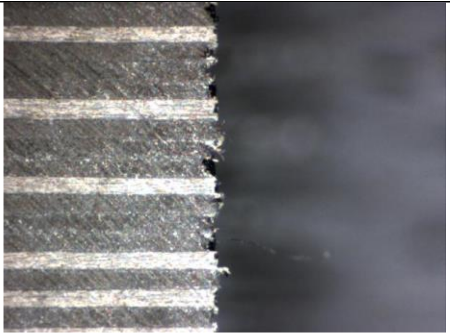	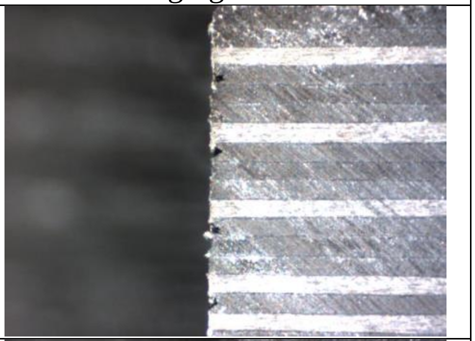
		1-R	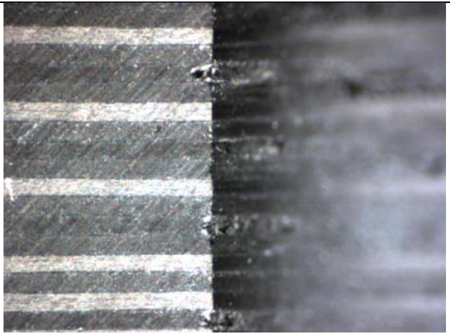	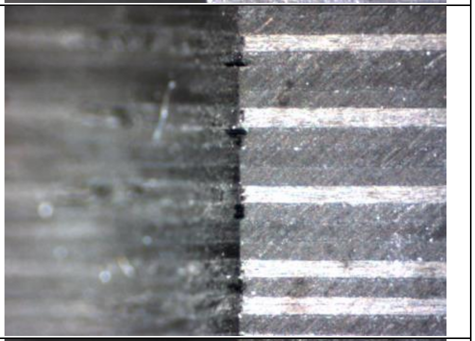
		2-L	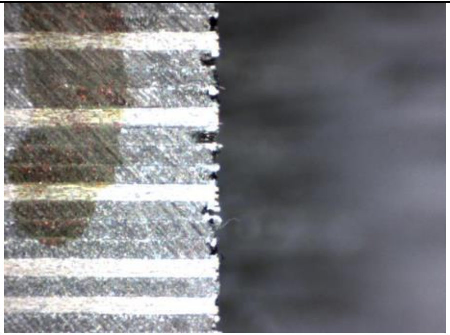	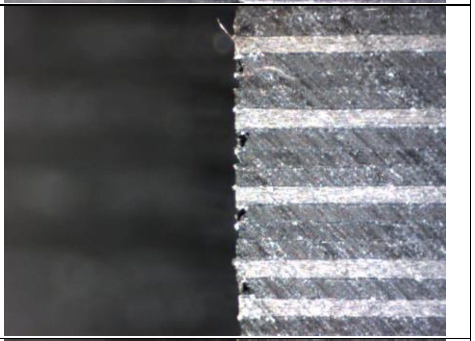
		2-R	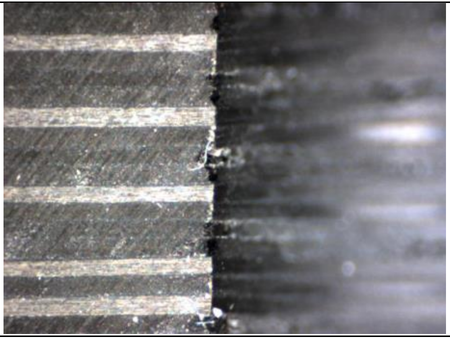	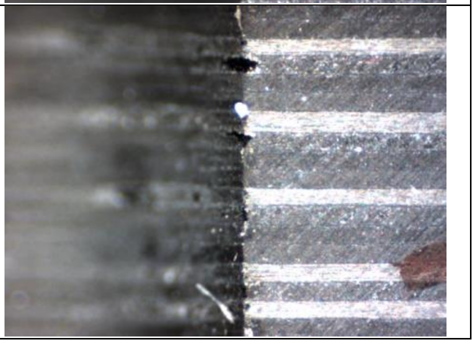

Table C. 2. Continued

Speed	Feed	Hole	Imaging Area – 1	Imaging Area – 4
6000 rpm	50 µm/rev	3-L	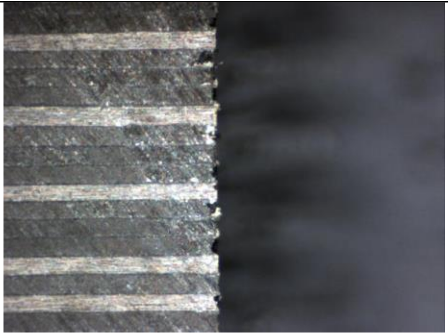	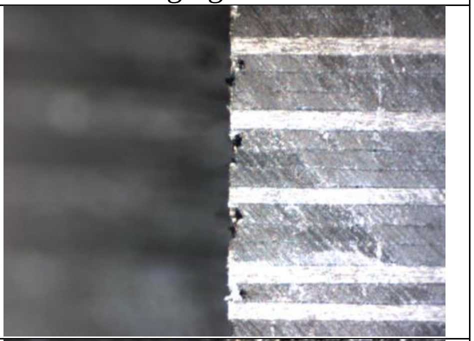
		3-R	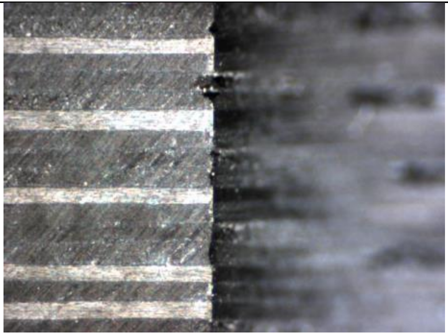	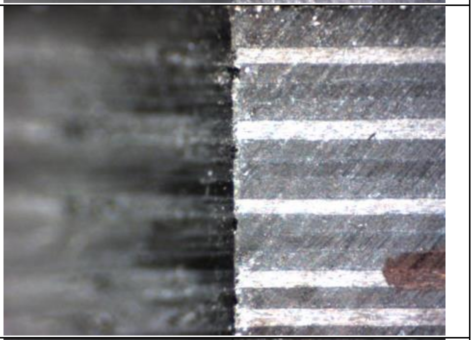
		4-L	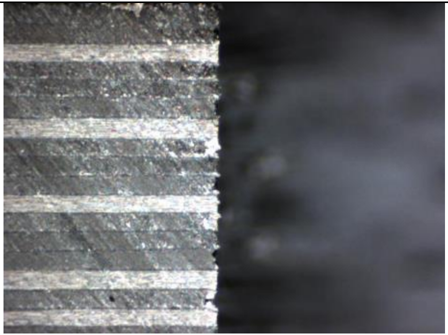	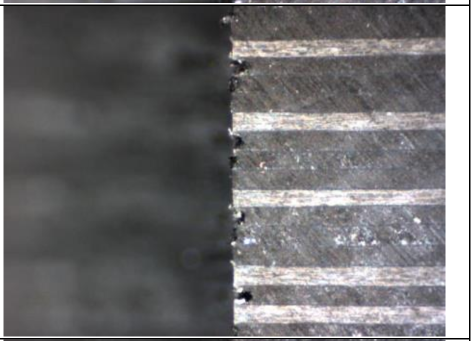
		4-R	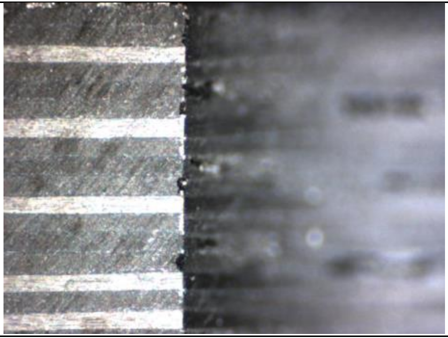	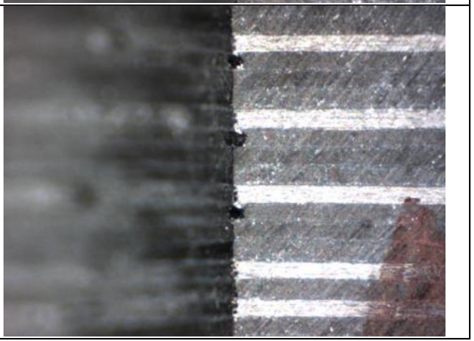

Table C. 2. Continued

Speed	Feed	Hole	Imaging Area – 2	Imaging Area – 3
6000 rpm	50 µm/rev	1-L	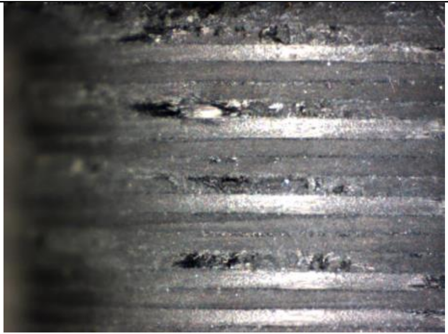	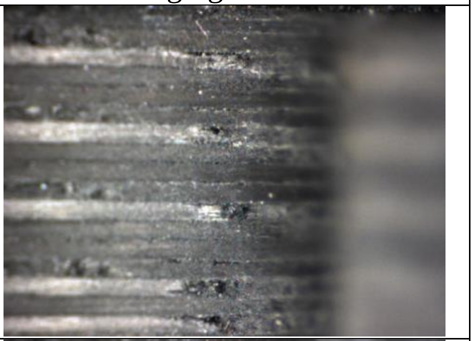
		1-R	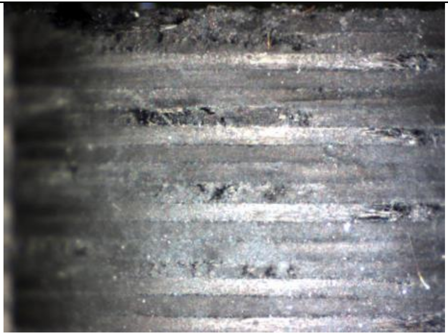	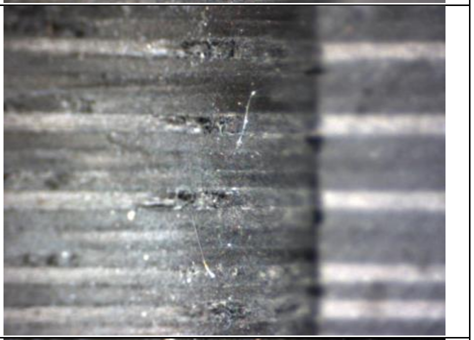
		2-L	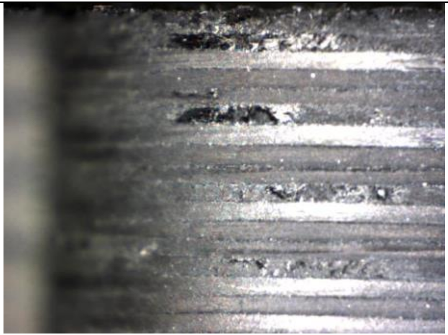	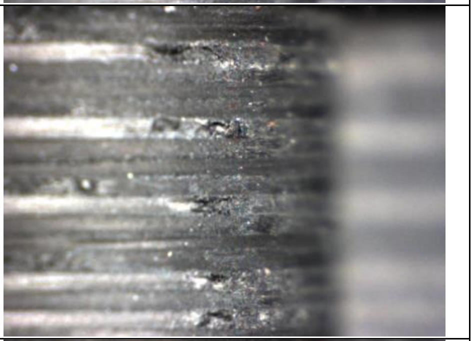
		2-R	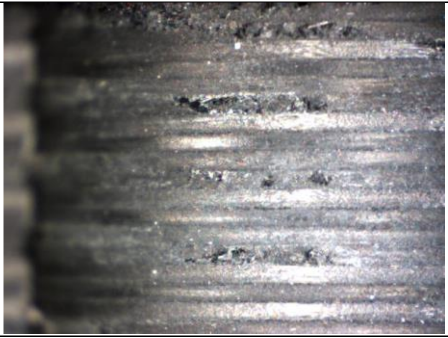	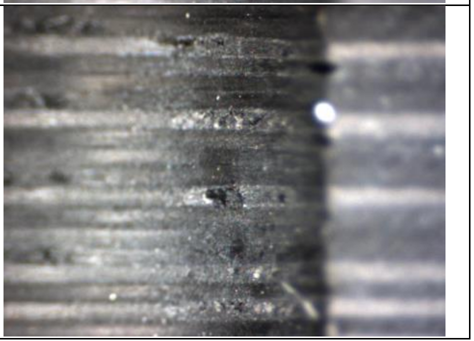

Table C. 2. Continued

Speed	Feed	Hole	Imaging Area – 2	Imaging Area – 3
6000 rpm	50 µm/rev	3-L	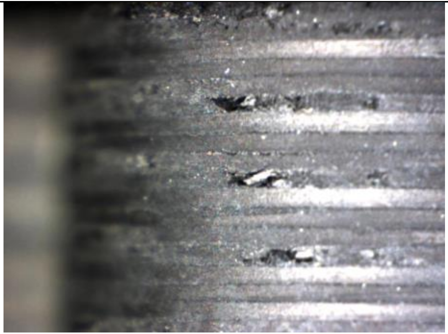	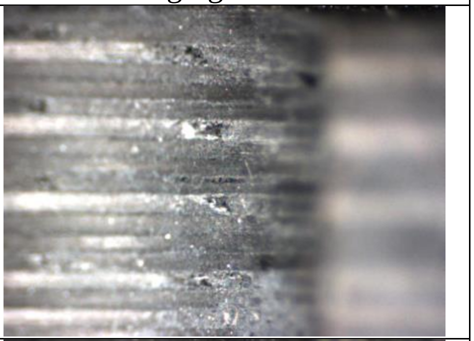
		3-R	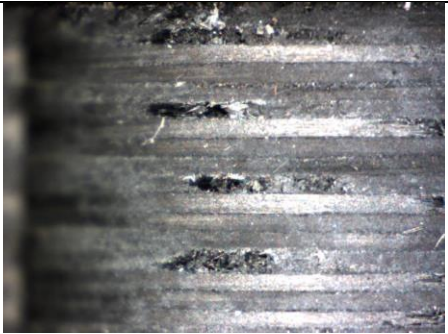	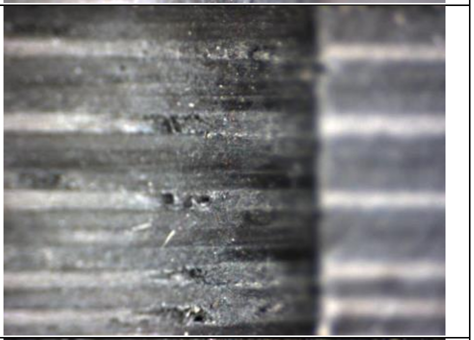
		4-L	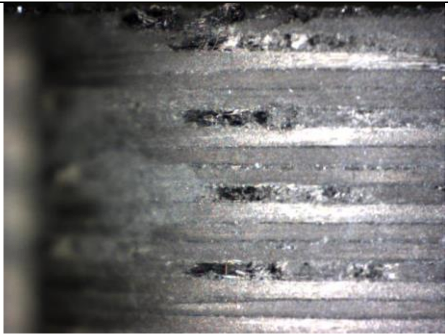	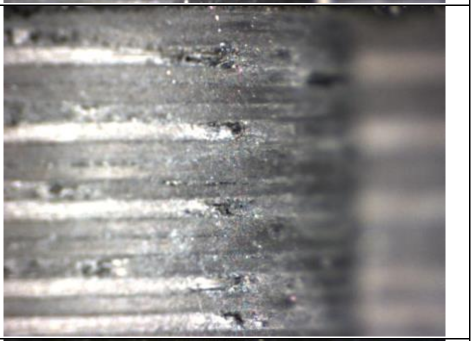
		4-R	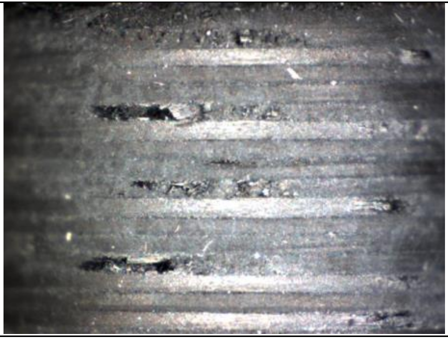	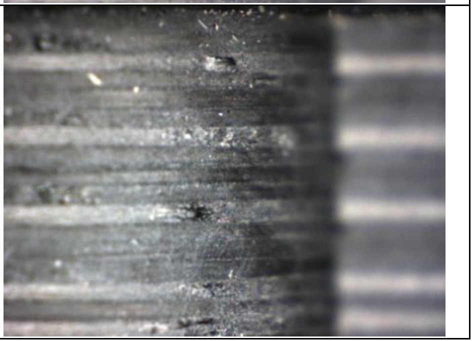

Table C. 2. Continued

Speed	Feed	Hole	Imaging Area – 5	Imaging Area – 8
6000 rpm	50 µm/rev	1-L	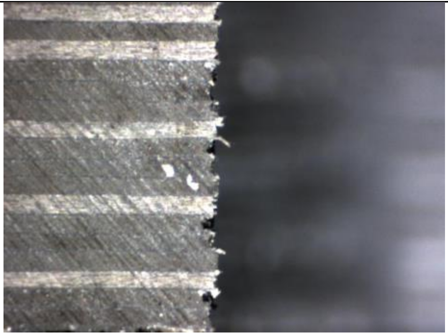	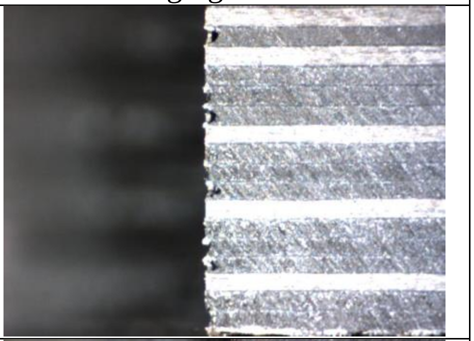
		1-R	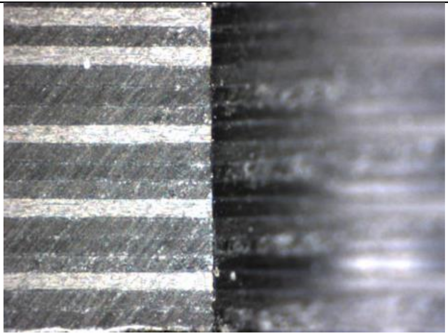	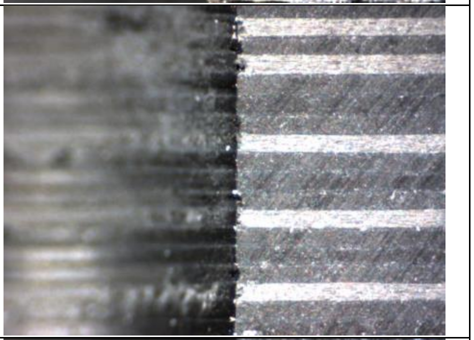
		2-L	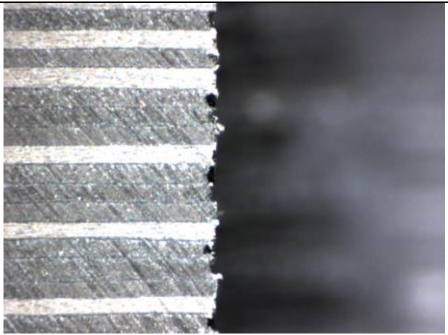	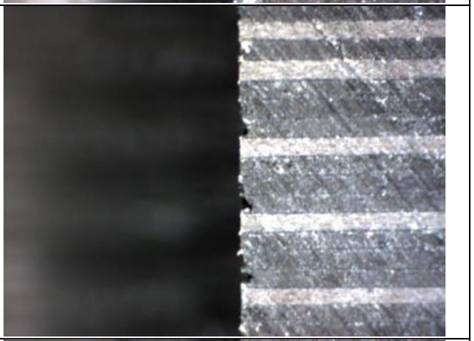
		2-R	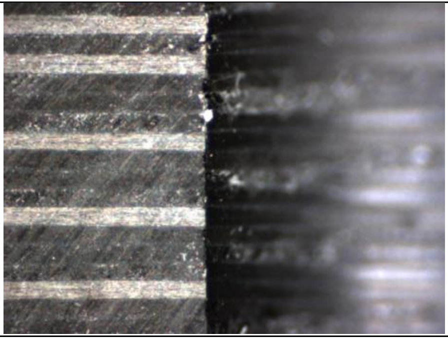	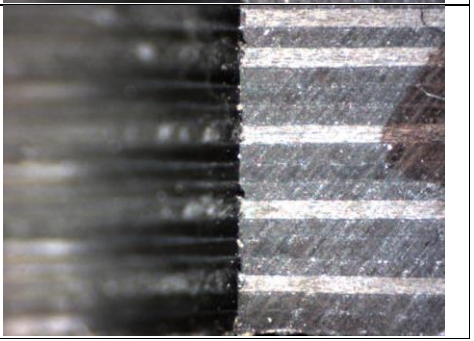

Table C. 2. Continued

Speed	Feed	Hole	Imaging Area – 5	Imaging Area – 8
6000 rpm	50 µm/rev	3-L	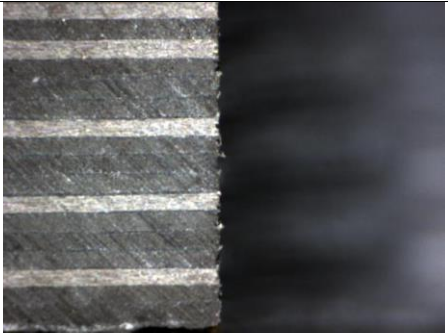	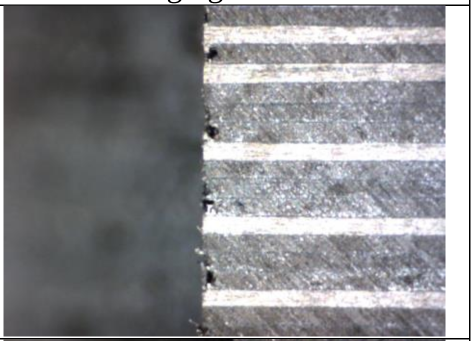
		3-R	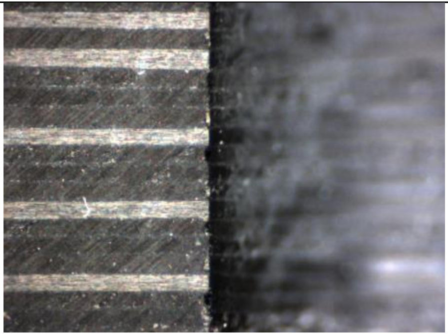	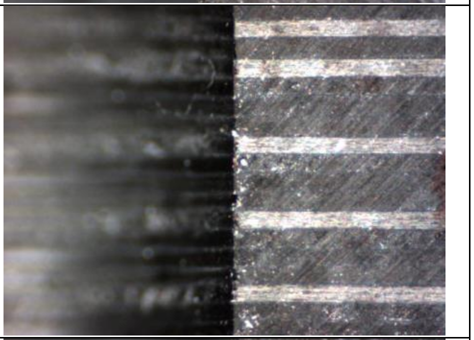
		4-L	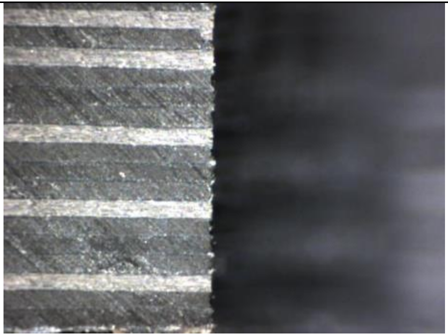	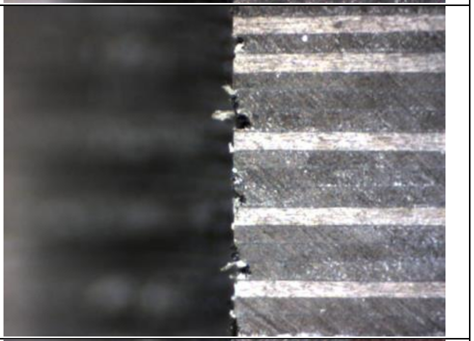
		4-R	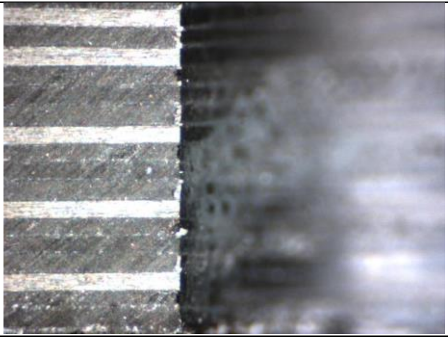	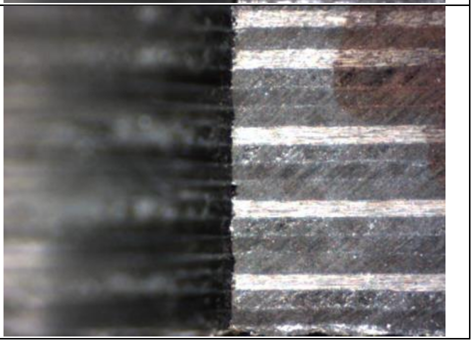

Table C. 2. Continued

Speed	Feed	Hole	Imaging Area – 6	Imaging Area – 7
6000 rpm	50 µm/rev	1-L	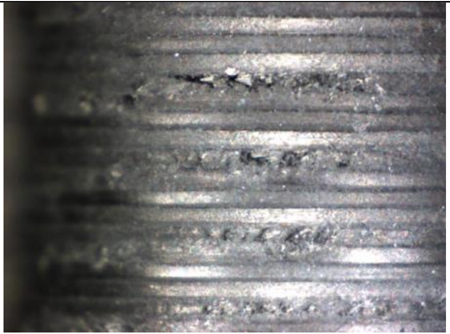	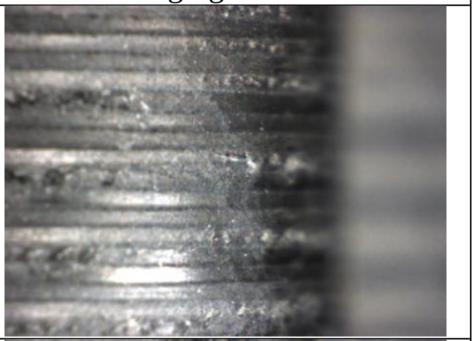
		1-R	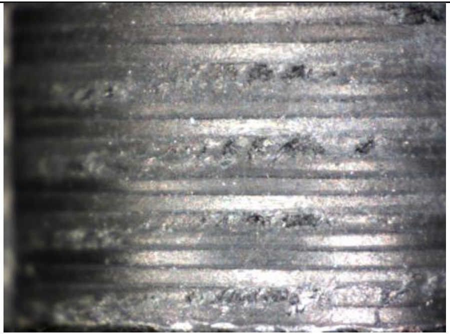	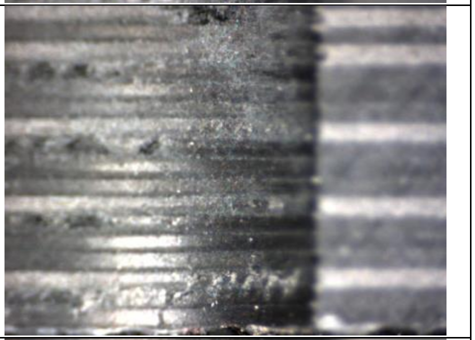
		2-L	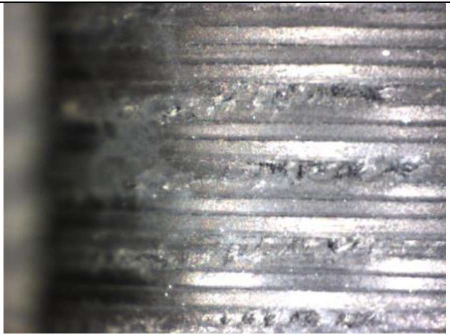	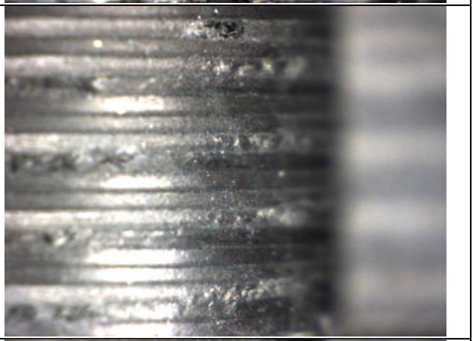
		2-R	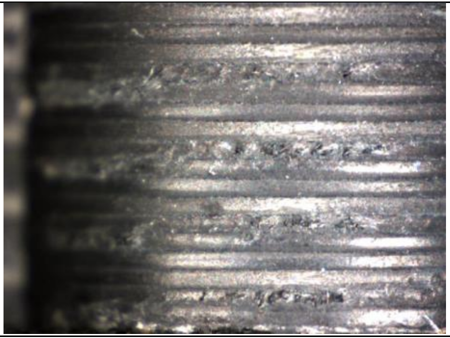	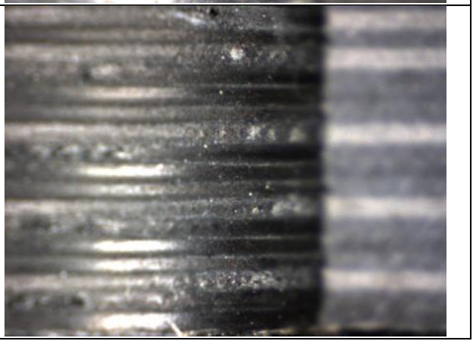

Table C. 2. Continued

Speed	Feed	Hole	Imaging Area – 6	Imaging Area – 7
6000 rpm	50 µm/rev	3-L	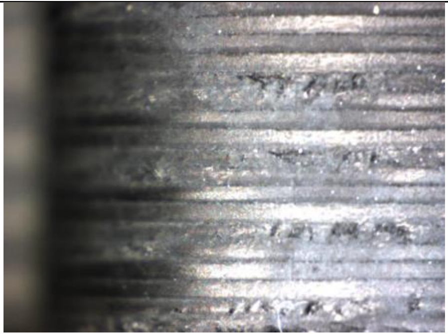	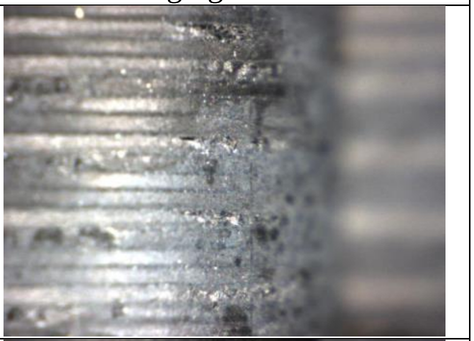
		3-R	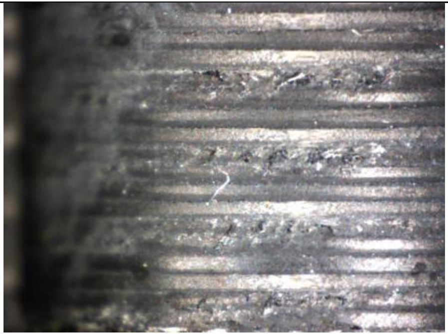	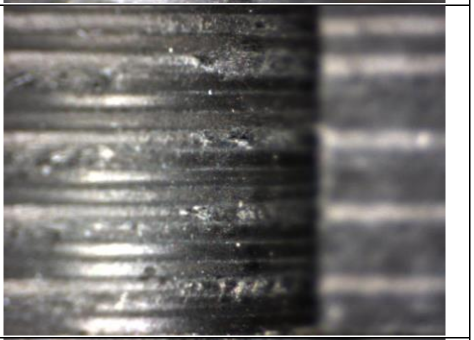
		4-L	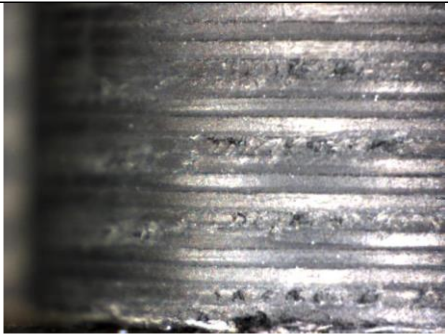	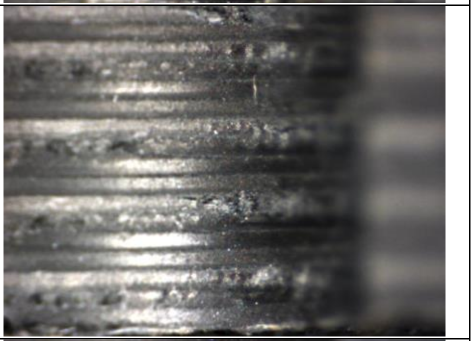
		4-R	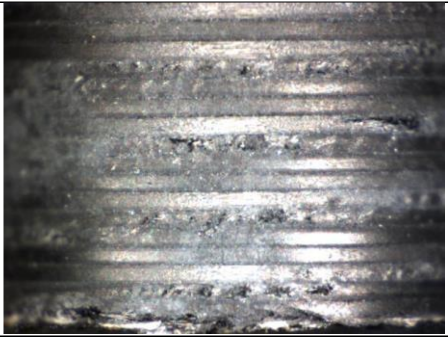	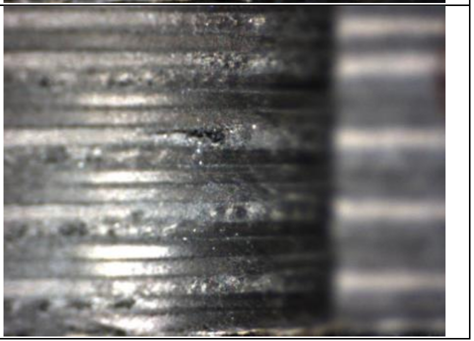

Table C. 2. Continued

Speed	Feed	Hole	Imaging Area – 1	Imaging Area – 4
6000 rpm	200 µm/rev	1-L	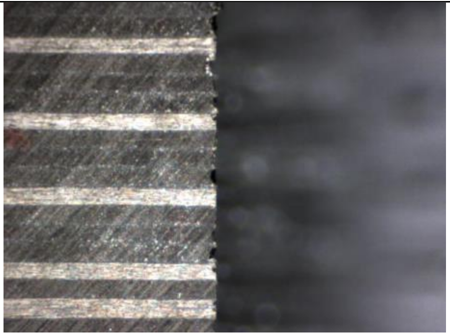	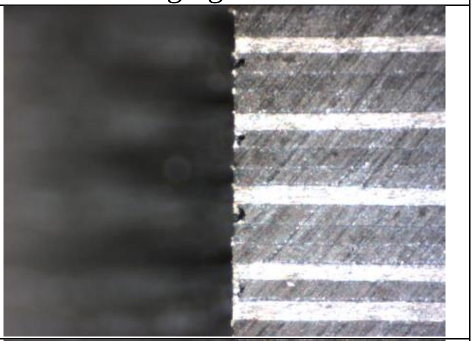
		1-R	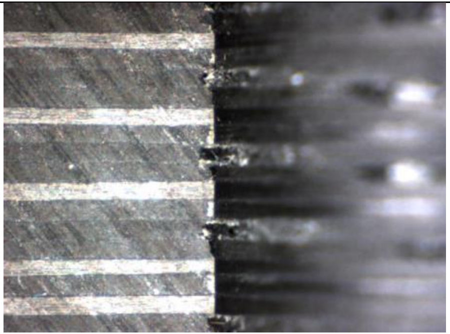	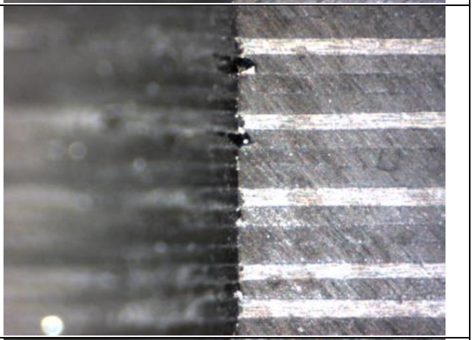
		2-L	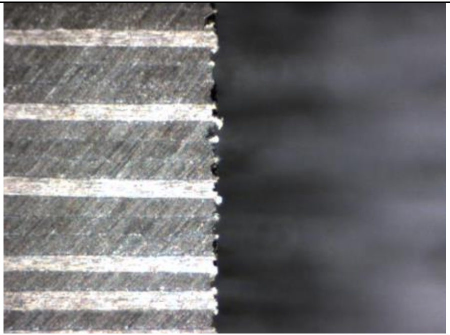	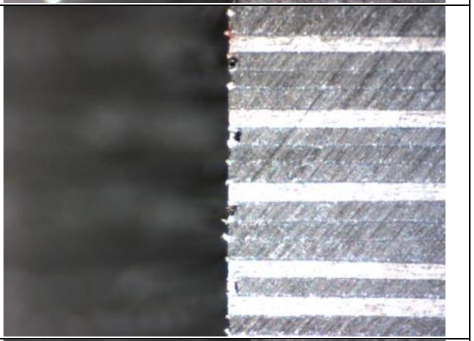
		2-R	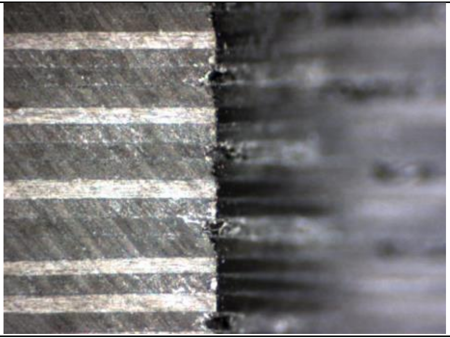	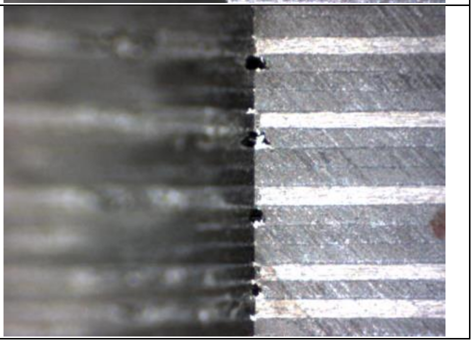

Table C. 2. Continued

Speed	Feed	Hole	Imaging Area – 1	Imaging Area – 4
6000 rpm	200 µm/rev	3-L	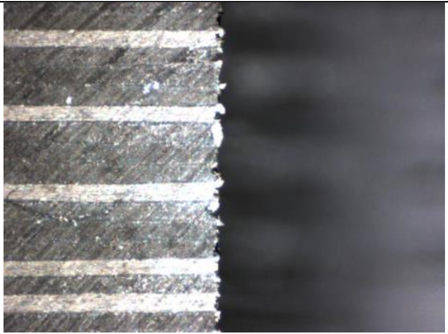	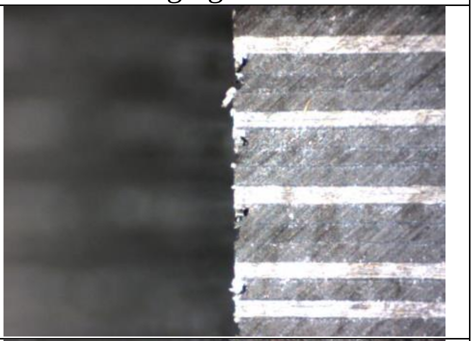
		3-R	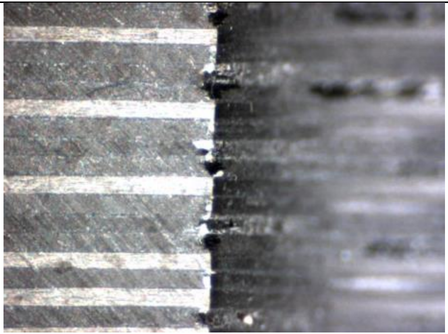	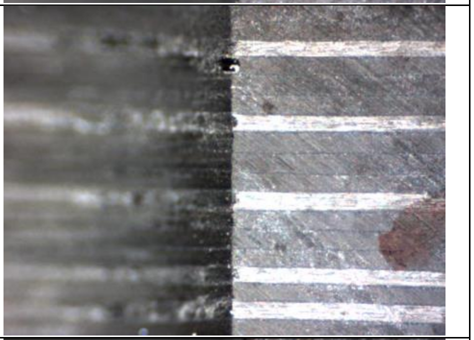
		4-L	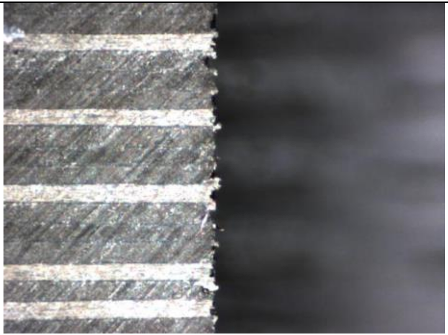	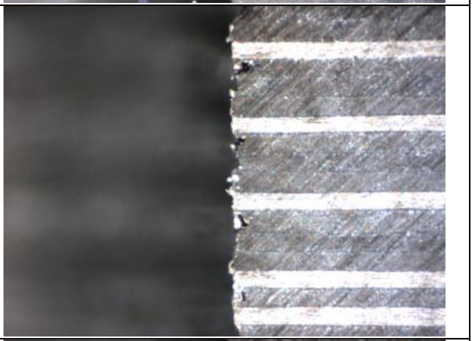
		4-R	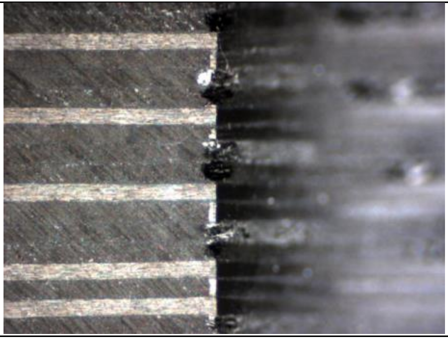	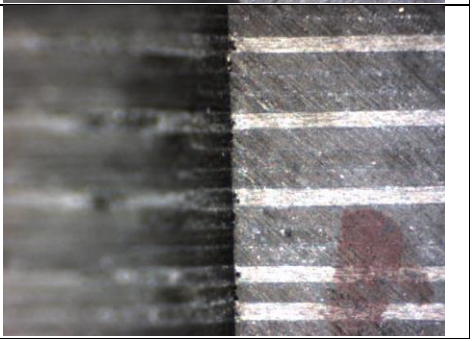

Table C. 2. Continued

Speed	Feed	Hole	Imaging Area – 2	Imaging Area – 3
6000 rpm	200 µm/rev	1-L	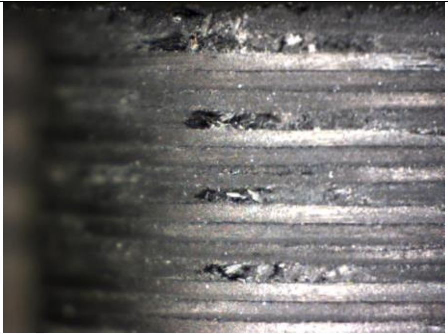	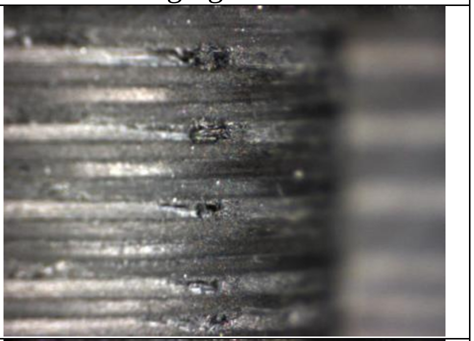
		1-R	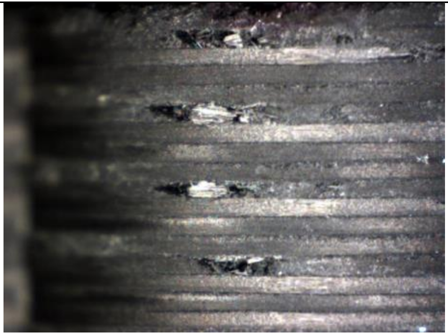	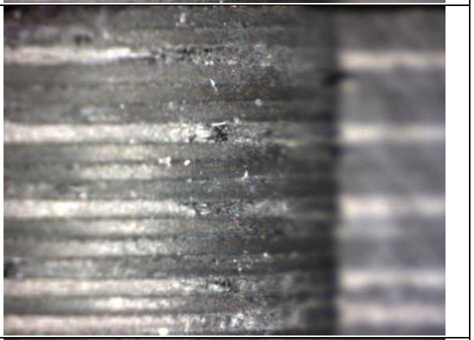
		2-L	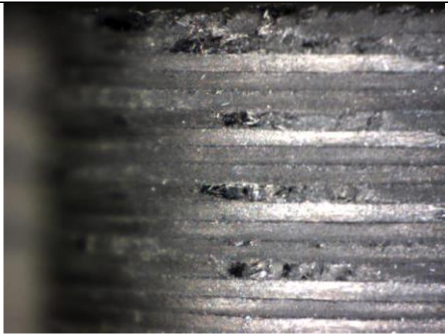	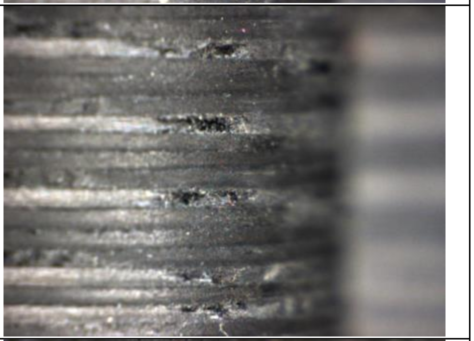
		2-R	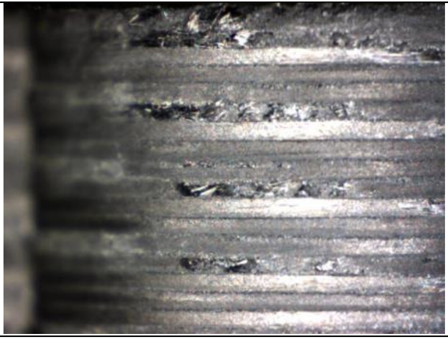	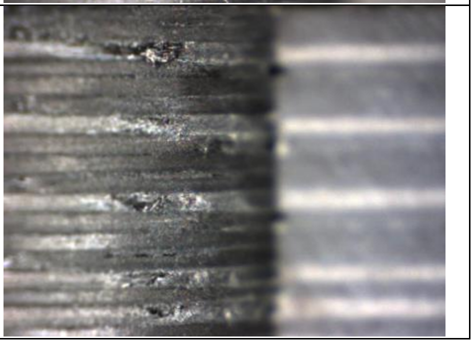

Table C. 2. Continued

Speed	Feed	Hole	Imaging Area – 2	Imaging Area – 3
6000 rpm	200 µm/rev	3-L	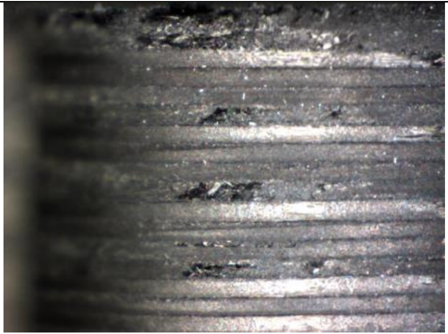	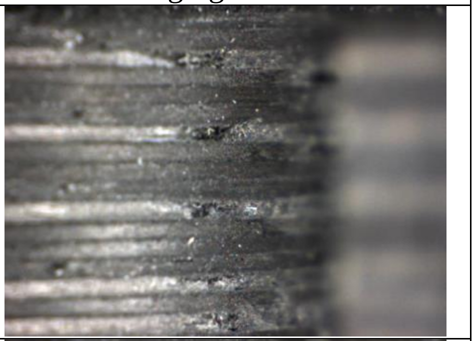
		3-R	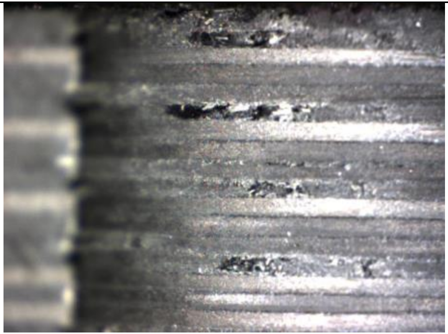	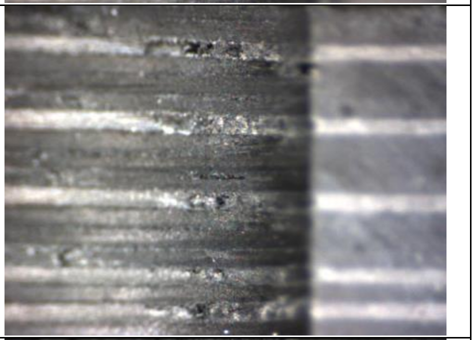
		4-L	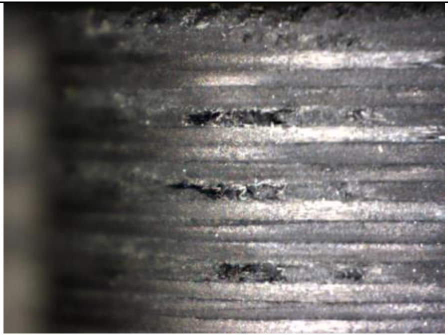	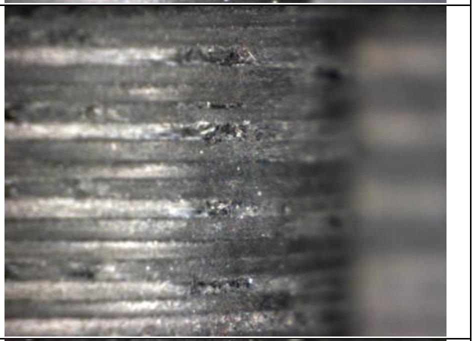
		4-R	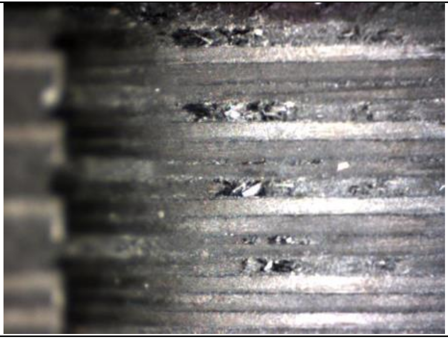	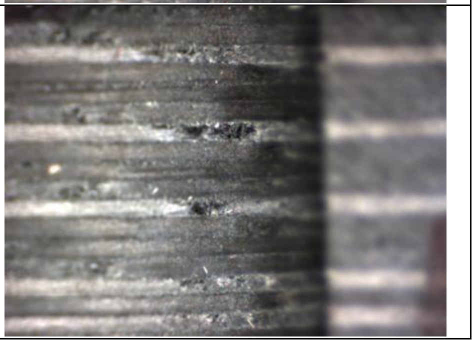

Table C. 2. Continued

Speed	Feed	Hole	Imaging Area – 5	Imaging Area – 8
6000 rpm	200 µm/rev	1-L	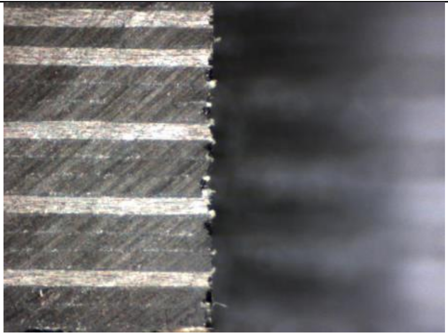	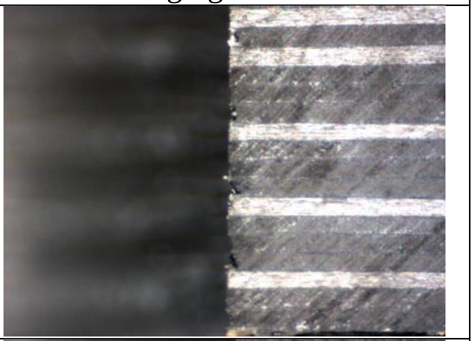
		1-R	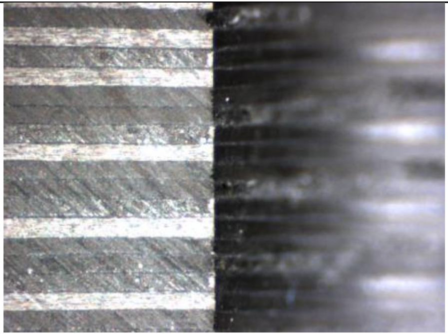	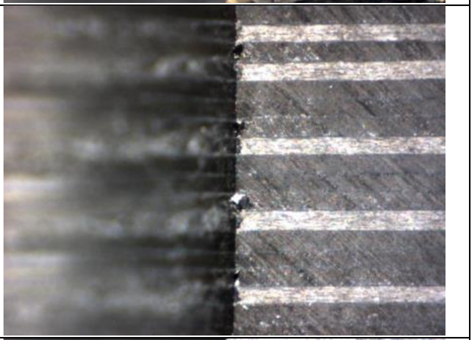
		2-L	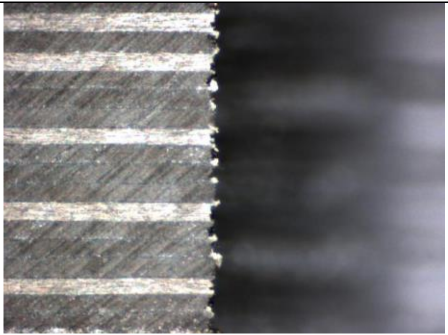	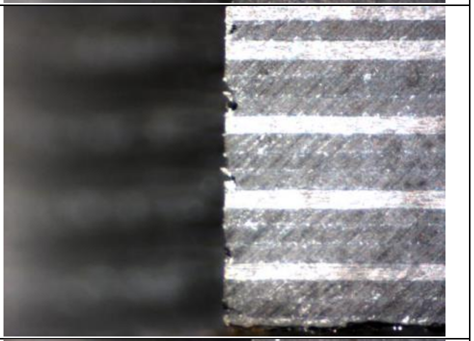
		2-R	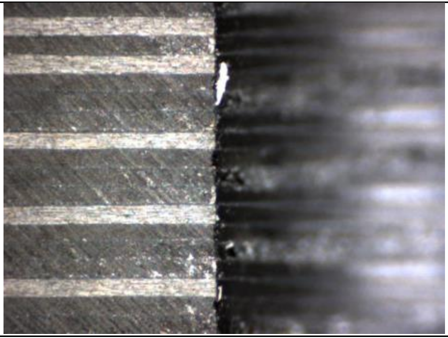	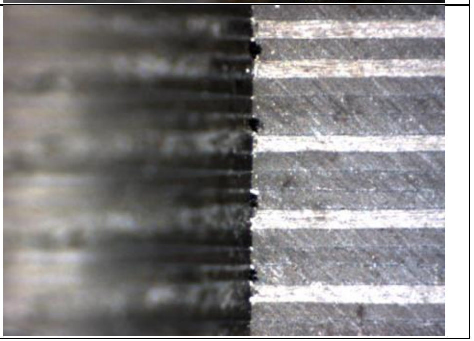

Table C. 2. Continued

Speed	Feed	Hole	Imaging Area – 5	Imaging Area – 8
6000 rpm	200 µm/rev	3-L	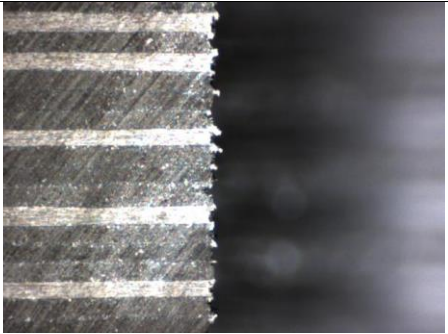	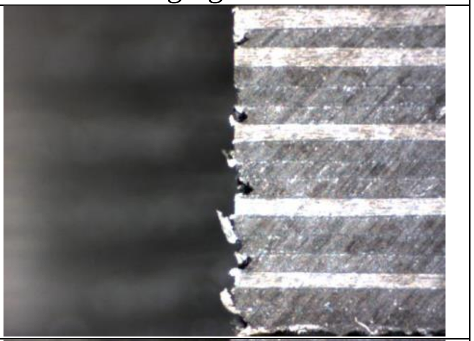
		3-R	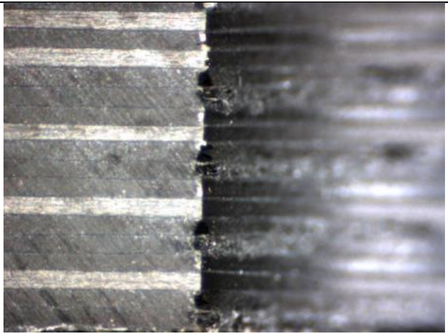	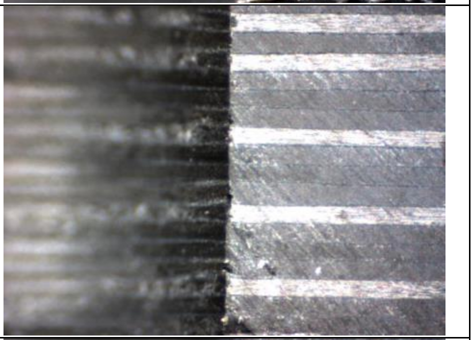
		4-L	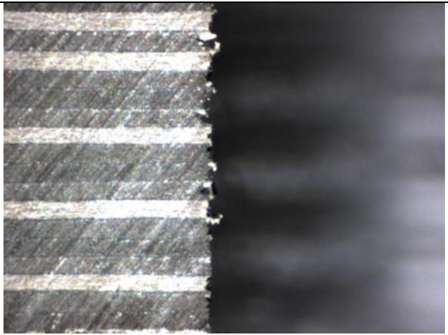	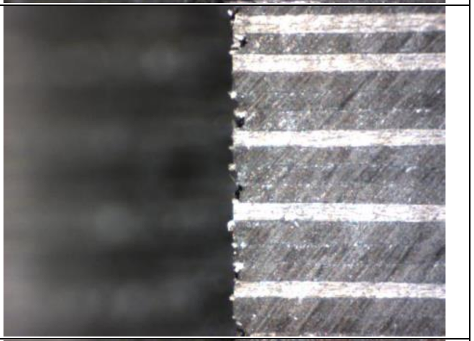
		4-R	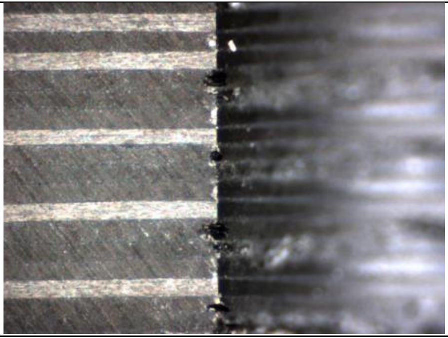	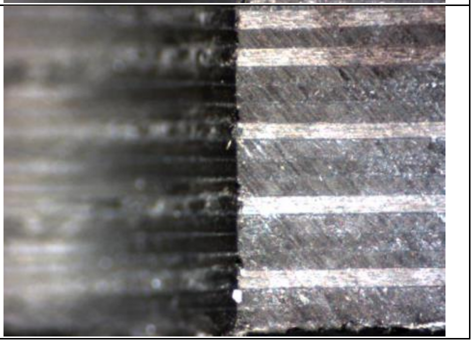

Table C. 2. Continued

Speed	Feed	Hole	Imaging Area – 6	Imaging Area –7
6000 rpm	200 µm/rev	1-L	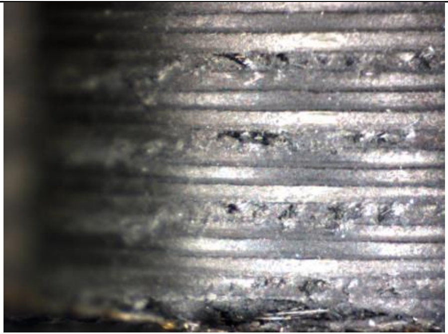	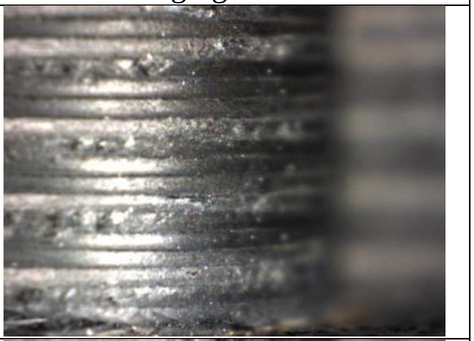
		1-R	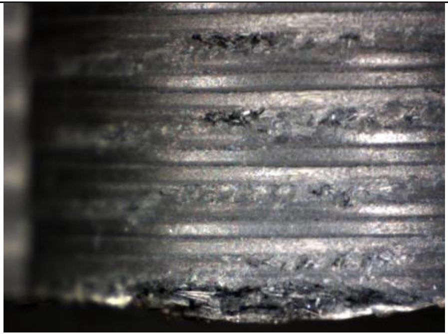	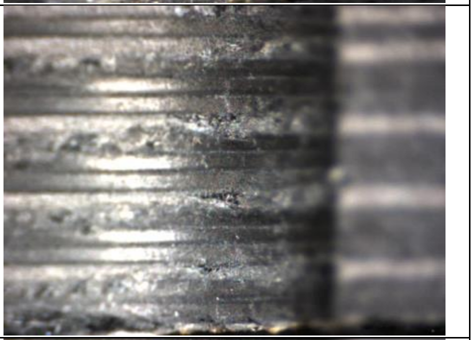
		2-L	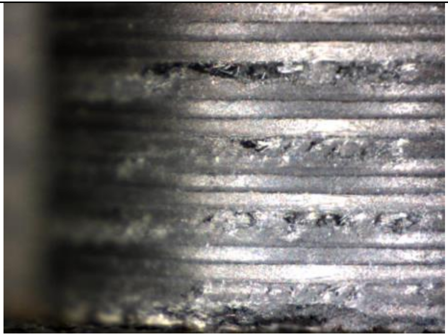	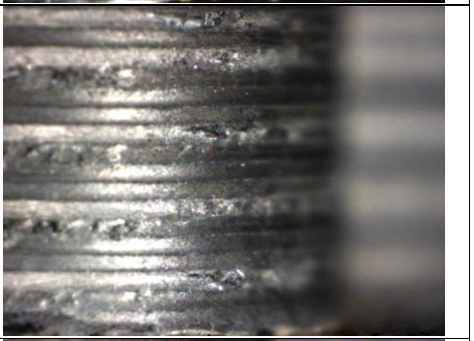
		2-R	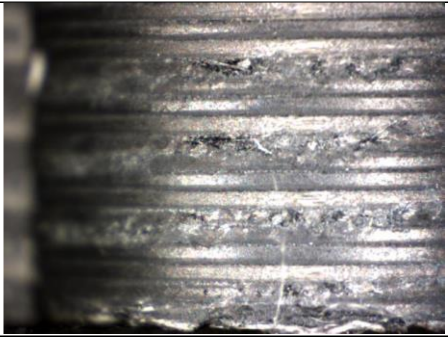	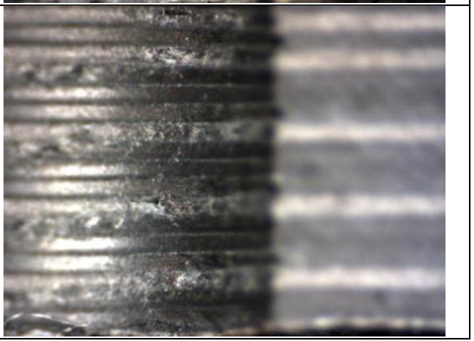

Table C. 2. Continued

Speed	Feed	Hole	Imaging Area – 6	Imaging Area – 7
6000 rpm	200 µm/rev	3-L	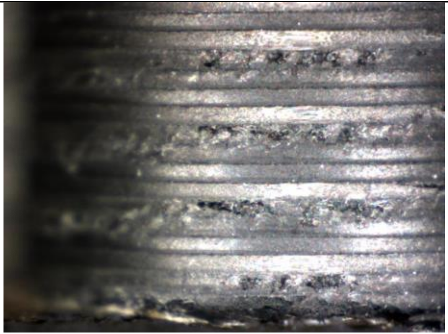	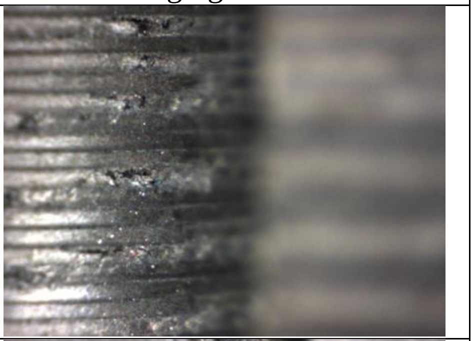
		3-R	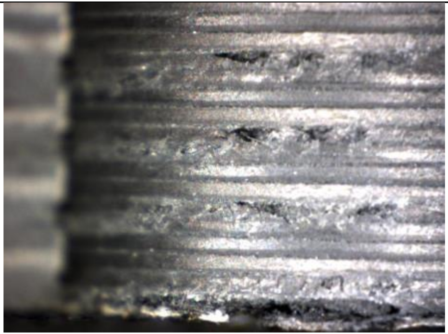	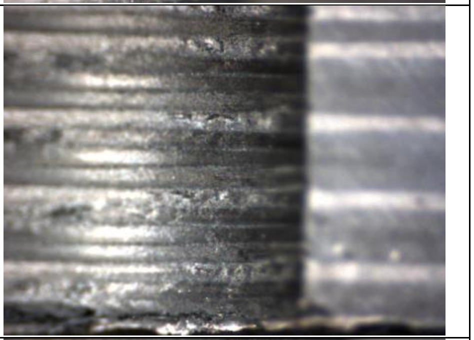
		4-L	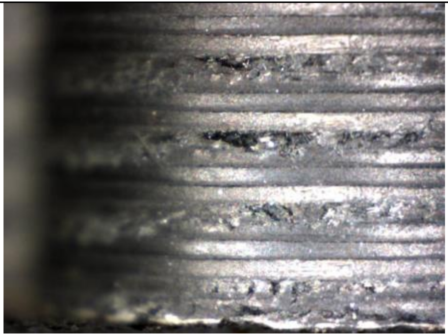	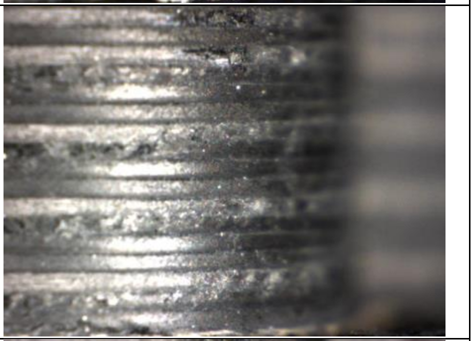
		4-R	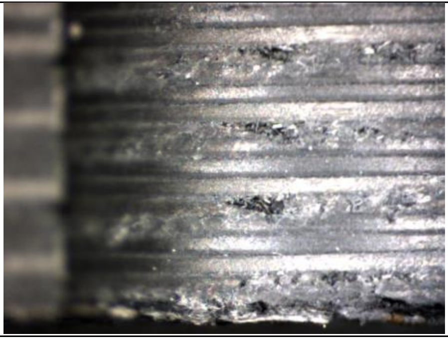	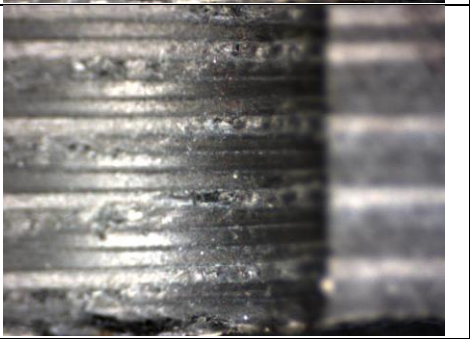

APPENDIX D – FIBER PULLOUT MEASUREMENTS FOR MULTI-DIRECTIONAL CFRP WITH FIBERGLASS SCRIM SURFACE PLIES

Fiber pullout measurements were taken at the edge of the sectioned hole at the left and right side of the sectioned halves and the depth and width of measured fiber pullout values are given with the individual ply orientation.

Table D. 1. Fiber pullout values for fiberglass scrim surface ply multi-directional CFRP

Cutting Speed	Feed Rate	Hole Number	Measured Side	Ply Number	Orientation of Plies (Degree)	Width (μm)	Depth (μm)
3000 rpm	50 μm/rev	1	Left	2	-45	147.1	80.3
				4	45	144.7	89.5
				8	45	137.8	87.2
				10	-45	140.1	135.3
				12	45	144.7	80.3
				16	45	126.4	96.4
				24	45	163.1	94.1
				28	45	142.4	64.2
			Right	6	-45	142.4	96.4
				10	-45	144.8	80.3
				14	-45	131	183.5
				26	-45	163.1	112.4
				38	-45	114.9	178.9
		2	Left	2	-45	112.6	48.2
				4	45	73.5	45.9
				10	-45	140.1	100.9
				12	45	87.3	43.6
				14	-45	142.4	195
				36	45	135.5	66.5
				38	-45	126.3	73.4
			Right	2	-45	158.5	71.2
				6	-45	172.9	243.2
				10	-45	151.6	234
				14	-45	149.3	183.5
				26	-45	121.7	103.2
				30	-45	135.5	123.9
				34	-45	158.5	100.9
				38	-45	156.2	126.2

Table D. 1. Continued

Cutting Speed	Feed Rate	Hole Number	Measured Side	Ply Number	Orientation of Plies (Degree)	Width (µm)	Depth (µm)
3000 rpm	200 µm/rev	1	Left	3	0	165.4	71.1
				4	45	126.4	68.8
				29	0	172.3	105.5
				37	0	156.2	144.5
			Right	2	-45	147	156
				6	-45	140.1	133
				10	-45	121.8	94
				14	-45	192.9	156
				26	-45	121.7	128.5
				30	-45	151.7	103.2
				34	-45	133.2	243.2
		2	Left	2	-45	144.7	146.8
				4	45	158.5	59.6
				16	45	158.5	55
				17	0	96.5	48.2
				29	0	130.9	119.3
				33	0	188.4	98.6
				36	45	135.6	52.8
				37	0	183.8	105.5
			Right	2	-45	137.8	57.3
				6	-45	158.5	229.4
				14	-45	144.7	119.3
				26	-45	167.7	162.9
				30	-45	188.4	169.8
				34	-45	137.8	80.3
				38	-45	163.1	176.7
6000 rpm	50 µm/rev	1	Left	4	45	149.3	270.7
				8	45	165.4	236.3
				12	45	144.8	270.7
				16	45	172.3	151.4
				24	45	142.5	266.1
				28	45	131	263.8
				32	45	163.1	227.1
				36	45	156.2	263.8
			Right	4	45	170	229.4
				5	90	181.5	126.2
				8	45	133.3	300.5
				12	45	119.7	220.2
				16	45	128.7	213.2
				24	45	188.4	121.9
				28	45	122.1	218
				32	45	172.4	174.6
				36	45	160.8	250.1

Table D. 1. Continued

Cutting Speed	Feed Rate	Hole Number	Measured Side	Ply Number	Orientation of Plies (Degree)	Width (µm)	Depth (µm)
6000 rpm	50 µm/rev	2	Left	4	45	165.4	114.8
				8	45	186.1	119.4
				12	45	183.8	75.7
				16	45	190.8	190.4
				24	45	172.3	201.9
				28	45	126.4	268.4
				32	45	181.6	250.1
				36	45	176.9	218
			Right	4	45	154	192.7
				8	45	131	158.4
				12	45	137.8	178.9
				16	45	147.1	188.1
				24	45	163.1	201.7
				28	45	147.1	176.6
				32	45	126.4	167.5
				36	45	121.8	151.4
		3	Left	4	45	135.6	165.2
				8	45	186.1	179
				12	45	142.4	160.8
				16	45	209.1	213.5
				24	45	158.5	119.3
				28	45	140.1	247.8
				32	45	144.7	144.6
				36	45	140.2	328.1
			Right	4	45	151.6	183.5
				5	90	154.4	94.2
				8	45	179.2	130.8
				12	45	142.5	158.3
				16	45	147.0	144.5
				24	45	160.8	130.8
				28	45	188.4	121.6
				32	45	140.2	140.0
				36	45	156.2	112.4
		4	Left	4	45	135.5	190.5
				8	45	156.2	112.4
				12	45	147	169.8
				16	45	174.7	220.2
				24	45	156.2	156.1
				28	45	151.6	181.3
				32	45	151.9	169.8
				36	45	135.6	199.6

Table D. 1. Continued

Cutting Speed	Feed Rate	Hole Number	Measured Side	Ply Number	Orientation of Plies (Degree)	Width (μm)	Depth (μm)
6000 rpm	50 μm/rev	4	Right	4	45	156.2	176.6
				8	45	183.8	110.1
				12	45	131	133.1
				16	45	142.5	137.6
				24	45	144.8	172.1
				28	45	156.2	172.2
				32	45	158.5	151.5
				36	45	154.1	68.8
6000 rpm	200 μm/rev	1	Left	2	-45	165.4	71.1
				4	45	211.4	119.3
				27	90	147	73.4
				28	45	142.4	103.2
				30	-45	156.2	66.5
				32	45	174.6	119.3
				38	-45	176.9	75.7
				39	90	165.4	82.6
			Right	4	45	137.9	96.3
				8	45	126.3	100.9
				12	45	153.9	119.3
				16	45	151.6	98.6
				24	45	202.2	94
				28	45	153.9	82.6
				32	45	147	94.1
				35	90	188.3	59.6
				36	45	174.6	101
		2	Left	2	-45	135.5	75.7
				4	45	160.8	66.5
				5	90	147	71.1
				8	45	163.1	144.5
				13	90	144.7	66.5
				16	45	158.5	75.7
				18	90	190.7	61.9
				20	90	160.8	59.6
				22	90	156.2	91.8
				24	45	124	91.7
				38	-45	144.7	80.3

Table D. 1. Continued

Cutting Speed	Feed Rate	Hole Number	Measured Side	Ply Number	Orientation of Plies (Degree)	Width (µm)	Depth (µm)
6000 rpm	200 µm/rev	2	Right	4	45	133.3	100.9
				5	90	131	64.2
				8	45	163.1	68.8
				12	45	163.1	80.3
				16	45	130.9	107.8
				24	45	151.7	103.3
				27	90	144.7	87.2
				28	45	163.1	110.1
				32	45	135.5	130.8
				39	90	170	10.5
		3	Left	2	-45	147.1	78
				4	45	114.9	126.2
				6	-45	153.9	71.1
				8	45	140.1	123.9
				12	45	151.6	149.1
				24	45	179.2	80.3
				26	-45	147	64.2
				32	45	149.3	137.6
			Right	4	45	163.1	91.7
				5	90	172.3	89.7
				8	45	174.6	114.7
				12	45	156.2	121.6
				13	90	144.7	52.8
				16	45	172.3	126.2
				20	90	234.4	52.7
				24	45	176.9	174.3
				28	45	165.4	121.6
				32	45	144.7	169.8
				35	90	149.3	75.7
				36	45	112.6	158.3
				39	90	176.9	153.7
		4	Left	2	-45	169.9	94.1
				4	45	149	165.1
				12	45	172.3	137.6
				16	45	149.3	133
				24	45	119.4	139.9
				27	90	183.8	87.2
				28	45	165.4	135.3
				32	45	156.2	133

Table D. 1. Continued

Cutting Speed	Feed Rate	Hole Number	Measured Side	Ply Number	Orientation of Plies (Degree)	Width (µm)	Depth (µm)
6000 rpm	200 µm/rev	4	Right	4	45	140.2	139.9
				8	45	87.3	112.4
				9	90	160.8	62
				12	45	158.5	126.2
				16	45	149.3	114.7
				18	90	179.2	52.8
				20	90	142.4	61.9
				22	90	193	97.1
				24	45	149.4	133
				28	45	163.1	105.5
				32	45	153.9	94.1

APPENDIX E – DELAMINATION FACTOR VALUES FOR MULTI-DIRECTIONAL CFRP WITH FIBERGLASS SCRIM SURFACE PLIES

Table E. 1. Delamination factor values for fiberglass scrim surface ply multi-directional CFRP

Cutting speed (RPM)	Feed Rate (µm/rev)	Hole Number	Delamination Factor
3000	50	1	1.686
		2	1.524
	200	1	1.606
		2	1.456
6000	50	1	1.158
		2	1.117
		3	1.116
		4	1.173
	200	1	1.563
		2	1.216
		3	1.526
		4	1.283

APPENDIX F – SURFACE ROUGHNESS RESULTS FOR MULTI-DIRECTIONAL CFRP WITH WOVEN FABRIC SURFACE PLIES

F. 1 SURFACE ROUGHNESS PROFILES FOR MULTI-DIRECTIONAL CFRP WITH WOVEN FABRIC SURFACE PLIES

The profiles of the hole surface and the values of roughness parameter are given in Table F. 1 and F. 2 respectively.

Table F. 1. Surface profiles for multi-directional CFRP with woven fabric surface plies

Speed	Feed	Section	Location	Profiles
3000 rpm	50 µm/rev	1-L	Center	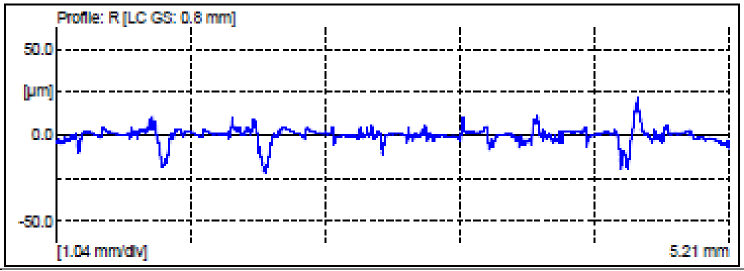
		1-L	Left	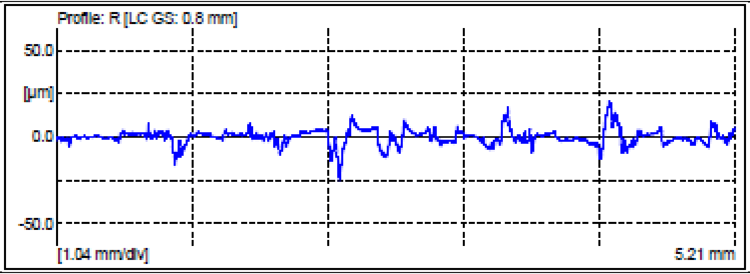
		1-L	Right	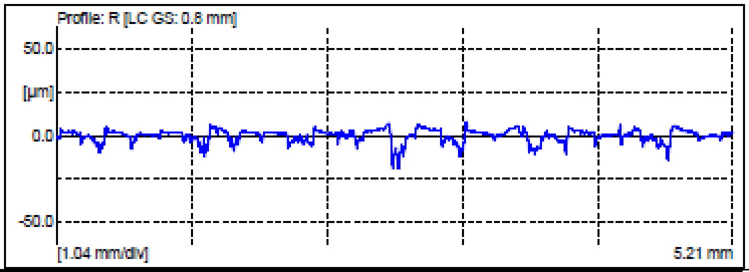
		1-R	Center	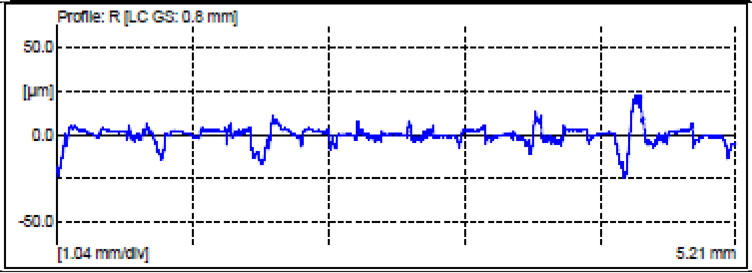
		1-R	Left	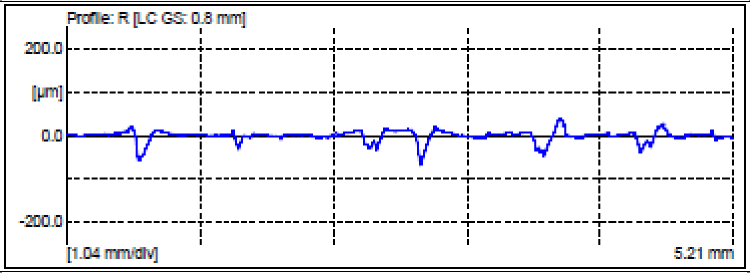
		1-R	Right	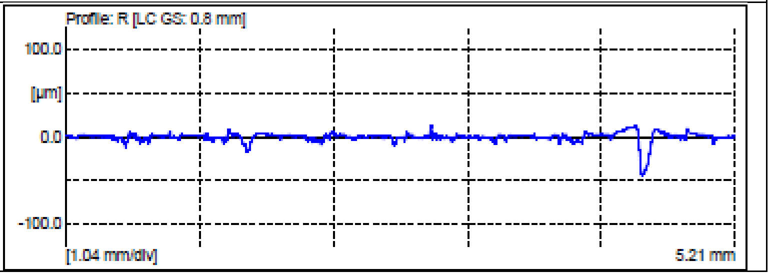

Table F. 1. Continued

Speed	Feed	Section	Location	Profiles
3000 rpm	50 µm/rev	2-L	Center	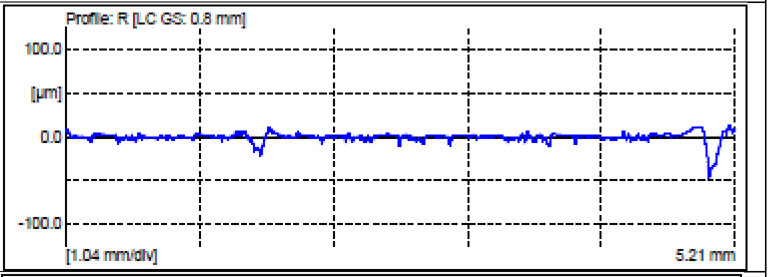
		2-L	Left	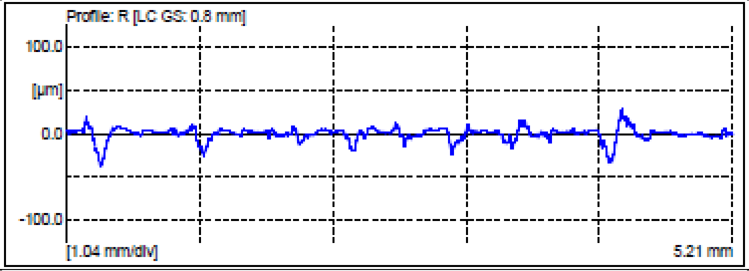
		2-L	Right	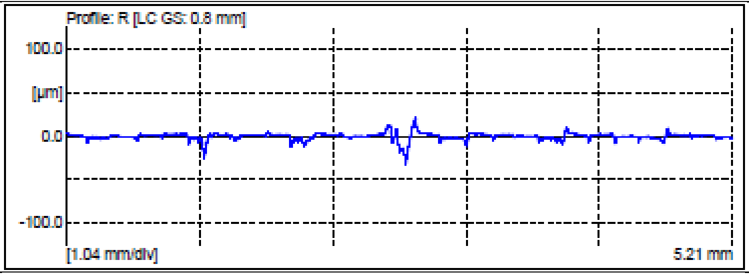
		2-R	Center	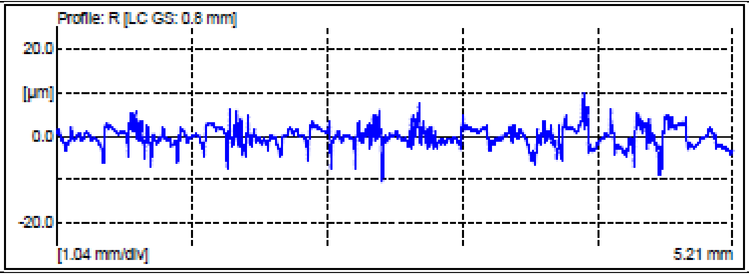
		2-R	Left	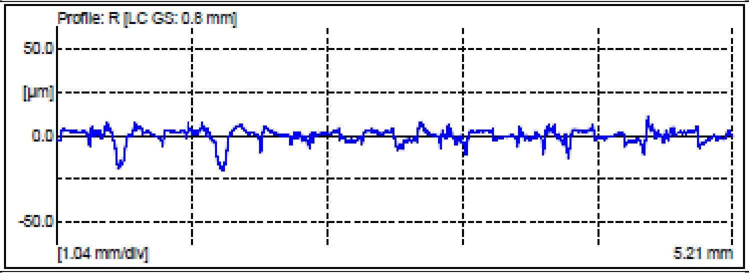
		2-R	Right	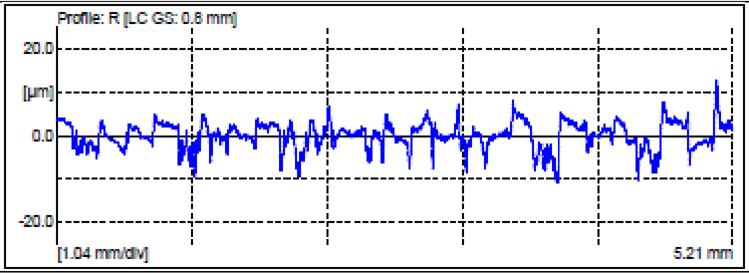

Table F. 1. Continued

Speed	Feed	Section	Location	Profiles
3000 rpm	200 µm/rev	1-L	Center	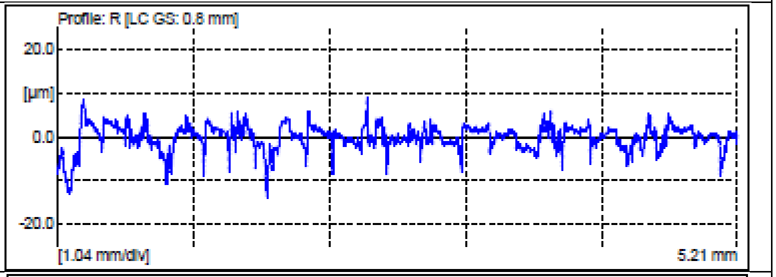
		1-L	Left	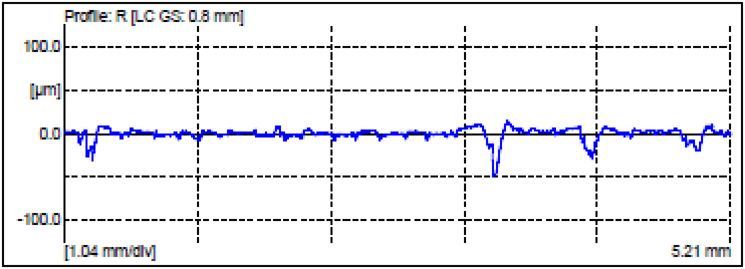
		1-L	Right	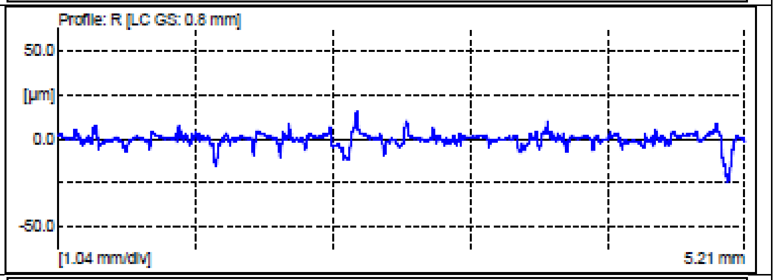
		1-R	Center	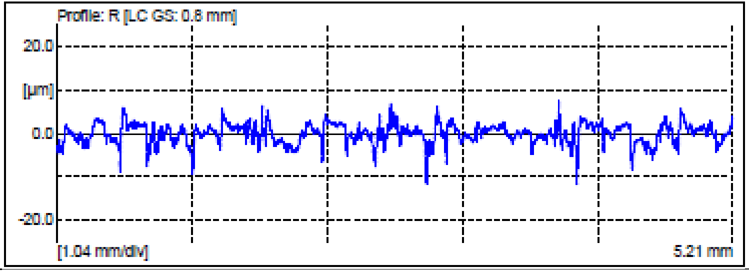
		1-R	Left	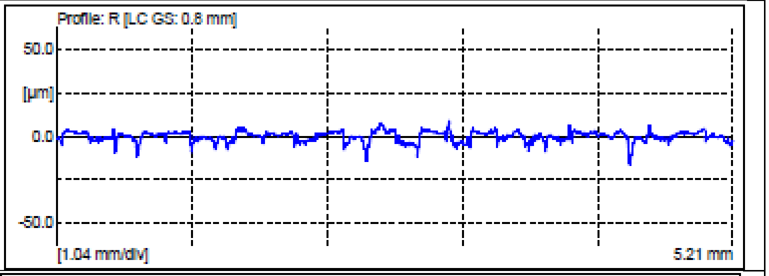
		1-R	Right	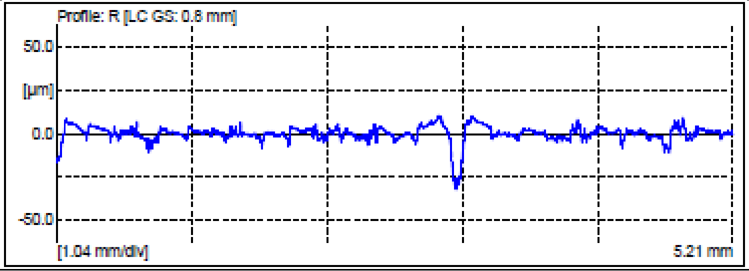

Table F. 1. Continued

Speed	Feed	Section	Location	Profiles
3000 rpm	200 µm/rev	2-L	Center	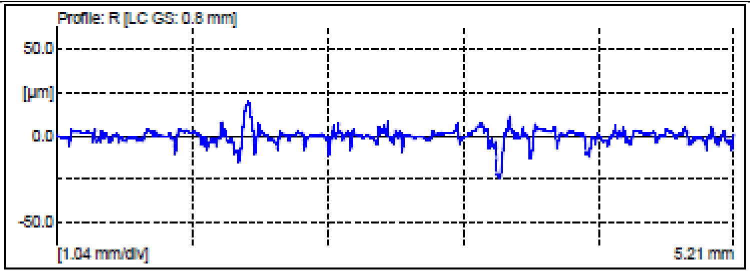
		2-L	Left	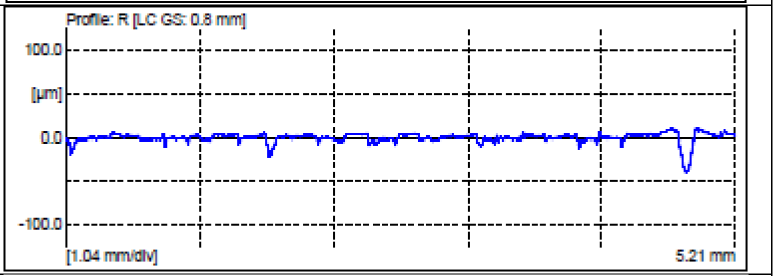
		2-L	Right	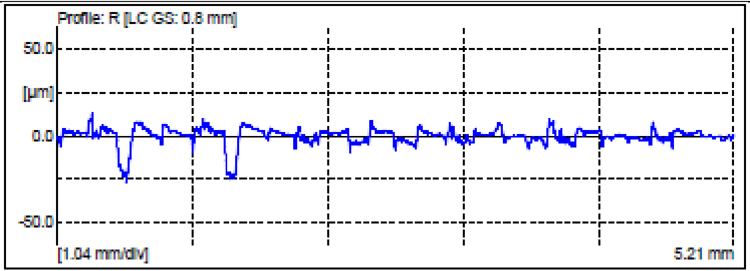
		2-R	Center	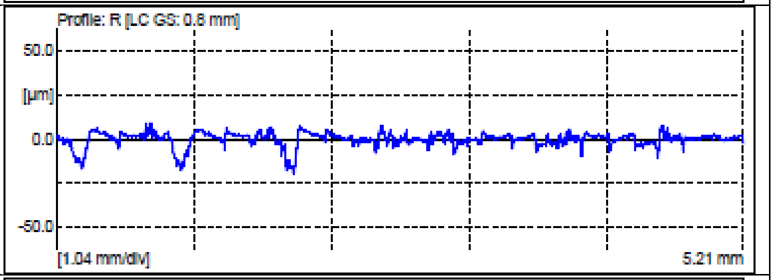
		2-R	Left	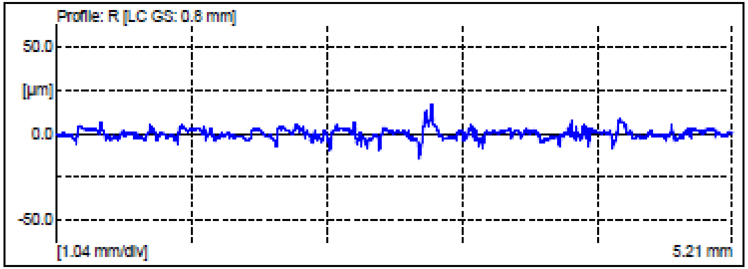
		2-R	Right	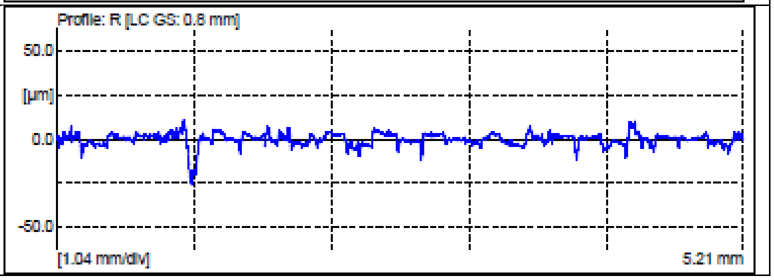

Table F. 1. Continued

Speed	Feed	Section	Location	Profiles
6000 rpm	50 µm/rev	1-L	Center	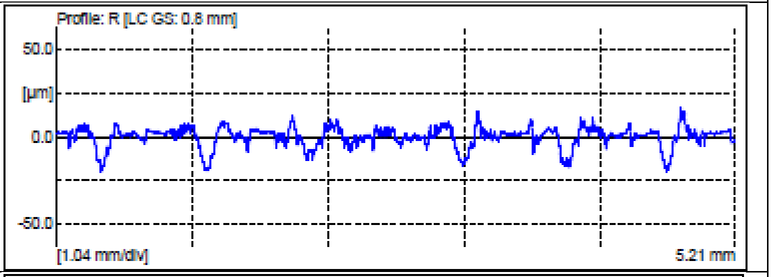
		1-L	Left	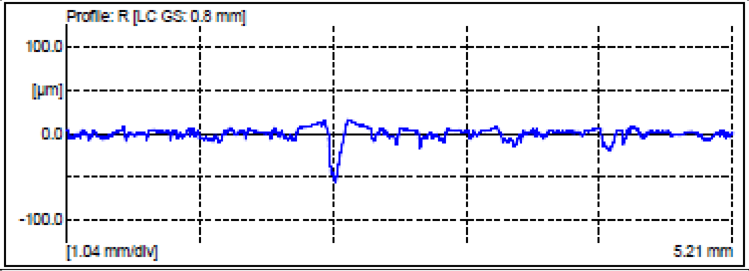
		1-L	Right	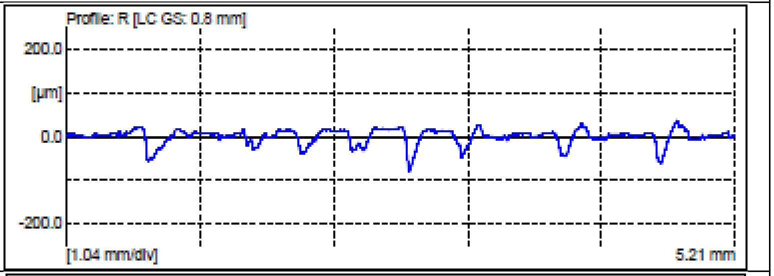
		1-R	Center	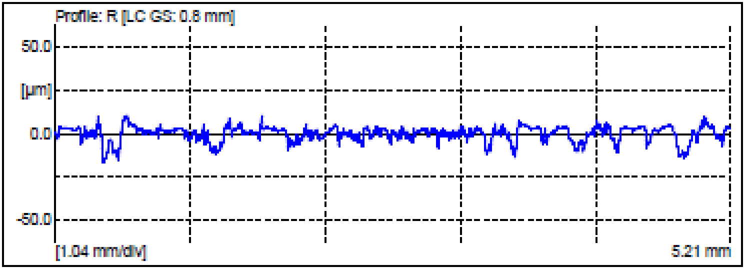
		1-R	Left	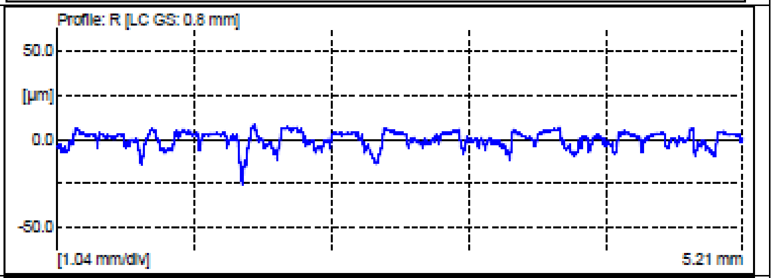
		1-R	Right	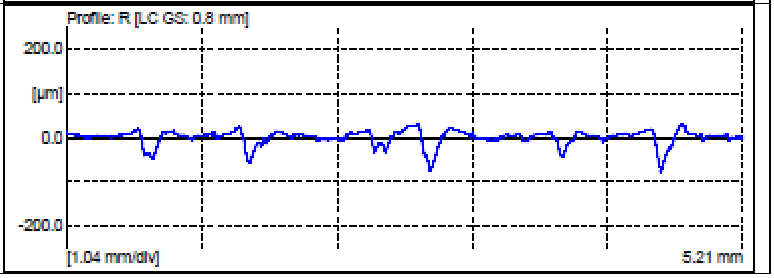

Table F. 1. Continued

Speed	Feed	Section	Location	Profiles
6000 rpm	50 µm/rev	2-L	Center	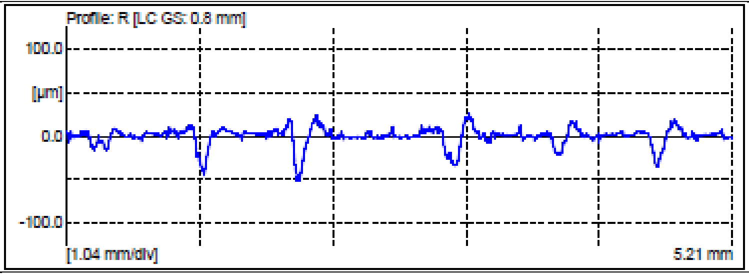
		2-L	Left	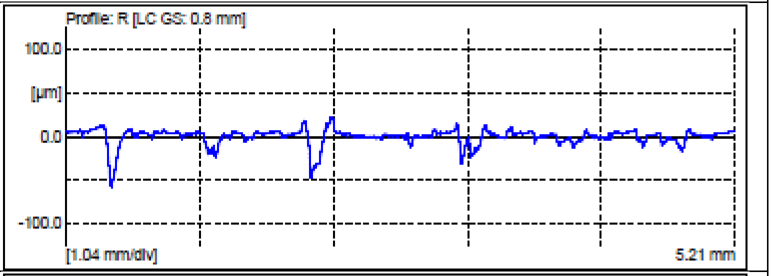
		2-L	Right	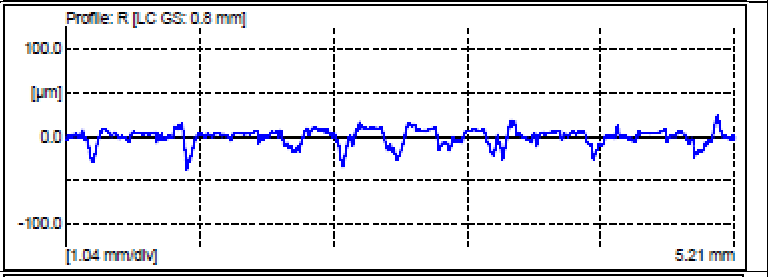
		2-R	Center	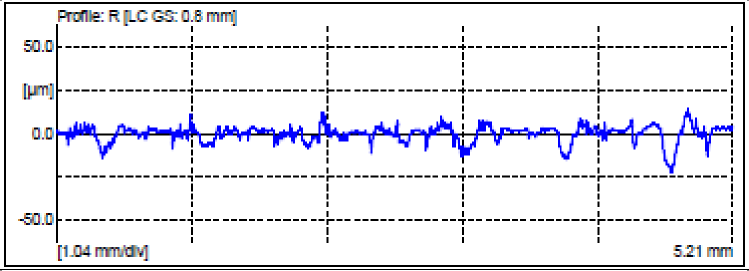
		2-R	Left	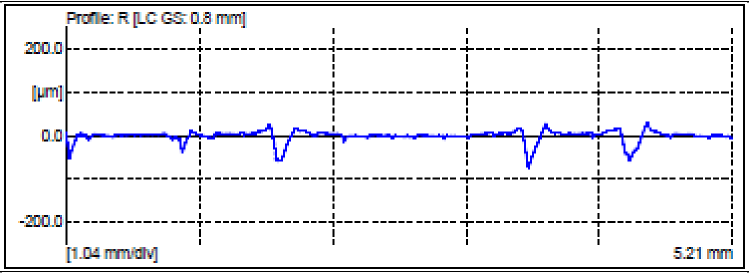
		2-R	Right	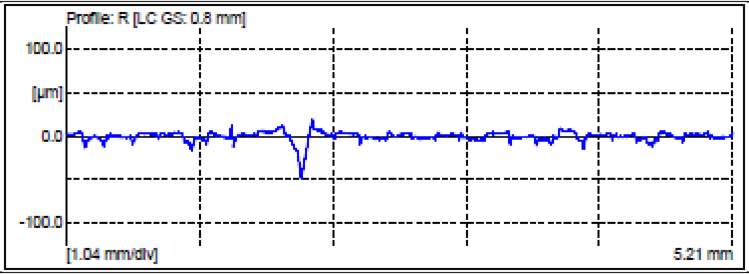

Table F. 1. Continued

Speed	Feed	Section	Location	Profiles
6000 rpm	50 µm/rev	3-L	Center	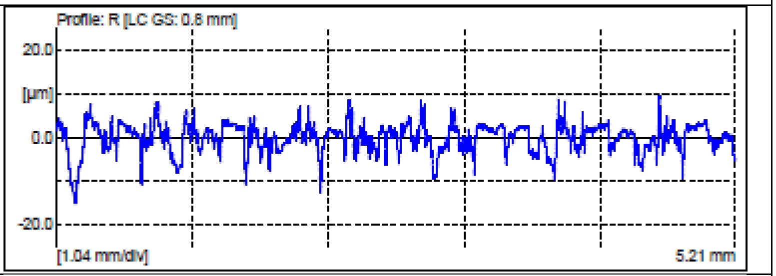
		3-L	Left	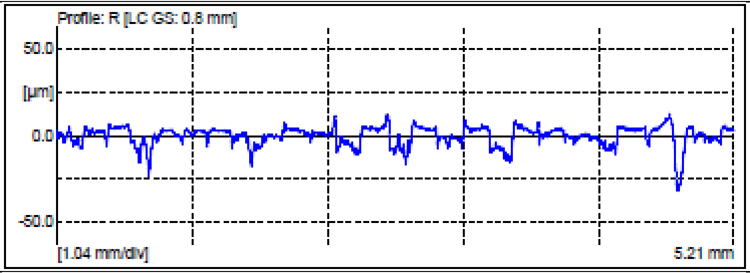
		3-L	Right	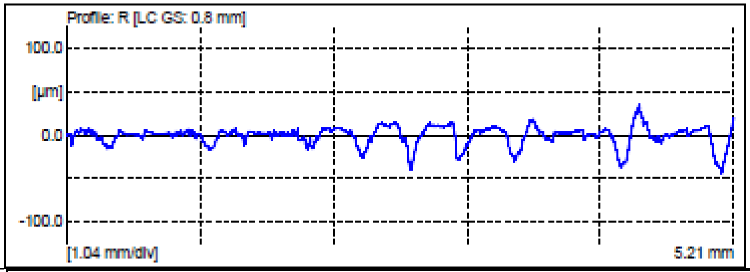
		3-R	Center	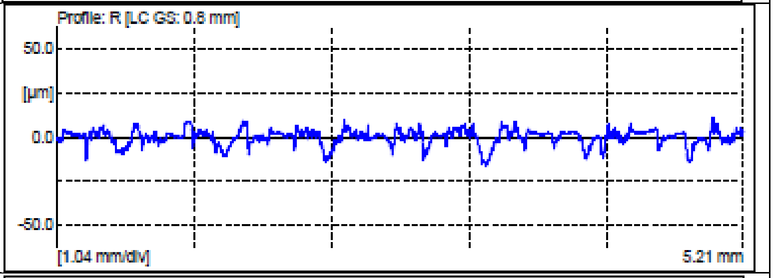
		3-R	Left	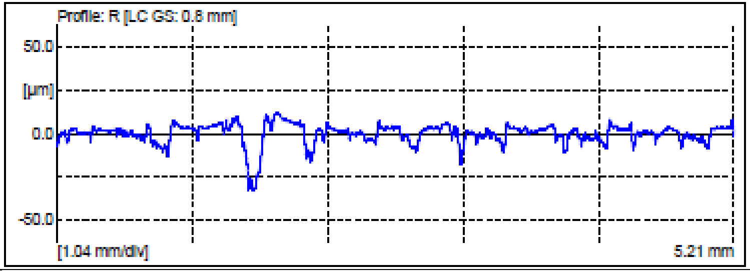
		3-R	Right	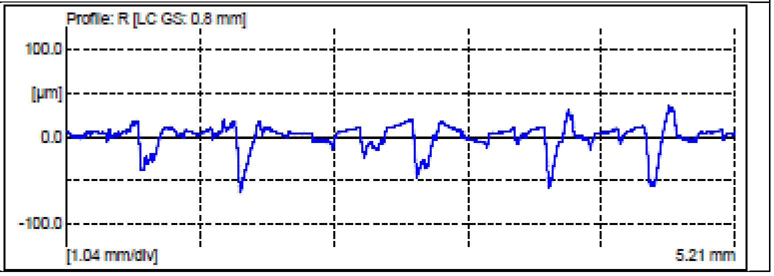

Table F. 1. Continued

Speed	Feed	Section	Location	Profiles
6000 rpm	50 µm/rev	4-L	Center	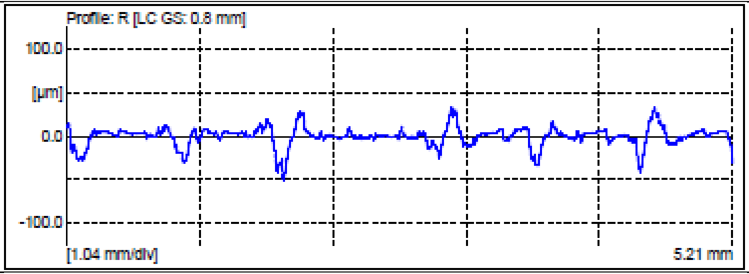
		4-L	Left	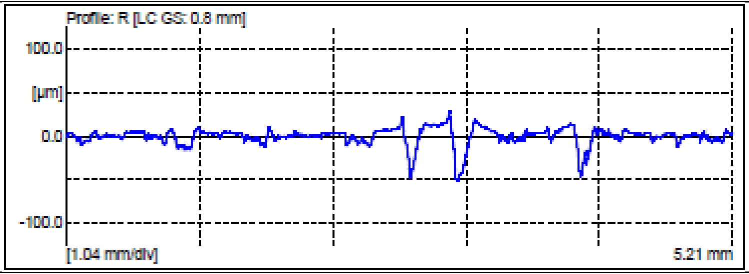
		4-L	Right	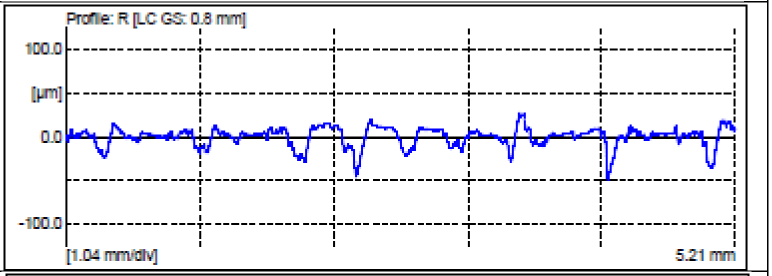
		4-R	Center	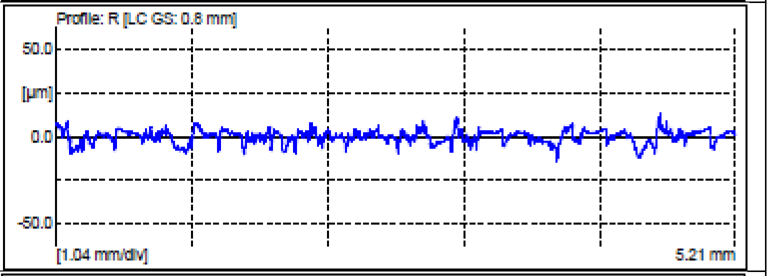
		4-R	Left	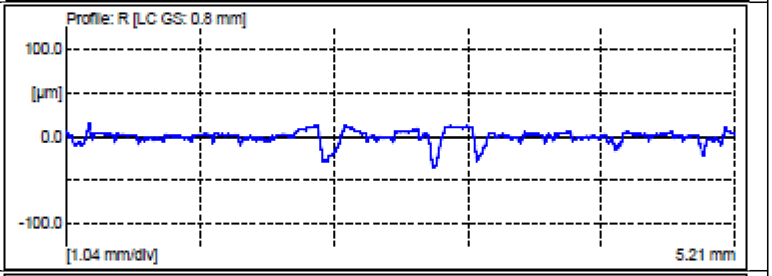
		4-R	Right	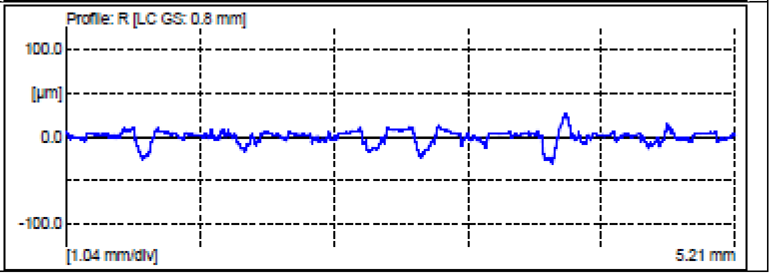

Table F. 1. Continued

Speed	Feed	Section	Location	Profiles
6000 rpm	200 µm/rev	1-L	Center	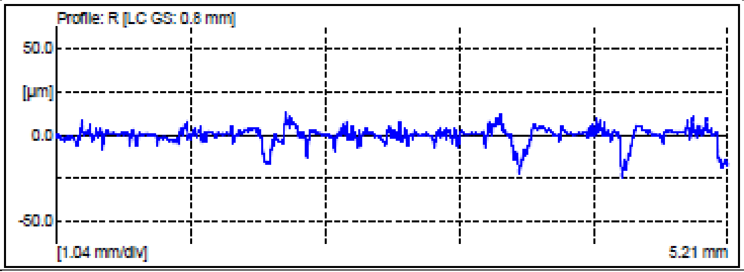
		1-L	Left	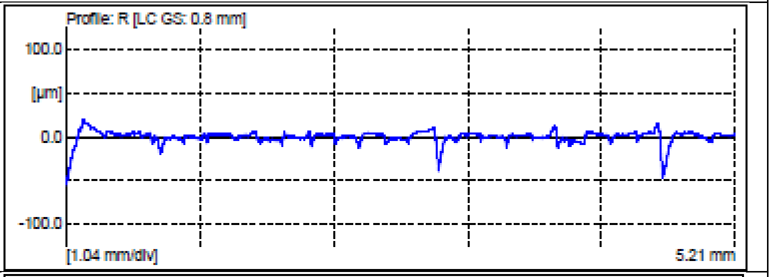
		1-L	Right	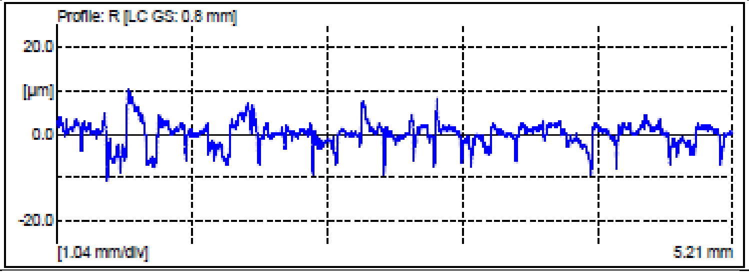
		1-R	Center	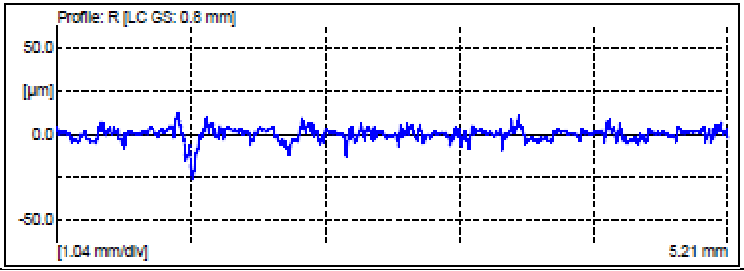
		1-R	Left	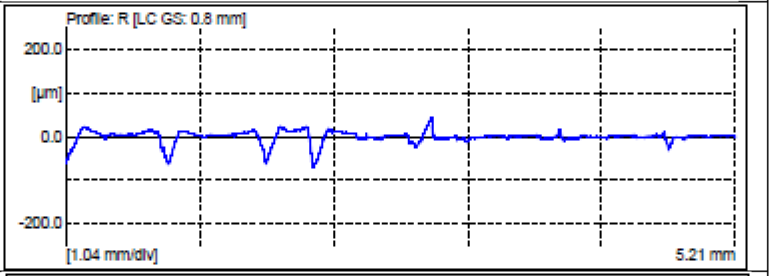
		1-R	Right	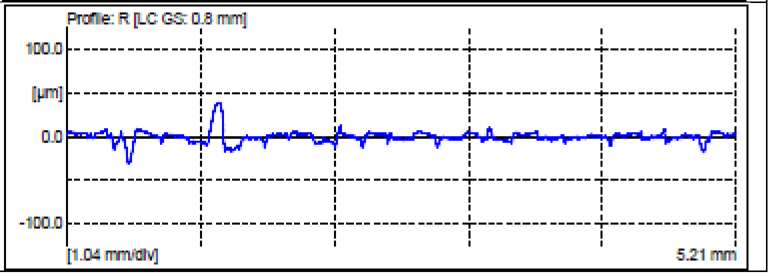

Table F. 1. Continued

Speed	Feed	Section	Location	Profiles
6000 rpm	200 µm/rev	2-L	Center	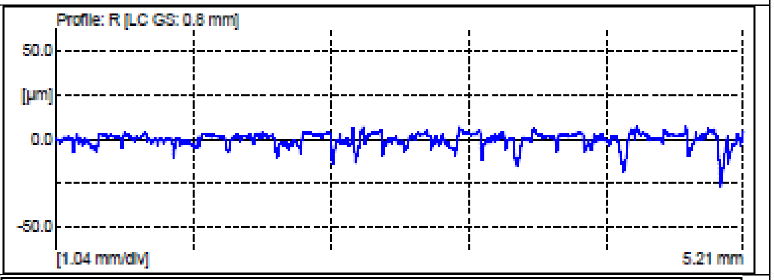
		2-L	Left	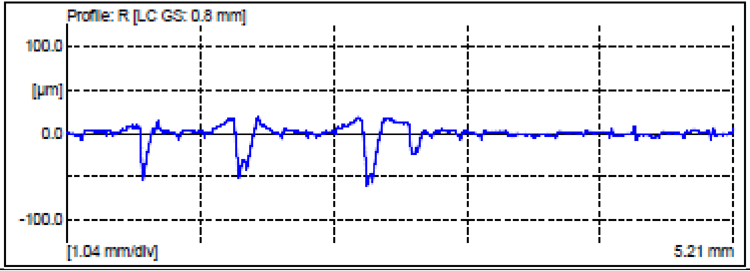
		2-L	Right	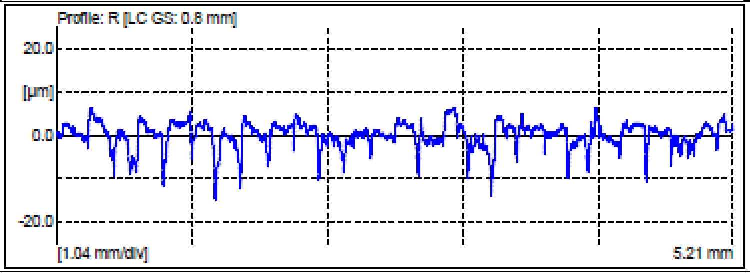
		2-R	Center	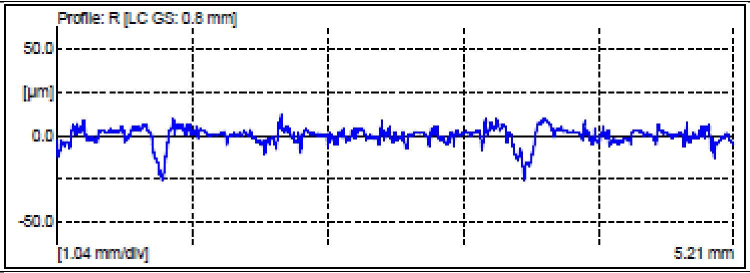
		2-R	Left	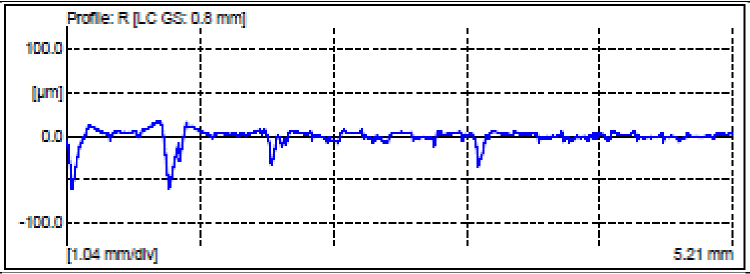
		2-R	Right	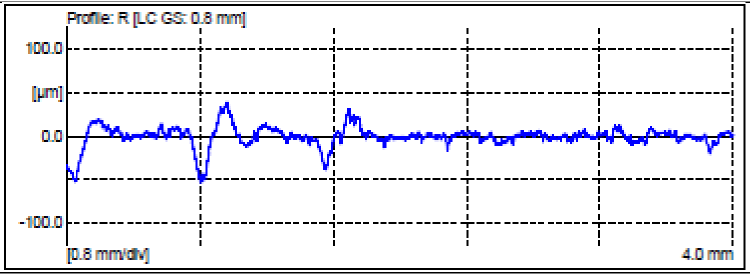

Table F. 1. Continued

Speed	Feed	Section	Location	Profiles
6000 rpm	200 µm/rev	3-L	Center	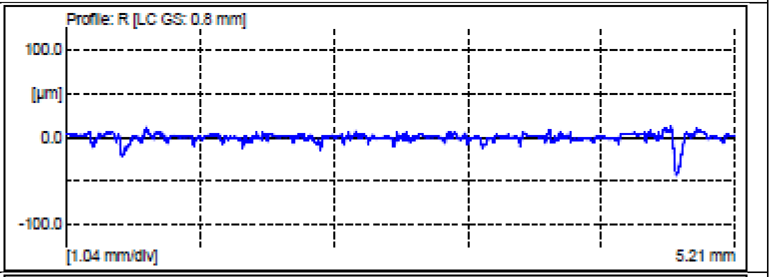
		3-L	Left	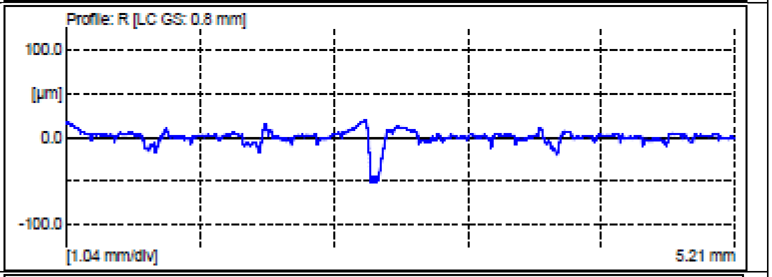
		3-L	Right	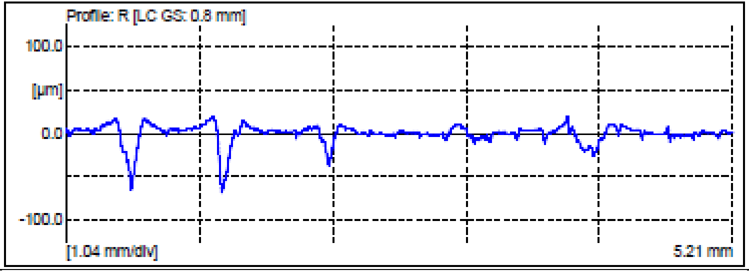
		3-R	Center	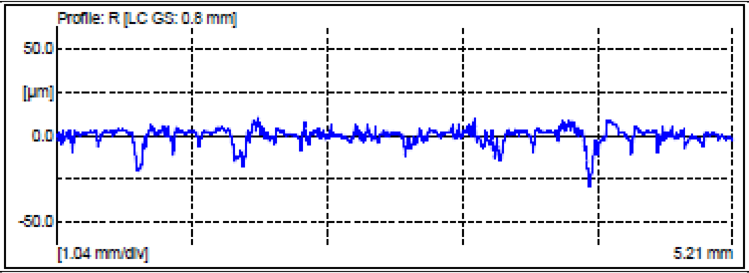
		3-R	Left	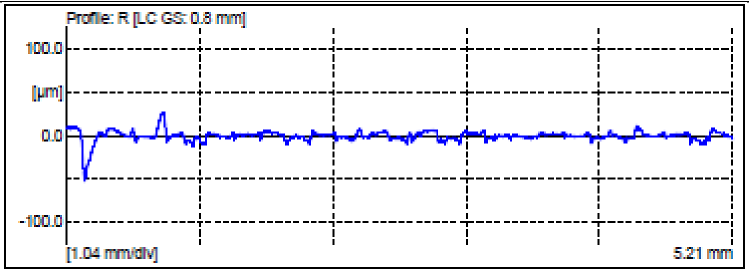
		3-R	Right	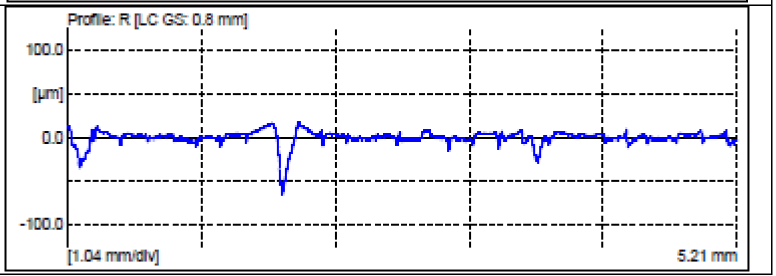

Table F. 1. Continued

Speed	Feed	Section	Location	Profiles
6000 rpm	200 µm/rev	4-L	Center	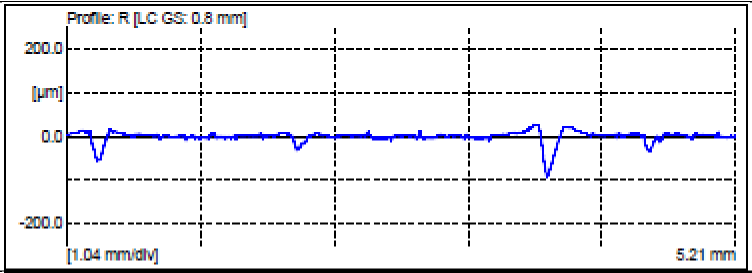
		4-L	Left	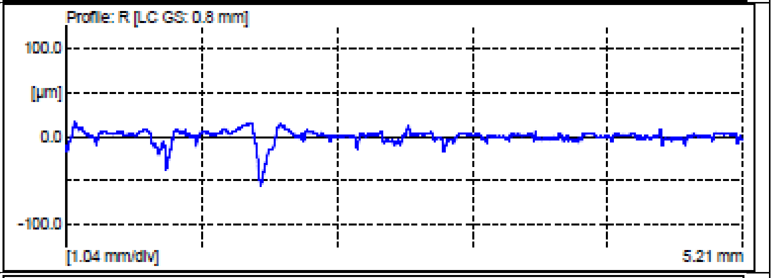
		4-L	Right	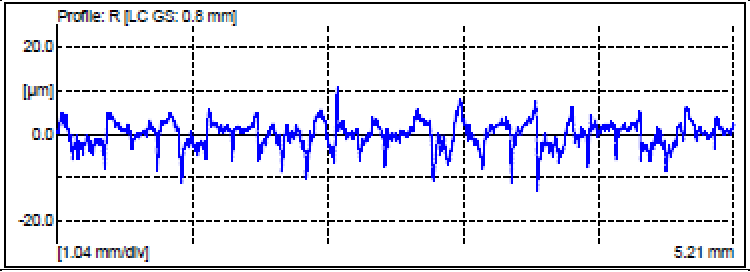
		4-R	Center	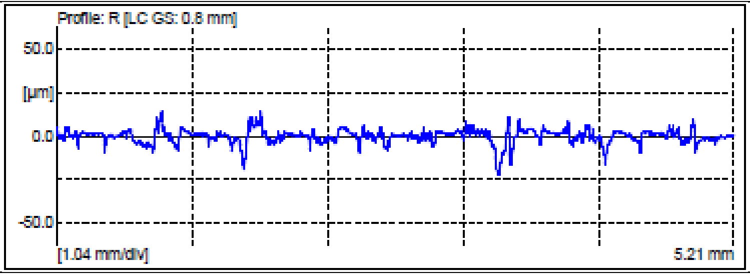
		4-R	Left	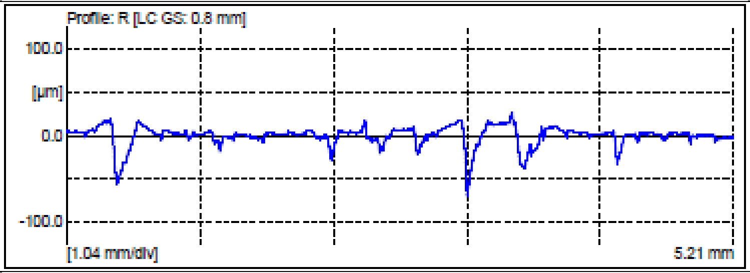
		4-R	Right	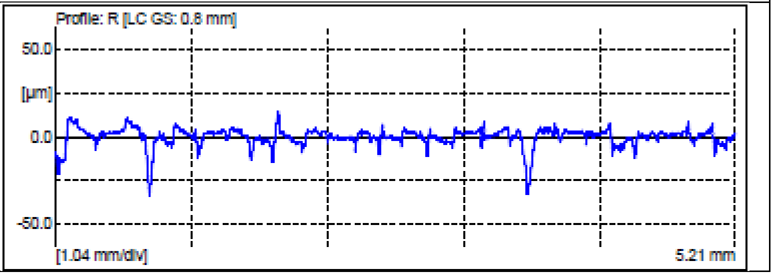

F. 2 ROUGHNESS PARAMETER VALUES FOR MULTI-DIRECTIONAL CFRP WITH WOVEN FABRIC SURFACE PLIES

Table F. 2. Roughness parameter values for woven fabric surface ply multi-directional CFRP

Speed	Feed	Section	Location	Ra (µm)	Rq (µm)	Rz (µm)	Rt (µm)
3000 rpm	50 µm/rev	1-L	Left	3.229	4.595	28.013	54.168
			Center	2.773	4.486	27.990	43.771
			Right	2.730	3.642	19.636	26.811
		1-R	Left	8.036	12.889	93.022	107.491
			Center	3.229	5.136	29.188	46.936
			Right	2.868	5.509	27.463	57.278
		2-L	Left	5.013	7.608	44.362	67.413
			Center	2.896	5.629	28.479	61.124
			Right	2.805	4.308	27.753	55.247
		2-R	Left	2.281	4.029	22.519	31.377
			Center	1.746	2.292	15.289	20.636
			Right	2.391	3.087	16.613	23.762
	200 µm/rev	1-L	Left	4.330	7.181	32.772	64.234
			Center	2.143	2.939	17.148	22.750
			Right	2.379	3.761	23.548	40.345
		1-R	Left	2.406	3.087	18.444	25.776
			Center	1.841	2.375	16.453	19.322
			Right	3.905	4.664	24.878	42.530
		2-L	Left	3.235	5.546	26.755	50.700
			Center	2.762	4.210	24.246	44.377
			Right	2.193	2.994	17.987	21.312
		2-R	Left	2.221	2.920	17.938	31.253
			Center	2.713	4.086	20.919	29.036
			Right	2.569	3.704	24.478	36.681
6000 rpm	50 µm/rev	1-L	Left	4.820	7.732	40.578	72.189
			Center	4.111	5.772	30.633	36.416
			Right	12.163	17.245	82.227	117.880
		1-R	Left	3.539	4.450	21.956	34.444
			Center	3.311	4.362	21.413	26.811
			Right	11.110	16.635	83.903	111.980
		2-L	Left	5.681	9.221	50.071	79.939
			Center	6.651	10.625	56.031	79.315
			Right	6.339	8.633	43.794	61.388
		2-R	Left	7.676	13.597	70.700	102.509
			Center	3.428	4.791	25.556	36.329
			Right	3.767	5.874	29.782	68.057

Table F. 2. Continued

Speed	Feed	Section	Location	Ra (µm)	Rq (µm)	Rz (µm)	Rt (µm)
6000 rpm	50 µm/rev	3-L	Left	4.121	5.572	30.229	44.587
			Center	2.554	3.363	19.656	24.813
			Right	7.792	11.094	46.215	78.887
		3-R	Left	4.058	5.963	25.184	45.320
			Center	3.242	4.404	23.690	27.999
			Right	9.781	14.542	77.103	99.255
		4-L	Left	6.520	10.255	43.590	81.067
			Center	7.508	11.318	62.570	86.384
			Right	7.942	10.923	54.680	76.410
		4-R	Left	4.757	7.254	37.442	51.939
			Center	2.873	3.662	20.752	27.365
			Right	5.280	7.441	37.425	57.064
	200 µm/rev	1-L	Left	4.269	7.279	45.732	75.173
			Center	3.150	4.879	26.899	37.574
			Right	2.071	2.807	15.978	21.088
		1-R	Left	8.493	14.067	63.751	114.081
			Center	2.583	3.724	25.121	38.818
			Right	4.071	6.633	32.872	70.110
		2-L	Left	5.960	10.907	49.027	79.330
			Center	2.850	4.053	21.247	34.156
			Right	2.193	2.994	17.987	21.312
		2-R	Left	5.280	9.441	38.493	76.897
			Center	3.336	4.905	25.999	38.709
			Right	7.701	12.364	63.476	98.279
		3-L	Left	4.722	8.068	36.739	71.655
			Center	3.020	5.225	29.338	55.603
			Right	6.765	11.270	52.246	87.546
		3-R	Left	3.701	6.157	30.099	79.448
			Center	3.150	4.719	26.550	39.918
			Right	4.647	8.294	41.790	83.377
		4-L	Left	4.675	7.626	37.561	73.561
			Center	6.982	13.192	58.465	120.179
			Right	2.334	3.007	17.818	23.657
		4-R	Left	7.349	11.595	65.674	95.952
			Center	2.944	4.181	26.722	36.860
			Right	3.386	5.244	30.839	48.907

APPENDIX G – FIBER PULLOUT MEASUREMENTS FOR MULTI-DIRECTIONAL CFRP WITH WOVEN FABRIC SURFACE PLIES

Table G. 1. Fiber pullout values for woven fabric surface ply multi-directional CFRP

Cutting Speed	Feed Rate	Hole Number	Measured Side	Ply Number	Orientation of Plies (Degree)	Width (µm)	Depth (µm)
3000 rpm	50 µm/rev	1	Left	3	45	197.6	73.4
				7	45	156.2	94.1
				11	45	174.6	73.4
				13	-45	126.4	110.1
				15	45	199.9	110.1
				23	-45	142.4	119.3
				25	45	149.3	126.2
				29	45	176.9	119.3
				33	45	159.3	112.3
				37	45	165.4	121.6
			Right	5	-45	117.2	105.5
				9	-45	181.5	73.4
				13	-45	158.5	103.2
				17	-45	140.1	87.2
				23	-45	181.5	114.7
				27	-45	135.6	112.4
				31	-45	147	149.1
				35	-45	181.5	165.2
		2	Left	3	45	179.2	66.5
				5	-45	140.2	156
				7	45	160.8	66.5
				9	-45	117.2	123.9
				11	45	117.2	83.9
				13	-45	130.9	73.4
				15	45	153.9	66.5
				23	-45	128.6	117
				25	45	172.3	62
				27	-45	105.7	149.1
				29	45	131	66.5
				31	-45	140.1	142.2
				37	45	170	98.6
			Right	4	0	168	66.5
				5	-45	157	181.2
				8	0	183.9	75.7

Table G. 1. Continued

Cutting Speed	Feed Rate	Hole Number	Measured Side	Ply Number	Orientation of Plies (Degree)	Width (µm)	Depth (µm)
3000 rpm	50 µm/rev	2	Right	9	-45	158.5	183.5
				12	0	165.4	71.1
				13	-45	128.7	185.8
				16	0	190.7	55.1
				17	-45	156.2	174.3
				22	0	156.2	73.4
				23	-45	195.3	197.3
				27	-45	121.7	167.4
				31	-45	172.3	183.5
				35	-45	1473	137.6
	200 µm/rev	1	Left	3	45	142.4	146.8
				7	45	166.7	130.8
				11	45	167.7	123.9
				15	45	151.6	105.5
				23	-45	119.4	91.8
				25	45	179.2	96.4
				29	45	174.6	55.1
				31	-45	144.7	149.1
				33	45	151.6	50.5
			Right	5	-45	131	82.6
				9	-45	151.6	75.7
				13	-45	140.1	78
				17	-45	172.3	101
				23	-45	153.9	52.8
				31	-45	121.7	75.7
				35	-45	144.8	45.9
		2	Left	3	45	209.2	107.8
				7	45	174.6	94.1
				11	45	172.3	84.9
				15	45	172.3	128.4
				23	-45	174.6	176.6
				25	45	147	91.8
				29	45	153.9	71.1
				33	45	151.7	94.1
				37	45	172.3	103.2
			Right	5	-45	204.3	110.1
				9	-45	147.1	78
				17	-45	124.1	78
				23	-45	124	48.2
				27	-45	142.5	96.3
				31	-45	186.1	75.7
				35	-45	163.1	89.5

Table G. 1. Continued

Cutting Speed	Feed Rate	Hole Number	Measured Side	Ply Number	Orientation of Plies (Degree)	Width (µm)	Depth (µm)
6000 rpm	50 µm/rev	1	Left	6	90	153.9	96.4
				7	45	153.9	165.2
				10	90	183.8	144.5
				11	45	160.8	103.2
				14	90	165.4	100.9
				18	0	128.7	68.8
				20	0	176.9	73.4
				22	0	153.9	89.5
				24	0	147	119.3
				27	-45	147	61.9
				28	0	117.2	89.5
				32	0	126.4	87.7
				36	0	151.6	91.8
			Right	3	45	148.5	257.9
				7	45	154.9	83.8
				11	45	148.5	74.2
				15	45	177.6	109.6
				25	45	167.9	151.5
				29	45	133.5	128.9
				33	45	158.1	138.7
				37	45	145.2	183.8
		2	Left	6	90	126.4	123..9
				14	90	160.8	146.8
				19	90	163.1	165.1
				21	90	142.2	142.2
			Right	3	45	160.8	162.9
				11	45	167.7	100.9
				15	45	131	123.9
				25	45	181.5	100.9
				29	45	167.7	94
				33	45	144.7	135.3
		3	Left	6	90	110.3	87.2
				10	90	117.1	114.7
				19	90	163.1	89.5
				21	90	144.7	71.1
			Right	3	45	158.5	167.5
				7	45	158.5	162.9
				11	45	126.7	146.8
				15	45	165.4	243.1
				25	45	152.6	220.2
				29	45	133.2	151.4
				33	45	160.8	135.3
				37	45	158.5	94

Table G. 1. Continued

Cutting Speed	Feed Rate	Hole Number	Measured Side	Ply Number	Orientation of Plies (Degree)	Width (µm)	Depth (µm)
6000 rpm	50 µm/rev	4	Left	5	45	87.3	82.8
				11	45	112.2	98.7
			Right	3	45	179.2	215.6
				7	45	188.4	169.8
				11	45	130.9	174.3
				15	45	112.6	231.7
				25	45	85	167.4
				29	45	133.5	160.6
				33	45	101.1	160.6
				37	45	112.6	234
	200 µm/rev	1	Left	3	45	160.8	126.2
				6	90	167.7	119.3
				7	45	147	87.2
				11	45	140.1	103.2
				15	45	148	117
				25	45	153.9	117
				29	45	159	119.3
				30	90	176.9	133.1
				33	45	165.4	126.2
			Right	5	-45	156.2	169.8
				9	-45	112.6	91.7
				13	-45	170	119.3
				17	-45	170	206.5
				23	-45	89.6	121.6
				35	-45	163.1	84.9
		2	Left	7	45	126.4	66.5
				29	45	170	61.9
				33	45	130.9	84.9
			Right	4	0	160.8	96.3
				5	-45	179.2	208.8
				9	-45	176.9	105.5
				13	-45	190.3	100.9
				17	-45	206.8	133
				23	-45	181.5	89.5
				27	-45	183.8	107.8
				31	-45	160.8	135.3
				35	-45	174.6	121.6

Table G. 1. Continued

Cutting Speed	Feed Rate	Hole Number	Measured Side	Ply Number	Orientation of Plies (Degree)	Width (µm)	Depth (µm)
6000 rpm	200 µm/rev	3	Left	3	45	153.9	126.2
				7	45	166.7	78
				11	45	216	121.6
				15	45	135.6	82.6
				25	45	131	149.1
				29	45	160.8	75.7
				33	45	158.5	100.9
				37	45	151.7	91.7
			Right	5	-45	140.1	165.2
				9	-45	133.3	107.8
				13	-45	140.2	215.6
				17	-45	140.2	121.6
				23	-45	144.7	220.2
				27	-45	153.9	75.7
				31	-45	160.8	96.3
				35	-45	158.5	91.8
		4	Left	3	45	176.4	91.7
				7	45	85	59.6
			Right	5	-45	149.3	112.4
				9	-45	142.5	78
				13	-45	126.4	162.9
				17	-45	131	75.7
				23	-45	149.3	105.5
				27	-45	165.4	114.7
				30	90	126.4	43.6
				31	-45	170	114.7
				35	-45	165.4	82.6

APPENDIX H – DELAMINATION FACTOR VALUES FOR MULTI-DIRECTIONAL CFRP WITH WOVEN FABRIC SURFACE PLIES

Table H. 1. Delamination factor values for Woven fabric surface ply multi-directional CFRP

Cutting Speed (RPM)	Feed Rate (µm/rev)	Hole Number	Delamination Factor
3000	50	1	1.125
		2	1.097
	200	1	1.336
		2	1.202

Table H. 1. Continued

Cutting Speed (RPM)	Feed Rate (µm/rev)	Hole Number	Delamination Factor
6000	50	1	1.185
		2	1.178
		3	1.116
		4	1.107
	200	1	1.231
		2	1.360
		3	1.160
		4	1.274

APPENDIX I – SEM MICROGRAPHS OF THE HOLE SURFACE OF QUASI – ISOTROPIC CFRP LAMINATES

An SEM micrograph of the sectioned halves of the hole surface was taken at three locations to cover the full sectioned halve. SEM images were taken at the right side, at the center, and at the left side, then reconstructed to form the sectioned halve as shown in Figure I. 1. From this, major damages and defects were identified and SEM micrographs for low and high level combination of feed rate and cutting speed are shown in detail in Figures I. 2 to I. 5.

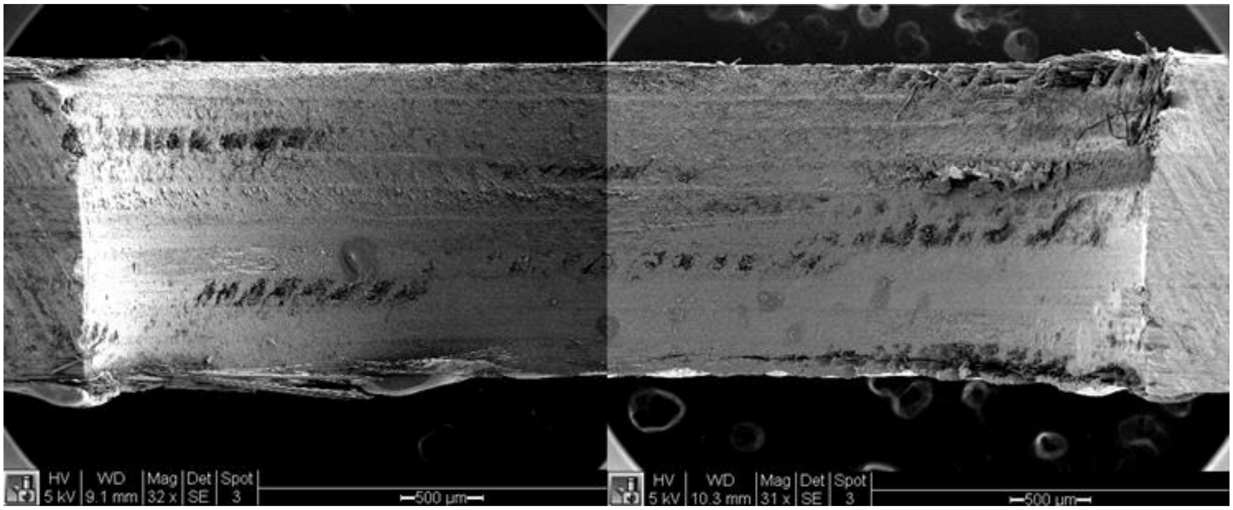

Figure I. 1. Reconstructed SEM micrograph of sectioned halve of a hole

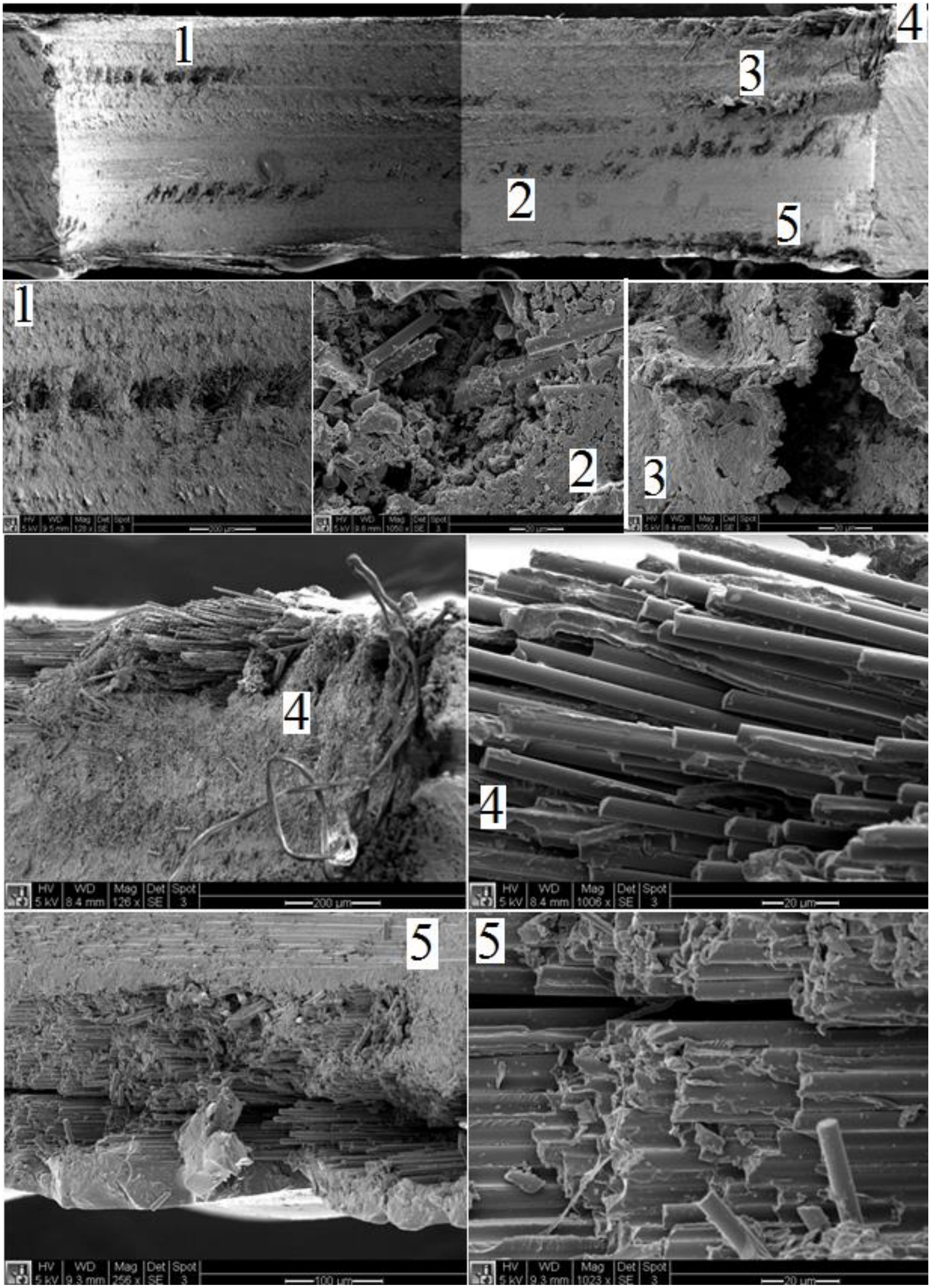

Figure I. 2. SEM micrograph of a hole drilled at 3000 rpm and 50 µm/rev

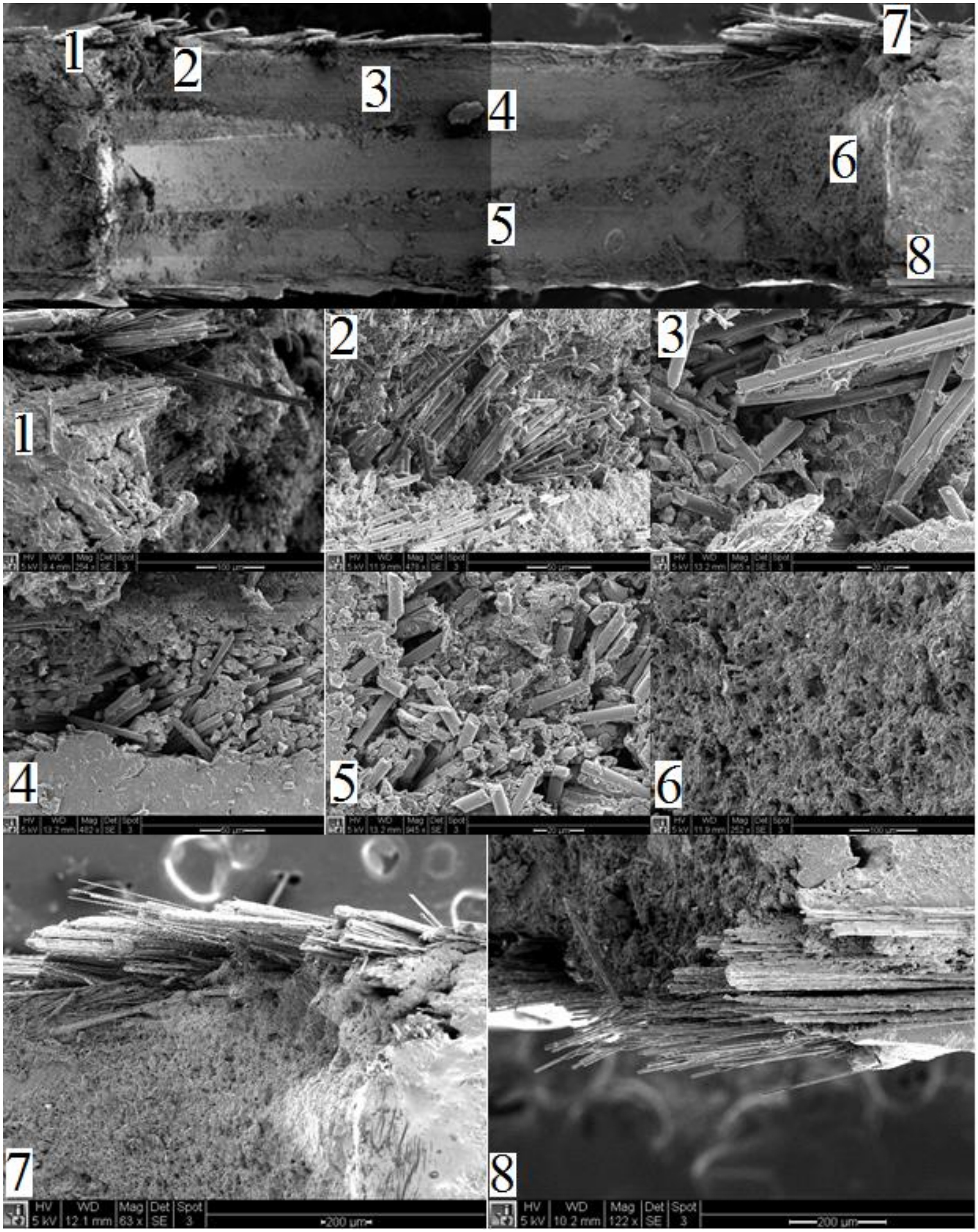

Figure I. 3. SEM micrograph of a hole drilled at 3000 rpm and 200 µm/rev

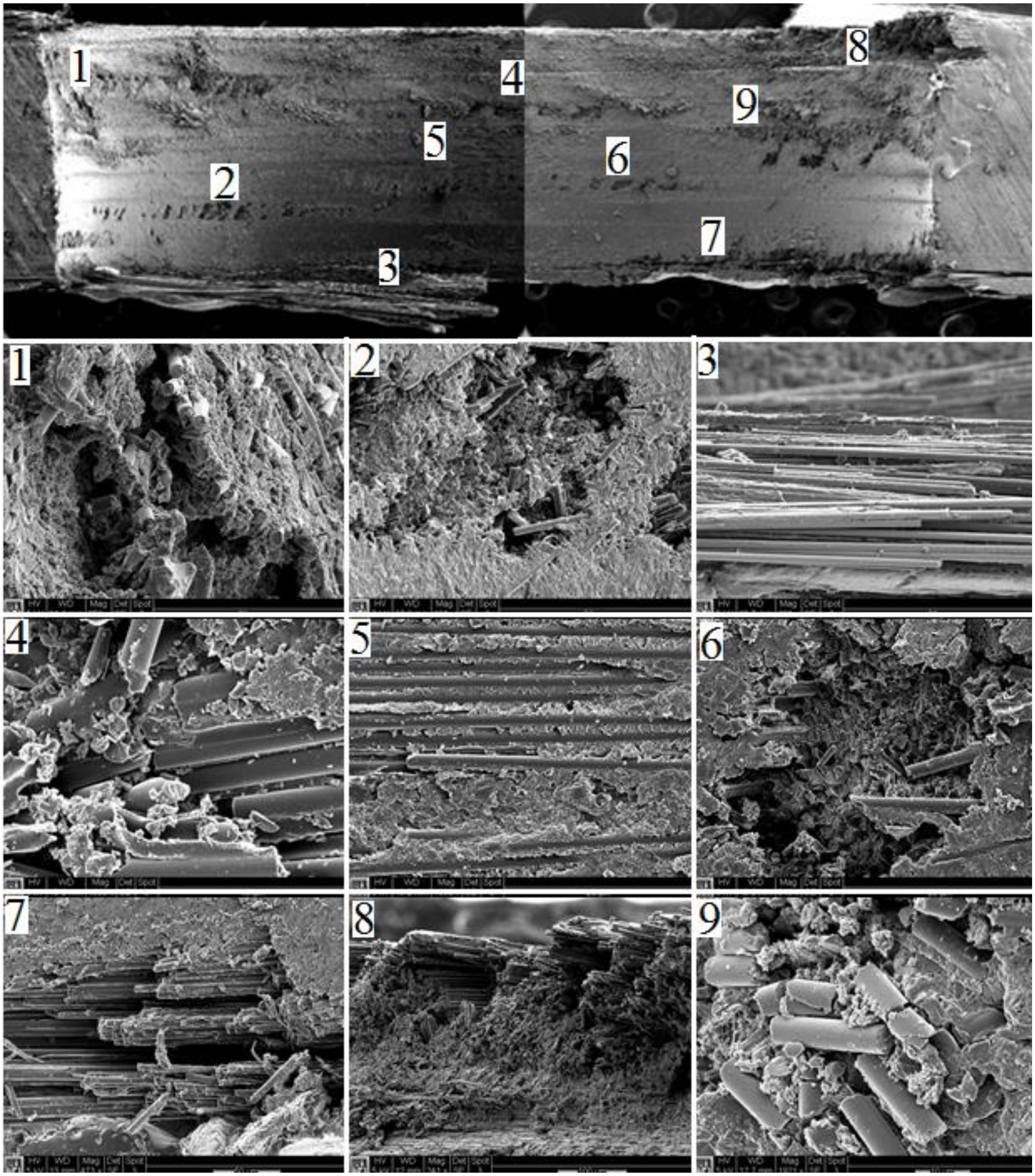

Figure I. 4. SEM micrograph of a hole drilled at 6000 rpm and 50 µm/rev

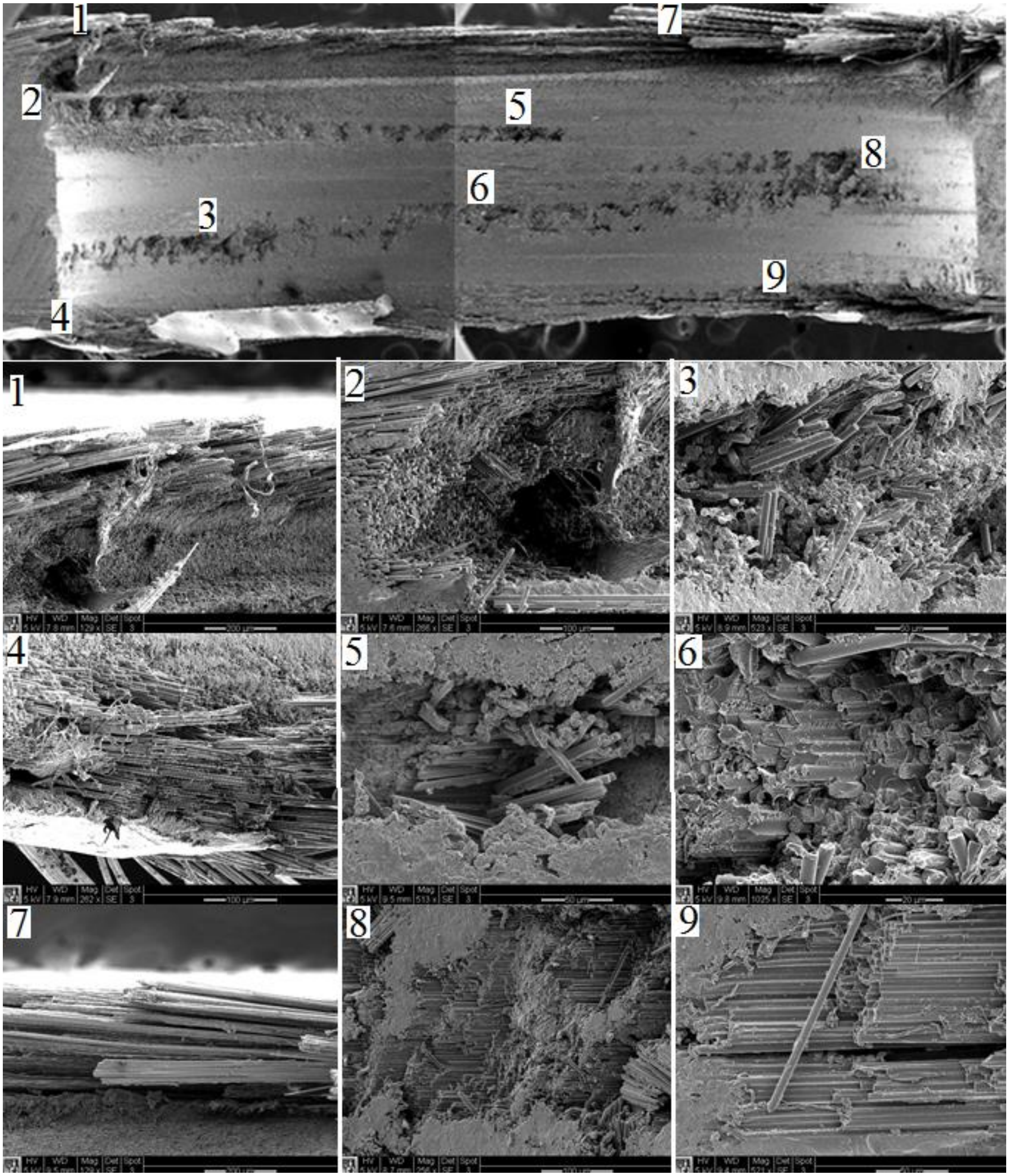

Figure I. 5. SEM micrograph of a hole drilled at 6000 rpm and 200 µm/rev

APPENDIX J – RAW ACOUSTIC EMISSION SIGNAL PROFILES WHEN DRILLING QUASI – ISOTROPIC CFRP LAMINATES

Acoustic emission signal was collected when drilling quasi-isotropic CFRP laminate and the raw acoustic emission signal profiles for holes drilled at different combinations of cutting speed and feed rate are shown in Figures from J. 1 to J. 8.

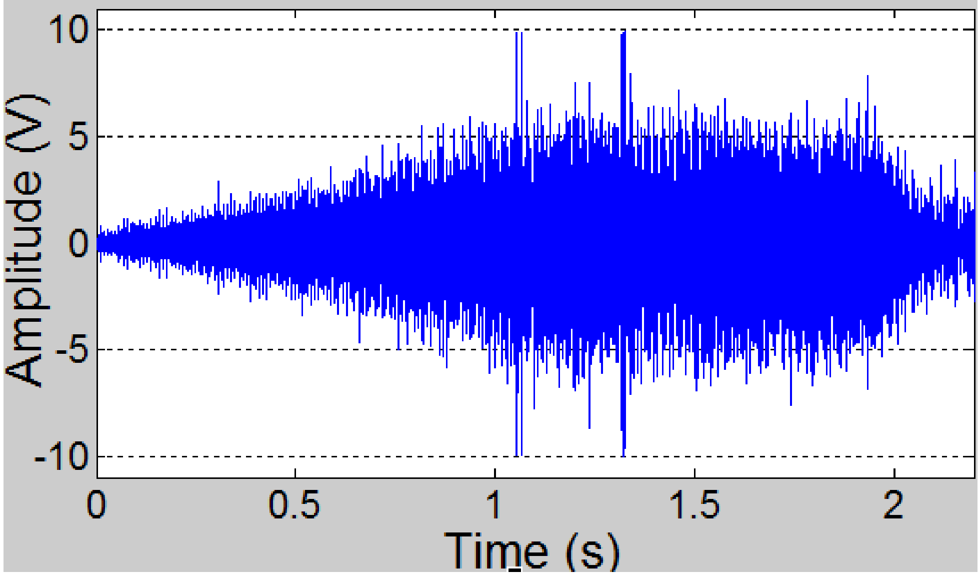

Figure J. 1. Raw acoustic emission signal profile for 3000 rpm and 50 µm/rev

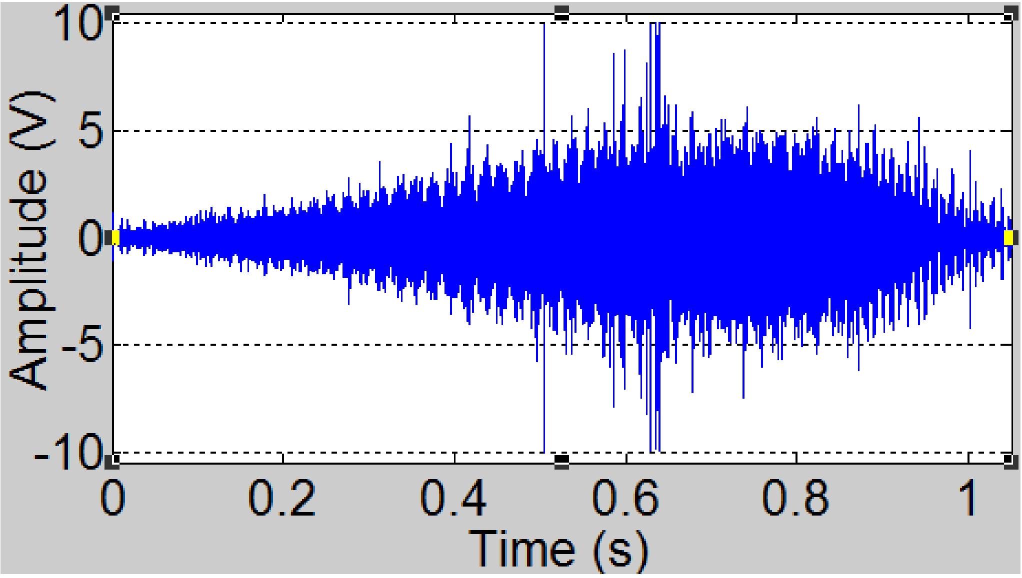

Figure J. 2. Raw acoustic emission signal profile for 3000 rpm and 100 µm/rev

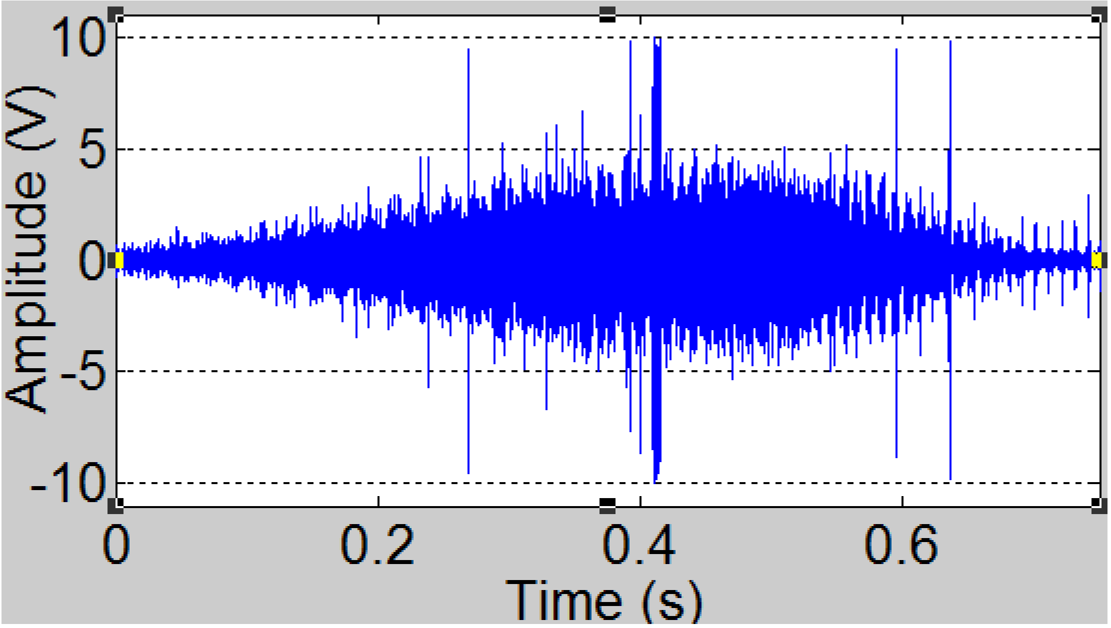

Figure J. 3. Raw acoustic emission signal profile for 3000 rpm and 150 µm/rev

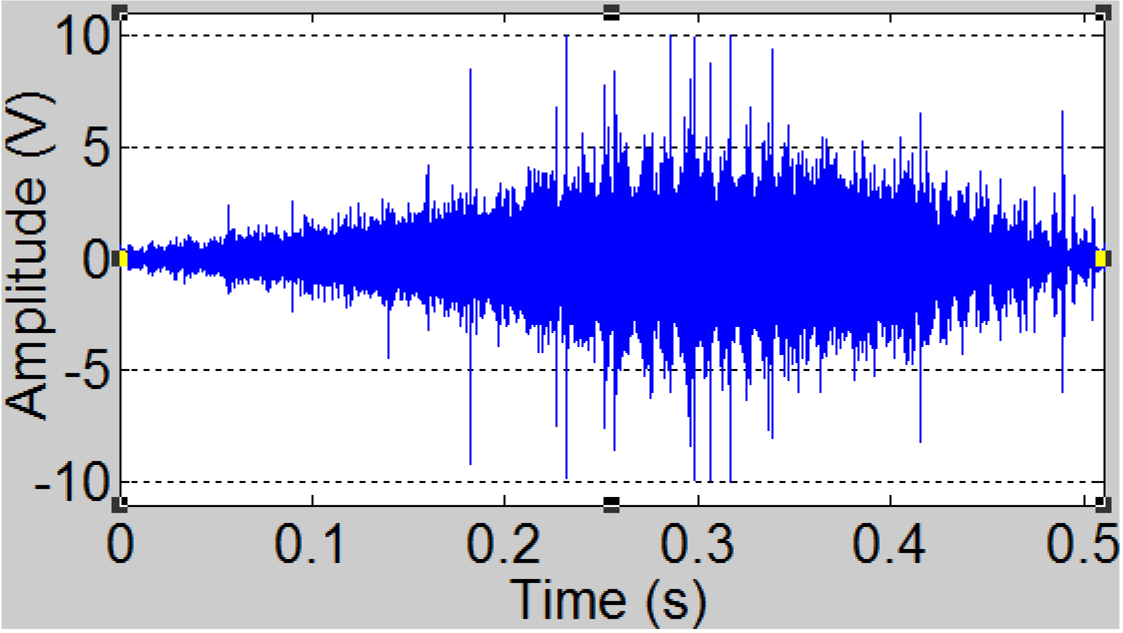

Figure J. 4. Raw acoustic emission signal profile for 3000 rpm and 200 µm/rev

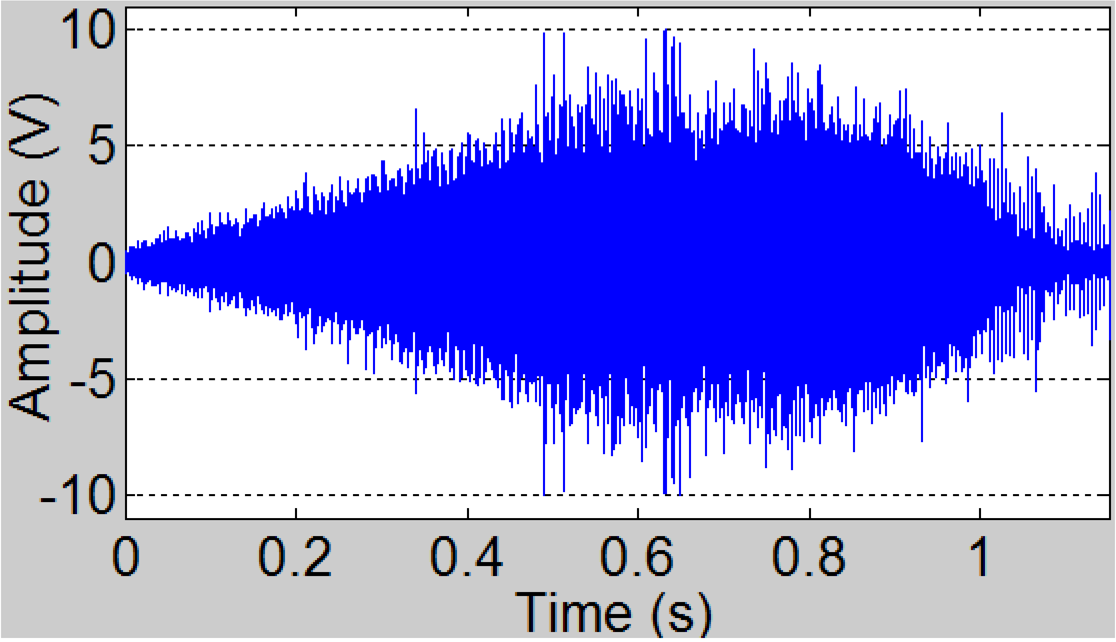

Figure J. 5. Raw acoustic emission signal profile for 6000 rpm and 50 µm/rev

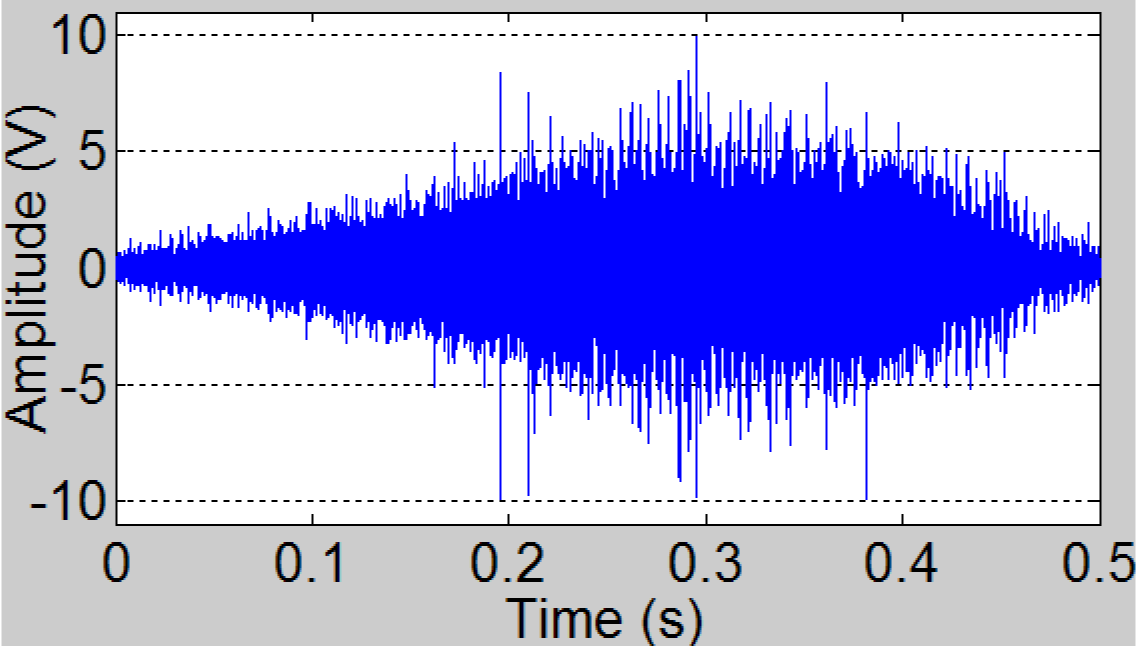

Figure J. 6. Raw acoustic emission signal profile for 6000 rpm and 100 µm/rev

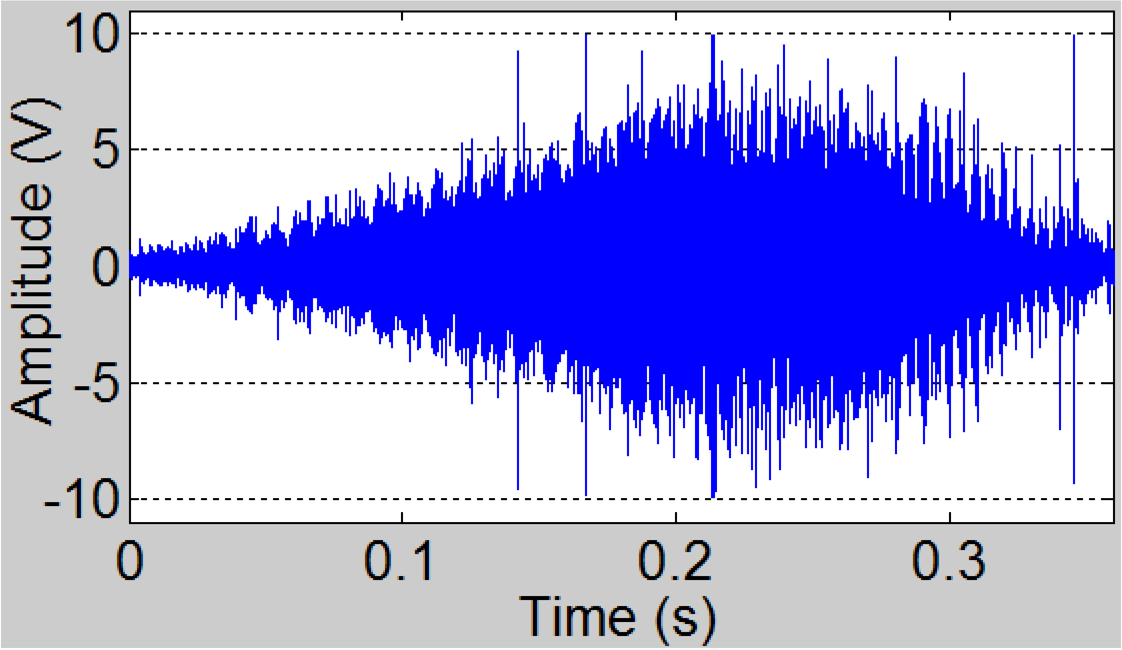

Figure J. 7. Raw acoustic emission signal profile for 6000 rpm and 150 µm/rev

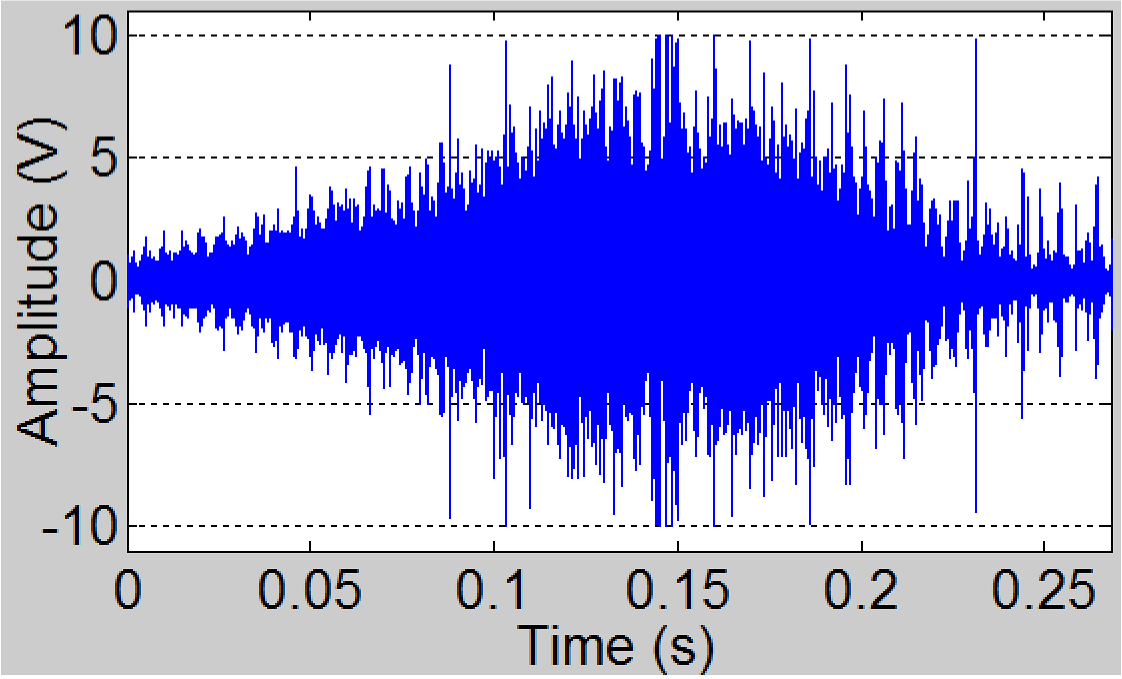

Figure J. 8. Raw acoustic emission signal profile for 6000 rpm and 200 µm/rev

APPENDIX K – ANOVA ANALYSIS AND SURFACE RESPONSE MODEL RESULTS OF THRUST FORCE AND TORQUE FOR UNI-DIRECTIONAL CFRP COMPOSITES

Table K. 1. ANOVA table for thrust force surface response model

Source	Sum of Squares	DF	Mean Square	F Value	p-value prob>F
Model	28008.51	5	5601.7	325	< 0.0001
A-Speed	231.04	1	231.04	13.4	0.0026
B-Feed	27757.09	1	27757.09	1610.42	< 0.0001
AB	5.54	1	5.54	0.32	0.5796
A$^{\wedge 2}$	11.86	1	11.86	0.69	0.4208
B$^{\wedge 2}$	2.97	1	2.97	0.17	0.6843
Residual	241.3	14	17.24		
Cor Total	28249.81	19			
Thrust = 115.95 – 4.56*A + 52.68*B – A*B-1.73*A$^{\wedge 2}$ + 0.92*B$^{\wedge 2}$					

Table K. 2. ANOVA table for torque surface response model

Source	Sum of Squares	DF	Mean Square	F Value	p-value prob>F
Model	0.68	5	0.14	520.09	< 0.0001
A-Speed	0.005476	1	0.005476	20.91	0.0004
B-Feed	0.67	1	0.67	2572.91	< 0.0001
AB	0.001152	1	0.001152	4.4	0.0546
A$^{\wedge 2}$	0.000289	1	0.000289	1.1	0.3115
B$^{\wedge 2}$	0.000302	1	0.000302	1.15	0.3013
Residual	0.003667	14	0.000262		
Cor Total	0.68	19			
Torque= 0.46 -0.022*A +0.26*B-0.014*A*B- 8.55 E-3*A$^{\wedge 2}$ - 9.286 E-3*B$^{\wedge 2}$					

APPENDIX L – SURFACE ROUGHNESS RESULTS FOR UNI-DIRECTIONAL CFRP

L. 1 SURFACE PROFILES FOR UNI-DIRECTIONAL CFRP

Table L. 1. Surface profiles for uni-directional CFRP Composite

Speed	Feed	Section	Location	Profiles
1500 rpm	64 µm/rev	Left Half	Center	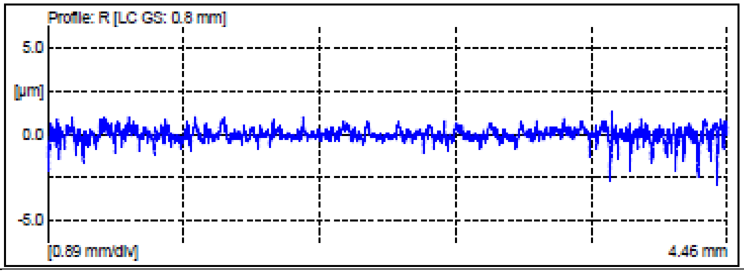
			Left	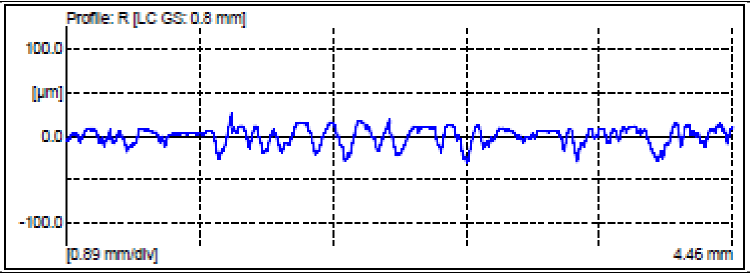
			Right	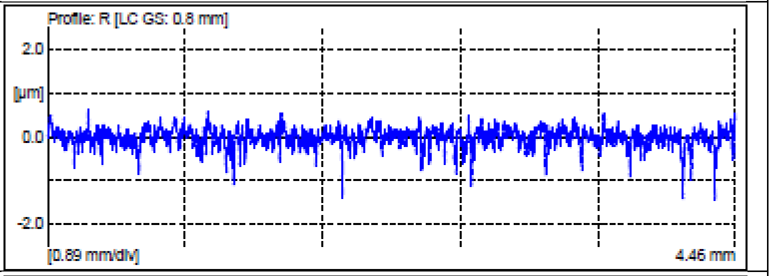
		Right Half	Center	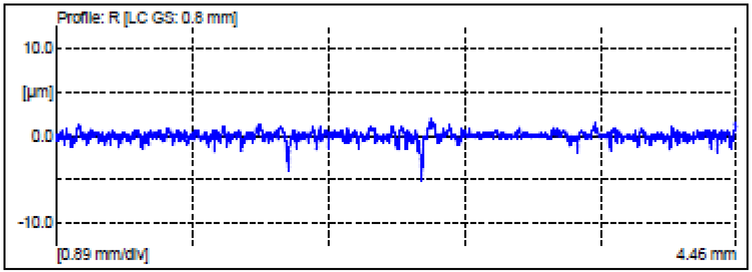
			Left	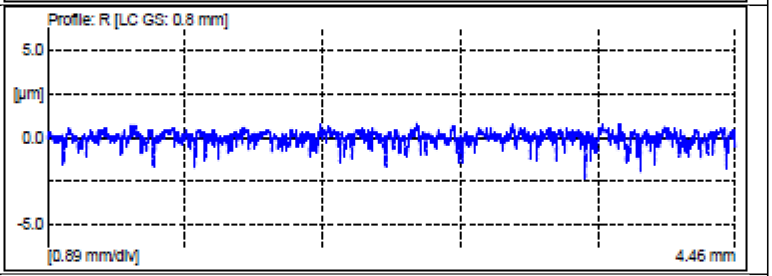
			Right	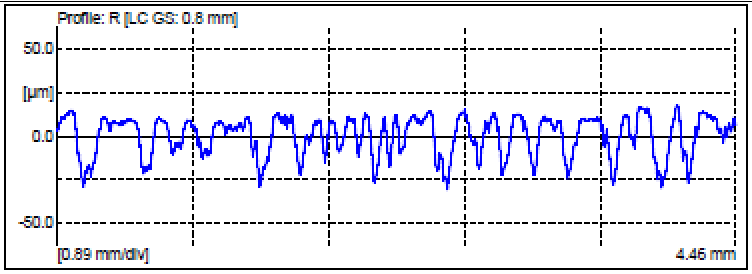

Table L. 1. Continued

Speed	Feed	Section	Location	Profiles
1500 rpm	128 µm/rev	Left Half	Center	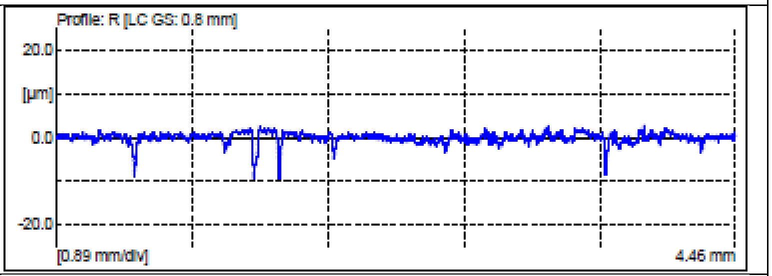
			Left	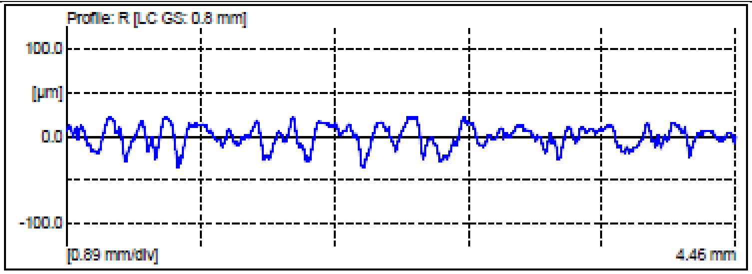
			Right	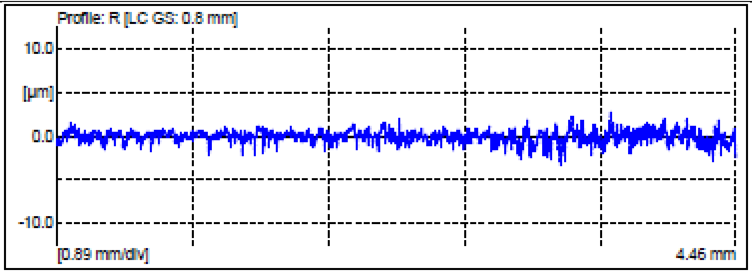
		Right Half	Center	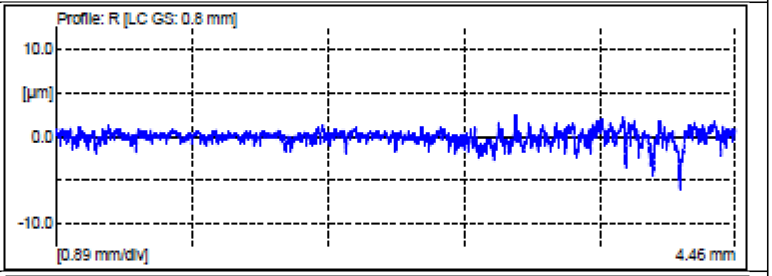
			Left	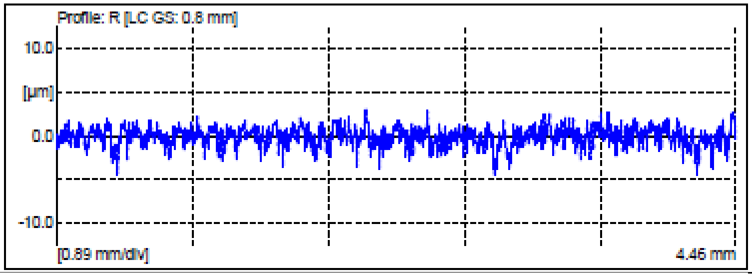
			Right	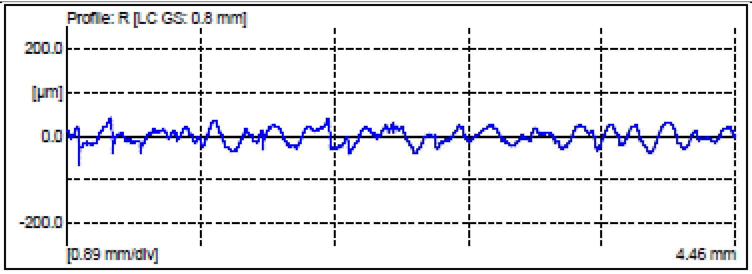

Table L. 1. Continued

Speed	Feed	Section	Location	Profiles
1500 rpm	192 µm/rev	Left Half	Center	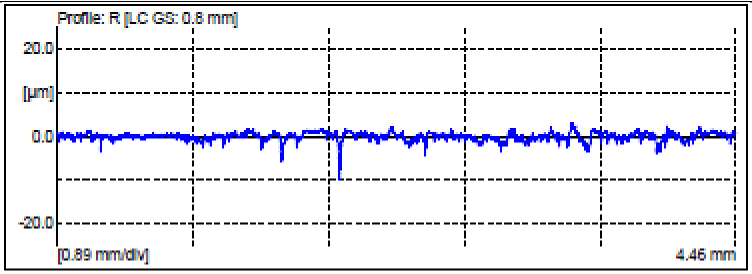
			Left	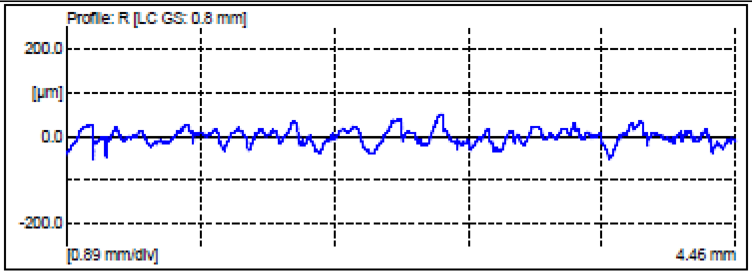
			Right	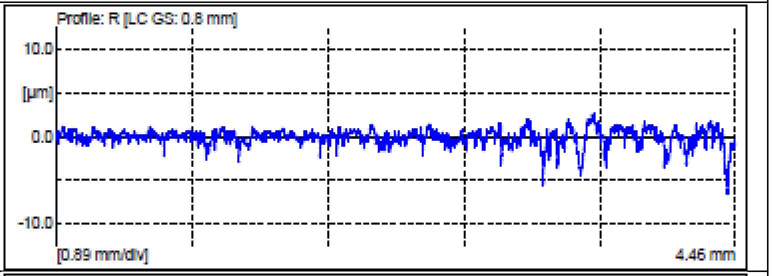
		Right Half	Center	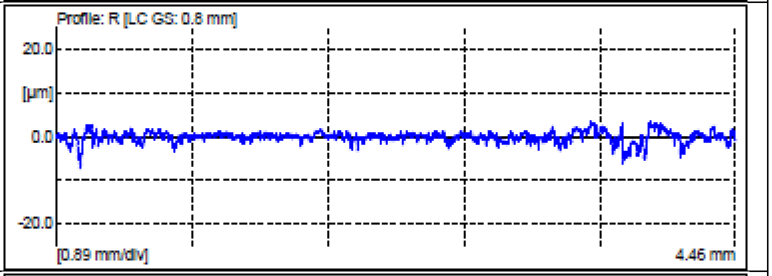
			Left	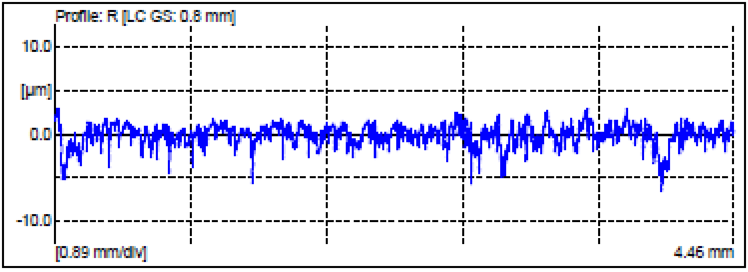
			Right	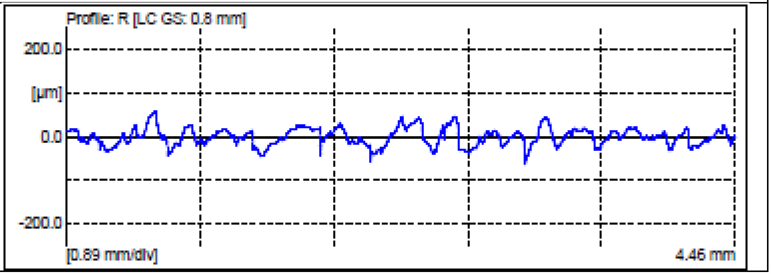

Table L. 1. Continued

Speed	Feed	Section	Location	Profiles
1500 rpm	256 µm/rev	Left Half	Center	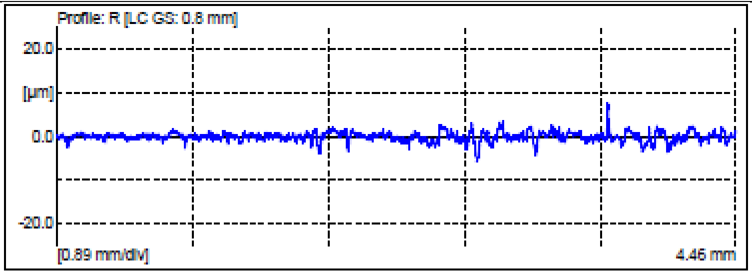
			Left	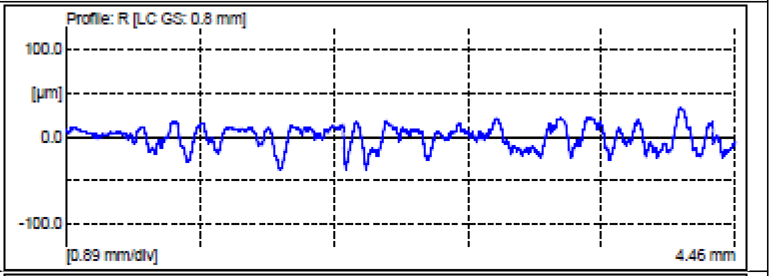
			Right	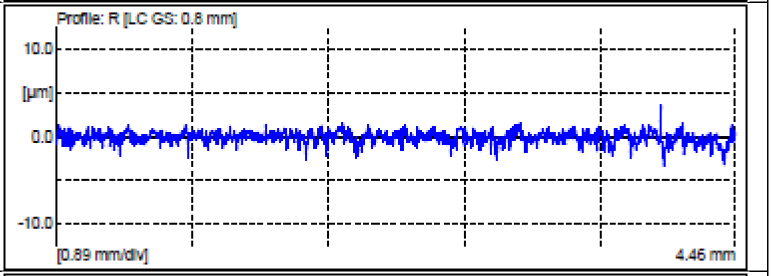
		Right Half	Center	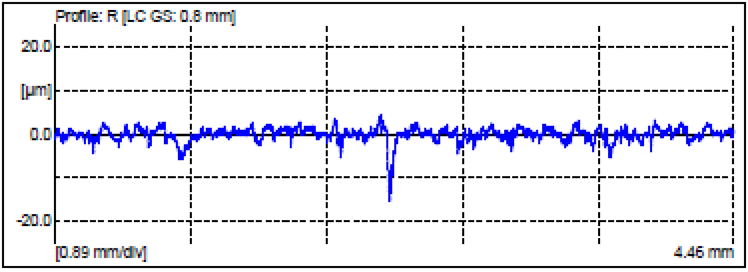
			Left	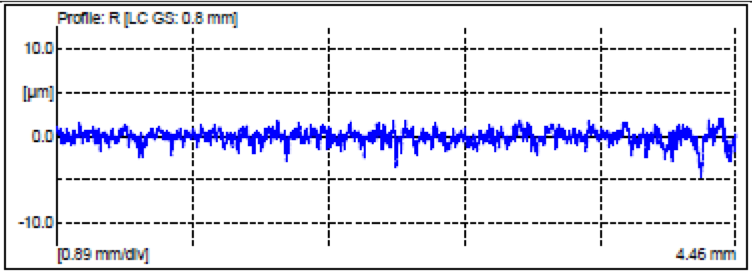
			Right	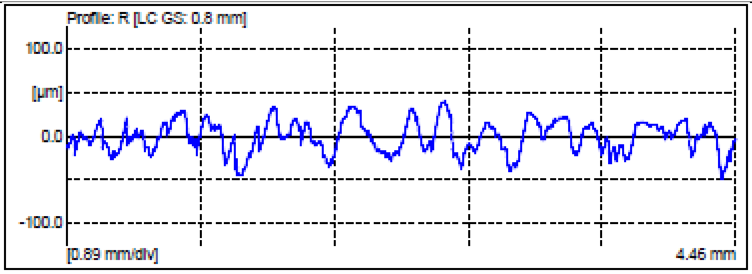

Table L. 1. Continued

Speed	Feed	Section	Location	Profiles
1500 rpm	320 µm/rev	Left Half	Center	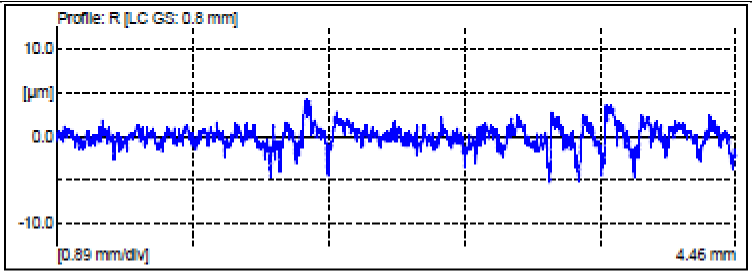
			Left	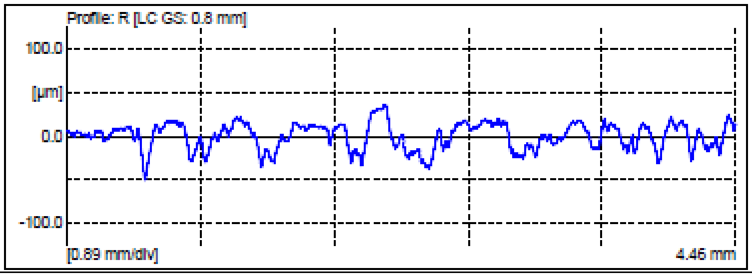
			Right	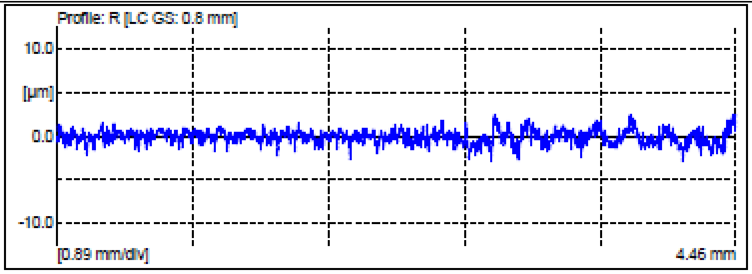
		Right Half	Center	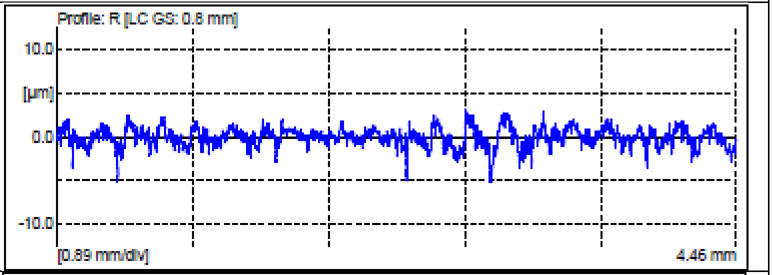
			Left	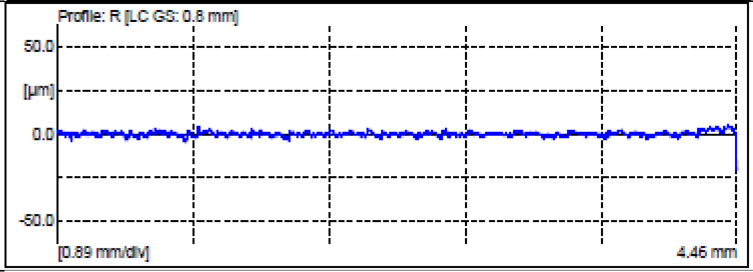
			Right	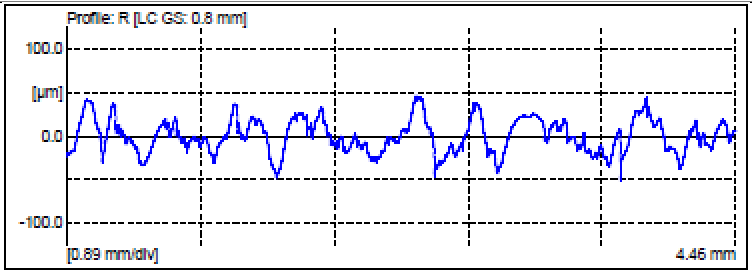

Table L. 1. Continued

Speed	Feed	Section	Location	Profiles
3000 rpm	64 µm/rev	Left Half	Center	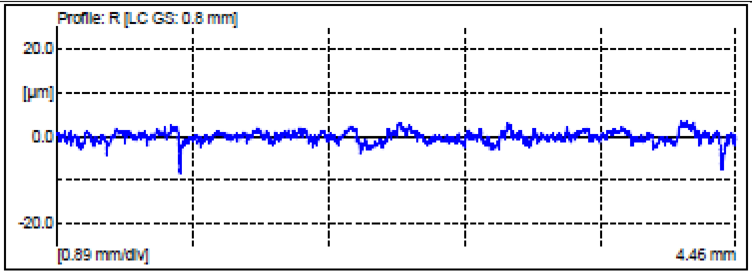
			Left	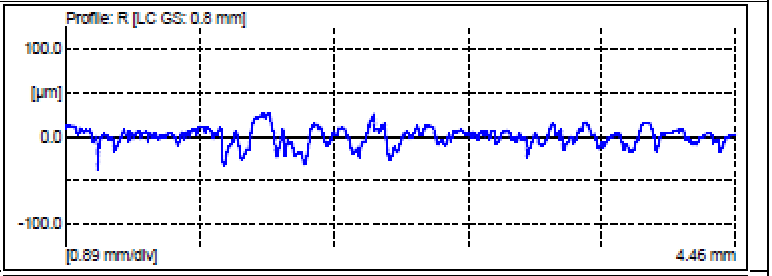
			Right	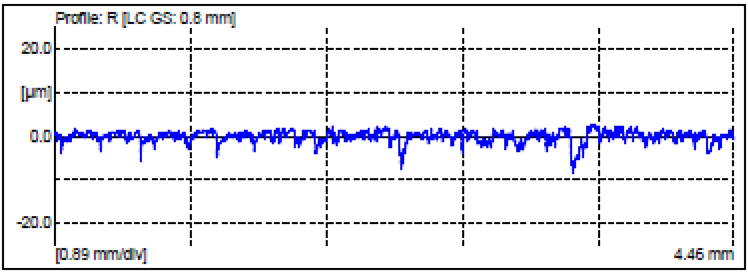
		Right Half	Center	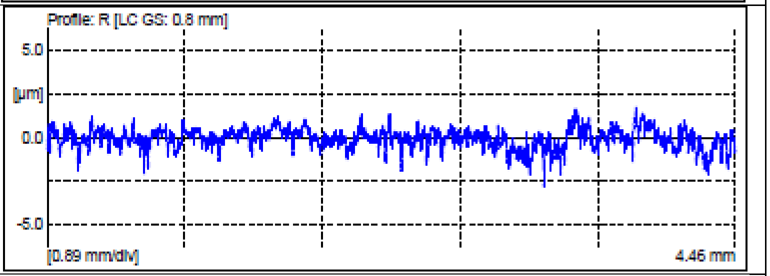
			Left	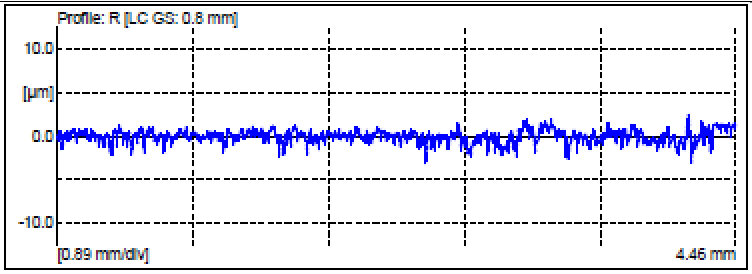
			Right	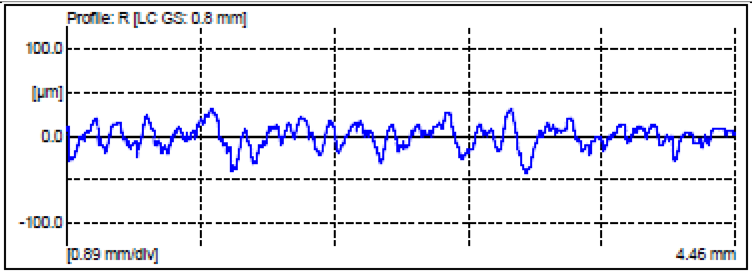

Table L. 1. Continued

Speed	Feed	Section	Location	Profiles
3000 rpm	128 µm/rev	Left Half	Center	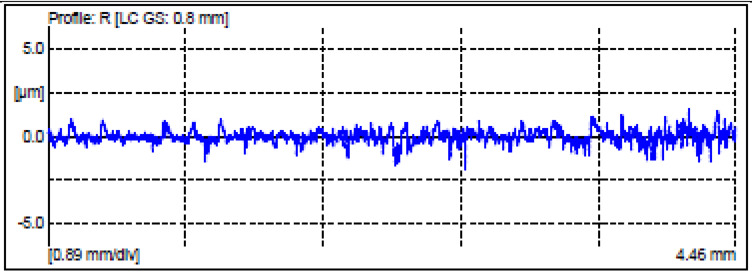
			Left	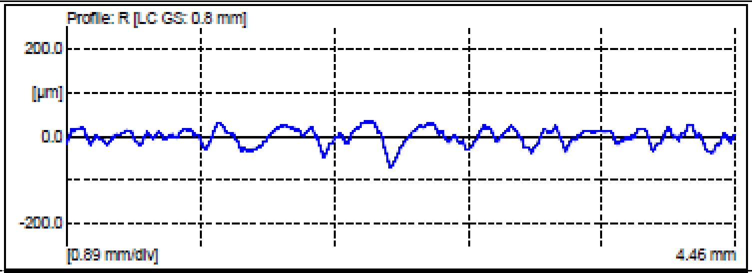
			Right	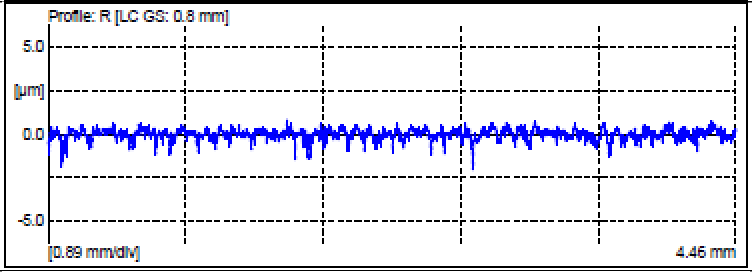
		Right Half	Center	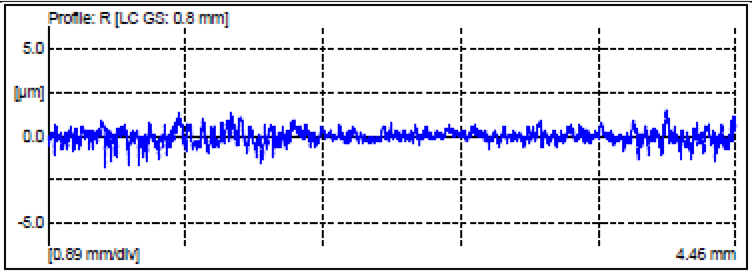
			Left	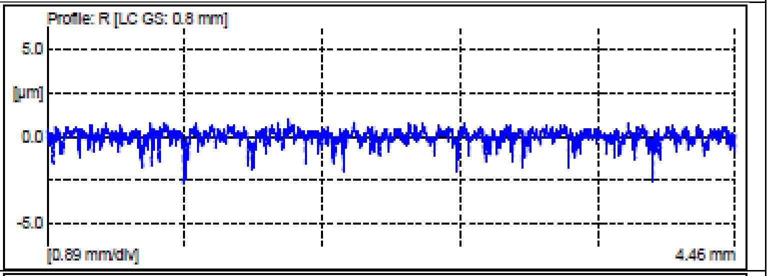
			Right	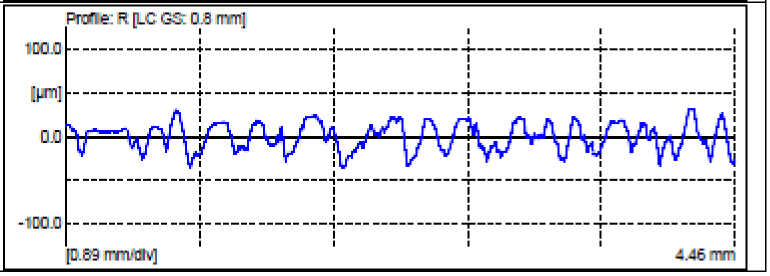

Table L. 1. Continued

Speed	Feed	Section	Location	Profiles
3000 rpm	192 µm/rev	Left Half	Center	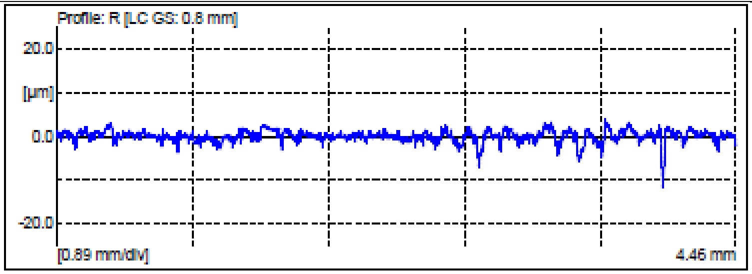
			Left	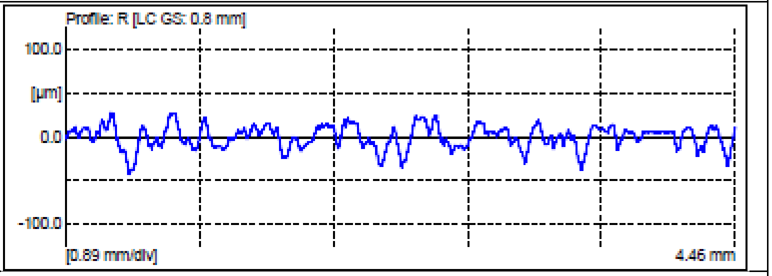
			Right	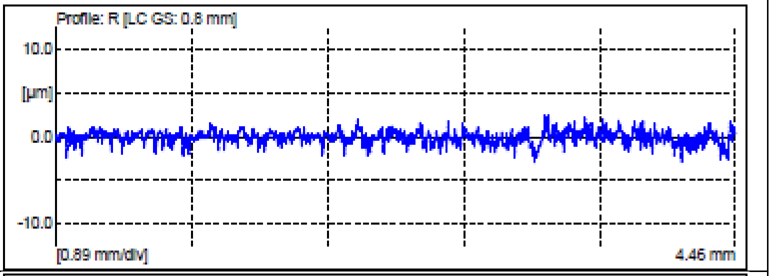
		Right Half	Center	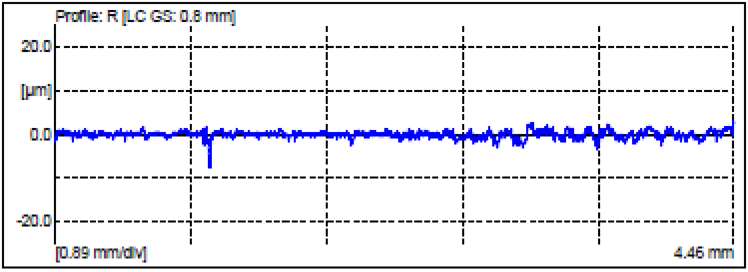
			Left	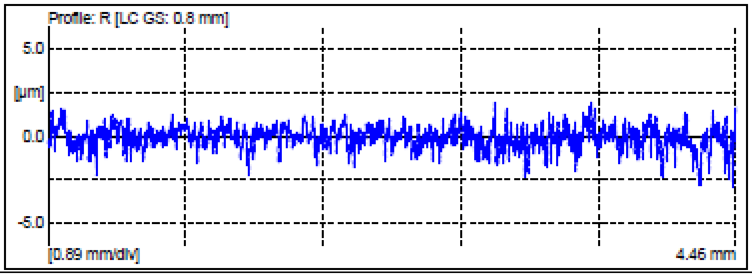
			Right	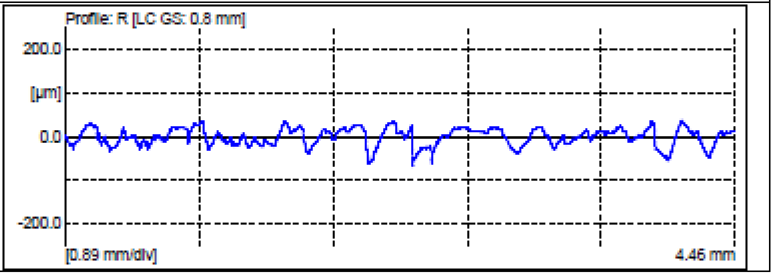

Table L. 1. Continued

Speed	Feed	Section	Location	Profiles
3000 rpm	256 μm/rev	Left Half	Center	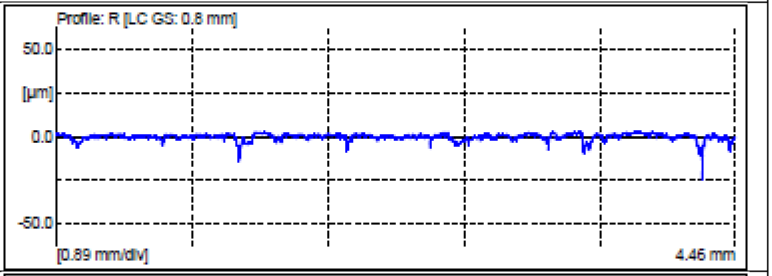
			Left	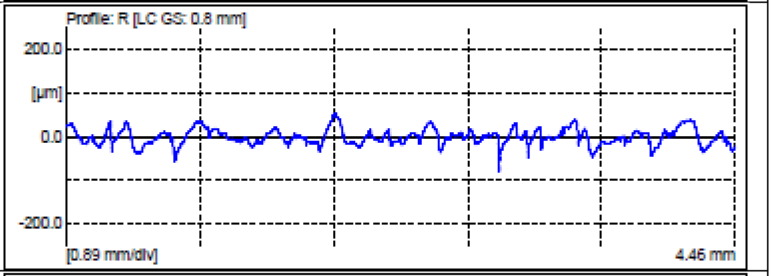
			Right	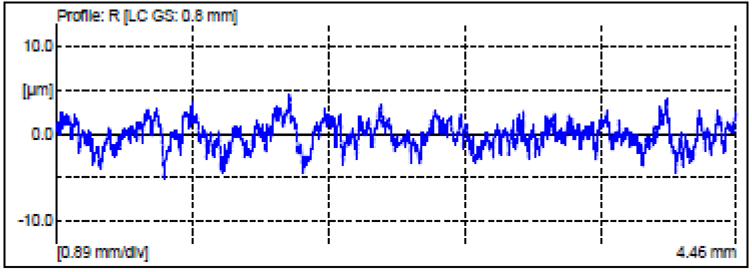
		Right Half	Center	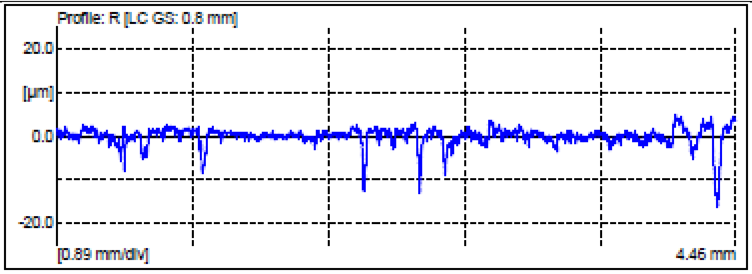
			Left	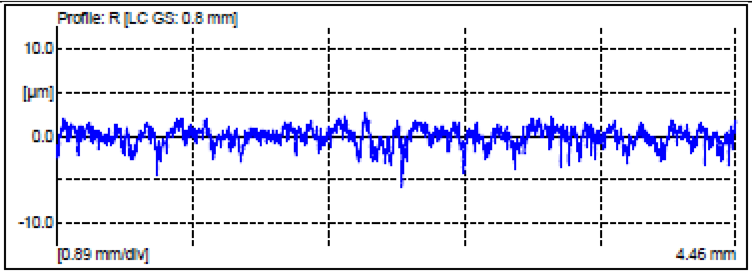
			Right	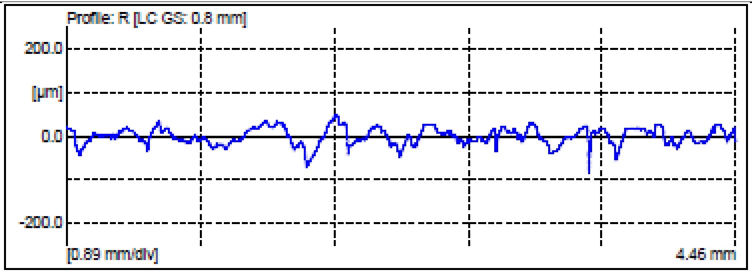

Table L. 1. Continued

Speed	Feed	Section	Location	Profiles
3000 rpm	320 µm/rev	Left Half	Center	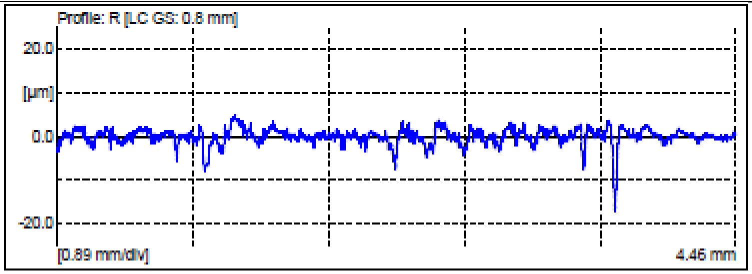
			Left	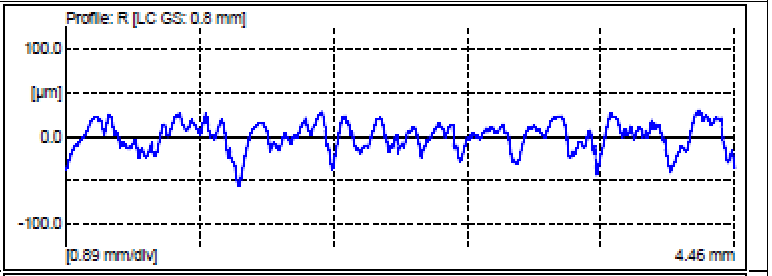
			Right	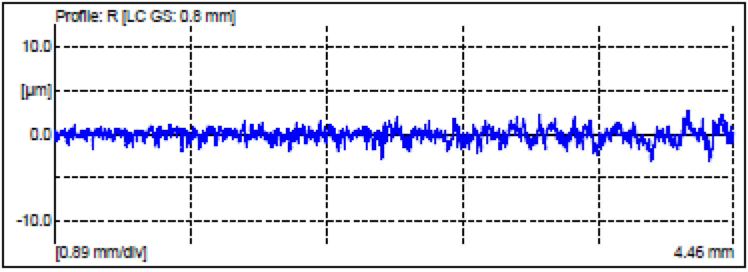
		Right Half	Center	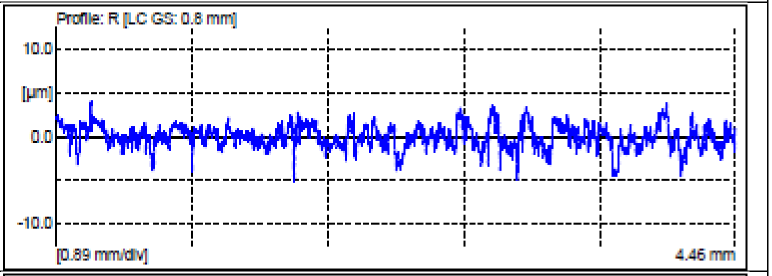
			Left	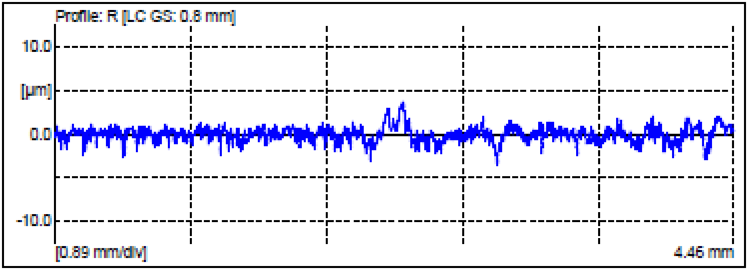
			Right	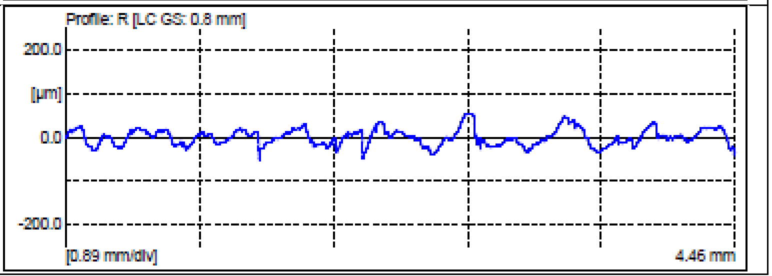

Table L. 1. Continued

Speed	Feed	Section	Location	Profiles
4500 rpm	64 µm/rev	Left Half	Center	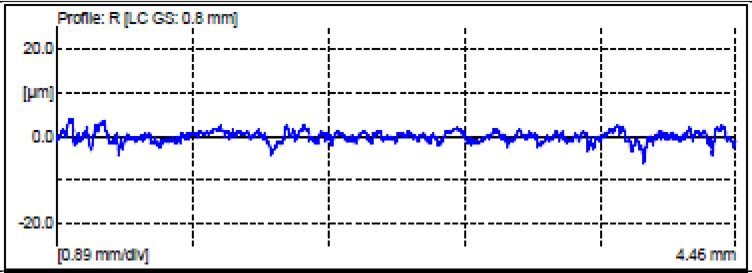
			Left	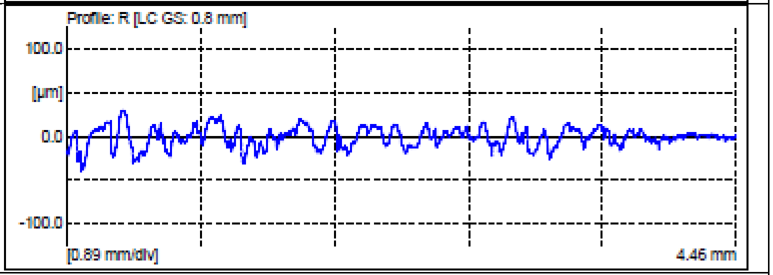
			Right	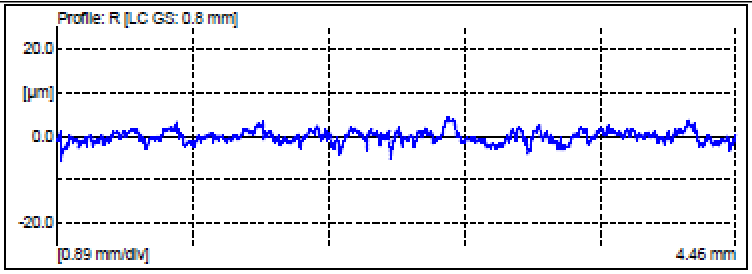
		Right Half	Center	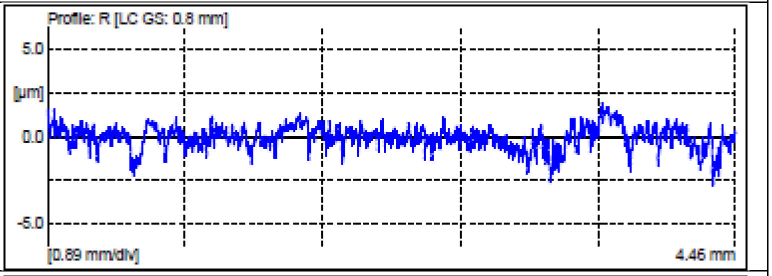
			Left	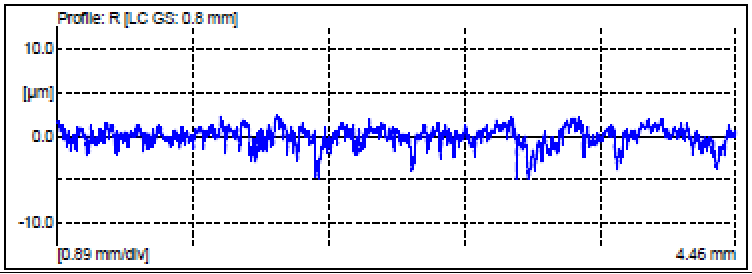
			Right	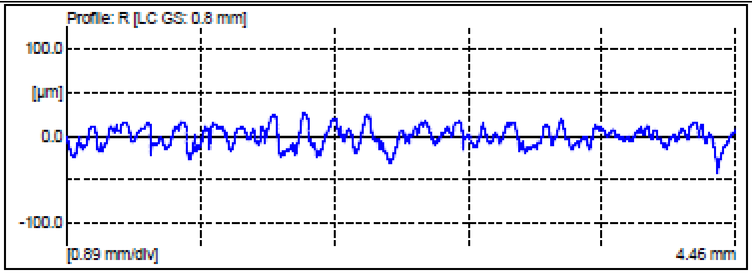

Table L. 1. Continued

Speed	Feed	Section	Location	Profiles
4500 rpm	128 µm/rev	Left Half	Center	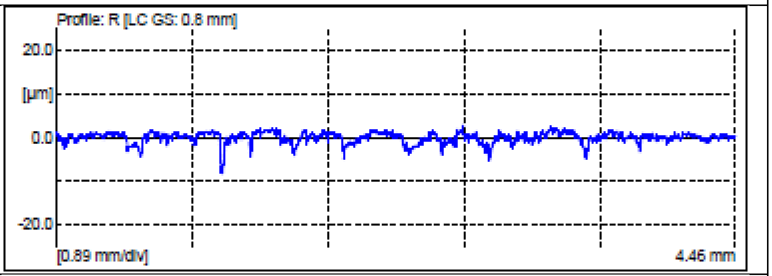
			Left	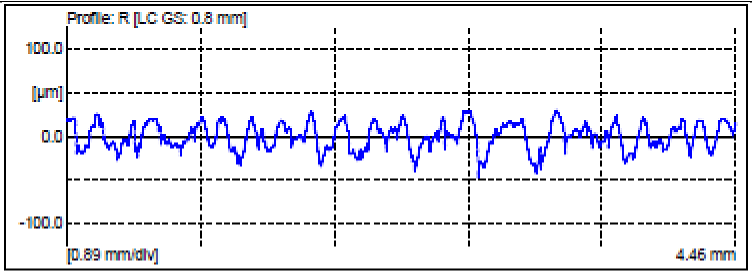
			Right	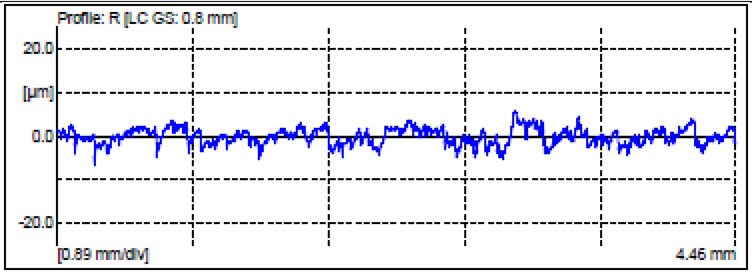
		Right Half	Center	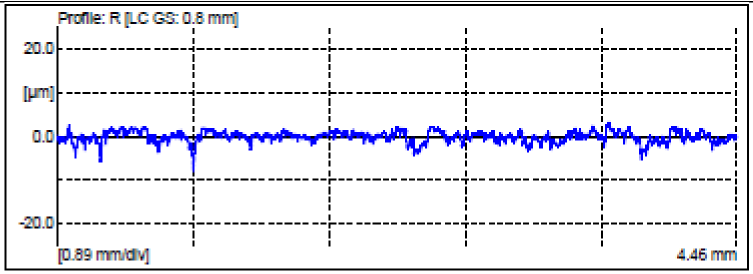
			Left	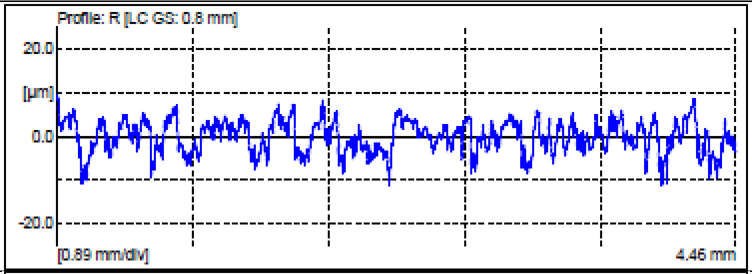
			Right	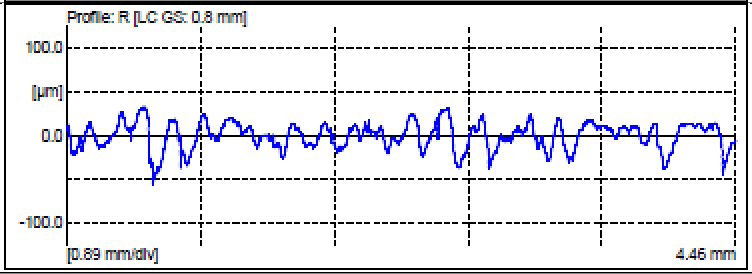

Table L. 1. Continued

Speed	Feed	Section	Location	Profiles
4500 rpm	192 µm/rev	Left Half	Center	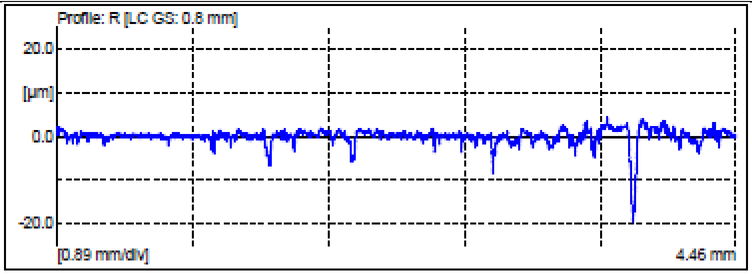
			Left	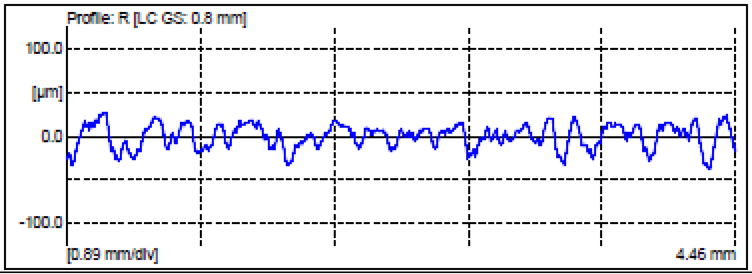
			Right	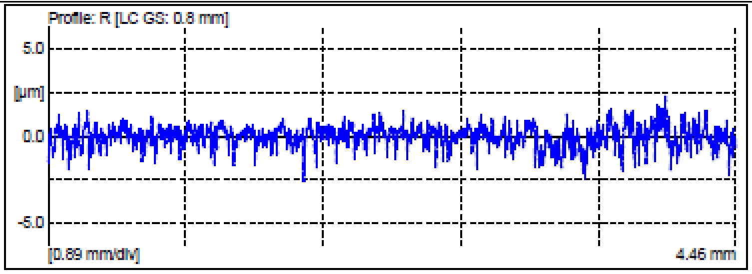
		Right Half	Center	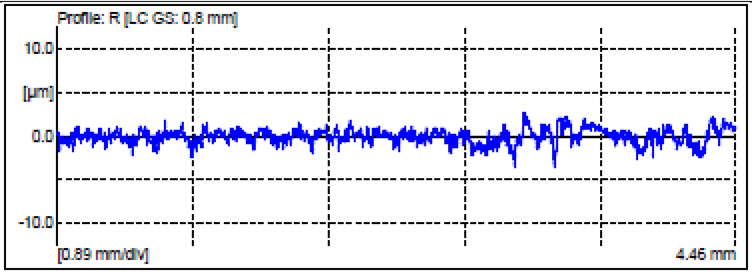
			Left	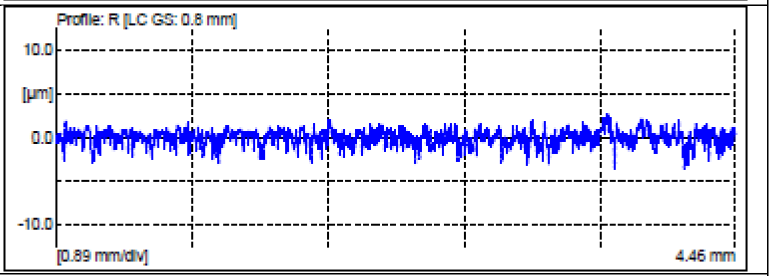
			Right	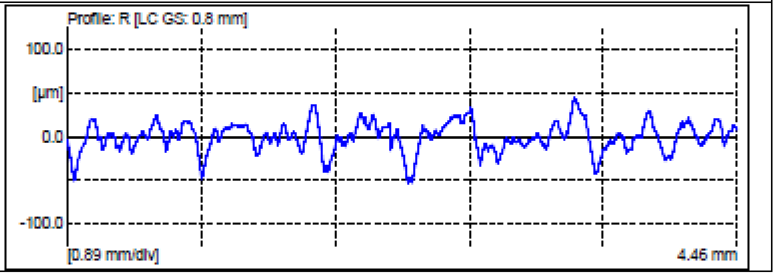

Table L. 1. Continued

Speed	Feed	Section	Location	Profiles
4500 rpm	256 µm/rev	Left Half	Center	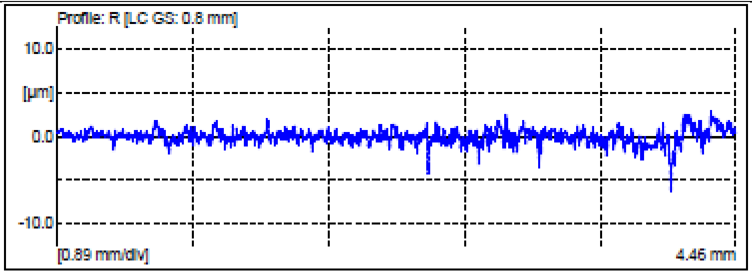
			Left	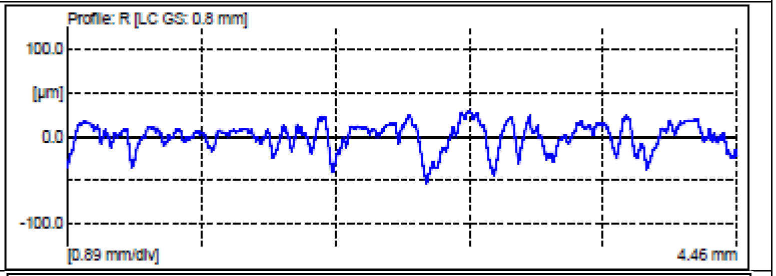
			Right	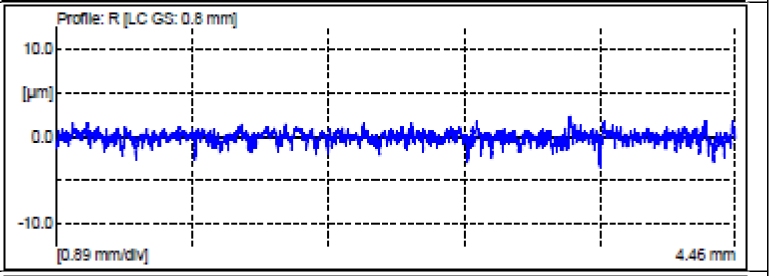
		Right Half	Center	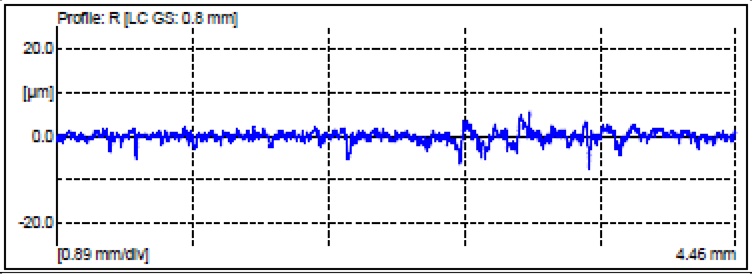
			Left	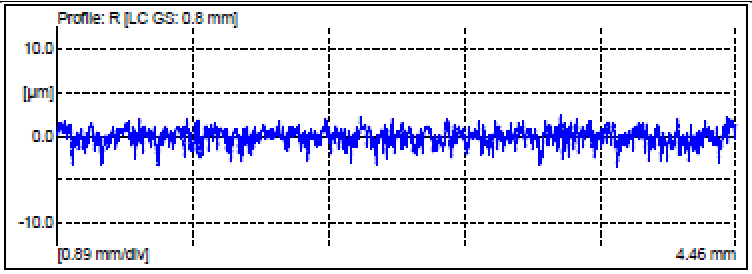
			Right	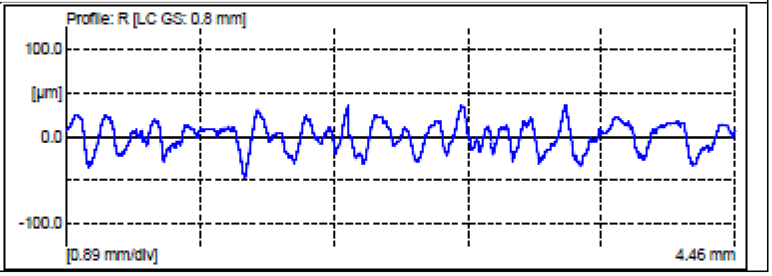

Table L. 1. Continued

Speed	Feed	Section	Location	Profiles
4500 rpm	320 µm/rev	Left Half	Center	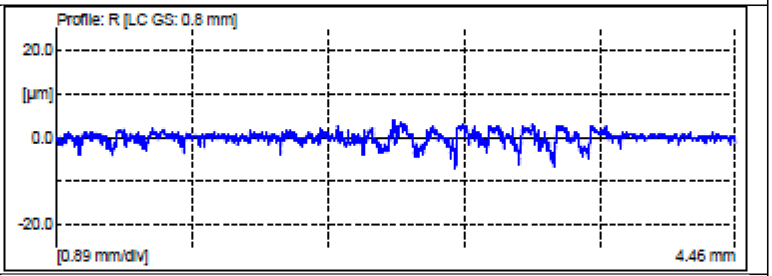
			Left	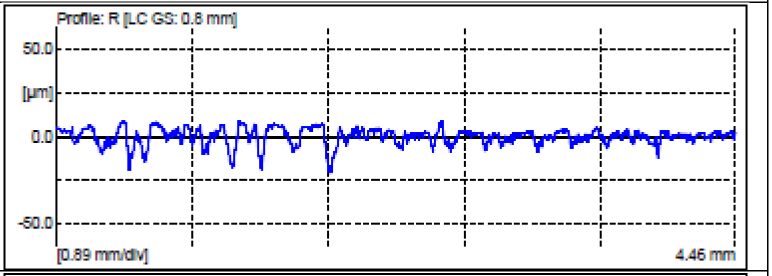
			Right	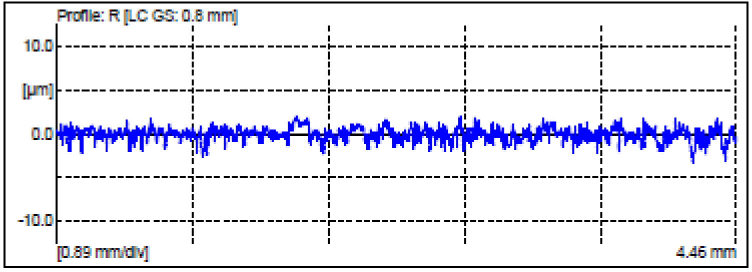
		Right Half	Center	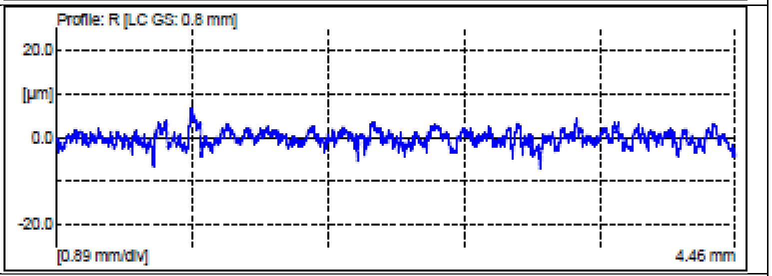
			Left	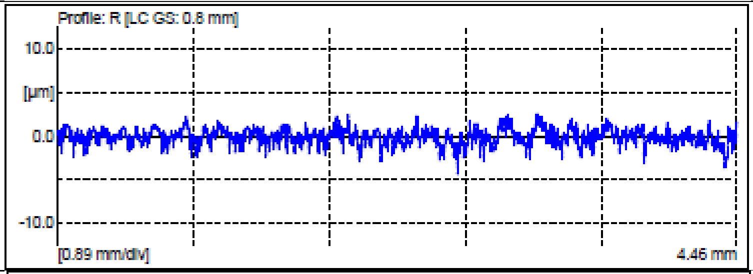
			Right	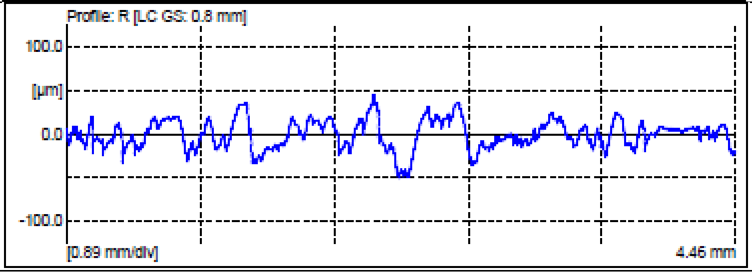

Table L. 1. Continued

Speed	Feed	Section	Location	Profiles
6000 rpm	64 µm/rev	Left Half	Center	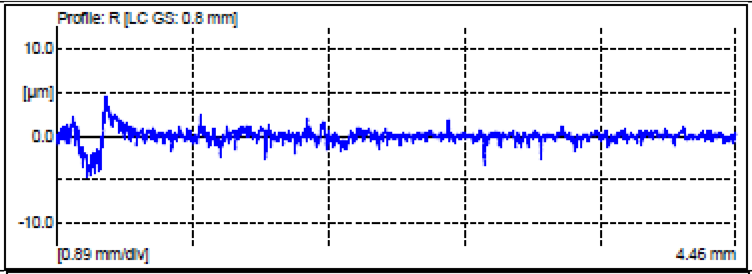
			Left	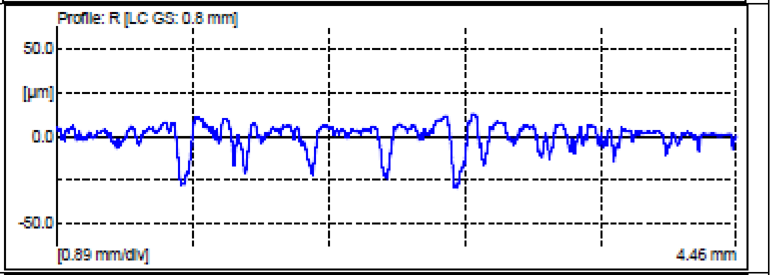
			Right	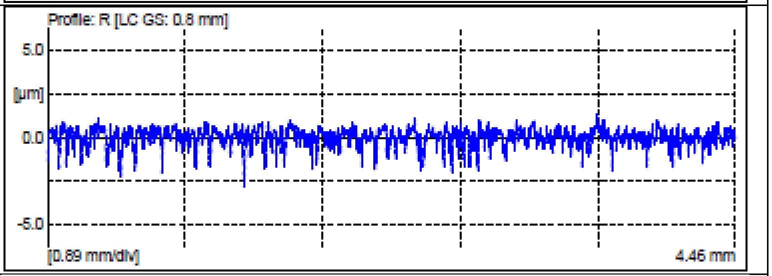
		Right Half	Center	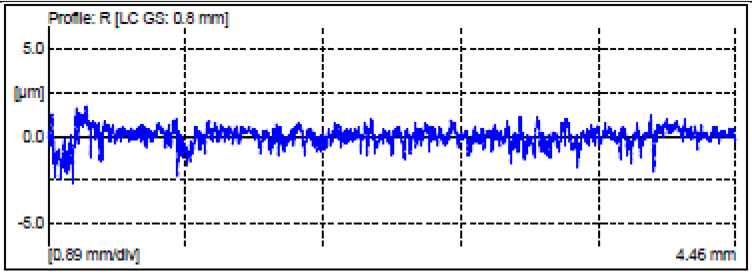
			Left	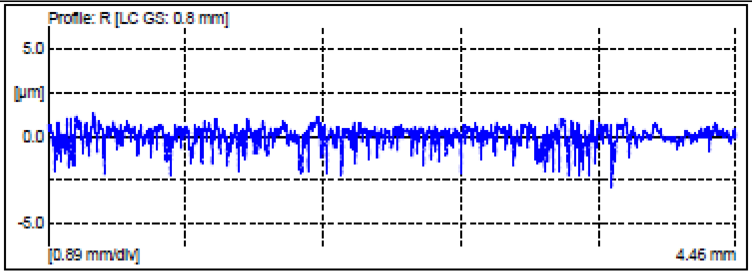
			Right	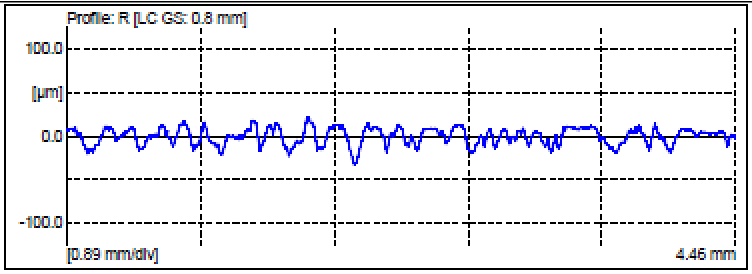

Table L. 1. Continued

Speed	Feed	Section	Location	Profiles
6000 rpm	128 µm/rev	Left Half	Center	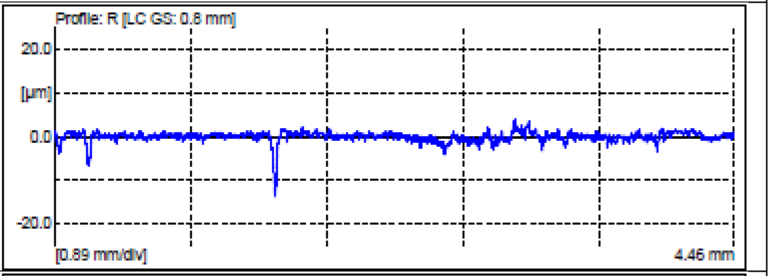
			Left	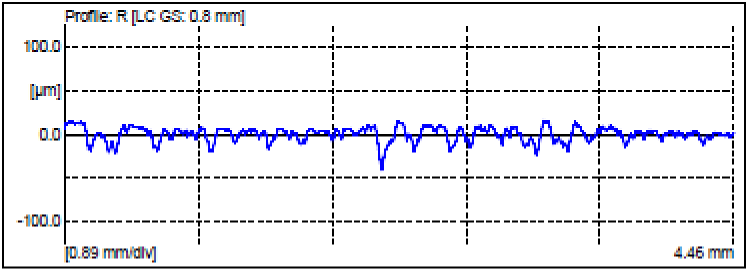
			Right	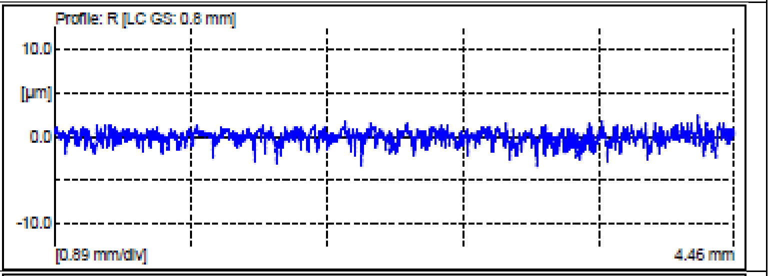
		Right Half	Center	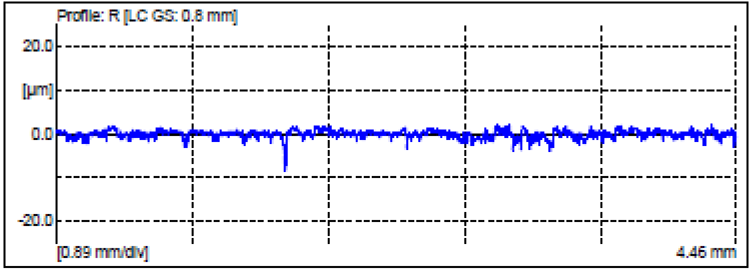
			Left	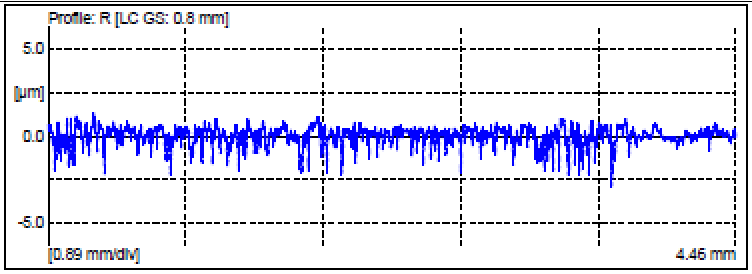
			Right	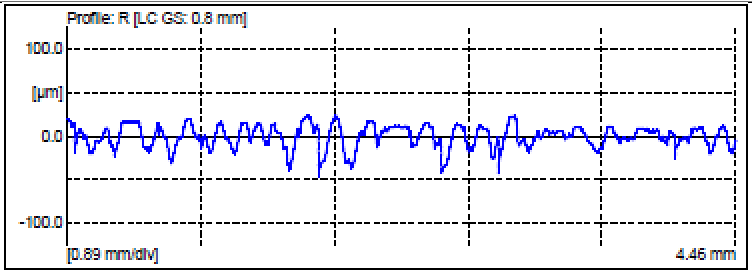

Table L. 1. Continued

Speed	Feed	Section	Location	Profiles
6000 rpm	192 µm/rev	Left Half	Center	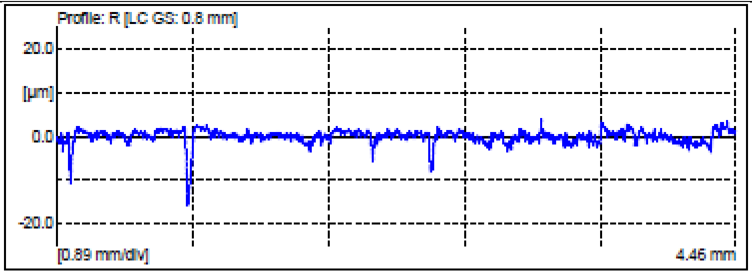
			Left	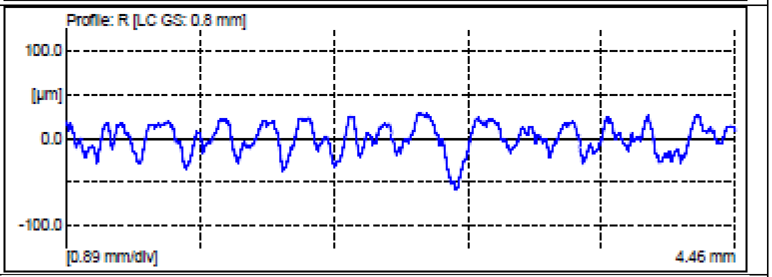
			Right	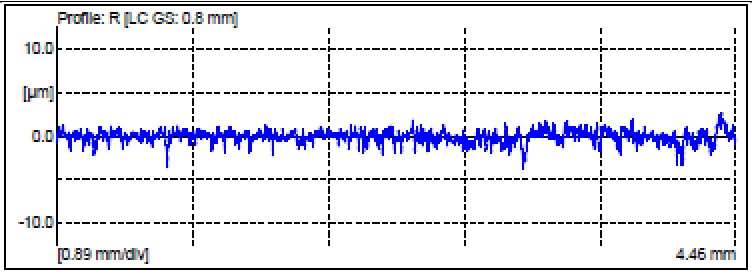
		Right Half	Center	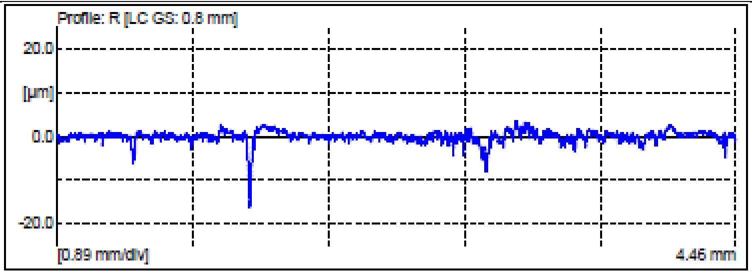
			Left	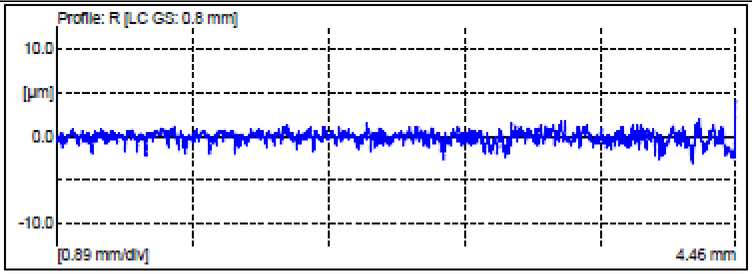
			Right	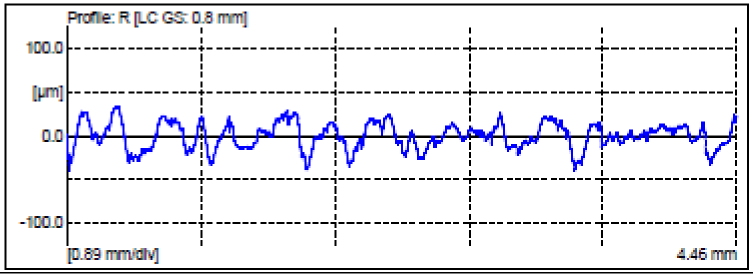

Table L. 1. Continued

Speed	Feed	Section	Location	Profiles
6000 rpm	256 µm/rev	Left Half	Center	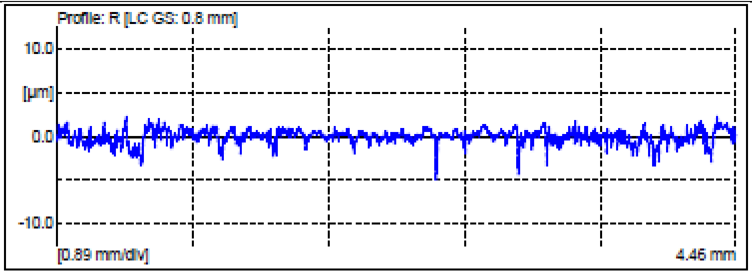
			Left	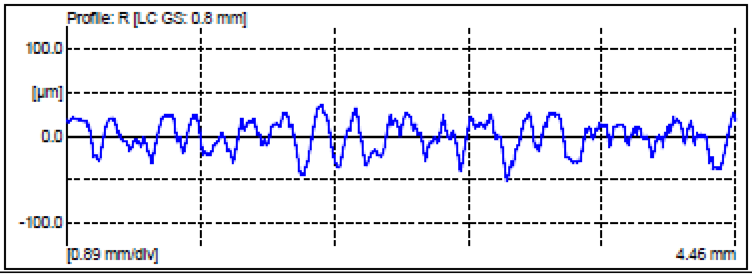
			Right	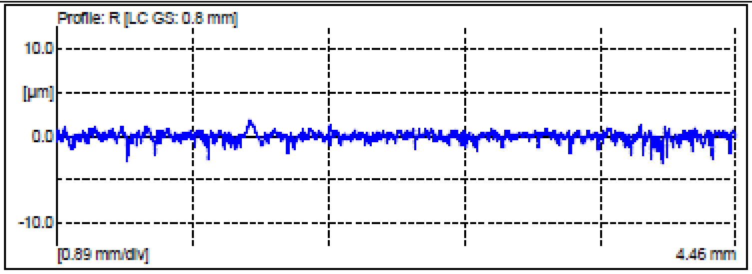
		Right Half	Center	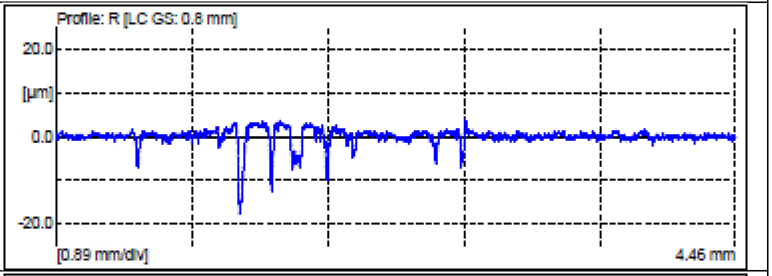
			Left	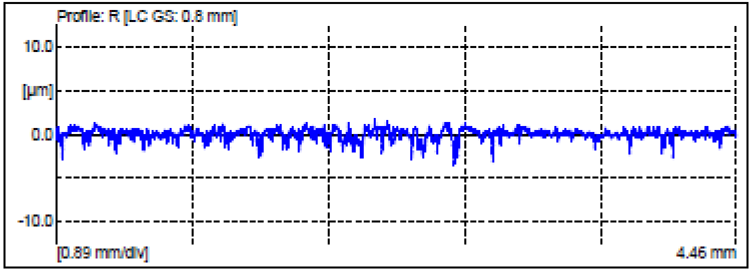
			Right	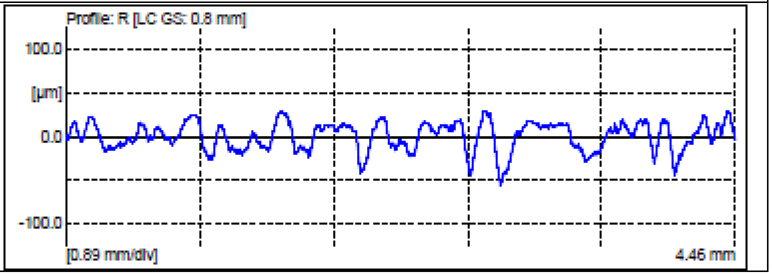

Table L. 1. Continued

Speed	Feed	Section	Location	Profiles
6000 rpm	320 µm/rev	Left Half	Center	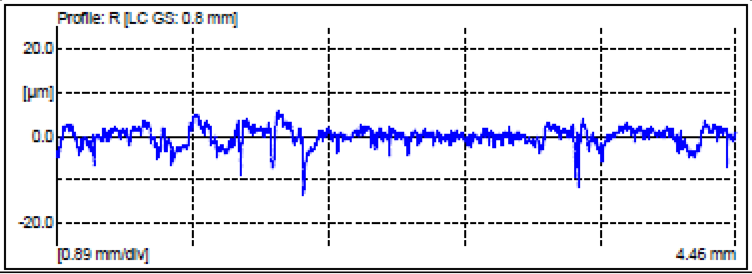
			Left	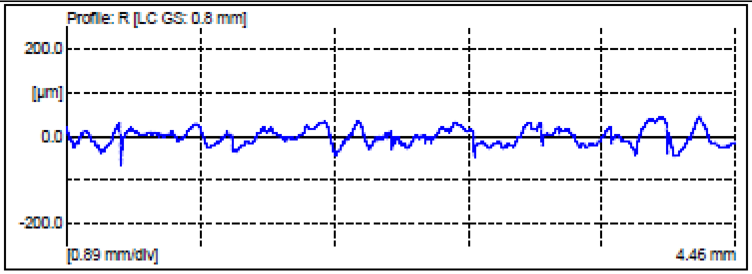
			Right	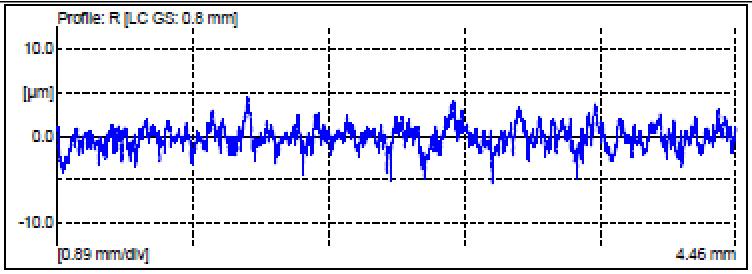
		Right Half	Center	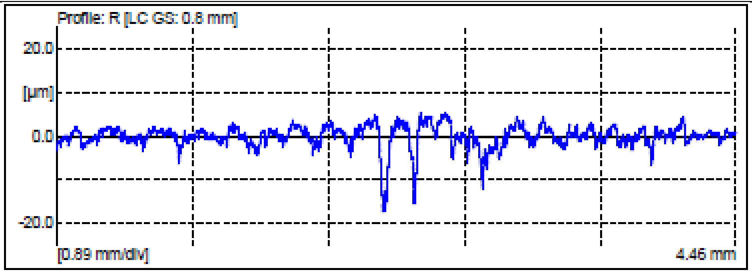
			Left	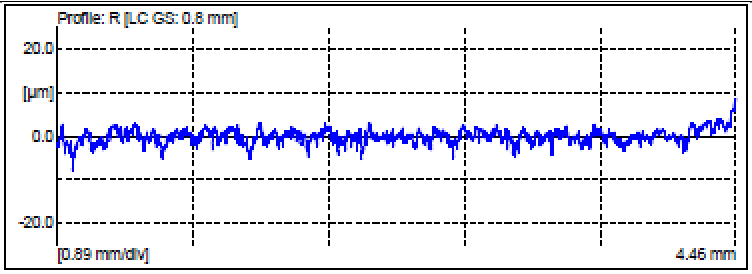
			Right	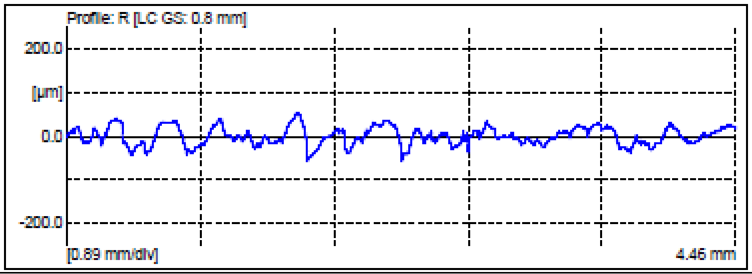

L. 2 SURFACE ROUGHNESS PARAMETER VALUES FOR UNI-DIRECTIONAL CFRP

Table L. 2. Roughness parameter values for uni-directional CFRP

Speed (rpm)	Feed Rate (µm/rev)	Surface Parameter	Left Halve			Right Halve		
			Center	Left	Right	Center	Left	Right
1500	64	Ra	0.297	8.252	0.156	0.379	0.264	9.667
		Rq	0.413	10.104	0.214	0.566	0.361	11.323
		Rz	2.6824	43.0898	1.7172	4.414	2.6002	43.769
		Rt	4.227	56.826	2.056	7.043	3.144	48.323
	128	Ra	0.797	9.881	0.523	0.525	0.853	14.357
		Rq	1.290	12.147	0.703	0.756	1.090	17.130
		Rz	9.1061	49.5208	4.2796	4.5358	6.5636	76.6498
		Rt	12.308	58.639	6.087	8.501	7.444	108.104
	192	Ra	0.697	13.369	0.650	0.853	0.912	15.881
		Rq	1.008	16.984	0.938	1.228	1.231	19.759
		Rz	7.4304	78.4452	5.5282	6.8206	7.8279	88.1425
		Rt	12.990	102.456	9.210	10.551	9.457	121.189
	256	Ra	0.754	10.367	0.489	1.095	0.562	14.650
		Rq	1.067	12.605	0.654	1.657	0.765	17.792
		Rz	7.1377	61.8591	4.492	9.7792	4.8359	69.0673
		Rt	13.241	71.099	6.886	19.656	6.594	89.429
	320	Ra	0.927	12.223	0.582	0.803	0.971	16.020
		Rq	1.252	14.825	0.753	1.058	0.645	19.423
		Rz	7.2058	59.9154	4.4238	6.7214	10.212	86.0193
		Rt	9.455	87.258	5.343	8.289	25.780	97.365
3000	64	Ra	0.944	7.449	0.966	0.430	0.549	10.790
		Rq	1.280	9.824	1.357	0.563	0.719	13.557
		Rz	7.8407	47.2892	8.1675	3.4525	4.3502	59.9042
		Rt	11.946	65.348	10.971	4.541	5.650	74.742
	128	Ra	0.282	14.247	0.236	0.294	0.287	12.605
		Rq	0.379	18.042	0.318	0.391	0.401	14.919
		Rz	2.5327	70.8781	2.3035	2.3552	3.1145	57.9309
		Rt	3.411	106.995	2.866	3.318	3.669	67.513
	192	Ra	0.932	10.196	0.542	0.602	0.486	16.011
		Rq	1.353	12.754	0.720	0.850	0.645	19.519
		Rz	8.7889	56.0838	4.382	5.4174	3.8198	78.4526
		Rt	15.374	70.617	5.472	10.337	4.831	104.388
	256	Ra	1.289	13.969	1.197	1.284	0.812	15.168
		Rq	2.025	17.902	1.489	2.146	1.036	18.863
		Rz	14.7415	93.1829	7.7283	12.9842	6.1951	96.3399
		Rt	26.994	133.032	9.576	21.051	8.492	132.511
	320	Ra	1.241	12.741	0.553	1.025	0.629	14.686
		Rq	1.882	15.715	0.729	1.315	0.847	18.378
		Rz	12.6251	68.2293	4.2834	7.9524	4.8793	80.6145
		Rt	22.168	85.224	5.751	9.254	7.136	106.233

Table L. 2. Continued

Speed (rpm)	Feed Rate (µm/rev)	Surface Parameter	Left Halve			Right Halve		
			Center	Left	Right	Center	Left	Right
4500	64	Ra	0.933	8.729	1.100	0.487	0.847	9.022
		Rq	1.207	11.197	1.388	0.643	1.120	11.073
		Rz	6.612	46.775	7.695	3.527	6.028	48.563
		Rt	10.097	69.159	10.102	4.710	7.339	67.960
	128	Ra	0.860	13.313	1.036	0.847	2.210	11.193
		Rq	1.203	16.892	1.298	1.384	2.864	13.722
		Rz	6.863	72.864	6.627	8.648	15.595	60.622
		Rt	11.037	91.207	8.257	12.620	21.571	72.579
	192	Ra	1.015	11.132	0.451	0.639	0.657	12.611
		Rq	1.893	13.423	0.591	0.825	0.848	16.557
		Rz	11.247	54.231	3.684	4.487	4.978	76.703
		Rt	24.001	65.266	4.879	6.159	6.180	97.793
	256	Ra	0.569	11.658	0.461	0.898	0.718	0.718
		Rq	0.810	14.858	0.621	1.275	0.922	15.701
		Rz	5.671	66.230	4.523	8.422	5.438	65.586
		Rt	9.088	82.269	5.759	12.950	5.872	83.395
	320	Ra	0.971	3.394	0.571	1.296	0.703	13.104
		Rq	1.350	4.608	0.751	1.648	0.909	16.247
		Rz	7.390	22.894	4.328	10.293	5.288	64.628
		Rt	10.830	29.538	5.268	13.779	6.898	94.900
6000	64	Ra	0.488	5.162	0.382	0.377	0.401	8.037
		Rq	0.823	7.294	0.506	0.514	0.539	9.618
		Rz	4.869	31.627	3.261	3.029	3.365	39.410
		Rt	9.244	42.325	4.141	4.427	4.206	54.997
	128	Ra	0.739	6.249	0.562	0.657	0.565	10.309
		Rq	1.251	8.052	0.735	0.925	0.744	12.793
		Rz	8.488	36.397	4.608	6.074	4.547	58.426
		Rt	17.703	57.077	5.861	10.577	5.835	69.895
	192	Ra	1.023	13.514	0.538	0.849	0.486	12.200
		Rq	1.685	16.569	0.723	1.463	0.663	14.863
		Rz	9.717	61.859	4.764	10.212	4.383	64.325
		Rt	19.679	88.067	6.467	19.742	7.136	73.222
	256	Ra	0.795	10.367	0.273	0.504	0.323	10.533
		Rq	1.223	13.277	0.373	0.962	0.442	12.799
		Rz	8.032	60.995	2.651	5.938	2.793	55.940
		Rt	13.114	85.922	3.937	11.362	3.432	68.916
	320	Ra	1.524	15.278	1.039	1.718	1.249	16.511
		Rq	2.038	18.635	1.343	2.615	1.641	20.224
		Rz	12.467	82.330	7.977	13.354	9.546	83.808
		Rt	19.400	111.685	9.884	22.767	16.707	109.748

L. 3 ANOVA ANALYSIS AND SURFACE RESPONSE MODEL RESULTS OF ROUGHNESS PARAMETERS R_a AND R_t FOR UNI-DIRECTIONAL CFRP COMPOSITES

Table L. 3. ANOVA table for roughness parameter Ra surface response model

Source	Sum of Squares	DF	Mean Square	F Value	p-value prob>F
Model	58.79	5	11.76	1.74	0.1908
A-Speed	17.02	1	17.02	2.51	0.1351
B-Feed	29.74	1	29.74	4.39	0.0547
AB	0.78	1	0.78	0.12	0.7391
$A^{\wedge 2}$	1.27	1	1.27	0.19	0.6712
$B^{\wedge 2}$	9.98	1	9.98	1.47	0.2447
Residual	94.75	14	6.77		
Cor Total	153.54	19			
$Ra = 11.92 – 1.24*A + 1.72*B + 0.37*A*B +0.57*A^{\wedge 2} – 1.69* B^{\wedge 2}$					

Table L. 4. ANOVA table for roughness parameter Rt surface response model

Source	Sum of Squares	DF	Mean Square	F Value	p-value prob>F
Model	3645.49	5	729.1	2.52	0.0795
A-Speed	460.18	1	460.18	1.59	0.2281
B-Feed	2243.29	1	2243.29	7.74	0.0147
AB	29.19	1	29.19	0.1	0.7556
$A^{\wedge 2}$	120.36	1	120.36	0.42	0.5296
$B^{\wedge 2}$	792.47	1	792.47	2.74	0.1204
Residual	4055.79	14	289.7		
Cor Total	7701.28	19			
$Rt = 93.17 – 6.44*A + 14.98*B + 2.29*A*B – 5.52*A^{\wedge 2} – 15.05*B^{\wedge 2}$					

APPENDIX M – SEM MICROGRAPH OF DRILLING INDUCED DAMAGE AND DEFECTS WHEN DRILLING UNI-DIRECTIONAL CFRP COMPOSITE

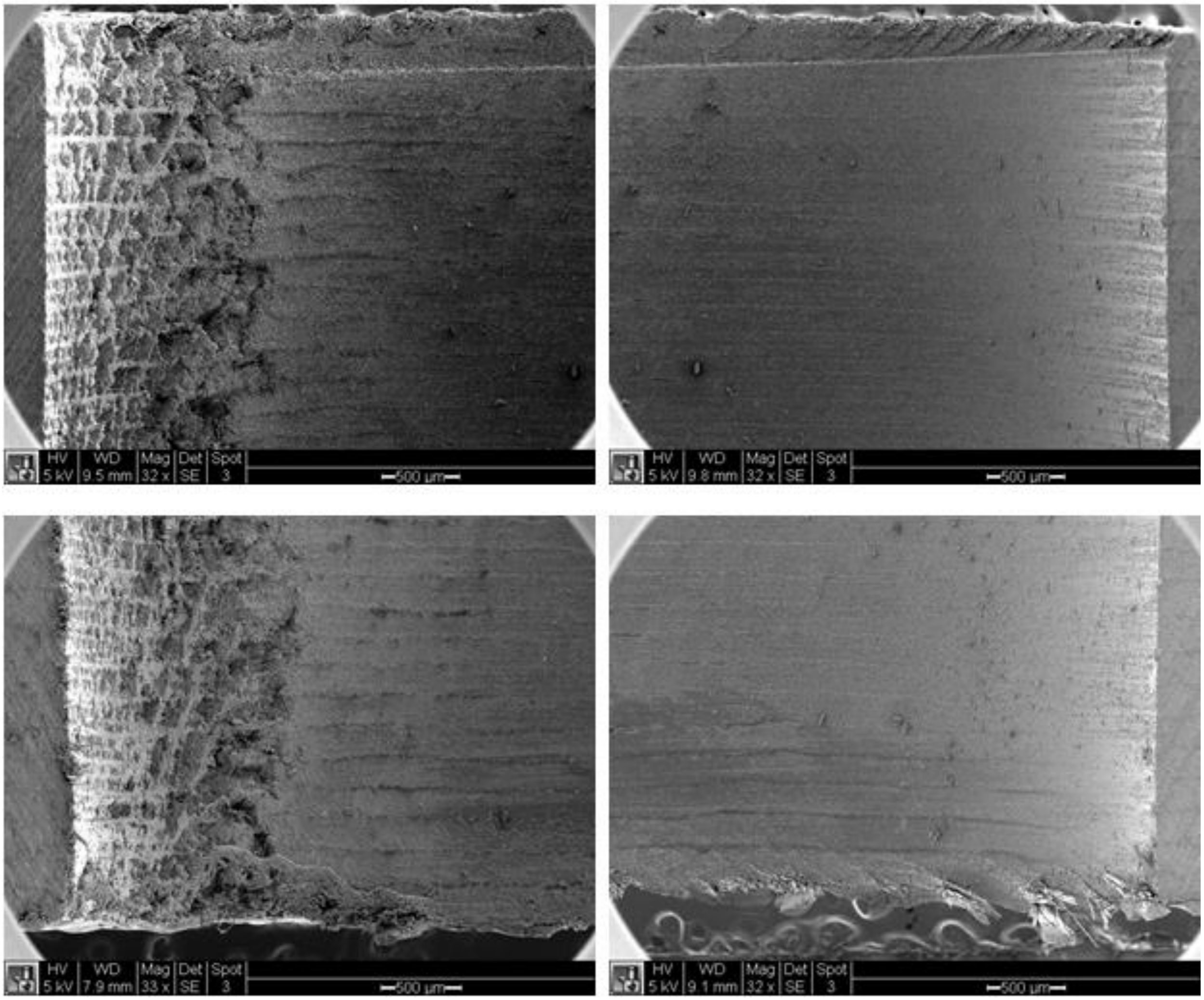

Figure M. 1. SEM micrograph of sectioned hole drilled at 4500 rpm and 128 µm/rev

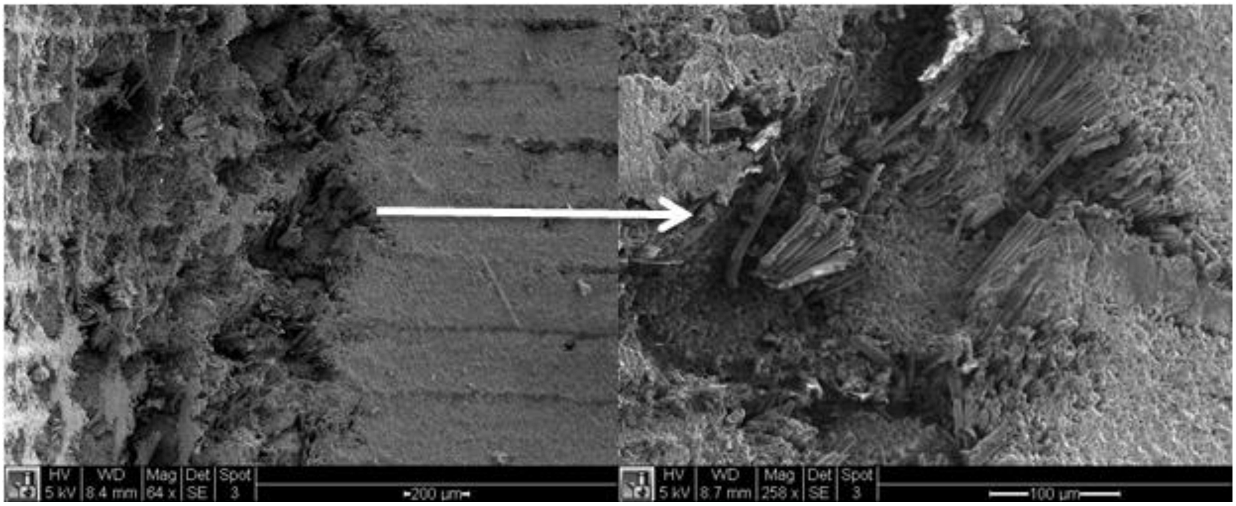

Figure M. 2. SEM micrograph of fiber pullout at 3000 rpm and 192 µm/rev

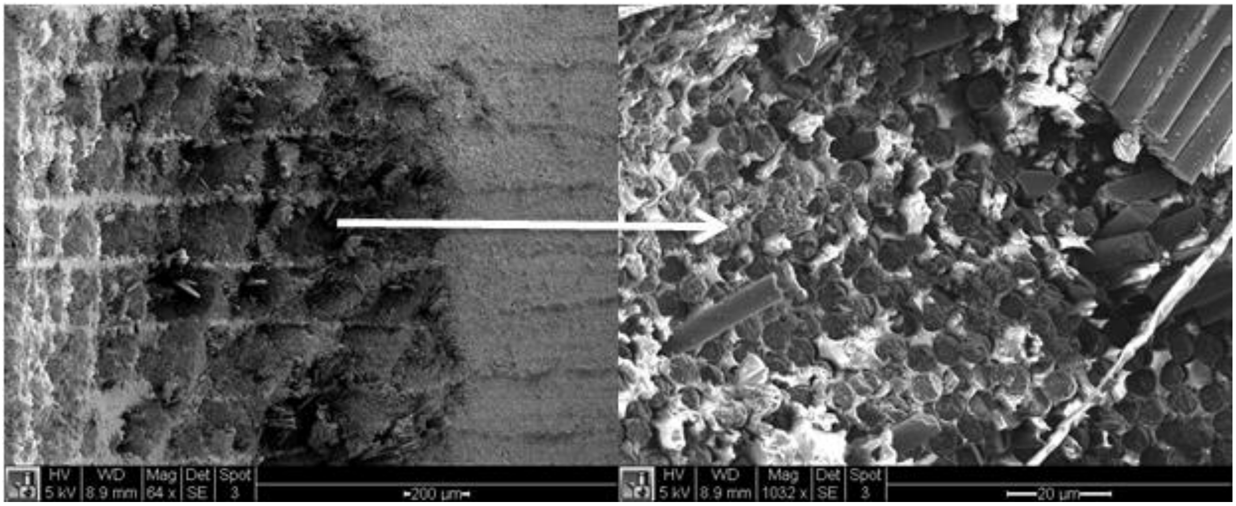

Figure M. 3. SEM micrograph of fiber pullout at 1500 rpm and 192 µm/rev

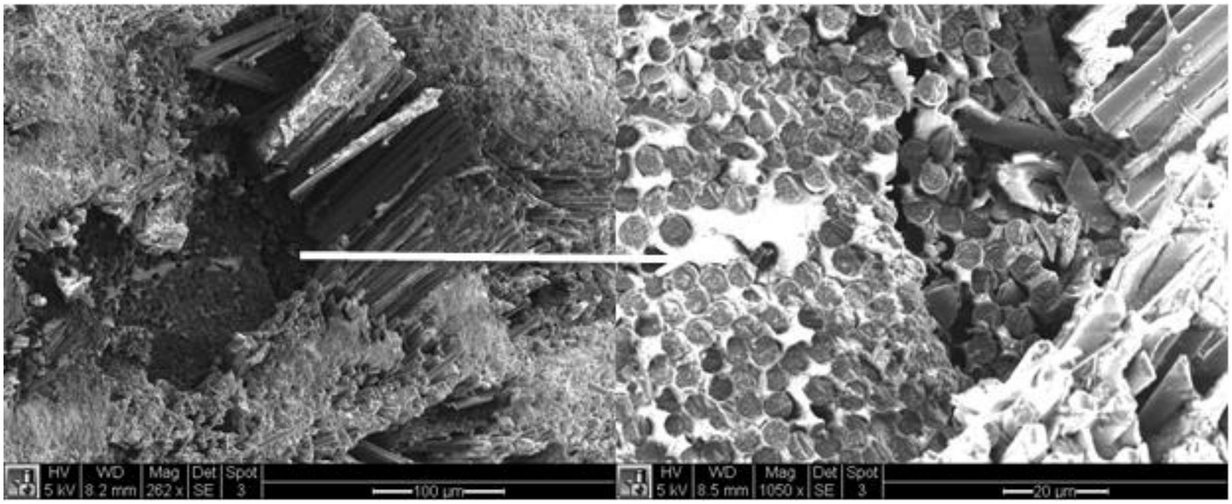

Figure M. 4. SEM micrograph of fiber pullout at 1500 rpm and 320 µm/rev

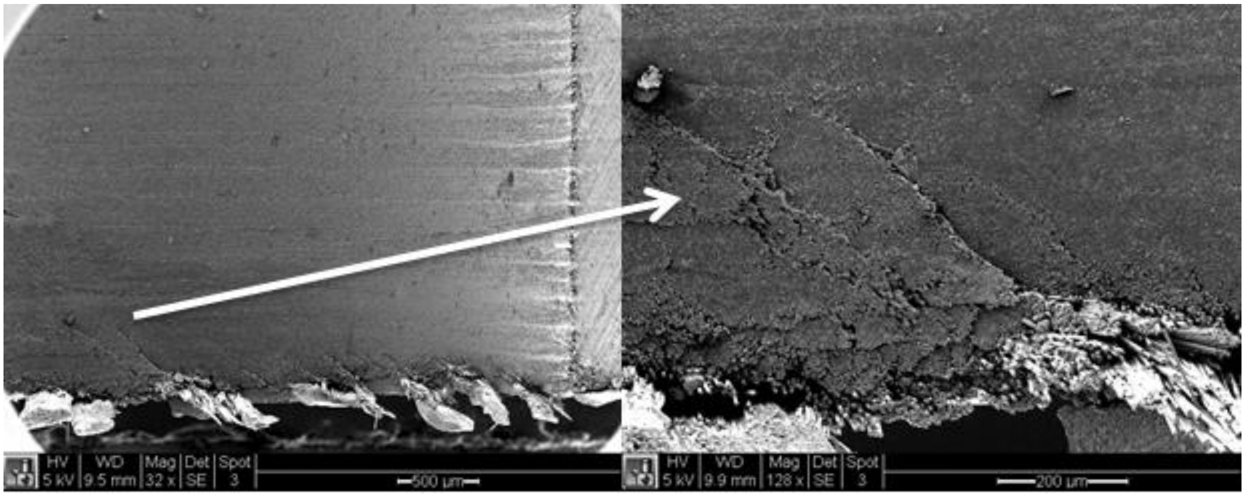

Figure M. 5. SEM micrograph of matrix crack at drill exit at 3000 rpm and 256 µm/rev

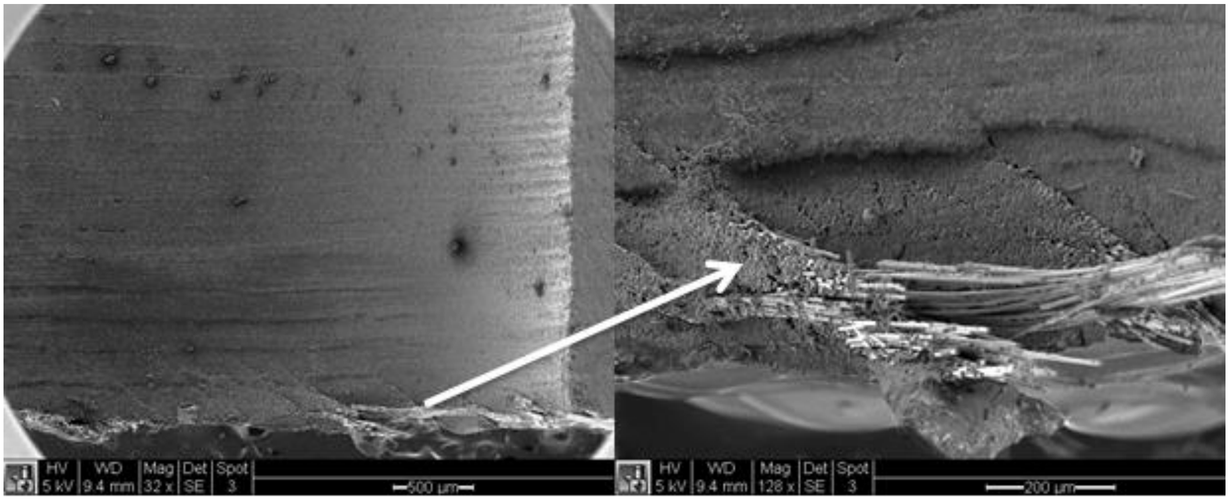

Figure M. 6. SEM micrograph of matrix crack at drill exit at 4500 rpm and 128 µm/rev

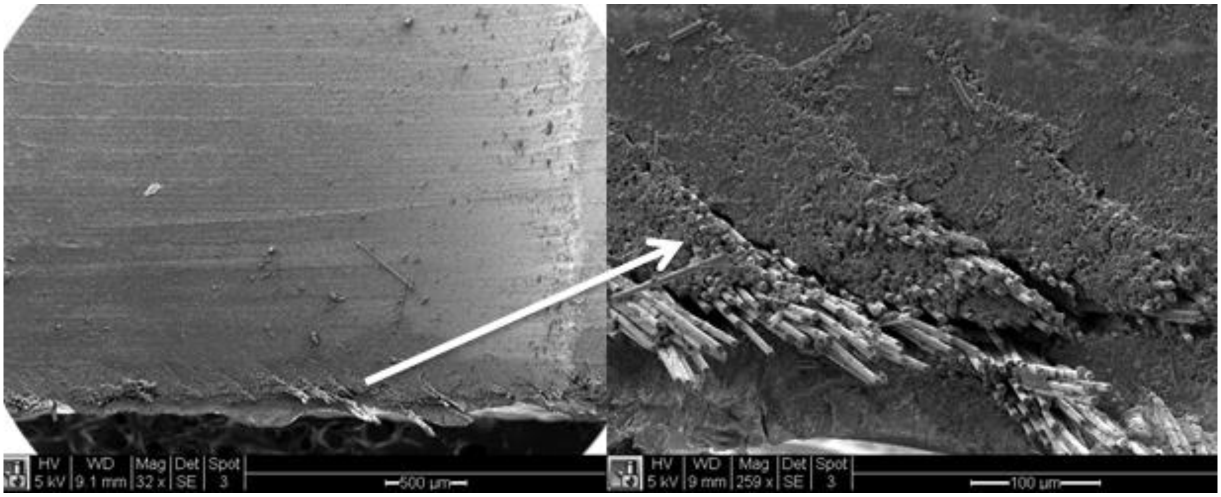

Figure M. 7. SEM micrograph of matrix crack at drill exit at 4500 rpm and 64 µm/rev

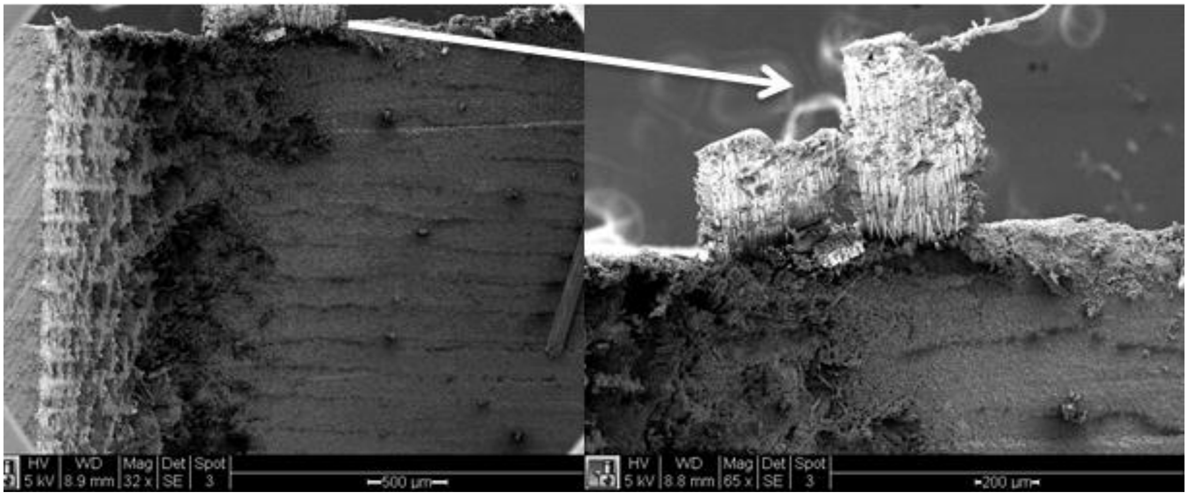

Figure M. 8. SEM micrograph of delamination at drill entrance at 3000 rpm and 320 μm/rev

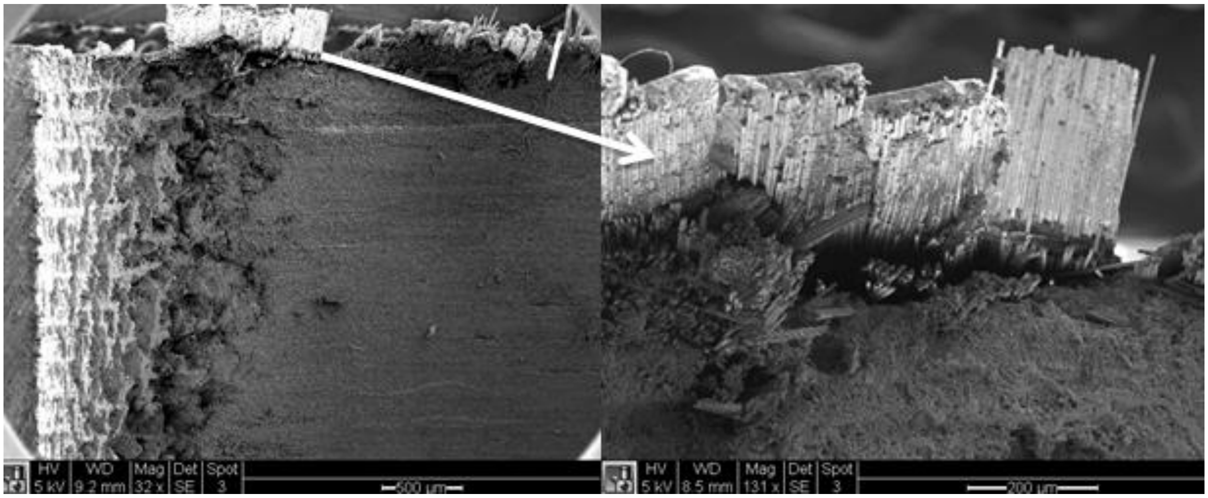

Figure M. 9. SEM micrograph of delamination at drill entrance at 6000 rpm and 320 μm/rev

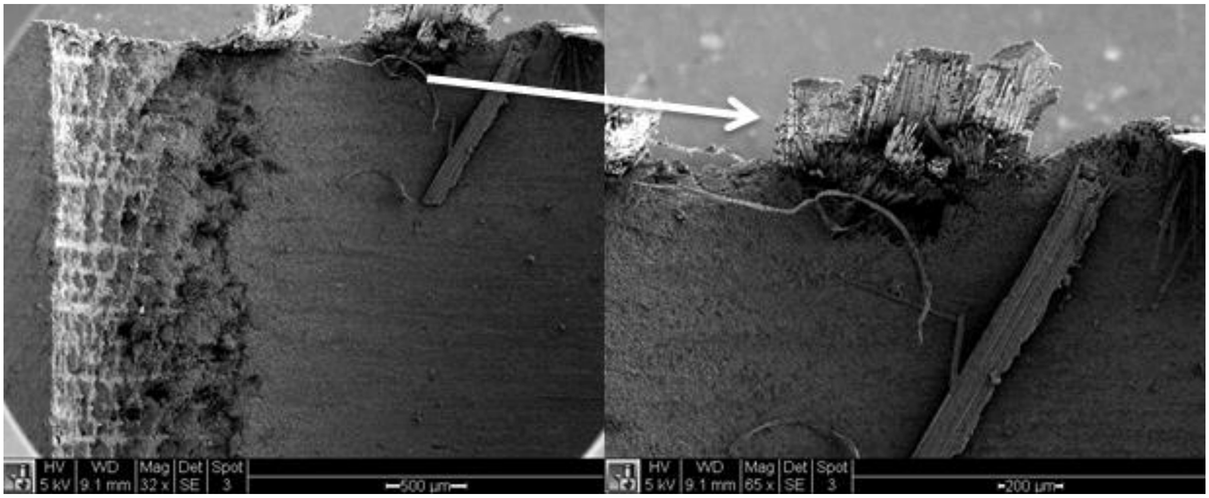

Figure M. 10. SEM micrograph of delamination at drill entrance at 1500 rpm and 192 μm/rev

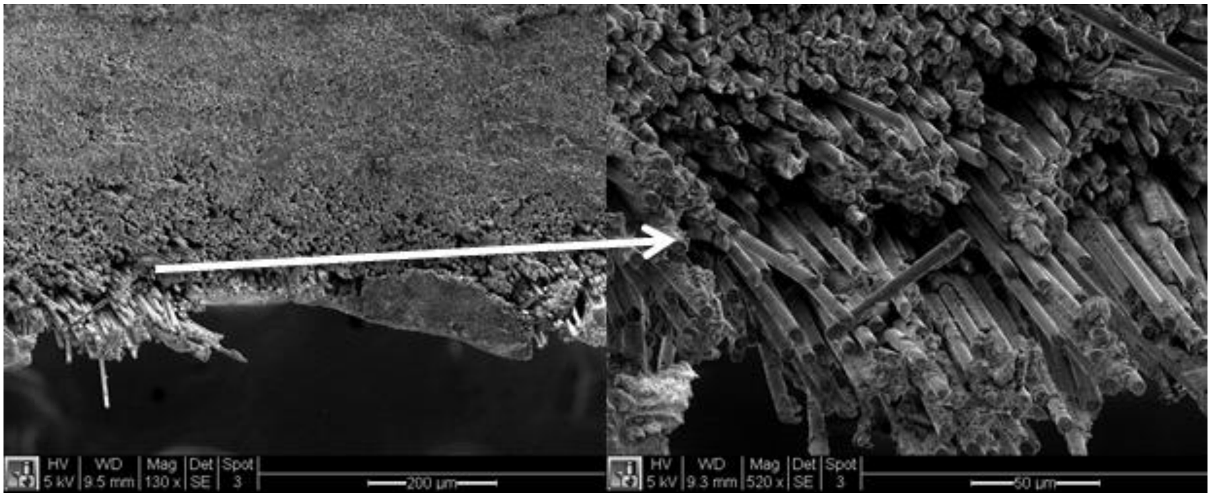

Figure M. 11. SEM micrograph of delamination at drill exit at 1500 rpm and 128 µm/rev

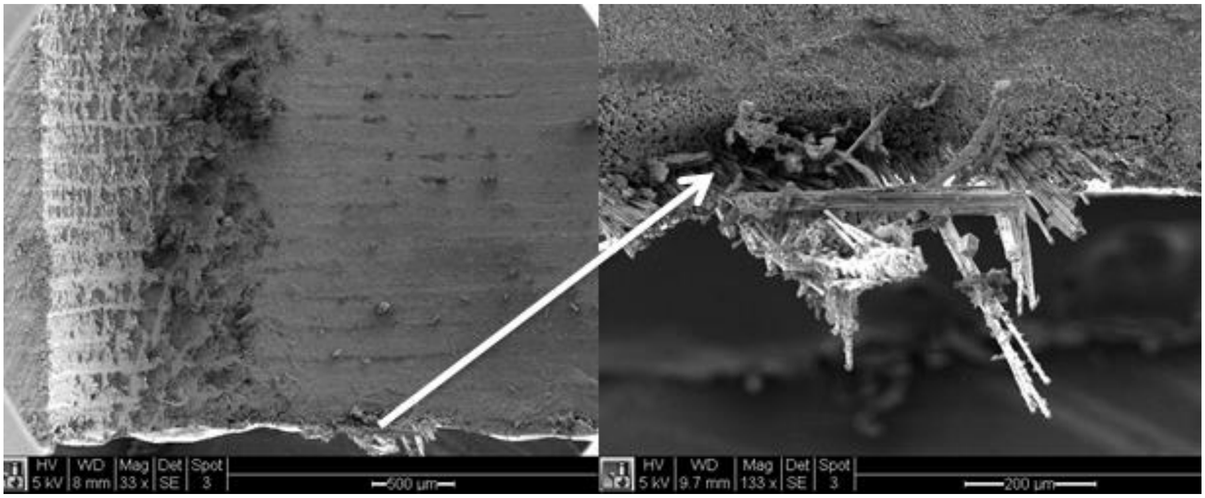

Figure M. 12. SEM micrograph of delamination at drill exit at 6000 rpm and 192 µm/rev

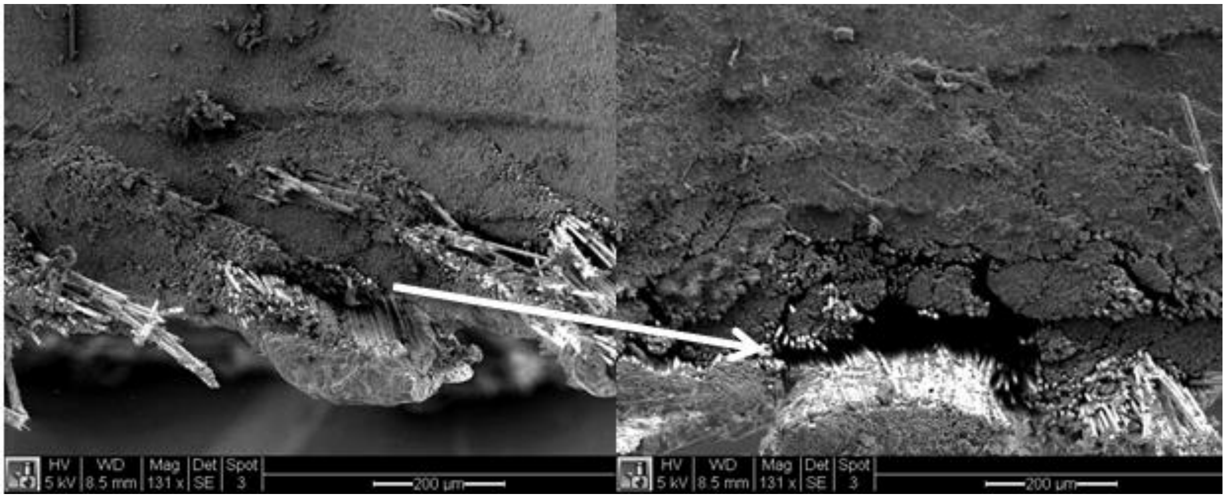

Figure M. 13. SEM micrograph of delamination at drill exit at 1500 rpm and 320 µm/rev

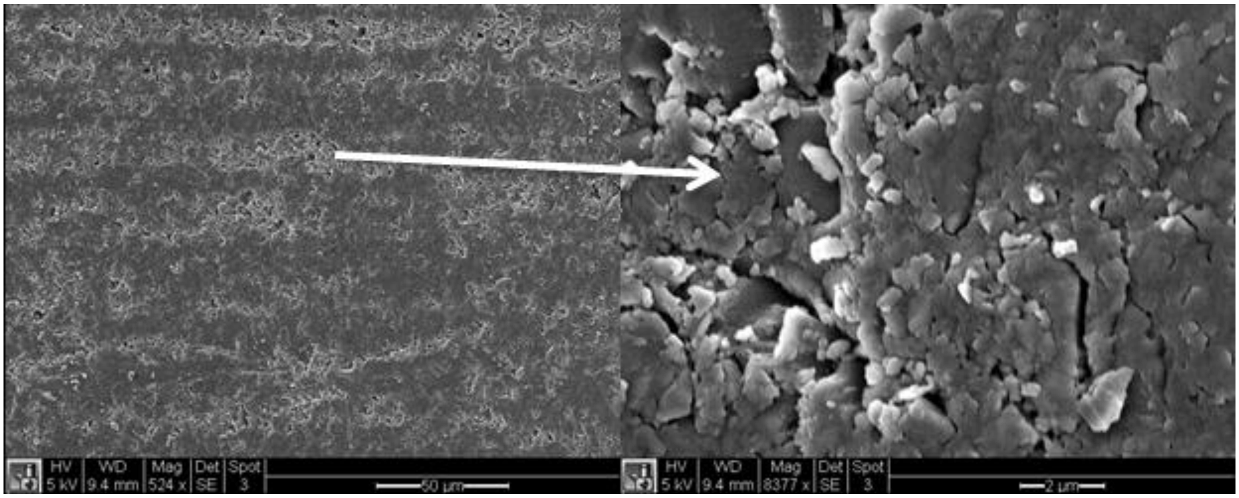

Figure M. 14. SEM micrograph of matrix smearing on hole surface at 6000 rpm and 192 µm/rev

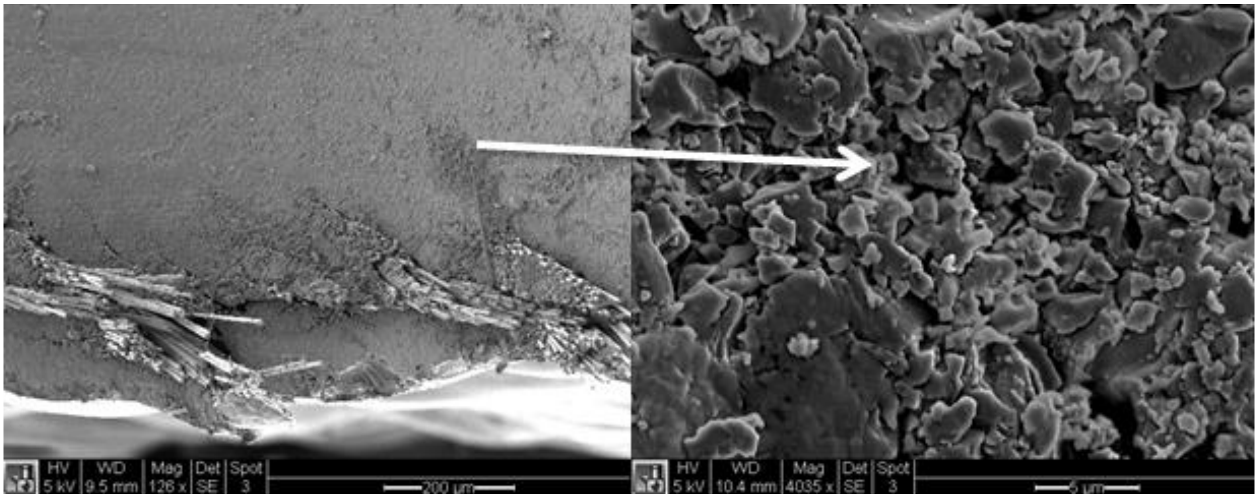

Figure M. 15. SEM micrograph of matrix smearing on hole surface at 3000 rpm and 64 µm/rev

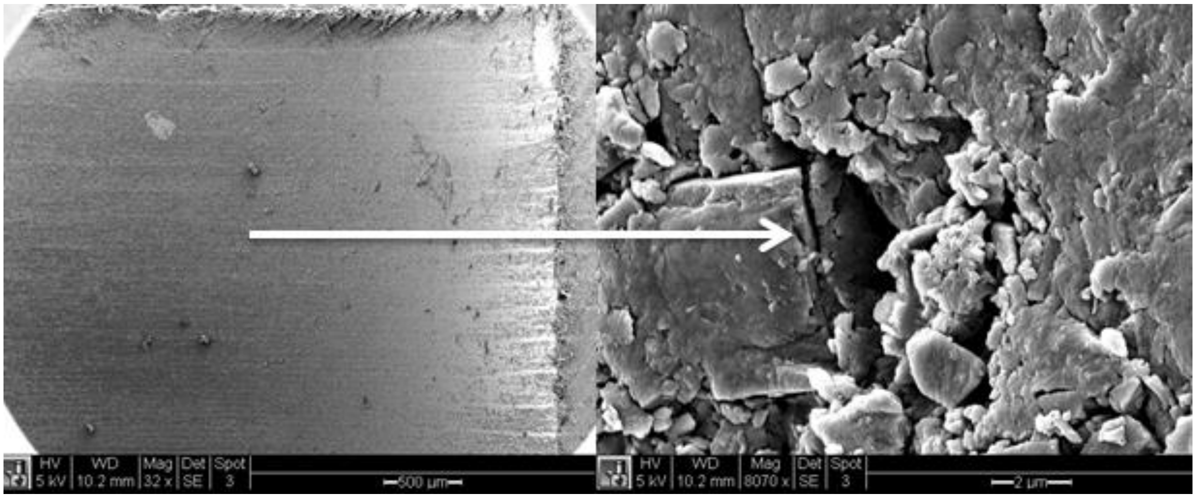

Figure M. 16. SEM micrograph of matrix smearing on hole surface at 3000 rpm and 64 µm/rev

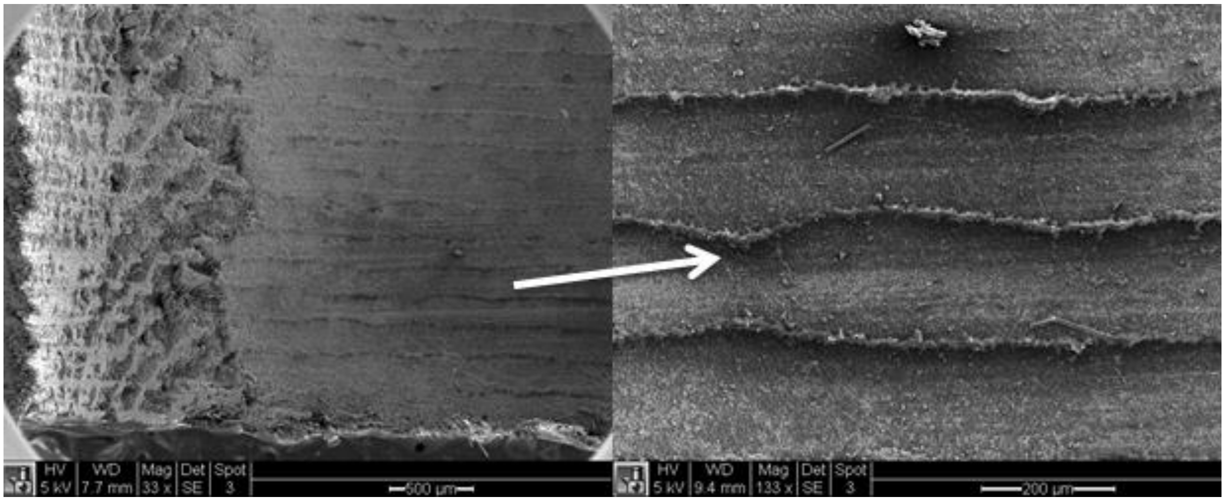

Figure M. 17. SEM micrograph of matrix melting at ply interface at 4500 rpm and 128 μm/rev

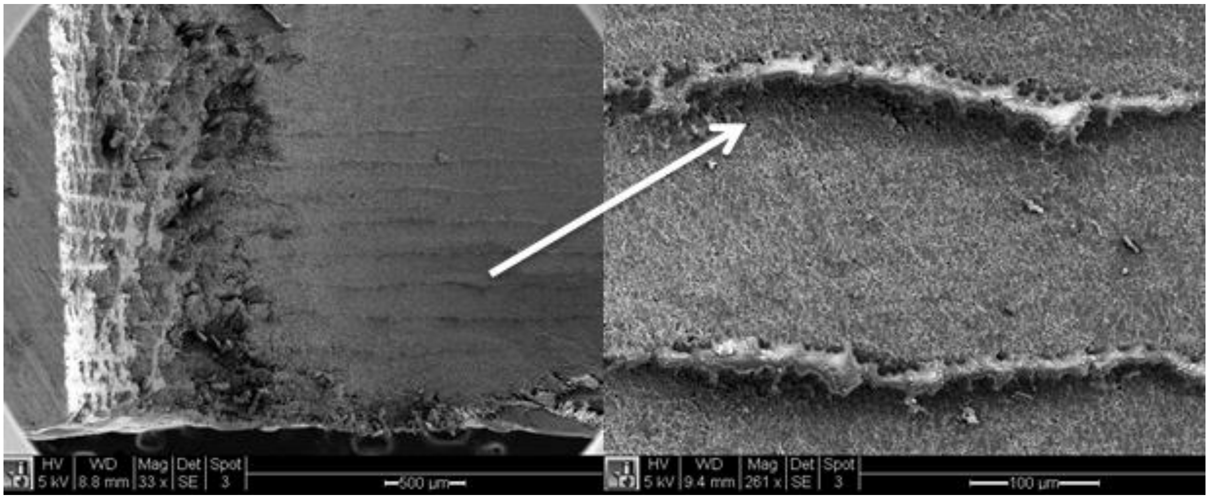

Figure M. 18. SEM micrograph of matrix melting at ply interface at 3000 rpm and 320 μm/rev

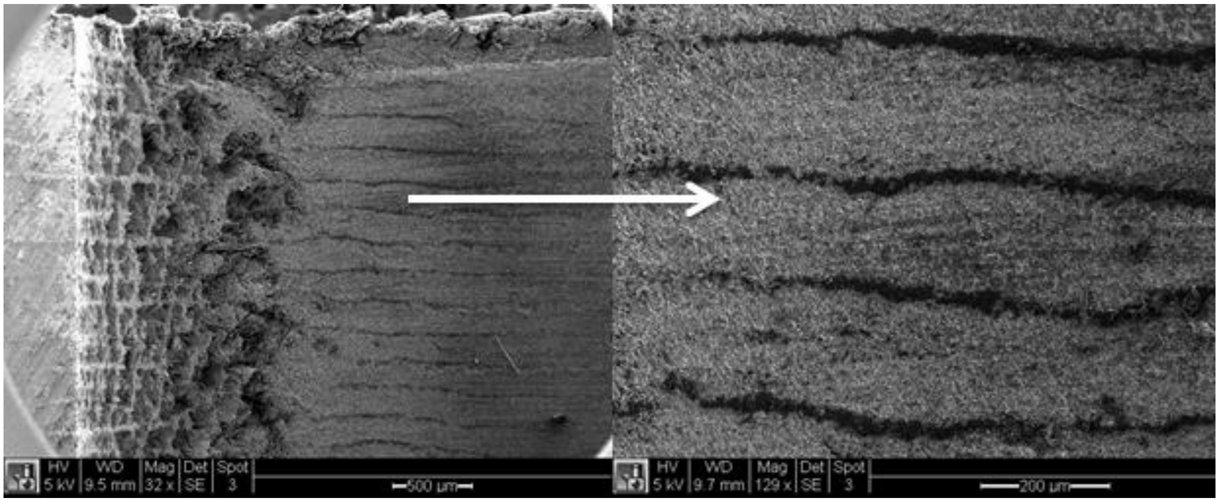

Figure M. 19. SEM micrograph of matrix melting at ply interface at 3000 rpm and 192 μm/rev

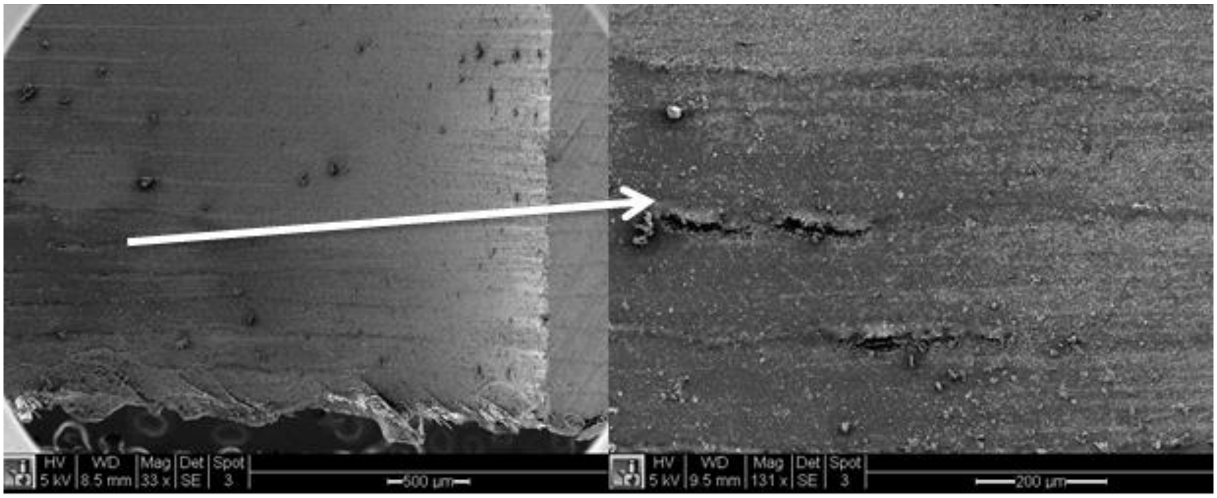

Figure M. 20. SEM micrograph of internal delamination at 4500 rpm and 128 µm/rev

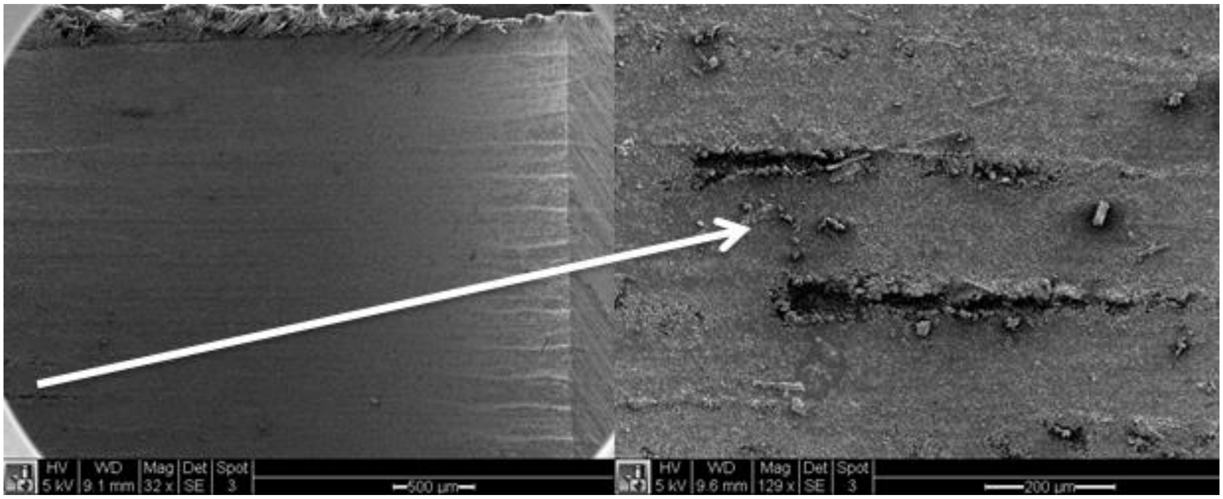

Figure M. 21. SEM micrograph of internal delamination at 6000 rpm and 320 µm/rev

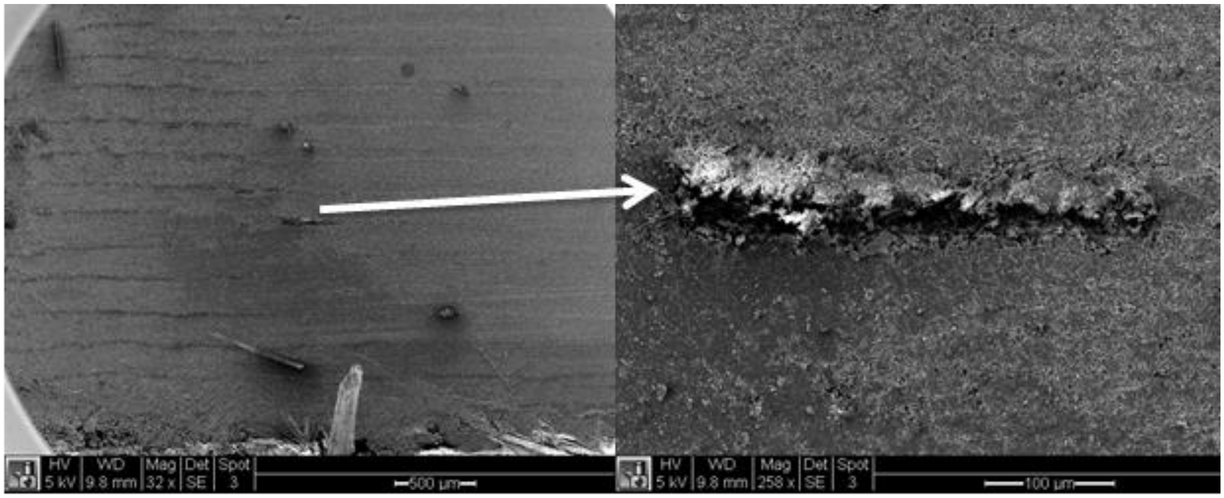

Figure M. 22. SEM micrograph of internal delamination at 4500 rpm and 320 µm/rev

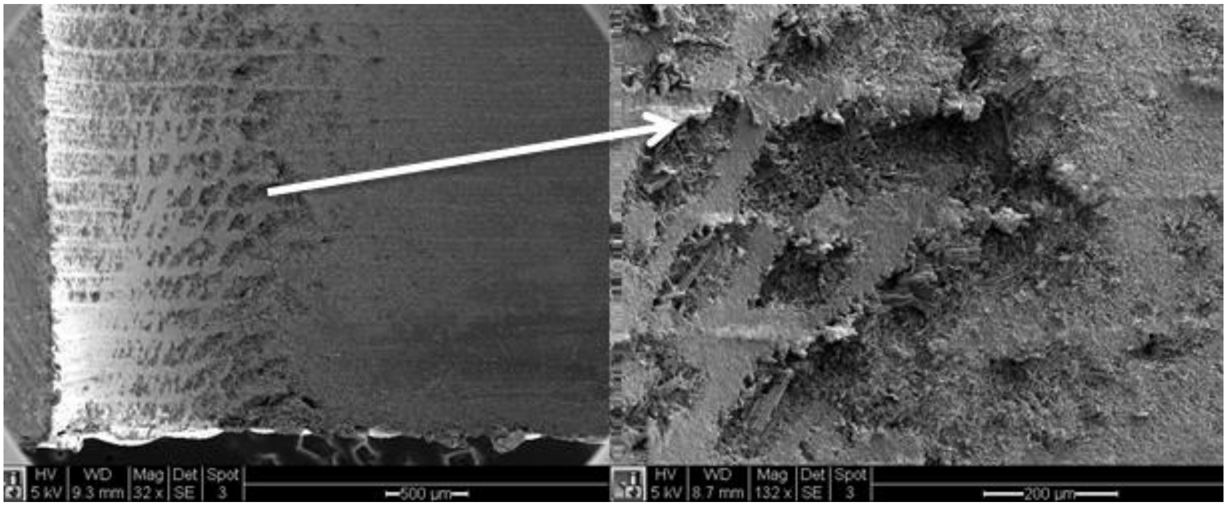

Figure M. 23. SEM micrograph of matrix poor area at 4500 rpm and 320 µm/rev

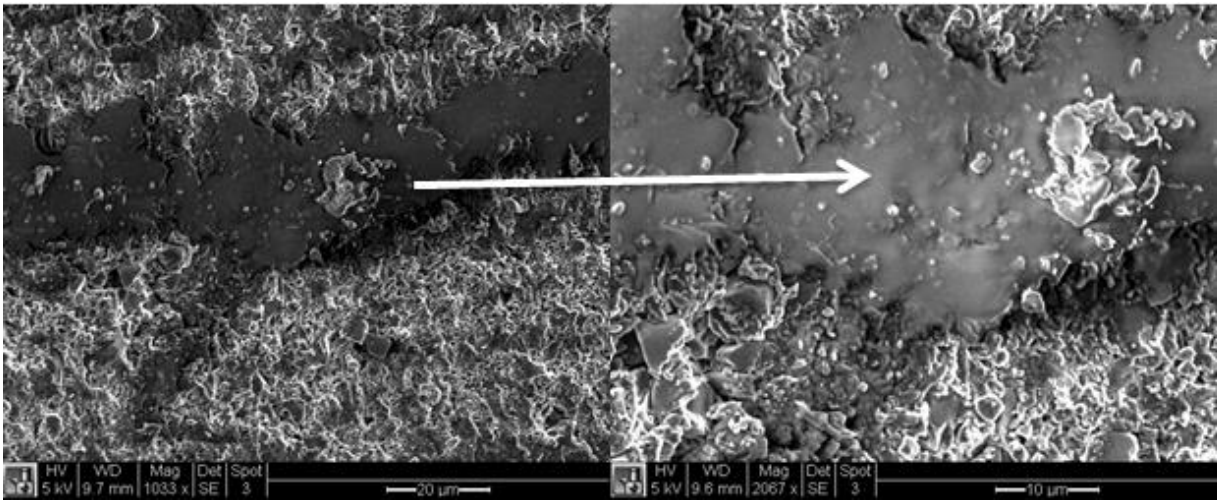

Figure M. 24. SEM micrograph matrix melting at ply interface at 3000 rpm and 256 µm/rev

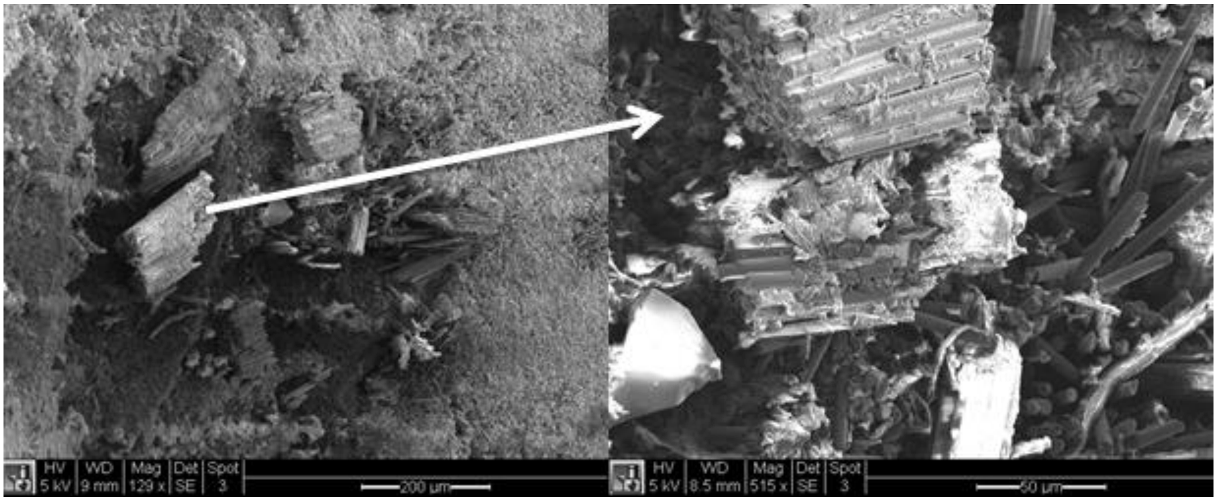

Figure M. 25. SEM micrograph of fiber bundle breakout at 1500 rpm and 256 µm/rev

APPENDIX N – OPTICAL MACROGRAPHS AT THE DRILL ENTRY AND EXIT FOR UNI-DIRECTIONAL CFRP

Table N. 1. Optical macrographs at the drill entry and exit for uni-directional CFRP

Speed (rpm)	Feed Rate (µm/rev)	Entrance	Exit
1500	64	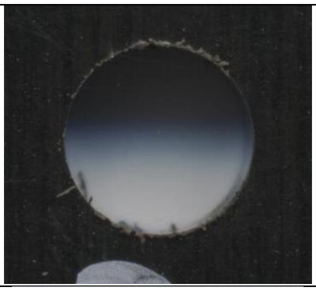	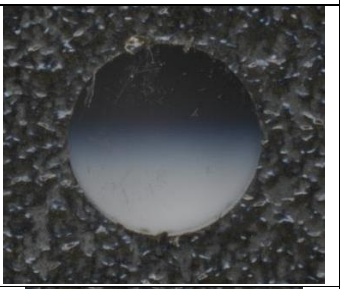
	128		
	192		
	256		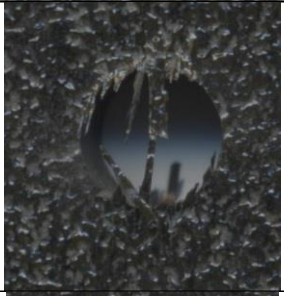
	320	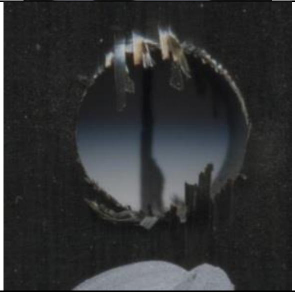	

Table N. 1. Continued

Speed (rpm)	Feed Rate (μm/rev)	Entrance	Exit
3000	64	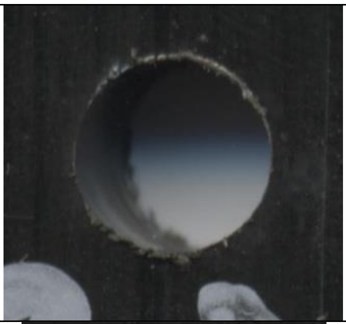	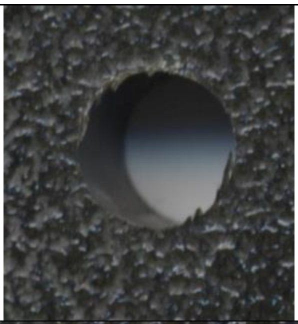
	128		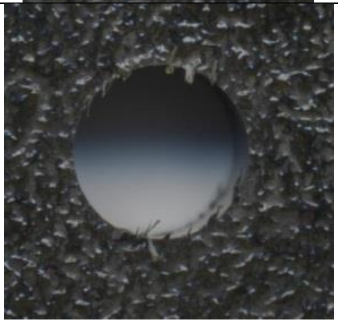
	192	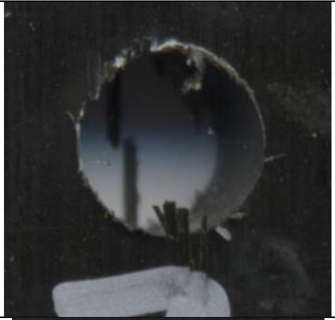	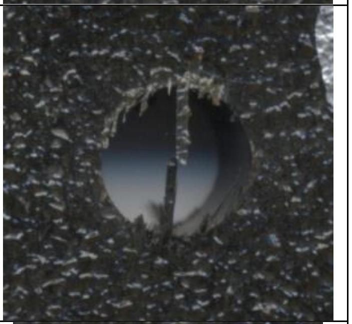
	256	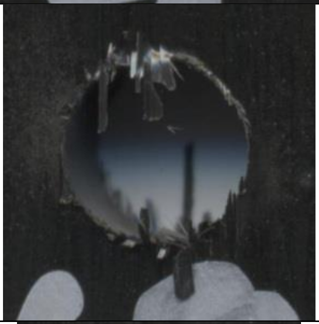	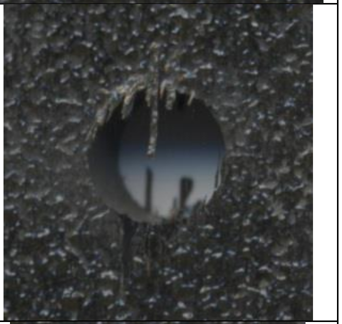
	320	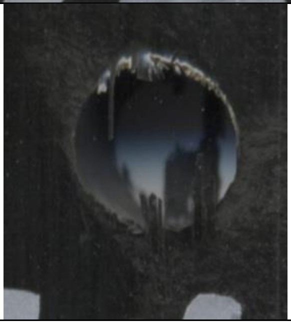	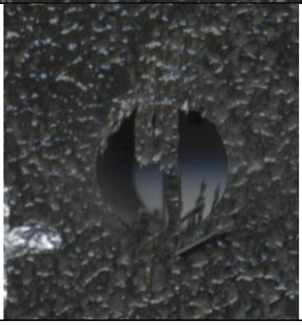

Table N. 1. Continued

Speed (rpm)	Feed Rate (µm/rev)	Entrance	Exit
4500	64		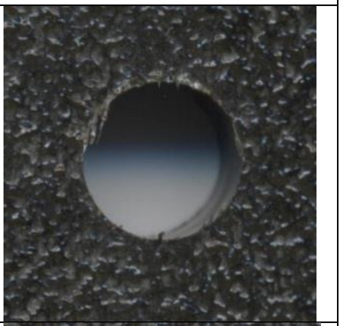
	128		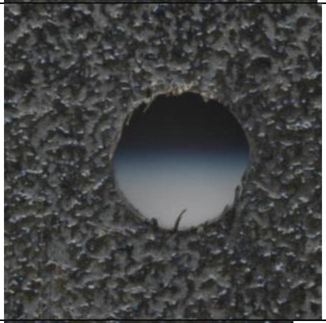
	192		
	256		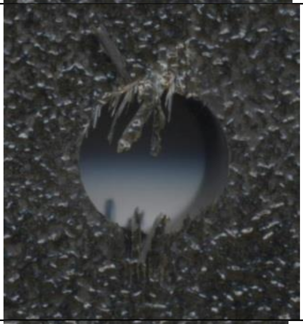
	320		

Table N. 1. Continued

Speed (rpm)	Feed Rate (µm/rev)	Entrance	Exit
6000	64	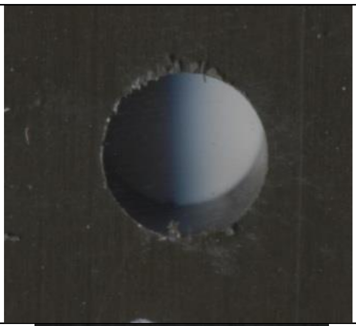	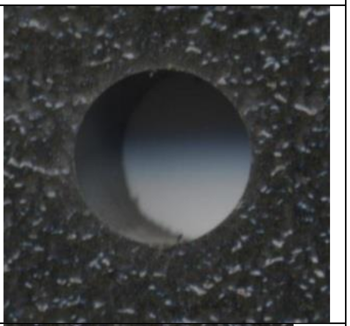
	128		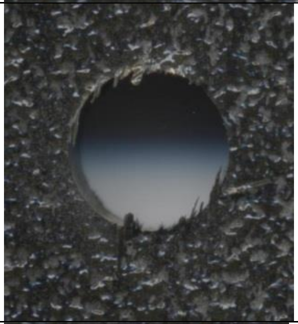
	192		
	256	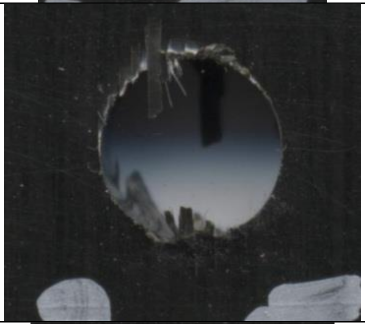	
	320		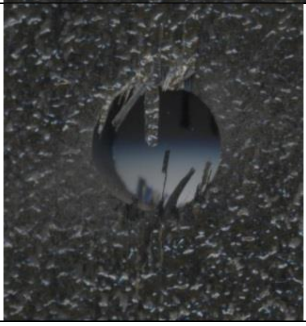

APPENDIX O – AUDIO MICROPHONE RAW SIGNAL PROFILES WHEN DRILLING MULTI-DIRECTIONAL CFRP WITH HSS DRILL

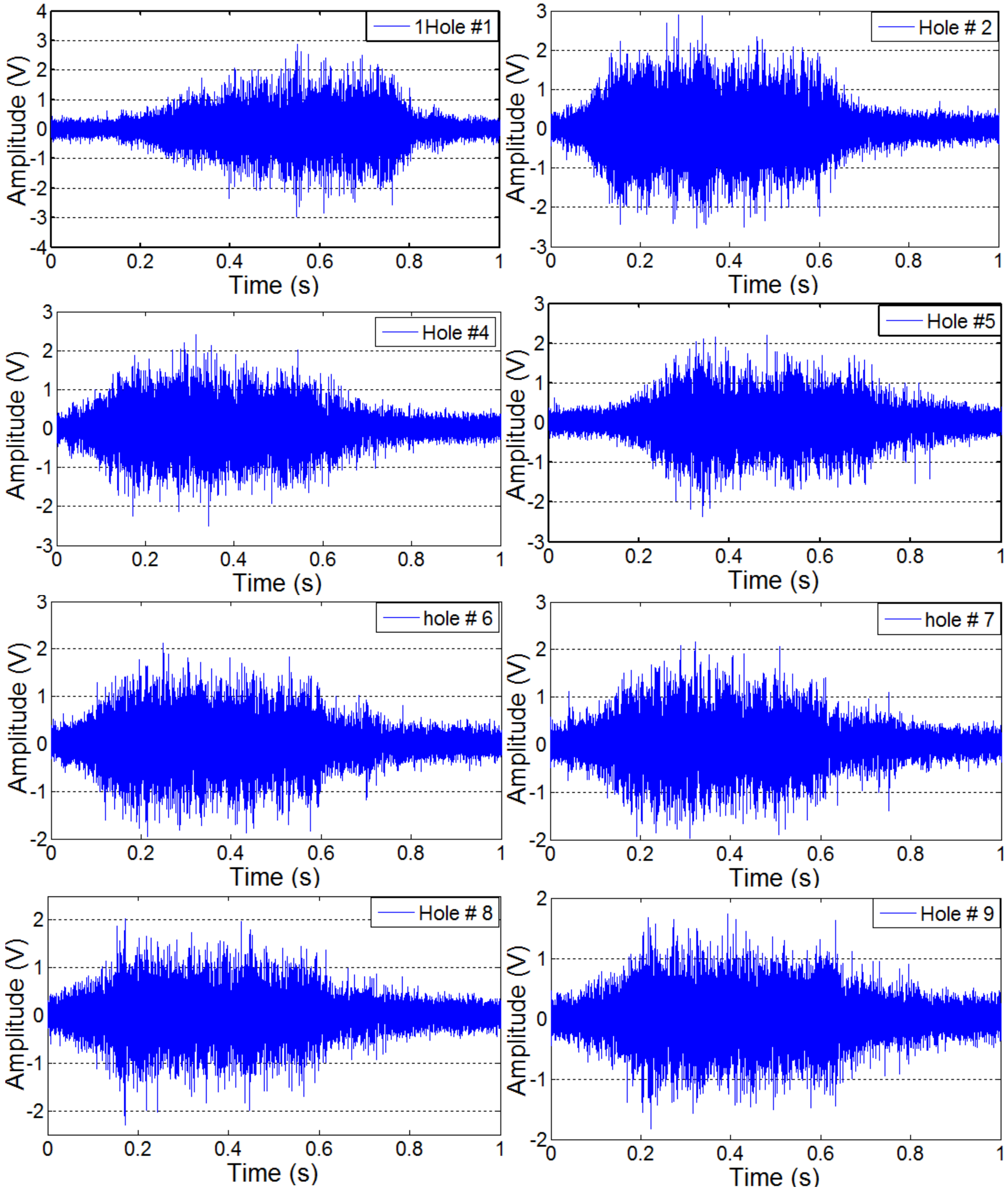

Figure O. 1. Audio microphone raw signal profiles when drilling multi-directional CFRP with HSS

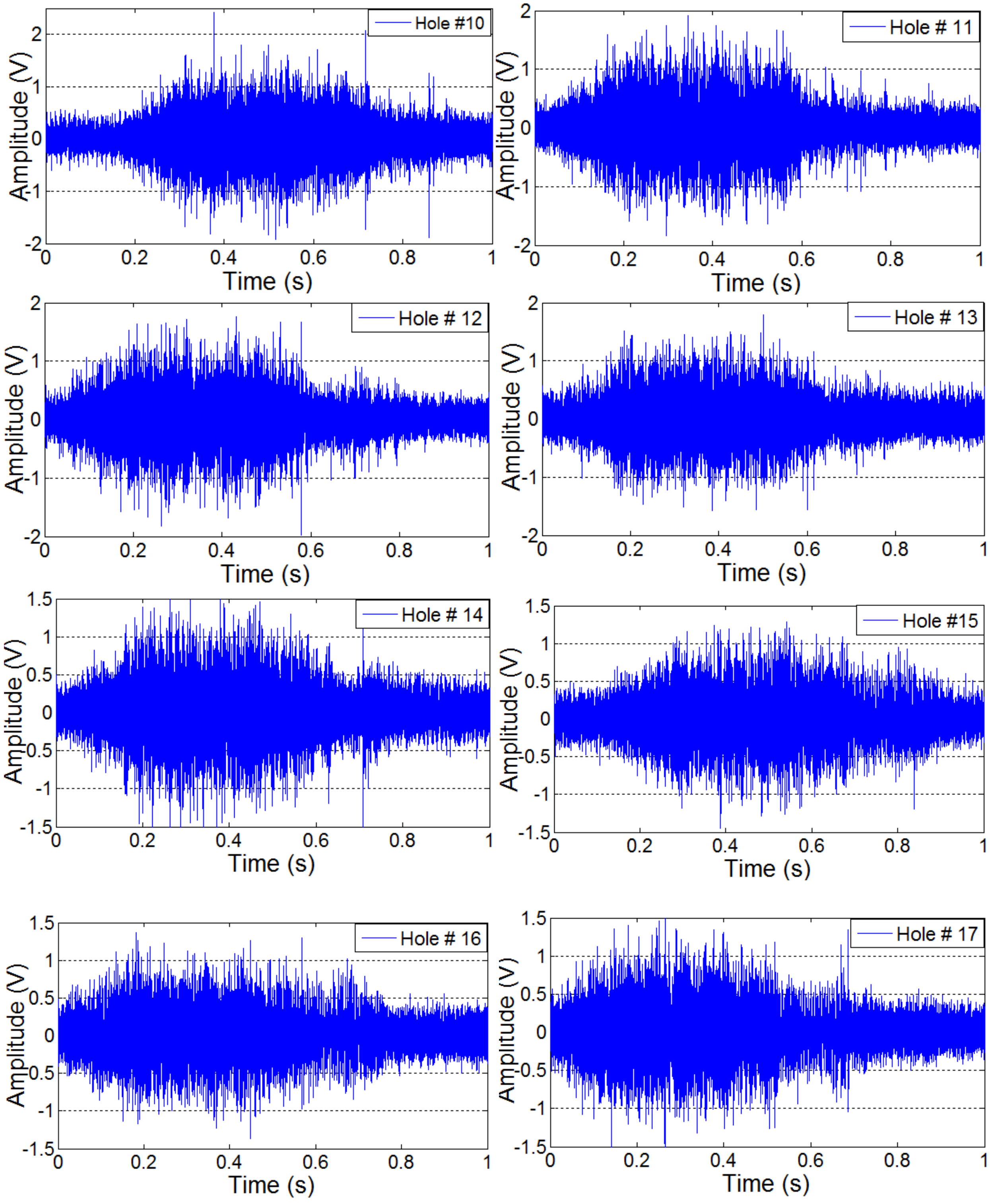

Figure O. 1. Continued

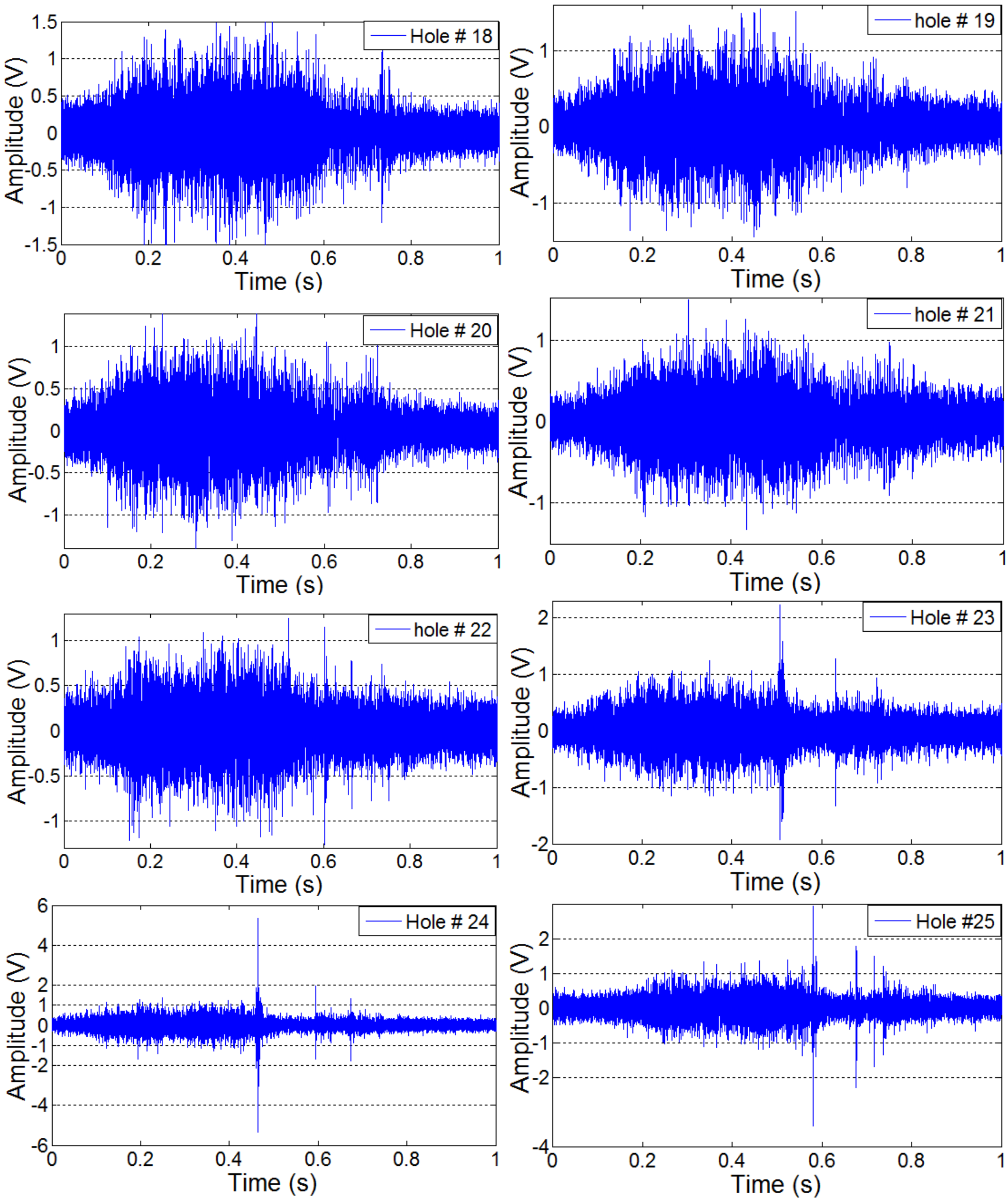

Figure O. 1. Continued

APPENDIX P – AUDIO MICROPHONE RAW SIGNAL PROFILES WHEN DRILLING UNI-DIRECTIONAL CFRP WITH HSS DRILL

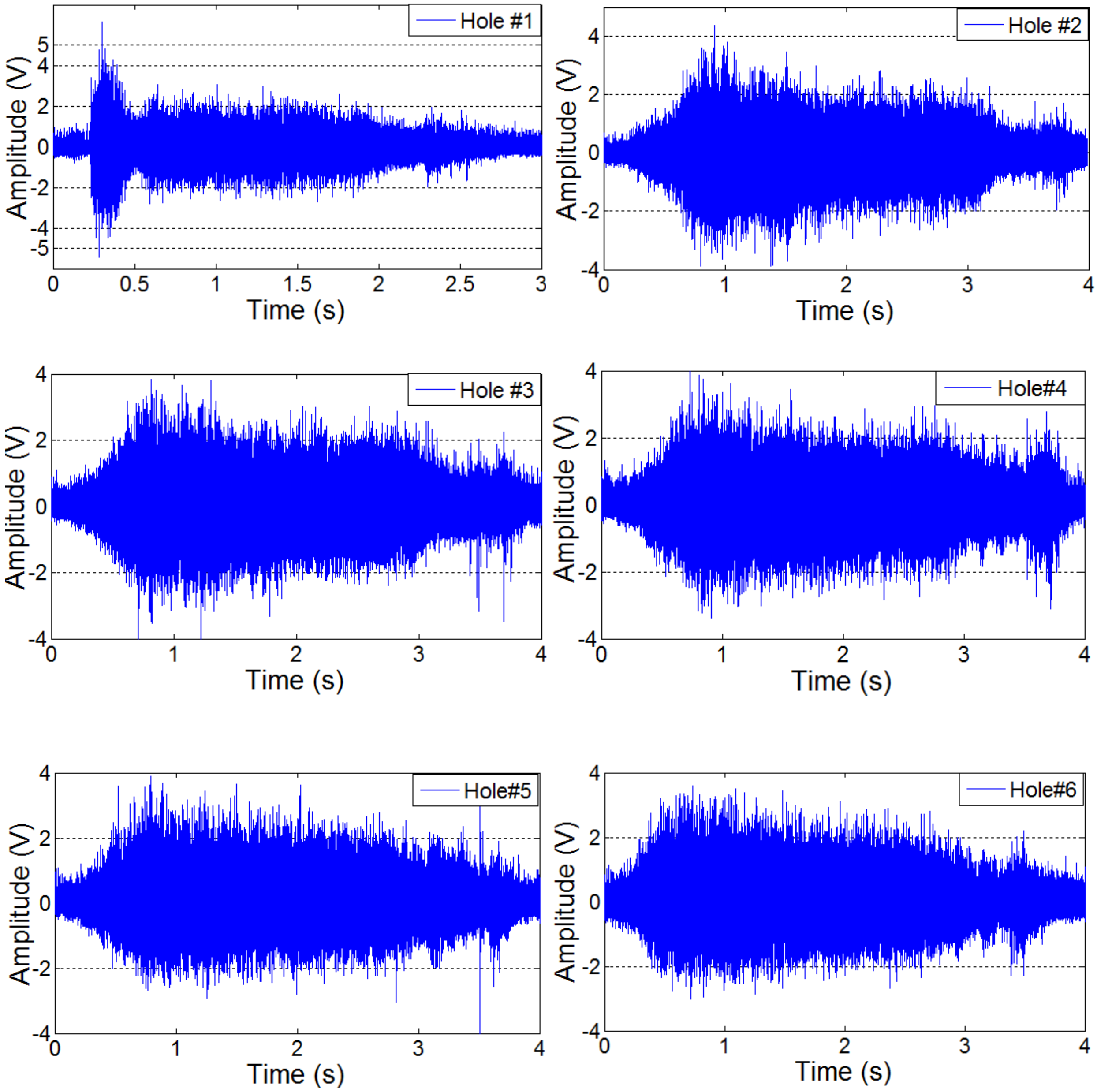

Figure P. 1. Audio microphone raw signal profiles when drilling uni-directional CFRP with HSS

APPENDIX Q – OPTICAL IMAGE OF DRILL CUTTING EDGE AND FLANK WEAR PROGRESSION OF CARBIDE DRILL TOOL

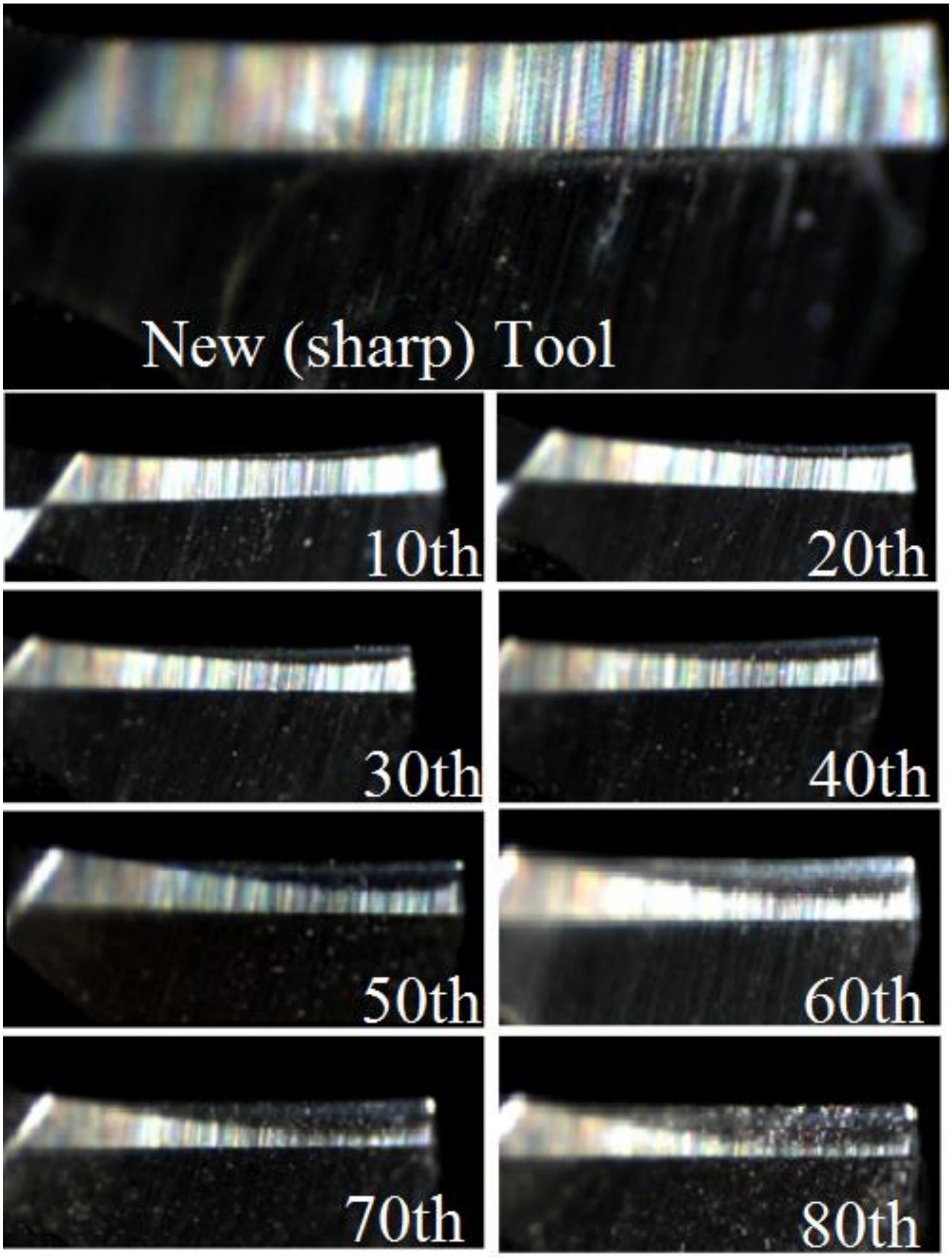

Figure Q. 1. Optical image of the cutting edge of drilling Condition II

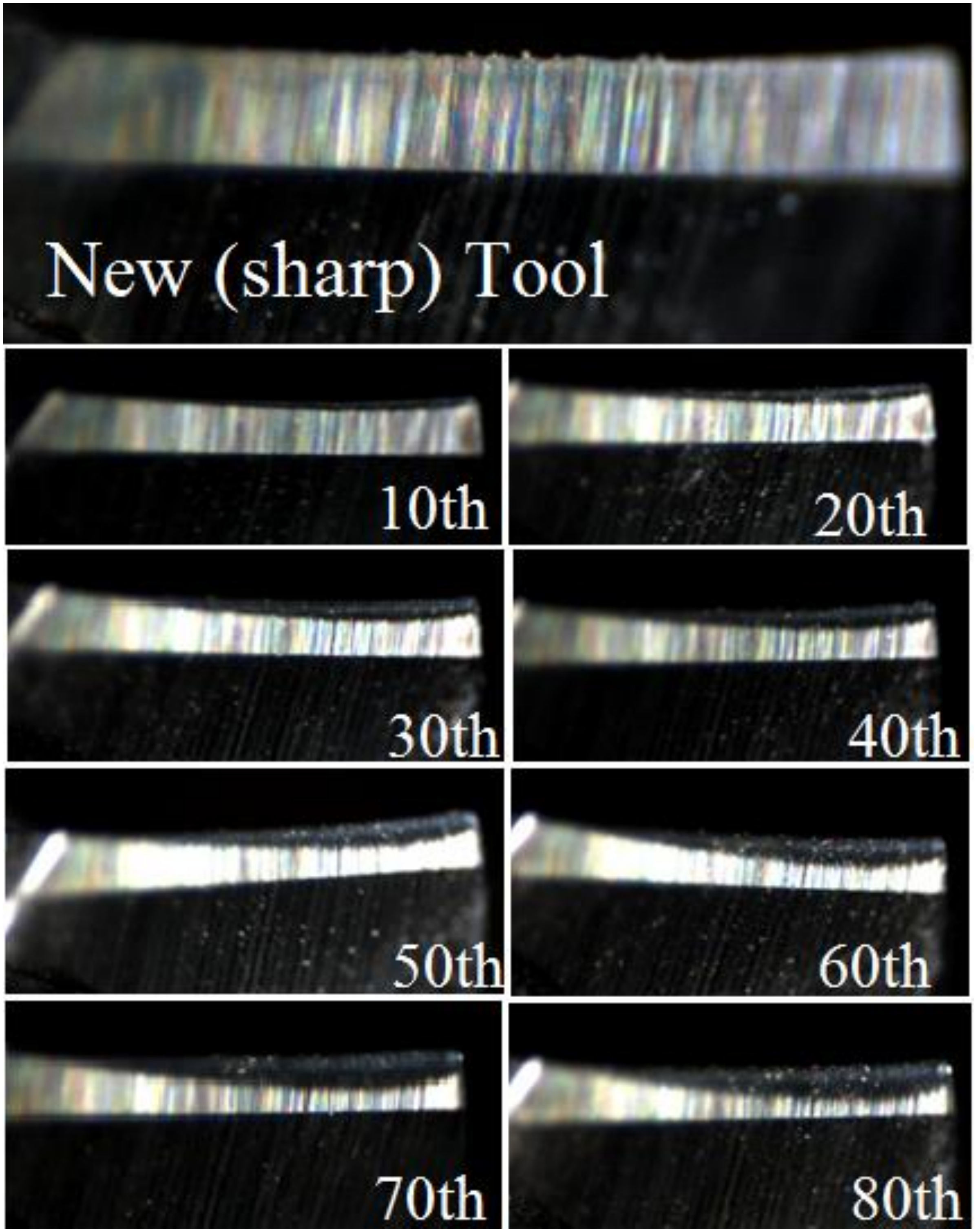

Figure Q. 2. Optical image of the cutting edge of drilling Condition III

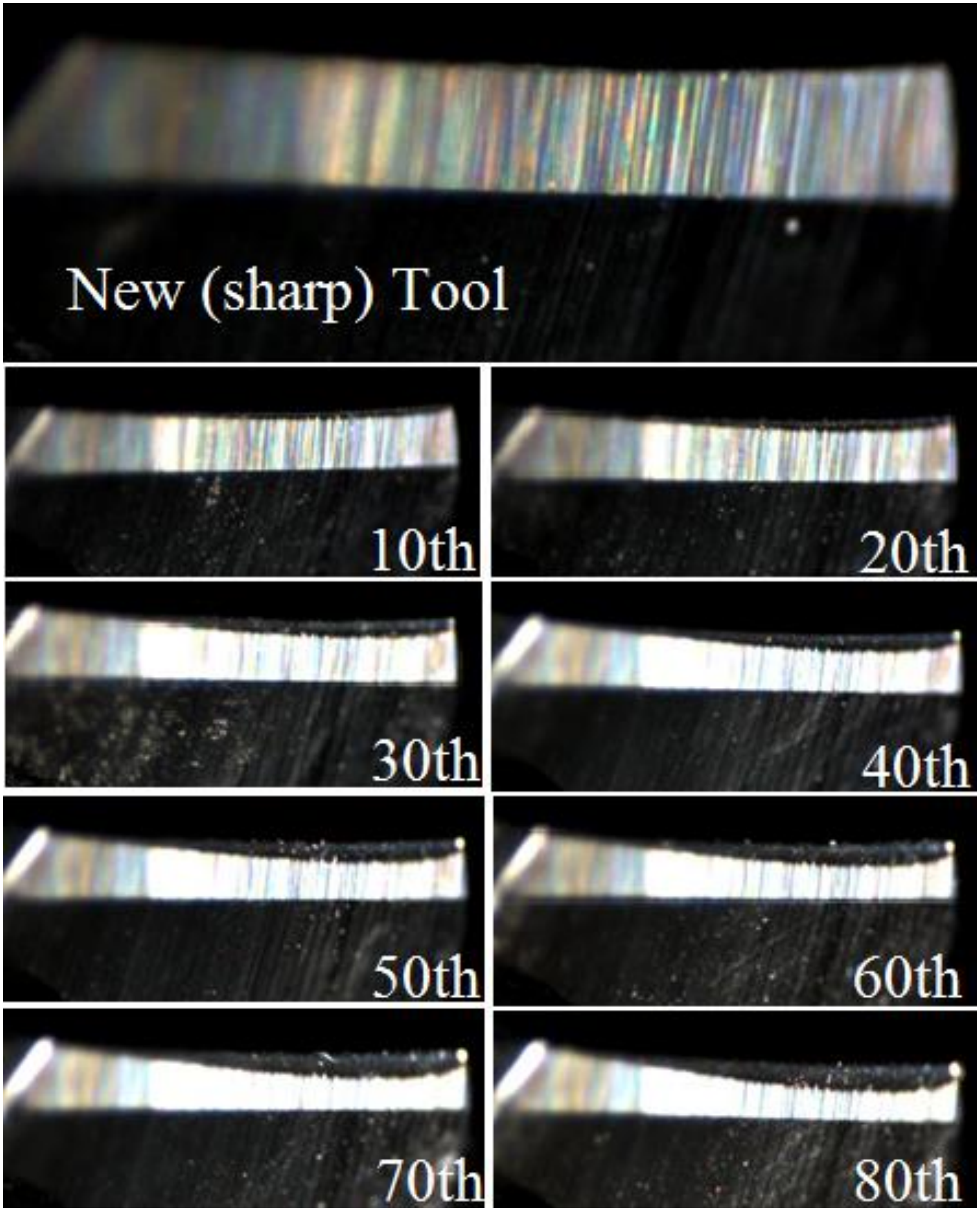

Figure Q. 3. Optical image of the cutting edge of drilling Condition IV

APPENDIX R– THRUST FORCE PROFILES WHEN DRILLING UNI-DIRECTIONAL CFRP WITH CARBIDE DRILL

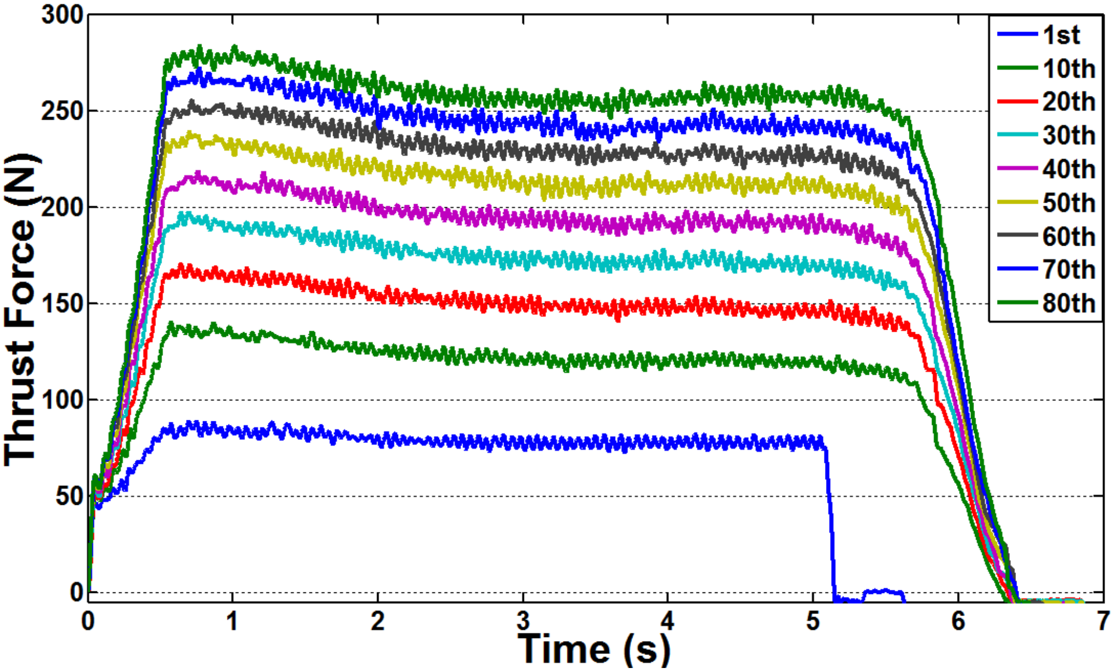

Figure R. 1. Thrust force profiles of drilling condition II for every tenth hole

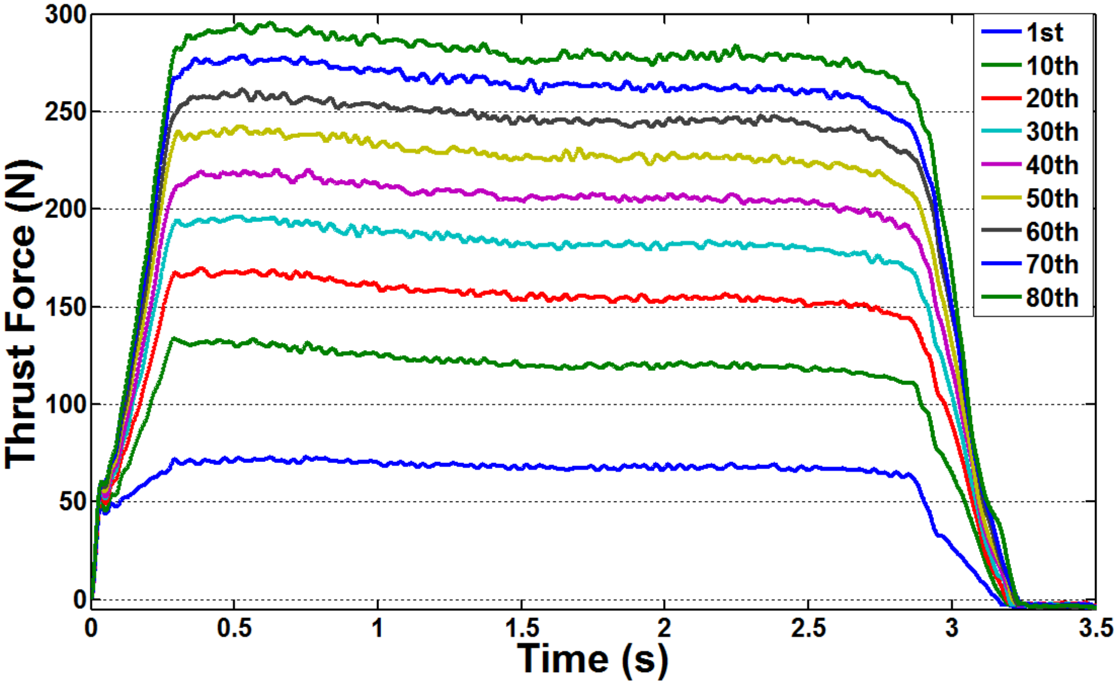

Figure R. 2. Thrust force profiles of drilling condition III for every tenth hole

APPENDIX S – TORQUE PROFILES WHEN DRILLING UNI-DIRECTIONAL CFRP WITH CARBIDE DRILL

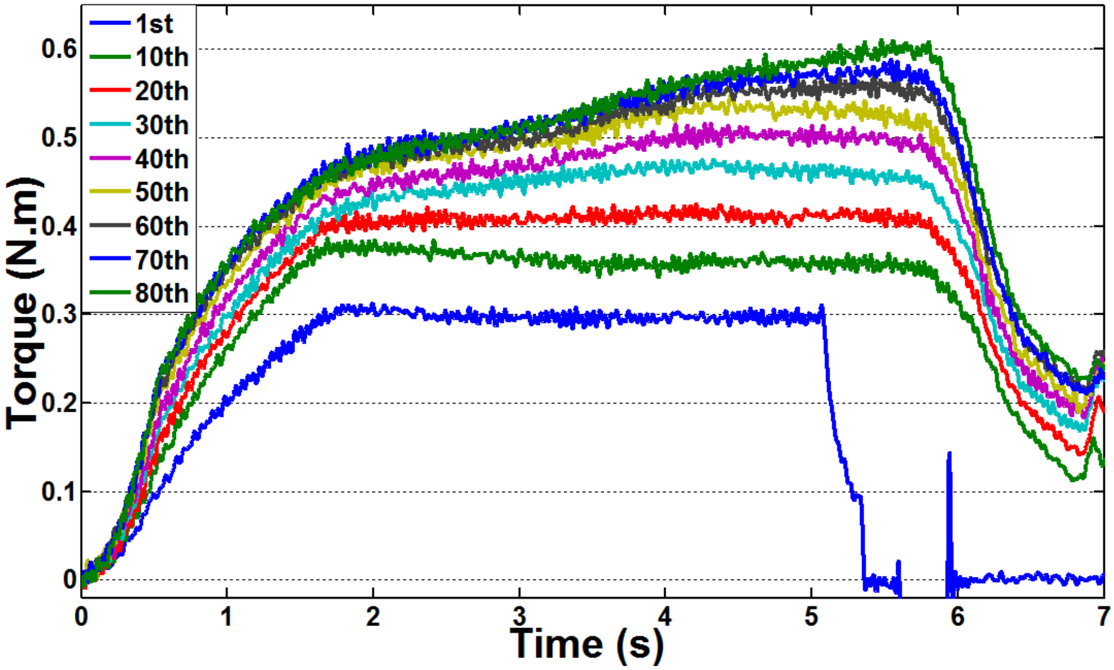

Figure S. 1. Torque profiles of drilling condition II for every tenth hole

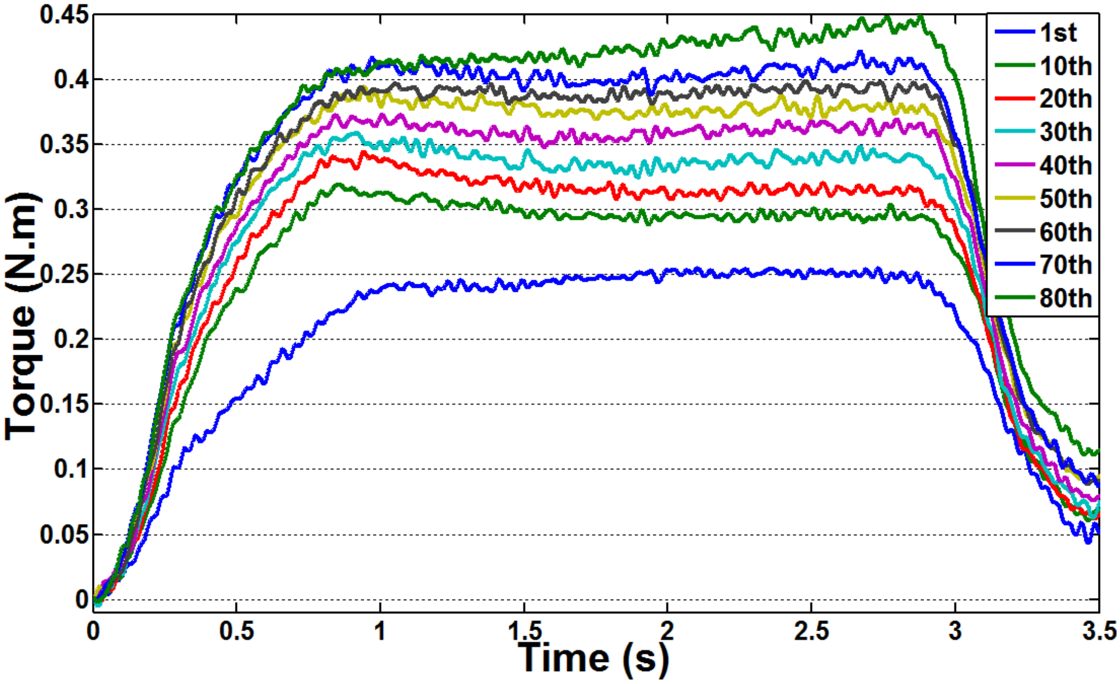

Figure S. 2. Torque profiles of drilling condition III for every tenth hole

APPENDIX T – AUDIO MICROPHONE RAW SIGNAL PROFILES WHEN DRILLING UNI-DIRECTIONAL CFRP WITH CARBIDE DRILL

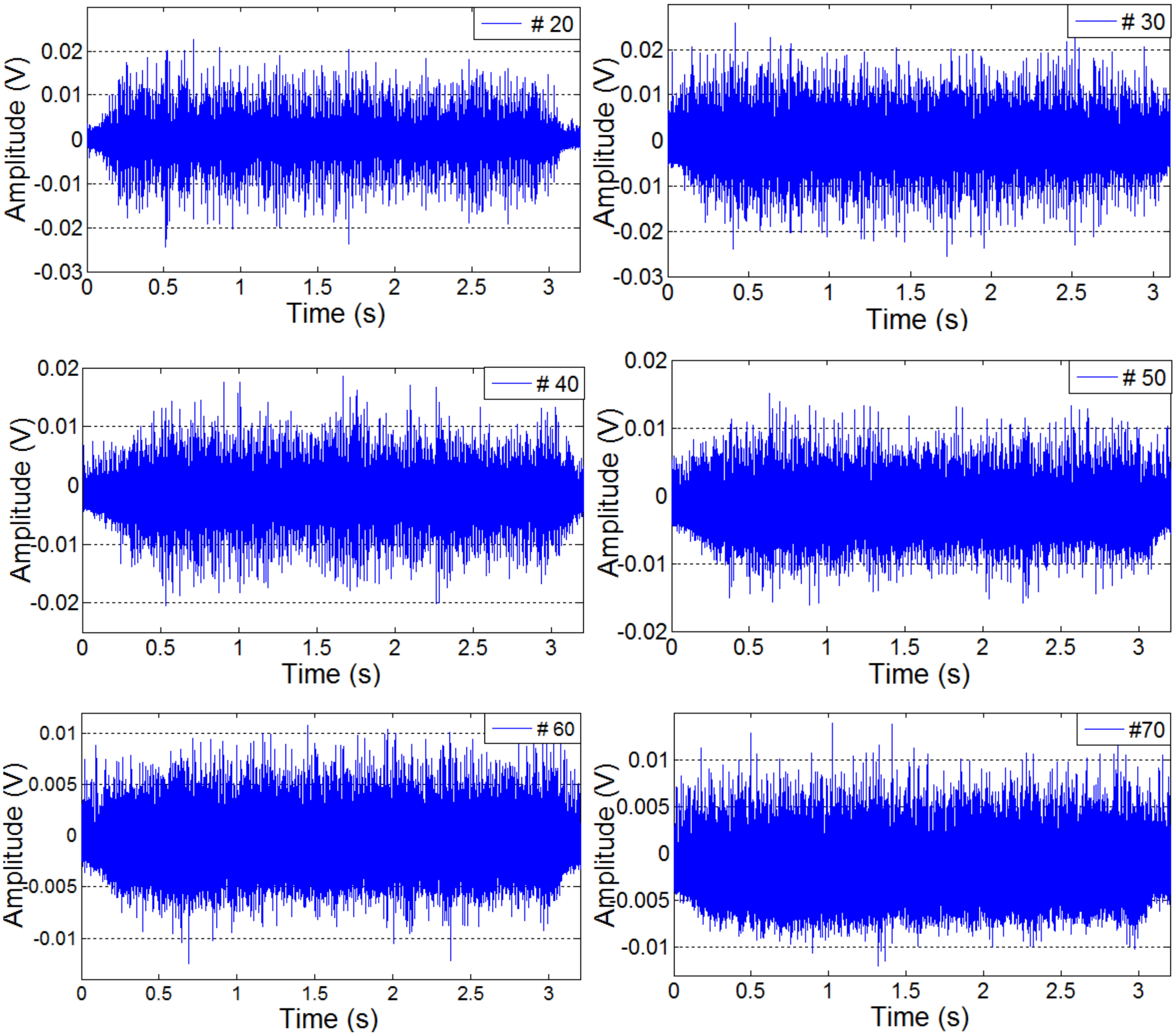

Figure T. 1. Audio microphone raw signal profiles when drilling uni-directional CFRP with carbide tool for drilling Condition I

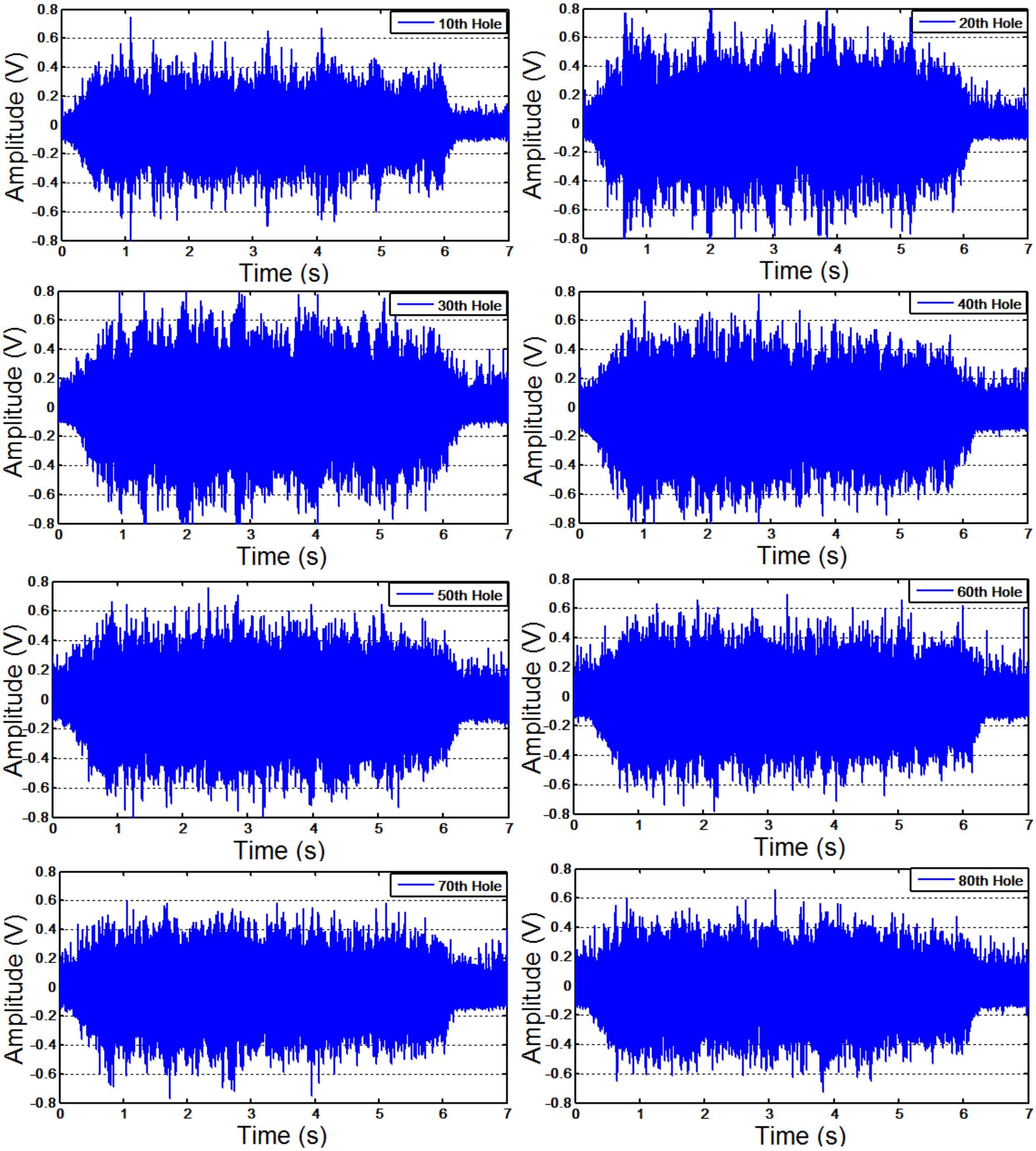

Figure T. 2. Audio microphone raw signal profiles when drilling uni-directional CFRP with carbide tool for drilling Condition II

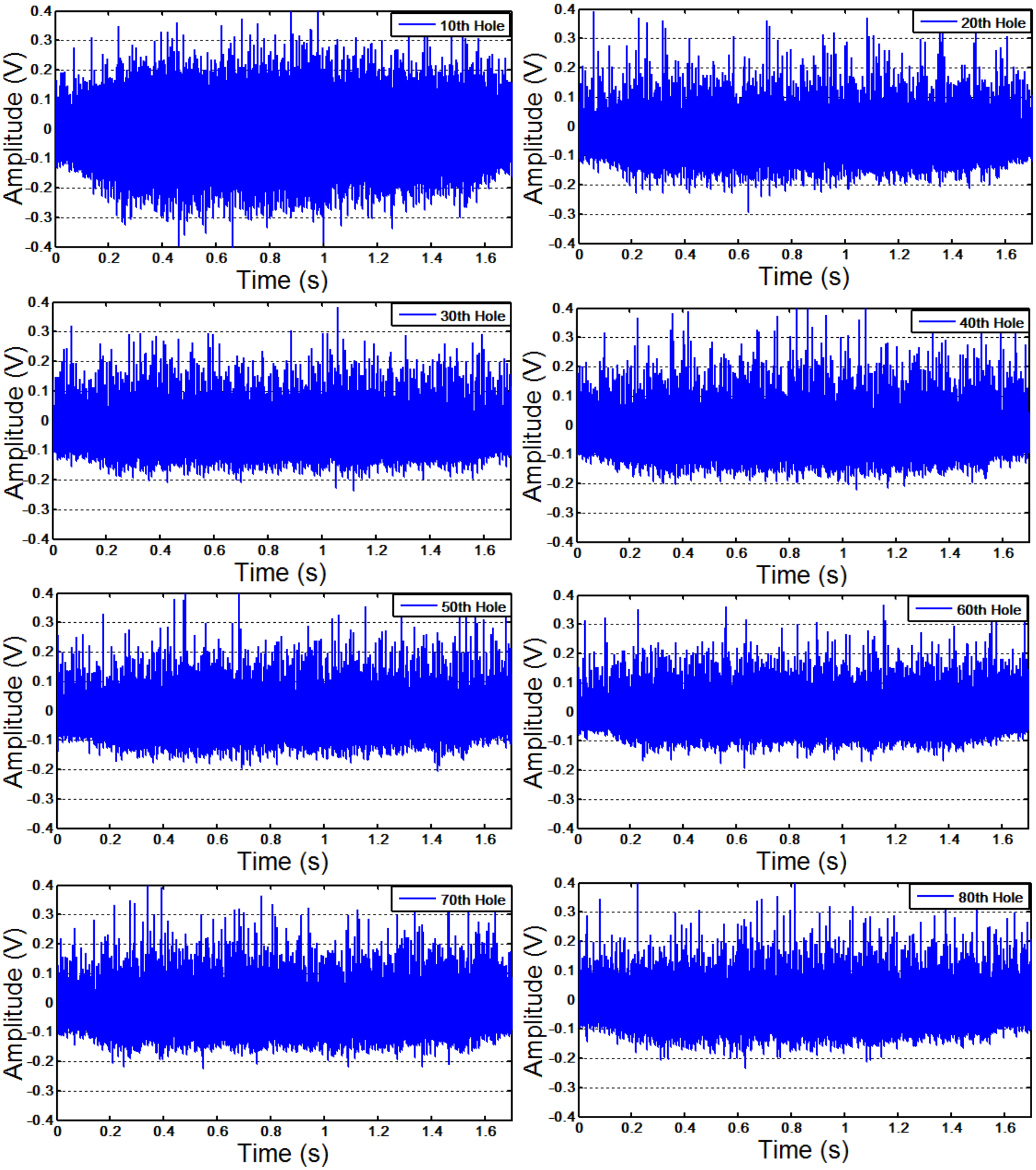

Figure T.3. Audio microphone raw signal profiles when drilling uni-directional CFRP with carbide tool for drilling Condition IV

APPENDIX U – RAW SIGNAL PROFILES OF ACOUSTIC EMISSION WHEN DRILLING UNI-DIRECTIONAL CFRP WITH CARBIDE DRILL

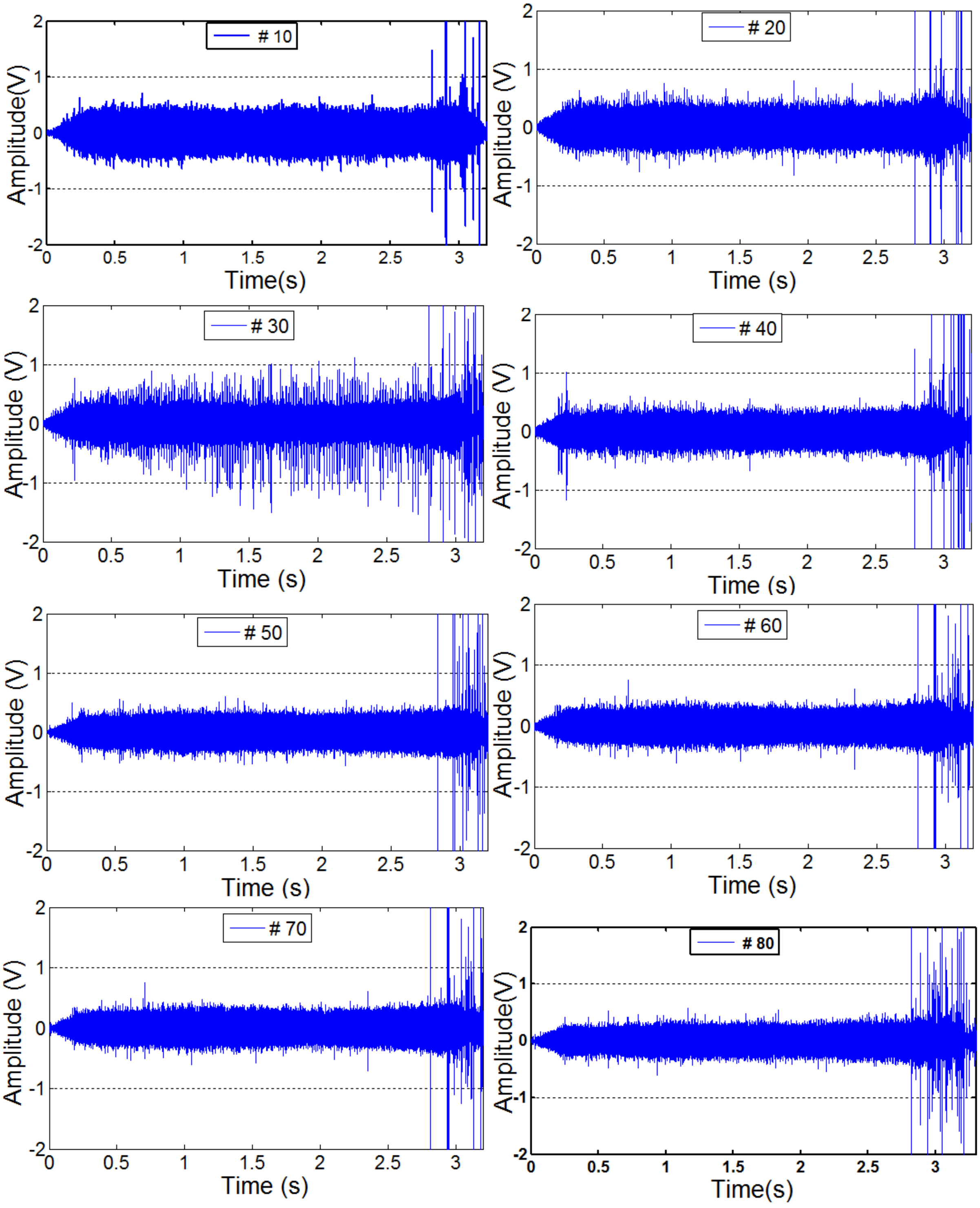

Figure U. 1. Acoustic emission raw signal profiles when drilling uni-directional CFRP with carbide tool for drilling Condition I

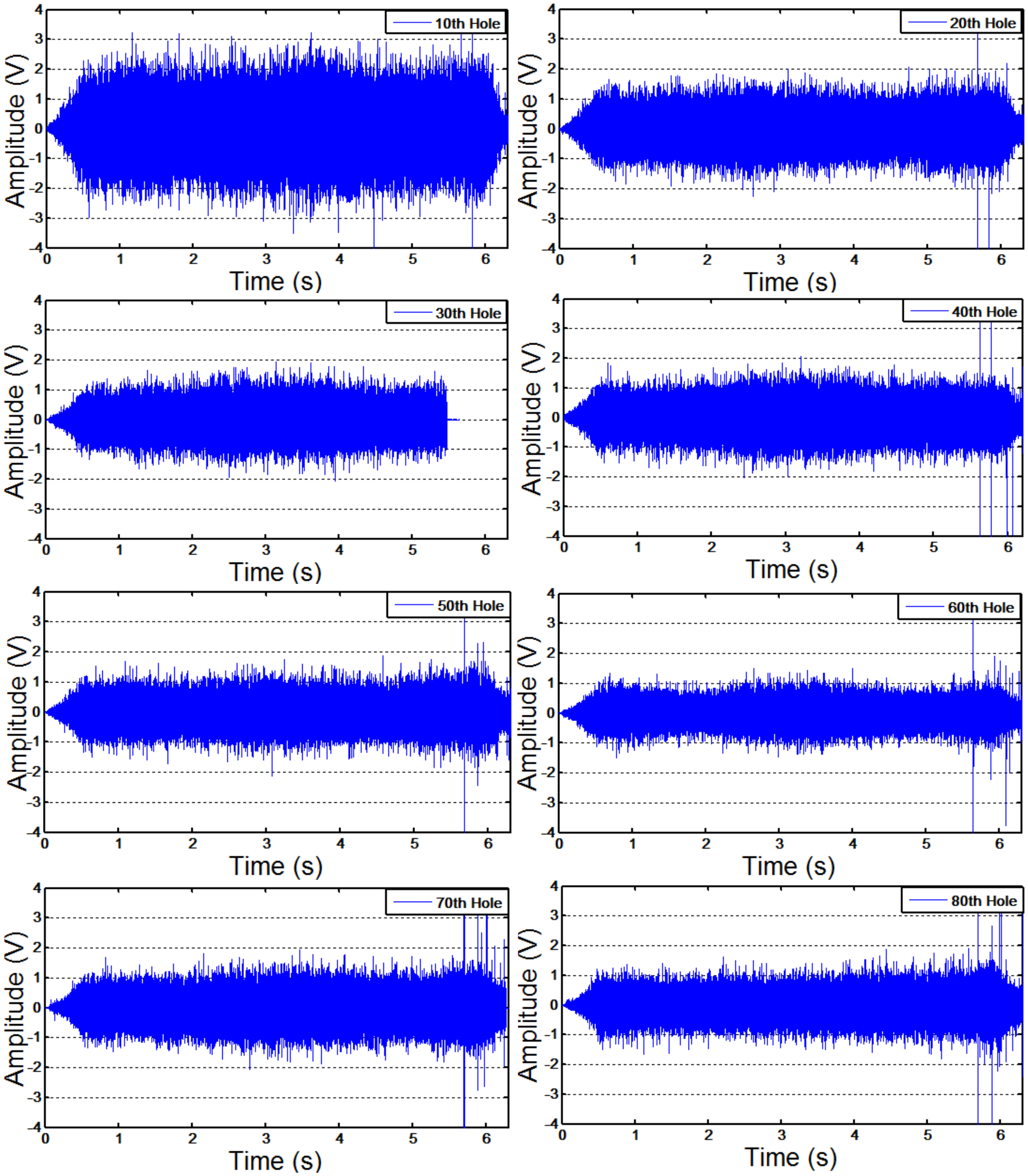

Figure U. 2. Acoustic emission raw signal profiles when drilling uni-directional CFRP with carbide tool for drilling Condition II

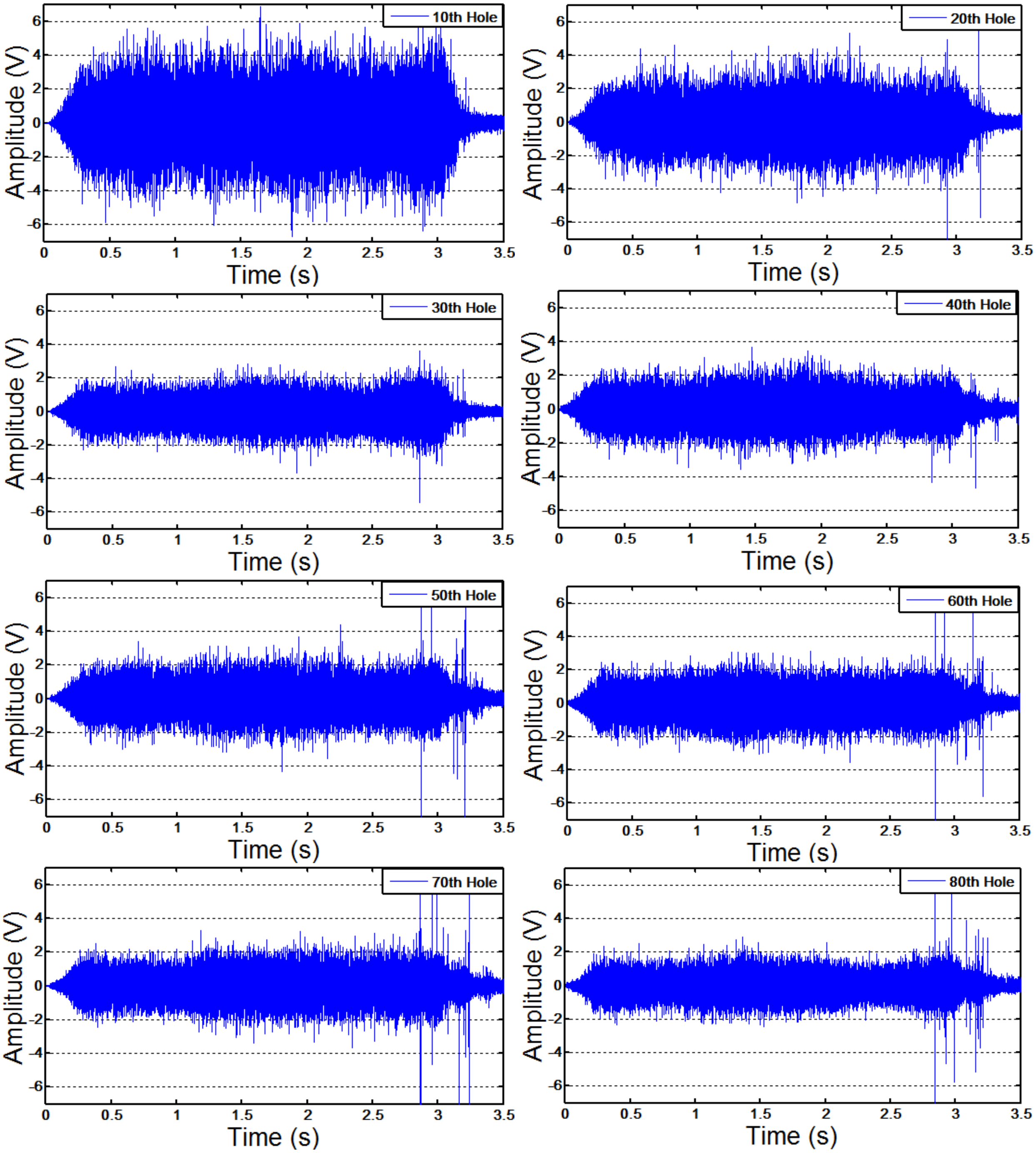

Figure U. 3. Acoustic emission raw signal profiles when drilling uni-directional CFRP with carbide tool for drilling Condition III

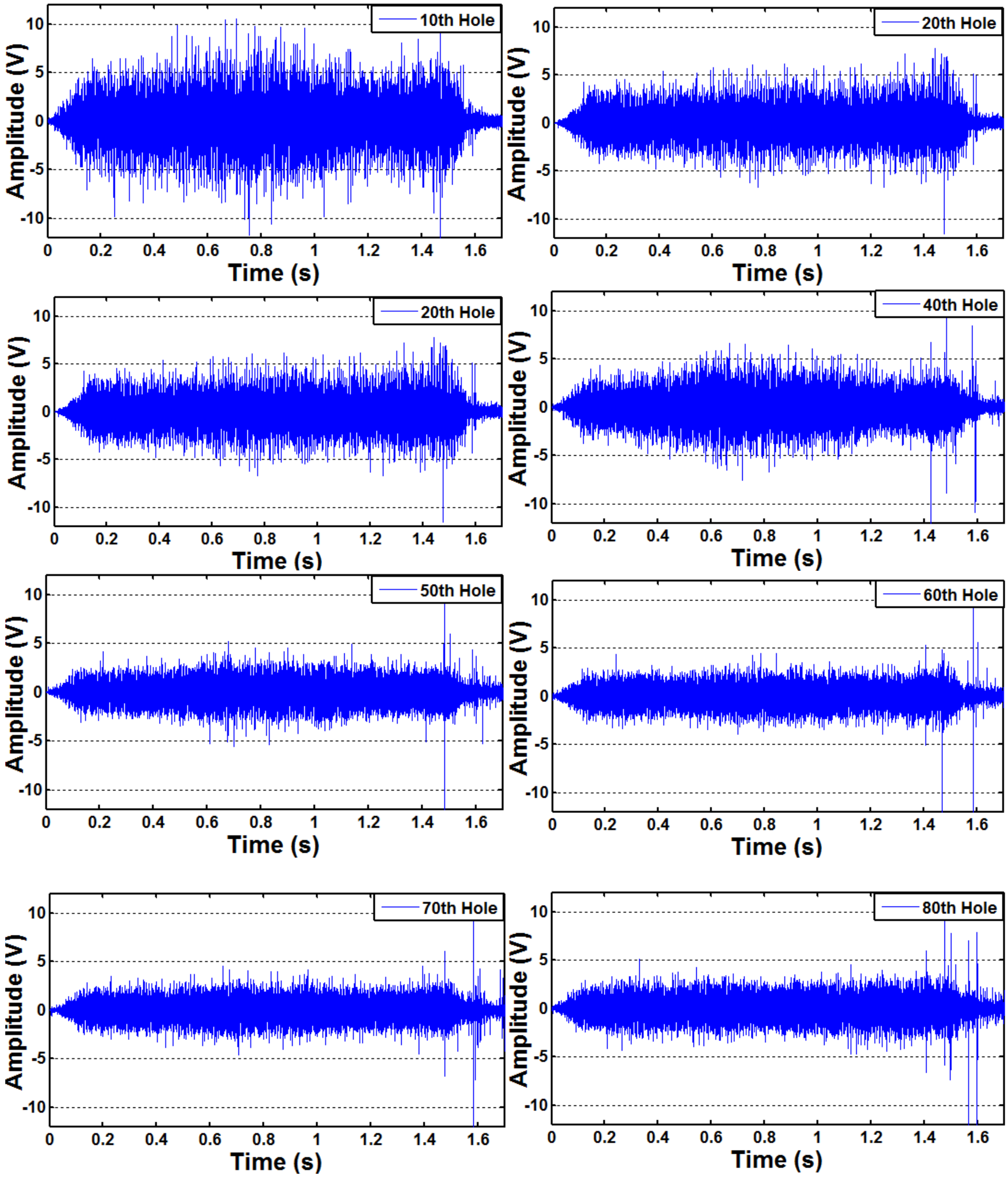

Figure U. 4. Acoustic emission raw signal profiles when drilling uni-directional CFRP with carbide tool for drilling Condition IV

APPENDIX V – SURFACE ROUGHNESS VALUES MEASURED AT 0^0 INTERACTION ANGLE WHEN DRILLING UNI-DIRECTIONAL CFRP WITH CARBIDE DRILL

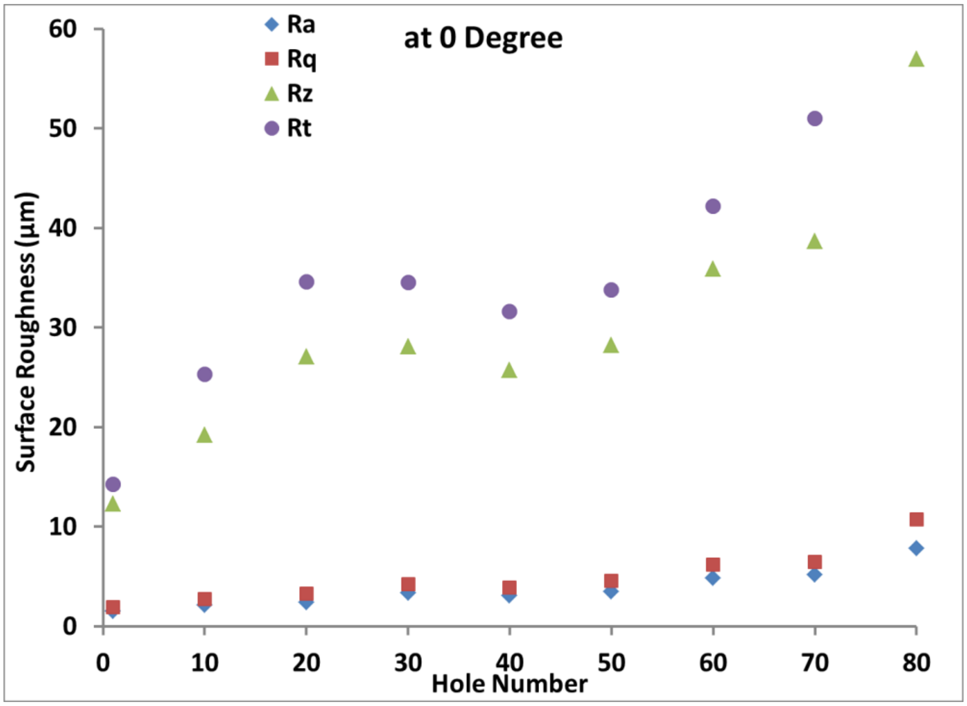

Figure V. 1. Surface roughness values measured at 0^0-interaction angle for drilling condition II

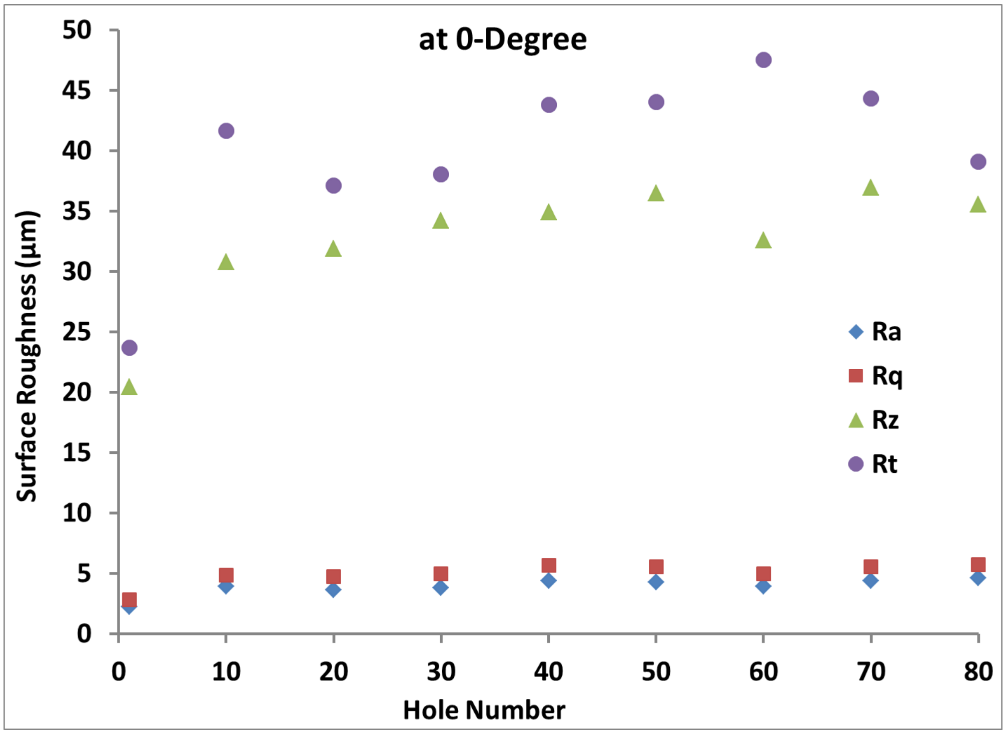

Figure V. 2. Surface roughness values measured at 0^0-interaction angle for drilling condition III

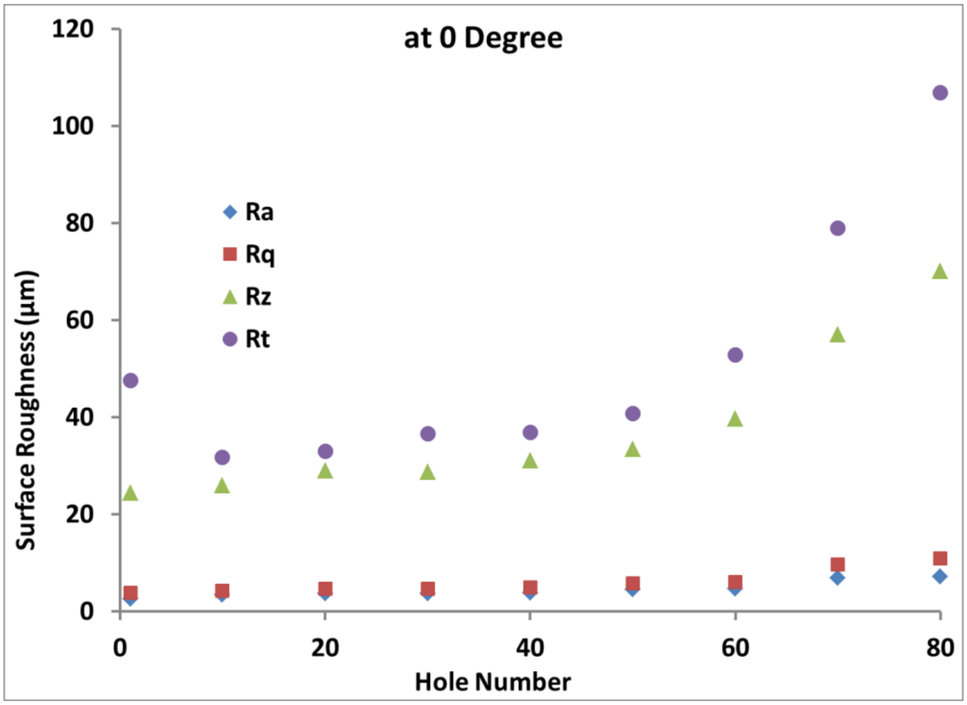

Figure V. 3. Surface roughness values measured at 0^0-interaction angle for drilling condition IV

APPENDIX W – SURFACE ROUGHNESS VALUES MEASURED AT 45^0 INTERACTION ANGLE WHEN DRILLING UNI-DIRECTIONAL CFRP WITH CARBIDE DRILL

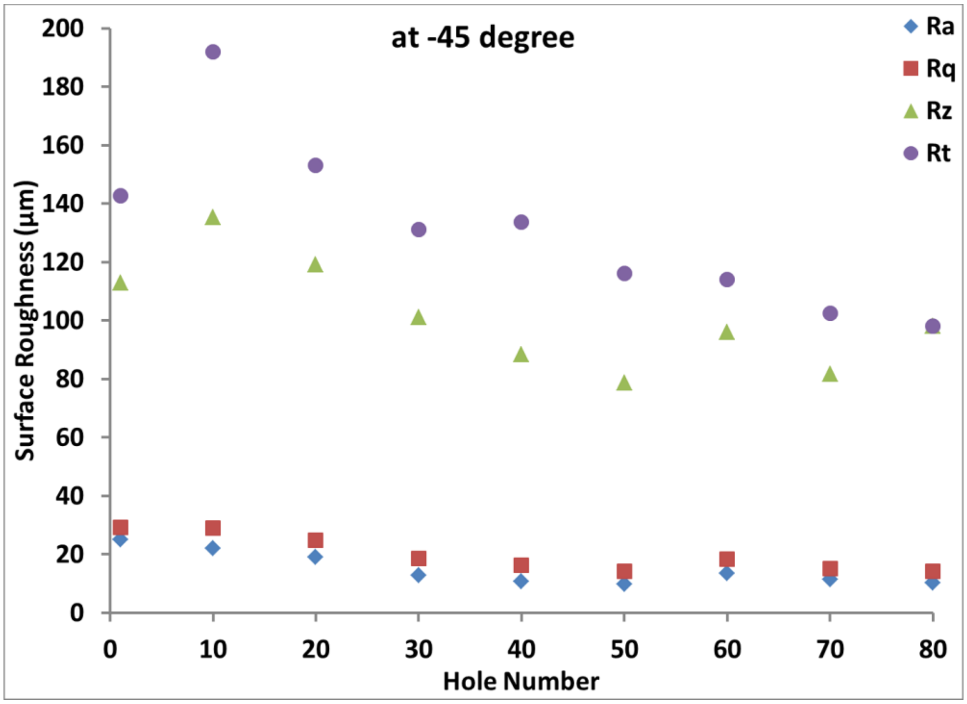

Figure W. 1. Surface roughness values at 45^0-interaction angle for drilling condition II

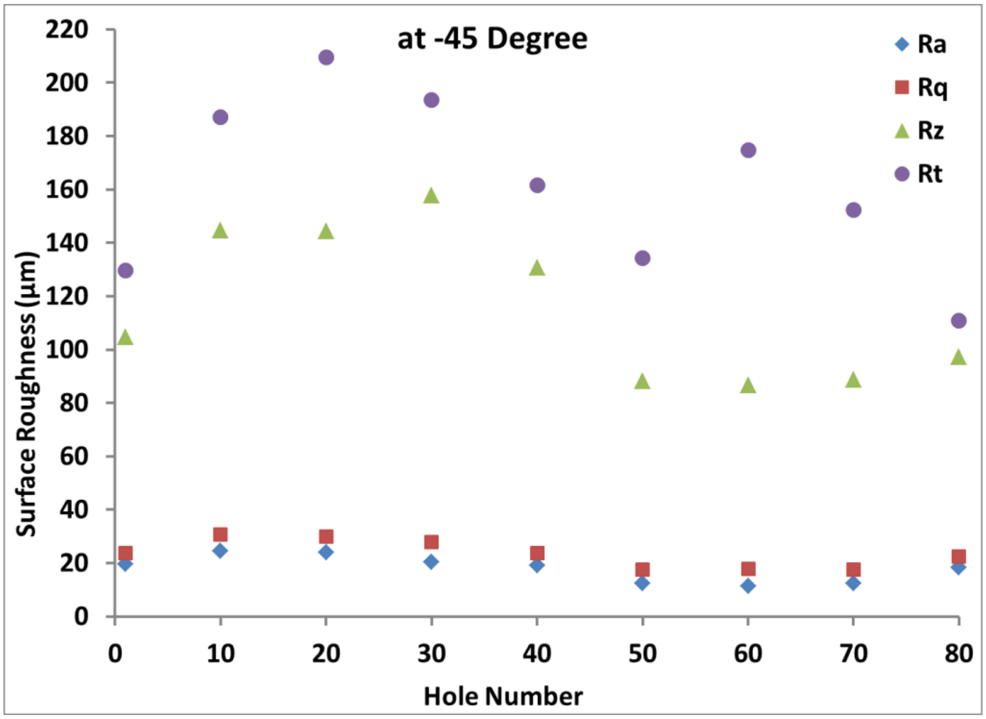

Figure W. 2. Surface roughness values at 45^0-interaction angle for drilling condition III

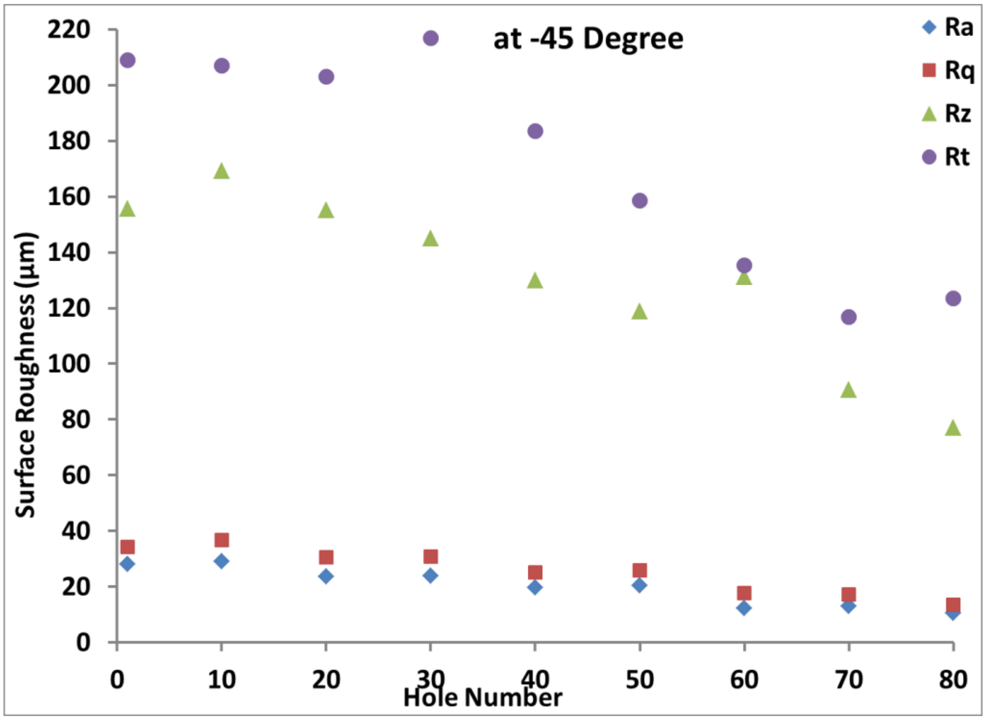

Figure W. 3. Surface roughness values at 45^0-interaction angle for drilling condition IV

APPENDIX X – OPTICAL IMAGE OF HOLE CIRCULARITY AT ENTRANCE WHEN DRILLING UNI-DIRECTIONAL CFRP WITH CARBIDE DRILL

Hole #	Optical Image	Circularity Error (mm)	Hole #	Optical Image	Circularity Error (mm)
10	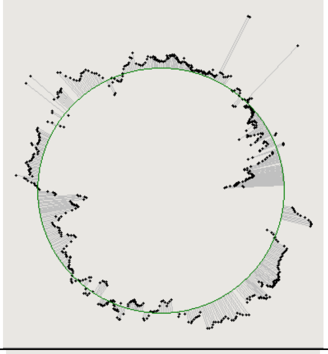	0.1717	50	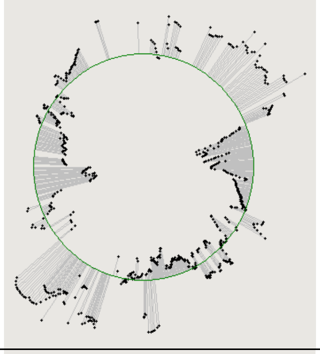	0.1964
20		0.1566	60	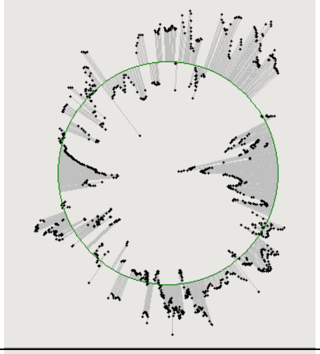	0.2452
30	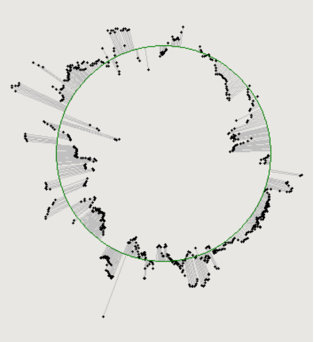	0.1859	70	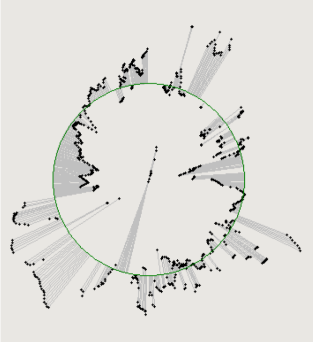	0.3281
40		0.1392	80	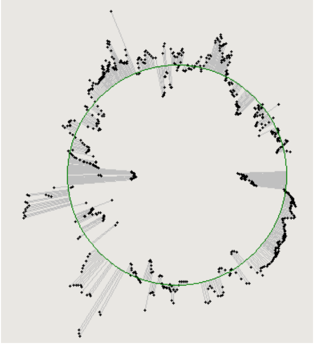	0.2084

Figure X. 1. Optical representation of runoff points of circularity error for drilling condition II

Hole #	Optical Image	Circularity Error (mm)	Hole #	Optical Image	Circularity Error (mm)
10		0.2323	50	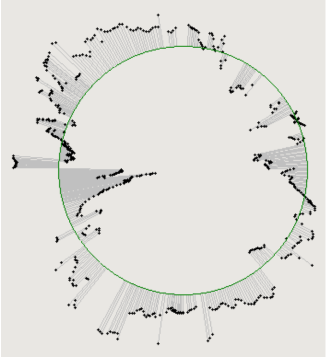	0.1928
20	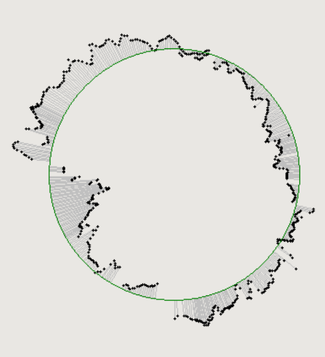	0.1205	60		0.2068
30	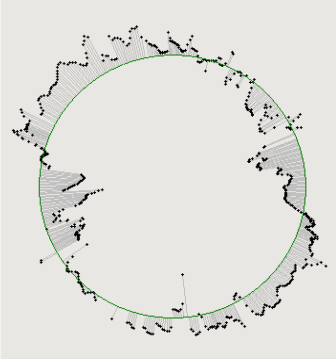	0.1237	70		0.1966
40	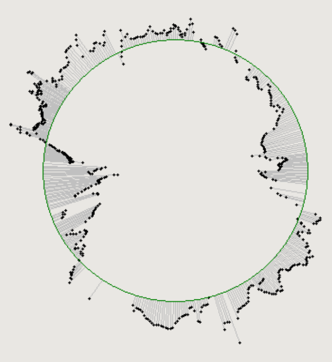	0.1502	80	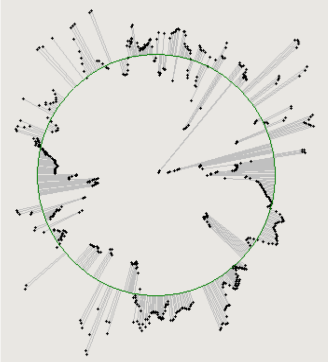	0.2511

Figure X. 2. Optical representation of runoff points of circularity error for drilling condition III

Hole #	Optical Image	Circularity Error (mm)	Hole #	Optical Image	Circularity Error (mm)
10	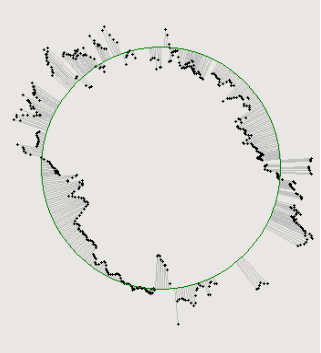	0.1136	50	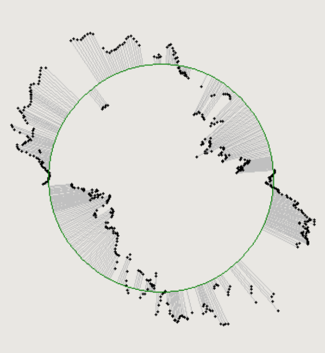	0.1843
20	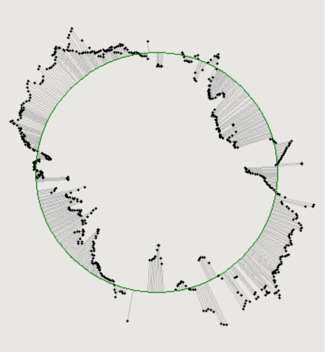	0.1339	60		0.2229
30		0.1625	70		0.2443
40	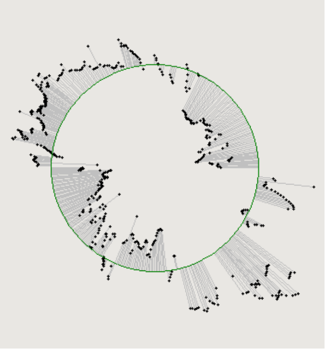	0.2219	80		0.2246

Figure X. 3. Optical representation of runoff points of circularity error for drilling condition IV

APPENDIX Y – SEM MICROGRAPHS OF DRILLED SURFACE FOR VARIOUS NUMBERS OF PLIES DRILLED

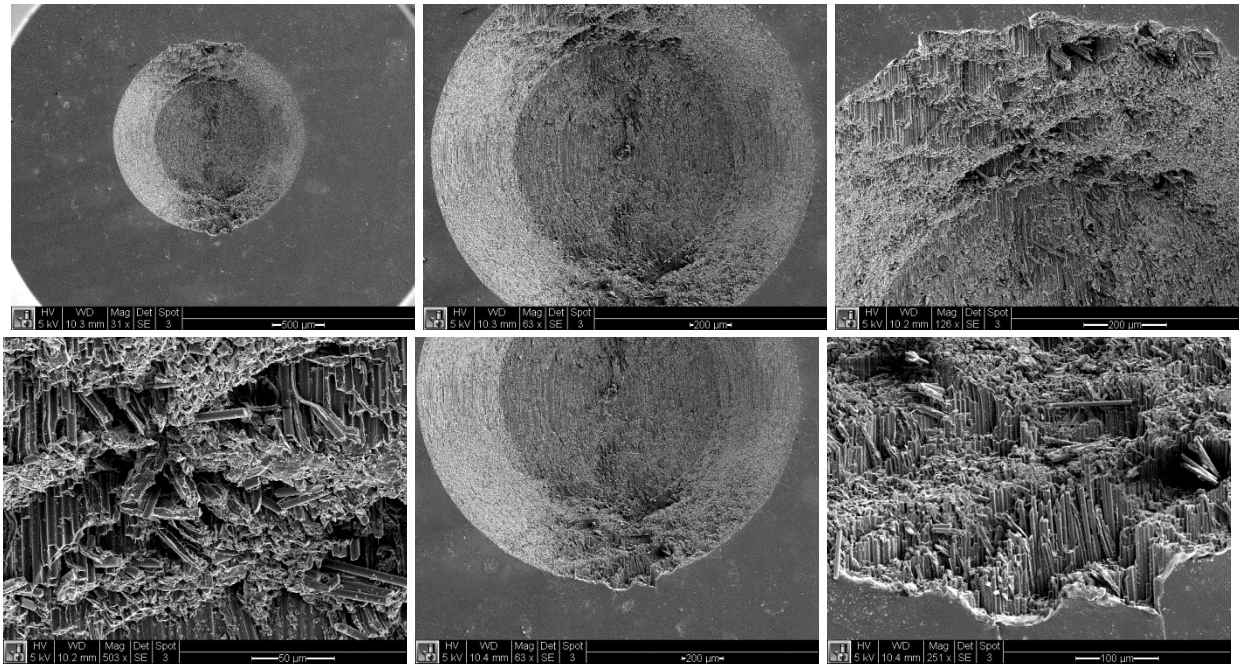

Figure Y. 1. SEM micrographs when two plies drilled

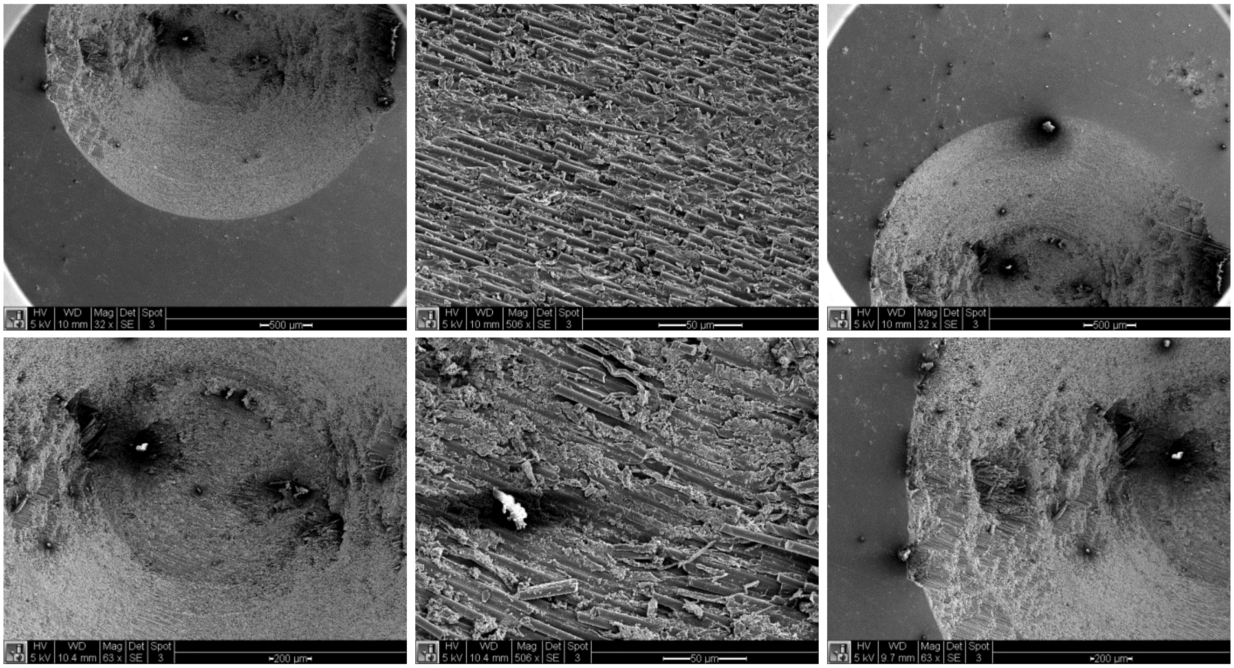

Figure Y. 2. SEM micrographs when four plies drilled

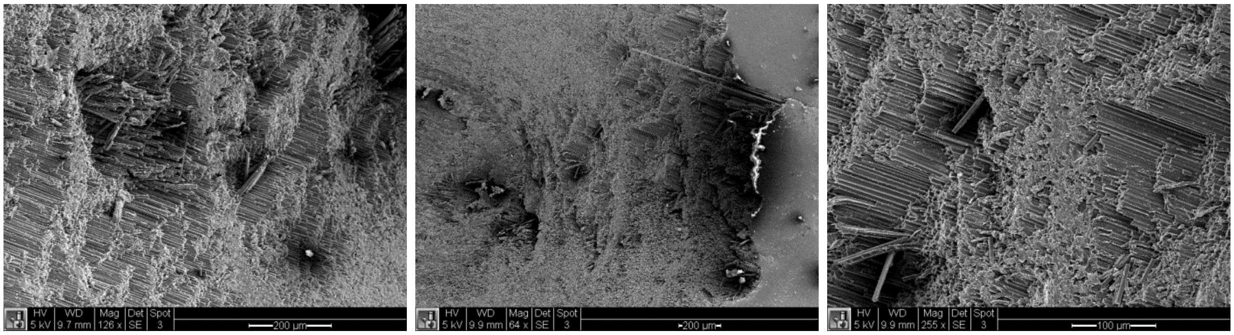

Figure Y. 2. Continued

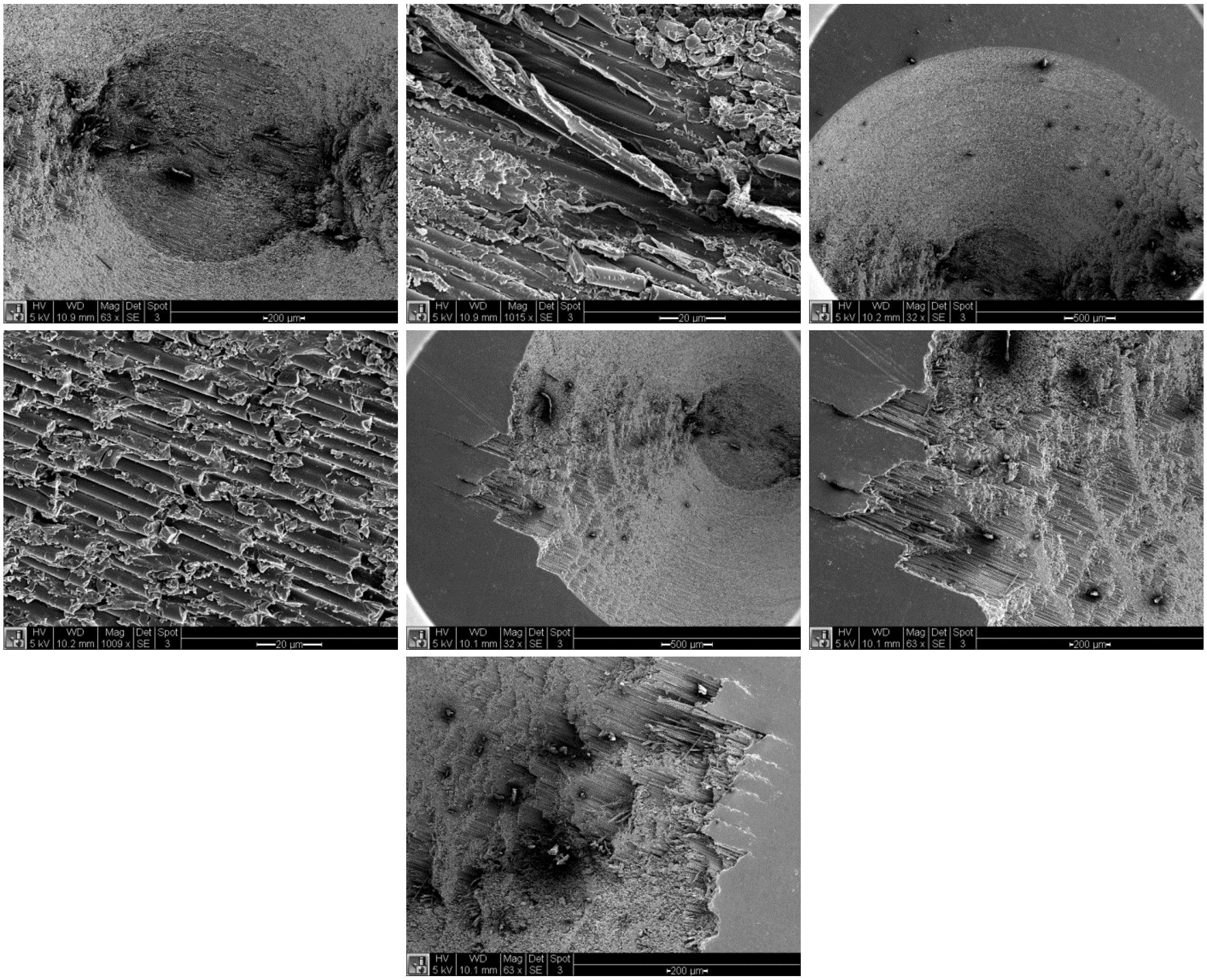

Figure Y. 3. SEM micrographs when six plies drilled

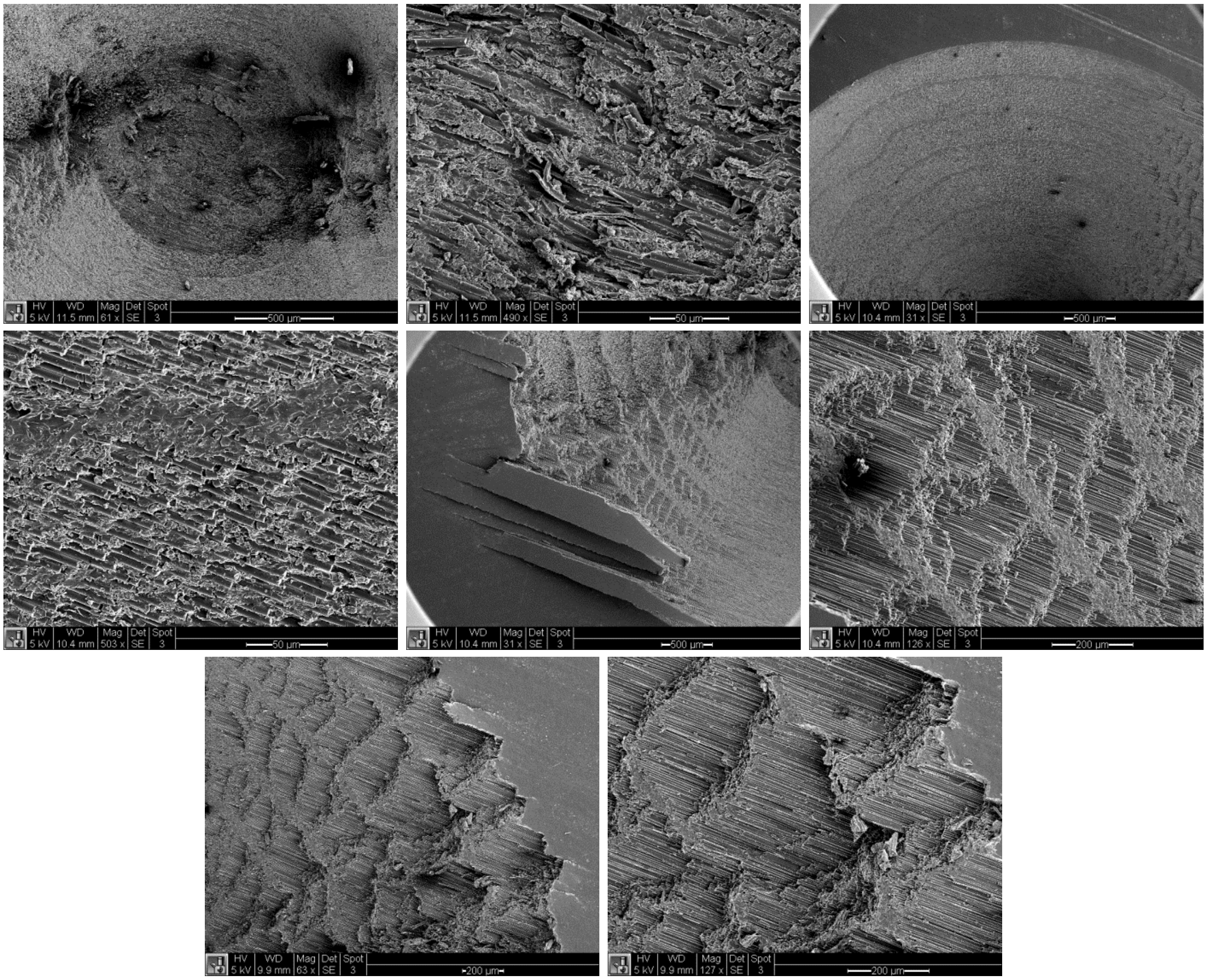

Figure Y. 4. SEM micrographs when eight plies drilled

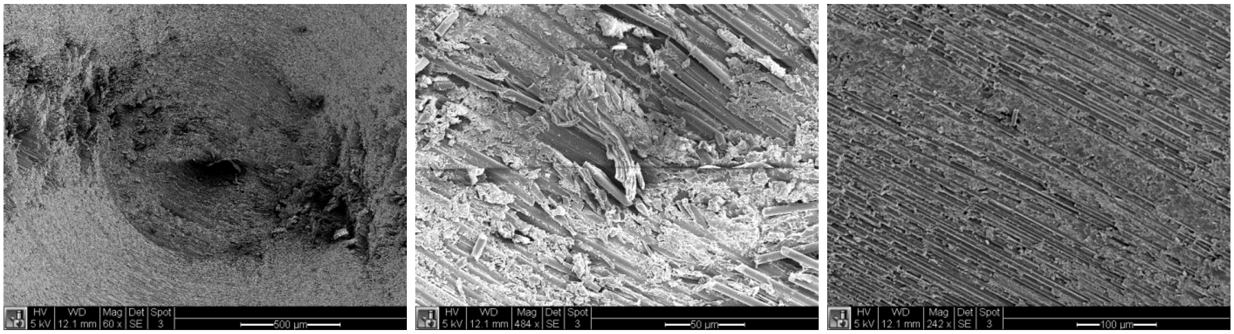

Figure Y. 5. SEM micrographs when ten plies drilled

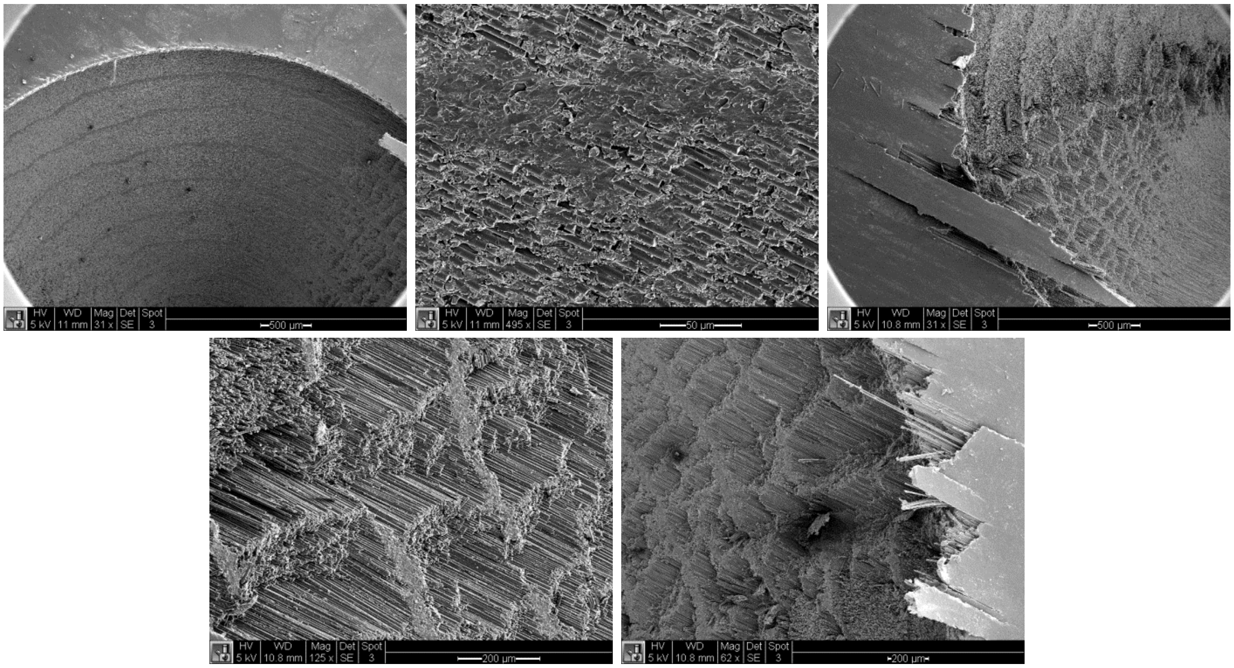

Figure Y. 5. Continued

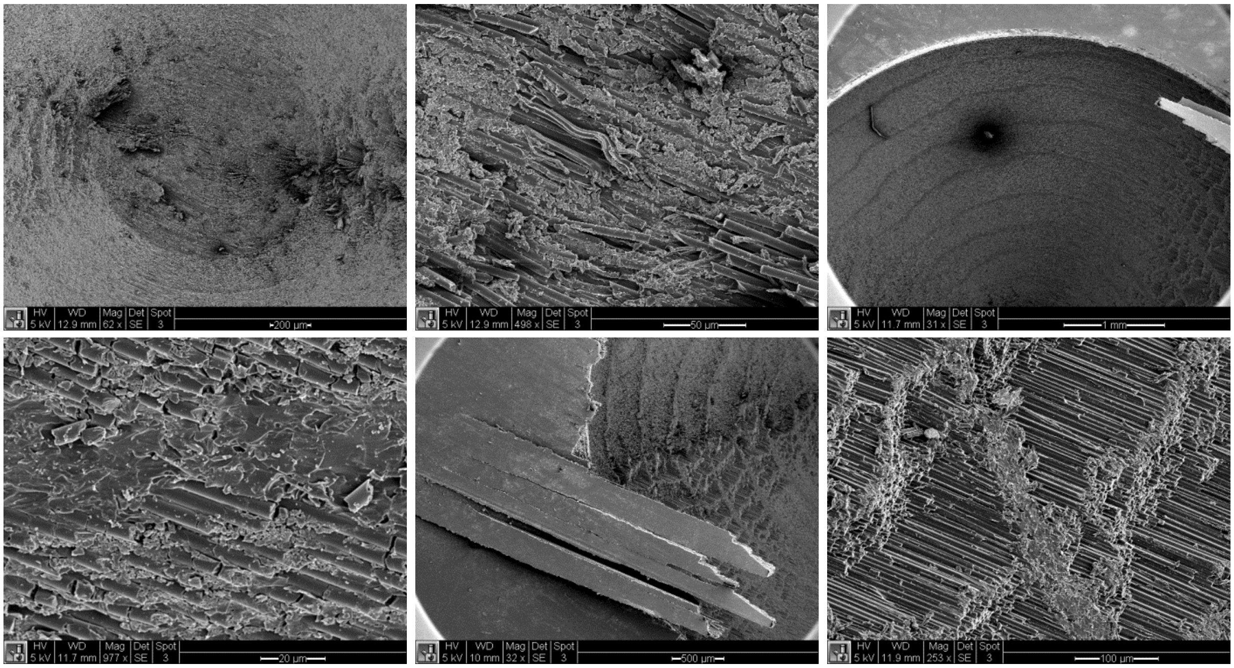

Figure Y. 6. SEM micrographs when twelve plies drilled

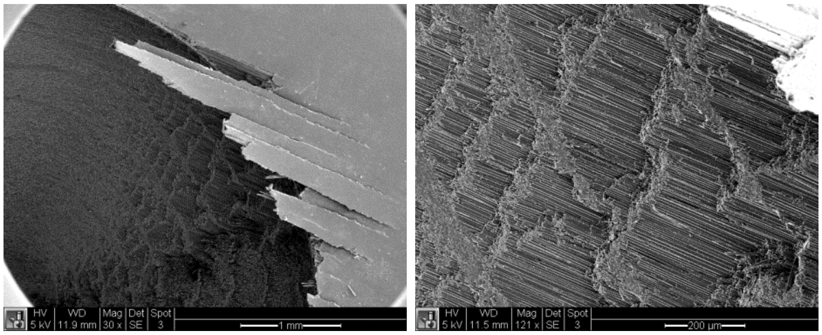

Figure Y. 6. Continued

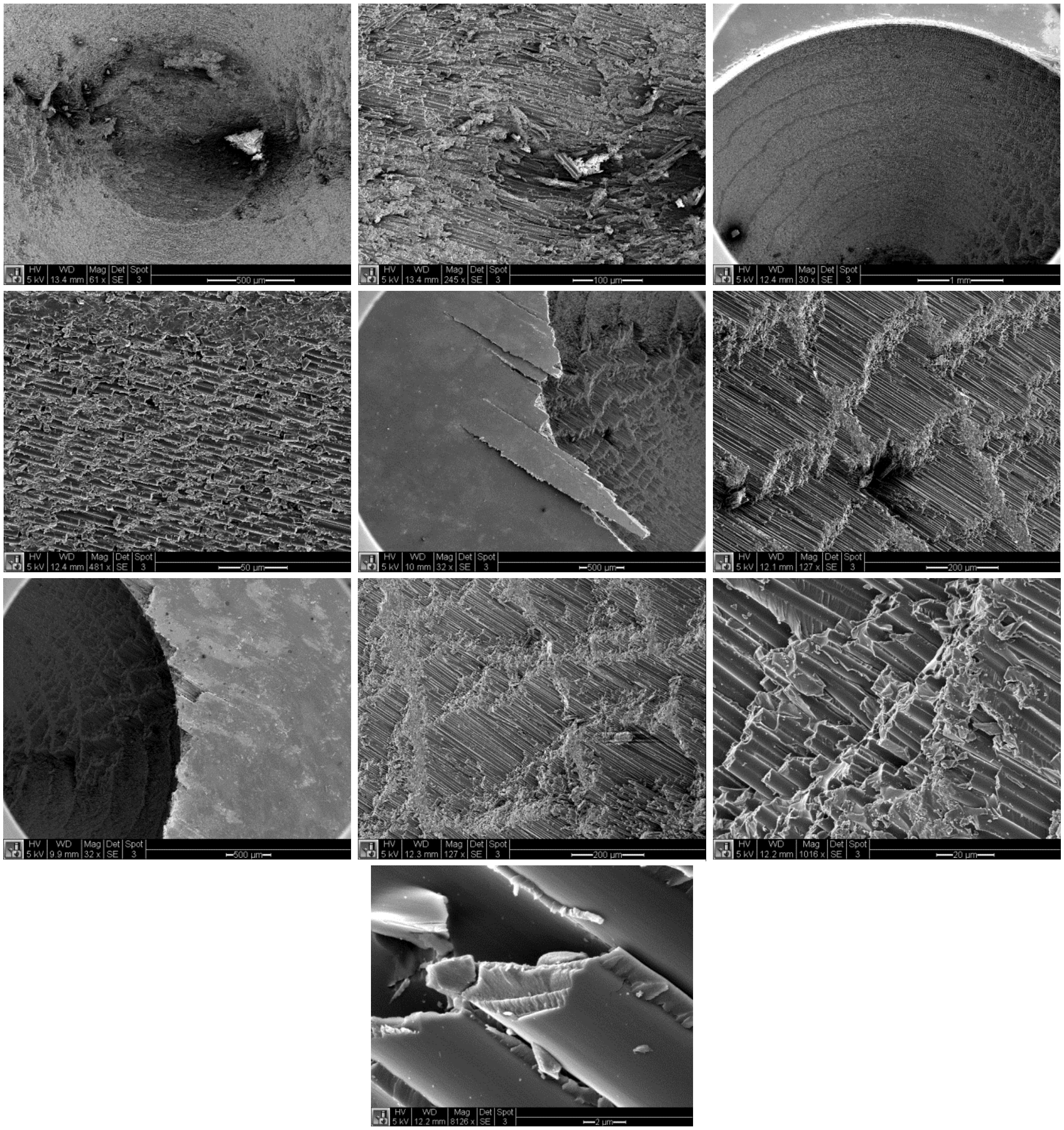

Figure Y. 7. SEM micrographs when fourteen plies drilled

APPENDIX Z – THRUST FORCE MODEL FOR DRILLING OF UNIDIRECTIONAL CFRP COMPOSITE USING A CARBIDE DRILL TOOL

A thrust force model for drilling of unidirectional CFRP composite using a carbide drill tool was developed by adopting and modifying a model developed by Langella et al. [72]. To capture the thrust force contribution of the chisel edge and the cutting edge experimentally, a pilot hole experiment was also conducted. The model is based on an assumption that orthogonal cutting takes place in an infinitesimal instant and acting over an elementary area on the cutting lip and each elementary force is integrated throughout the cutting lip length to calculate thrust force. This modified model and the pilot hole experiment were not included in the body of this dissertation, whereas, the original model by Langella et al. was discussed in chapter two.

The vertical and horizontal forces adopted from orthogonal cutting was given by the following expressions

$$F_{vu} = B \times 10^{-a\gamma} t^{.5} \left[{}^{N}\!/_{mm} \right] \qquad \text{(a)}$$

$$F_{hu} = A + B \times 10^{-b\gamma} t \left[{}^{N}\!/_{mm} \right] \qquad \text{(b)}$$

Coefficients a and b are given as 1.089

From the geometry of the drill cutting edge and chisel edge shown in Figure Z. 1, geometric relationships between the drill diameter, feed rate, and other drill geometries can be defined. A normalized radial coordinate ρ is defined, which is equal to the ratio of the radial distance of a cutting point from the axis of the tool measured on a plane perpendicular to the axis (r) to the nominal radius of the drill (R). The formulation of this model is mainly focused on the influence of the feed rate (f), point angels (ε), and the geometric relationship of the drill elements.

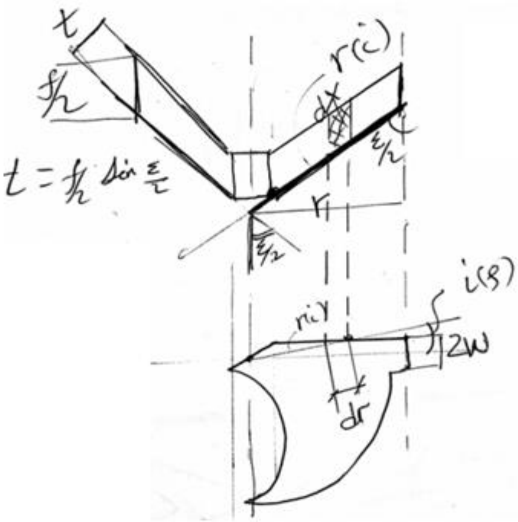

Figure Z. 1. Geometric relationship of chip load and cutting edge

$$dA = dx * \frac{f}{2} \tag{Z.1}$$

$$dx = dr * \cos(i(\rho)) \tag{Z.2}$$

$$\rho = \frac{r}{R} \rightarrow r = \rho * R \rightarrow dr = Rd\rho \tag{Z.3}$$

$$dx = cos(i(\rho))Rd\rho \tag{Z.4}$$

$$\sin\left(\frac{\varepsilon}{2}\right) = \frac{r}{r(i)} \qquad \text{and} \qquad r(i) = \frac{w}{sin(i(\rho))} \tag{Z.5}$$

$$w = \frac{r}{sin\left({}^{\varepsilon}/_{2}\right)} * sin(i(\rho)) \tag{Z.6}$$

$$i(\rho) = sin^{-1}\left[\frac{w}{\rho * R} * sin\left({}^{\varepsilon}/_{2}\right)\right] \tag{Z.7}$$

Knowing that $cos = \sqrt{1 - sin^2}$ we have

$$cos(i(\rho)) = 1 - \frac{w^2 sin^2(\varepsilon/2)}{2\rho^2 R^2} \tag{Z.8}$$

Where: *w* is half of the thickness of the chisel edge and *i (ρ)* is the inclination angle of the cutting lip for the tool considered.

The resultant tangential and vertical forces exerted on the cutting lip can be found by integrating over the cutting lip as shown in Equation 9.

$$F_v = \int_\tau^1 F_{vu} d_x \;= \int_\tau^1 [B \times 10^{-1.089*\gamma} t^{.5}]\, d_x \qquad \text{(Z.9)}$$

And since $t = \frac{f}{2} * sin(\varepsilon/2)$ and $dx = cos(i(\rho))Rd\rho$

$$F_v = \int_\tau^1 \left[(B \times 10^{-1.089\gamma}) \left(\frac{f}{2}\right)^{0.5} \left(sin(\varepsilon/2)\right)^{0.5} \left(1 - \frac{w^2 sin^2(\varepsilon/2)}{2\rho^2 R^2}\right) \right] Rd\rho \qquad \text{(Z.10)}$$

$$F_h = \int_\tau^1 F_{hu} dx \quad = \quad \int_\tau^1 [A + B \times 10^{-1.089\gamma}] dx$$

$$F_h = \int_\tau^1 \left[\left(A + B \times 10^{-1.089\gamma} \frac{f}{2}\right) \left(sin(\varepsilon/2)\right) \left(1 - \frac{w^2 sin^2(\varepsilon/2)}{2\rho^2 R^2}\right) \right] Rd\rho \qquad \text{(Z.11)}$$

The integration limit can be deduced from the Figure Z.2 shown below

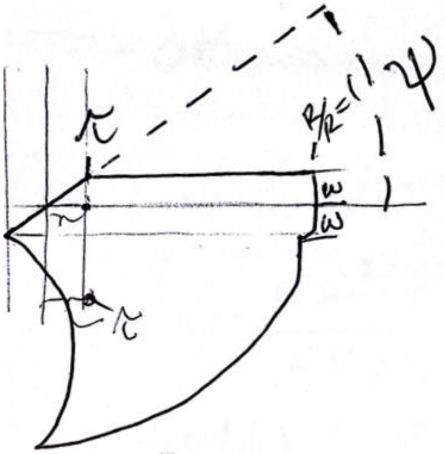

Figure Z. 2. Cutting edge end chisel edge of the drill

Inegration limits are based on the nondimentional coordinate $\rho = \frac{r}{R}$

So the upper limit is when r = R => $\frac{r}{R} = 1$

and the lower limit is => $\tau = \frac{w/\tan(\psi)}{R} = \frac{w}{R * \tan(\psi)}$ (Z.12)

The vertical force *Fv* shown on the Figure Z. 3 below can be resolved in to two components (Fr and Fa) which are perpendicular and parallel to the axis of the drill respectively.

- Fr is canceled by equivalent and opposite Fr generated by the other cutting lip
- Fa generates a resultant thrust force
- Multiplying Fh by the distance r from the drill axis gives the torque δM

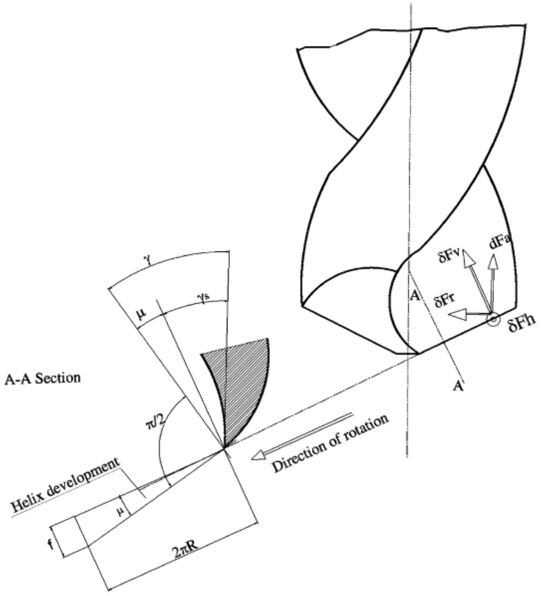

Figure Z. 3. The forces exerted on a main cutting lip and the drilling rake angle [72]

Therefore, from the figure we have

$$\delta F_a = \delta F_v sin\left({}^{\varepsilon}/_{2}\right) \qquad \text{(Z.13)}$$

$$\delta M = \delta F_h \times r = \delta F_h \times \rho R \qquad \text{(Z.14)}$$

Using equations Z.10, Z.11, Z.13, and Z.14 we have

$$T = \int_{\tau}^{1} \left[\left(B \times 10^{-1.089\gamma}\right) \left(\frac{f}{2}\right)^{0.5} \left(sin(\varepsilon/2)\right)^{3/2} \left(1 - \frac{w^2 sin^2(\varepsilon/2)}{2\rho^2 R^2}\right)\right] R d\rho \qquad \text{(Z.15)}$$

$$M = \int_{\tau}^{1} \left[\left(A + B \times 10^{-1.089\gamma} \frac{f}{2}\right) \left(sin(\varepsilon/2)\right) \left(1 - \frac{w^2 sin^2(\varepsilon/2)}{2\rho^2 R^2}\right)\right] \rho R^2 d\rho \qquad \text{(Z.16)}$$

Actual rake angle is given as a sum of static rake (γ_s) and dynamic rake (μ) as shown in the above figure and based on this an average value of the rake angle γ_m is given as shown below

$$\gamma_m = \frac{\int_{\tau}^{1} \left[tan^{-1}\left(\frac{\rho \tan(\theta)}{sin(\varepsilon/2)}\right) + tan^{-1}\left(\frac{f}{2\pi\rho R}\right)\right] d\rho}{\int_{\tau}^{1} d\rho} \qquad \text{(Z.17)}$$

And the new adjusted thrust force and torque are:

$$T' = \left(B \times 10^{-1.089\gamma}\right) \left(\frac{f}{2}\right)^{0.5} G' \ \ [N] \qquad \text{(Z.18)}$$

$$M' = \left(A + B \times 10^{-1.089\gamma} \frac{f}{2}\right) G \qquad \text{(Z.19)}$$

Here the value G and G' refers to the integrals in equations (15) and (16)

$$G = \int_{\tau}^{1} \left[\left(sin(\varepsilon/2) \right) \left(1 - \frac{w^2 sin^2(\varepsilon/2)}{2\rho^2 R^2} \right) \right] \rho R^2 d\rho$$

$$G = \frac{Sin(^{\varepsilon}/_{2})[(1-\tau^2)R^2 + w^2 sin^2(^{\varepsilon}/_{2}) \ln \tau]}{2} \qquad \text{(Z.20)}$$

$$G' = \int_{\tau}^{1} \left[\left(sin(\varepsilon/2) \right)^{3/2} \left(1 - \frac{w^2 sin^2(\varepsilon/2)}{2\rho^2 R^2} \right) \right] R d\rho$$

$$G' = \frac{\left(sin(\varepsilon/2) \right)^{3/2} (1-\tau) \left(2R^2\tau - \left(sin(\varepsilon/2) \right)^2 w^2 \right)}{2\tau R} \qquad \text{(Z.21)}$$

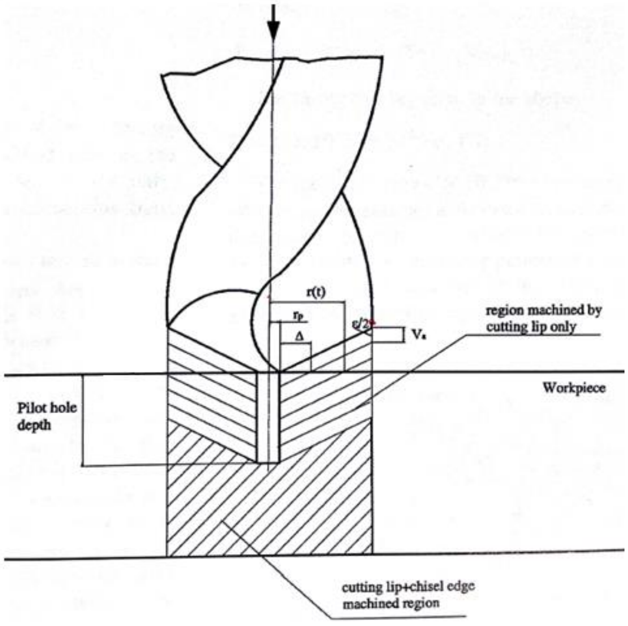

Figure Z. 4. Workpiece section with pilot hole and region machined differently [72]

Using the pilot hole the variation of thrust force and torque along the cutting lip without the chisel edge contribution can be determined based on Figure Z. 4. Here the integration limit varies with time.

Let $r_u(t)$ and $r_l(t)$ be the upper limit and the lower limit respectively at any given instant time, the thrust force and torque at the cutting lip becomes

$$T = \left(B \times 10^{-1.089\gamma}\right)\left(\frac{f}{2}\right)^{0.5} \int_{r_l(t)/R}^{r_u(t)/R} \left[\left(sin(\varepsilon/2)\right)^{3/2}\left(1 - \frac{w^2 sin^2(\varepsilon/2)}{2\rho^2 R^2}\right)\right] R d\rho \quad \text{(Z.22)}$$

$$M = \left(A + B \times 10^{-1.089\gamma}\frac{f}{2}\right) \int_{r_l(t)/R}^{r_u(t)/R} \left[\left(sin(\varepsilon/2)\right)\left(1 - \frac{w^2 sin^2(\varepsilon/2)}{2\rho^2 R^2}\right)\right] \rho R^2 d\rho \quad \text{(Z.23)}$$

The two integration limits can be calculated from material thickness, tool geometry, and the relation given by Figure Z. 4.

Let r_p be the radius of pilot hole, t_h be thickness of the material, L_h be length of cutting lip measured parallel to the drill axis, and t be the drilling time, based on this, the following relation can be constructed.

$$V_a = f * v \quad [^{mm}/_{s}] \qquad \text{(Z.24)}$$

$$\Delta(t) = t * V_a tan\left(^{\varepsilon}/_{2}\right) \qquad \text{(Z.25)}$$

$$L_h = \frac{R - r_p}{tan\left(^{\varepsilon}/_{2}\right)} \qquad \text{(Z.26)}$$

Using the above Figure Z. 4 and Equations (Z.24 – Z.26), the integration limits are expressed as

$$r_u(t) = \begin{cases} r_p + \Delta, & t * V_a \le L_h \\ R, & t * V_a \ge L_h \end{cases} \qquad \text{(Z.27)}$$

$$r_l(t) = \begin{cases} r_p, & t * V_a \le t_h \\ r_p + (t * V_a - t_h) tan\left(^{\varepsilon}/_{2}\right), & t_h \le t * V_a \le t_h + L_h \\ R, & t * V_a \ge t_h + L_h \end{cases} \qquad \text{(Z.28)}$$

The constants A and B from equation (a) and (b) are related to the specific cutting energies as follows

$$B \times 10^{-1.089\gamma} = K_n \qquad \left[^{N}/_{mm^2}\right] \qquad \text{(Z.29)}$$

$$\frac{A}{^{f}/_{2}} + B \times 10^{-1.089\gamma} = K_t \qquad \left[^{N}/_{mm^2}\right] \qquad \text{(Z.30)}$$

The following relations were suggested to derive the specific cutting energies from experimental results

$$K_n = \frac{T_{exp}}{2\left({}^{f}/_{2}\right)^{0.5} G'} \qquad \left[{}^{N}/_{mm^2}\right] \tag{Z.31}$$

$$K_t = \frac{M_{exp}}{2\left({}^{f}/_{2}\right) G} \qquad \left[{}^{N}/_{mm^2}\right] \tag{Z.32}$$

In order to capture the thrust force by the cutting edge only without the contribution of the chisel edge, a pilot hole experiment was conducted. Using cobalt HSS drill with diameter equal to 1.17 mm, which is the width (length) of the chisel edge, a pilot hole was drilled on unidirectional CFRP at a feed rate of 200 µm/rev and with a cutting speed of 3000 and 6000 rpm. The thrust force profiles for the pilot hole, for the cutting edge (with pilot hole), and for the hole drilled without a pilot hole are given in Figure Z. 5 – Z. 7.

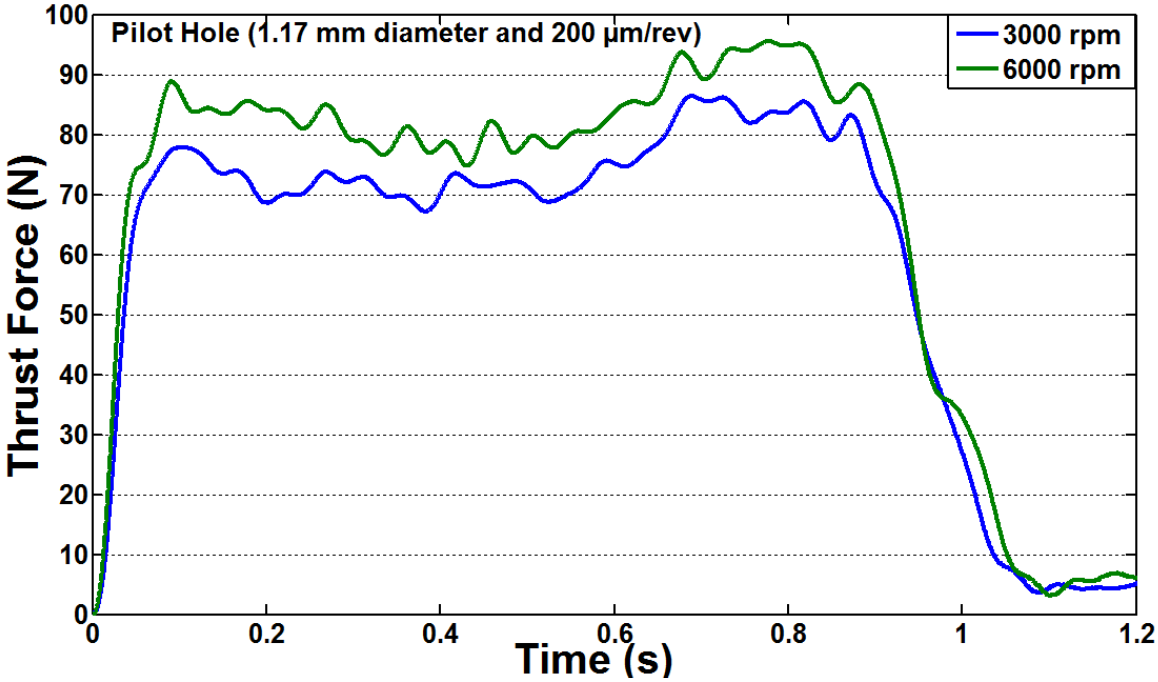

Figure Z. 5. Thrust force profile of the pilot hole

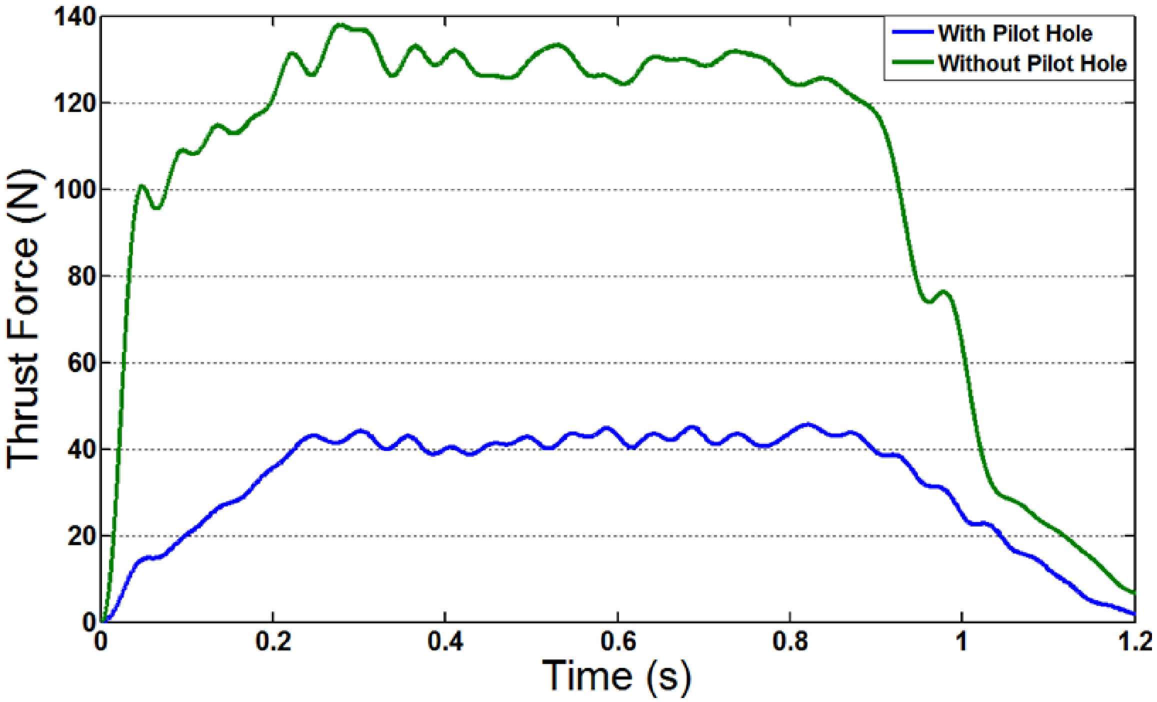

Figure Z. 6. Thrust force profiles at 3000 rpm for with and without a pilot hole

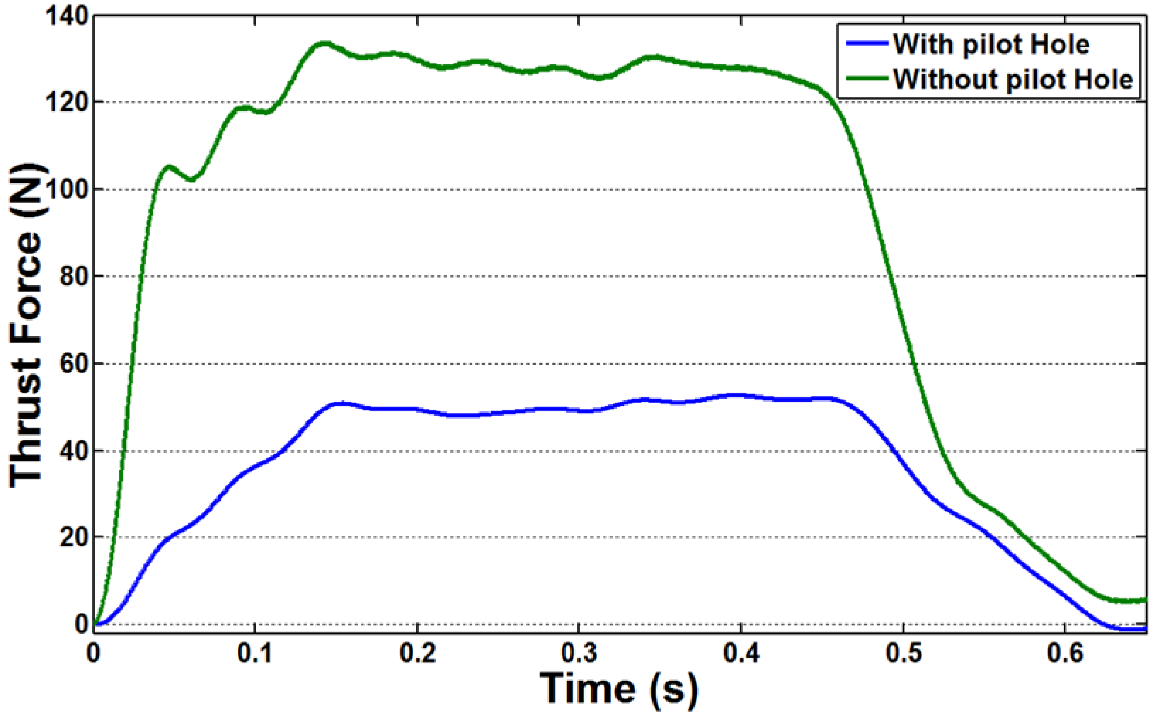

Figure Z. 7. Thrust force profiles at 6000 rpm for with and without a pilot hole

As it can be seen form Figure Z. 6 and Z. 7, the magnitude the thrust force caused by the cutting edge is almost one third of the total thrust force magnitude. In all cases of drilling conditions, the chisel edge contributes almost 62 % of the total thrust force. Using the experimental value of the thrust force of the cutting edge, which is the thrust force acquired when drilling with a pilot hole, the specific energy of Equation (Z.31) was calculated. Once the value of the specific cutting energy is found, prediction of the thrust force for the cutting edge was made using Equation (Z.22) and the integration limits given by Equation (Z.27 and Z.28). Cutting edge thrust force values measured experimentally and predicted by the force model is shown in Figure Z.8. As it can be seen from the figure, the predicated value agrees well with the experimental result except the observed time delay or difference. The maximum value of the thrust force, the gradient at drill entrance, and the gradient at the drill exit agreed with the experimental result very well. After the prediction of the cutting edge thrust force value, we can easily get the total drilling thrust force value by multiplying the cutting edge force value by 5/2, since we know the contribution of the cutting edge to the total drilling thrust force is only 40 %.

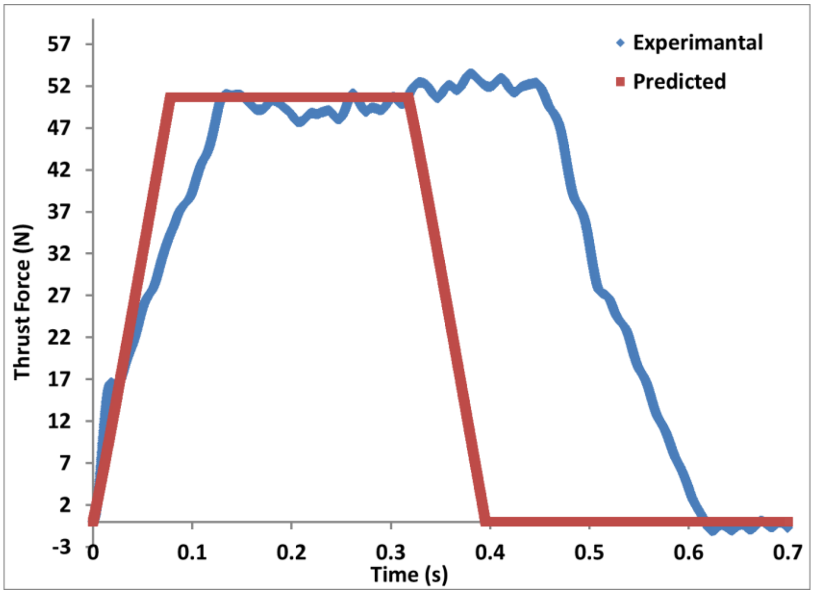

Figure Z. 8. Measured and predicted values of thrust force for cutting edge

APPENDIX AA – MATLAB CODES

AA. 1 HILBERT ENVELOPE – FOR ACCELEROMETER SIGNAL

```
function accEnv1( fileName )

%Import desired text file
importfile( fileName );

%time axis
time = data( :, 1 );

%torque
Fz = data( :, 2 );

%Hilbert envelope
FzEnvelope = hilbertEnv( Fz );

plot( time, FzEnvelope );

 end

function importfile(fileToRead1)
%IMPORTFILE(FILETOREAD1)
%  Imports data from the specified file
%  FILETOREAD1:  file to read

%  Auto-generated by MATLAB on 10-May-2011 14:46:15

DELIMITER = '\t';
HEADERLINES = 22;

% Import the file
newData1 = importdata(fileToRead1, DELIMITER, HEADERLINES);

% Create new variables in the base workspace from those fields.
vars = fieldnames(newData1);
for i = 1:length(vars)
    assignin('caller', vars{i}, newData1.(vars{i}));
end

end

function xEnv = hilbertEnv( x )
    xEnv = abs( x ).^2;
end
```

AA. 2 HILBERT ENVELOPE – FOR MICROPHONE SIGNAL

```
function micEnv( fileName )

%Import desired text file
importfile(fileName );

%time axis
time = data( :, 1 );

%torque
m = data( :, 5 );

%Hilbert envelope
mEnvelope = hilbertEnv( m );

plot( time, mEnvelope );

end

function importfile(fileToRead1)
%IMPORTFILE(FILETOREAD1)
%  Imports data from the specified file
%  FILETOREAD1:  file to read

%  Auto-generated by MATLAB on 10-May-2011 14:46:15

DELIMITER = '\t';
HEADERLINES = 22;

% Import the file
newData1 = importdata(fileToRead1, DELIMITER, HEADERLINES);

% Create new variables in the base workspace from those fields.
vars = fieldnames(newData1);
for i = 1:length(vars)
    assignin('caller', vars{i}, newData1.(vars{i}));
end

end

function xEnv = hilbertEnv( x )
    xEnv = abs( x ).^2;
end
```

AA. 3 HILBERT ENVELOPE – FOR ACOUSTIC EMISSION SIGNAL

```
function AeEnv( fileName )

%Import desired text file
importfile(fileName );

%time axis
time = data( :, 2 );

%torque
m = data( :, 3 );

%Hilbert envelope
mEnvelope = hilbertEnv( m );

plot( time, mEnvelope );
 end
 function importfile(fileToRead1)
%IMPORTFILE(FILETOREAD1)
%  Imports data from the specified file
%  FILETOREAD1:  file to read

DELIMITER = '\t';
HEADERLINES = 50;

% Import the file
newData1 = importdata(fileToRead1, DELIMITER, HEADERLINES);

% Create new variables in the base workspace from those fields.
vars = fieldnames(newData1);
for i = 1:length(vars)
    assignin('caller', vars{i}, newData1.(vars{i}));
end

end

function xEnv = hilbertEnv( x )
    xEnv = abs( x ).^2;
end
```

AA. 4 FILTER FOR SIGNAL AMPLITUDE

```
% x is the signal to be filtered
% fc if teh filtering frequency
%fs is the sampling frequency of teh signal to be filtered

function [ xsmooth ] = smoothDyno( x, fc, fs )

hn = designfilter( [0 fc /(fs / 2) ], 'pass' );
xsmooth = narrowbandfilter( x, hn );

end
```

AA. 5 DEMEAN SPECTROGRAM

```
function op = demeanSpect(sig,w,noverlap,nfft,fs)

win = hamming(w);
sig = sig(:);
win = win(:);
nwind = length(win);
nsig = length(sig);
ncol = fix((nsig-noverlap)/(nwind-noverlap));

% Pre-process X
colindex = 1 + (0:(ncol-1))*(nwind-noverlap);
rowindex = (1:nwind)';
sigin = zeros(nwind,ncol);

sig = detrend(sig);
% filter out the very low frequencies, incl. DC in filtMicHenvSq
fOrder = 3000;
fCutoff = 25; % Hz
h = fir1(fOrder, fCutoff / (fs/2), 'high');
sig = (filter(h, 1, sig));

% Put x into columns of xin with the proper offset
sigin(:) = sig(rowindex(:,ones(1,ncol))+colindex(ones(nwind,1),:)-1);

% demean
for cnt = 1 : ncol
%     sigin(:,cnt) = detrend(sigin(:,cnt));
    sigin(:,cnt) = sigin(:,cnt) - mean(sigin(:,cnt));
end

% Apply the window to the array of offset signal segments.
sigin = win(:,ones(1,ncol)).*sigin;

% demean again ???
% for cnt = 1 : ncol
% %     sigin(:,cnt) = detrend(sigin(:,cnt));
%     sigin(:,cnt) = sigin(:,cnt) - mean(sigin(:,cnt));
% end

op = fft(sigin,nfft);
op = op(1:nfft/2+1,:);
```